MONASH University

INVESTIGATION OF BOND STRENGTH OF SMA BARS IN CONCRETE UNDER HIGH TEMPERATURE

Parag T. Moon
BE Civil, M Tech in Structural Engineering

A thesis submitted for the degree of
Doctor of Philosophy
at
Monash University in 2020
Department of Civil Engineering

Abstract

Concrete is a very strong material in compression and the steel reinforcement in tension. The bonding between them is vital for structural strength and serviceability. The strength is reflective of bond stress between concrete and the steel reinforcement when subjected to loading. Whenever external load is applied on concrete, reinforcing bar receives a part of the load through load transfer mechanism from concrete to steel. When tensile force is applied to the rebar, it develops stresses that are both tangential and normal to the contact surface. The stress parallel to bar is termed bond stress. Interaction between concrete and reinforcing bar is due to chemical adhesion, friction, mechanical interlock and shear along the cylindrical concrete surface between adjacent ribs. The first two properties contribute more in the case of plain rebar. For deformed rebar, the surface roughness and closely spaced ribs produce great interlocking with bearing against the key formed between concrete and ribs. For a given concrete grade, pull-out strength is related to bond stress between concrete and the rebar. In the pull-out tests, the force at the interface can be represented by;

1) A force component that is parallel to rebar (which is responsible for the breakdown of adhesion and frictional resistance that leads to pull-out failure)

2) The perpendicular component which creates circumferential or radial stress (which lead to splitting type of failure)

Such failures get exacerbated in events such as fire in building where steel is used as reinforcement in the concrete. Significant scrutiny on the failure mechanisms of concrete and rebars using both physical tests (pull-out tests) and numerical modelling techniques using commercially available software such as ANSYS can be found in the literature. These studies primarily focus on failure mechanisms at standard room temperature conditions and assisting in the design of reinforced structural elements to address such conditions. However, there is plenty of evidence in the literature that suggest the loss of both life and property due to events such as fire. The loss of property can primarily be attributed to the failure of structural elements in the buildings affected by fire events and as an extension the loss of valuable lives too. The

development of modern materials such as smart materials may provide a means to addressing the above-mentioned problem.

In this study, smart materials (SMAs) are investigated for their ability to gain strength at elevated temperatures (such as event of fire). While steel rebars lose strength at higher temperatures, SMAs can be trained to gain strength at such high temperatures. This novel thought of using SMA reinforcement alongside traditional steel reinforcement in concrete is new to literature. In doing so, the advantages of steel rebars and SMA can be exploited under normal conditions and at higher temperatures respectively. Since steel rebars have been in existence for many decades they were subjected to in depth scrutiny in the literature. The method of strength testing steel-reinforced concrete under standard conditions (both experimentally and numerically) is well defined in the literature. However, there is only minimal data to model the effects of fire on the steel rebar-concrete bond stress and more so on SMA rebars and concrete.

Therefore, physical experiments were conducted as a part of this thesis to generate the required data sets on the bond stress between 1) Steel Rebar-Concrete and 2) SMA-Concrete specimens not only at room temperature but in various conditions of fire. In all, 24 specimens were tested (12 each for Steel and SMA) for different rebar embedded lengths (150mm and 300mm) and for different fire exposure time periods (no fire, 30 and 60 minutes fire exposure). The methodology for physical experiments was developed based on established processes and methods found in the literature (for example pull-out test). Differential scanning calorimeter DSC 8500 was used to measure the transformation temperatures of SMA NiTi alloy (Nickel Titanium) samples extracted from the SMA rebars. It was essential to understand the maximum heat treatment temperature since the SMA material loses its memory retaining ability beyond this temperature. The due execution of physical experiments on several concrete specimens resulted in the generation of the bond stress and slip data for use in numerical studies, thereby achieving the first aim of this thesis.

Such data sets from the physical experiments was drawn upon as inputs to define the parameters of the CZM bilinear model required for defining the material characteristics

of the interface in the structural analysis. Data derived and observations made from such experimentation builds on the existing knowledge in the literature. More importantly, such data sets were employed in examining the interface of the specimens (concrete and SMA/steel rebar) that were subjected to conditions of fire and structural loading using numerical methodology that was adopted (from literature) and improvised in this work.

The novel numerical method developed in this work employs a cohesive zone modelling (CZM) technique that combines both thermal and structural effects and hence allowed for the examination of the interface bond stress for the first time taking into account both the conditions of fire and structural loading. Physical experiments were duplicated in the numerical methods to study the discrepancies and to validate the novel numerical method developed in this work. Such numerical studies duplicated the geometry, conditions of fire, rebar embedded (insert) length, rebar material etc. The bond stress values from both numerical and physical experiments were compared and found to be in tight agreement thereby validating the novel numerical method developed and thus achieving the second aim of this work.

The results of both physical and numerical experiments are presented in Chapter 5; wherein they are compared and comprehensively analysed for accuracy and agreement. It was established that the numerical model and methodology developed in this work predicted the bond stress values between SMA-Concrete and Steel-Concrete with a good accuracy against corresponding values from physical experiments for all of the specimen cases that were considered. The accuracy was in the range of (2% to 12%). In developing such a numerical model that predicts the bond stress between SMA rebar and concrete for various conditions as mentioned earlier (including that of fire exposure), a novel non-destructive method is confirmed to have been developed.

In the process of validating the results of both the physical and numerical experiments, various observations were made. Equipped with the new non-destructive, cost effective and time saving numerical modelling tool this study set out to test the influence of several other parameters on the bond stress at the interface. The

parameters considered were various bar diameters, concrete grade, embedded length of rebar, material of rebar, sand coated SMA and different fire conditions. On identifying the key parameters, regression analysis was carried out to develop a new empirical formula that will allow for quick assessment of the bond stresses at the interface that holistically takes into account the influence of thermal and structural loading on a given reinforced concrete specimen. Such a formula will come handy to design engineers in performing quick assessment of the bond stress in an SMA reinforced concrete structural element. Development of such a formula achieves the third and final aim of this thesis.

Summary of significant contributions

A novel numerical model is developed in this work to examine the bond stress behaviour between both steel and SMA reinforced concrete specimens. The model takes into account the effect of fire and the duration of fire on the rebars and allows the user to model and predict the strength of structural members in such scenarios. The observations made in this work can potentially give rise to the use of SMA rebars alongside steel rebars in reinforced concrete design. Such a novel approach is expected to enhance and build on the existing knowledge on the passive mechanism of addressing fire related issues and structural failures. The significant contributions of this study can be summarised into the following points:

- A data set is produced from physical experiments that establishes specific values for bond stress at the interface of SMA reinforcement and concrete that is subjected to fire over a period of 60 minutes;
- A new numerical method is developed for examining and evaluating the bond stress at the interface in reinforced concrete that takes into account the influence of thermal and structural loading;
- An empirical formula is developed for quick assessment of bond stress between SMA and concrete in conditions ranging from room temperature to conditions that prevail during a fire event in a building;

- A method of strengthening concrete is proposed that utilises both steel and SMA rebars in concrete, potentially could save properties and lives; and
- The developed methods and proposed techniques assist greatly in improving the fire rating of buildings.

Declaration by author

This thesis is composed of my original work, and contains no material previously published or written by another person except where due references have been made in the text. I have clearly stated the contribution by others to jointly-authored works that I have included in my thesis.

I have clearly stated the contribution of others to my thesis as a whole, including data analysis, significant technical procedures, professional editorial advice, and any other original research work used or reported in my thesis. The content of my thesis is the result of work I have carried out since the commencement of my research higher degree candidature.

This work has not previously been submitted for a degree or diploma in any university. To the best of my knowledge and belief, the thesis contains no material previously published or written by another person except where due references are made in the thesis itself.

Signature: ……

Print Name: Parag T Moon.

Date: ……10 May 2020…….

Publications during candidature

Under Publication

Moon, P. T., Wong, B. M., Heidarpour, A., and Bhamare, R. (2020) “Investigation of bond strength of SMA bars in concrete under high temperature” Modern Methods and Advances in Structural Engineering and Construction, International Structural Engineering and Construction Society (ISEC-SEC 5)

Moon, P. T., Wong, B. M., Heidarpour, A., and Bhamare, R. (2020), ‘Study of bond stress of SMA rebars in concrete under elevated temperature’, *Institution of Civil Engineers*.

Acknowledgements

PhD is a roller-coaster ride and it gets even more challenging when it's a part time over eight long years. It is nearly impossible for anyone to endure this ride successfully without significant support from family, supervisors, colleagues, friends and all other well-wishers. I believe this is the best opportunity for me to thank all those who supported me through this exiting journey. Thank you all for your constant support. Words cannot express my grateful feelings to all of you.

First, I would like to thank my Principal supervisor, Dr. Bill Wong, for accepting me as his student to pursue research in an area that he is so passionate about: the application of smart materials in civil engineering. He gave me constant encouragement and support to perform this research. His valuable advice and guidance kept me focused and prevented me from losing my way. My special thanks and appreciation to Bill who spent many valuable hours of his personal time in improving my work.

I would also take this opportunity to thank my other Principal supervisor Dr. Amin Heidarpour for his guidance and providing valuable insights that eventually resulted in a better presentation of the topic and results. Thanks to Amin for taking time and for your valuable inputs that got me through several technical challenges.

My family is my greatest asset for they have supported me all through my life so far and I am sure they would continue doing so well into the future. I would like to take this opportunity to thank my wife Dr. Rupali S Bhamare, who was my inspiration to getting into the PhD program. You truly proved to be my better half in the way you supported me to overcome the most challenging times over eight long year. I could not have got through the PhD program without your support in my research. The motivation, encouragement and strength you provided are highly appreciated. Thanks for being there with our two little kids Harshul and Anshul and supporting them while I was engrossed in the PhD work. I would like to thank them both for being so cooperative and understanding. You both gave us so much joy that in your company I was relieved of the immense stress and pressure that I was in during the course of my

studies. Thanks to my parents Mrs. Manorama and Mr. Tarachand Moon who instilled the character, determination and work ethics in me that has made me what I am today. Thank you for everything that you have done to get me to here.

I also like to take this opportunity, to thank Mr. Long Goh, Sarvanan, and other staff of the civil engineering department at Monash University for your generous support and help in getting the physical experiments at the lab done on time. Thank you all for the great support you had been.

I would also like to thank my colleague and manager, Peter Allison for his support and granting me the time required for the study. I would also like to thank all my other colleague from Frontline Australasia Pty Ltd Sean, Mike, Sally, Alex, Kani, Babu, Octavian for helping me with the design and fabrication of the test jig and the testing apparatus.

Last but not the least; I would like to thank my friends for their irreplaceable friendship. Thanks to Chinmay, Dr. Raju Kadam for your support and help. Special thanks to Dr. Venkata Vijay Kumar Maddali for your valuable support from the time I commenced of my PhD. Your support with my thesis writing is much appreciated. Thank you for being there when I needed the most, a true reflection of good friends that you have always been.

Keywords

Bond stress, Bond Slip, Smart Material Rebars, Improved fire rating, Passive methods of addressing fire, Hybrid-Rebar concrete model, CZM Bilinear Modelling of SMA, Cohesive zone modelling.

Dedicated to

My loving Parents

Mrs. Manorama & Mr. Tarachand Moon

Notation and Abbreviation:

30F	30min of fire exposure
60F	60min of fire exposure
ASCE	American Society of Civil Engineering
$\{F^a\}$	Applied load vector
A_f	Austenitic finish temperature
A_s	Austenitic start temperature
τ	bond stress
BCA	Building Code of Australia
CCAA	Cement Concrete and Aggregate Australia
CPU	Central Processing Unit
$f_{c'}$	Characteristic strength of concrete.
CZ	Cohesive Zone
CZM	Cohesive Zone Method
CAD	Computer Aided Design
δ_C	Critical value interfacial separation
ρ	Density
d_b	Diameter of the rebar
DSC	Differential scanning calorimetry
u	Displacement
l_d	Embedment length
σ_f,	Final stress level
FEM	Finite Element Method
FRL	Fire Resistance Level
K_{ic} ,J_{ic}	Fracture toughness parameter
GPU	Graphics Processing Unit
$\{Q^a\}$	Heat flow vector
HSC	High strength concrete
HTSMA	High Temperature Shape Memory Alloys
HHT	Hilber-Hughes-Taylor
δ	Interfacial separation
a	length between transversal ribs
P	Load
M_f	Martensitic finish temperature

M_s	Martensitic start temperature
τ_t^{max}	Max tangential stress
σ_{cu}	Maximum compressive strength
T_t^{max}	Maximum tangential cohesive traction
δ_t^{max}	Maximum tangential displacement jump
σ_{max}	Maximum tangential traction
MDF	Medium Density Fibre board
E_c	Modulus of elasticity
NiTi	Nickel Titanium
NF	No fire exposure
$\{\ddot{u}(t)\}$	Nodal acceleration vector
$u(t)$	Nodal displacement vector
$\{u_n\}$	Nodal DOF value at time t_n
$\{\dot{u}(t)\}$	Nodal velocity vector
d	Nominal rebar diameter
δ_n	Normal direction displacement
NSC	Normal strength concrete
OHS	Occupational Health and Safety
μ	Poisson's ratio
PVC	Poly Vinyl Chloride
σ_{zp}	Principal stress in the z direction
σ_{xp}	Principal stresses are in the x
σ_{yp}	Principal stresses are in the y
S_{PR}	projective area of transversal ribs
R_m	Rebar modulus
β_1, β_2	Regression coefficients
β_3, β_4	Regression coefficients
RC	Reinforced Concrete
R	Resultant force
R_f	Rib factor
K_R	Sand roughness factor
α	Sand size coefficient
SMA	Shape Memory Alloy
SME	Shape Memory Effect
β_t	Shear transfer coefficient

δ_t^c	Slip at failure of bond
δ_t^*	Slip at Max tangential Stress
α_1	Slope of transversal ribs
p_2	SMA area ratio of the cross-section
ASMA	SMA reinforcement area
S_R	Spacing of transversal ribs
cp	Specific heat
σ_s	Start stress level
μ	Static coefficient of friction of rebar with concrete
A_s	Steel area
p_1	Steel area ratio of the cross-section
ε	Strain
G_c	Strain energy release rate
σ_{SMA}	Stress in SMA
$[C]$	Structural damping matrix
$[M]$	Structural mass matrix
$[K]$	Structural stiffness matrix
K_t	Tangential cohesive stiffness
T_t	Tangential cohesive traction
δ_t	Tangential direction displacement
δ_t	Tangential displacement jump
δ_t^c	Tangential displacement jump at the completion of debonding
δ_t^*	Tangential stiffness jump
T	Temperature
f_R	The relative rib area
λ	Thermal conductivity
$\{\dot{u}\}$	Time rate of the DOF values
$\{\dot{u}_n\}$	Time rate of the nodal DOF values at time t_n
C	Transient integration parameter
θ	Transient integration parameter
TWSME	Two Way Shape Memory Effect
ε_{cu}	Ultimate strain
f_c	Ultimate uniaxial compressive strength
f_t	Ultimate uniaxial tensile strength
$\{u\}$	Vector of DOF values

WBZ	Wood-Bosak-Zienkiewicz
f_{sy}	Yield stress of steel

TABLE OF CONTENT

CHAPTER 1: INTRODUCTION 1

1.1 Statement of problem 1
1.2 Background 3
1.3 Shape Memory Alloys (SMA) 5
1.4 Major issues and limitations of current SMA's 7
1.5 Research Significance and Innovation 8
1.6 The purpose of this study 10
1.7 Outline of Thesis 11

CHAPTER 2: LITERATURE REVIEW 14

2.1 Background 14
2.2 Behaviour of reinforced concrete building under fire 15
2.2.1 Effect of fire on concrete 15
2.2.2 Response of concrete to fire 18
2.2.2.1 Chemical changes 19
2.2.2.2 Effect of fire on steel reinforcement in reinforced concrete 20
2.2.2.3 Spalling 22
2.2.3 Bond-Strength of reinforced concrete 22
2.2.4 Bond failure mechanism 30
2.2.5 Assessment of fire damage 32
2.2.6 Fire resistance level (FRL) of reinforced concrete 35
2.3 Shape Memory Alloy (SMA) 38
2.3.1 How shape memory alloy works 39
2.3.2 NiTi Based shape memory alloy 41
2.3.3 High Temperature Shape Memory Alloys 43
2.3.4 Surface condition of the SMA bar 43
2.3.5 Passive design for increasing the FRL in SMA-Concrete 44
2.4 Application of SMA in Civil and Structural Engineering 48
2.5 Other Applications of shape memory alloy 52
2.5.1 Aerospace 52
2.5.2 Automotive 54
2.5.3 Bio-medical 55
2.6 Concluding remarks on literature survey 57
2.7 Gaps in the Literature review 59
2.8 Specific Aims and Objectives 60

CHAPTER 3: EXPERIMENTAL STUDIES.....63

3.1 Introduction.....63

3.2 Experiments: Framework.....66

3.2.1 Concrete Grade: M30.....67

3.3 The Specimens: Preparation and Process.....68

3.3.1 Concrete Mix Design.....68

3.3.2 Rebar materials.....73

3.3.3 SMA rebar characterisation: DSC experiment.....74

3.3.3.1 The process.....75

3.3.4 Heat treatment of SMA rebars.....80

3.3.5 Rebar lengths.....81

3.3.6 Concrete casting.....82

3.4 Experiments: Nomenclature.....87

3.4.1 Equipment and Instrumentation employed -Thermocouples.....87

3.4.2 SE 309 Thermometer.....88

3.4.3 NCDT 2300 Sensor.....89

3.4.4 Load Cell.....91

3.4.5 Jetflow Furnace.....92

3.4.6 Custom designed gripper.....95

3.5 Risk Assessment.....96

3.6 Experiment.....97

3.7 Experimental Studies - Results and Discussion.....101

3.7.1 Introduction.....101

3.7.2 Specimens response to Thermal Loading and Pull.....102

3.7.3 Failure Modes in the tested physical specimens.....114

3.8 Chapter Summary.....116

CHAPTER 4: NUMERICAL STUDIES.....122

4.1 Introduction.....122

4.2 Numerical Model Framework.....124

4.2.1 Concrete Model.....124

4.2.2 Steel-Concrete interface modelling.....127

4.2.3 Cohesive zone cracking.....129

4.2.4 SMA – rebar modelling.....133

4.2.5 Governing equations – Numerical modelling.....135

4.3 Develop and Benchmark the Numerical Model.....141

4.3.1 Concrete Model Validation.....141

4.3.2 Interface Bond Model Verification *143*
4.3.3 Transient Thermal Analysis Verification *147*
4.4 Numerical Model to study bond stress/bond slip at Rebar-Concrete interface 149
4.4.1 Establishing the goal and domain identification *150*
4.4.2 Step 1-CAD Model *152*
4.4.3 Step 2-Meshing *153*
4.4.4 Step 3-Materials *155*
4.4.4.1 Concrete: 155
4.4.4.2 SMA NiTi – Material 156
4.4.4.3 Steel: 157
4.4.5 CZM Bilinear Model-Modelling the interface between SMA and Concrete *158*
4.5 Step 4-Numerical Analysis 161
4.5.1 Thermal Analysis: Modelling the specimen response to fire *162*
4.5.2 Structural Analysis – Modelling specimen response to pull-out testing *168*
4.5.3 Convergence accuracy and results *180*
4.6 Numerical Studies – Results and Discussion 182
4.6.1 Results- Thermal Analysis *182*
4.6.1.1 Concrete-Steel Specimen Thermal Analysis results 183
4.6.1.2 Concrete-SMA Specimen Thermal Analysis results 194
4.6.2 Results- Nonlinear structural analysis *203*
4.6.2.1 Bond stress between Steel-concrete 203
4.6.3 Validation of Numerical Method developed in this work- A comparison with Physical Experiments 212
4.7 Numerical Studies - Results and Discussion 234
CHAPTER 5: PARAMETRIC STUDIES 243
5.1 The parametric studies 244
5.1.1 Effect of bar diameter *244*
5.1.2 Effect of concrete grade *246*
5.1.3 Effect of embedded length *248*
5.1.4 Effect of fire exposure duration *250*
5.1.5 Effect of sand coating *252*
5.1.6 Key highlights of the parametric studies *253*
5.2 Empirical Equation 256
5.2.1 Regression Analysis – Discussion on Case studies *257*
5.2.2 Validation of case studies for empirical equation *270*
5.2.3 Estimating the error margin *275*
5.2.4 Summary of Parametric Studies and Regression Analysis *277*

CHAPTER 6: SUMMARY OF RESULTS AND KEY HIGHLIGHTS 281

6.1 Introduction 281

6.2 Results – Physical Experiments 281

6.3 Results – Numerical Studies 288

6.4 Compare and contrast experimental Vs numerical results 291

6.4.1 The thermal input conditions 292

6.4.2 Failure mode analysis 293

6.4.3 Normalised bond stress: response of specimen to thermal and structural loading 294

6.4.4 Bond Stress comparison - Numerical Vs Physical Experiments 296

6.4.5 Estimating the error margin 297

6.5 Results - Parametric Studies and Development of Empirical Formula 299

CHAPTER 7: CONCLUSIONS AND RECOMMENDATIONS 308

7.1 Introduction 308

7.2 Conclusions 309

7.3 Main findings, significance and contributions 311

7.4 Limitation and constraints of the current studies 323

7.5 Recommendation for future works 323

TABLE OF FIGURES

Figure 1.1: Temperature induced phase transformation of SMA (temperature induced) (Lagaudas et al. SMA book)..... 6
Figure 1.2 Thesis outline..... 13
Figure 2.1: Stress-strain curves for normal-strength concrete at various temperatures (CCAA T61)..... 16
Figure 2.2: Relative strength reduction (Guide to fire safety of concrete building 2010)..... 17
Figure 2.3: Degradation of compressive strength of normal strength concrete (ASCE Model)..... 18
Figure 2.4: Degradation of compressive strength of high strength concrete (Kodur Model)..... 18
Figure 2.5: Chemical transformation in concrete at high temperature..... 19
Figure 2.6: Effect of elevated temperature on Young's Modulus (Elghazouli et al. 2009)..... 20
Figure 2.7: Reduction factors at the elevated temperatures (Xuhong et al. 2012)..... 21
Figure 2.8: Stress-strain curves at the elevated temperatures (Amin H et al. 2014)..... 21
Figure 2.9: Internal cracks around the reinforcing rebar embedded in concrete (Goto, 1971)..... 23
Figure 2.10: Rebar rib types (One Steel – essential technical data on the steel reinforcement)..... 24
Figure 2.11: Definition of relative rib area, f_R. (Jokela 1979)..... 25
Figure 2.12: Specimens used in relative rib area measurement (testing year 1999)..... 26
Figure 2.13: Bond stress vs slip with 16 mm at 150 mm embedment in M40 concrete (Apparao et al. 2002)..... 28
Figure 2.14: (a) Local bond response - scale of the reinforcement (b) Bond response – scale of reinforcement lugs (Goto 1971)..... 30
Figure 2.15: Reactive forces acting on concrete during rebar pull-out..... 31
Figure 2.16: Hengzhou building in Hengyang city (Yi et al. 2015)..... 33
Figure 2.17: Spalling and visible reinforcement (Yi et al. 2015)..... 33
Figure 2.18: The photographs of the Plasco building – (a) During the fire (b) After its collapse (Mehmet et al. 2018)..... 33
Figure 2.19: Spalling and visible reinforcement (Mehmet et al. 2018)..... 34
Figure 2.20: Standard time temperature curve (AS 1530.4)..... 36
Figure 2.21: Temperature-induced phase transformation of an SMA without loading (Lagoudas, D.,C., Kumar, P., K., Introduction to Shape Memory Alloys)..... 39
Figure 2.22: Stress–strain curve of the super elastic behaviour (Lagoudas D.C and Kumar P.K)..... 40
Figure 2.23: A-Original parent phase, b-self-accommodated martensite, c-deformation in martensite, d-reverse transformation (upon heating above A_f)..... 41
Figure 2.24: Shape memory effect in SMA (Lagoudas, D.,C., Kumar, P., K., Introduction to Shape Memory Alloys)..... 42
Figure 2.25: Sand coating of SMA rebar (a) Bonded length (b) Epoxy application (c) Sand coating (d) Sand coated rebars (Muntasir et al. 2016)..... 44
Figure 2.26: Effect of sand coating on SMA rebar at room temperature (Muntasir et al. 2016)..... 44

Figure 2.27: Concrete strength used in 500°C isotherm method (from Eurocode 2)....45
Figure 2.28: Hybrid SMA-Steel reinforced concrete beam (Wong et al. 2014)....46
Figure 2.29: Plot of bending moment of hybrid SMA-RC beam with fire duration (Wong et al. 2014)....47
Figure 2.30: SMA device for earthquake suitable connection of historic gable (Menna et al. 2015) Applications of Shape Memory Alloys in structural engineering)....48
Figure 2.31: behaviour of incorporated SMA devices (Menna et al. 2015)....49
Figure 2.32: SMA wire Steel beam composite beam (Sadiq et al. 2013)....49
Figure 2.33: (a) SMA Reinforcement details (b) Test performed with SMA rebars (Li et al. 2008)....50
Figure 2.34: (a) Schematic illustration the concept of using pre-strained SMA hoops to apply external confining pressure on RC bridge columns (b) SMA confined test specimen after cyclic compressive test....51
Figure 2.35: Stress – Strain curve of SMA under high temperature (Sadiq et al. 2013)....52
Figure 2.36: SMA Cyrofit tube coupling....53
Figure 2.37: SMA composite chevron....53
Figure 2.38: SMA-actuated mirror....54
Figure 2.39: Automatic oil valve adjusting device for the Shinkansen....54
Figure 2.40: Simon filter: A-filter in the recovery form, B- filter release....55
Figure 2.41: Self-expanding stents....55
Figure 2.42: (A) Orthopedic staples, (B) Staples placed in human foot, (C) X-ray showing staple....56
Figure 2.43: SMA plates used to repair injured area....57
Figure 2.44: Bending moment capacity – concrete beam with and without SMA (Wong et al. 2015)....58
Figure 2.45: Mid-span displacement – concrete beam with and without SMA (Wong et.al. 2015)....58
Figure 3.1: Organisation structure....65
Figure 3.2: Experiment boundary....66
Figure 3.3: Water /cement ratio for M30 concrete is around 0.65 (AS 1379 -2007)....71
Figure 3.4: Water-Cement ratio chart....72
Figure 3.5: Sieve analysis of aggregate....72
Figure 3.6: Steel and SMA rebar 10mm diameter....74
Figure 3.7: Differential scanning calorimeter DSC 8500....76
Figure 3.8: Preparation of SMA sample material characterisation (a) cutting thin slice (b) material shredding....77
Figure 3.9: Classification, Identification and Storage of SMA samples....77
Figure 3.10: Aluminum container to place the sample for testing in DSC....78
Figure 3.11: Placement of sample and activation of test program through computer....79
Figure 3.12: Phase transformation of samples at different heat treatment....79
Figure 3.13: Annealing of SMA rebars at 400°C for 30min....81
Figure 3.14: Cut SMA rebar of length 450 and 350mm....81
Figure 3.15: Schematic diagram of rebars (length 450 and 300mm) embedded in concrete specimens....82
Figure 3.16: Jigs for positioning the rebars....83

Figure 3.17: Mould for casting sample with rebar and thermocouple positioner....84
Figure 3.18: Cast test specimen with SMA rebar and thermocouple. 84
Figure 3.19: (a) specimens in the oven (b) specimens heated to 50℃ for 6 hrs....85
Figure 3.20: Samples ready for testing....85
Figure 3.21: Schematic diagram of experimental setup and nomenclature 87
Figure 3.22: Thermocouple position in the concrete specimen....88
Figure 3.23: Test Link SE309 ILD2300 Opto NCDT....89
Figure 3.24: ILD 2300 Opto NCDT-device for slip measurement....90
Figure 3.25: ILD 2300 Opto NCDT- Definition of terms....90
Figure 3.26: ILD 2300 Opto NCDT-LASER displacement Measurement arrangement....91
Figure 3.27: Load cell arrangement....92
Figure 3.28: Load Cell AC2500 and reader....92
Figure 3.29: Jetflow Furnace....93
Figure 3.30: Furnace inside: Specimen holding position (rear end view)....94
Figure 3.31: Frame work for the front door insulation and sample placement....94
Figure 3.32: Insulation of furnace & test specimen feed....95
Figure 3.33: Input temperature curve to furnace 95
Figure 3.34: Collet gripper slips during the test. 96
Figure 3.35: Bolted gripper (specifically design for this study). 96
Figure 3.36: Isolation of test setup and OHS 97
Figure 3.37: Schematic of experiment setup....98
Figure 3.38: Actual picture of test apparatus (view from front corner end)....98
Figure 3.39: Actual images of test apparatus (view from front top end) 99
Figure 3.40: Test Setup (No Fire & Fire Condition)....99
Figure 3.41: Inside the electric oven (front and rear door removed)....101
Figure 3.42: Parameters considered....102
Figure 3.43: Thermocouple T1, T2 and T3 position in specimen....103
Figure 3.44: The temperature trend curve of furnace and specimen as recorded during the physical experiments....103
Figure 3.45: The trend curve of furnace and specimen temperature measured on billet heating (Chen et al. 2015)....104
Figure 3.46: Bond Stress-Slip plot for NF-FL-E1-SMA....106
Figure 3.47: Bond Stress-Slip plot for NF-FL-E1-SMA (max. bond stress)....107
Figure 3.48: Steel-concrete a) half embedded and b) full embedded, bond stress at various conditions and parameters....110
Figure 3.49: SMA-concrete a) half embedded and b) full embedded, bond stress at various conditions and parameters....111

Figure 3.50: The 12 specimens....114
Figure 3.51: Failure Modes: Pull out test under high temperature....115
Figure 3.52: Various aspects that were considered in the experimental studies undertaken....116
Figure 3.53: Achievement of the objectives of AIM 1....119
Figure 3.54: Data flow from physical experiments (Chapter 3) to Numerical experiments (Chapter 4)....121
Figure 4.1: Typical stress strain for concrete material (Ansys help documentation)....124
Figure 4.2: Concrete Solid65 Element geometry and shapes (Ansys help documentation)....125
Figure 4.3: Failure surface for concrete -ANSYS Concrete Solid65 (Ansys help documentation)....126
Figure 4.4: Interface element Inter 205 – ANSYS element (Ansys help documentation)....128
Figure 4.5: Debonding: (a) Normal separation (b) Shear (tangential) separation....128
Figure 4.6: Cohesion zone modelling at interface (Ansys help documentation)....129
Figure 4.7: Traction – separation laws for cohesive zone models a) Bilinear, b) Exponential, c) Trapezoidal, and d) Trilinear laws....130
Figure 4.8: Cohesive zone model used to model the bond slip (Ansys help documentation)....131
Figure 4.9: Cohesive zone element -INTER 205 (Ansys help documentation)....132
Figure 4.10: SMA Shape Memory Effect -SME (Lagoudas D.C and Kumar P.K)....134
Figure 4.11: Solid185 – 8 node brick element -rebar modelling (Ansys help documentation)....135
Figure 4.12: Geometry, loading and beam reinforcements (dimensions in cm)....142
Figure 4.13: Crack generated under bending load....142
Figure 4.14: Typical specimen for pull out testing (Apparao et al. 2002)....144
Figure 4.15: Fine mesh at the concrete – steel interface (a and b)....144
Figure 4.16: Zoomed crack growth at the steel-concrete interface....145
Figure 4.17: Progressive crack growth during the different stages of the pull-out....146
Figure 4.18: RC beam with fire on all exposed surface....147
Figure 4.19: Temperature profiles a) contour plot and b) Iso-lines at 30, 60 and 90 minutes....148
Figure 4.20: Temperature profiles Iso-line at 30, 60 and 90 minutes (quarter-section): EN 1992-1-2 :2004-left: FEA right)....148
Figure 4.21: Simulation workflow....149
Figure 4.22: Adaptive simulation method and the software tools employed....150
Figure 4.23: Experiment apparatus developed in Chapter 3....150
Figure 4.24: CAD model of the experiment apparatus (developed in Chapter 3). 151
Figure 4.25: CAD model side view (Thermal and Structural Domain)....151
Figure 4.26: a) Symmetric Model b) Wedge 152
Figure 4.27: Simplified CAD domain modelled for numerical analysis 153
Figure 4.28: Meshing of the symmetric model and mesh at the rebar-concrete interface....154
Figure 4.29: Concrete-Relative tensile strength degradation with temperature 155
Figure 4.30: Concrete-Relative compressive strength degradation with temperature....155

Figure 4.31: Relative elastic modulus degradation with temperature (Concrete) 156
Figure 4.32: Relative elastic modulus variation with temperature (steel) 157
Figure 4.33: Relative yield strength variation with temperature (steel) 158
Figure 4.34: Relative compressive strength degradation with temperature 159
Figure 4.35: The association between chapters and the data flow 162
Figure 4.36: Sequential coupling flow 163
Figure 4.37: Thermal boundary condition as applied 164
Figure 4.38: Temperature-time fire curve 165
Figure 4.39: 3D expanded view of temperature profile a) at 30 mins duration b) at 60 mins duration 166
Figure 4.40: Temperature profile at 30 mins fire duration 166
Figure 4.41: Temperature profile at 60 mins fire duration 167
Figure 4.42: Temperature profiles of the specimen 168
Figure 4.43: CAD model of the experiment apparatus (developed in Chapter 3). 169
Figure 4.44: 3D CAD model of the Rebar-Concrete Model showing the Three components 170
Figure 4.45: 2D wedge of the Rebar-Concrete Model (location of the wedge as showing the inset) 170
Figure 4.46: Numerical Model – Showing element type and the respective material 173
Figure 4.47: Numerical Model – Domain Mesh 173
Figure 4.48: Load and Boundary condition – Pull-out simulation 176
Figure 4.49: Concrete-Relative degradation with temperature a) tensile strength b) compressive strength and c) elastic modulus 178
Figure 4.50: Steel-Relative degradation with temperature a) yield strength and b) elastic modulus 179
Figure 4.51: Specimen interface-bond stress vs slip 179
Figure 4.52: Convergence chart 181
Figure 4.53: Thermal load on specimen 182
Figure 4.54: Temperature profile SMA rebar full insert: Experimental Vs Numerical 184
Figure 4.55: 3D CAD of Concrete-Steel rebar and the interface 185
Figure 4.56: 3D Cross-section identifying the locations (to read thermal profiles) 185
Figure 4.57: Bond strength degradation between concrete and steel rebars (Lublóy et al. 2014) 186
Figure 4.58: 3D Thermal profile of the Concrete-Steel Rebar and interface at (a) Start (b) 30min and (c) 60min fire exposure 188
Figure 4.59: 2D Axial Thermal profile of the Concrete-Steel Rebar and interface at (a) Start (b) 30min and (c) 60min fire exposure 189
Figure 4.60: 2D Radial Thermal profile of the Concrete-Steel Rebar and interface at (a) Start (b) 30min and (c) 60min fire exposure 190
Figure 4.61: 2D Radial Thermal profile of the Concrete at (a) Start (b) 30min and (c) 60min fire exposure 191
Figure 4.62: 2D Radial Thermal profile of the Concrete-Steel Rebar Interface at (a) Start (b) 30min and (c) 60min fire exposure 192

Figure 4.63: 2D Radial Thermal profile of the Steel Rebar at (a) Start (b) 30min and (c) 60min fire exposure ..193
Figure 4.64: 3D Thermal profile of the Concrete-SMA Rebar and interface at (a) Start (b) 30min and (c) 60min fire exposure ..195
Figure 4.65: 2D Axial Thermal profile of the Concrete-SMA Rebar and interface at (a) Start (b) 30min and (c) 60min fire exposure..196
Figure 4.66: 2D Radial Thermal profile of the Concrete-SMA rebar and the interface at (a) Start (b) 30min and (c) 60min fire exposure ..197
Figure 4.67: 2D Radial Thermal profile of the Concrete (specimen with SMA rebar) at (a) Start (b) 30min and (c) 60min fire exposure..198
Figure 4.68: 2D Radial Thermal profile of the Concrete-SMA Rebar Interface at (a) Start (b) 30min and (c) 60min fire exposure ..199
Figure 4.69: 2D Radial Thermal profile of the SMA Rebar at (a) Start (b) 30min and (c) 60min fire ..200
Figure 4.70: Similarities in thermal profiles between Steel and SMA rebar concrete specimens..201
Figure 4.71: Temperature profiles of the specimens (both steel and SMA) as a close approximation..202
Figure 4.72: a) Symmetric Model b) Wedge ..204
Figure 4.73: Resultant force for full insert Steel rebar-Concrete Specimen at a) No Fire b) 30min of Fire exposure (c) 60min of Fire exposure ..206
Figure 4.74: Full insert Steel rebar displacement profile for a) No Fire b) 30min of Fire exposure (c) 60min of Fire exposure and for respective loads shown in Figure 4.73 ..207
Figure 4.75: Full insert Concrete interface element displacement profile for a) No Fire b) 30min of Fire exposure (c) 60min of Fire exposure and for respective loads shown in Figure 4.73 ..208
Figure 4.76: Axial section view of Full insert steel rebar Concrete interface element displacement profile for a) No Fire b) 30min of Fire exposure (c) 60min of Fire exposure and for respective loads shown in Figure 4.73 ..209
Figure 4.77: Bond Stress at interface from numerical Analysis for full steel rebar insert under No Fire, 30min and 60min of Fire exposure for respective loads shown in Figure 4.73 ..211
Figure 4.78: Comparison of Bond Stress values from (a) numerical experiments results and (b) Physical experiment results..212
Figure 4.79: Resultant force for half insert Steel rebar-Concrete Specimen at a) No Fire b) 30min of Fire exposure (c) 60min of Fire exposure ..215
Figure 4.80: Half insert Steel rebar displacement profile for a) No Fire b) 30min of Fire exposure (c) 60min of Fire exposure and for respective loads shown in Figure 4.79. ..216
Figure 4.81: Half insert Concrete interface element displacement profile for a) No Fire b) 30min of Fire exposure (c) 60min of Fire exposure and for respective loads shown in Figure 4.79. ..217
Figure 4.82: Axial section view of half insert steel rebar Concrete interface element displacement profile for a) No Fire b) 30min of Fire exposure (c) 60min of Fire exposure and for respective loads shown in Figure 4.79. ..218

Figure 4.83: Bond Stress at interface from numerical Analysis for full steel rebar insert under No Fire, 30min and 60min of Fire exposure for respective loads shown in Table 4.13 220
Figure 4.84: Comparison of Bond Stress values from (a) numerical experiments results and (b) Physical experiment results 221
Figure 4.85: Resultant force for Full insert SMA rebar-Concrete Specimen at a) No Fire b) 30min of Fire exposure (c) 60min of Fire exposure 222
Figure 4.86: Full insert SMA rebar; displacement profile for a) No Fire b) 30min of Fire exposure (c) 60min of Fire exposure and for respective loads shown in Figure 4.85. 223
Figure 4.87: Full insert SMA rebar; Concrete interface element displacement profile for a) No Fire b) 30min of Fire exposure (c) 60min of Fire exposure and for respective loads shown in shown in Figure 4.85 224
Figure 4.88: Axial section view of Full insert SMA rebar Concrete interface element displacement profile for a) No Fire b) 30min of Fire exposure (c) 60min of Fire exposure and for respective loads shown in Figure 4.85 225
Figure 4.89: Bond Stress at interface from numerical Analysis for full SMA rebar insert under No Fire, 30min and 60min of Fire exposure for respective loads shown in Table 4.14 227
Figure 4.90: Comparison of Bond Stress values from (a) numerical experiments results and (b) Physical experiment results 228
Figure 4.91: Resultant force for half insert SMA rebar-Concrete Specimen at a) No Fire b) 30min of Fire exposure (c) 60min of Fire exposure 229
Figure 4.92: Half insert SMA rebar; displacement profile for a) No Fire b) 30min of Fire exposure (c) 60min of Fire exposure and for respective loads shown in Figure 4.91. 230
Figure 4.93: Half insert SMA rebar; Concrete interface element displacement profile for a) No Fire b) 30min of Fire exposure (c) 60min of Fire exposure and for respective loads shown in Figure 4.91 231
Figure 4.94: Axial section view of Half insert SMA rebar Concrete interface element displacement profile for a) No Fire b) 30min of Fire exposure (c) 60min of Fire exposure and for respective loads shown in Figure 4.91 232
Figure 4.95: Bond Stress at interface from numerical Analysis for full SMA rebar insert under No Fire, 30min and 60min of Fire exposure for respective loads shown in Table 4.15 234
Figure 4.96: 2D Radial Thermal profile at 60min of thermal exposure (a) Concrete (b) Concrete-SMA rebar interface and (c) SMA Rebar 235
Figure 4.97: Failure Modes: Pull out test under high temperature a) physical experiment and b) numerical study 236
Figure 4.98: Comparison of Bond Stress values from (a) numerical experiments results and (b) Physical experiment results 237
Figure 4.99: Effect of fire duration on bond stress of Half embedded rebar – SMA and Steel M30) 239
Figure 4.100: Effect of fire duration on bond stress of Full embedded rebar – SMA and Steel M30) 239
Figure 4.101: Experimental and FEA correlation 240

Figure 4.102: Interaction of numerical results with other Chapters....242
Figure 5.1: Effect of bar diameter on bond stress (Half embedded length)....245
Figure 5.2: Effect of bar diameter on bond stress (Full embedded length)....246
Figure 5.3: Effect of concrete grade on bond stress a) SMA Half embedded and b) SMA Full embedded....247
Figure 5.4: Effect of embedded length on bond stress (No Fire condition – M50)....248
Figure 5.5: Effect of embedded length of SMA rebar on bond stress in M50 concrete at a) 30min and b) 60min fire exposure....249
Figure 5.6: Effect of fire duration on bond stress (rebar half insert)....251
Figure 5.7: Effect of fire duration on bond stress (rebar full insert)....251
Figure 5.8: Effect of sand coating on bond stress (Full embedded length – M30)....252
Figure 5.9: Effect of sand coating on bond stress (Full embedded length - SMA-steel – M30)....253
Figure 5.10: Influence of parameters on (a) 8mm (b) 10mm and (c) 12mm diameter SMA fully embedded rebar....254
Figure 5.11: Influence of parameters on (a) 8mm (b) 10mm and (c) 12mm diameter SMA half embedded rebar....255
Figure 5.12: Regression Analysis – Coefficient for parameter....263
Figure 5.13: Regression analysis – Statistics....265
Figure 5.14: Line fit plot for the embedded length variable....266
Figure 5.15: Line fit plot for the bar diameter variable....266
Figure 5.16: Line fit plot for the concrete modulus variable....267
Figure 5.17: Line fit plot for the rebar modulus variable....267
Figure 5.18: Definition of relative rib area, F_R. (Jokela 1979)....268
Figure 5.19: FEA-Test-Empirical formula comparison (SMA)....271
Figure 5.20: FEA-Test-Empirical formula comparison (Steel)....272
Figure 5.21: Bond-slip response pull-out test (Apparao et al. 2002)....272
Figure 5.22: Katz Test-Empirical formula comparison (Steel Test)....274
Figure 5.23: Parameters considered for further studies....277
Figure 5.24: Achieving AIM 1, 2 and 3 (Results flow)....280
Figure 6.1: Steel-Concrete a) half embedded and b) full embedded, bond stress at various conditions and parameters....284
Figure 6.2: SMA-Concrete a) half embedded and b) full embedded, bond stress at various conditions and parameters....285
Figure 6.3: 2D Radial Thermal profile at 60min of thermal exposure (a) Concrete (b) Concrete-SMA rebar interface and (c) SMA Rebar....289
Figure 6.4: Axial section view of Full insert SMA rebar Concrete interface element displacement profile for a) No Fire b) 30min of Fire exposure (c) 60min of Fire exposure and for respective loads shown in Figure 4.81....290

Figure 6.5: Bond Stress at interface from Numerical Analysis for full SMA rebar insert under No Fire, 30min and 60min of Fire exposure for respective loads shown in Table 4.14 291
Figure 6.6: Temperature profile SMA rebar full insert: Experimental Vs Numerical 292
Figure 6.7: Failure Modes: Pull-out test under high temperature a) physical experiment and b) numerical study 293
Figure 6.8: Experimental and FEA correlation 294
Figure 6.9: Comparison of Bond Stress values from (a) Numerical experiments results and (b) Physical experiment results 296
Figure 6.10: Line fit plot for the Embedded length variable 300
Figure 6.11: Line fit plot for the Bar diameter variable 300
Figure 6.12: Line fit plot for the concrete modulus variable 301
Figure 6.13: Line fit plot for the rebar modulus variable 301
Figure 6.14: Bond-slip response pull-out test (Apparao et al. 2002) 303
Figure 6.15: Bond stress benchmark numerical (FEA), physical (Test) and empirical formula comparison (steel) 305
Figure 6.16: Bond stress benchmark Numerical (FEA), Physical (Test) and Empirical formula comparison (SMA) 305
Figure 6.17: Achieving AIM 1, 2 and 3 (Results flow) 307
Figure 7.1: Phase transformation of samples at different heat treatment 312
Figure 7.2: 3D Thermal profile of the Concrete-Steel Rebar and interface at (a) Start (b) 30min and (c) 60min fire exposure 316
Figure 7.3: Failure Modes: Pull out test under high temperature a) physical experiment and b) numerical study 318
Figure 7.4: Experimental and FEA correlation 319
Figure 7.5: Effect of fire duration on bond stress of Half embedded rebar – SMA and Steel M30) 319
Figure 7.6: Effect of fire duration on bond stress of Full embedded rebar – SMA and Steel M30) 320
Figure 7.7: Effect of sand coating on bond stress (Full embedded length - SMA-steel – M30) 320
Figure 7.8: Influence of parameters on (a) 8mm (b) 10mm and (c) 12mm diameter SMA fully embedded rebar 322

TABLE OF TABLES

Table 2.1: Relative rib area....26
Table 2.2: Description of rebars....27
Table 3.1: Compressive strength of crushed and uncrushed aggregates....69
Table 3.2: Approximate free- water content (Kg/m^3) for various levels of workability....70
Table 3.3: Fineness Modulus....73
Table 3.4: List of pull-out specimens tested....86
Table 3.5: List of pull-out specimens tested....102
Table 3.6: SMA rebar- concrete pull out tests results on specimen NF-FL-E1-SM....105
Table 3.7: Summary of data on concrete-SMA rebar pull out tests....107
Table 3.8: Summary of data on concrete-SMA rebar pull out tests....109
Table 3.9: Summary of data on concrete-steel rebar pull out tests....109
Table 3.10: Summary of data on Maximum tangential traction, Tangential Displacement, Ratio and Non dimensional weigh parameter....113
Table 3.11: List of pull-out specimens tested....118
Table 3.12: Summary of data on Maximum tangential traction, Tangential Displacement, Ratio and Non dimensional weigh parameter....120
Table 4.1: Comparison of FE model with hand calculations....142
Table 4.2: Comparison of pull out forces in bond strength test (experimental Vs numerical)....144
Table 4.3: Relative strength degradation properties of Concrete under fire condition....156
Table 4.4: Relative strength degradation properties of Steel under fire condition....158
Table 4.5: CZM Bilinear Model Parameters....160
Table 4.6: List of CZ parameters extracted from the experimental test study....160
Table 4.7: Profile and statistics of the specimen domain....171
Table 4.8: Mesh controls....174
Table 4.9: Mesh settings and statistics....175
Table 4.10: Material model used in analyses....177
Table 4.11: Bond Stress at interface from numerical Analysis for full steel rebar insert....210
Table 4.12: List of specimens examined using numerical method developed in this work....214
Table 4.13: Bond Stress at interface from numerical Analysis for half insert steel rebar....219
Table 4.14: Bond Stress at interface from numerical Analysis for full insert SMA rebar....226
Table 4.15: Bond Stress at interface from numerical Analysis for half insert SMA rebar....233
Table 5.1: Partial list of dependent and independent variables as derived from parametric studies....258
Table 5.2: Coefficient for parameters in Empirical equation....262
Table 5.3: Coefficient for parameters in Empirical equation: Weightage and Interpretation....263
Table 5.4: Statistics used for bond stress evaluation for pullout test (Apparao Rao)....273
Table 5.5: Material degradation used for evaluation....273

Table 5.6: Statistics used for bond stress evaluation for pullout test (Katz et al. 1999) 274
Table 5.7: Comparison of bond stress (Katz et al. 1999) 274
Table 5.8: Estimation of error in empirical equation with respect to physical test and numerical model 275
Table 5.9: The parameter variance 278
Table 5.10: Number of Parametric Numerical Simulation 278
Table 6.1: Summary of data on SMA-concrete rebar pull-out tests 283
Table 6.2: Summary of data on steel-concrete rebar pull-out tests 283
Table 6.3: Displacement, Ratio and Non dimensional weigh parameter 287
Table 6.4: Estimation of error in bond stress between results from physical and numerical experiments for (a) SMA and (b) Steel rebar 298
Table 6.5: Statistics used for bond stress evaluation for pullout test (Apparao et al. 2002) 303
Table 6.6: Comparison of bond stress (Katz et al. 1999) 304
Table 6.7: Statistics used for bond stress evaluation for pullout test (Katz et al. 1999) 304
Table 7.1: Summary of data on Maximum tangential traction, Tangential Displacement, Ratio and Non dimensional weigh parameter 314

CHAPTER 1: Introduction

1.1 Statement of problem

Concrete has excellent inherent fire resistive properties such as non-combustibility and high thermal resistivity. However, during an event of fire (at high temperature), several physio-chemical transformations take place in the concrete resulting in a drop in its strength and stiffness. In addition, the chemical disintegration of major constituents of concrete enables crack propagation and/or explosive spalling. In reinforced concrete members, such changes are reflected by a reduction in the mechanical properties and an increase in the permeability of concrete. Furthermore, weakening in the bond strength between embedded rebar and concrete is well documented in the literature.

The strength of reinforced concrete structure purely depends on the concrete and reinforcing rebar (which is steel in most of the cases). The purpose of providing the reinforcement is to increase the strength of concrete in tension, which in turn depends on the bonding between the two materials (i.e. concrete and reinforcing rebar). The bond strength is measured by calculating the bond stress. The design bond stress is defined as the shear force per unit nominal surface area of reinforcement bar (rebar). The stress acts on the interface between rebars and the surrounding concrete (along the direction parallel to the rebars).

Bond strength is derived from various parameters, such as bond stress at the interface of concrete and the rebar and the pressure of the hardened concrete against the rebar (due to the drying shrinkage of the concrete) to name a few. Likewise, friction interlock between the rebar surface, deformations, projections and the micro movements of the tensioned rebar in the concrete results in the increased resistance to slippage. In short, bond strength is governed by the following key factors:

- Adhesion between the concrete and the reinforcing rebar;

- Gripping effect resulting from the drying shrinkage of the surrounding concrete and the shear interlock between the rebar deformations and the surrounding concrete;
- Frictional resistance to sliding and interlock of reinforcement;
- Effect of concrete grade, strength in tension and compression; and
- Diameter, shape, ribs type, ribs spacing and reinforcement spacing.

The response of structures exposed to fire is usually described in terms of fire resistance level (FRL). FRL is defined as the period of time (in minutes) within which a specimen is subjected to conditions of fire defined by a standard fire time-temperature curve at which time the specimen reaches the prescribed form of "limiting behaviour". For example, in performance-based design, this limiting behaviour may be defined as real structural collapse or as a failure of structural integrity (generally defined in terms of a deflection limit). The design for fire safety includes the following measures:

- Passive measures: Fire resisting beams, columns, floors and walls (preventing structural collapse); and
- Active measures: Automatic fire alarms, sprinkler systems, smoke control fans and smoke vents (controlling or preventing fire itself, facilitating the evacuation of occupants).

Passive fire protection measures can be defined as products that are built in as part of the building or structure which helps to limit the development and spread of fire, thereby increasing the FRL. Passive fire safety covers all those aspects of fire protection that are involved in the design of a building, the building materials and the structural maintenance. The three main failure criteria under fire condition, in relation to concrete structures are:

- Structural adequacy (which is the ability to resist load);
- Integrity (which is the ability to resist the passage of flames); and

- Insulation (the ability to prevent fire spread due to unacceptable temperature rise of the non-heated face).

Passive fire protection products and systems are those that are considered to be always 'switched on' and do not require activating in order to fulfil their roles. In contrast, active fire protection devices require some form of a response and/or motion in order to perform their desired functions. A further differentiation is that active fire protection systems are added to the building after construction, as opposed to being part of the building itself. The limitations that are typical to passive measures are that of reduction in strength and stiffness with the increase in the temperature, a short window of time before failure to name a few. To overcome the above-mentioned limitations of the passive measures, there is a need to strengthen and improve the FRL of the passive measures.

1.2 Background

In today's construction industry reinforced concrete is adjudged as one of the main construction materials owing to its strength and durability. However, under conditions of fire (high temperature exposure) both concrete and reinforcement steel lose their respective strength, leading to catastrophic failure of structures and leaving short time for rescue and fire prevention operation. A structure's fire resistance capacity is determined by the period for fire resistance level (FRL) under specific fire conditions such as the standard fire curve. The standard fire curve predicts that the ambient temperature can reach as high as 900°C in less than 60 minutes of fire exposure. In reinforced concrete, the temperature of reinforced steel can be significantly high in fire, leading to deteriorating conditions which may cause structural collapse or a failure of integrity. Design for fire safety includes numerous active and passive measures. However, these measures, especially for structural fire protection of concrete elements, have their own limitations such as continuous weakening of structural materials in rising fire temperature, etc.

Moreover, another important component of reinforced concrete is steel. It is very important to understand how steel in the reinforced concrete behaves under fire. Studies on the effect of rising temperature on the strength of steel are well published

in the literature. It has been noted that the on average steel loses around 50% of its strength when the temperature reaches around 400°C. During a fire event, the rising temperature of the steel reinforcement reduces the load carrying capacity of steel, resulting in catastrophic failure of the structure. To reduce the rate of heating to the reinforcement, generally increased concrete cover or providing insulation on the concrete is recommended. However, the increased cover or insulation provision for all structural elements in a concrete structure is not practical. In addition, it will make the design inefficient and construction cost exceedingly high as well as increasing the risk of concrete spalling.

To overcome these limitations of structural fire design, smart materials such as shape memory alloy (SMA) are employed to enhance the integrity of the structural elements in the event of fire. The excellent physical and mechanical properties of SMA have made them successful candidates for use in structural engineering applications. The use of shape memory alloys (SMAs) has increasingly expanded in recent decades. Undeniably, the number of commercial applications is increasing each year. SMA is popular in market segments represented by actuators and motors, which is amongst the largest applications of SMA materials. Primarily, SMAs play a key role in the development and implementation of smart devices, which can be integrated into structures to provide functions such as sensing, energy dissipation, actuation, monitoring, self-adapting, and healing or rehabilitation of structures.

In recent decades, intensive research has been carried out on SMA for its application in the field of structural engineering (such as smart engineered systems with a particular emphasis on seismic response control of structures). Such systems mainly use NiTi (Nickle Titanium) and Copper based SMAs, typically aimed at absorbing a part of the seismic energy acting on a structure (for example, damping control, structural retrofit etc.). SMAs come in many shapes and configurations, such as single and stranded wires, ribbons, strips, tubing, and rebars. SMA is characteristically defined by their super elastic behaviour and large recoverable strain that confers a remarkable fatigue resistance. It is for this reason that SMA can follow large mechanical strain without significant irreversible strain. Some of the highlights on the SMA as evidenced in the literature are discussed in this section.

1.3 Shape Memory Alloys (SMA)

Shape Memory Alloys (SMA's) are relatively novel materials which have the ability to return to a predetermined shape when heated. When SMA is cold, or below its transformation temperature, it has a very low yield strength and can be deformed quite easily into any new shape, which can be retained. However, when the material is heated up above its transformation temperature, it undergoes a change in crystal structure which causes it to return to its original shape. If the SMA encounters any resistance during this transformation, it can generate extremely large forces. The shape memory effect is the ability of an SMA to remember and return to its predetermined shape even after several deformations when subjected to heating to a certain temperature. This shape recovery is the result of phase transformations that can be induced by either a stress or a temperature change. In addition to these key aspects, other excellent properties of SMAs have been exploited in civil engineering applications, such as durable fatigue strength, corrosion resistance, large damping capacity, and a good versatility in terms of their many possible shapes and configurations (refer Chapter 2). SMAs have the potential to have a significant impact in the field of structural engineering; for example, rehabilitation/restoration of structures, adaptable structures for seismic or shock loading to developing solutions for structures undergoing cyclic or fatigue loading.

A metallurgical phase diagram for a metallic alloy is a schematic representation of the equilibrium conditions between distinct phases. Phase diagrams consist of equilibrium lines or phase boundaries that separate different phases from each other. For an SMA alloy consisting of Nickle (Ni) and Titanium (Ti), the phase transformation (Figure 1.1) is represented in temperature along the ordinate axis. In the typical operating temperature range, SMAs have two phases, each with a different crystal structure and therefore different properties. One is the high temperature phase called austenite (A) and the other is the low temperature phase called martensite (M). There are four characteristic temperatures associated with the phase transformation. The detailed process of how the Shape Memory Effect works is described in the next Chapter (refer Chapter 2). The following are the distinct temperature induced phases;

- (M_s): martensitic start temperature
- (M_f): martensitic finish temperature
- (A_s): austenitic start temperature
- (A_f): austenitic finish temperature

The variable stiffness in super elastic behaviour ($T > A_f$) can be used to provide force and displacement control within the three characteristic strain regimes:

- at low strains ($\varepsilon < 1\%$), the elastic modulus of the austenite phase can be used to limit strains under service load conditions;
- at intermediate strains ($1\% < \varepsilon < 6\%$; i.e., in the super elastic plateau), the reduced modulus can be used to limit the force transmitted to the structure while it undergoes rather large displacements; and
- at large strains ($\varepsilon > 6\%$), the increased modulus in the stress-induced martensite phase can be used to control displacements under severe loadings.

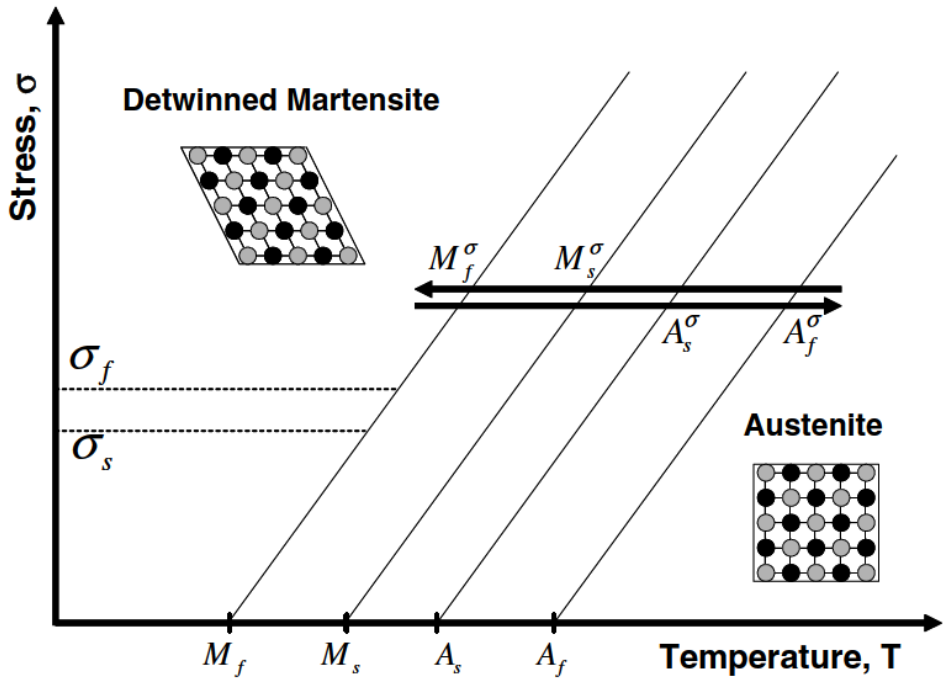

Figure 1.1: Temperature induced phase transformation of SMA (temperature induced) (Lagaudas et al. SMA book)

SMA is used in base isolation through SMA sliding device, where the resistance to sliding was achieved by opposing pairs of Nitinol tension elements. The isolated structure exhibited noticeable improvement in terms of inter-story drifts, and column rotational demands (Casciati et al. 2007). Another application is that of SMA springs that are activated in a base isolation system as a response to the vibration caused by structural resonance frequency during the high loading (Dolace et al. 2007).

SMA's super elastic capability is used to dissipate significant amount of energy through phase transition-induced hysteresis of SMA. For example, a hybrid SMA-based super elastic semi-active base isolation system was used for the moderation of seismic motions; as a result, it reduced base drifts by 18% achieving a satisfactory superstructure seismic response (Shook et al. 2008). Elsewhere, SMA-based damping devices have been used as external damping systems to obtain better effectiveness and combine good corrosion-resistance properties. Deng et al. 2006 assessed the effectiveness of SMA NiTi wires for use in damping devices to reduce the vibration amplitudes on realistic full-scale cable samples. The authors noted that the cable oscillation amplitudes (in the cable with SMA damper) were reduced by 25% with respect to the unequipped cable. SMA has been used in full scale rehabilitation or restoration of structures of historic importance. Li et al. 2008 explored the SMA's shape memory effect capability in Reinforced Concrete (RC) beam, where it is reported to have recovered to its original shape (SMA wires when heated have closed the crack and reduced the mid-span deflection) on heating. Like any material, SMAs have limitations too.

1.4 Major issues and limitations of current SMA's

SMA has been successfully used in many applications under low to mid-temperature. The concept of using SMA is gaining popularity. For example, Wong et al. 2014, examined the concept of hybrid SMA-reinforced steel concrete using analytical techniques. However, a majority of studies mentioned in the literature are focused on SMA wires that are latched on to the structure with additional anchoring system, leading to a very costly installation process (Menna et al. 2015). Mounting the SMA wires externally to retrofit a structure is a challenging affair that requires physical intervention on the structure itself. Secondly, SMA based reinforced concrete has not

been studied under high temperature condition; in other words, FRL of SMA-reinforced concrete is unknown. If SMA rebars were to be used along with the steel rebar in a hybrid reinforced concrete structure, it's imperative to understand the bond behaviour of SMA-reinforced concrete. Moreover, SMA wires require additional insulation in order to delay the temperature rise to a value that is beyond the optimal phase transformational value for practical use of SMA. Following are three key limiting factors for the use of SMA in civil engineering applications:

- Mostly SMA wires have been used to retrofit the damaged and displaced structure;
- SMA have not been studied thoroughly under high temperature in conjunction with concrete; and
- No experimental-based studies have been done to use SMA rebar as a measure to improve the fire resistance level.

It is evident in the literature that the bond stress is critical for the behaviour of reinforced concrete at higher temperature. However, no previous work in the literature exists on the bond stress of SMA-concrete interface that is subjected to conditions of fire (during the fire event). It is important to understand the bond behaviour at high temperature for the use of SMA in reinforced concrete to improve the fire resistance level (FRL) of the building, which is an important factor to be considered while designing for fire safety. In the present situation, the issues and limitations restrict the application of SMA's in construction industry.

1.5 Research Significance and Innovation

The strength of reinforced concrete is derived from the combination of the strength of both the rebar and concrete which gives it the desired results in tension and compression. The interaction between reinforcement and the surrounding concrete is termed as bond behaviour or bond mechanism. Bond behaviour is crucial to the structural strength of concrete elements as it does the transfer of stresses from concrete to rebar. It is this transfer of stresses that makes it possible to take advantage of the compressive strength of the concrete and the tensile strength of the

reinforcement in reinforced concrete structures. Hence, bond strength is a vital factor when the performance of reinforced concrete is assessed. Muntasir et al. 2015 carried out research on bond behaviour of SMA while others (Sadiq et al. 2013) have evaluated the SMA performance under high temperature. For example, Andrawes et al. 2010 examined the use of SMA wires mostly to retrofit structures externally. By using such smart materials one can limit the number of active measures that are otherwise required to address the situation that arises during a fire event. Analytical studies have shown that a hybrid steel-SMA reinforced concrete beam is able to increase fire resistance level of the beam in regard to its bending capacity and deflection as compared to a steel-reinforced concrete beam with similar strength (Wong et al. 2014).

Most of the experimental investigations found in literature are limited to finding ultimate bond stress and bond-slip of a concrete specimen for varying parameters and under standard room temperature conditions. Finite element modelling (FEM) has found acceptance in the literature as a method that can address many issues that are normally associated with physical experiments such as cost, time etc. Several authors employed the FEM and studied the stress distribution in reinforced concrete (Ngo and Scordeis, 1967; Bamonte et al. 2003; Sezen and Mohle, 2003; Jendele and Cervenka, 2006, Khalfallah and Ouchenane, 2007, and Shafaie et al. 2009) Numerical prediction of bond-slip behaviour in simple pull-out test was investigated by Al-Zuhairi and Al-Fatlawi (2013). It is understood that proper modelling can replicate the results of the physical experiments.

In view of drawbacks mentioned in the previous section and based on the work carried out in the literature on the use of SMA in civil engineering applications (as discussed above), the idea of hybrid SMA RC beam is a possibility that might provide an alternative solution to improve the FRL of structures. The application of the aforementioned concept has huge potential in fire-resistant structural design. Therefore, the hypothesis of the current research is that the performance of the SMA reinforced concrete beam will be much better under fire as compared to conventional RC beam. While steel strength deteriorates as its temperature increases, SMA can make up for the lost strength by its ability to strengthen at high temperatures. For

example, a simple reinforced concrete (RC) beam under fire will have large deflection, which will lead to a collapse state of high stress. By using SMA in reinforced concrete beams the SMA will gain the strength and stiffness at higher temperature, subsequently reducing the otherwise large deflection as well as increasing the fire resistance level of the beams. FEM could potentially be used as a tool to study the bond stress between the SMA reinforcement and concrete.

1.6 The purpose of this study

The purpose of this thesis is twofold 1) to scrutinize and characterise the bond stress distribution between the concrete and the smart materials (SMA) based reinforcement bar and 2) to examine the specimen's response to heat exposure in an event of fire. More particularly, this thesis for the first time develops a numerical model to examine the bond stress of SMA-concrete under high temperature. This research will introduce a novel concept of SMA rebar embedded in concrete (Reinforced Concrete with Shape Memory Alloy rebar) to enhance the fire safety of RC elements. The smart materials based RC developed in this research will improve on the existing passive measures for fire safety known in the literature. This research will help enhance a structure's ability to withstand large displacement, larger strain and higher fatigue strength by transforming back to the original shape/position after being subjected to extreme heat (a fire event), extreme loading (experienced during earthquakes), wind loading or vibration etc. In summary, the general aims are:

1. To review the literature and study SMA materials in order to identify an SMA with a potential to improve fire resistance level in concrete structures;
2. To conduct experimental studies in order to understand the bond behaviour between SMA and concrete that is subjected to significantly high temperature (which occurs in a fire event);
3. To develop a numerical model by incorporating data from experimental studies and carry out parametric studies by using the factors that influence the SMA-Concrete bond strength; and
4. To formulate an empirical equation for quick evaluation of bond stress in a SMA-Concrete structural element.

The specific aims and objectives of this study are framed on reviewing the literature and are presented at the end of the following chapter (Chapter 2).

1.7 Outline of Thesis

This report is divided into six chapters i.e. Introduction, Literature review, Experimental testing, Numerical analysis, Results discussion and Development of Empirical formula, Conclusions & Recommendation.

Chapter 1: It presents the background, statement of the problem and background to the current research study that highlights the significance of SMA and their application in the present scenario. The generic aims of the research work are established which formed the basis for the literature review.

Chapter 2: In the literature review, a thorough study was undertaken on existing research on the bond stress modelling, SMA and its application, SMA rebar bond stress evaluation. Extensive review of the relevant technical literature on strength degradation of the concrete and steel material, case studies of the structures under fire conditions and damage or failure of structures due to behaviour of material at high temperature was taken up. In specific, the behaviour of materials such as concrete, steel and SMA under high temperatures, the shape memory alloys and their applications in wider industries such as automotive, aerospace, biomedical, etc. are examined including that of application of SMA in structural and construction industry. The gaps in the literature were identified based on which specific aims and objective of this research work are established.

Chapter 3: An aim of this research is to conduct experiments on SMA-CONCRETE structural elements. In this chapter, experiments were designed and conducted to understand the bond behaviour of SMA-CONCRETE structural elements at high temperature (replicating a fire event). To this extent, the methodology for sample preparation, the physical testing setup, the apparatus and equipment used and the data that was gathered that assists in the numerical studies is also discussed in detail. Failure analysis of the specimens tested was documented for comparative studies with the numerical results.

Chapter 4: The FEM numerical methodology (numerical model creation, approach, verification and validation with experimental work of other researchers) to conduct numerical experiments was established in this chapter. Numerical parametric studies were conducted on the finite element model using ANSYS software. Finite element models were developed that replicate the geometry employed in the experimental studies. Thermal and structural analyses were carried out on specimens; the results of which were validated against the failure modes documented in the physical experiments. The fire exposure duration was studied for three durations of 1) no fire exposure, 2) 30 minutes fire exposure and 3) 60 minutes fire exposure. On validation, parametric studies were undertaken to identify the parameters that most significantly influence the bond stresses. The information gathered from the results of the parametric study assisted in the development of an empirical formula (discussed towards the end of the following chapter).

Chapter 5: In this chapter, the results from both the physical experiments and the numerical studies (including parametric studies) are presented. Such results are compared and analysed to establish and validate the novel numerical method developed in this study. In addition, the data sets were used to understand the factors affecting bond stress such that an empirical formulation of bond strength could successfully be developed. Thorough regression analyses were carried out on the factors such as concrete grade, rebar diameter, embedded length and strength reduction for high temperature under different fire duration times. The effects of these factors were studied. The influencing parameters are combined and correlated to generate a new empirical equation that can be employed to assess the maximum bond stress value for structures that are subjected to thermal and structural loading. A quick mathematical tool is hence developed to predict the bond strength at high temperature.

Chapter 6: It summarises the research undertaken in this work, major conclusions are drawn, and recommendations are provided for future research in this area. Some of the limitations endeavoured in this thesis are discussed for consideration in future research undertaking.

Chapter 1 **Problem identification and definition**

Statement of purpose | Background | Purpose of study

Aims

1. To review the literature and study SMA materials in order to identify an SMA with a potential to improve fire resistance level in concrete components.
2. To conduct experimental studies to understand the bond behaviour between a suitable SMA and concrete and to also understand the strength of SMA-CONCRETE component under significantly high temperature which occurs in a fire event.
3. To develop a numerical model by incorporating data from experimental studies and perform parametric studies on that factors that influence the SMA-CONCRETE bond strength.
4. To formulate an empirical equation for quick evaluation of bond stress in a SMA-CONCRETE structural element.

Chapter 2 **Literature review**

Bond stress modelling
SMA and its application

Fire temperature
Fire damage failure
Material degradation
Fire resistance level

Chapter 3 **Experimental studies**

Experiment studies
Experimental setup
specimen casting
SMA characterisation

Parameters
Embedment Length
Fire Duration
Bar Material

Chapter 4 **Numerical parametric studies**

Numerical Model
Concrete Model
Nonlinear Model
High Temperature, CZM

Parameters
Bar diameter, Fire duration
Embedment Length
Concrete Grade, Bar material

Chapter 5 **Results and Discussion**

Experimental and numerical results presentation and discussion

Empirical formula

Chapter 6 **Conclusion**

Conclusion and future recommendations

Figure 1.2 Thesis outline

CHAPTER 2: Literature Review

In this chapter, an extensive review of the relevant technical literature on reinforced concrete and its strength behaviour under high temperature condition was carried out. The specific areas covered in this chapter include fire statistics & modelling analysis, behaviour of concrete under fire and effect of fire on bond strength. Also, shape memory alloy and its mechanism and applications are studied in detail to understand its behaviour in fire resisting structures. The bond failure mechanism and bond strength are crucial part of this research which has been studied and collated for reinforced concrete structure. The critical research problem was identified based on the gaps that were established in the course of literature review. Specific aims and objectives that would address the stated research problem were developed towards the end of this chapter. The theoretical framework, mathematical models and the methodology that form the basis of achieving some of the aims are presented in Chapter 3.

2.1 Background

Concrete has an excellent inherent fire-resistant property. It is non-combustible and has a high thermal resistivity which significantly slows down the spread of heat through concrete elements. The behaviour of concrete under high temperature condition was critically examined in several studies (Ulrich (1988), Naus (1995), Hager (2013), Kodur (2014)). Various aspects such as evaporation, condensation, heat conduction & advection, phase expansion, thermo-chemical changes and damage, thermo-mechanical damage, spalling and crack initiation and propagation were considered. For example, Heikal (2000), and Xu et al. 2001, studied the physical, chemical and mechanical aspects that lead to the deterioration of concrete. It is understood that such aspects may result in undesirable structural failures (Kalifa et al. 2000; Cioni et al. 2001; Poon et al. 2004; Georgali et al. 2005 and Janotka et al. 2005). Therefore, an understanding of the properties of concrete (both before and after a fire event) is of significant importance for determining its fire resistance level (FRL). Fire resistance of materials is quantified by means of fire resistance rating. Fire resistance rating is

typically determined by measuring the ability of a passive fire protection material or assembly to withstand a standard fire resistance test. This is quantified either as a measure of period of time for which a material or assembly withstands a specific fire resistance test, or by evaluating through quantifiable criteria set by a specific fire resistance test, the ability of a material or assembly to perform a specific structural functionality (D. Panias et al. 2015). The standard fire curve can reach 900°C in just 60 minutes of fire exposure in reinforced concrete and the temperature of reinforcing steel can be significantly high, leading to deteriorating conditions which may result in structural collapse. It is for this reason that the behaviour of concrete needs to be well understood more so in conditions of fire event. In the next section some of the most important aspects that govern the reinforced concrete behaviour under both normal and fire conditions are discussed.

2.2 Behaviour of reinforced concrete building under fire

Although there are many fire incidents in buildings that have occurred in past, only the unusual or remarkable ones are reported in the public and in technical literature. The ones that are important to this study and are reported in the technical literature is discussed in the following sections.

2.2.1 Effect of fire on concrete

Kodur et al. 2006 illustrated the performance of concrete under fire conditions in regards to its material, structural and fire characteristics. Results from a number of fire resistance tests showed that the strength of concrete has significant influence on fire performance of concrete members.

Youssef et al. 2007 provided formulations for estimating the behaviour of unconfined and confined concrete under various temperature conditions for various parameters. These parameters are concrete compressive strength, concrete tensile strength, concrete compressive strain at peak stress, initial modulus of elasticity of concrete, transient creep strain mechanism, thermal strain, yield stress and bond strength of reinforcing rebars. To evaluate strength and behaviour of materials under elevated temperature conditions, tests are carried out by increasing the temperature of the

small specimen using some form of heating under various conditions. Based on such testing and models developed and proposed by Schneider et al. 1981, Cement Concrete and Aggregate Australia (CCAA) developed stress-strain relationships at different temperature for normal-strength concrete (Figure 2.1).

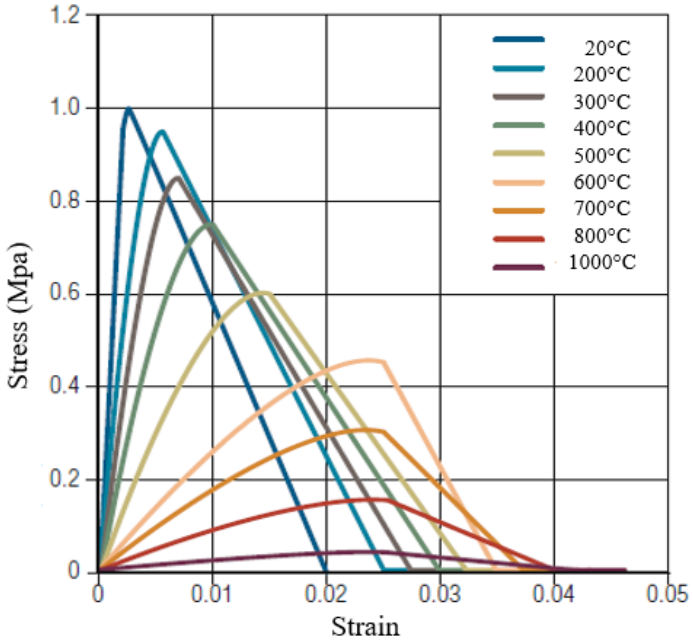

Figure 2.1: Stress-strain curves for normal-strength concrete at various temperatures (CCAA T61)

The higher the strength (along with associated lower permeability) of concrete, the higher the probability of spalling (Dwaikat et al. 2009). Spalling is a process of surface failure in which spall is shed. Spalling can occur in all concrete types when exposed to rapid heating during fire conditions. The results from past studies on concrete column and steel hollow section filled with concrete showed that concrete strength reduced significantly under fire event (Mohamed et al. 2014 and Shan-Shan et al. 2013). As per National Institute of Standards and Technology Internal Report (NISTIR 5934), the compressive strength of concrete with a value that is more than more than 40MPa is referred to as high strength concrete (HSC), whereas the concrete with compressive strength between 20 MPa to 40 MPa is referred as normal strength concrete (NSC).

It is understood that the reduction of strength of HSC when heated under stress is around 30% for temperature between 100-400°C and is comparable to NSC (refer Figure 2.2).

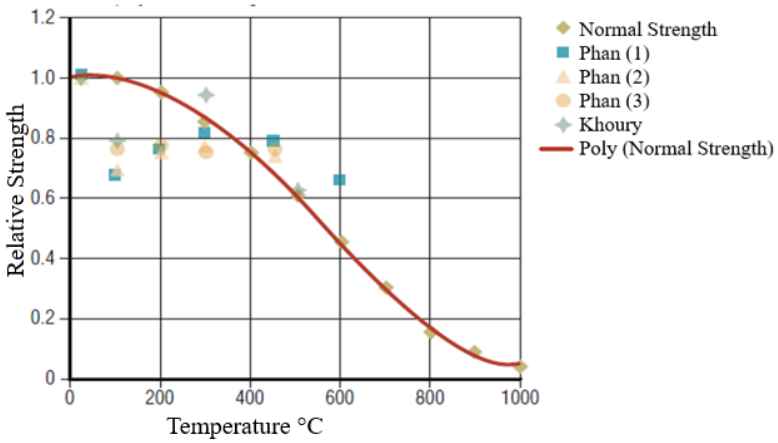

Figure 2.2: Relative strength reduction (Guide to fire safety of concrete building 2010)

The study on normal strength concrete was conducted to understand the strength and behaviour of concrete material under elevated temperature conditions; however, the specimen was not exposed to actual fire conditions. The specimen in the above-mentioned studies was soaked at a given temperature to achieve close to uniform temperature conditions throughout the specimen. Based on such testing, various complex models (small cylinders) which include effect of creep have been developed and studied (Schneider et al. 1981).

The mechanical properties such as compressive strength, tensile strength, elastic modulus and stress-strain response in compression under high temperature conditions are important when designing for fire resistance or design for increased fire resistance level. Kodur studied the behaviour of concrete under high temperature. It is understood that both ASCE model (ASCE 1992) (Figure 2.3) and Kodur model (Kodur et al. 2008) (Figure 2.4) demonstrate the variation of compressive strength ratio for NSC and HSC at elevated temperatures respectively. Furthermore, when such data is compared with the values of compressive strength generated by Eurocode (EN-2004) and Kodur (Kodur et al. 2014), it is observed that there is a large but uniform variation in the compressive strength data for NSC between the

temperature range 20–800°C. However, for HSC the variation seems to be more profound between the temperature of 200-500°C and less pronounced above 500°C.

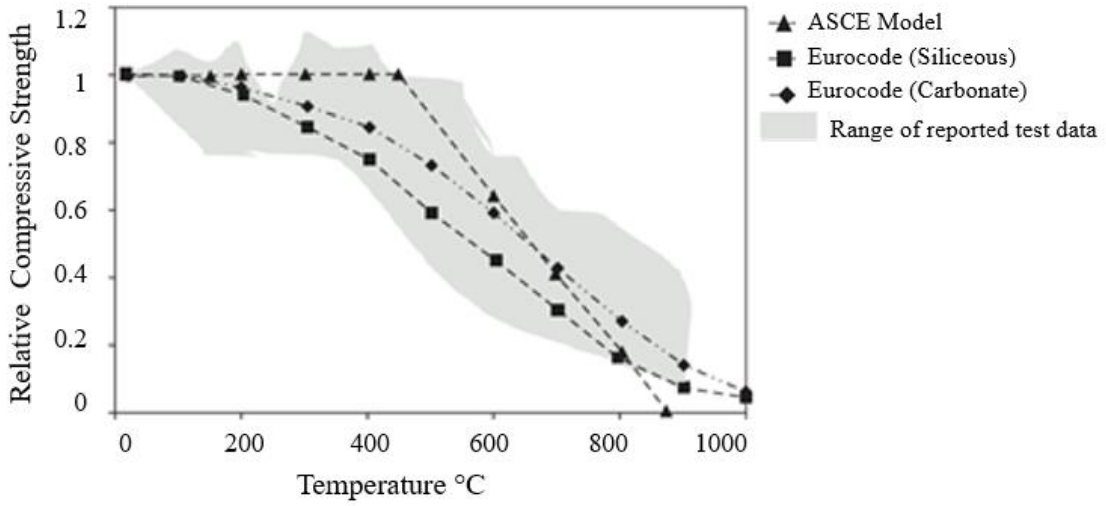

Figure 2.3: Degradation of compressive strength of normal strength concrete (ASCE Model)

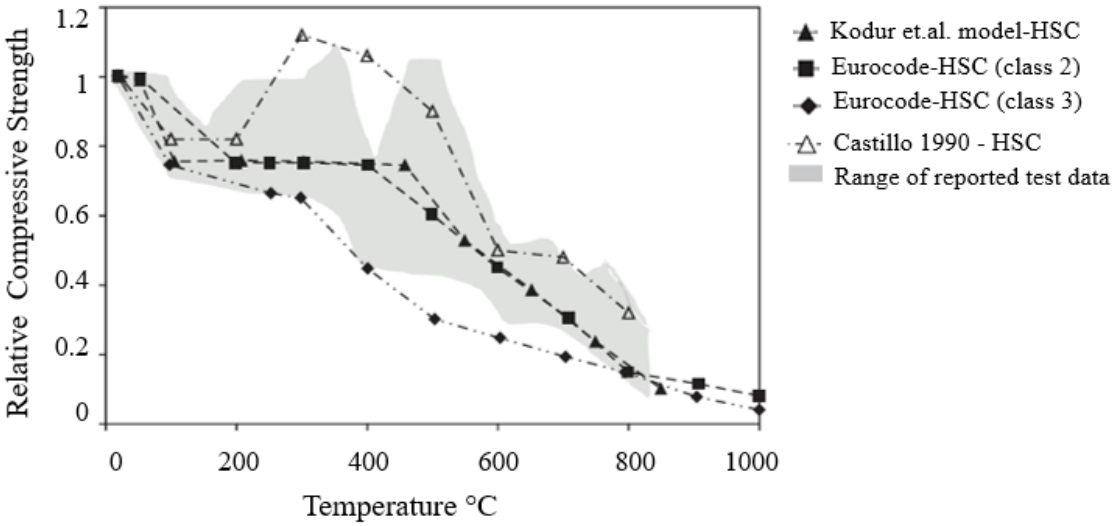

Figure 2.4: Degradation of compressive strength of high strength concrete (Kodur Model)

2.2.2 Response of concrete to fire

Concrete responds to fire in many different ways and the most significant ones among them are 1) change in chemistry of the cement, 2) spalling and 3) loss of bond strength between cement and the reinforcement rods. In an event that cement starts responding to fire, any or all of the aspects mentioned may happen at varying rates, eventually leading to the catastrophic failure of the structural elements of the building.

It is therefore important to review and understand the above-mentioned aspects in detail.

2.2.2.1 Chemical changes

When a concrete is subjected to heat, it undergoes several changes depending on the temperature and the duration it is exposed to the heat. Owing to the heterogeneous nature of the material (i.e. sand, cement and aggregate), the changes that occur in concrete are multidimensional and complicated. In addition, it has shown that some changes are linear such as strain with in elastic limit and can be reversed. However, there are other non-linear aspects to concrete (such as thermal expansion, cracks and their propagation, material strength etc.) that undergo permanent physical change.

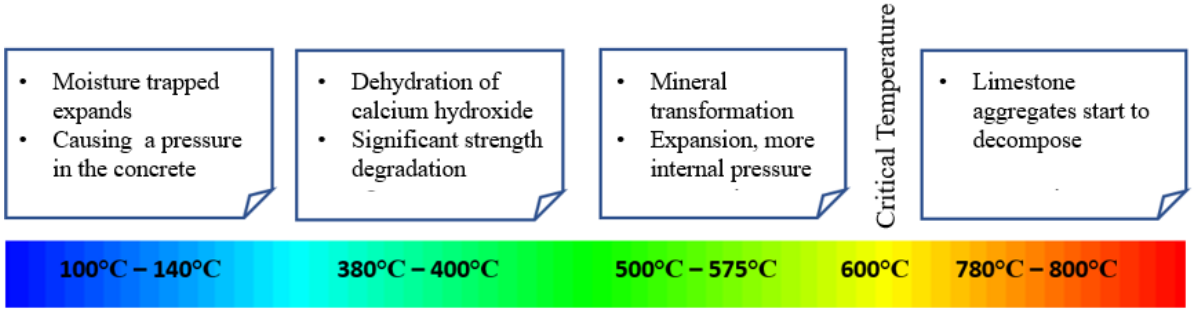

Figure 2.5: Chemical transformation in concrete at high temperature

As the temperature approaches to about 100-140°C, the moisture trapped in the pores of concrete expands and evaporates causing a pressure built-up in the concrete (Hager 2013). Likewise, as the temperature reaches close to 400°C the dehydration of calcium hydroxide further accelerates the vapour pressure build-up leading to significant drop in strength of concrete. At further elevated temperatures (around 575°C) quartz-based aggregate undergo mineral transformation resulting in volumetric expansion further adding to the internal pressure in the concrete. At around 800°C, limestone aggregates decompose (Figure 2.5). At this juncture, there exists a differential expansion rates between quartz and limestone aggregates leading to cracking and spalling of the concrete. These physical and chemical changes in concrete significantly lower the compressive strength of the concrete. It is for this reason the concrete starts losing its compressive strength significantly around 600°C; identified as critical temperature ranges for concrete (Kodur 2014). In reinforced

concrete in addition to the chemical mixtures of concrete it also includes reinforcement rebars. The effect of fire on such reinforcing rebars also needs to be understood.

2.2.2.2 Effect of fire on steel reinforcement in reinforced concrete

An important constituent of reinforced concrete is steel. It is therefore important to understand how the steel in the reinforced concrete behaves during a fire event. Elghazouli et al. 2009, investigated the influence of elevated temperatures on the mechanical properties of steel reinforcement. The experimental study focused on assessing the performance of reinforcement, with particular focus on the influence of temperature on enhancing the ductility of the reinforcement.

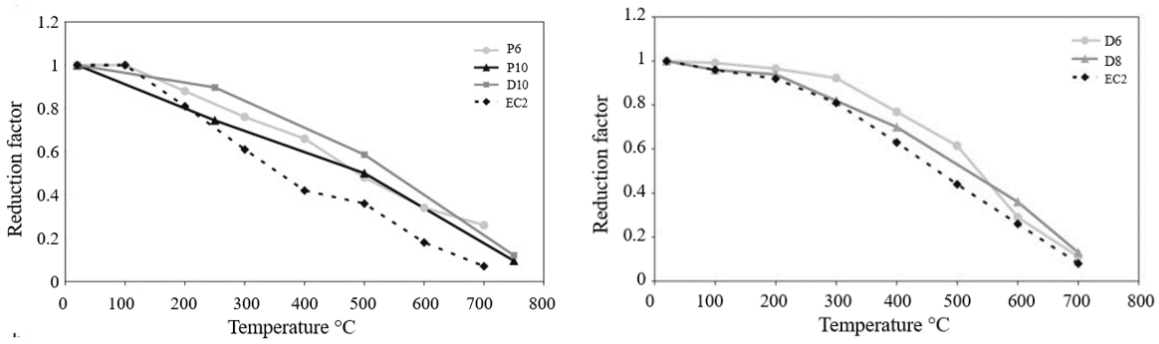

(a) Hot-rolled specimens (b) Cold-worked specimens

Figure 2.6: Effect of elevated temperature on Young's Modulus (Elghazouli et al. 2009)

The reduction factors obtained by Elghazouli et al. 2009 and Eurocode (Eurocode 2, 2004) are compared in Figure 2.6. It is noted that in the event of fire, the rise in the temperature of the reinforcing steel significantly affects the load carrying capacity of steel. It is also noted that all specimens behaved rather similarly in terms of the overall degradation. The temperature range at which point the reduction was notably varied was between 250-400°C.

Xuhong (Xuhong et al. 2012) examined the tensile strength of steel over the temperature range 20-700°C. Specimens considered in these experiments were made up of structural steel (grade S460N and S460M). The data from the above-mentioned experiments were further compared to the design standards and plotted as shown in Figure 2.7 . By comparing the results, it was found that the deterioration of mechanical

properties of structural steel at elevated temperature is dependent on steel quality and grades. The stress-strain relation at elevated temperature is presented in (Figure 2.8). Furthermore, unique predictive equations were proposed and validated by the researchers to study deterioration of high strength structural steel (grade S460) at elevated temperatures (Xuhong et al. 2012; Amin H et al. 2014; Wang et al. 2014; Chiew (2014)).

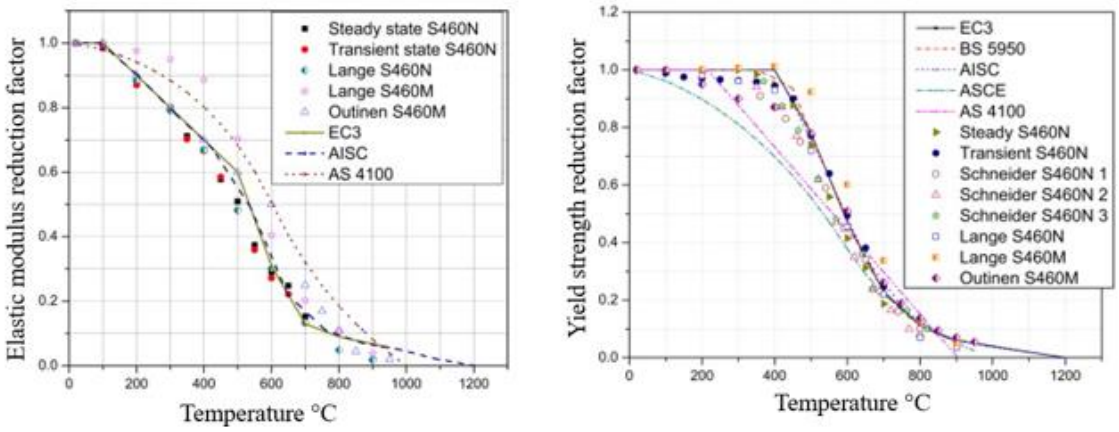

(a) Comparison of Elastic modulus reduction factors

(b) Comparison of yield strength reduction factors

Figure 2.7: Reduction factors at the elevated temperatures (Xuhong et al. 2012)

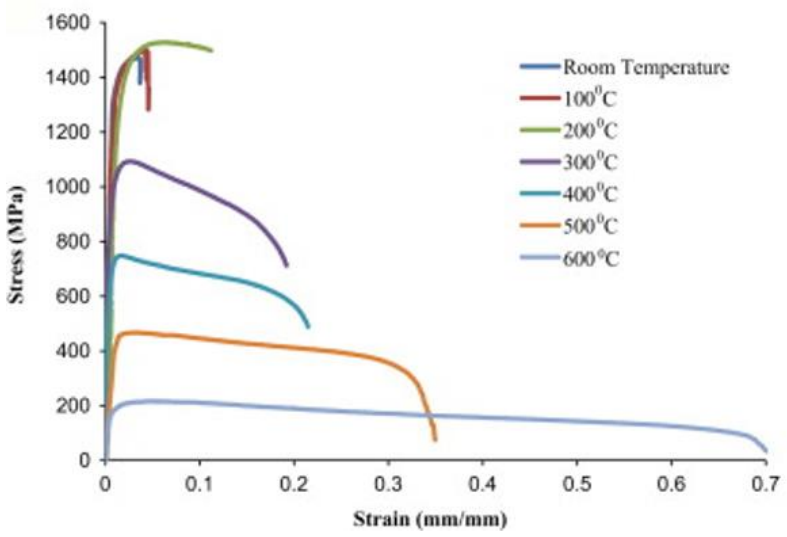

Figure 2.8: Stress-strain curves at the elevated temperatures (Amin H et al. 2014)

2.2.2.3 Spalling

Like chemical changes and steel exposure to fire, spalling is also a failure mechanism in concrete. Spalling is the process of concrete breaking apart into smaller pieces from the parent concrete surface. If spalling occurs at significantly high rates it is often referred as explosive spalling; such a situation normally occurs at elevated temperatures. However, in cases where moisture content is present in the pores of concrete, spalling can occur at a lower temperature. Severe spalling occurs where there is limited or no concrete cover present on the reinforcing steel. In such a situation, the reinforcement steel is exposed directly to high temperature during a fire event. As a consequence, the reinforcement rebars lose their strength. High strength concrete (HSC), (which has higher compressive strength than normal strength concrete) is considerably less porous. Such low porosity leads to other problems; it makes it harder for water vapor to escape the concrete block during heat build-up leading to catastrophic failures. At this juncture, it is important to understand yet another failure mechanism in concrete i.e. the bond stress of cement aggregate and steel in reinforced concrete.

2.2.3 Bond-Strength of reinforced concrete

Bond is necessary not only to ensure adequate level of safety allowing composite action of steel and concrete, but also to control structural behaviour along with sufficient ductility. The bond in reinforced concrete (RC) members depends on a number of factors such as reinforcing unit (rebar or multi wire) and stress state in both reinforcing unit and surrounding concrete. Other parameters such as concrete cover, space between rebars, number of layers and bundled bars, casting direction and rebar position play important role.

Mathey and Watstein (1961) reported that the bond stress decreases as the embedment length increases. Hansen and Liepins (1962) reported an increase in the bond stress under dynamic loading over static loading. Also, the author reported progressive bond failure and large slip from large repeated loading. Ferguson and Thomson (1962) studied the development length of rebars and the effect of confinement on such bars. The author noted that the bond stress varies as a function

of development length rather than rebar diameter. Ultimate bond stress varies as concrete grade changes when other factors kept constant. Furthermore, Thomson observed that the bond stress is dependent on concrete tensile strength.

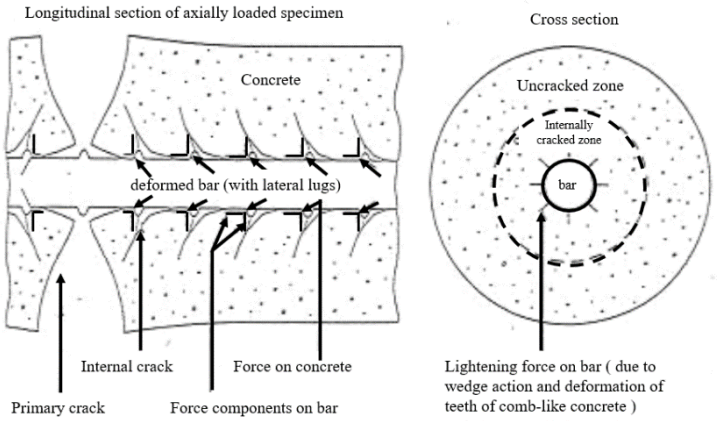

Figure 2.9: Internal cracks around the reinforcing rebar embedded in concrete (Goto, 1971).

Goto (1971) reported on the influence of deformation patterns and rib geometry on bond stress. The author noted that the bond behaviour is influenced by the rib face angle. However, when the rib face angle is less than 30°, the bond behaviour is different (Figure 2.9).

The three main influencing parameters to the bond stress between cement aggregate and steel reinforcement in concrete are 1) adhesion, 2) friction and 3) mechanical bond. While the adhesion bond is dependent on capillary forces and adhesion forces between the concrete and rebar, the frictional bond is based on the friction and shear resistance between the roughness of the rebar surface and the concrete interface. The adhesion and frictional bonds play only a minor role and they affect only lighter loads and smaller slips. Unlike the adhesion and frictional bonds, the mechanical bond is a strong bond that occurs as a result of the mechanical interlocking between rebar and concrete (assisted by the lugs or ribs in rebar). It is for this reason that a great deal of importance is placed on the geometrical features of the ribs on deformed rebar (Figure 2.10).

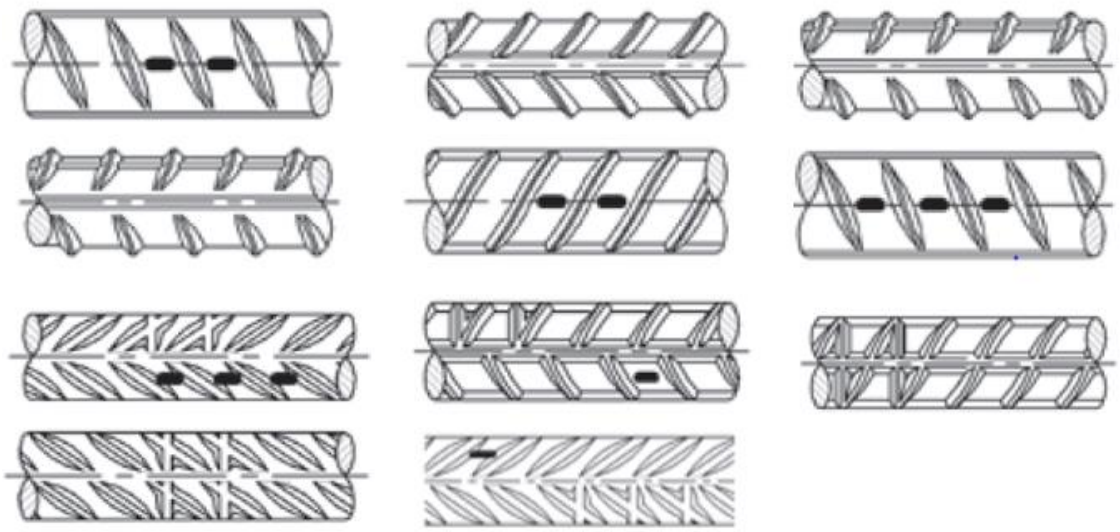

Figure 2.10: Rebar rib types (One Steel – essential technical data on the steel reinforcement)

Based on Jokela (1979) equation presented in study conducted by Esko (Esko et al. 2005), geometric information of the ribs allows one to calculate the relative rib area (f_R), and the angle of slope of transversal ribs (α_1). The relative rib area (f_R) is a parameter which takes account of height and occurrence, or the distance of transversal ribs. It is the ratio between the projected rib area and the cylindrical surface area of one rib space. Relative rib area (Figure 2.12) increases if rib height increases or the number on ribs per unit of length increases. Relative rib area (f_R), is calculated as per Equation 2.1 which is written as follows:

$$f_R = \frac{\sum S_{PR}}{\pi \, d \, a} \qquad \text{Equation 2.1}$$

where,

d: is the nominal rebar diameter

a: is the length between transversal ribs and

S_{PR}: is the projective area of transversal ribs (Figure 2.11)

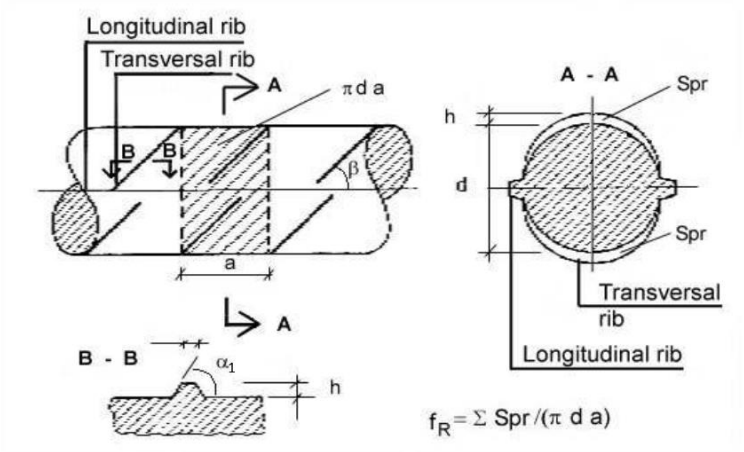

Figure 2.11: Definition of relative rib area, f_R. (Jokela 1979)

Some of the earliest tests to study deterioration of bond stress in concrete-steel rebar with respect to increasing temperature were conducted by Diederichs and Schneider (1981). The authors conducted the concentric pull-out tests on normal strength concrete (NSC) specimens between 20°C-800°C temperature range under both steady state and transient thermal conditions. They concluded that shape of the rebar (ribbed or smooth) has significant influence on bond stress besides temperature itself.

Slipping and fracturing can occur in either of the two ways 1) depending on the properties of concrete and 2) the geometry of the reinforcement rebar. In the case of geometry of the reinforcement rebar:

- If the ribs are high and are situated close to one another, breaking takes place on the cylindrical plane at the outermost edges of the ribs; and
- If the ribs are lower or apart from one another, breaking occurs behind the ribs, where the hardened cement paste will be pulverised and the concrete gets broken in a wedge-shaped formation.

Galvanised steel reinforcement is used to reduce the corrosion. Esko et al. 2005, studied the effect of galvanisation on steel reinforcing rebars and its effect on the relative rib area. It was found that ribbed black steel reinforcement had better bonding compared to galvanising steel rebar. Figure 2.12 shows relative rib area calculations

for each rebar. The mean values of relative rib area, length between transversal ribs, the angle of slope of transversal ribs and the angle of slope longitudinal ribs of the specimens are shown in Table 2.1 and Table 2.2 (testing year 2001) (Sistonen et al. 2002).

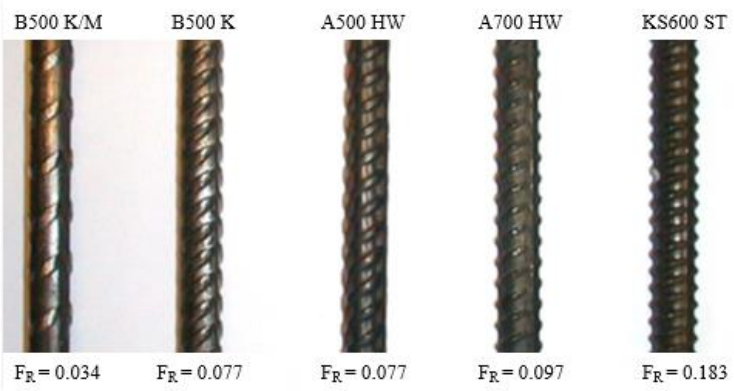

Figure 2.12: Specimens used in relative rib area measurement (testing year 1999)

Table 2.1: Relative rib area

Reinforcement rebar type	**Relative rib area**	**Minimum allowed relative rib area**	**Length between transversal ribs**	**The angle of slope of transversal ribs**	**The angle of slope of longitudinal ribs**
	F_R	**F_R min**	**a (mm)**	**α (°)**	**β (°)**
A500HWMep.Zn	0.074	0.063	14.6/7.3	34	69/63
A700HW.Zn	0.101	0.063	6.3/6.2	41	70/70
KS600ST.Zn	0.126	-	5.1/5.1	34	62/62
B500K..Zn	0.032	0.064	7.5	34	60
B500Kmod.Zn	0.071	0.064	15	33	57
A500HW Rotorcut, Zn	0.089	0.063	14.7/7.2	34	70/61
A500HW Mep. ref	0.071	0.063	14.7/7.2	39	69/63
A700HW. ref	0.087	0.063	6.1/6.1	46	70/69
KS600ST. ref	0.149	-	5.1/5.1	45	62/62
B500K. ref	0.032	0.064	7.4	39	60
B500K. mod. ref	0.073	0.064	14.9	42	57
A500HW Rotorcut ref.	0.090	0.063	14.6/7.2	43	70/61

Table 2.2: Description of rebars

	Reinforcement rebar type	Remark
A500HWMep.Zn	Finnish weldable hot rolled ribbed steel rebar	Hot- dip galvanised
A700HW.Zn	Finnish weldable hot rolled ribbed steel rebar	Hot- dip galvanised
KS600ST.Zn	Swedish weldable hot rolled ribbed steel rebar	Hot- dip galvanised
B500K..Zn	Finnish cold worked ribbed steel rebar	Hot- dip galvanised
B500Kmod.Zn	Finnish cold worked ribbed steel rebar	
A500HW Rotorcut, Zn	Finnish weldable hot rolled ribbed steel rebar	Hot- dip galvanised
A500HW Mep .ref	Finnish weldable hot rolled ribbed steel rebar	
A700HW. ref	Finnish weldable hot rolled ribbed steel rebar	
KS600ST. ref	Swedish weldable hot rolled ribbed steel rebar	
B500K. ref	Finnish cold worked ribbed steel rebar	
B500K. mod. ref	Finnish cold worked ribbed steel rebar	Modified, every other transversal rib removed
A500HW Rotorcut ref.	Finnish weldable hot rolled ribbed steel rebar	

The utility of reinforced concrete as a structural material is derived from the combination of concrete (which is strong and relatively durable in compression) and reinforcing steel (which is strong and ductile in tension).

Apparao et al. 2002, studied the parameters that influence the bond stress in reinforced concrete. The bond stress-slip curves were drawn from experimental observations of load vs. slip data (at the free and loaded ends) (Figure 2.13). The bond stress (τ) was calculated as the stress developed over an equivalent surface area using the following formula (Equation 2.2):

$$\tau_{max} = \frac{P}{\pi\, d_b\, l_d} \qquad \text{Equation 2.2}$$

where,

P: load (N),

l_d: embedment length (mm), and

d_b: diameter of the rebar (mm)

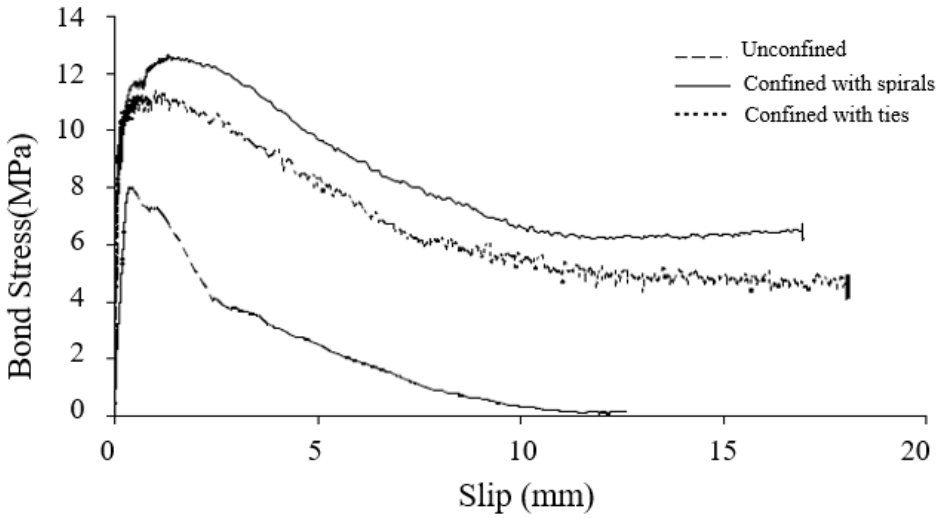

Figure 2.13: Bond stress vs slip with 16 mm at 150 mm embedment in M40 concrete (Apparao et al. 2002)

Chih et al. 2003 studied the change in bond stress due to effects of changes in strength, stiffness, toughness, bond strength of the rebar etc. The experimental results of post-fire pull-out tests showed a substantial decrease in bond stress as the temperature exceeds 200°C.

Haddad et al. 2008 studied the effect of elevated temperature on the bond between steel reinforcement and fiber reinforced concrete members through double pull-out tension tests for temperatures ranging from 350°C to 700°C. The specimens were heated to a temperature within aforementioned range without any applied load during heating, and then cooled down at room temperature before loading to failure. The authors concluded that there is significant reduction in bond stress between concrete and rebar as the temperatures exceed 400°C.

While experimental methods were quite popular in studying the bond stress of RC, non-destructive numerical methods were developed to facilitate a much faster

experimentation process. Numerical models developed prior to 2010 (Huang 2010, Bartina et al. 2007, Capua et al. 2007) assumed a perfect bond stress between rebar and concrete throughout the temperature range of 20°C-800°C. The authors opined that assuming a perfect bond between rebar and concrete at elevated temperatures may lead to un-conservative predictions of fire resistance in RC beams in certain scenarios. Nevertheless, the effect of rate of temperature induced bond degradation or the influence of different concrete strengths on fire resistance could not be quantified in these studies. Both Huang (2010) and Gao et al. 2013 incorporated the variation of temperature induced bond between rebar and concrete. The authors incorporated the influence of bond degradation utilizing zero thickness bond-link (spring) elements in evaluating the response of RC beams under fire. The separation of the bond-link elements was governed by set of equations based on the temperature of the elements.

Thanyawat et al. 2012 proposed a mechanical model for evaluating the bond strength between steel rebar and concrete at elevated temperatures. The model is based on the smear crack theory. The study establishes a relationship between the splitting bond strength and the inner crack radius of the concrete. It is established by taking into account the thermal properties of the rebar and the concrete, specifically their respective differential thermal coefficient of expansions.

Later, Zhong et al. 2012 investigated the effects of fire exposure on the residual bond strength between the encased steel section and concrete. Zhong et al. 2012, considered the following parameters:

- Fire exposure time;
- Thickness of concrete cover;
- Concrete strength; and
- Tie arrangement.

Zhong et al. 2012 compared the measured bond stress-slip curves and the predictions made by an existing model. The authors opined that the influence of the thickness of

concrete cover on residual bond strength is not appropriate and significant and that there is significant bond strength deterioration after long fire exposure. On the contrary, the authors suggested that the lateral reinforcement was effective for concrete experiencing long fire exposure.

Pothisiri and Panedpojaman (2012) developed a mechanical model for predicting bond strength between rebar and concrete at elevated temperatures by incorporating smear crack theory. The authors concluded that the bond strength predictions using empirical models developed using experimental data to be un-conservative when the ratio of concrete cover thickness to rebar diameter is less than two.

2.2.4 Bond failure mechanism

The nature of bond failure is dependent on factors such as 1) rebar spacing, 2) beam width, 3) end anchorage, 4) flexural bond and 5) anchorage bond (Ferguson et al. 1966). Goto suggested that complex stress, strain and damage fields define the lug-scale behaviour at the rebar concrete interface as shown in Figure 1.14 (Goto 1971).

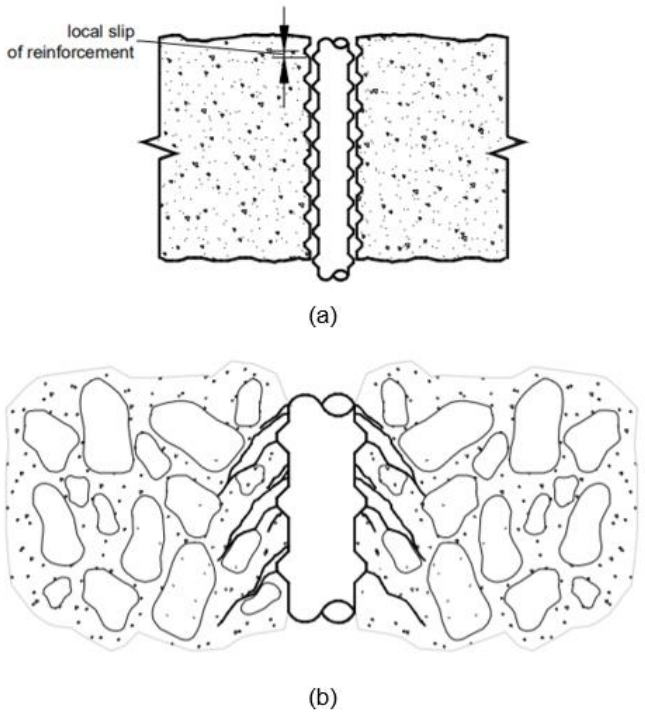

Figure 2.14: (a) Local bond response - scale of the reinforcement (b) Bond response – scale of reinforcement lugs (Goto 1971)

From the analytical and experimental studies, the authors concluded that load transfer between concrete and steel is attributed to three forces 1) chemical adhesion, 2) friction and 3) mechanical interaction of the lugs (the deformed reinforcement bearing on the surrounding concrete area). The authors also noted the mechanical interaction is quite a dominant response mechanism for ribbed rebars. Slip between the rebar and concrete is mainly due to crushing of concrete in front of the reinforcement lugs and increased level of slip (splitting of concrete due to wedging action of the lugs bearing on the concrete) (Figure 2.15).

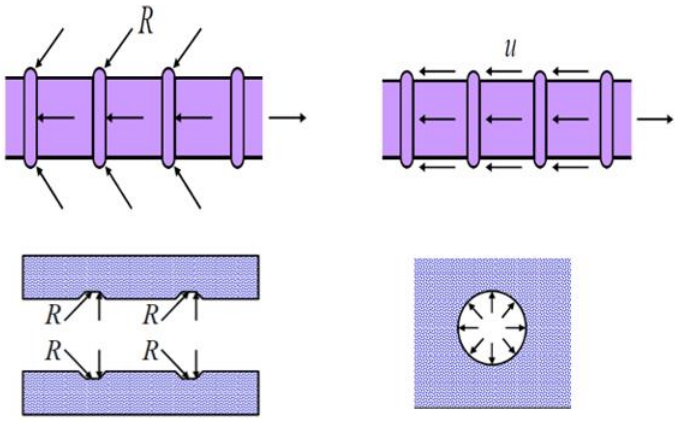

Figure 2.15: Reactive forces acting on concrete during rebar pull-out

Three modes of system failure are proposed: 1) elastic, 2) partially cracked-elastic and 3) plastic (Goto 1971, Lutz et al. 1967). The elastic mode of failure describes a system in which the concrete surrounding the reinforcing rebar exhibits a linearly-elastic material response and bond strength corresponds to the concrete carrying a peak tensile stress equal to the concrete tensile strength. The partially cracked-elastic mode of failure defines a system in which radial cracks initiate in the concrete at the concrete-steel interface but do not propagate to the surface of the specimen. The cracked concrete is assumed to have no tensile strength and bond strength corresponds to the un-cracked concrete carrying a maximum stress equal to the tensile strength. The plastic failure mode describes a system in which all of the concrete surrounding the anchored rebar is assumed to carry a tensile hoop stress equal to the concrete tensile strength (Figure 2.15).

Tepfers pioneered an analytical model in which the concrete surrounding a single reinforcing rebar is characterized as a thick-walled cylinder subjected to internal shear and pressure. In this analogy the internal shear and pressure correspond respectively to the bond and radial stresses developed at the concrete-steel interfaces. Tepfers proposed that bond strength is determined by the capacity of the concrete nearby the reinforcing bars to carry the hoop stresses (Tepfers 1979).

2.2.5 Assessment of fire damage

Although fire is one of the major adversities that can affect a structure infrequently; it may nevertheless induce unpredictable damage that could be termed severe (Folic et al. 2002, Garlock et al. 2012, Ha et al. 2016). Exposure to heat due to fire (on steel reinforcement) can cause thermal buckling or elongation of structural members beyond the strain limit of the materials employed. Such effects can lead to catastrophic failure of load bearing member and cause unbalanced load transfers from damaged members to intact members (Yaqub et al. 2011). Such catastrophic failure may allow no or significantly small time to conduct rescue operations and to minimize the damage. Two recent examples of fire related catastrophes in buildings are discussed in the following paragraph to understand the devastating loss of property as well as human lives.

Yi et al. 2015 conducted a fire assessment which showed that around 46% of the bottom reinforced concrete loadbearing structure experienced temperatures in excess of 800°C. The two central internal columns (Figure 2.17) of the building experienced temperatures close to 1300°C. The building subsequently collapsed, triggering a progressive catastrophic failure in which twenty fire fighters died and sixteen more were injured (Figure 2.16).

Figure 2.16: Hengzhou building in Hengyang city (Yi et al. 2015)

Figure 2.17: Spalling and visible reinforcement (Yi et al. 2015)

Figure 2.18: The photographs of the Plasco building – (a) During the fire (b) After its collapse (Mehmet et al. 2018)

Figure 2.19: Spalling and visible reinforcement (Mehmet et al. 2018)

Mehmet et al. 2018 documented the fire damage of the Plasco Building, a seventeen-story high-rise RC building in Tehran (Figure 2.18). The building collapsed as a result of fire; leading to several casualties. Mehmet et al. 2018 observed that the cross-section area of the some of the beams decreased as a result of spalling of concrete cover. Longitudinal rebars and stirrup were bared and direct that the flame attacked the reinforcements on many beams (Figure 2.19). Furthermore, many beams were vertically deformed and cracked with the loss of the cross-section which lead to significant material strength reduction. Bending capacity of a beam largely depends on strength and elastic modulus of the materials, cross section of the beam and reinforcement characteristics. Any significant damage to any or all of the aforementioned parameters will lead to the catastrophic failure. For the above-mentioned reasons, it is important to study and understand the behaviour of fire in the building environment. An understanding of the Fire Resistance Level (FRL) of a material allows for proper design of buildings and structural elements.

2.2.6 Fire resistance level (FRL) of reinforced concrete

Fire resistance level (FRL) of a material is the measure of the capacity of the material to resist fire with respect to 1) Structural adequacy, 2) Integrity and 3) Insulation wherein:

- Structural adequacy: Material has to show a) ability to resist the load and b) to maintain the structural adequacy under the high temperature condition;
- Structural integrity: material has to not only keep the integrity of the structure (i.e. not allowing the fire to break/damage the material) intact but also keep the integrity of materials (i.e. stop the flames to reach core of the material) intact; and
- Insulation: protects the structure from unwarranted temperature rise in the inner layer of materials.

As per the Building Code of Australia (BCA), the technical/appropriate term for fire ratings is 'Fire Resistance Level (FRL)'. It is important to understand a) what the different components of FRL are, b) how they are determined and c) what they mean in regards to passive fire protection. The FRL is a rating period represented by time in minutes without any failures. As per AS 1530.4 fire test failure criteria, it is expressed in particular order. The FRL is expressed as structural adequacy/integrity/insulation (SA/INT/INS). For example, FRL 60/60/60 means it has the structural adequacy of 60 minutes, structural integrity of 60 minutes and insulation of 60 minutes. The terms structural adequacy, integrity and insulation are defined as below:

1. Structural adequacy: It is a measure of load bearing capacity or to carry a predetermined load during fire event. As per AS 1530, the structure is deemed to fail in structural adequacy if the structure collapses or when the maximum rate of deflection exceeds the limits provided in AS 1530.4;
2. Integrity: It is the measure of fire resistance capacity of the material to restrict the passage of flames and hot gases through the material; and

3. Insulation: It is a measure of the temperature rise on the non-exposed surface of the fire-resistant separating barrier. AS 1530 limits average temperature rise to 140°C and maximum temperature rise to 180°C (Figure 2.20).

Based on the ability to resist the fire in the aforementioned three key aspects, there are various fire resistance levels (FRL) or grading periods recognised in the Australian Standards (AS 1530) such as 30, 60, 90, 120, 180 and 240 minutes. This represents the time duration up to which the material will resist the fire without undergoing any of the failure due to fire. The higher fire resistance levels are generally applicable for the insulated non-load bearing materials. For the load bearing material, the FRL levels are generally considered as 60 minutes.

The term 'Real fire' is commonly referred to the fire that can happen within buildings which are initiated either accidentally or deliberately. 'Real fire' is differentiated from the 'Standard fire'. 'Standard fire' is referenced by the deemed to satisfy (DTS) provisions of the Building Code of Australia (BCA), Australian Standards for concrete structures (AS 3600) and Australian Standards – Methods for fire tests on building (AS 1530.4); which is characterised by a standard fire temperature versus time relationship (Figure 2.20).

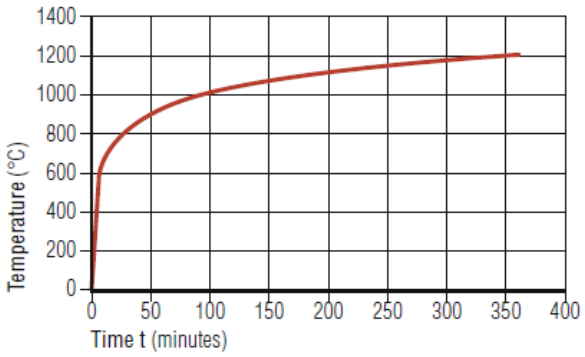

Figure 2.20: Standard time temperature curve (AS 1530.4)

Concrete structures are generally known for providing better fire resistance when compared to other equivalent building materials. When chemically fused and under normal conditions concrete is chemically inert, non-corrosive, exhibits high heat

capacity, has low thermal conductivity. It is this slow rate of heat transfer and strength loss that enables concrete to act as an effective fire shield not only between adjacent spaces but also to protect itself from fire damage. The behaviour of concrete structural members when exposed to fire is dependent on thermal, mechanical, and deformation properties of concrete. Similar to other materials, the thermo-physical, mechanical and deformation properties of concrete change substantially in temperature range that is normally associated with building fires. These properties vary as a function of temperature and depend on the composition and characteristics of concrete. The strength of concrete has significant influence on its properties at both room and high temperatures. For example, the FRL for a non-loadbearing external wall of a building of class 2, 3 or 4 is 60 minutes. A structure can however be designed to be fire resistant in two ways, i.e. 1) Active and 2) Passive. The active way of fire resistance is generally provided by the mechanism of alerting alarm, providing the insulated material to stop further spread, or providing rescue floor, escape path, sprinklers or other fire mechanism to put off the fire.

Passive fire safety covers all those aspects of fire protection that are involved in the design of a building, the building materials and the structural maintenance. Passive measures also include designing structural members with fire resisting capability such as fire resisting beams, columns, floors and walls (preventing structural collapse). Passive fire protection products and systems are named as such because they are considered to be always 'switched on' and do not require activating in order to fulfil their role. In contrast, active fire protection devices require some form of response and/or motion in order to work. Moreover, active fire protection systems are added to the building after construction, in contrast to passive fire protection system which are being part of the building itself. Structural elements can be designed with fire resistance for either controlling the spread of fire or preventing structural collapse, or both. Structural design for fire safety is a subset of fire resistance. Passive fire safety elements essentially allow more time for the fire fighters and rescue team to carry out their duties.

As noted thus far, fire related issues are significant in the construction and building industry. The design criterion for fire safety includes both active and passive

measures. However, these measures, especially for structural fire protection of concrete elements, have their own limitations. The most significant limitation is the continuous weakening of structural materials during a fire event. To overcome these limitations for structural fire design, Sadiq et al. 2013 suggested the need for employing smart material such as shape memory alloy (SMA) to enhance the integrity of the structural elements.

2.3 Shape Memory Alloy (SMA)

Shape Memory Alloy (SMA) is novel material which has the ability to return or regain their original shape or to a predetermined shape when heated. When SMA is cold (or below its transformation temperature) it exhibits relatively low yield strength and can be deformed quite easily into any new shape which it will retain. However, when the material is heated above the transformation temperature it undergoes a change in crystal structure which causes it to return to its original shape. If the SMA encounters any resistance during this transformation, it can generate extremely large forces.

In other words, remembering the original shape and restoring to its original shape under the application of thermal load is particularly unique to shape memory alloy. For the same reason they are classified as “Smart material”. This property of remembering the shape comes from the SMA’s capability of phase shift, where-in the crystal structure is reorganised. This atomic rearrangement can also occur when a stress field is imposed wherein, the thermal and mechanical fields show a reciprocal influence and the action of each of the two amends the characteristic values of the other. The two phases that exist in SMA are stable at low and high temperature respectively. The first phase at low temperature or “Cold” phase is called martensite, which gets its name from renowned German physicist Adolf Martens and the second phase which occurs at high temperature is called “hot” phase; also called as austenite or austenite phase. The hot phase gets its name after the English physicist Charles Austen. To be employed in a structural element of a building it is important to understand how the shape memory alloy works.

2.3.1 How shape memory alloy works

SMAs have two phases, each phase has a different crystal structure and therefore different properties. As mentioned earlier, the high temperature phase is called austenite (A) and the low temperature phase is called martensite (M). Austenite (generally cubic) has a different crystal structure and orientation from martensite (tetragonal, orthorhombic or monoclinic).

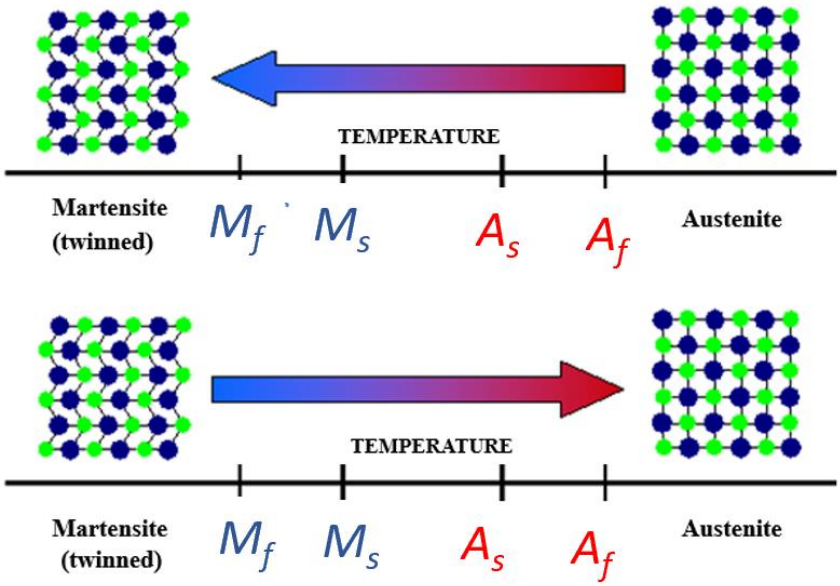

Figure 2.21: Temperature-induced phase transformation of an SMA without loading (Lagoudas, D.,C., Kumar, P., K., Introduction to Shape Memory Alloys)

A schematic of the crystal structures of twinned martensite and austenite for an SMA and the transformation between them is shown in Figure 2.21. There are four characteristic temperatures associated with the phase transformation. During the forward transformation, austenite, under zero load, begins to transform to twinned martensite at the martensitic start temperature (M_s) and completes transformation to martensite at the martensitic finish temperature (M_f). At this stage, the transformation is completed and the material is fully in the twinned martensitic phase. Similarly, during heating, the reverse transformation initiates at the austenitic start temperature (A_s) and the transformation is completed at the austenitic finish temperature (A_f) (Kumar and Lagoudas 2008).

Some SMA's also exhibit super elastic behaviour. For example, Ni–Ti alloy (a type of SMA) is associated with the recovery of the deformation upon unloading. The super elastic behaviour is observed during loading and unloading above A_f and is associated with stress–induced martensitic transformation and the reversal to austenite upon unloading. For NiTi alloy when subjected to external stress at a temperature above A_f, it deforms transforming into a detwinned martensite (which is unstable at high temperatures). However, when the load is removed the NiTi alloy transforms back into austenite and the original shape of the alloy is fully recovered. The loading and unloading paths do not coincide, with the unloading path being a lower stress plateau compared to the loading plateau. Figure 2.22 represents a typically stress–strain curve of the super elastic behaviour under particular load and unload condition.

An SMA exhibits the shape memory effect (SME) when it is deformed in the twinned martensitic phase and then unloaded while at a temperature below A_s. When it is subsequently heated above A_f, the SMA will regain its original shape by transforming back into the parent austenitic phase as shown in (Figure 2.23).

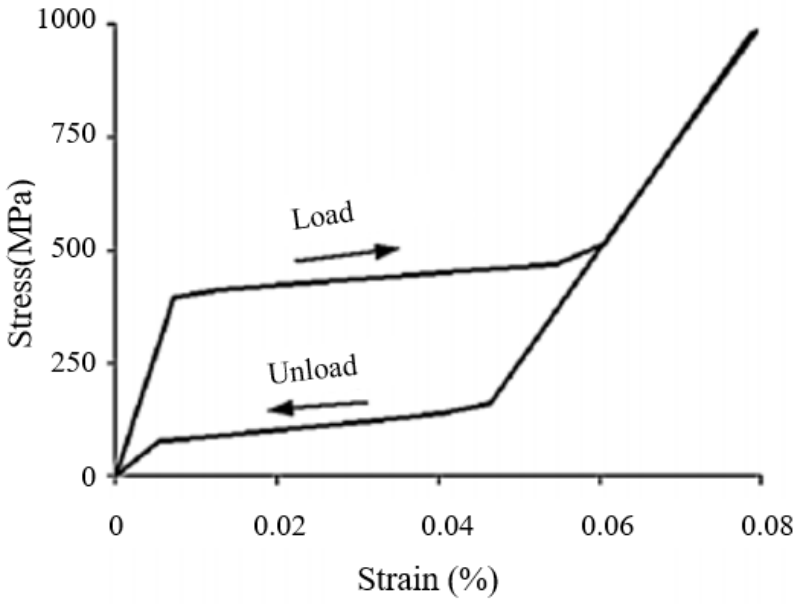

Figure 2.22: Stress–strain curve of the super elastic behaviour (Lagoudas D.C and Kumar P.K)

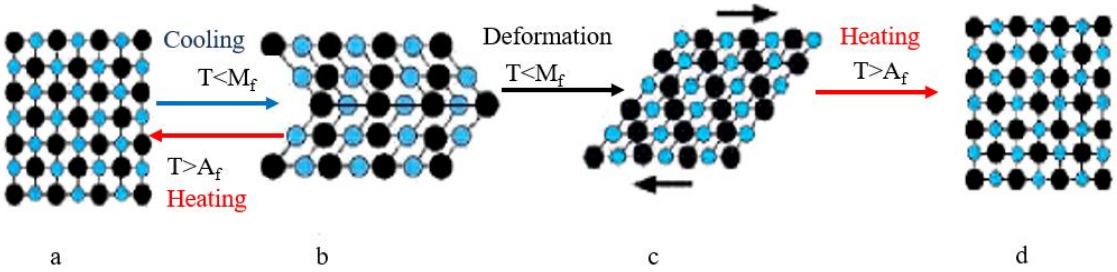

Figure 2.23: A-Original parent phase, b-self-accommodated martensite, c-deformation in martensite, d- reverse transformation (upon heating above A_f)

2.3.2 NiTi Based shape memory alloy

Shape memory alloy can be categorised into copper based, iron based and NiTi based. The NiTi alloy system has been studied most extensively and is used in the greatest number of commercial applications. This NiTi alloy exhibits strong Shape Memory Effect (SME), Two Way Shape Memory Effect (TWSME), and pseudo elastic behaviour under the right conditions, which make this material ideal for a variety of applications. It also exhibits resistance to corrosion and is biocompatible, making it suitable for use in biomedical applications. Compared to the less widely used alloys, the crystallography and thermomechanical properties and response of NiTi are well understood, as are the effects of heat treatment and the variation of transformation temperatures with changes in composition. In this section we briefly discussed the NiTi system, including the NiTi based ternary alloys.

The nature of the NiTi alloy can be better understood by following the thermomechanical processing and loading path in a combined stress-strain-temperature space as shown in Figure 2.24; where NiTi specimen is tested under uniaxial loading. The stress σ is the uniaxial stress on the specimen due to an applied load. The corresponding strain ε is the change in the length of the specimen along the direction of applied load, normalized by the original length starting from the parent phase (point A in, the stress-free cooling of austenite below the forward transformation temperatures (M_s and M_f) results in the formation of twinned martensite (point B) (Figure 2.24).

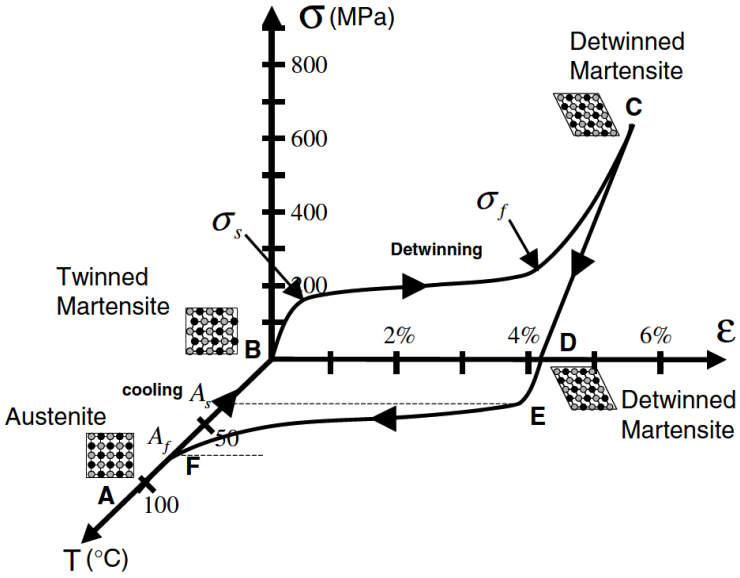

Figure 2.24: Shape memory effect in SMA (Lagoudas, D.,C., Kumar, P., K., Introduction to Shape Memory Alloys)

When the twinned martensite is subjected to applied stress that exceeds the start stress level (σ_s), the reorientation process is initiated, resulting in the growth of certain favourably oriented martensitic variants that grow at the expense of other less favourable variants. The stress level for reorientation of the variants is far lower than the permanent plastic yield stress of martensite. The detwinning process is completed at a stress level, σ_f, that is characterized by the end of the plateau in the σ-ε diagram in Figure 2.24. The material is then elastically unloaded from C to D and the detwinned martensitic state is retained. Upon heating in the absence of stress, the reverse transformation initiates as the temperature reaches A_s, (at E) and is completed at temperature A_f (point F), above which only the parent austenitic phase exists. In the absence of permanent plastic strain generated during detwinning, the original shape of the SMA is regained (indicated by A). The strain recovered due to the phase transformation from detwinned martensite to austenite is termed as the transformation strain (ε_t). Subsequent cooling to martensite will again result in the formation of self-accommodated twinned martensitic variants with no associated shape change, and the whole cycle of the SME can be repeated. The above described phenomenon is called one-way shape memory effect, or simply SME, because the shape recovery is achieved only during heating after the material has been detwinned by an applied

mechanical load. Where applications involve high temperature, special NiTi alloys are employed as SMA.

2.3.3 High Temperature Shape Memory Alloys

High Temperature Shape Memory Alloys (HTSMAs) are a unique class of SMAs that have transformation temperatures greater than 100°C and are capable of actuating under high temperature deformations and conditions. These alloys are produced by adding ternary elements such as palladium, platinum, hafnium, gold, and zirconium to NiTi, for which the transformation temperatures can be shifted anywhere in the range of 100‑800°C. The primary limitations of HTSMAs are that the transformation strains associated with the material are approximately 3%, and that these materials have a low critical stress for slip.

2.3.4 Surface condition of the SMA bar

In general, steel rebars possess ribs and lugs with rough surface finish. Such rough surface finish provides good surface for bonding with concrete and enables the transfer of forces through mechanical interlock and friction. In sharp contrast, SMA rebar surface is typically smooth with no ribs or lugs. In addition, it is not only very hard to machine the SMA rebar machining activities such as threading. However, such operation may reduce the bar strength significantly (Alam et al. 2007). A method of addressing the smooth surface finish issue is by coating the rebar with some granular material. Such coatings improve the surface friction and provide additional resistance in order to transfer the bond forces through the bar. Sand coating on steel rebars using epoxy adhesive was experimented by Muntasir et al. 2016, to provide an understanding of the bond stress in such SMA rebars at room temperature. Different rebar diameter (20 mm and 32 mm), length of sand coating and grain size of sand used for coating (Figure 2.25) were considered by Muntasir et al. 2016.

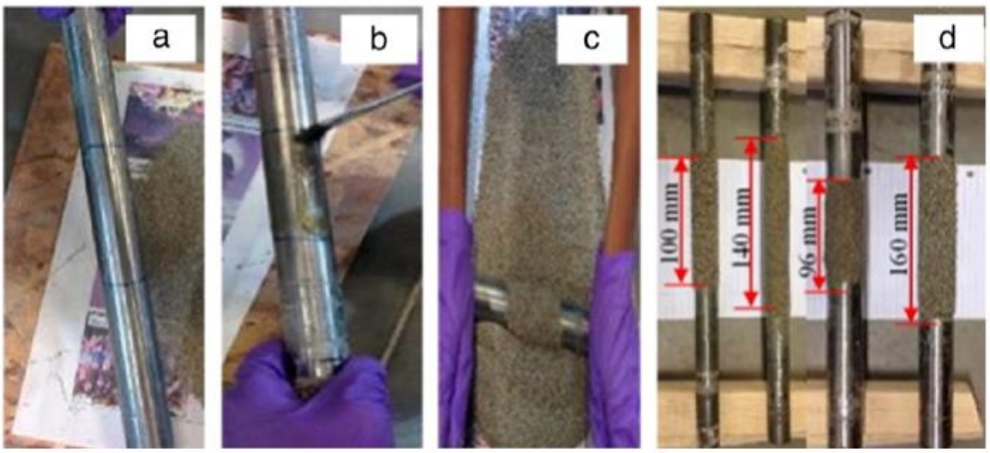

(a) bonded length, (b) epoxy application (c) sand coating and (d) sand coated rebars

Figure 2.25: Sand coating of SMA rebar (a) Bonded length (b) Epoxy application (c) Sand coating (d) Sand coated rebars (Muntasir et al. 2016)

Based on the experimental outcomes, Muntasir et al. 2016 reported that there is significant increase in bond stress with the increased sand grain size coating (Figure 2.26). The authors also suggested an empirical formula to include the sand roughness factor to evaluate the increased bond stress.

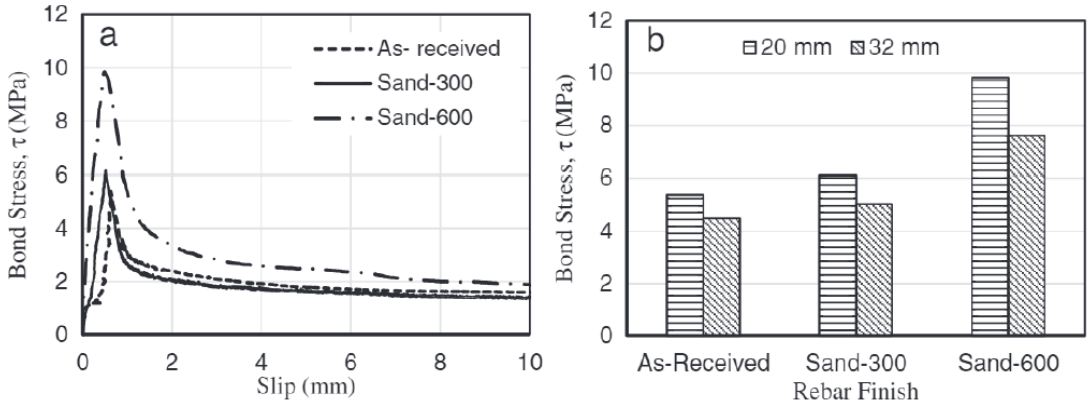

Figure 2.26: Effect of sand coating on SMA rebar at room temperature (Muntasir et al. 2016)

2.3.5 Passive design for increasing the FRL in SMA-Concrete

Hybrid reinforced concrete using steel and SMA rebars can be designed considering the varying properties of concrete, steel and SMA. The difficulty to determine the temperature rise in concrete beam is addressed by the 500°C isotherm method' given in Eurocode 2 (2004). The 500°C isotherm method is a simplified procedure to

determine the virtual reduction in size of the cross-section of the concrete beam at high temperatures. It is based on standard fire test results. So far researchers have studied various sizes of beams heated to different fire resistance periods, namely from 30 minutes up to 240 minutes.

The hypothesis has been made to understand that any element with a temperature higher than 500°C in the cross-section of the concrete beam is assumed to have no strength, whereas the remaining area is assumed to have properties pertaining to room temperature (Figure 2.27). For example, Wong et al. 2014 studied the bending moment capacity of a reinforced concrete beam at high temperature based on Isotherm 500.

Based on the understanding of SMA and concrete thus far, it can be said that SMA reinforced concrete beam will exhibit better performance characteristics compared to conventional RC beam in a fire event. SMA behaviour under fire can be combined with reinforced concrete and a composite SMA-steel reinforced concrete section can be designed to have an increased strength under fire conditions. This will also allow the structure to increase the fire resistance levels (FRLs).

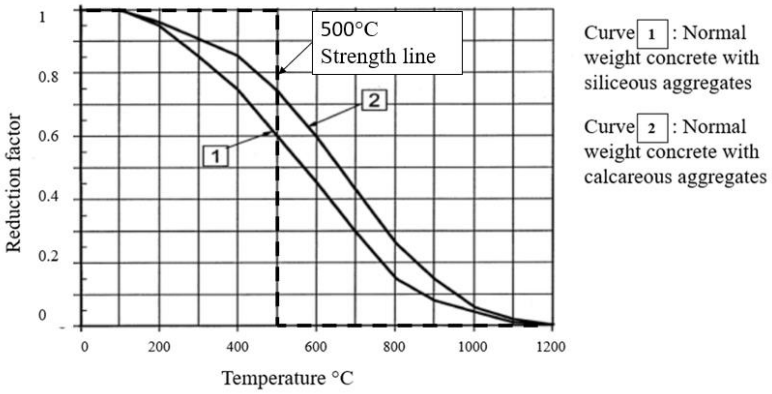

Figure 2.27: Concrete strength used in 500°C isotherm method (from Eurocode 2)

Wong et al. 2014 considered the use of SMA and steel reinforcement in concrete. The considered a rectangular cross-section width b (200mm), effective depth d (300mm), and steel and SMA as reinforcements being placed at the same depth (Figure 2.28).

The authors derived the bending moment capacity (M_u) of the section as a function of the temperatures as shown in
Equation 2.3.

$$M_u = \left(A_s f_{sy} + A_{SMA}\sigma_{SMA}\right)d\left(1 - \frac{1}{2\alpha_2}\frac{\left(p_1 f_{sy} + p_2\sigma_{SMA}\right)}{f_c'}\right) \qquad \text{Equation 2.3}$$

where,
A_s = steel area, f_{sy} = yield stress of steel, ASMA = SMA area, σ_{SMA} = stress in SMA, p_1 = steel area ratio of the cross-section, p_2 = SMA area ratio of the cross-section, $f_{c'}$ = characteristic strength of concrete.

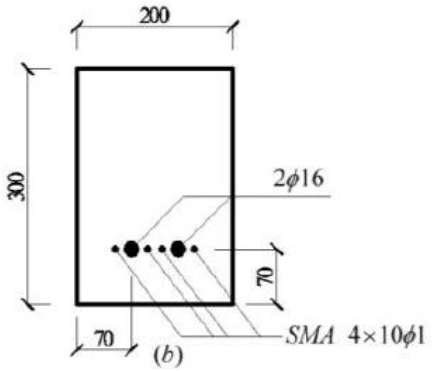

Figure 2.28: Hybrid SMA-Steel reinforced concrete beam (Wong et al. 2014)

Wong et al. 2014 demonstrated that the bending moment capacity of a hybrid steel-SMA reinforced concrete beam can be optimised by varying the distances of both the steel rebars and SMA wires such that a unique set of axial distances for the steel and SMA can be obtained. The authors further reported that there is a gain in the bending moment capacity with the duration of fire and/or with the increase in the temperature (refer Figure 2.29).

Wong and Liu (2013) identified two major factors which are interrelated and influence the ultimate bending capacity of the beam in fire. The two main factors are 1) total area and 2) axis distance (concrete cover) of the reinforcements. More the area of

reinforcement greater the bending capacity of the beam would be. Moreover, the position of reinforcements in the concrete section also make a difference in the bending moment capacity. When the concrete cover is more i.e. when the Steel and SMA rebars are located further from exposed surface, for the same fire duration exposure there will be lower temperature which will bring higher strength but on the other hand more the reinforcement towards the centre of section lower will be the moment capacity. Figure 2.29 shows the plot of ultimate bending moment as presented by the authors Wong and Liu (2013) for two particular cases of hybrid reinforcement i.e. SMA and Steel.

1) Cs = Csma = 70mm
2) Cs= 75mm: Csma= 85mm

Where, Cs and Csma indicate the cover distance of steel and SMA respectively. The sharp drop in bending moment is due to the loss in the cross-section area and cover to the reinforcement. The steel reinforcement loses the strength significantly with the rising temperature and the temperature after 80 mins is over 900°C. Moreover, SMA can be strengthened for up to around 400°C beyond which its strength will drop as well. Therefore, delaying the temperature rise in SMA using appropriate concrete cover SMA have been implemented in many civil and structural engineering application.

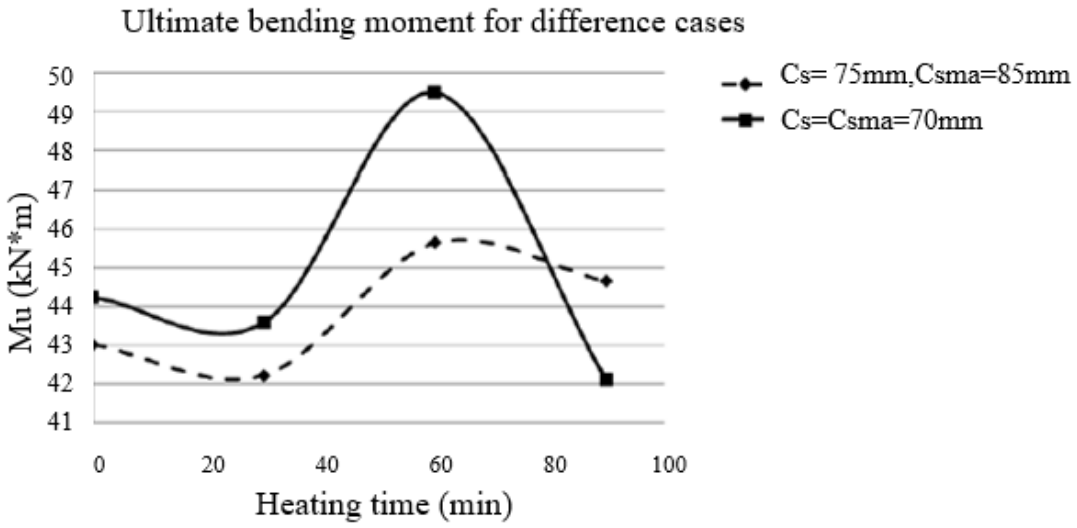

Figure 2.29: Plot of bending moment of hybrid SMA-RC beam with fire duration (Wong et al. 2014)

Considering this unique characteristic that SMA's exhibit, many applications in civil and structural engineering have implemented.

2.4 Application of SMA in Civil and Structural Engineering

Graesser et al. 1991 successfully used NiTi SMA for damping of seismic loads while Wittig et al. 1992 employed SMAs as a tension damper (where the bending and torsional characteristics of SMA are used). Cardone et al. 2004 compared his work on super elastic bracing of RC-frames with classic steel bracings. A real scale application of a super elastic SMA device can be found in an earthquake restraint (Castellano et al. 2000). The historic gable was connected with the main structure using SMA rods (Figure 2.30). The NiTi SMA rods were subjected to tension, although they were designed to take tension and compression forces (Menna et al. 2015).

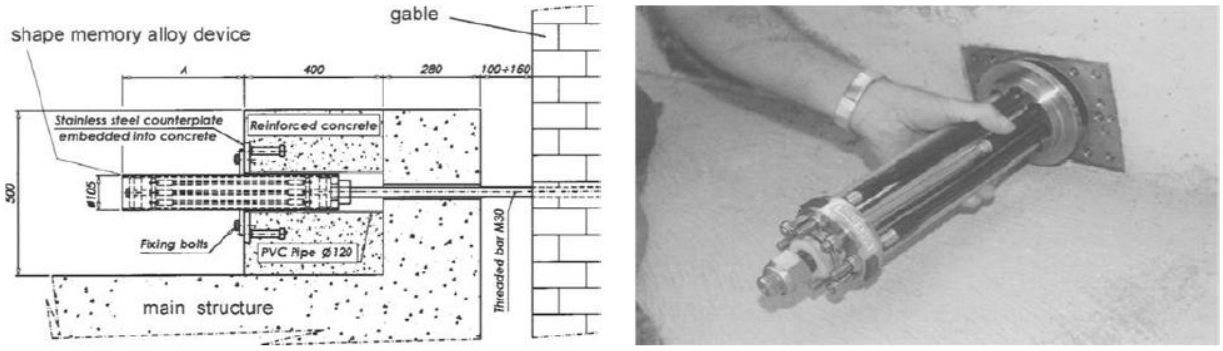

Figure 2.30: SMA device for earthquake suitable connection of historic gable (Menna et al. 2015) Applications of Shape Memory Alloys in structural engineering)

SMA was also used in a retrofit project of a bell tower (at the Church of San Giorgio, Italy (Figure 2.31)) requiring earthquake protection. In the case of the bell tower, steel tendons were added to increase the tilt resistance with intermediary super elastic SMA devices to act as load limiters to prevent the masonry from compression failure.

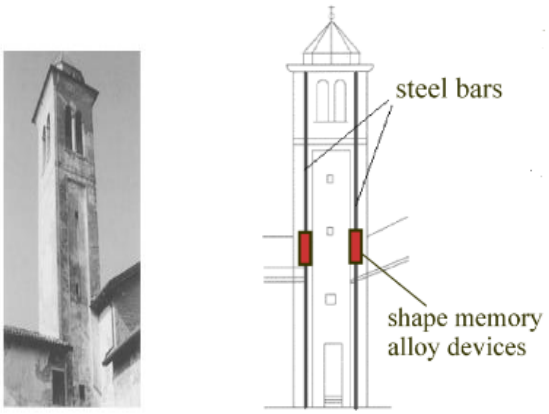

Figure 2.31: behaviour of incorporated SMA devices (Menna et al. 2015)

In another striking application, Sadiq et al. 2013 demonstrated that the Steel-NiTi composite beam showed up to 3 times increase in the stiffness where the temperature of the NiTi (Shape memory alloy) went to 300°C under the fire event (Figure 2.32).

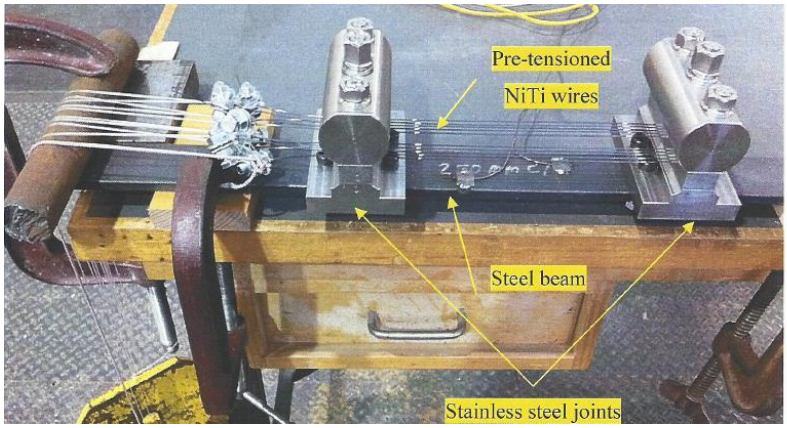

Figure 2.32: SMA wire Steel beam composite beam (Sadiq et al. 2013)

Song et al. 2007 introduced a concept of intelligent reinforced concrete (where the actuation property of the SMA is exploited) in SMA wires. Stranded martensite SMA wires were used for post-tensioning reinforced concrete specimens. By heating the SMA wire through electricity, the wires contracted the concrete structure and hence reduced the crack openings. This concept was successfully employed to rehabilitate a concrete structure.

Later, Li et al. 2008 proposed a two-phase repair method for RC beams strengthened with CFRP (carbon fiber reinforced plastic) plates in combination with SMA. RC specimens were temporarily strengthened by SMA wires (heated by electrical current), resulting in the generation of a recovery force which in turn reduced the deformation. When the permanent mid-span deformation under load is under the acceptable limit, then the CFRP plate was bonded to the bottom of the specimen using epoxy resins, completing the strengthening process called the permanent damage repair process (Figure 2.33).

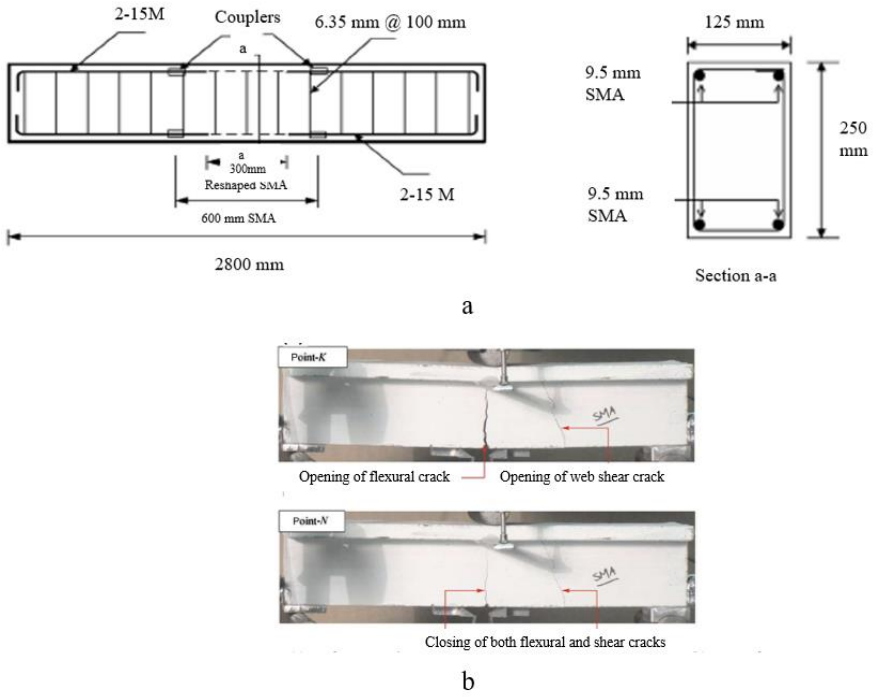

Figure 2.33: (a) SMA Reinforcement details (b) Test performed with SMA rebars (Li et al. 2008)

The absence of flexural ductility is a common problem in bridge pier especially under large displacement demands of ground motion. To improve the ductility and the strength of reinforced pier or columns, a technique called the lateral confinement of concrete is used. In this technique, the pressure is applied perpendicular to the direction of the loading. Both passive and active concrete confinement techniques are employed to achieve the desired results. In the case of active confinement, SMA-based systems were proposed, mainly due to their shape memory effect and their

ability to recover their original shape after experiencing large deformations without the need of mechanical prestressing.

Shin and Andrawes (2010) investigated the uniaxial compression behaviour of concrete confined with (NiTi) SMA spirals; used either solely or in conjunction with glass fiber reinforced polymer wraps. SMA wires were initially restrained to approximately 6% strain and then wrapped around the concrete element in the form of a spiral; after heating, the SMA spirals were activated through the shape memory recovery, resulting in a large confining pressure on the wrapped element.

Similarly, Choi et al. 2010 reported that the SMA wire jackets increased the ultimate strength and the ductility compared to the plain concrete cylinders without flexural strength degradation (Figure 2.34). The authors based their observation on the experimental tests on concrete cylinders and RC columns (0.4 m in diameter and 1.4 m in height) confined with NiTiNb and NiTi wires (400 mm height with 2 mm pitch). The high recovery stress by shape recovery of SMAs provided a reliable external active confining pressure on RC bridge columns by improving the column ductility. Also, the analytical results obtained under displacement-controlled cyclic loading and a suite of strong earthquake records revealed that, the SMA retrofitted columns exhibited an increase in strength that was 38% higher compared to carbon fiber reinforced polymer (CFRP) wrapped columns. Further Andrawes et al. 2010 observed that there was improvement in effective stiffness and column residual drifts in cases where SMA was employed.

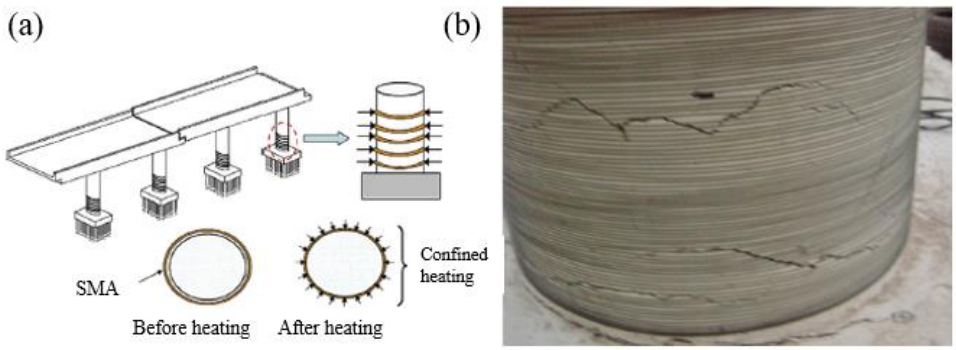

Figure 2.34: (a) Schematic illustration the concept of using pre-strained SMA hoops to apply external confining pressure on RC bridge columns (b) SMA confined test specimen after cyclic compressive test

SMA materials have its inherent physical properties of increasing stiffness and strength at increasing temperature. Sadiq et al. 2013 showed that the recovery stress of SMA increases around 300°C; after this temperature the recovery stress starts to decrease. Figure 2.35 shows the tensile test results of NiTi-based SMA at high temperature. For example, restraining the strain recovery of the SMA wire pre-strained at about 4%, a recovery stress of 1400 MPa is generated when heated from room temperature to 200°C. However, it can be seen from Figure 2.35 that at around 600°C, only small amount of recovery stress remains though high ductility is still maintained. Therefore, SMA can be used for structural fire protection applications more effectively as long as SMA materials can be insulated for the desired fire resistance period.

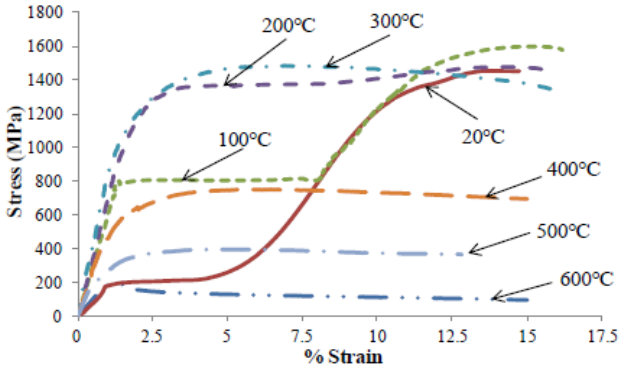

Figure 2.35: Stress – Strain curve of SMA under high temperature (Sadiq et al. 2013)

Besides civil and structural engineering applications the SMAs have found their way into other commercial applications.

2.5 Other Applications of shape memory alloy

The application of SMA can be found in a wide variety for industrial sectors such as aerospace, automotive, biomedical, oil exploration and construction. Over the past decade, the SMAs have been explored for their microstructural mechanisms, engineering effects and applications of shape memory alloys in general engineering. Some of these are presented below.

2.5.1 Aerospace

The first successful demonstration of a shape memory alloy for U.S. Navy F-14 fighter aircraft was Cryofit tube coupling (Figure 2.36).

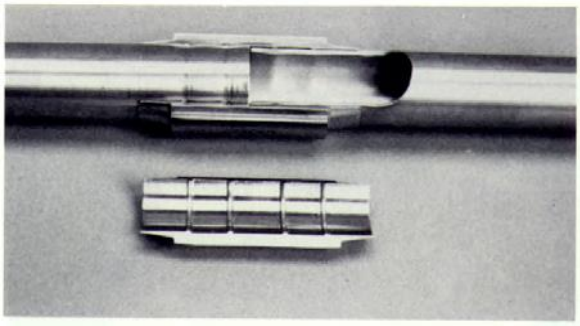

Figure 2.36: SMA Cyrofit tube coupling

Another application of SMA in the aircraft industry is to optimize the trade-off between noise mitigation (at take-off and landing) and performance at altitude. Such engine noise levels are often highly regulated by various civil agencies. Often flow mixing devices known as “chevrons” are statically installed along the trailing edges of the exhaust nozzles (Figure 2.37). Here the composite chevrons were designed to be reconfigurable with SMA beam components embedded inside. In addition, actuation was based on the principle of changing flow temperature with altitude. The SMA beam elements are formed such that they force the chevron inward and mix the flow of gases (reducing noise) at low altitudes and low speeds where the engine temperature is high. They then relax and straighten up at high altitude and high speeds, increasing engine performance.

Figure 2.37: SMA composite chevron

2.5.2 Automotive

Eric et al. 2010 developed a second generation SMA-actuated mirror (Figure 2.38). A robust control algorithm was developed for the mirror to provide stable and accurate positioning.

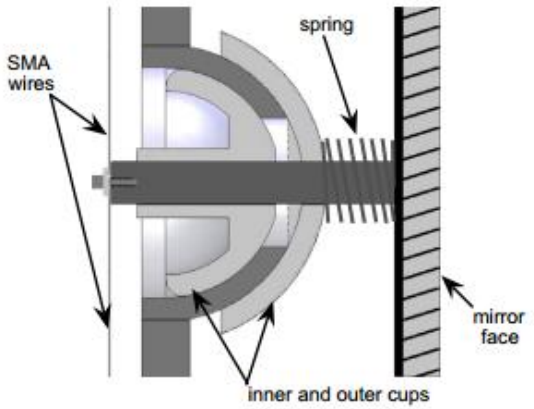

Figure 2.38: SMA-actuated mirror

In another example, an SMA oil controller was developed for the purpose of reducing loss in stirring lubricant in a gear of a Shinkansen, a Japanese bullet train. In the train, lubricant contained in a gearbox is dispersed by a pitch wheel and directly splashed on bearings (Figure 2.39). This lubricating method is not adequate for a high-speed Shinkansen, (because the high ram speed increases lubricant stirring loss). Particularly in the case of a rapid Shinkansen, such loss is significant, raising gear temperature (Kato 2011). The SMA oil controller addressed the above-mentioned issues.

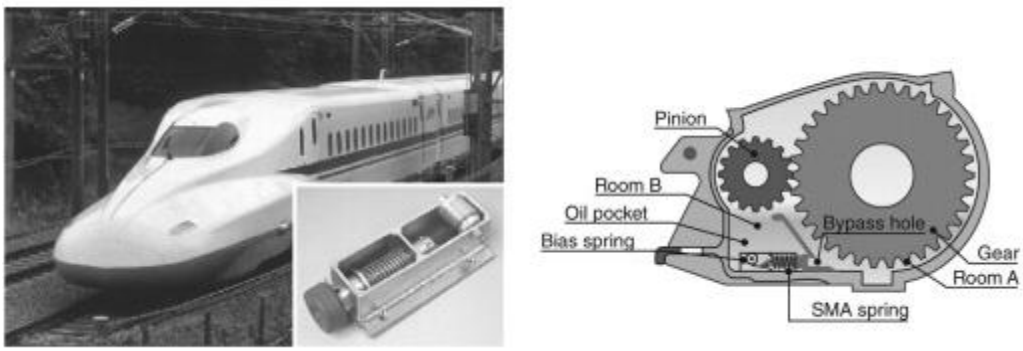

Figure 2.39: Automatic oil valve adjusting device for the Shinkansen

2.5.3 Bio-medical

The very first cardiovascular device developed with shape memory alloy was the Simon filter. The Simon filter (Figure 2.40) represents a new generation of device that is used for blood vessel interruption in order to prevent pulmonary embolism. Patients who cannot take anticoagulant medicines are the major users of the Simon filter. The purpose of this device is to filter clots that travel inside the bloodstream (Machado and Savi 2003).

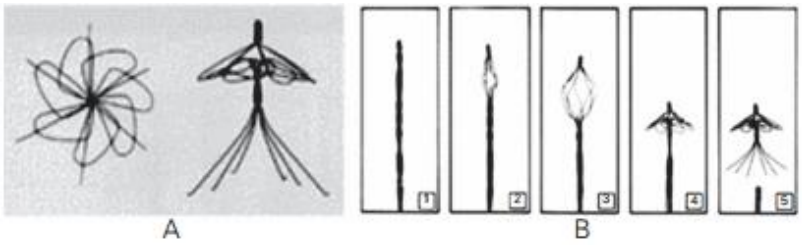

Figure 2.40: Simon filter: A-filter in the recovery form, B- filter release

Self-expanding stents is yet another important cardiovascular application that is used to maintain the inner diameter of a blood vessel. In this type of application, a cylindrical scaffold with shape memory (Figure 2.41) is placed, for example, reaching inside a blood vessel through a catheter. Initially, this scaffold is pre-compressed in its martensitic state. As the scaffold is heated, due to the body temperature, it tends to recover its original shape, expanding itself. This technique is employed in the treatment of aneurysms; a support mechanism for weakened vessel.

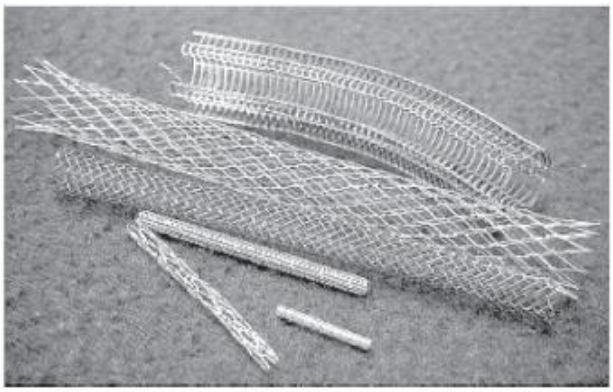

Figure 2.41: Self-expanding stents

Another application can be found in the orthopaedic area and is related to the healing process of broken and fractured bones. Several types of shape memory orthopaedic staples are used to accelerate the healing process of bone fractures, exploiting the shape memory effect. The shape memory staple, in its opened shape, is placed at the site where one desires to rebuild the fractured bone. Through heating, this staple tends to close, compressing the separated part of bones. It is important to note that an external device performs the heating, and not the temperature of the body. The force generated by this process accelerates healing, reducing the time of recovery. In Figure 2.42 an application of these staples during the healing process of a patient's foot fracture is shown.

Figure 2.42: (A) Orthopedic staples, (B) Staples placed in human foot, (C) X-ray showing staple

With respect to the healing of fractured bones, it is important to note that shape memory plates are also used for the recovery of bone. These plates are primarily used in situations where a cast cannot be applied to the injured area, i.e., facial areas, nose, jaw and eye socket (Figure 2.43). The plates are placed on the fracture and affixed with screws, maintaining the original alignment of the bone and allowing cellular regeneration. Because of the shape memory effect, when heated these plates tend to recover their former shape, exerting a constant force that tends to join parts separated by fractures, helping with the healing process (Figure 2.43).

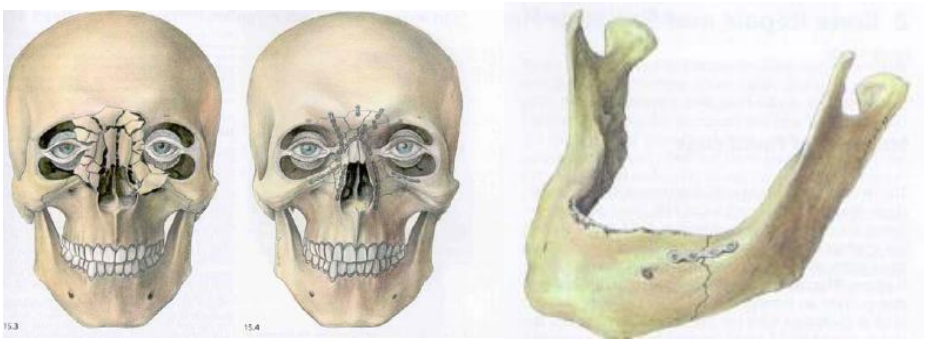

Figure 2.43: SMA plates used to repair injured area

2.6 Concluding remarks on literature survey

From the literature survey it can be concluded that reinforced concrete loses its strength significantly under increased or elevated temperature condition and as such this can lead to catastrophic failure of a structure leaving a short time frame for rescue and fire prevention operation. From the case studies of fire damage and other failure, it can be said that there is an opportunity for increasing the fire resistance level especially from the structural adequacy point of view through a passive method. It is well understood and elaborated in the literature that SMA's possess a unique quality of gaining in strength with increase in temperature. SMA's have been used in civil engineering applications for retrofitting structures such as closing the shear crack in beam, increasing the ductility of the column or bridge piers, relocating bridge at deck-abutment interface to reduce the hinge opening etc. However, the SMA used in such civil applications was very much restricted to the use of wires and mostly in external application only. A novel concept of hybrid reinforced structure has been studied analytically (Wong et al. 2014) which showed significant improvement in the bending moment at around 1-hour fire duration, and as a consequence increases the FRL (Fire resistance level) of system. This is because at room temperature the stronger steel reinforcement with higher yield stress can compensate for the weaker SMA wires whereas at high temperatures the stronger SMA with high recovery stress can compensate for the weaker steel.

Wong et al. 2015, demonstrated further advantage of SMA RC by studying a 4m long simply supported concrete beam reinforced with both steel bars and SMA wires

subjected to 3-sided fire attack of a standard fire. The total area of steel was 320mm^2 and that of SMA was 59 mm^2 embedded in a rectangular cross-section beam (180mm × 250mm). For comparison purposes, the same beam with and without SMA are studied. The response of both the bending moment capacity and the mid-span deflection under a load of 20kN were calculated. The results of the analysis for the first 30 minutes of the standard fire are shown in Figure 2.44 and Figure 2.45. In the case of the beam with SMA, both the bending capacity and deflection remain virtually unchanged whereas the one without SMA has the bending capacity deteriorated by 14% and the deflection increased by 37% at the end of the 30 minutes of fire. The increase in ultimate bending moment capacity and reduction in displacement under high temperature under fire conditions shows potential of SMA to be used as hybrid SMA RC beams.

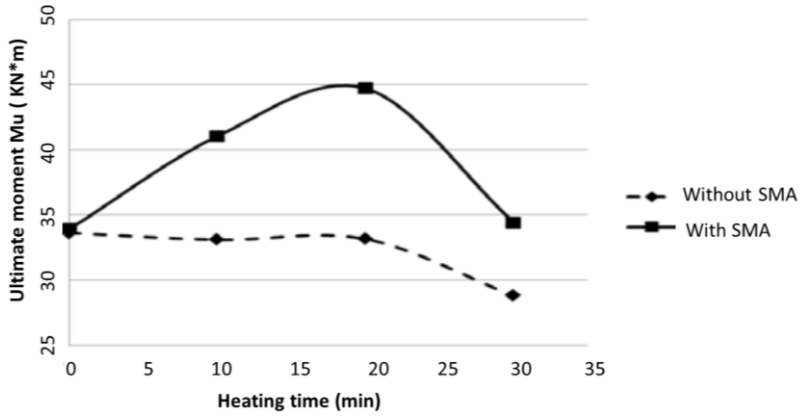

Figure 2.44: Bending moment capacity – concrete beam with and without SMA (Wong et al. 2015)

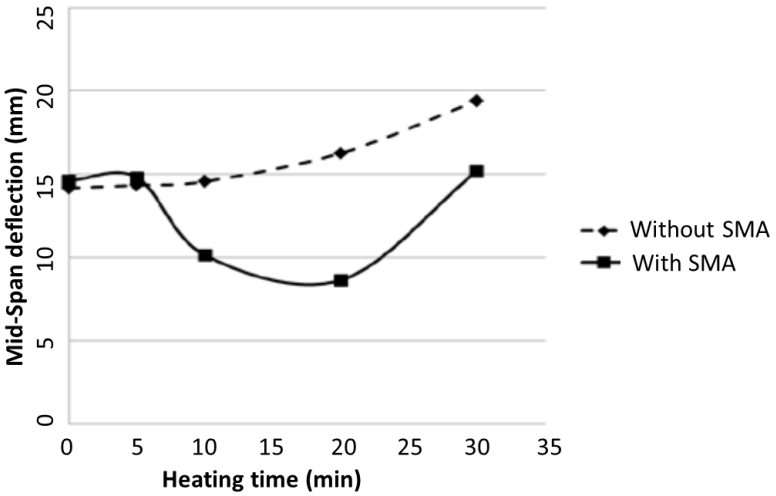

Figure 2.45: Mid-span displacement – concrete beam with and without SMA (Wong et al. 2015)

Bond stress is understood to be a critical aspect governing the SMA-concrete interaction at the concrete-rebar interface and more so at elevated temperatures. The interaction is a complex mechanism that is dependent on various aspects including rebar surface characteristics, concrete properties, heating conditions and other characteristics. Only a very limited number of studies considered the incorporation of temperature induced bond degradation in evaluating fire resistance of RC structural members. The swapping of SMA for steel rebar in steel reinforced concrete beam is understood to increase in the stiffness at high temperatures. Likewise, the bond strength is also a vital aspect when the performance of reinforced concrete is considered. There exists very limited literature on the bond behaviour of SMA under very high temperature (during the fire event). Significant amount of literature is available on SMA wires which are found to be used to retrofit structures externally. However, SMA-RC rebar embedded in concrete (Reinforced Concrete with Shape Memory Alloy rebars) has not been studied.

The significant gaps in the literature are presented below. These gaps form the basis to establishing the specific aims and respective objectives of this thesis.

2.7 Gaps in the Literature review

From the extensive literature survey carried out on the SMA for civil engineering applications the following three significant gaps have been identified:

1. While SMA wires were subject to several studies as passive measure to improve the fire resistance level and for its use in external application of a structure, very limited number of studies examined the use of SMA rebars as reinforcement inside the concrete. Also, there is complete absence of any studies on the reaction and bond behaviour of SMA rebar-concrete at high temperature (experienced typically during a fire event). Such a study is critical to establish the suitability of SMA rebar as reinforcement in hybrid reinforced concrete structure.

2. Numerical modelling for bond slip in steel rebar and concrete is extensively covered in the literature. However, no literature is available on numerical

modelling of SMA-concrete bond strength behaviour under very high temperature. The development of such numerical model will assist in the development of non-destructive parametric studies that are cheaper and quicker to perform. The product development cycle of SMA-concrete elements can be shortened several folds when such numerical models are developed.

3. The literature also lacks any quick assessment tools to gauge the bond stress of SMA-concrete that is exposed to high temperature in a fire event. Such an assessment tool will assist design engineers to quickly asses the FRL of the reinforced concrete that are made with SMA rebars.

Based on the above identified gaps in the literature, the specific aims and objectives of this thesis are developed and are as presented below.

2.8 Specific Aims and Objectives

The three specific aims of this thesis address the three gaps identified in the previous section respectively. The three main aims and their objectives are presented below.

AIM 1

Conduct experiments to examine and develop two data sets on the bond stress between 1) SMA rebars and concrete and 2) Steel and Concrete in the cohesive zone and to also study the strength of SMA-Concrete specimens in conditions that replicate a fire event. The objectives of which are to:

- Develop a theoretical framework that is based on established principles from the literature that aids in the design of experiments on SMA-Concrete elements;
- Prepare specimens;
- Design of concrete;
- Characterisation of SMA to identify the maximum operational temperature for heat treatment in order to train the material for its memory retaining ability;
- Heat treatment of SMA rebars to achieve shape retaining ability;

- Design and development of jigs and fixture for concrete moulds;
- Preparation and casting of concrete specimens for pull testing;
- Identify suitable equipment and instruments and prepare for installation and setup;
- Identify all relevant equipment and instruments that assists in collecting the data of interest;
- Install all instrumentation such as thermocouples, thermometers, load cells etc. at a suitable time on to the test apparatus;
- Conduct risk assessment of the test rig and the location surrounding the same to prevent any unwarranted event. Address any issues as required;
- Design and develop the experiment apparatus which includes equipment and instrumentation that would assist in the conduct of experiments and capture the relevant data;
- Install the test apparatus as per the design of experiments;
- Install instruments and equipment as per the design requirement;
- Simulate fire conditions in the furnace using fire curve data;
- Conduct pull test and record all relevant data;
- Conduct tests at various temperatures, different fire duration and for different concrete samples with varying rebar materials and depths; and
- Document all data for further use.

AIM 2

Develop a numerical model to study the bond stress and bond slip behaviour in the cohesive zone of SMA-Concrete and Steel-Concrete specimens under various fire conditions; the objectives of which are;

- Establish the numerical framework;
- Develop numerical models;
- Validate the developed model against studies in literature;
- Examine the bond stress behaviour at the cohesive zone using appropriate modelling tools and data gathered from physical experiments;

- Identify a suitable numerical model to study and characterise the bond stress between rebar and concrete in the cohesive zone;
- Adopt data generated from physical experiments carried out in AIM 1 as required
- Conduct numerical experiments using CZM bilinear modelling;
- Obtain required data sets for use in the study;
- Conduct numerical experiments to study bond stress behaviour between the SMA-Concrete and Steel-Concrete specimens on the whole by employing the validated Numerical model and inputs from the CZM bilinear modelling that fully takes into account both the thermal and structural conditions;
- Develop CAD Model of the domain of interest;
- Apply suitable meshing conditions and generate the mesh;
- Select suitable material properties for the components of the specimen;
- Apply boundary conditions and perform transient Thermal analysis based on temperature time fire curve;
- Utilise appropriately the data from the Thermal analysis to examine the structural response of the specimen using Structural analysis incorporating the data available from the CZM bilinear modelling;
- Follow the above steps and conduct parametric studies on various specimens developed; and
- Document results for a comparative analysis between physical and numerical experiments.

AIM 3

Development of empirical equation for the quick assessment of bond stress based on numerical model developed in AIM2. The objectives of which are;

- Regression analysis of parametric study;
- Empirical equation considering the effect of the parameters affecting bond stress; and
- Validation of empirical equation with experimental studies results

CHAPTER 3: Experimental Studies

3.1 Introduction

This chapter outlines the details of the experiment design and methods undertaken in this work to address a research aim discussed in Chapter 2. The manner in which this chapter fits into the thesis organisation can be identified in Figure 3.1. In the previous chapter a comprehensive survey of literature was undertaken to understand the topic of SMA-concrete and related bond stress which led to identifying the gaps in the literature on the above said topic. The gaps helped develop the three aims of this thesis. One of the aims is addressed in this chapter. More specifically, the Aim 1 of this research is:

- To conduct experimental studies to understand the bond stress behaviour of concrete-steel rebar and concrete-SMA rebars that are subjected to high temperature

Essentially the objectives that assist in successfully achieving the Aim 1 are as follows:

- Develop a theoretical framework that is based on established principles from the literature that aids in the design of experiments on SMA-concrete;
- Prepare of experimental setup allowing the sample to be heated to a high temp as per standard fire curve;
- Identify and setup the equipment's to apply loading, measurements, recording etc.;
- Characterisation of SMA and preparing the samples;
- Casting of concrete pull-out test specimens; and
- Performing the pull-out test at various temperatures

All aspects concerning the theoretical framework, the design of experiments, the method and conduct of physical experiments, the specimen preparation methodology, the various specimens developed for the experimental studies, the equipment and

instruments employed in the course of experimentation, the experiment process and procedures that leads to the generation of various data sets are dealt with in this chapter. Such data sets are further employed in the development of numerical models and experiments in Chapter 4 and in the Results section of this Thesis (Chapter 5).

The results and discussion on the physical experiments concludes in this chapter with the development data sets on the bond stress and displacement values of the various specimens involved there by achieving the Aim 1 of this thesis. Such data sets are further employed in the development of numerical models and experiments in Chapter 4 and discussed in the Results section of this thesis (Chapter 5). The manner in which the Aim 1 and the corresponding objectives were achieved is presented as follows.

Chapter 1 Problem identification and definition

Statement of purpose | Background | Purpose of study

Aims

1. To review the literature and study SMA materials in order to identify an SMA with a potential to improve fire resistance level in concrete components.
2. To conduct experimental studies to understand the bond behaviour between a suitable SMA and concrete and to also understand the strength of SMA-CONCRETE component under significantly high temperature which occurs in a fire event.
3. To develop a numerical model by incorporating data from experimental studies and perform parametric studies on that factors that influence the SMA-CONCRETE bond strength.
4. To formulate an empirical equation for quick evaluation of bond stress in a SMA-CONCRETE structural element.

Chapter 2 Literature review

Bond stress modelling
SMA and its application

Fire temperature
Fire damage failure
Material degradation
Fire resistance level

Chapter 3 Experimental studies

Experiment studies
Experimental setup
specimen casting
SMA characterisation

Parameters
Embedment Length
Fire Duration
Bar Material

Chapter 4 Numerical parametric studies

Numerical Model
Concrete Model
Nonlinear Model
High Temperature, CZM

Parameters
Bar diameter, Fire duration
Embedment Length
Concrete Grade, Bar material

Chapter 5 Results and Discussion

Experimental and numerical results presentation and discussion

Empirical formula

Chapter 6 Conclusion

Conclusion and future recommendations

Figure 3.1: Organisation structure

3.2 Experiments: Framework

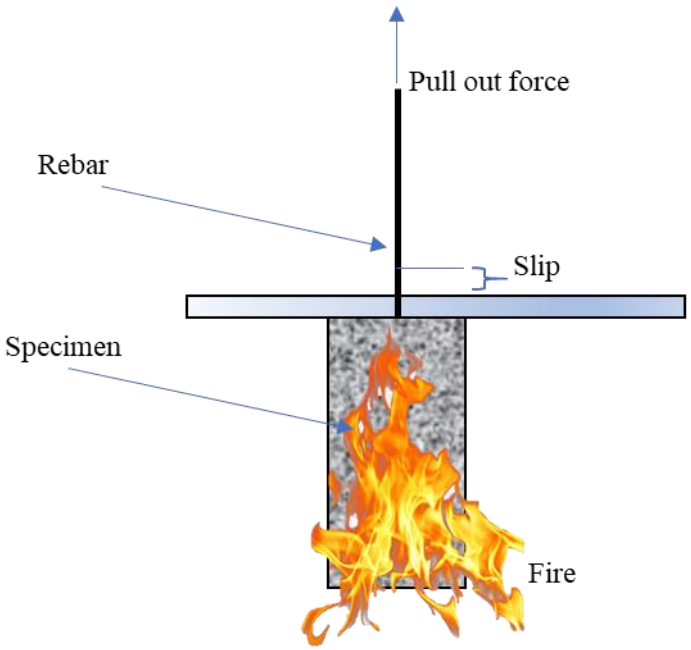

Figure 3.2: Experiment boundary

In Figure 3.2 a schematic diagram is shown of the experiment boundary. It mimics a fire event in a building. What is studied is the effect of such fire on the concrete-rebar bond strength. That is 1) Specimen with SMA rebar and 2) Specimen with steel rebar. Such an examination will provide an in-depth understanding of the failure mechanisms of SMA-concrete specimens and will also allow for a comparative study and characterization of SMA-concrete with respect to standard concrete specimen with steel rebars.

In order to understand the bond behaviour between SMA and concrete, and to also examine the strength of SMA-concrete specimen that is exposed to high temperature (which occurs in a fire event), it is important to identify and adopt suitable techniques and methodologies from the literature. To this extent the following key aspects have been identified from the literature that would assist in the design and development of the physical experiments in this work.

Pull-out test is very common and effective way to understand the bond stress between concrete and rebar. For example, Goto (1971) did the pull-out test to study the crack propagation and failure mechanism around the rib area of rebar. Eligehausen et al. 1983 examined the effect of steel bar diameter embedded in NSC and claimed that the maximum bond capacity decreases slightly with increasing bar diameter. The authors also claimed that frictional bond resistance was not influenced by the bar diameter, lug spacing or relative rib area. In another study, Larrard et al. 1993 investigated the effect of bar diameter on bond strength. The authors noted that the bond strength is directly proportional to tensile strength of concrete. The rate of increase in bond stress is higher with smaller bar diameter. Based on pull-out test conducted on bond stress, Tepfers and Lorenzis (2003) opined that the bond stress decreases as the bar diameter increases. Extensive studies were conducted using pull out tests to study the influence of various parameters on bond such as bar diameter, strength of concrete, lateral confinement and embedment length (Al-Sulaimani et al. 1990; Cairns and Abdullah 1995; Benmokrane et al. 1996; Tighiouart et al. 1998; Andrade et al. 2001; Belaid et al. 2001). Apparao et al. 2002 were of the view that the pull-out tests are also valid in determining relative performance or bond behaviour between different types of concretes and reinforcing bar coatings. It can therefore be said that the pull-out test methodology is very well understood and employed in the literature and one that is suitable to examine the SMA-concrete bond stress and its characterisation in this work. Having identified the methodology to conduct experiments, it was important to adopt techniques that will allow for the preparation of SMA-concrete specimens. This aspect is dealt with as follows.

3.2.1 Concrete Grade: M30

A grade of concrete is identified by its compressive strength (in MPa) that it gains after 28 days of curing and is denoted by letter “M”. On the basis of the compressive strength of the concrete, they are classified as ordinary concrete (M5 to M20), normal concrete (M25 to M45) and high strength concrete (M50 to M70). Concrete more than M25 grade are also called as design mix concrete; commonly used in the construction of large structures having high strength requirements. Typically for such work, higher

grade concrete such as M30 or above is used. The grade of concrete is essentially selected based on structural requirements of the project at hand.

High strength concrete (HSC) typically has a reduced water/cement ratio. Both high strength concrete (HSC) and normal strength concrete (NSC) will show reduction in strength when exposed to high temperatures. Considering the fact that the experiments conducted in this work are to mimic a fire event in the building as explained earlier, it can be said that the concrete specimen will be subjected to a high temperature. As a consequence, it can be expected that the strength of concrete is reduced leading to plausible spalling of concrete and leading to the exposure of reinforcement rebar to high temperature. It is evidenced in the literature that concrete spalling increases with lower water to cement ratio in concrete structures. HSC is much more likely than NSC to fail through spalling at very high temperatures (Bastami et al. 2011). Considering the above M30 concrete grade has been selected for casting the samples and subsequent tests for the current investigation. The 28-day concrete compressive strengths averaged 32.7 MPa for the target strength of 30 MPa. The measured slumps for the mixes were 83 mm.

3.3 The Specimens: Preparation and Process

The experiments require the preparation of various specimens and the physical development of a testing apparatus (with due care given to the experimental setup and the instrumentation employed in such an apparatus). In the following two sections, the matters concerning 1) the preparation of specimens and 2) the various aspects that are critical to the development of experimental apparatus/setup are elaborated in detail.

3.3.1 Concrete Mix Design

The concrete design involves 1) the selection of a suitable concrete grade (such as M15, M25, M30 etc.), 2) design of concrete by way of selecting suitable aggregate materials including that of cement and 3) casting the specimen, testing the specimen and cross-verifying the compressive strength obtained with the standards for the selected grade of concrete.

The design of concrete mix defines the heat resistance capacity of concrete structure. Spalling is one of the main factors in addressing the performance of concrete under fire. For example, the spalling tendency increases with the water content in the concrete at the time of exposure to fire. The presence of siliceous aggregates can also cause spalling. When exposed to high temperature, concrete undergoes dehydration which results in shrinkage. Furthermore, the extreme heat due to rising temperature causes expansion of aggregates. Such typical response of concrete made using traditional concrete mix leads to internal stress as results spalling that inevitably occurs during fire exposed conditions. The concrete grade considered in this work is Grade M30 and is based on the explanation provided earlier in this chapter (Section 3.2.1). The design of specimens based on M30 grade concrete is explored as below. There are essentially five steps to concrete design. The first step involves the determination of the compressive strength of the aggregates that are used in the cement mixture. Such a determination a can be made as explained in the steps 1 to 5 as follows.

Step 1

For assumed free w/c = 0.5 the compressive strength for general purpose cement and crushed aggregate can be determined from Table 3.1.

Table 3.1: Compressive strength of crushed and uncrushed aggregates

Type of Cement	**Type of coarse aggregate**	**Compressive Strengths (MPa)**			
		Age (days)			
		3	**7**	**28**	**91**
Type GP or	Uncrushed	17	24	38	45
Type SR	Crushed	22	31	42	54
Type HE	Uncrushed	24	36	47	52
	Crushed	31	39	52	60

Step 2

In Step 2, the designing of concrete is to establish the free water content based on the desired slump values. From Table 3.2, free water content based on slump 60-100 is 210kg/m^3. The desired values for the specimens for the slump are in the range of 60-

100mm. The aggregate size considered in this work is 20mm for the type being "Crushed". Based on the above two pieces of information, the Free Water Content can be established from Table 3.2 to be 210 kg/m^3.

Table 3.2: Approximate free- water content (Kg/m^3) for various levels of workability

Maximum Size aggregate (mm)	Type of aggregate	Slump (mm)				
		0-10	10-30	30-60	60-100	100-160
10	Uncrushed	135	160	195	210	225
	Crushed	160	185	220	235	235
20	Uncrushed	120	140	170	185	185
	Crushed	150	170	200	210	210
30	Uncrushed	100	125	155	170	180
	Crushed	140	155	180	195	200

Step 3

In Step 3, cement content in the concrete is estimated by basing on w/c ratio of 0.65. The w/c ratio of 0.65 is adopted from the figure for corresponding M30 grade cement. For the assumed concrete design strength of 30 MPa the cement content in concrete can be expressed as Cement Content = Free Water Content/(w/c).

where,

Design w/c = 0.65 (from Figure 3.3)

crushed aggregate with max. size = 20mm (assumed)

Design slump = 60-100 mm (from Step 2)

Free Water content (w/c) = 210kg/m^3 (from Table 3.2)

Therefore, the cement content can be calculated as Cement Content = 210/0.65 = 323kg/m^3

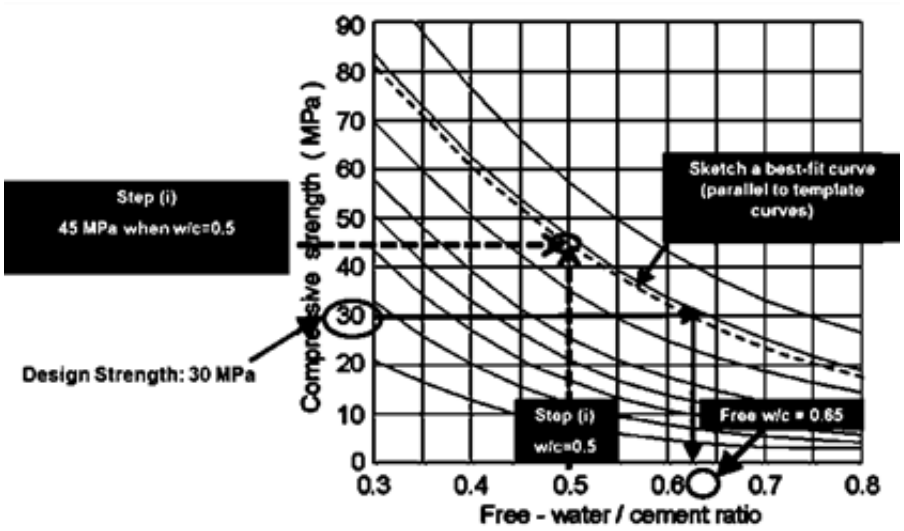

Figure 3.3: Water /cement ratio for M30 concrete is around 0.65 (AS 1379 -2007)

Step 4

The next step (Step 4) in the design of concrete is the estimation of the total aggregate in the concrete. Typically, Wet Density (of concrete) is calculated as the summation of the total aggregate in the concrete, cement and the free water content expressed as Wet Density (concrete) = Total aggregate + cement + free water. Therefore, the Total aggregate can be represented as Total aggregate = Wet Density (concrete) - free water content - cement content. For Wet density, the specific gravity of aggregate need to be specified and this value can be identified from Figure 3.3 for given free water content.

For, water content of 210 kg/m^3 (derived in Step 3), the specific gravity can be noted as being 2.65 approximately (Refer Figure 3.4) and the corresponding wet density of concrete can be noted to be 2350 kg/m^3. The specific gravity of Australian aggregate generally ranges from 2.5 to 2.9. With the above information the Total aggregate content can be calculated as the difference between Wet (concrete) and the sum of Free water and cement content densities respectively; which stands to be 1815 kg/m^3 (refer Figure 3.4).

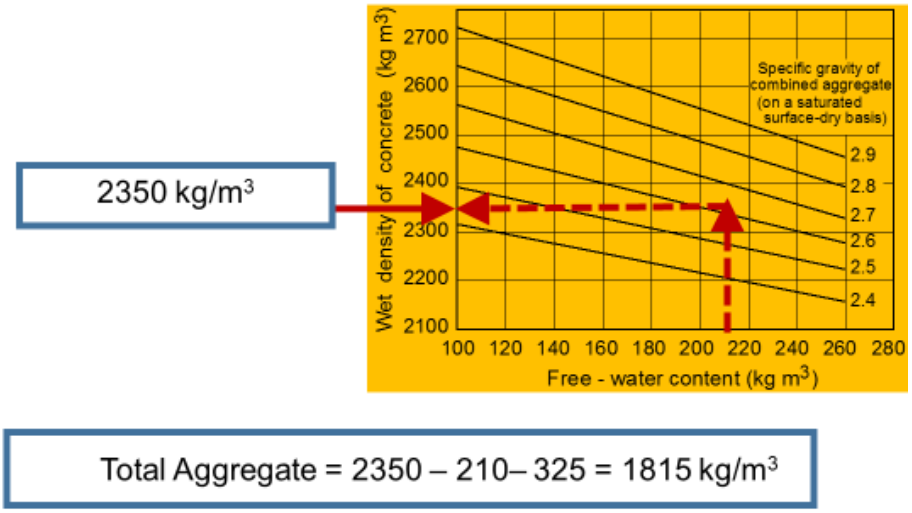

Figure 3.4: Water-Cement ratio chart

Step 5

Finally (Step 5), the aggregates at hand were subjected to a sieve analysis to understand the proportion of fine/coarse aggregate that will be present in the concrete mixture (Figure 3.5). Data from the analysis are presented in Table 3.3.

Figure 3.5: Sieve analysis of aggregate

Table 3.3: Fineness Modulus

Sieve Size (mm)	Mass retained (g)	% Retained	% Cumulative retained
4.75	6	2	2
2.36	31	10.1	12
1.18	30	9.8	22
0.6	59	19.2	41
0.3	107	34.9	76
0.15	53	17.3	93
0.075	21	6.8	-
Total	307		Total = 246
	Fineness Modulus		2.46

From the above data, the Fineness modulus was calculated as below (refer Table 3.3). Having estimated the Total aggregate which is of value 1815 kg/m^3 (earlier calculation), the density of Fine Aggregate is calculated as a product of the percentage of fine aggregate to total aggregate (Fine Aggregate = % Fine Aggregate * Total Aggregate) and this value is calculated to be 816 kg/m^3 (45% of 1815 kg/m^3). Having identified the density of fine aggregate, the density of the coarse aggregate is calculated as the difference between the total and fine aggregate (Coarse Aggregate = Total Aggregate – Fine Aggregate) and this value is calculated to be 998 kg/m^3 (1815 – 816 kg/m^3). Having designed the concrete, the specimen (a cylinder of 150mm diameter x 300mm height) was cast with two different rebars materials 1) Steel and 2) SMA.

3.3.2 Rebar materials

SMA and steel bars were used in the specimen preparation. The SMA and steel bars are shown in Figure 3.6 SMA bar can be identified by their smooth and shiny surface finish.

Figure 3.6: Steel and SMA rebar 10mm diameter

1) Steel material

Mild steel 10mm plain rebar is considered in this work to maintain the geometric relevance to the diameter chosen for SMA rebars. Mild steel has the following engineering properties; elastic modulus of 210 GPa, yield strength of 260 MPa, ultimate tensile strength to be around 385 MPa and a density of 7889.4 kg/mm^3 when tested at room temperature.

2) SMA material

In this research SMA NiTi with, 10mm diameter and 750mm long plain rebar was supplied by university. The yield strength of SMA rebar was around 385.2 MPa, Elastic modulus of 65 GPa, and density was 6600 kg/m^3 when the 10mm rebar being tested in Universal Testing Machine (UTM) at room temperature.

Furthermore, the characterisation of SMA rebars was essential to the understanding of the response of the material to various temperature conditions and to ascertain the maximum temperature limit beyond which the SMA does not exhibit any further phase transformation or, in other words failure to remember and regain its original shape. To this extent, samples were extracted from the bar and heat treated at various temperature (150°C, 200°C and 400°C). Such heat-treated samples were studied using Differential Scanning Calorimeter DSC experiments.

3.3.3 SMA rebar characterisation: DSC experiment

Differential scanning calorimetry is a technique in which the heat flux (power) to the sample is monitored against time or temperature while the temperature of the sample, in a specified atmosphere, is programmed. In practice, the difference in heat flux to a

pan containing the sample and an empty pan is monitored. The instrument used is a differential scanning calorimeter or DSC.

DSC has two nearly identical (in terms of heat losses) measuring cells, one for the sample and one reference holder. Both cells are heated with separate heaters and their temperatures are measured with separate sensors. The temperature of both cells can be linearly varied as a function of time being controlled by an average-temperature control loop. A second-differential-control loop adjusts the power input as soon as a temperature difference starts to occur due to some exothermic or endothermic process in the sample. The differential power signal is recorded as a function of the actual sample temperature.

One single heater is used in the heat-flux DSC to increase the temperature of both the sample cell and the reference cell. Small temperature differences occurring due to exothermic/endothermic effects in the sample are recorded as a function of the programmed temperature. Both systems are extensively described in the available literature.

3.3.3.1 The process

In this study, Differential scanning calorimeter DSC 8500 (Figure 3.7) was used to measure the transformation temperatures of SMA NiTi alloy samples extracted from the SMA rebars. The transformation temperatures are typically the martensite and austenite start and finish temperatures M_s, M_f, A_s and A_f respectively or in other words the phase transformation temperatures. The DSC 8500 is capable of measuring the transformations only in stress free condition. The scanning temperature of this machine is from -180°C to 750°C, with heat varying from 5 - 20°C/min.

To perform the phase transformation study using DSC 8500, the sample needed to be small and weigh around 10mg. Typically, NiTi based SMA's used (in applications such as structural rehabilitation or retrofitting and in experimental studies found in literature) are wires of less than 2mm, hence cutting into small samples for any experimentation was relatively an easy exercise. However, in this research work the SMA material

under investigation are 10mm diameter rebars. NiTi based SMA's are hard materials and cutting the 10mm bars proved challenging. Hence, a couple of different approaches were employed to extract small amounts of material from the bars.

Figure 3.7: Differential scanning calorimeter DSC 8500

1) Approach 1

The first approach used was to make 1mm thin slice of rebar, and cut it further to achieve samples that weigh 10mg. The slicing of material into 1mm thin slice was an extremely difficult task. The smallest piece that could be obtained after several attempts of cutting was a sample that was about 10mm in diameter, 1mm thick and weighed about 38mg (Figure 3.8a). The sample obtained was not a suitable candidate from reasons mentioned earlier. Therefore, another approach was adopted.

2) Approach 2

It was decided to make shavings of material from the sample obtained in the first approach to minimize loss of material on the bars available. After a few attempts, thin material shavings were carved out form the sample as shown in Figure 3.8b.

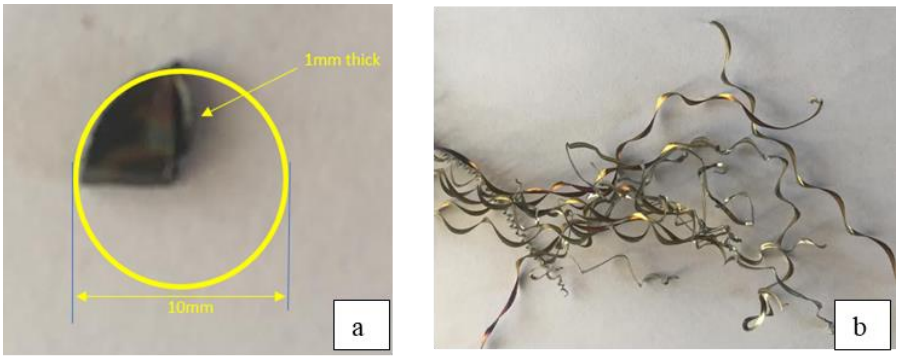

Figure 3.8: Preparation of SMA sample material characterisation (a) cutting thin slice (b) material shredding

The shavings were then segregated into three groups and annealed at three different temperature, (150°C, 200°C and 400°C) respectively. In each of the above cases, the oven was raised to the respective annealing temperatures and maintained for 30min before it was allowed to cool down. The cooled samples were sorted into respective bags and labelled as shown in Figure 3.9.

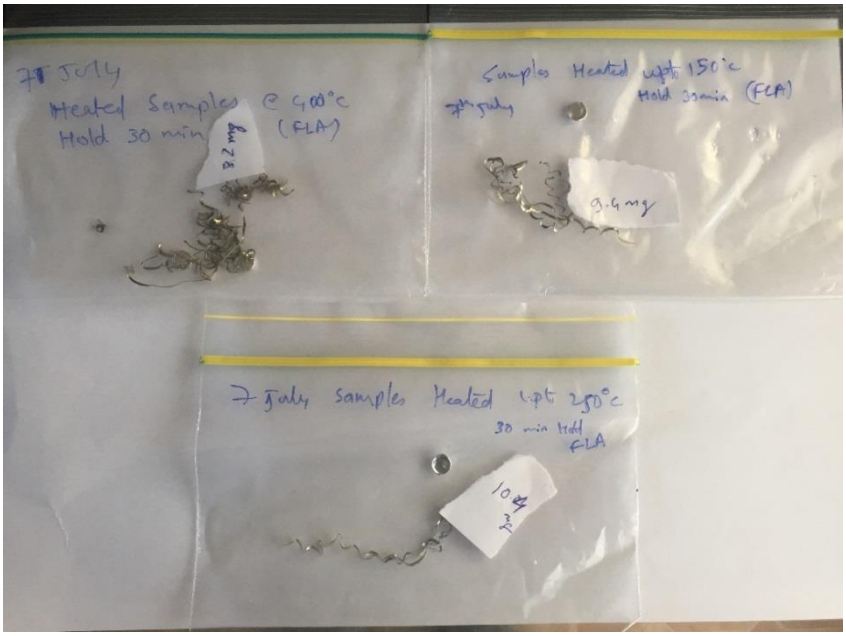

Figure 3.9: Classification, Identification and Storage of SMA samples

The above annealed samples were then prepared to be suitable for DSC experiments. The following steps were adopted to study the samples:

- Prepare samples with small weights;
- Weigh the sample using electronic balance;
- Put the sample into the aluminium container, ensuring that the sample is placed in the middle of the container while the container lid is placed flat;
- Crimp the container using the crimper with minimal force just to close the lid (Figure 3.10);
- Place the crimped sample container into the left pan and an empty container into the right pan of the DSC machine using the suction pen. Then, place the metal cover of the pan on top of both containers using the suction pen (Figure 3.11.); and
- Place the crimped sample container into the left pan and an empty container into the right pan of the DSC machine using the suction pen. Then, place the metal cover of the pan on top of both containers using the suction pen.

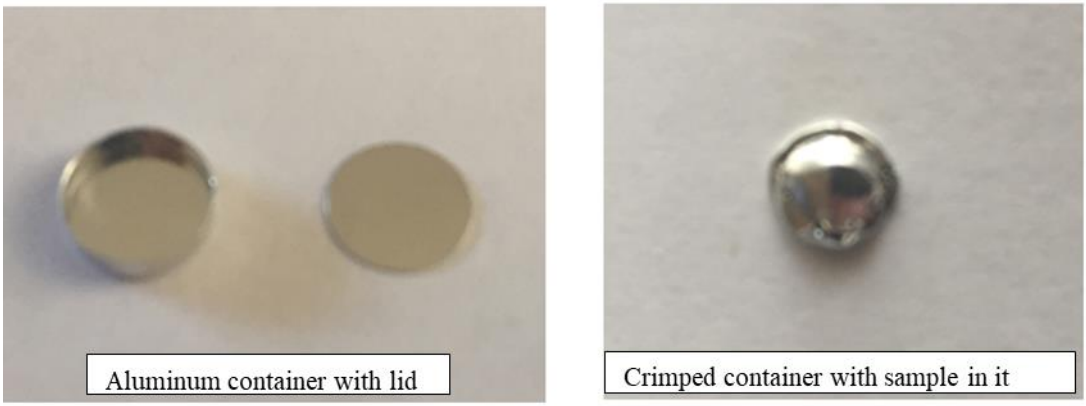

Figure 3.10: Aluminum container to place the sample for testing in DSC

The pan holding the sample and with a chromel wafer immediately underneath is placed on a constantan disc (a platform) in the DSC (Figure 3.11). A chromel-alumel thermocouple positioned under the constantan disc measures the sample temperature. An empty reference pan (with similar arrangement as mentioned above) sits on a symmetric platform within the DSC.

Figure 3.11: Placement of sample and activation of test program through computer

In this study, in order to measure the heat flux (for reasons discussed earlier in this section) the following steps were undertaken. It was observed at the start of the process that the sample temperature fluctuated within +/- 0.010°C. Therefore, the temperature was held at -50°C for 1 min to stabilise the readings. Then the sample was heated from -50°C to 150°C at 10°C per min. At this point, the temperature was held the same and maintained for 1 min before the cooling cycle began. The sample was then cooled from 150°C to -50°C at 10°C /min and held for 1 min at -50°C.

The heat flow through the specimen and the reference were monitored for any differential heating. Any difference in the heat flow indicated that an endothermic or exothermic transformation had occurred in the tested material. In Figure 3.12, the data obtained during the testing on the phase transformations of the three sample (annealed at 150, 250 and 400°C) is presented.

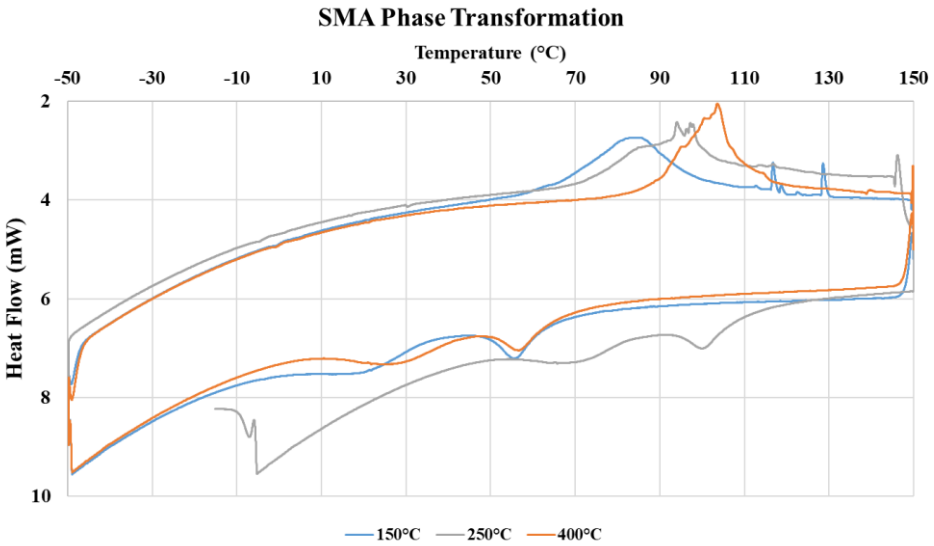

Figure 3.12: Phase transformation of samples at different heat treatment

Typically, in the DSC method, the phase transition is established by identifying the peak of the curve, where the peak of the curve represents the change of phase from martensite (M) to that of austenite (A). The phase transition of three samples annealed at 150, 250 and 400°C respectively are plotted showing their peaks at 80, 95 and 105°C respectively. These peaks in the respective plots establish the occurrence of the phase transition. No crystallized structures were examined in this study for the reason that such studies are only required for the designing the phase transformation.

The data suggests that in the case of the SMA samples, the phase transformation limit increases with the increase in the heat treatment temperature. The highest phase transformation temperature for the SMA under investigation was found to be 105°C for a sample that was annealed at 400°C. Based on these observations, all of the SMA rebars used in this thesis were heat treated at 400°C (Figure 3.12). The process of heat treatment is explained below.

3.3.4 Heat treatment of SMA rebars

The SMA rebars (12 in total) were placed in an oven that was maintained at 400°C for a period of 30min. Figure 3.13 shows the temperature profile of the oven during the heat treatment phase of rebars. The initial drop in temperature (at time 9:50:24) is when the door was opened to place the rebars (Figure 3.13). Then, temperature is maintained for 30 mins and then rebars taken out and quenched in water to be cooled down. The heat treated rebars were cleaned and dried before they were cut into different sizes and casted into the concrete specimen. This aspect is dealt next.

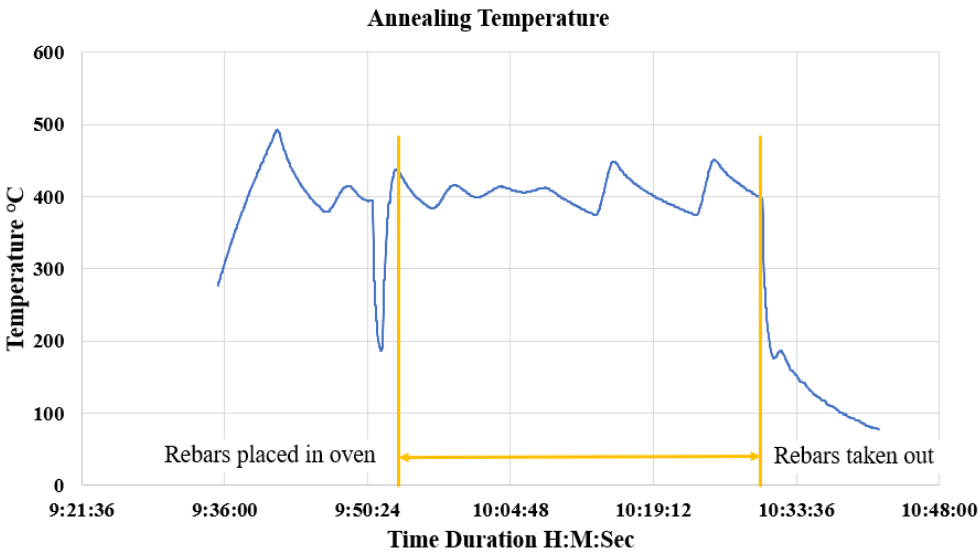

Figure 3.13: Annealing of SMA rebars at 400°C for 30min

3.3.5 Rebar lengths

In the course of preparing the specimens, such bars were each cut into two pieces of length 450mm and 300mm respectively (Figure 3.14). The long and short rebars were full embedded and half embedded into the concrete respectively. A schematic diagram of this arrangement is shown in Figure 3.15. The embedment length is a crucial parameter for the bond strength in this study.

Figure 3.14: Cut SMA rebar of length 450 and 350mm

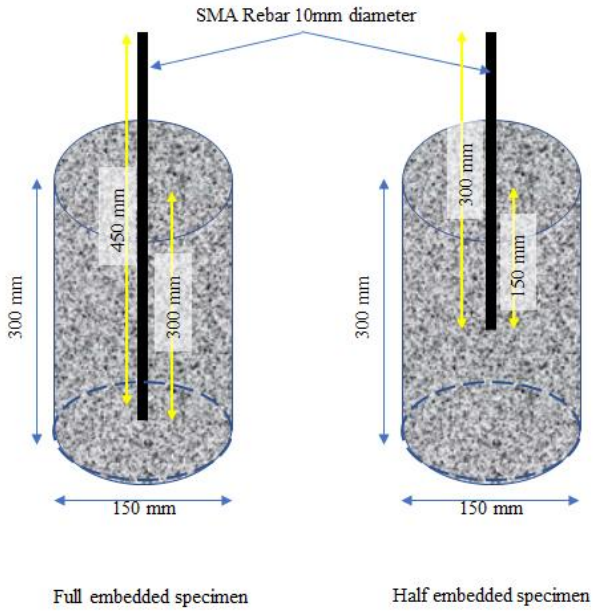

Figure 3.15: Schematic diagram of rebars (length 450 and 300mm) embedded in concrete specimens

3.3.6 Concrete casting

The test specimens consist of cylindrical concrete sample with either a standard steel rebar or an SMA rebar positioned at the centre of the sample. SMA bar embedded coaxially conform to AS/NZS 4671 standards. PVC moulds were specifically designed for this purpose (150mm diameter PVC pipe that is 5mm thick). A PVC pipe was then cut at height of 300mm. The PVC cut section was then mounted on a strong MDF board and sealed in place with the silicon sealant. The inner surfaces of the moulds were all coated in oil to facilitate the easy removal of the cast specimens. A jig (as shown in Figure 3.16) was designed and developed to position the rebar and thermocouples in place as shown in Figure 3.17. In the case of steel rebars, they were used was without any pre-treatment. However, the SMA bars were annealed at 400°C for half an hour. The oxides layer on the SMA bars was washed out and the bars were cleaned and dried out before casting. Two types of reinforced concrete specimens were developed involving 1) standard steel bars and 2) SMA bars. The concrete design method is discussed next.

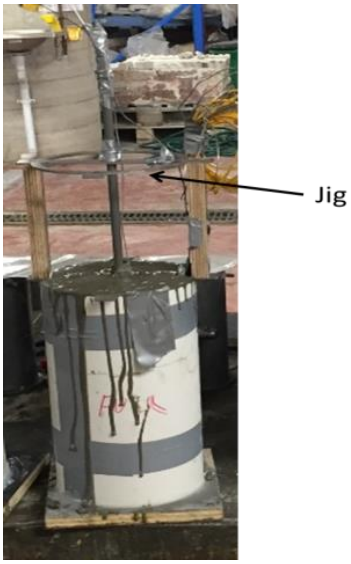

Figure 3.16: Jigs for positioning the rebars

Concrete mixing was carried out using a 115 litres drum mixer. The aggregate quantity for each batch was as per the concrete mix design as discussed in section 3.3.1. The volume from each batch allowed for the production of six specimens. Due care was taken to ensure that all batches of concrete produced were consistent throughout. This included pre-blending the sand from the saturated stockpile and regularly assessing the moisture content of the sand and stone that was used. The mixing of concrete was carried out with the help of a qualified and experienced technician. The surface of the drum mixer was saturated using a damp cloth before adding two thirds of the total water, half the amount stone, sand and cement and mixed well before adding all of the remaining aggregates and cement. The mixing was continued for three minutes until the mix was homogenous in consistency. Once mixing was complete, fresh concrete was poured into the moulds to achieve M30 grade concrete cylinders (with rebars and thermocouples in place). The moulds were then subjected to vibration by placing them on a vibration table in order to remove all of the trapped air. The exposed top surface was finished using a trowel after sample had been removed from the vibration table. The specimens were then left to harden (Figure 3.18). The jigs and moulds were removed after 24 hours after pouring. The specimens (now concrete cylinders) were kept in a curing tank and at room temperature for a further 28-day period from the time of casting.

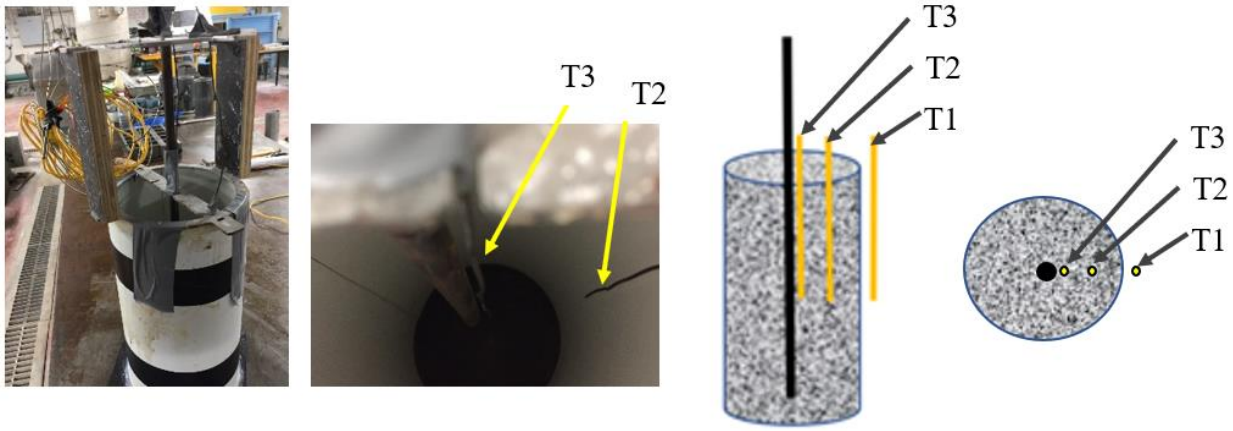

Figure 3.17: Mould for casting sample with rebar and thermocouple positioner

Figure 3.18: Cast test specimen with SMA rebar and thermocouple.

At the time of curing, the weather was cold and the temperature in the curing tank was lower than average room temperature of 23°C. On removing the specimens from the curing tanks, they were to be dried. Any increase in humidity in the air leads to more spalling and cracking during the test under high temperature. To avoid such a situation, the samples were oven dried at 50°C for 6 hours (refer Figure 3.19) using an oven built by Labec. After the curing process was completed, specimens were transported and stored at the testing facility until the time of testing (Figure 3.20).

(a) (b)

Figure 3.19: (a) specimens in the oven (b) specimens heated to 50°C for 6 hrs.

Figure 3.20: Samples ready for testing

In all, 24 specimens were cast (12 with SMA and 12 with steel rebars) the details of which are as follows:

- 6 samples for SMA half-length embedded;
- 6 Samples for SMA Full-length embedded;
- 6 samples for steel half-length embedded; and
- 6 samples for steel Full- length embedded.

The list of specimens with different parameters tested in the pull-out test have been presented in Table 3.4.

Table 3.4: List of pull-out specimens tested

Sr No	Name	Bar Diameter (mm)	Embedded length	Concrete Grade	Fire Duration	Bar Material
1	NF-FL-E1-SMA	10	Full	M30	Zero	SMA
2	30F-FL-E1-SMA	10	Full	M30	30 min	SMA
3	60F-FL-E1-SMA	10	Full	M30	60 min	SMA
4	NF-HL-E1-SMA	10	Half	M30	Zero	SMA
5	30F-HL-E1-SMA	10	Half	M30	30 min	SMA
6	60F-HL-E1-SMA	10	Half	M30	60 min	SMA
7	NF-FL-E2-SMA	10	Full	M30	Zero	SMA
8	30F-FL-E2-SMA	10	Full	M30	30 min	SMA
9	60F-FL-E2-SMA	10	Full	M30	60 min	SMA
10	NF-HL-E2-SMA	10	Half	M30	Zero	SMA
11	30F-HL-E2-SMA	10	Half	M30	30 min	SMA
12	60F-HL-E2-SMA	10	Half	M30	60 min	SMA
13	NF-FL-E1-Steel	10	Full	M30	Zero	Steel
14	30F-FL-E1-Steel	10	Full	M30	30 min	Steel
15	60F-FL-E1-Steel	10	Full	M30	60 min	Steel
16	NF-HL-E1-Steel	10	Half	M30	Zero	Steel
17	30F-HL-E1-Steel	10	Half	M30	30 min	Steel
18	60F-HL-E1-Steel	10	Half	M30	60 min	Steel
19	NF-FL-E2-Steel	10	Full	M30	Zero	Steel
20	30F-FL-E2-Steel	10	Full	M30	30 min	Steel
21	60F-FL-E2-Steel	10	Full	M30	60 min	Steel
22	NF-HL-E2-Steel	10	Half	M30	Zero	Steel
23	30F-HL-E2-Steel	10	Half	M30	30 min	Steel
24	60F-HL-E2-Steel	10	Half	M30	60 min	Steel

For the ease of identifying a particular specimen, the specimens were named in a unique way using the convention Fire exposed duration-Embedded Length-Experiment specimen-material. For example: 30F-FL-E1-SMA represents specimen

exposed to fire for 30min--full embedment--experiment test 1 specimen--SMA rebar. All test samples used were M30 concrete grade having a bar diameter of 10 mm into the concrete.

The concrete specimens produced were subjected to testing to ensure the concrete produced is of M30 grade. The testing examined and cross-verified the compressive strength results of the specimen produced against the values of Grade M30 specified in the Concrete Standards.

3.4 Experiments: Nomenclature

A schematic diagram of the experimental set-up is shown in Figure 3.21. The various equipment and testing gear employed in the experiments and their respective positions are as indicated in Figure 3.21. The manner in which such equipment were connected and their specific purpose is elaborated as follows.

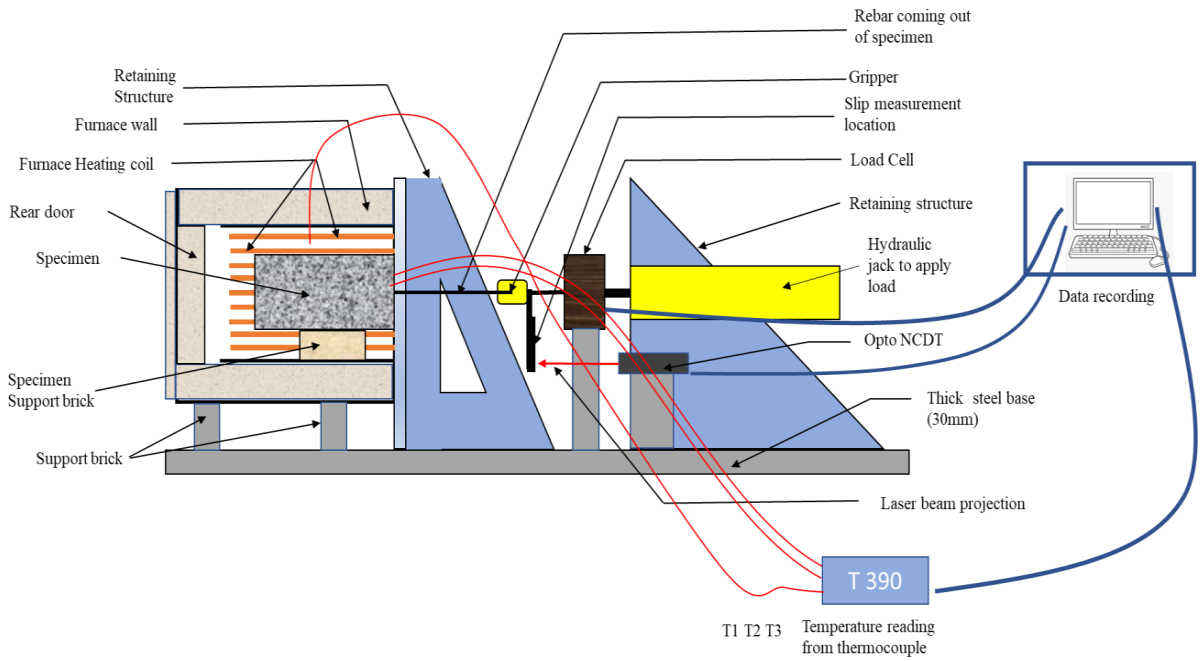

Figure 3.21: Schematic diagram of experimental setup and nomenclature

3.4.1 Equipment and Instrumentation employed -Thermocouples

Thermocouples are the devices used to measure the temperature at a specific location. Three thermocouples were employed in this work to measure the radial

temperature profiles on the specimen 1) to measure the temperature on the surface (T1), 2) Halfway inside the specimen (T2) and 3) at the bar concrete interface (T3) as shown in Figure 3.22. More specifically K Type Thermocouples, which are capable of measurements up to 1200^{o}C were used. The Thermocouple probes were connected to thermometer (SE3094 channel) which recorded the data on to a computer. The temperature profile was constantly monitored as per the fire exposure duration time i.e. 30mins and 1hour. Once the desired temperature was reached the pull-out test was performed.

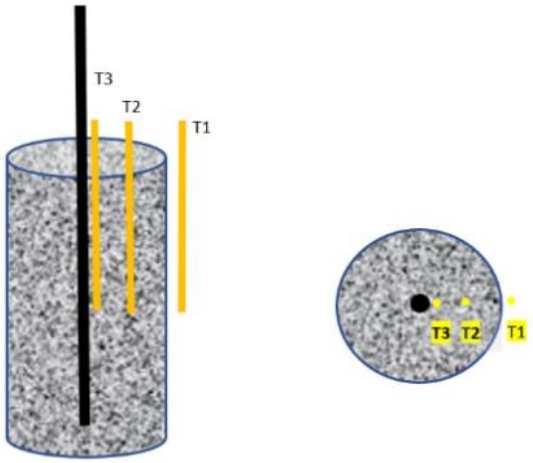

Figure 3.22: Thermocouple position in the concrete specimen

3.4.2 SE 309 Thermometer

TestLink SE309 is a type of four channel thermocouple thermometers which are microcontroller-based testers. These thermometers are equipped with RS232 interface for advanced applications. The 309 series, has the ability to read data from more than two points and up to four points. Since the work in this thesis requires reading of the temperature at three locations the SE 309 series of TestLink was selected. The thermocouple SE309 is shown operational in Figure 3.23 during the testing phase.

Figure 3.23: Test Link SE309 ILD2300 Opto NCDT

3.4.3 NCDT 2300 Sensor

The NCDT 2300 sensor is an optical system for measurements of displacement with micrometre accuracy. While the Opto NCDT 2300 system is designed for use in both industrial and laboratory applications for various measurement considerations (measuring displacement, distance, position and elongation, in-process quality control and dimensional testing). The manner in which the sensor was connected to the computer in this work is shown in Figure 3.24.

The Opto NCDT 2300 operates according to the principle of optical triangulation, i.e. a visible, modulated point of light was projected onto the target surface. The system can operate in both direct and diffuse reflection modes (Figure 3.25). With diffuse arrangement, the sensor measures distances while directly arranged the sensor measures distances or the thickness of a transparent measurement object (Figure 3.24, Figure 3.25). The sensor's operating temperature: 0-50 °C (+32 up to +104 °F).

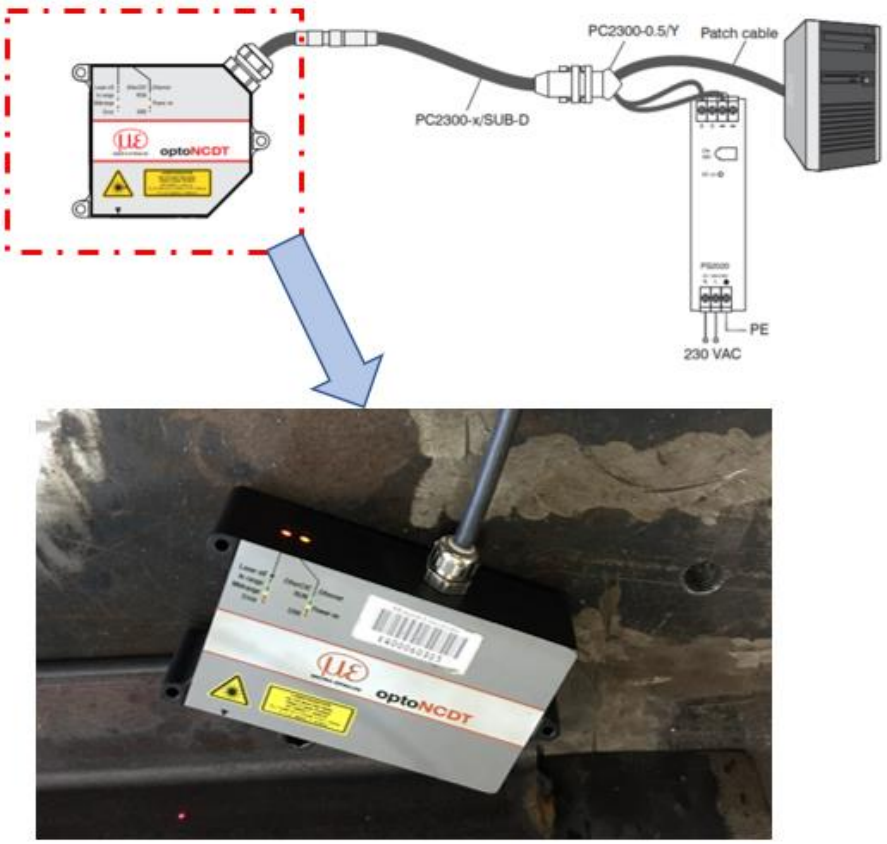

Figure 3.24: ILD 2300 Opto NCDT-device for slip measurement

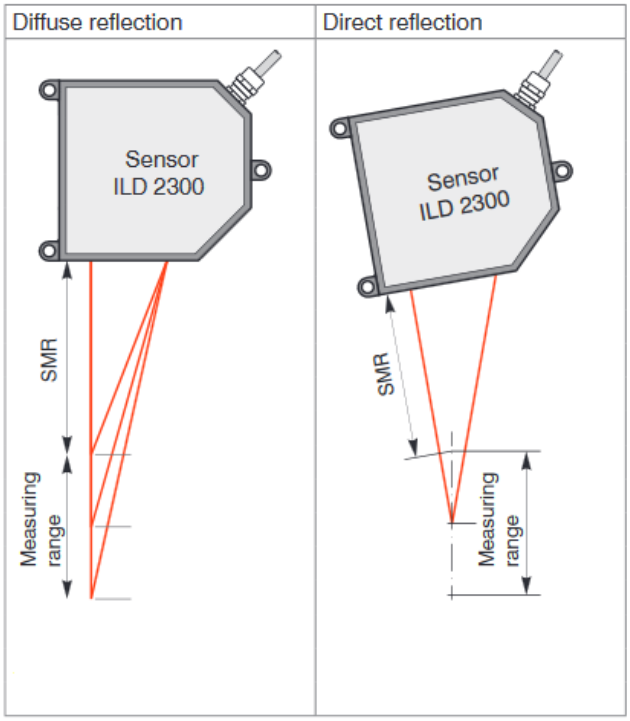

Figure 3.25: ILD 2300 Opto NCDT- Definition of terms

In this thesis, the direct reflection mode was employed to measure the elongation of the steel/SMA rebars during the pull test. The displacement/elongation of the rebars is measured by projecting and directly reflecting a LASER in the sensor onto an arm that is radially attached to the bar as shown in Figure 3.26.

The data obtained from the Opto NCDT 2300 sensor is fed into ILD 2300 DAQ Tool V3.4.0 for the documentation of displacement data in a coma separated value- csv file format for further analysis.

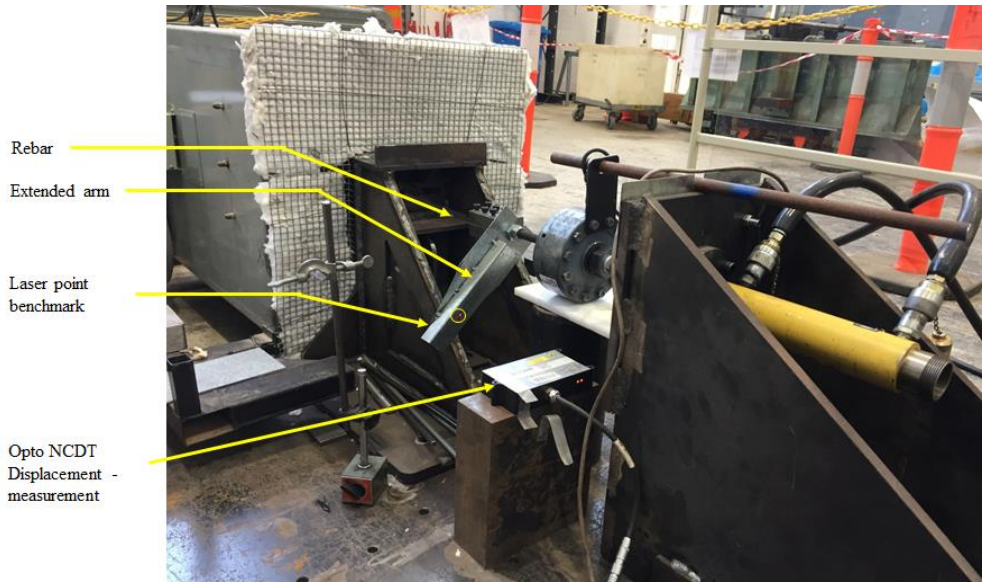

Figure 3.26: ILD 2300 Opto NCDT-LASER displacement Measurement arrangement

3.4.4 Load Cell

A load cell or force sensor is a device which converts load or force into an electrical signal. Tension/compression load cells measure the force applied on to the load cell. The capacity of the load cell employed in this work is 60kN. In this study, the load cell was connected between the free end of the rebar and the hydraulic jack as shown in (Figure 3.27 and Figure 3.28). During the pull-out tests, the load values were displayed on the load cell reader for recording purpose (Figure 3.28).

Figure 3.27: Load cell arrangement

Figure 3.28: Load Cell AC2500 and reader

3.4.5 Jetflow Furnace

In order to mimic a fire event in a building as discussed in Section 3.2, one end of the specimen is enclosed in a furnace as shown in Figure 3.29 and Figure 3.30. The other end of the specimen was held by grippers (refer Figure 3.29) so as to support the bar and to assist in gripping the rebar during the pull-out test. In this work, a Jetflow furnace (Figure 3.29) was employed within which the specimen was exposed to fire. A retaining structure was designed to take the load off the oven and to act as a solid wall against which the samples were pulled. The furnace was modified to have a door at the front end (the rear end door being a standard). The modified door had a slot cut into it such that the rebar and the thermocouples extend out through the slot (Figure 3.30,Figure 3.31, Figure 3.32). The special door was insulated from inside as well as from the outside to avoid the loss of heat and heat transfer to other part of the system.

FP21 controller was used to control the fire by following a time dependent temperature curve (Figure 3.33). The Australian Standard Fire curve was approximated to fit the 5-step linear time temperature curve.

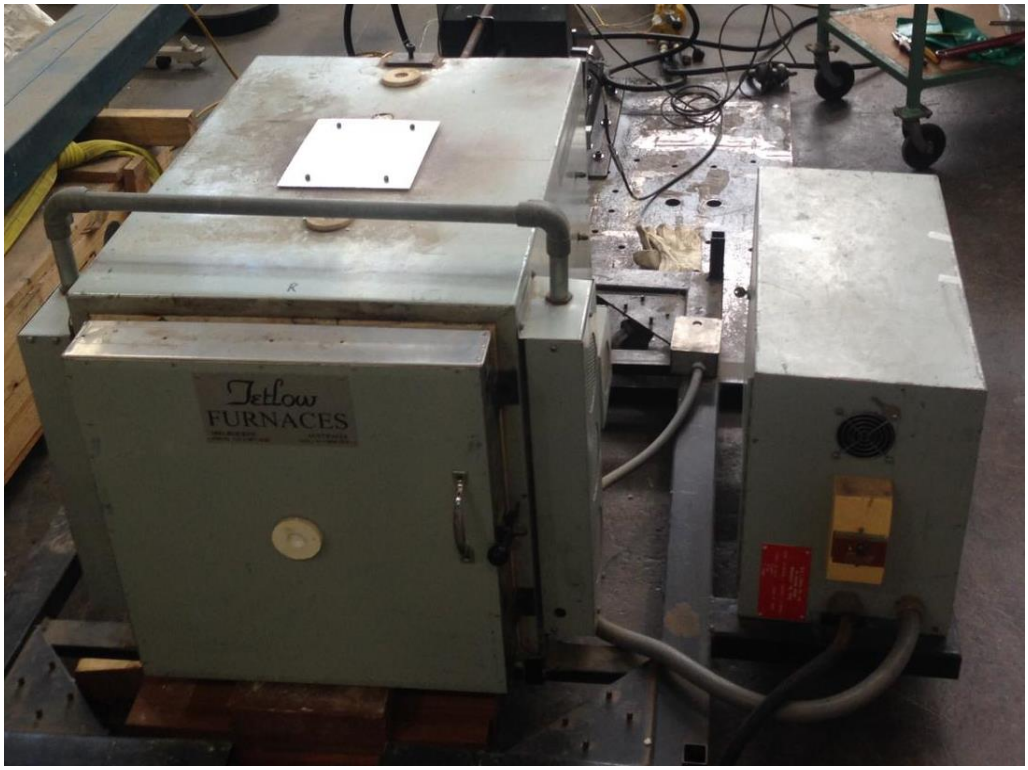

Figure 3.29: Jetflow Furnace

Figure 3.30: Furnace inside: Specimen holding position (rear end view)

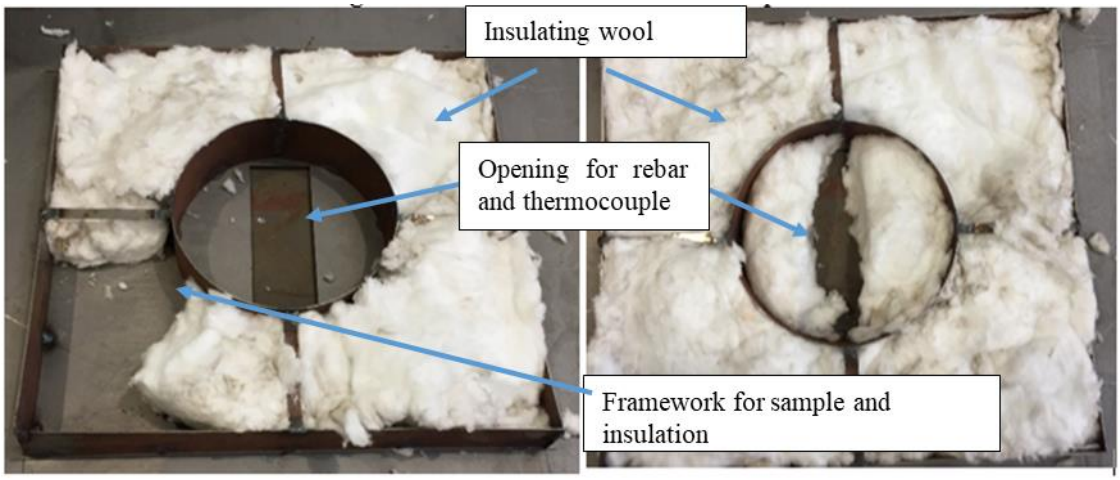

Figure 3.31: Frame work for the front door insulation and sample placement

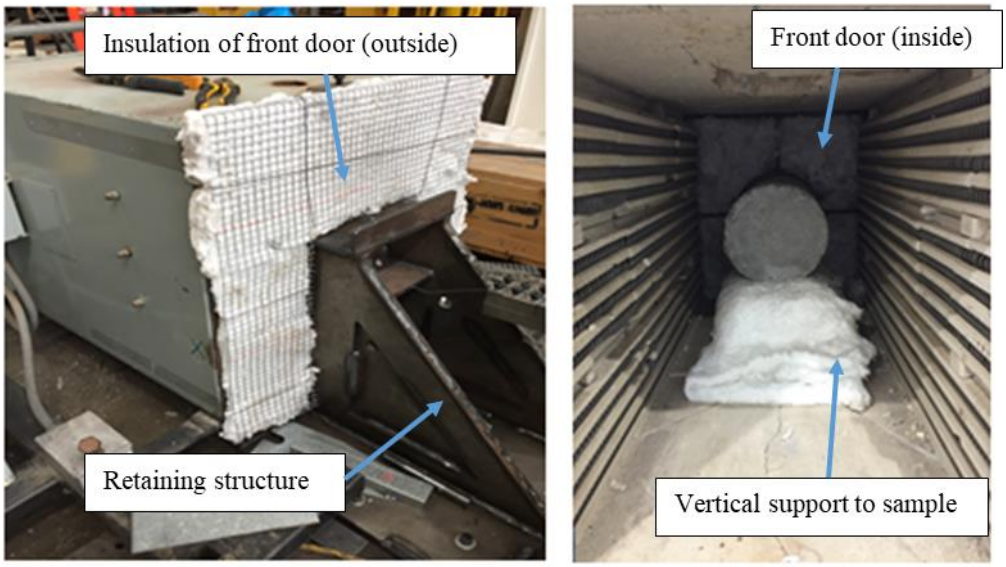

Figure 3.32: Insulation of furnace & test specimen feed

Figure 3.33: Input temperature curve to furnace

3.4.6 Custom designed gripper

When conducting a pull-out test, due care needs to be given to secure the specimen in place. In this study, initially a collet was used to connect the rod; however, the collet could not provide the desired grip to pull the rebar out (Figure 3.34) and it slipped out. Hence a new gripper was designed specifically to connect the rebar to the load cell from a single solid metal piece. A bolted gripper was specifically designed for this study to prevent any slip during the pulling experiments. The successful design of the gripper was confirmed by no notable shift in the markings made on the rebar in relation to the

gripper during the pull experiments. Hence measurement of the gripper slip was deemed not applicable.

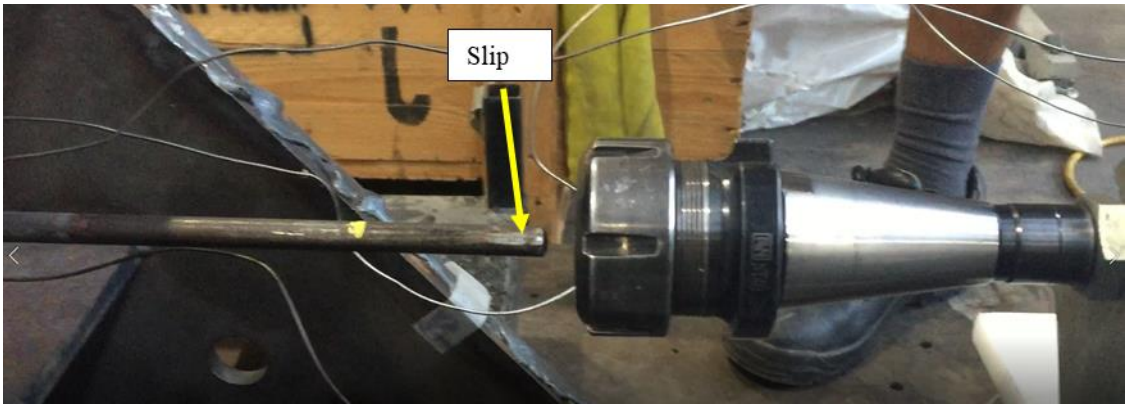

Figure 3.34: Collet gripper slips during the test.

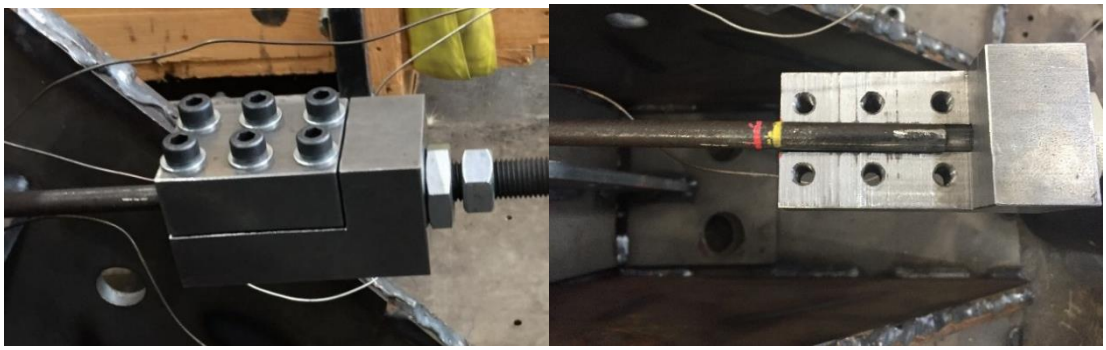

Figure 3.35: Bolted gripper (specifically design for this study).

3.5 Risk Assessment

The test apparatus involved both high temperature equipment (such as furnace) and high-power hydraulic equipment. This warrants a safe work zone and operational conditions. A detailed risk analysis was carried out. The risk involved was documented and classified into low, medium and high risks. The existing safety controls were understood from lab technicians and safety officers while new controls were discussed and put in place to mitigate the specific risks identified. For example, proper signage and screens were used to isolate the test area and to inform the other users of the lab. Figure 3.36 shows the isolation of the test setup and OHS warning signs.

Figure 3.36: Isolation of test setup and OHS

3.6 Experiment

The apparatus to conduct the pull-out test under the fire condition (under high temperature) was designed and fabricated as shown in Figure 3.37 and Figure 3.38. The entire test apparatus was assembled on to a rigid platform to provide the required stability. To provide structural support to the entire apparatus two retaining walls were built as shown in Figure 3.39 and Figure 3.40. The front door and retaining wall sit snug fit and hence the resistance is provided by the retaining wall and not door of furnace. The walls were designed to handle load which is up to 60kN.

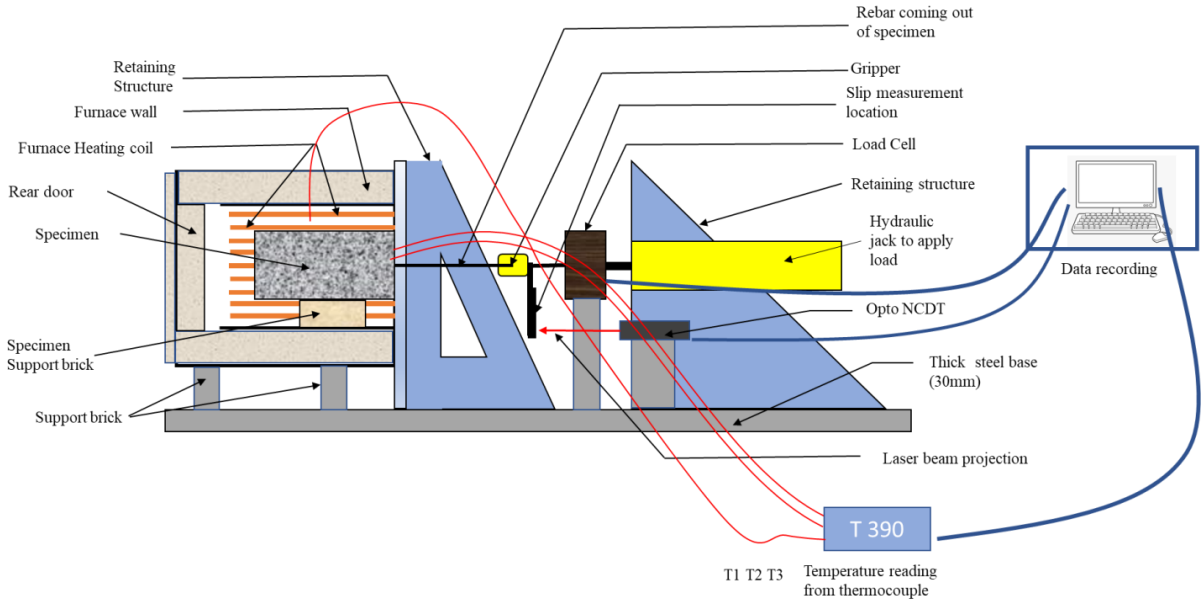

Figure 3.37: Schematic of experiment setup

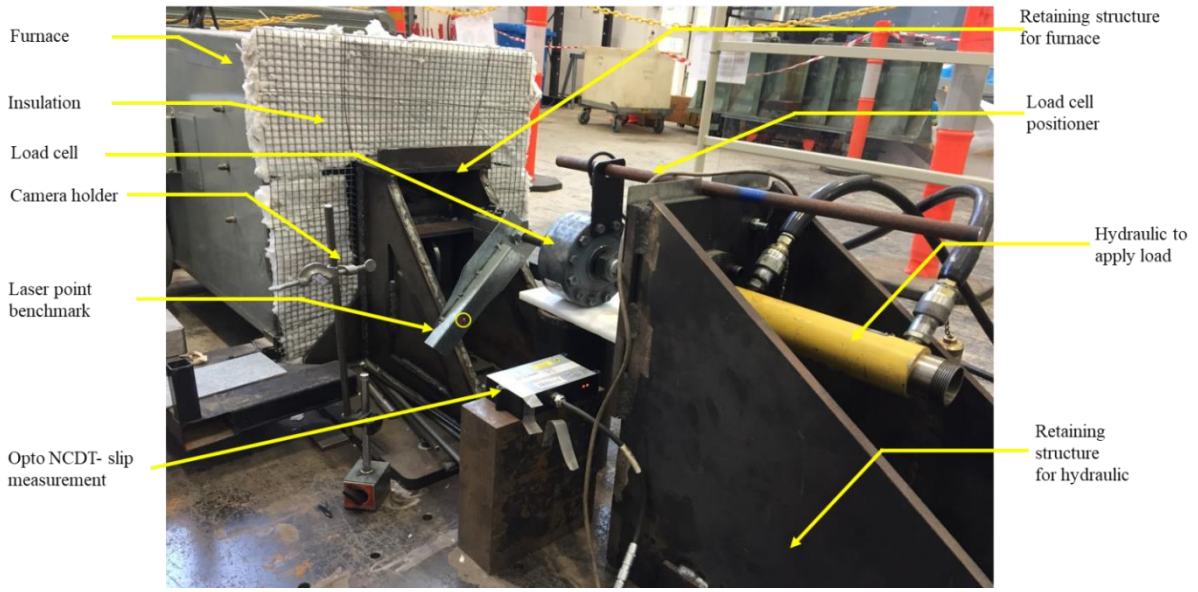

Figure 3.38: Actual picture of test apparatus (view from front corner end)

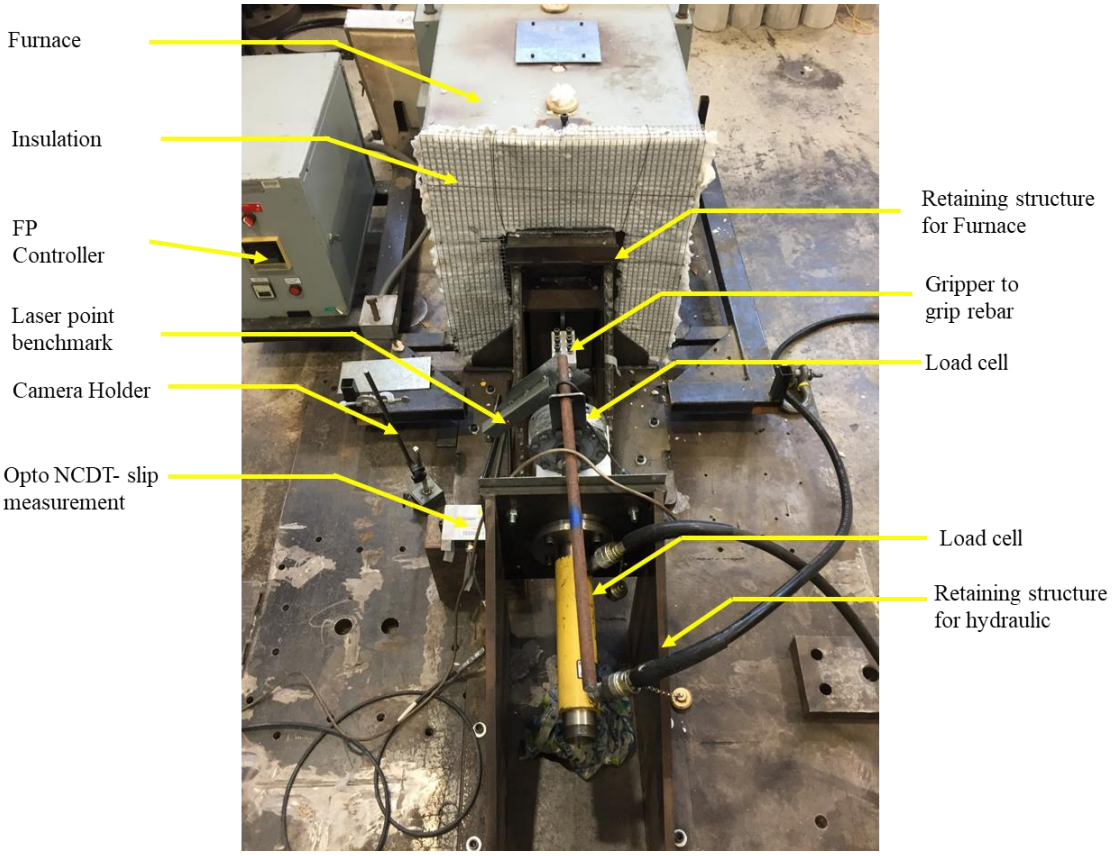

Figure 3.39: Actual images of test apparatus (view from front top end)

Figure 3.40: Test Setup (No Fire & Fire Condition)

Various components/equipment/instruments required for the pull-out test i.e. furnace (oven), retaining structure, gripper, load cell, hydraulic jack were placed in their respective positions and secured as shown in Figure 3.39 and Figure 3.40. The

specimen was positioned in the furnace through the rear access door of the furnace. The thermocouple probes were connected to thermometer (SE3094 channel) which was further connected to the computer to store the data. FP21 controller was used to control the fire applied on to the specimen in the furnace by following a time dependent temperature curve as explained earlier in section 3.4.5.

The pull-out test experiments were conducted at three temperature/time duration steps 1) room temperature/ no fire condition, 2) 30 mins fire duration and 3) 60 mins fire duration time. In each of the above-mentioned case, the temperature of the concrete specimen was recorded using 3 thermocouples as discussed in Section 3.4.1. For the above-mentioned steps, the sample was heated as per the fire curve in the Jetflow furnace, to reach the desired temperature for the respective time intervals of 30 min and 1-hour fire temperature.

The rebar's loose end was connected to the load cell through the gripper in a manner as discussed in Section 3.4.6 and Section 3.4.4. ILD2300 Opto NCDT laser was powered up and projected on to the extended arm which was connected to the rebar. Hydraulic cylinder was then used in each of the above case to pull the rebar in the pull-out test. The load was applied gradually at a rate of 0.1 kN/s. The load was applied till the bar slipped in each of the test case. The displacement of the rebar was measured through ILD2300 Opto NCDT under load and eventual slip. Both the load and slip distance were recorded. The force-displacement plot was then converted into bond stress-displacement plot.

In this experimental study over all 24 samples of M30 grade, half and full embedment lengths (Section 3.3.6) for three temperature conditions i.e. zero fire duration, 30 min fire duration and 60 min fire duration were tested and the average displacement value of the response was used in the evaluation of the results discussed in Chapter 5.

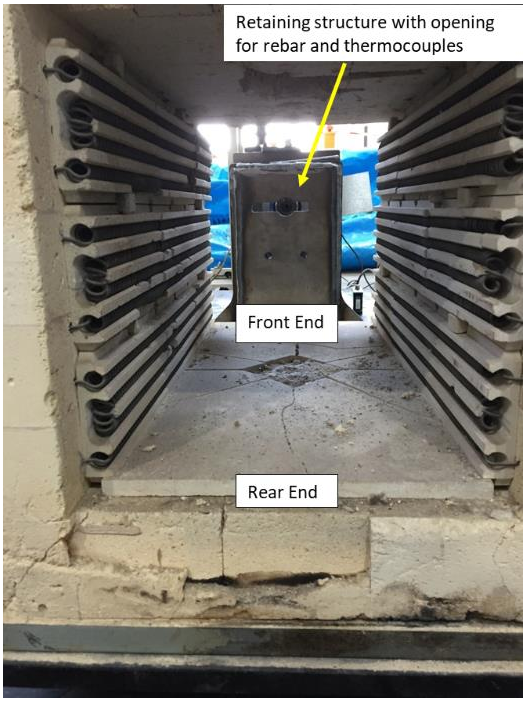

Figure 3.41: Inside the electric oven (front and rear door removed)

3.7 Experimental Studies - Results and Discussion

3.7.1 Introduction

The physical experiments conducted in this chapter, involved the design and development of testing apparatus to conduct pull-out test on various specimens designed. The specimen list and the conditions they were subjected to are presented in Table 3.5. Each of the specimens listed was tested to estimate the pull-out force such that corresponding bond stress values for each specimen case can be calculated. Bond stress Vs Displacement curves were plotted in order to establish the bond slip value for the observed maximum bond stress value. A comprehensive data set of the above said values feed into the numerical experiments that are conducted in the following chapter. The results obtained from the physical experiments are presented in this section as it forms a crucial aspect of the numerical studies. Failure analysis on the physical specimens completes this chapter.

3.7.2 Specimens response to Thermal Loading and Pull

The experimental samples are identified using general code of notation which was to be defined to identify the specific test specimen. For example, NF-HL-E1-SMA, sample is identified as No fire condition, half embedded, 1st test and SMA rebar. HL and FL refers to 150mm and 300mm depth of insert of the rebar into the concrete respectively (Figure 3.42).

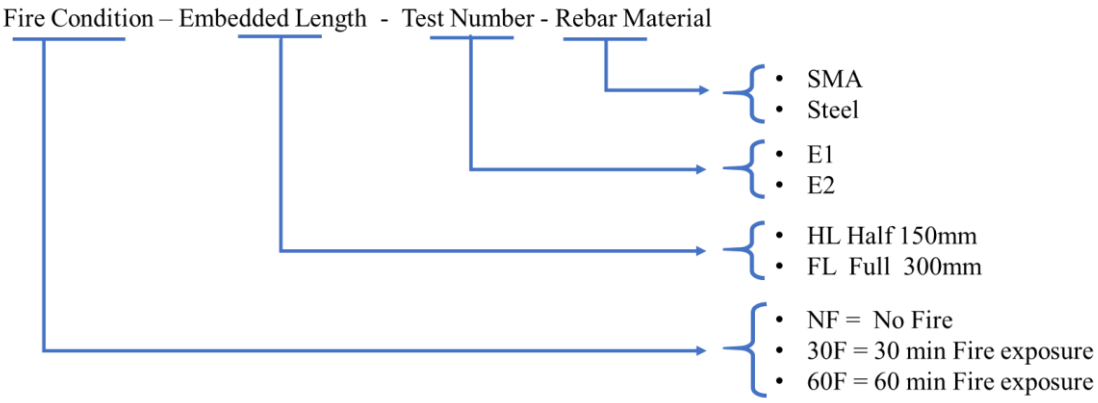

Figure 3.42: Parameters considered

Table 3.5: List of pull-out specimens tested

No	Name	Bar diameter (mm)	Embedded length	Concrete Grade	Fire Duration	Bar Material
1	NF-FL-E1-SMA	10	Full	M30	Zero	SMA
2	30F-FL-E1-SMA	10	Full	M30	30 min	SMA
3	60F-FL-E1-SMA	10	Full	M30	60 min	SMA
4	NF-HL-E1-SMA	10	Half	M30	Zero	SMA
5	30F-HL-E1-SMA	10	Half	M30	30 min	SMA
6	60F-HL-E1-SMA	10	Half	M30	60 min	SMA
7	NF-FL-E1-Steel	10	Full	M30	Zero	Steel
8	30F-FL-E1-Steel	10	Full	M30	30 min	Steel
9	60F-FL-E1-Steel	10	Full	M30	60 min	Steel
10	NF-HL-E1-Steel	10	Half	M30	Zero	Steel
11	30F-HL-E1-Steel	10	Half	M30	30 min	Steel
12	60F-HL-E1-Steel	10	Half	M30	60 min	Steel

Each of the specimens identified in Table 3.5 was monitored for its response to the thermal load applied on to the face of the concrete while they were being subjected to

a pull force. Temperature readings were obtained from the three thermocouples placed on/within the specimen as shown in Figure 3.43 (discussed earlier in Section 3.3.6 Chapter 3).

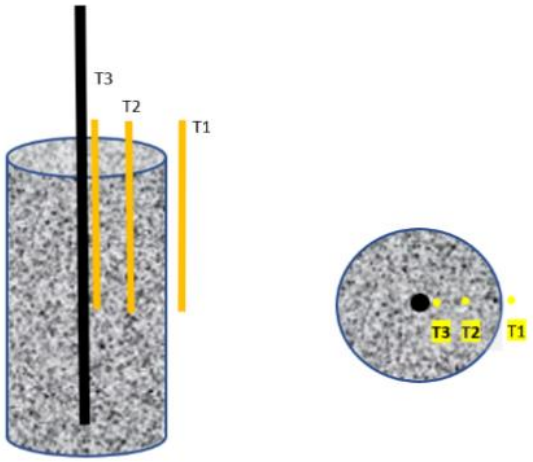

Figure 3.43: Thermocouple T1, T2 and T3 position in specimen.

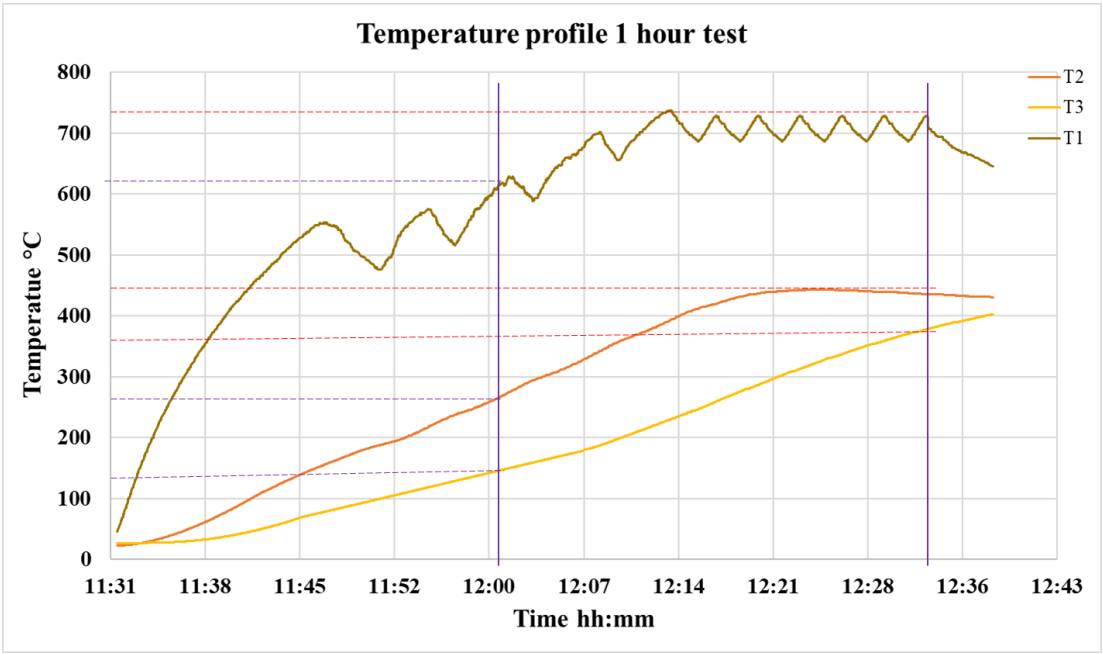

Figure 3.44: The temperature trend curve of furnace and specimen as recorded during the physical experiments

The thermal load that the specimens were subjected to is shown in Figure 3.44. It can be noted that there are three temperature readings that are plotted; one each for thermocouples T1, T2 and T3 (at locations as mentioned above) respectively. The

temperature plot for thermocouple T1 is from a location that is just outside of the specimen and in the furnace enclosure. The fluctuation observed in the plot is typical of electric heating of furnace and the specimen within as shown in Figure 3.45 and as noted by Chen et al. 2015. It is hence established that the furnace operated well as per its design specifications.

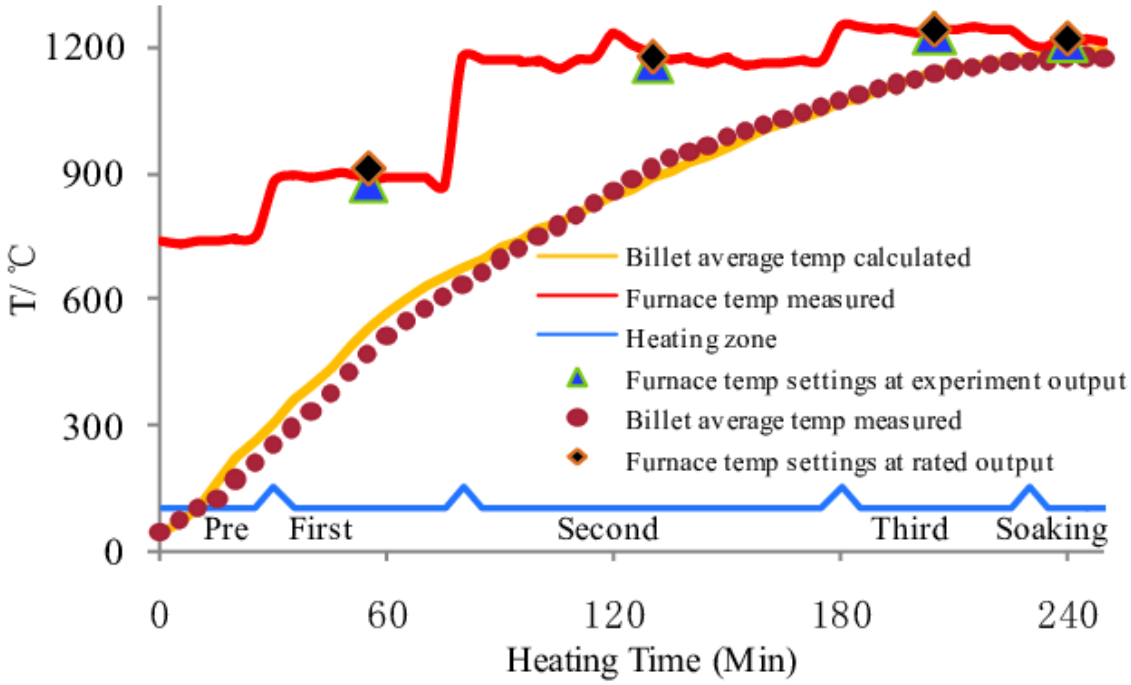

Figure 3.45: The trend curve of furnace and specimen temperature measured on billet heating (Chen et al. 2015)

When it comes to understanding the data from T2 and T3 thermocouples, it is important to make note of their respective temperature readings at 30min and 60min of operation. T1 provides information on the surface temperature of the concrete while T3 provides temperature at the core (typical location of the interface between concrete and rebar). From Figure 3.44, it can be said that the surface temperature of concrete and at the core is 280 and 110°C at 30min of testing and 450 and 380°C at 60mins of testing respectively. In either of the above-mentioned cases, it is evident that the temperature of the specimen did not exceed a value that is in excess of 380°C at the core for the entire duration of testing (physical experiments).

It is evident that the temperature of the specimen did not exceed a value that is in excess of 380°C at the core for the entire duration of testing (physical experiments).

The temperature value of 380°C that is stressed upon is significant to this study for two reasons:

1. The steel rebars that are typically used in reinforcing concrete will significantly lose their strength at such temperatures; and
2. On the contrary, the SMA rebar that is proposed in this work gains strength at this temperature due to its memory retaining capabilities. The effect of high temperature around 400°C on both steel and rebars is examined in this work by way of both physical and numerical experiments.

While there exist well established methods in the literature to study the bond stress between steel rebar and concrete at various temperatures, no such studies were found to be carried out using SMA rebar. Therefore, it was important to conduct several physical tests in order to obtain the data sets required to develop a numerical model that would replicate the physical experiment. The results of the physical experiments are discussed next, followed by the results from the numerical experiments.

The data concerning the maximum pull force for specimen NF-FL-E1-SMA is noted in Table 3.6. The reading was recorded from the load cell placed between the rebar and the hydraulic jack that was pulling the bar. Likewise, the data set for the maximum displacement (slip) of the bar during the pull-out test was noted from the reading provided (as shown in Figure 3.46) by the NCDT LASER device. The concrete grade considered in all of the specimens is M30.

Table 3.6: SMA rebar- concrete pull out tests results on specimen NF-FL-E1-SM

Specimen Tested	Rebar Material	Fire exposed duration (mins)	Embedded Length (mm)	Concrete Grade	Force (kN)	Max Bond Stress (Mpa)
NF-FL-E1-SMA	SMA	No Fire	300	M30	14.23	1.51

Equipped with information on force and displacement, the bond stress value was calculated using the formula shown below;

$$\tau = \frac{P}{\pi\, d_b\, l_b}$$ Equation 3.1

where,

P: Force (N),

l_b: Embedment length of the rebar (mm), and

d_b: Diameter of the rebar (mm)

τ: Bond Stress (MPa)

For example, in the case of NF-FL-E1-SMA;

where,

P=14.23 (kN), l_b= 300mm, d_b=10mm

τ= (14230)/(3.1416 x 300 x 10) = 1.51MPa

Therefore, the bond stress for specimen NF-FL-E1-SMA is established to be 1.51MPa. Having derived the bond stress value (as discussed above) and the recorded bond slip values from the observations made during the course of pull-out testing, a chart (stress vs slip) is plotted as shown in Figure 3.46.

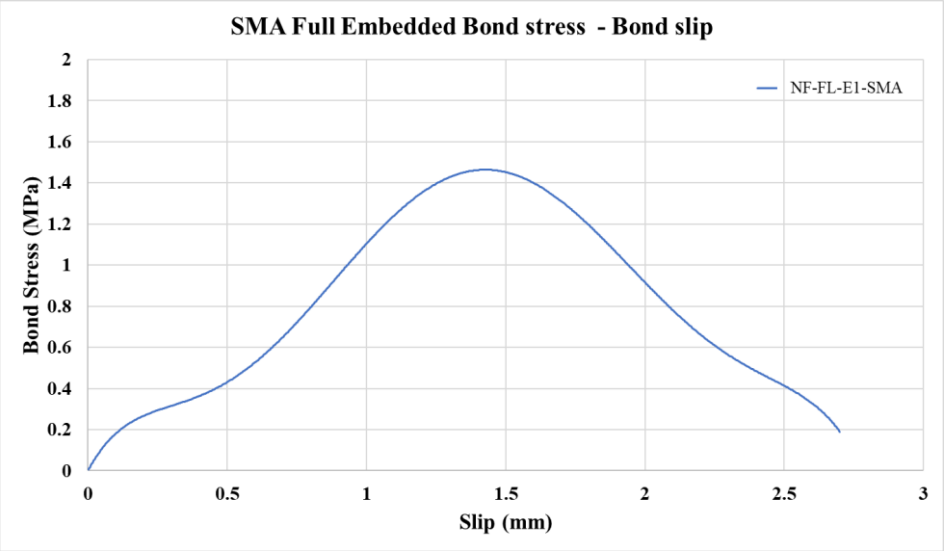

Figure 3.46: Bond Stress-Slip plot for NF-FL-E1-SMA.

The goal of the physical experiments was to extract two sets of data from each test carried out on the various specimens considered. The two data sets are 1) Bond Stress vs Slip for Steel (Data set 1) and 2) Bond Stress vs Slip for SMA (Data set 2). For the sample case under discussion (NF-FL-E1-SMA), the above mentioned two sets of data are noted from the plot provided in Figure 3.46. First the maximum stress value τ_t^{max} is noted (and recorded into Data set 1), a vertical line (red line shown in Figure 3.47) is then drawn from the point such that it intersects the X axis (Slip). The slip value at this point δ_t^* is noted and recorded into Data set 2. A subset of Data set 2 (ratio of δ_t^* to δ_t^c) is also created.

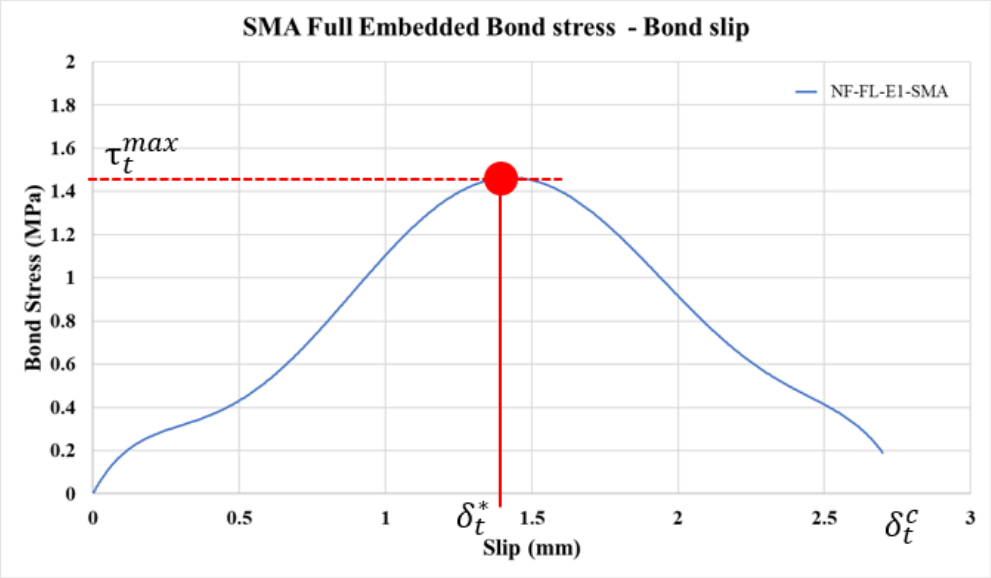

Figure 3.47: Bond Stress-Slip plot for NF-FL-E1-SMA (max. bond stress)

Table 3.7 A data set created as shown in the Table 3.7 for the specimen NF-FL-E1-SMA provides all the parameters required to define the interface material of the cohesive zone (CZM Bilinear model) in the numerical studies.

Table 3.7: Summary of data on concrete-SMA rebar pull out tests

Sno.	Specimen Name	Max. Traction (τ) MPa	Traction Displacement (δ*) mm	Ratio (δ*)/(δc)	Weight Parameter
1	NF-FL-E1-SMA	1.51	1.4	0.52	1

The above discussed process is from the literature as elaborately explained in Chapter 4 (Section 4.4.5). The same process is repeated for each of the 12 specimens considered in this work. The bond stress values between SMA-concrete and Steel-concrete specimens as calculated from the Force and other values as explained earlier for each of the specimens is tabulated in Table 3.8 and Table 3.9 respectively. It could be noted that there are 2 tests for each specimen type. The tests were duplicated to get the average values. However, for discussion sake only 12 specimens are worth mentioning.

Table 3.8: Summary of data on concrete-SMA rebar pull out tests

Specimen Tested	Rebar Material	Fire exposed duration (mins)	Embedded Length (mm)	Concrete Grade	Force (kN)	Max Bond Stress (Mpa)
NF-FL-E1-SMA	SMA	No Fire	300	M30	14.23	1.51
NF-FL-E2-SMA	SMA	No Fire	300	M30	14.04	1.49
30F-FL-E1-SMA	SMA	30	300	M30	11.12	1.18
30F-FL-E2-SMA	SMA	30	300	M30	10.18	1.08
60F-FL-E1-SMA	SMA	60	300	M30	8.95	0.95
60F-FL-E2-SMA	SMA	60	300	M30	7.5	0.8
NF-HL-E1-SMA	SMA	No Fire	150	M30	8.5	1.82
NF-HL-E2-SMA	SMA	No Fire	150	M30	8.24	1.75
30F-HL-E1-SMA	SMA	30	150	M30	6.5	1.39
30F-HL-E2-SMA	SMA	30	150	M30	7.02	1.49
60F-HL-E1-SMA	SMA	60	150	M30	6.36	1.35
60F-HL-E2-SMA	SMA	60	150	M30	6.55	1.39

Table 3.9: Summary of data on concrete-steel rebar pull out tests

Specimen Tested	Rebar Material	Fire exposed duration (mins)	Embedded Length (mm)	Concrete Grade	Force (kN)	Max Bond Stress (Mpa)
NF-FL-E1-Steel	Steel	No Fire	300	M30	31.53	3.34
NF-FL-E2- Steel	Steel	No Fire	300	M30	30.7	3.25
30F-FL-E1-Steel	Steel	30	300	M30	30.01	3.18
30F-FL-E2-Steel	Steel	30	300	M30	30.3	3.21
60F-FL-E1-Steel	Steel	60	300	M30	18.7	1.98
60F-FL-E2-Steel	Steel	60	300	M30	18.5	1.96
NF-HL-E1-Steel	Steel	No Fire	150	M30	17.01	3.61
NF-HL-E2-Steel	Steel	No Fire	150	M30	16.93	3.59
30F-HL-E1-Steel	Steel	30	150	M30	14.95	3.17
30F-HL-E2-Steel	Steel	30	150	M30	15.01	3.18
60F-HL-E1-Steel	Steel	60	150	M30	8.62	1.81
60F-HL-E2-Steel	Steel	60	150	M30	8.41	1.78

Bond stress vs bond slip charts were plotted one each for half and full embedded steel rebar inside concrete respectively (Figure 3.48a,b) and another similar set for half and full embedded SMA rebar inside concrete respectively (Figure 3.49 a,b).

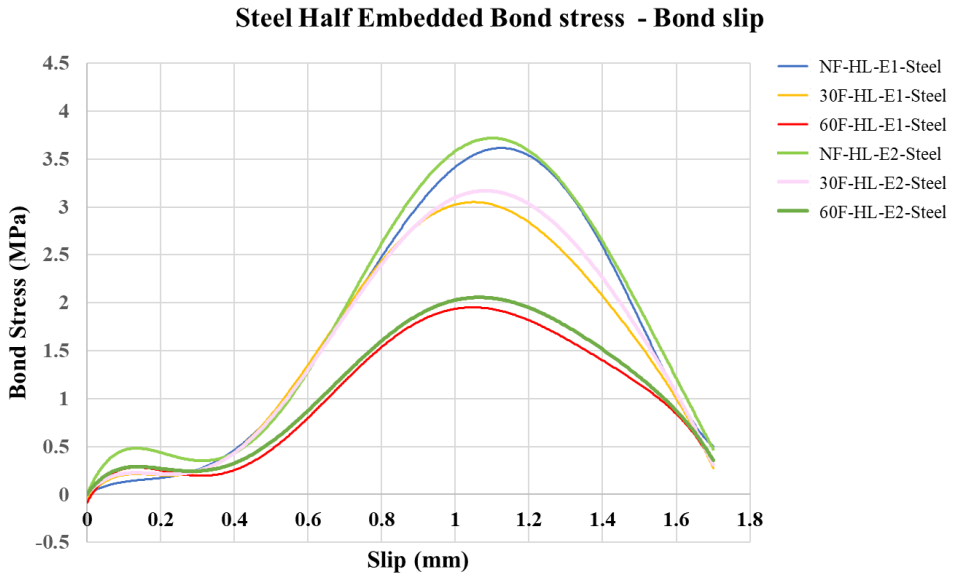

(a) Steel-concrete (half embedded)

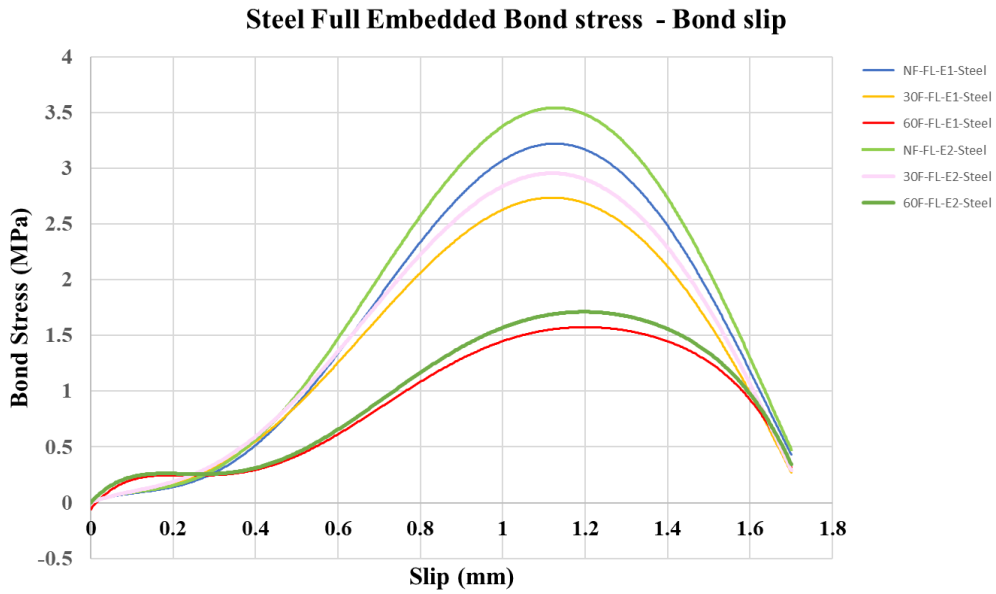

(b) Steel-concrete (full embedded)

Figure 3.48: Steel-concrete a) half embedded and b) full embedded, bond stress at various conditions and parameters

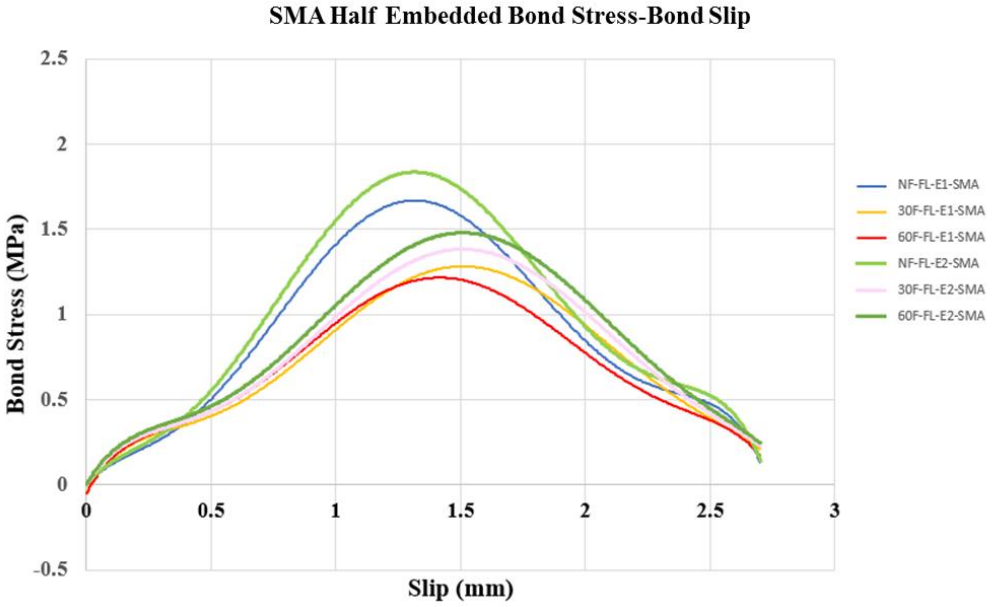

(a) SMA-concrete (half embedded)

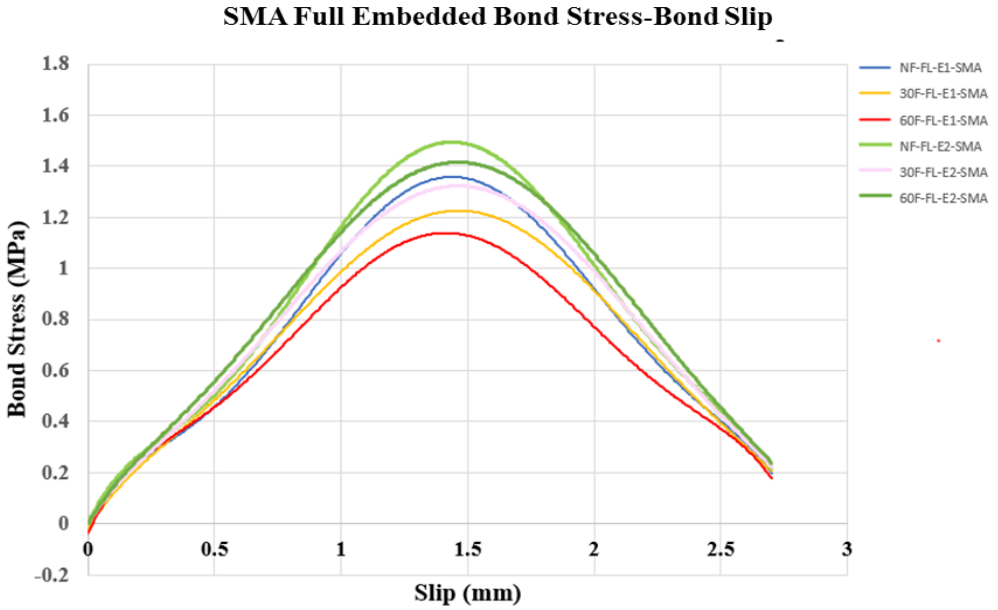

(b) SMA-concrete (full embedded)

Figure 3.49: SMA-concrete a) half embedded and b) full embedded, bond stress at various conditions and parameters

A data set created as shown in Table 3.10 for all the specimens considered in this work provides all of the parameters required to define the respective interface material of the cohesive zone (CZM Bilinear model) in the numerical studies. The experimental studies conducted and the resulting data set generated achieved AIM1 of this thesis.

Such a model takes into account the non-linear structural effects that are influenced by thermal loading. The absence of such temperature specific data and the model related information in the literature made the requirement of physical experiments an absolute necessity in this work. The information generated on the parameters as presented in Table 3.10 will contribute greatly to advance non-destructive testing method of analysing bond stress between SMA-concrete and Steel-concrete rebars that are exposed to high temperatures.

Table 3.10: Summary of data on Maximum tangential traction, Tangential Displacement, Ratio and Non dimensional weigh parameter

Sno.	Specimen Name	Max. Traction (τ) MPa	Traction Displacement (δ*) mm	Ratio (δ*)/(δc)	Weight Parameter
1	NF-FL-E1-SMA	1.51	1.4	0.52	1
2	NF-FL-E2-SMA	1.49	1.45	0.54	1
3	30F-FL-E1-SMA	1.18	1.5	0.56	1
4	30F-FL-E2-SMA	1.08	1.65	0.61	1
5	60F-FL-E1-SMA	0.95	1.5	0.56	1
6	60F-FL-E2-SMA	0.8	1.5	0.56	1
7	NF-HL-E1-SMA	1.82	1.3	0.48	1
8	NF-HL-E2-SMA	1.75	1.3	0.48	1
9	30F-HL-E1-SMA	1.39	1.5	0.56	1
10	30F-HL-E2-SMA	1.49	1.5	0.56	1
11	60F-HL-E1-SMA	1.35	1.4	0.52	1
12	60F-HL-E2-SMA	1.39	1.55	0.57	1
13	NF-FL-E1-Steel	3.34	1.15	0.67	1
14	NF-FL-E2-Steel	3.25	1.15	0.67	1
15	30F-FL-E1-Steel	3.18	1.15	0.67	1
16	30F-FL-E2-Steel	3.21	1.15	0.67	1
17	60F-FL-E1-Steel	1.98	1.15	0.67	1
18	60F-FL-E2-Steel	1.96	1.05	0.61	1
19	NF-HL-E1-Steel	3.61	1.15	0.67	1
20	NF-HL-E2-Steel	3.59	1.15	0.67	1
21	30F-HL-E1-Steel	3.17	1.05	0.61	1
22	30F-HL-E2-Steel	3.18	1.1	0.67	1
23	60F-HL-E1-Steel	1.81	1.1	0.67	1
24	60F-HL-E2-Steel	1.78	1.1	0.67	1

With the required data set generated as presented in Table 3.10 AIM 1 of this thesis stands successfully achieved

3.7.3 Failure Modes in the tested physical specimens

In all, 24 specimens (two of each type-1 set shown in Figure 3.50) were physically tested during the experimental program and the failure of each pull out test specimen was studied. Figure 3.51 shows:

a) the pull-out of SMA bar with no residuals of concrete on the bar meaning the bar slipped through the concrete;
b) the pull-out of steel bar with very fine dust like particles attached to the bar, which could still be considered a slip; and
c) the internal cut section of the smooth interface area between SMA and concrete where de-bonding occurred.

Figure 3.50: The 12 specimens

As the axially applied load is gradually increased during the pull-out test, the rebar over comes the chemical adhesion, frictional resistance and then the mechanical interlock developing large stress causing the concrete to fail in tension or compression leading to spitting failure. However, in the experiments carried out it was noticed (refer Figure 3.51) that smooth pull-out failure had occurred in (c). The bond resistance can

mainly be attributed to adhesion and the friction between the two materials rather than mechanical in nature. No splitting or cracking of the concrete was observed at the bond interface as shown in (c). There was no spalling of concrete during the experiment. Due to high temperature during the test, cracks were observed on the concrete as shown in (d). The failure mode was consistent across all the samples. No cracking or breaking of the specimen was observed because of the pull-out force.

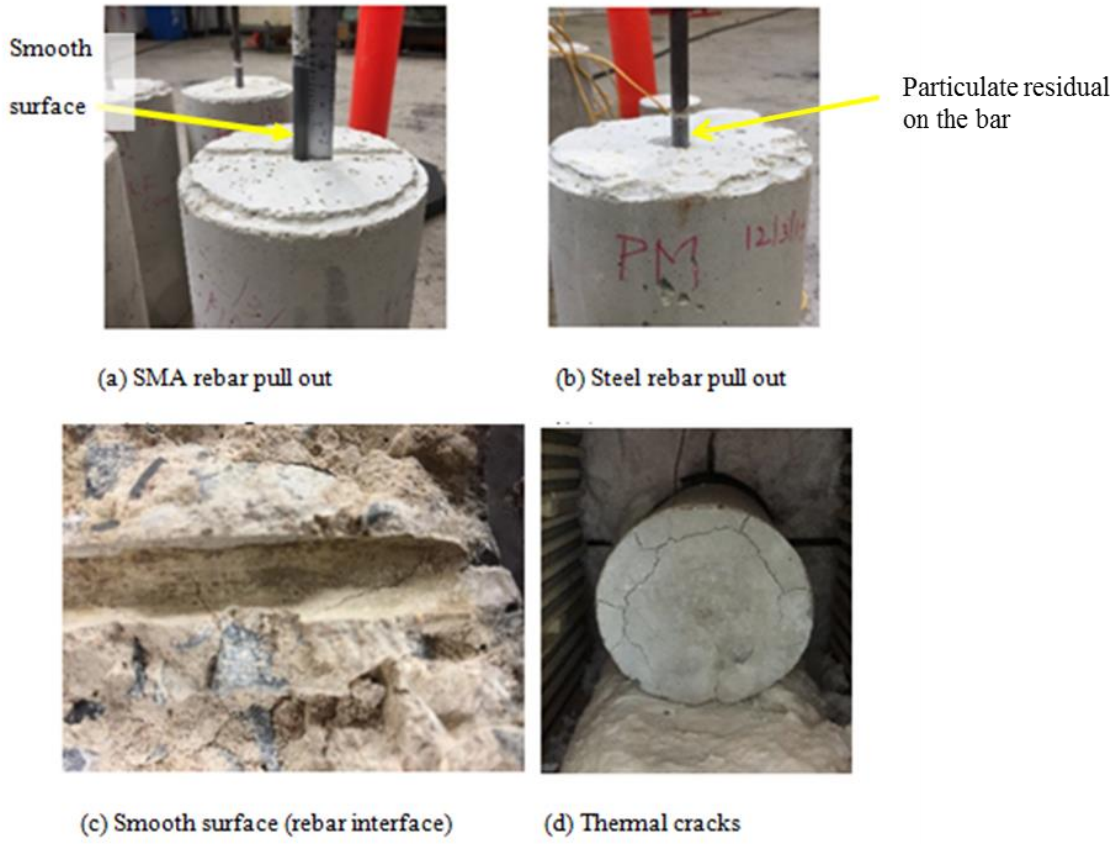

Figure 3.51: Failure Modes: Pull out test under high temperature

Having collected all of the data and information required from the experimental studies as explained thus far, numerical models were developed in Chapter 5 that would employ such data to conduct numerical experiments on the bond slip behaviour of the SMA-concrete and Steel-concrete interface specimens that are subjected to thermal exposure. The results of the numerical experiments are discussed next.

3.8 Chapter Summary

A gap in the literature review as identified in Chapter 2 was the lack of data on the bond stress behaviour between SMA-concrete. Such information was crucial to the development of non-destructive methods (numerical modelling) of analysing the bond stress characteristics of SMA-concrete which is an aim (AIM3) of this research work. In the absence of the relevant data in the literature on SMA-concrete as mentioned above, this thesis explored the physical experimentation path to extract the relevant data.

This chapter was aimed at the design and development of experiments in order to examine and study the bond stress behaviour between SMA-concrete. An overview of the test plan is shown in Figure 3.52 that identifies the various aspects that were considered in successfully executing the experiments.

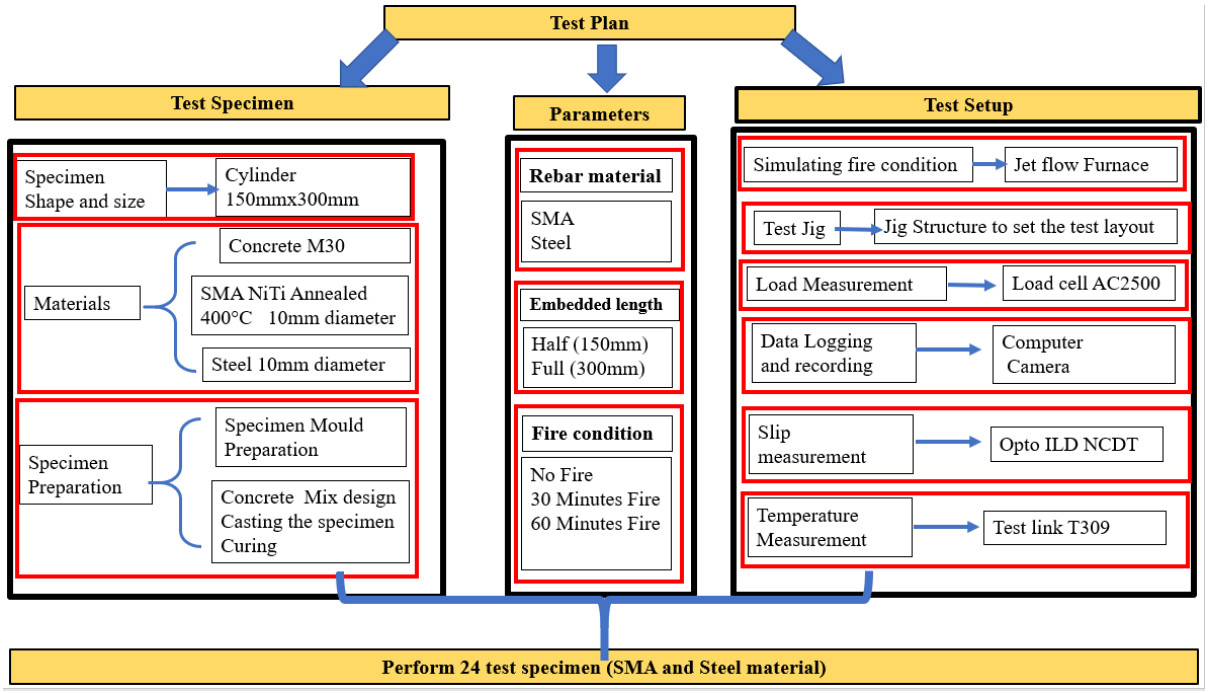

Figure 3.52: Various aspects that were considered in the experimental studies undertaken

A well-established experiment method laid out in the literature called the pull-out test was adopted in this work to assist in the above-mentioned work. To this extent, various equipment/instruments were identified. One such equipment is the furnace (Jetflow)

employed in this work with some modifications done to hold the specimen and allow for the instrumentation to be placed without any hindrance. A hydraulic cylinder and associated gear were employed to develop the required pull strength of 0.1kN. Various other instruments such as thermocouples (K type), temperature sensors, load cells, displacements sensors and other relevant software programs such as (x, y, z) were procured. All such gear mentioned above were assembled onto a test platform that provided the stability required for the pull-out test. Where possible all the data was collected on to computer for further analysis.

SMA rebars needed a heat treatment to activate and train the material for its memory retaining ability. It was important to establish the maximum operational temperature for such heat treatment in order to protect the material's shape retaining memory ability. To this extent, samples were extracted from the bar and heat treated at various temperatures. Such heat-treated samples were studied using DSC experiments (which record the response of the material for various heat treatment temperatures). These experiments provided an understanding on the phase change temperature for each of the heat-treated sample thereby establishing the maximum operational temperature (400°C). Beyond this heat treatment temperature, the sample exhibited no further phase transformation.

Tests were conducted on a total of 24 specimens (12 each for SMA-concrete and Steel-concrete) with varying rebar depths (150 and 300mm) and for varying fire conditions (No fire condition, fire conditions at 30min and fire conditions at 60min) as shown in Table 3.11.

Table 3.11: List of pull-out specimens tested

Sr. No.	Rebar material	Name	Bar Diameter (mm)	Embedded length (mm)	Fire Duration (mins)
1	SMA	NF-FL-E1-SMA	10	300	Zero
2		30F-FL-E1-SMA	10	300	30 min
3		60F-FL-E1-SMA	10	300	60 min
4		NF-HL-E1-SMA	10	150	Zero
5		30F-HL-E1-SMA	10	150	30 min
6		60F-HL-E1-SMA	10	150	60 min
7	Steel	NF-FL-E1-Steel	10	300	Zero
8		30F-FL-E1-Steel	10	300	30 min
9		60F-FL-E1-Steel	10	300	60 min
10		NF-HL-E1-Steel	10	150	Zero
11		30F-HL-E1-Steel	10	150	30 min
12		60F-HL-E1-Steel	10	150	60 min

Such a comprehensive study resulted in a significant data set on the bond stress values for each one of the above-mentioned cases. A snapshot of the same is showcased in Figure 3.48 (Steel-concrete bond stress) and Figure 3.49 (SMA-concrete bond stress). An extensive analysis of the results of the experiments is presented in Chapter 5 (Results and Discussion).

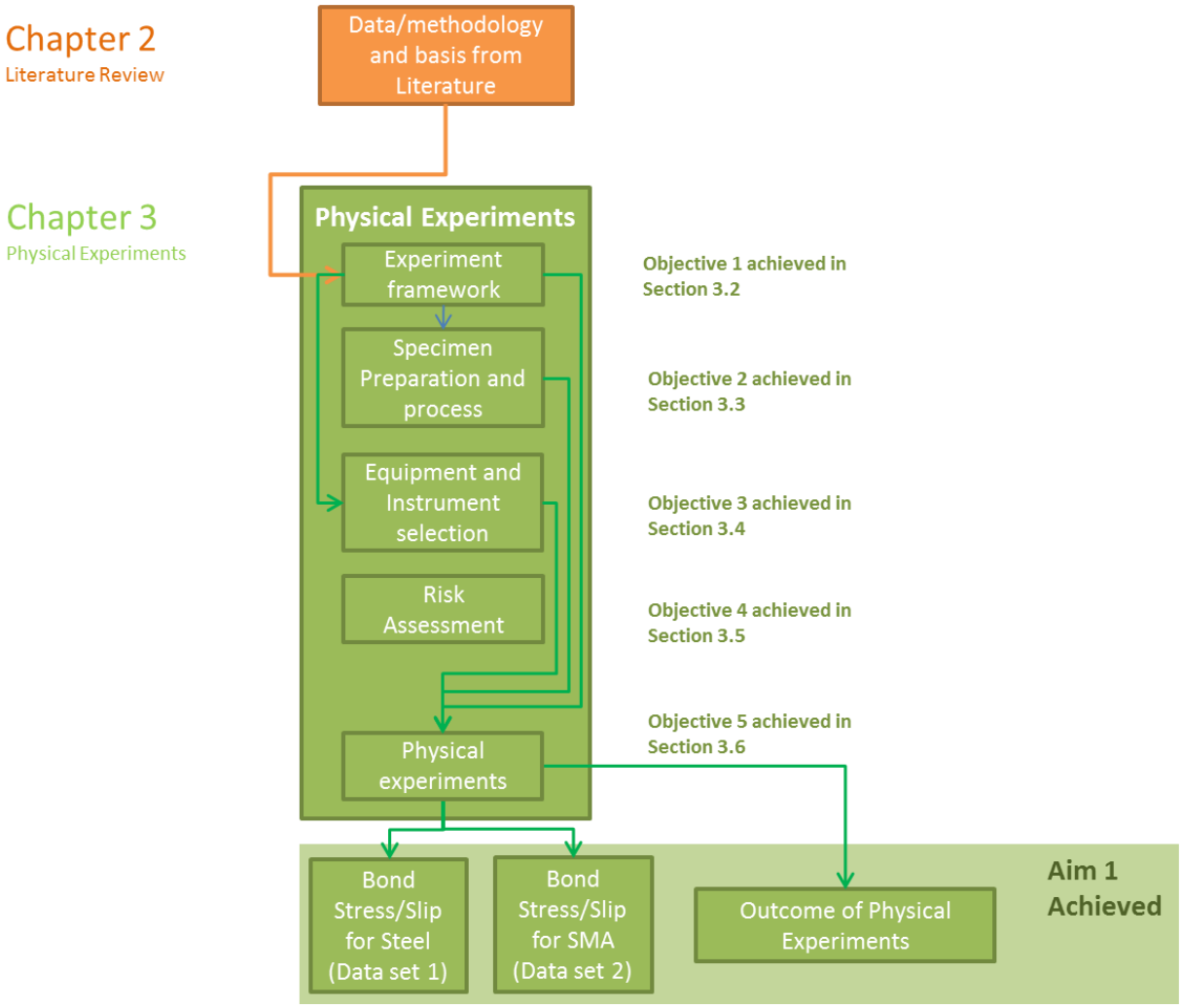

Figure 3.53: Achievement of the objectives of AIM 1

In summary, all the objectives that were set out to successfully achieve AIM 1 were achieved as shown in Figure 3.53. In extracting the required data sets as shown in

Table 3.12 on the bond stress/slip between steel-concrete and SMA-concrete, AIM 1 of this research is achieved; which is

- To conduct experimental studies to understand the bond stress behaviour of concrete-steel rebar and concrete-SMA rebars that are subjected to high temperature.

Table 3.12: Summary of data on Maximum tangential traction, Tangential Displacement, Ratio and Non dimensional weigh parameter

Sno.	Specimen Name	Max. Traction (τ) MPa	Traction Displacement (δ*) mm	Ratio (δ*)/(δc)	Weight Parameter
1	NF-FL-E1-SMA	1.51	1.4	0.52	1
2	NF-FL-E2-SMA	1.49	1.45	0.54	1
3	30F-FL-E1-SMA	1.18	1.5	0.56	1
4	30F-FL-E2-SMA	1.08	1.65	0.61	1
5	60F-FL-E1-SMA	0.95	1.5	0.56	1
6	60F-FL-E2-SMA	0.8	1.5	0.56	1
7	NF-HL-E1-SMA	1.82	1.3	0.48	1
8	NF-HL-E2-SMA	1.75	1.3	0.48	1
9	30F-HL-E1-SMA	1.39	1.5	0.56	1
10	30F-HL-E2-SMA	1.49	1.5	0.56	1
11	60F-HL-E1-SMA	1.35	1.4	0.52	1
12	60F-HL-E2-SMA	1.39	1.55	0.57	1
13	NF-FL-E1-Steel	3.34	1.15	0.67	1
14	NF-FL-E2-Steel	3.25	1.15	0.67	1
15	30F-FL-E1-Steel	3.18	1.15	0.67	1
16	30F-FL-E2-Steel	3.21	1.15	0.67	1
17	60F-FL-E1-Steel	1.98	1.15	0.67	1
18	60F-FL-E2-Steel	1.96	1.05	0.61	1
19	NF-HL-E1-Steel	3.61	1.15	0.67	1
20	NF-HL-E2-Steel	3.59	1.15	0.67	1
21	30F-HL-E1-Steel	3.17	1.05	0.61	1
22	30F-HL-E2-Steel	3.18	1.1	0.67	1
23	60F-HL-E1-Steel	1.81	1.1	0.67	1
24	60F-HL-E2-Steel	1.78	1.1	0.67	1

The above-mentioned data sets as enlisted in

Table 3.12 shall be used in the following Chapter for the development of numerical models (for testing the SMA-concrete bond stress at the cohesive zone). The manner in which the data flows from Chapter 3 to Chapter 4 and subsequently to Chapter 5 is shown in Figure 3.54.

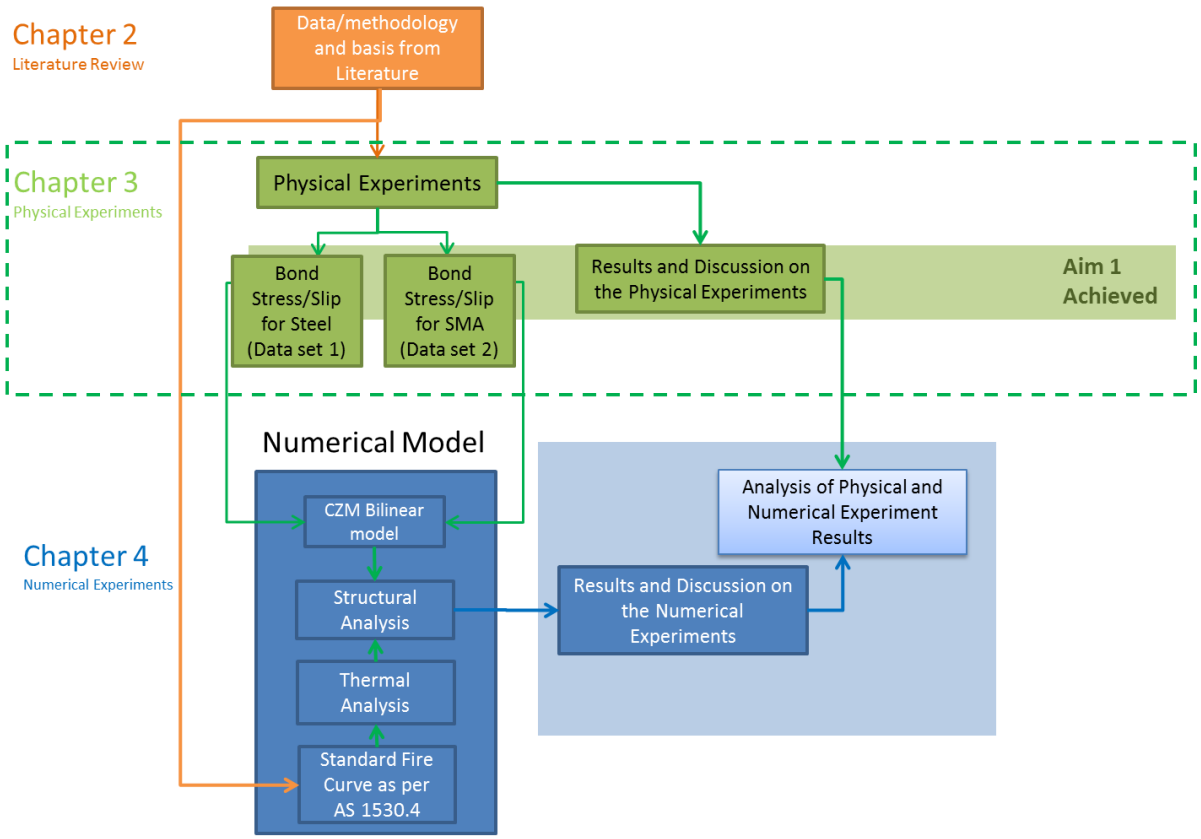

Figure 3.54: Data flow from physical experiments (Chapter 3) to Numerical experiments (Chapter 4)

CHAPTER 4: Numerical Studies

4.1 Introduction

This Chapter is aimed at developing a numerical model that allows for a quick and non-destructive method of examining bond stress between SMA-concrete. Since not much data was available in the literature on the above said topic, an extensive experimental study was undertaken in this work to generate the required data in Chapter 3. The data set is employed in this work as a basis on which numerical models are built. The data set also allows for the validation of the first of its kind Numerical model developed in this work. Essentially, this Chapter addresses AIM 2 of the thesis. The AIM2 and its objectives are:

AIM 2

- Develop a numerical model to study the bond stress and bond slip behaviour in the cohesive zone of SMA-concrete and Steel-concrete specimens under various fire conditions; the objectives of which are:
    - Establish the numerical framework;
    - Develop and benchmark an appropriate numerical model;
    - Conduct numerical experiments to study bond stress behaviour between the SMA-concrete and Steel-concrete specimens by employing the validated numerical model utilising inputs from CZM bilinear modelling mesh elements that fully takes into account both the thermal and non-linear structural conditions; and
        - Develop CAD model of the domain of interest;
        - Select suitable mesh element type and conditions and generate the mesh;
        - Apply appropriate material properties for the concrete and rebar of the specimen;
        - Apply boundary conditions and perform thermal analysis;

- Apply data generated from physical experiments (carried out in AIM 1) to define the material property of the interface of the concrete-rebar interface in structural analysis;
- Adopt thermal profile from the thermal analysis to examine the structural response of the specimen using structural analysis; and
- Validate the novel method developed by comparing the outcomes with numerical experiment.

- Document results for a comparative analysis between physical and numerical experiments.

To this extent, first the numerical framework is established that identifies topic that are of importance in the literature. The exercise is to identify a numerical process and potentially the parameters that are required to run the numerical simulations. Once identified, validation studies were taken up that verified the accuracy of the numerical model developed in this work as against other works from the literature. The developed numerical models were then adopted and the data from the experiments conducted in the previous chapter were deployed to study the numerical model's effectiveness to duplicate the observations made on the bond stress between SMA and the concrete.

As a step leading to the development of the appropriate numerical model, first the specimen is subjected to thermal analysis to extract the thermal profile which is then applied to the specimen during the course of the nonlinear structural analysis wherein the bond stress is examined as a response to pull-out testing. The failure modes observed in both numerical and physical experiments are closely examined to establish the accuracy of the novel numerical model developed in this work. On successfully establishing the accuracy of the numerical model it is further employed to examine the bond stress of the comparative specimens from the physical experiments. The results of all such numerical experiments conducted in this work conclude this Chapter. A new non-destructive method of testing SMA-concrete bond stress using numerical modelling is developed in this work which is a significant contribution to the literature. The successful development of such method achieves the Aim 2 of this thesis.

4.2 Numerical Model Framework

This section deals with the numerical modelling of concrete by itself and concrete-steel as identified in the literature. The framework forms the basis on which the numerical model for this work will be developed for studying the bond stress and bond slip behaviours of both SMA-concrete and steel-concrete specimens. More importantly suitable mesh element types need to be established so as to allow the numerical model developed in this work to fully replicate real time scenarios experienced by both concrete and the rebar materials under standard room temperature and during fire conditions. To this extent, for concrete the element type Solid65 and Solid185 elements were selected based on their application found in the literature for modelling concrete and rebar (both steel and SMA) respectively. More elaborate explanation is given below.

4.2.1 Concrete Model

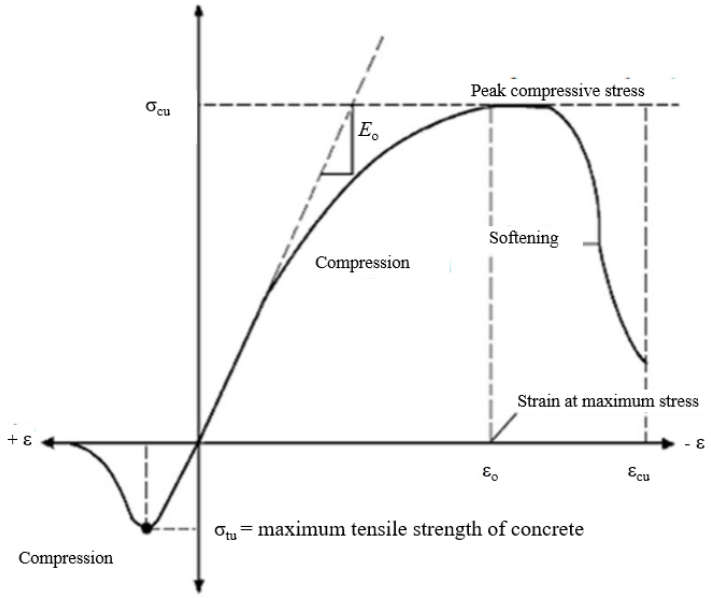

Figure 4.1: Typical stress strain for concrete material (Ansys help documentation)

The stress strain model for the concrete as suggested by Barbosa et al. 1998 is shown in Figure 4.1. In compression, the stress-strain curve for concrete is linearly elastic up to about 30 percent of the maximum compressive strength. Then from this point

onward, the stress increases gradually up to the maximum compressive strength. Once it reaches the maximum compressive strength σ_{cu}, the curve descends into a softening region and eventually crushing failure occurs at an ultimate strain ε_{cu}. Georgin et al. 2003 identified that, the stress-strain curve for concrete is approximately linearly elastic up to the maximum tensile strength in tension. After this point, the concrete cracks and the strength decreases gradually to almost zero. The same approach is used in this study to model the concrete material.

ANSYS, commercially available Finite Element Analysis software that has been used extensively in the literature was employed in this work to develop the numerical models. Concrete is a complex material to model and standard mesh elements do not have the capability to include the concrete material with specific details. Concrete Solid65 (Figure 4.2) a special purpose three-dimensional eight noded solid isoparametric element is used to model concrete element in the literature (Dahmani et al. 2010; Md Arman et al. 2015; Yongquan et al. 2016). It is based on a constitutive model for the triaxial behaviour of concrete and uses Williams and Warnke failure criteria. The concrete element includes a smeared crack analogy for cracking in tension zone and a plasticity algorithm to account for the possibility of concrete crushing in compression zone. It is for this reason that Concrete Solid65 elements were selected in this work for numerical studies.

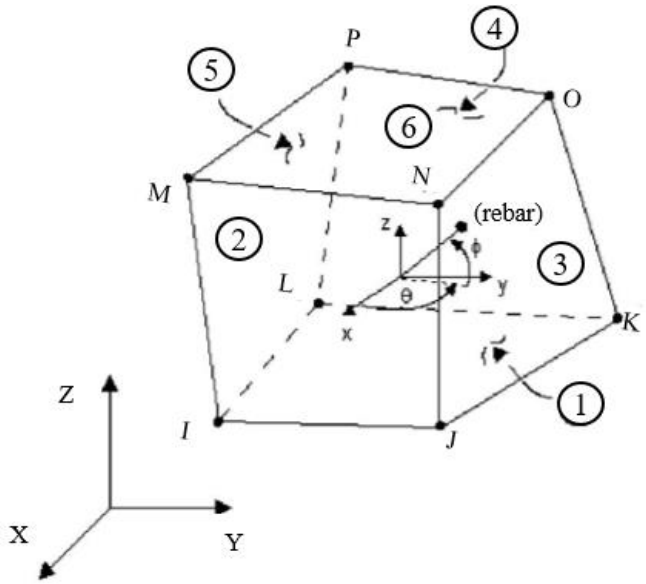

Figure 4.2: Concrete Solid65 Element geometry and shapes (Ansys help documentation)

Based on the literature, the Following data was collected and utilised in the numerical analysis as inputs to model the concrete behaviour in ANSYS:

- Modulus of elasticity (E_c);
- Ultimate uniaxial compressive strength (f_c);
- Ultimate uniaxial tensile strength (f_t);
- Poisson's ratio (ν);
- Shear transfer coefficient (β_t); and
- Compressive uniaxial stress-strain relationship for concrete.

The shear transfer coefficient, β_t, represents conditions of the crack face. The value of β_t ranges from 0.0 to 1.0, with 0.0 representing a smooth crack (complete loss of shear transfer) and 1.0 representing a rough crack (no loss of shear transfer). The value of β_t used in many studies of reinforced concrete structures varied between 0.05 and 0.25. A number of comparative analytical studies have been attempted by Kachlakev et al. 2001 to evaluate the influence of shear transfer coefficient. They are used for finite element models of reinforced concrete beams and bridge decks with β_t values within the range 0.05-0.25 and encountered convergence problems at low loads with β_t values less than 0.2. Therefore, a shear transfer coefficient of 0.2 has been used.

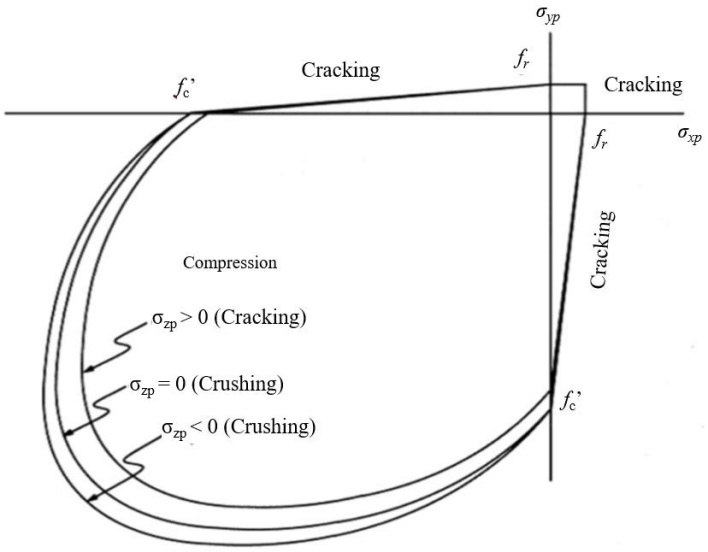

Figure 4.3: Failure surface for concrete -ANSYS Concrete Solid65 (Ansys help documentation)

Figure 4.3 illustrates the three-dimensional failure surface for concrete. From the figure it can be noted that the most significant nonzero principal stresses are in the x and y directions and are represented by σ_{xp} and σ_{yp}, respectively (Dahmani et al. 2010). Three failure surfaces are shown as projections on the σ_{xp}-σ_{yp} plane. The mode of failure is a function of the sign of σ_{zp} (principal stress in the z direction). Researchers T. Subramani et al. 2014 and Bangash (1989) established that when the principal tensile stress in any direction lies outside of the failure surface, cracking occurs in a concrete element. In the direction parallel to the principal tensile stress direction, the elastic modulus of the concrete element is set to zero after cracking (Nilson, 1968; Wahyuni et al. 2011). When all principal stresses are compressive and lie outside the failure surface, crushing occurs. Thereafter, the elastic modulus is set to zero in all directions and the element effectively disappears (Zhang et al. 2013). According to Mindess et al. 2003, crack's formation and thus concrete failure is attributed to the weakness of concrete in tension where the specimen is subject to a uniaxial compressive load in compression test. Secondary tensile strains caused by the impact of Poisson occurs perpendicular to the load.

Both cracking and crushing phenomena of failure modes are considered for concrete materials. To define a failure surface for the concrete, the data on ultimate tensile and compressive strengths from the literature has been used in this study. Since this study also aims at examining concrete with rebars (both SMA and steel) a method from the literature was sought to model the interface in the numerical studies. Since SMA-concrete studies on bond stress were absent in the literature (for which a numerical model is being developed in this work), well understood methods on Steel-concrete interface modelling from the literature is adopted in this work to develop a numerical Model for the SMA-concrete bond stress studies.

4.2.2 Steel-Concrete interface modelling

The steel-concrete bond interface modelling provides information on bond stresses. A numerical method known as Cohesive Zone Method is a method that is found to be employed in the literature for the numerical modelling of a two-material junction for interface delamination and progressive failure. This approach introduces a failure mechanism by gradually degrading the material elasticity between the surfaces. The

material behaviour at the interface is characterized by the stresses (normal and tangential) and separation distances (normal gap and tangential sliding). Modelling of cohesive zone between steel and concrete is achieved by employing interface elements that are meshed in between layers with initial zero thickness (Figure 4.4).

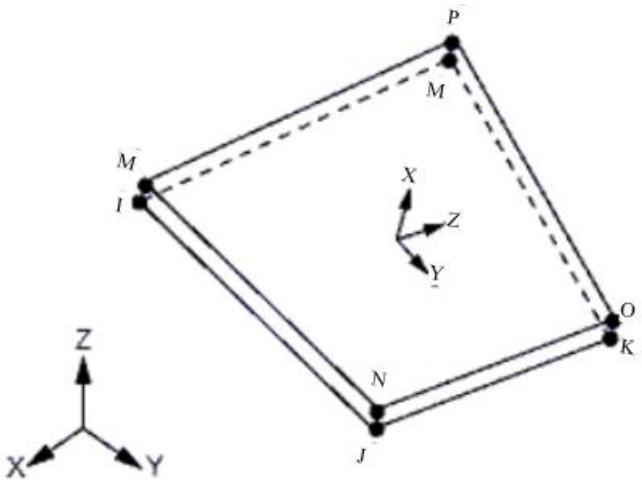

Figure 4.4: Interface element Inter 205 – ANSYS element (Ansys help documentation)

Interface elements use exponential material law for elasticity and debonding. The cohesive zone model can address three modes of separation as follows and as shown in Figure 4.5.

- Mode I: debonding for normal separation;
- Mode II: debonding for tangential separation; and
- Mode II: debonding for normal and tangential (Mixed mode) and

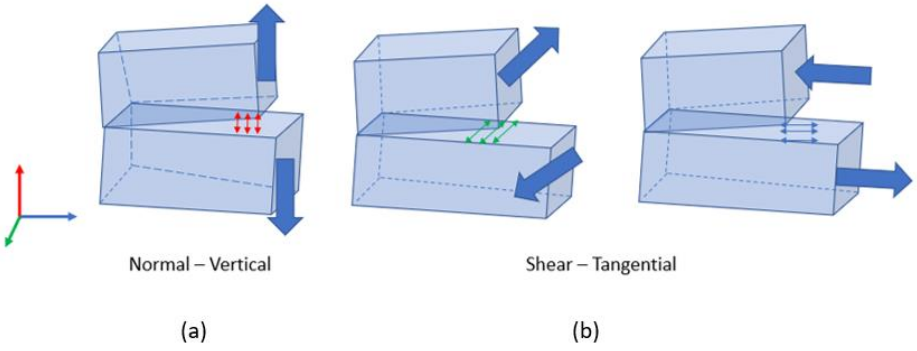

Figure 4.5: Debonding: (a) Normal separation (b) Shear (tangential) separation

For the above mentioned reasons the Cohesive Zone Method is adopted in this study to examine the bond strength and bond failure mechanism between Concrete and SMA/Steel rebars as shown in Figure 4.6.

4.2.3 Cohesive zone cracking

Cohesive zone cracking in a CZ model, interfacial separation occurs within a cohesive damage zone when the damage exceeds a pre-set limit. The stresses (normal and tangential) and separation distances (normal gap and tangential sliding) characterise the material behaviour at the interface. Within the cohesive zone, there are active traction stresses between the cohesive surfaces and that the interaction is governed by the traction separation law (Kyoungsoo et al. 2011). Before a load is applied, a CZ zone mesh element is said to be undamaged, while a fully damaged element is noted as completely separated and does not produce any force interactions between the cohesive surfaces. Figure 4.6 shows a cohesive zone model for interfacial separation.

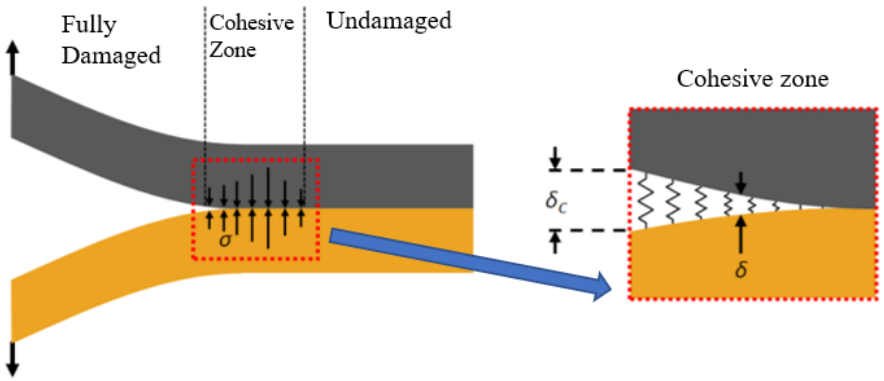

Figure 4.6: Cohesion zone modelling at interface (Ansys help documentation)

The traction σ is exerted by the interface until the interfacial separation δ reaches a critical value δ_c. σ is a function of δ given by traction-separation law. As the element becomes damaged, the area beneath the traction-separation law is the mechanical work needed to separate the element. Thus, the area beneath the traction-separation law is equivalent to critical strain energy release rate (G_c).

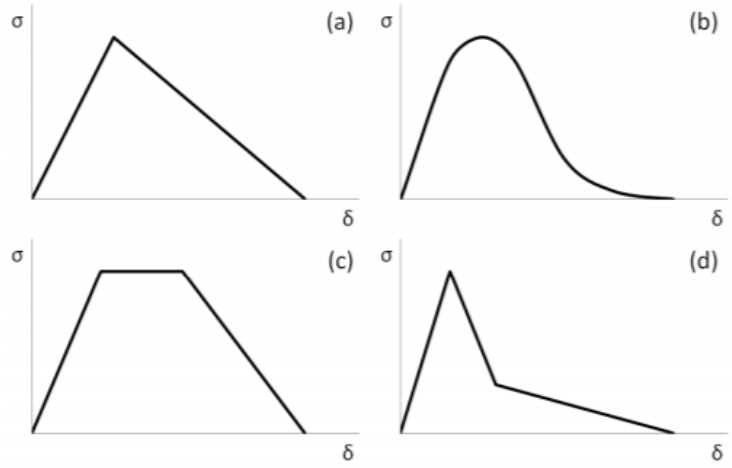

Figure 4.7: Traction – separation laws for cohesive zone models a) Bilinear, b) Exponential, c) Trapezoidal, and d) Trilinear laws.

There are many ways (such as bilinear, exponential, trapezoidal, and trilinear) in which the CZ law can be defined when describing material behaviours (Figure 4.7). Such laws allow for cohesive zone elements to model a wide range of material behaviour, including the nonlinear behaviours, fracture toughness parameter such as K_{ic} (Force) J_{ic} (energy) fatigue crack growth rate study (which has been applicable for ferrous and non-ferrous materials and alloys). In the experiments conducted in the previous Chapter (experimental studies) the SMA rebar and concrete material bond failure showed both normal and shear separation in the physical pull-out tests carried out. For reasons mentioned above, bilinear traction-separation law was found to be suitable for studying the bond stress and separation in this work.

In addition, a bilinear traction-separation law (Figure 4.7) is used because the curve is defined by only three parameters (maximum tangential traction σ_{max}, tangential displacement δ_c, and loading unloading ratio $\alpha = \delta^*/\delta_c$). The bilinear laws correspond to pure mode I and pure mode II delamination, and mixed-mode interpolation is adopted in this work. For all the above reasons, in this present study a bilinear law as shown in Figure 4.8 is used to model behaviour between SMA-concrete interface.
The mathematics that governs the traction law in the cohesion zone of rebar concrete interface is presented below.

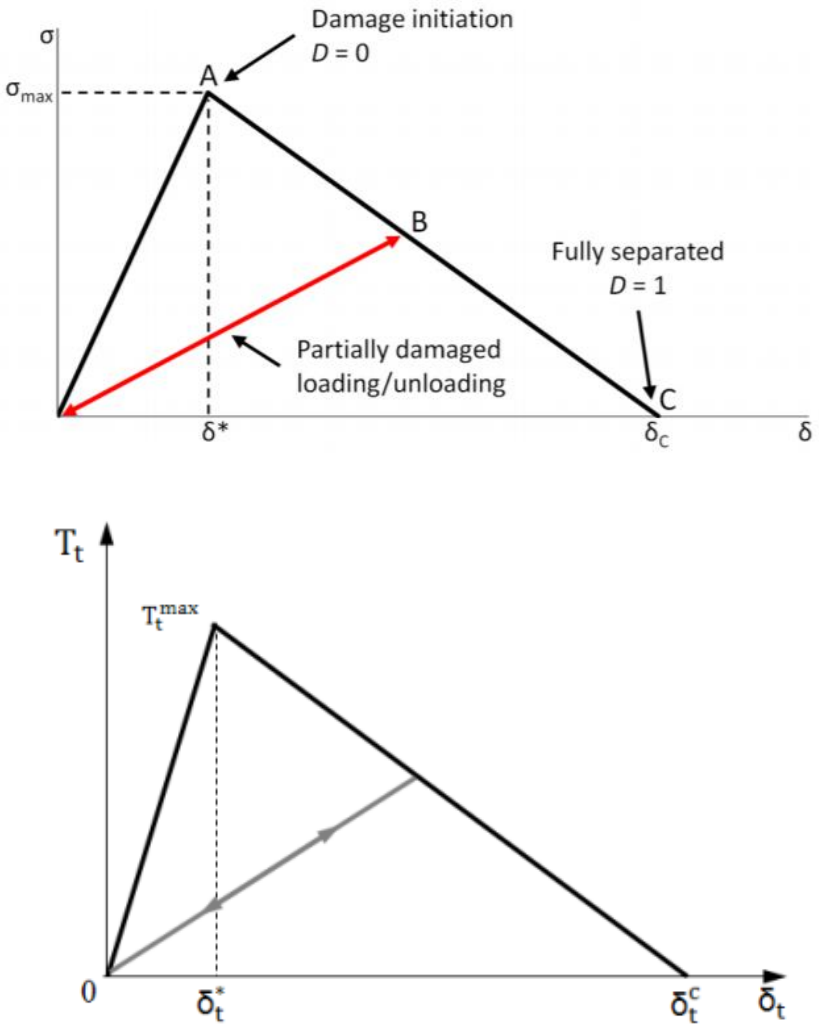

Figure 4.8: Cohesive zone model used to model the bond slip (Ansys help documentation)

The interface element offers resistance (traction) in normal and tangential (in plane) of the element. From the figure below, based on δ_n (normal direction displacement) and δ_t (tangential direction displacement) and the maximum stress capacity before they reach the maximum δ in each direction a peeling (normal separation) or slip (tangential separation) is modelled (Figure 4.9). Since the study in this research is on plain rebar, the failure is mostly in the shear or tangential.

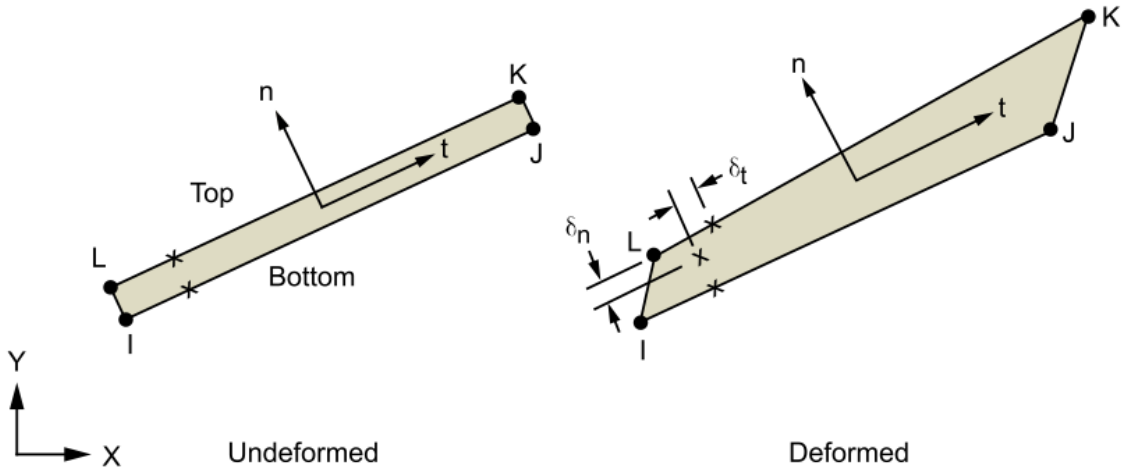

Figure 4.9: Cohesive zone element -INTER 205 (Ansys help documentation)

The relation between tangential cohesive traction T_t and tangential displacement jump δ_t can be expressed as:

$$T_t = K_t \delta_t (1 - D_t) \qquad \text{Equation 4.1}$$

where,

K_t = Tangential cohesive stiffness calculated internally by software

T_t^{max} = Maximum tangential cohesive traction

δ_t^* = Tangential stiffness jump at maximum tangential cohesive traction

δ_t^c = Tangential displacement jump at the completion of debonding

α = Ratio of δ_t^* to δ_t^c

δ_t^{max} = Maximum tangential displacement jump in the deformation history

$\max \delta_t^* \quad (\tau')$ Where $\quad 0 \leq \tau' \leq \tau$

$$D_t = \begin{cases} 0 & \delta_t^{max} \leq \delta_t^* \\ \left(\frac{\delta_n^{max} - \delta_t^*}{\delta_t^{max}}\right)\left(\frac{\delta_t^c}{\delta_t^c - \delta_t^*}\right) & \delta_t^* < \delta_t^{max} \leq \delta_t^c \\ 1 & \delta_t^{max} > \delta_t^c \end{cases}$$

In the above equations, it must be noted that, regardless of the current magnitude of δ, the damage value D can never decrease. In other words, unloading will not reduce the damage that has accumulated. Therefore, if a CZ element is unloaded while

partially damaged, from point B for example, it follows a path of reduced stiffness. When loading is resumed, the element will have the same reduced stiffness until it returns to point B, where further damage will initiate. When the damage parameter is set to D = 1, the CZ element is said to be fully damaged, and the stiffness of the cohesive zone element is zero. The cohesive zone method has been used for analysis to simulate the bonding behaviour between concrete and steel/SMA in this work.

4.2.4 SMA – rebar modelling

SMA is a unique alloy which remembers its shape. In loading and unloading cycles, it can undergo large deformation mechanisms without showing any indication of residual strain. This phenomenon of SMA is called pseudo elastic effect or super elasticity. SMA also possesses a quality of recovering to its original shape through thermal cycles, which is called as the shape memory effect. ANSYS offers two material models to input the data for SMA, one for super elasticity and other for shape memory effect. The super elastic model is more suitable for the SMA properties which undergo large deformation without showing permanent deformation under isothermal condition.

In addition, as the SME (Shape Memory Effect) occurs at low temperatures the material microstructure is initially composed of twinned martensite. In Figure 4.10 upon loading the SMA, the applied stress reaches the critical value for de-twinning at point 2 and at which point the martensite reorientation starts followed by macroscopic deformation (plateau 2-3) (Figure 4.10). At the end of the plateau, the martensite is completely de-twinned. At this point, any further loading only causes elastic deformation of the new microstructure (slope 3-4). Upon unloading, the macroscopic deformation is retained as all variants of martensite are equally stable along the curve leading to point 5. When the material is heated above its critical temperature, the martensite to austenite phase transition begins, allowing the material to recover up to 8% (macroscopic deformation) along the curve (points 6-7). During cooling, the transition from austenite to martensite occurs under no load, thus no macroscopic change can be observed between points 7-1. The described SME is also known as one-way SME, since only a high-temperature shape is memorized by the material. Indeed, no change in shape occurs upon cooling under no applied load condition (Figure 4.10, points 7-1).

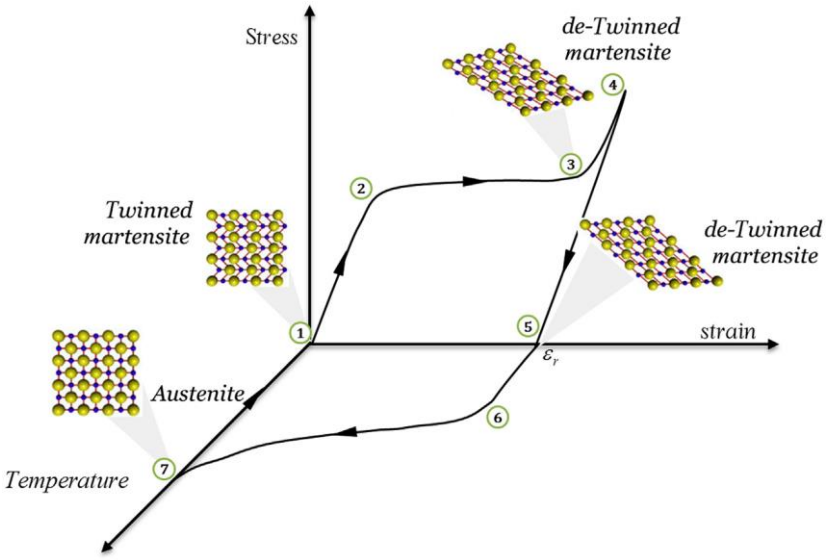

Figure 4.10: SMA Shape Memory Effect -SME (Lagoudas D.C and Kumar P.K)

In ANSYS, the shape memory effect can be specified by seven constants which includes hardening parameter, reference temperature, elastic limit, temperature scaling parameter, maximum transformation strain, martensite modulus lode and dependency parameters. These seven constants define the stress-strain behaviour of material in loading and unloading cycles for the uniaxial stress-state and thermal loading. In the present study, the SMA rebars used are of cylindrical shape (straight rod) at both low temperature as well as at high temperature. In other words, the rebar is not deformed at room temperature from its original shape. Also, The SMA rebars are not under any load or stress condition at low temperature. Hence, as the temperature of SMA rebars increases (considering a fire event) a phase change occurs from martensite to austenite. Under these conditions, the stiffness of rebar increases.

The elastic modulus of 65 GPa at room temperature is considered for SMA used in the numerical studies in this work. A suitable mesh element for modelling the rebar is one that is suitable for use in both thermal and structural type of numerical modelling studies. This is due to the fact that the temperature profiles that will generate from the thermal analysis need to be provided as inputs to the structural analysis. For the above reasons, solid 185 elements shown in Figure 4.11 is used in this work to model both

SMA and steel rebars. Such an element type was found to have been employed in various studies (Hui et al. 2017; Subramani et al. 2014) in similar applications.

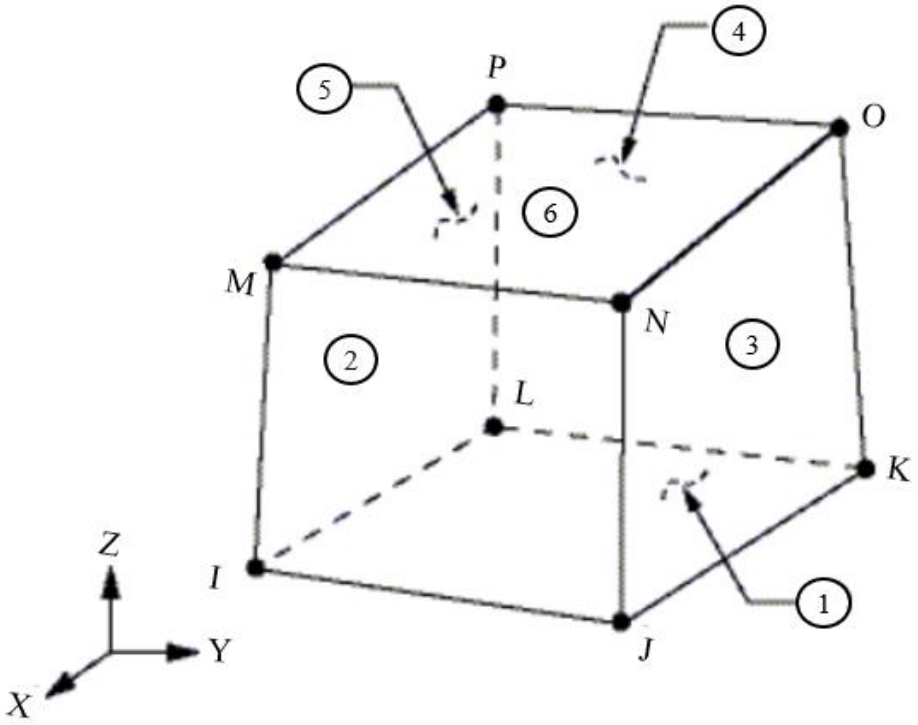

Figure 4.11: Solid185 – 8 node brick element -rebar modelling (Ansys help documentation)

4.2.5 Governing equations – Numerical modelling

For most structural dynamics problems of a mechanical system, the spatial discretization for the principle of virtual work using the finite element method gives the finite element semi-discrete equation of motion as follows:

$$[M]\{\ddot{u}(t)\} + [C]\{\dot{u}(t)\} + \{F^i(t)\} = \{F^a(t)\} \qquad \text{Equation 4.2}$$

where,

$[M]$= structural mass matrix

$[C]$= structural damping matrix

$\{\ddot{u}(t)\}$= nodal acceleration vector

$\{\dot{u}(t)\}$= nodal velocity vector

$\{F^i(t)\}$= internal load vector

$\{F^a(t)\}$= applied load vector

Three methods are available for solving Equation 4.2 central difference time integration method which is used for explicit transient analysis where the equation are not coupled and can be solved explicitly; Newmark time integration method is used for implicit transient analyses and Hilber–Hughes–Taylor (HHT) time integration method which is used also for implicit transient analyses, which is also an extension of the Newmark time integration method.

The structural dynamics problems concerned with the mechanical behaviour governed by the above differential equation can be classified into two classes; that is, linear and nonlinear problems. In linear structural dynamics systems, the internal load is linearly proportional to the nodal displacement, and the structural stiffness matrix remains constant. Therefore, Equation 4.2 can be rewritten as:

$$[M]\{\ddot{u}(t)\} + [C]\{\dot{u}(t)\} + [K]\{u(t)\} = \{F^a(t)\} \qquad \text{Equation 4.3}$$

where,
$[K]$= structural stiffness matrix
$u(t)$= nodal displacement vector

Among direct time integration methods for numerically solving the finite element semi-discrete equation of motion given in Equation 4.3, several methods such as the Newmark method are incorporated in the program. As the generalized- α method recovers the Wood-Bosak-Zienkiewicz method (also called WBZ-method), the Hilber-Hughes-Taylor method (also called HHT- method), and the Newmark family of time integration algorithms. The input parameters for these methods can be given through ANSYS commands.

4.2.5.1 Newmark Method

The Newmark family of time integration algorithms is one of the most popular time integration methods as a single step algorithm. The semi-discrete equation of motion given in Equation 4.2 can be rewritten as:

$$[M]\{\ddot{u}_{n+1}\} + [C]\{\dot{u}_{n+1}\} + [K]\{u_{n+1}\} = \{F^a_{n+1}\} \qquad \text{Equation 4.4}$$

where,

$\{\ddot{u}_{n+1}\}$= the nodal acceleration vector $\{\ddot{u}_{n+1}\}$ at time $\{t_{n+1}\}$

$\{\dot{u}_{n+1}\}$= the nodal velocity vector $\{\dot{u}_{n+1}\}$ at time $\{t_{n+1}\}$

$\{u_{n+1}\}$= the nodal displacement vector $\{u_{n+1}\}$ at time $\{t_{n+1}\}$

$\{F^a_{n+1}\}$= the applied load at time $\{t_{n+1}\}$

In addition to Equation 4.4, the Newmark family of time integration algorithms requires the displacement and velocity to be updated as follows:

$$\{\dot{u}_{n+1}\} = \{\dot{u}_n\} + [(1-\delta)\{\ddot{u}_n\} + \delta\{\ddot{u}_{n+1}\}]\Delta t \qquad \text{Equation 4.5}$$

$$\{u_{n+1}\} = \{u_n\} + \{\dot{u}_n\}\Delta t + [\left(\frac{1}{2} - \alpha\right)\{\ddot{u}_n\} + \alpha\{\ddot{u}_{n+1}\}]\,\Delta t^2 \qquad \text{Equation 4.6}$$

where,

α, δ= Newmark's integration parameters

$\{\ddot{u}_{n+1}\}$= nodal acceleration vector $\{\ddot{u}_n\}$ at time $\{t_n\}$

$\{\dot{u}_{n+1}\}$= nodal velocity vector $\{\dot{u}_n\}$ at time $\{t_n\}$

$\{u_{n+1}\}$ =nodal displacement vector $\{u\}$ at time (t_n)

Thus, the Newmark family of time integration algorithms can be determined by the Newmark integration parameters. In the end, the Newmark integration scheme consists of the three finite difference equations presented in Equation 4.4 through Equation 4.6, and the three $\{\ddot{u}_{n+1}\}$, $\{\dot{u}_{n+1}\}$, and $\{u_{n+1}\}$ can be numerically calculated by the three algebraic equations along with the three known quantities $\{\ddot{u}_n\}, \{\dot{u}_n\}$, and $\{u_n\}$ .By making use of the three algebraic equations given in Equation 4.4 through Equation 4.6, a single-step time integrator in terms of the unknown $\{u_{n+1}\}$ and the three known quantities can be written as:

$$(a_0[M] + a_1[C] + [K])\{u_{n+1}\} = \{F^a_{n+1}\} + [M](a_0\{u_n\} + a_2\{\dot{u}_n\} + a_3\{\ddot{u}_n\}) + [C](a_1\{u_n\} + a_4\{\dot{u}_n\} + a_5\{\ddot{u}_n\}) \quad \text{Equation 4.7}$$

where,

$$a_0 = \frac{1}{\alpha \Delta t^2}$$

$$a_1 = \frac{\delta}{\alpha \Delta t}$$

$$a_2 = \frac{1}{\alpha \Delta t}$$

$$a_3 = \frac{1}{2\alpha} - 1$$

$$a_4 = \frac{\delta}{\alpha} - 1$$

$$a_5 = \frac{\Delta t}{2}\left(\frac{\delta}{\alpha} - 2\right)$$

$$a_6 = \Delta t(1 - \delta)$$

$$a_7 = \delta \Delta t$$

First, the unknown $\{u_{n+1}\}$ is calculated using Equation 4.7 Then, the program computes the two unknowns $\{\dot{u}_{n+1}\}$ and $\{\ddot{u}_{n+1}\}$ by using the following equations:

$$\{\dot{u}_{n+1}\} = a_1(\{u_{n+1}\} - \{u_n\}) - a_4\{\dot{u}_n\} - a_5\{\ddot{u}_n\} \quad \text{Equation 4.8}$$

$$\{\ddot{u}_{n+1}\} = a_0(\{u_{n+1}\} - \{u_n\}) - a_2\{\dot{u}_n\} - a_3\{\ddot{u}_n\} \quad \text{Equation 4.9}$$

The most important factors in choosing an appropriate time integration scheme for the finite element semi-discrete equation of motion given in Equation 4.2 are accuracy, stability, and dissipation. In conditionally stable time integration algorithms, stability is affected by a chosen size of the time step whereas in unconditionally stable time integration algorithms, a time step size can be chosen independent of stability considerations.

In the Newmark method, the amount of numerical algorithm dissipation can be controlled by one of Newmark's parameters, δ, as follows $\delta \geq \frac{1}{2}$

$$\alpha \geq \frac{1}{4}\left(\frac{1}{2} + \delta\right)^2 \qquad \text{Equation 4.10}$$

With the Newmark parameters satisfying the above conditions, the Newmark family of methods may be unconditionally stable. By introducing the amplitude decay factor $\gamma \geq 0$, the above conditions can be written:

$$\delta = \frac{1}{2} + \gamma$$

$$\alpha = \frac{1}{4}(1 + \gamma)^2 \qquad \text{Equation 4.11}$$

$$\gamma \geq 0$$

Consequently, the program provides the user with the Newmark integration procedure, which is unconditionally stable via input of the amplitude decay factor γ. Alternatively, the α and δ parameters may be input directly using ANSYS command input when, the effect of velocity or acceleration is not significant in the response of the structure for the given loading condition, like in case of the pull-out test. The load application is gradual and much slower. The acceleration and velocity component can be removed and we can have a static analysis for which the equation can be

$$K]\{u\} = \{F\} \qquad \text{Equation 4.12}$$

For thermal analysis

The governing equation of interest is as follows

$$[C]\{\dot{u}\} + [K]\{u\} = \{F^a\} \qquad \text{Equation 4.13}$$

where,

$[C]$ = damping matrix

$[K]$= coefficient matrix

$\{u\}$= vector of DOF values

$\{\dot{u}\}$ = time rate of the DOF values

$\{F^a\}$ = applied load vector

In a thermal analysis,$[C]$ is the specific heat matrix,$[K]$the conductivity matrix, $\{u\}$the vector of nodal temperatures and$\{\dot{u}\}$the applied heat flows

Physics	Degrees of Freedom (DOF)	Load
Structural	$\{u\}$ Displacement	$\{F^a\}$ Force
Thermal	$\{T\}$ Temperature	$\{Q^a\}$heat flow

The procedure employed for the solution of Equation 4.13 is the generalized trapezoidal rule

$$\{u_{n+1}\} = \{u_n\} + (1-\theta)\Delta t\{\dot{u}_n\} + \theta\Delta t\,\{\dot{u}_{n+1}\} \qquad \text{Equation 4.14}$$

where,

$C =$ Transient integration parameter fed as input to software.

$\Delta t = t_{n+1} - t_n$

$\{u_n\}$= nodal DOF value at time t_n

$\{\dot{u}_n\}$= time rate of the nodal DOF values at time t_n (calculated from previous time step)

For Transient thermal analysis equation 11 can be written at time t_{n+1} as

$$[C]\{\dot{u}_{n+1}\} + [K]\{u_{n+1}\} = \{F^a\} \qquad \text{Equation 4.15}$$

Substituting $\{\dot{u}_{n+1}\}$ Equation 4.14 into Equation 4.15

$$\left(\frac{1}{\theta\Delta t}[C]+[K]\right)\{u_{n+1}\}=\{F^a\}+[C]\left(\frac{1}{\theta\Delta t}\{u_n\}+\frac{1-\theta}{\theta}\{\dot{u}_n\}\right) \quad \text{Equation 4.16}$$

The solution of Equation 4.16 employs the same solvers used for static analysis in Static Analysis. Once $\{u_{n+1}\}$ is obtained,$\{\dot{u}_{n+1}\}$ is updated using Equation 4.14. In a nonlinear analysis, the Newton-Raphson method (Newton-Raphson Procedure) is employed along with the generalized trapezoidal assumption.

The transient integration parameter θ defaults to 1.0 and can be changed via input command (backward Euler method). For all $\theta > 0$, the system equations that follow are said to be implicit. In addition, for the more limiting case of $\theta \geq \frac{1}{2}$, the solution of these equations is said to be unconditionally stable, i.e., stability is not a factor in time step (Δt) selection. The available range of θ is therefore limited to

$$\frac{1}{2} \leq \theta \leq 1 \quad \text{Equation 4.17}$$

which corresponds to an unconditionally stable, implicit method. The generalized-trapezoidal method requires that the values of $\{u_0\}$ and $\{\dot{u}_0\}$ at the start of the transient must be known. Nonzero initial conditions are input either directly (for $\{u_0\}$) or by performing a static analysis load step (or load steps) prior to the start of the transient itself. Static load steps are performed in a transient analysis which, by turning off the transient time integration effects is to start the transient immediately. This implies $\{u\}$=$\{\dot{u}\} = \{0\}$.

$$\{u_{n+1}\}=\{u_n\}+(1-\theta)\Delta t\{\dot{u}_n\}+\theta\Delta t\,\{\dot{u}_{n+1}\} \quad \text{Equation 4.18}$$

4.3 Develop and Benchmark the Numerical Model

4.3.1 Concrete Model Validation

To confirm the suitability of the numerical model developed in this work it was essential to benchmark the numerical model developed in this work. For this reason, a numerical model developed initially was benchmarked against a study found in the literature. To

this extent, Dahmani et al. 2010 numerical model was chosen for the purpose of benchmarking. The beam dimensions and support conditions were kept exactly the same as Dahmani to make sure all the parameters modelled are correct (Figure 4.12). From the numerical method in this section, it has been observed that the first crack generated (Figure 4.13) was at around 38.4 kN whereas form the analytical calculation shown by Dahmani, the first crack generated was at 40.46 kN (Dahmani et al. 2010). It is observed that the results matched well with the analytical method (Table 4.1). Such a close match in the results confirmed the suitability and accuracy of the numerical model developed in this work from which more comprehensive work evolves as discussed in the following sections. In addition, it is understood from the modelling (in this section) that, the parameters considered in numerical simulations are appropriate and can be used in further investigations concerning concrete.

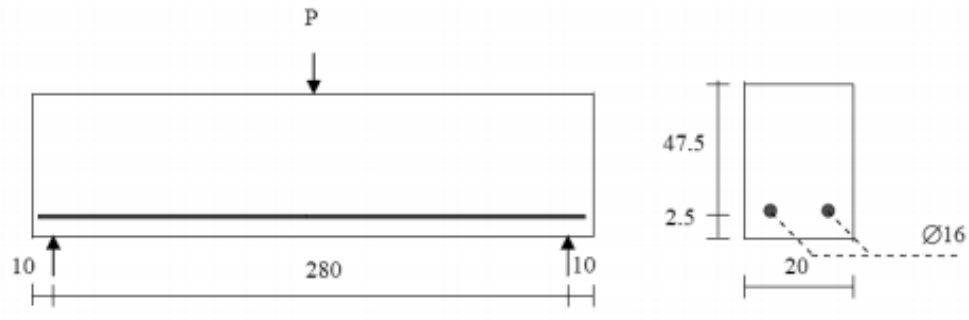

Figure 4.12: Geometry, loading and beam reinforcements (dimensions in cm)

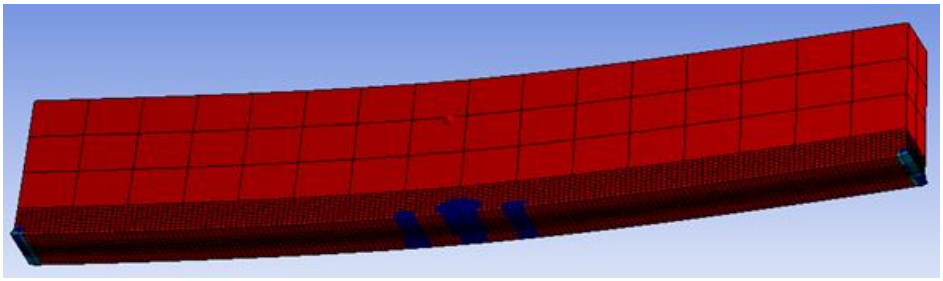

Figure 4.13: Crack generated under bending load

Table 4.1: Comparison of FE model with hand calculations

Model	Deflection (mm)	Load at first crack (kN)
Ansys model	0.32	38.4
Dahmani (Hand calculation)	0.29	40.46

4.3.2 Interface Bond Model Verification

Since this study involves the examination of the bonding between SMA-concrete, the interface needs to be modelled and verified before more complex work is undertaken. To this extent, the interface between the steel rebar and concrete is modelled with cohesive zone interface allowing the normal and shear separation (Figure 4.9). The model was created based on the specimen details from the experimental study conducted by Apparao et al. 2002. A very fine mesh was created at the concrete-steel interface to capture the crack initiation and growth in the concrete model (Figure 4.15). The cohesion zone normal and shear specimen limit was specified based on the grade of concrete and steel rebar materials mentioned by Apparao et al. 2002. Lugs were modelled as per rebar geometry to assist in the mechanical interaction of the rebars with the concrete at their interface. The constrained boundary condition was applied on the face of sample. A known (10mm) displacement was applied to the rod in co-axial direction to mimic the pull on the rebar for the pull-out and the reaction force is measured as the pull-out force. Concrete element (Solid 65) was used in the numerical model including cracking and crushing behaviour of concrete. The results showed crack propagation (Figure 4.16). The cracks originated at the location of the lug in radial direction because of the resistance to the pull-out action. The elements which were cracked are plotted in blue and the elements which were not cracked are plotted in red. Figure 4.16 shows the progressive growth of the crack during the pull out, highlighting the bond failure mechanism. It is observed that numerical and experimental pull out force matches quite closely for all different diameter of rebar and different embedment length (refer Table 4.2) crack propagation at different stages of pull out test is presented in Figure 4.17 and the numerical model developed to study the interface between the rebar and concrete hence stand validated and used to develop the numerical model to study SMA-concrete bond behaviour. This aspect is dealt with in the following section.

Figure 4.14: Typical specimen for pull out testing (Apparao et al. 2002)

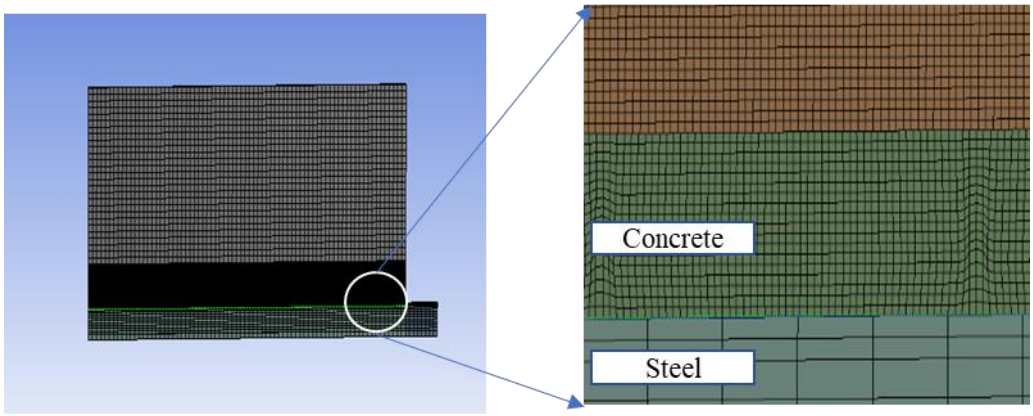

(a) Fine mesh at concrete steel interface (b) Zoomed view at concrete steel interface

Figure 4.15: Fine mesh at the concrete – steel interface (a and b)

Table 4.2: Comparison of pull out forces in bond strength test (experimental Vs numerical)

Pull out test model	**Pull out force (experiment) (kN) Apparao et al. 2002**	**Pull out force (FEA) (kN)**
M40, 16 mm dia, 150 mm	58.32 kN	60.32 kN
M40, 20mm dia, 75 mm	62.58 kN	62.00 kN
M40, 20mm dia, 150 mm	72.39 kN	75.40 kN

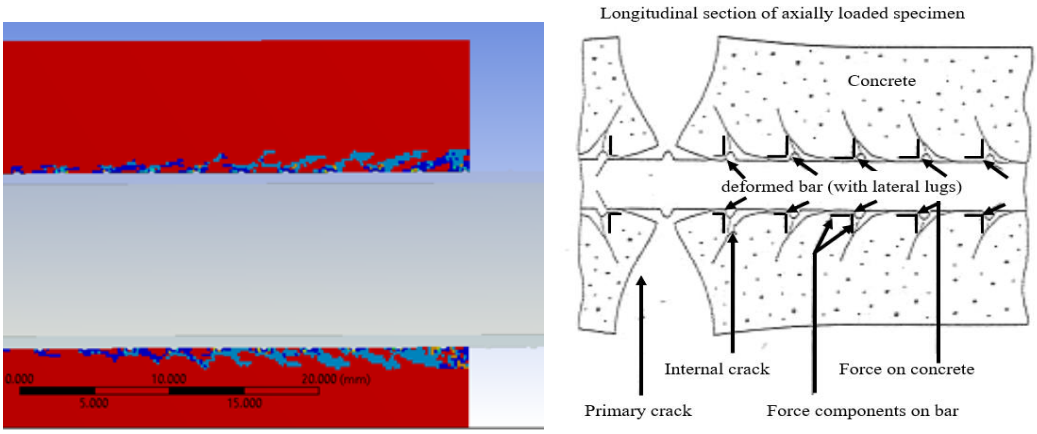

Figure 4.16: Zoomed crack growth at the steel-concrete interface

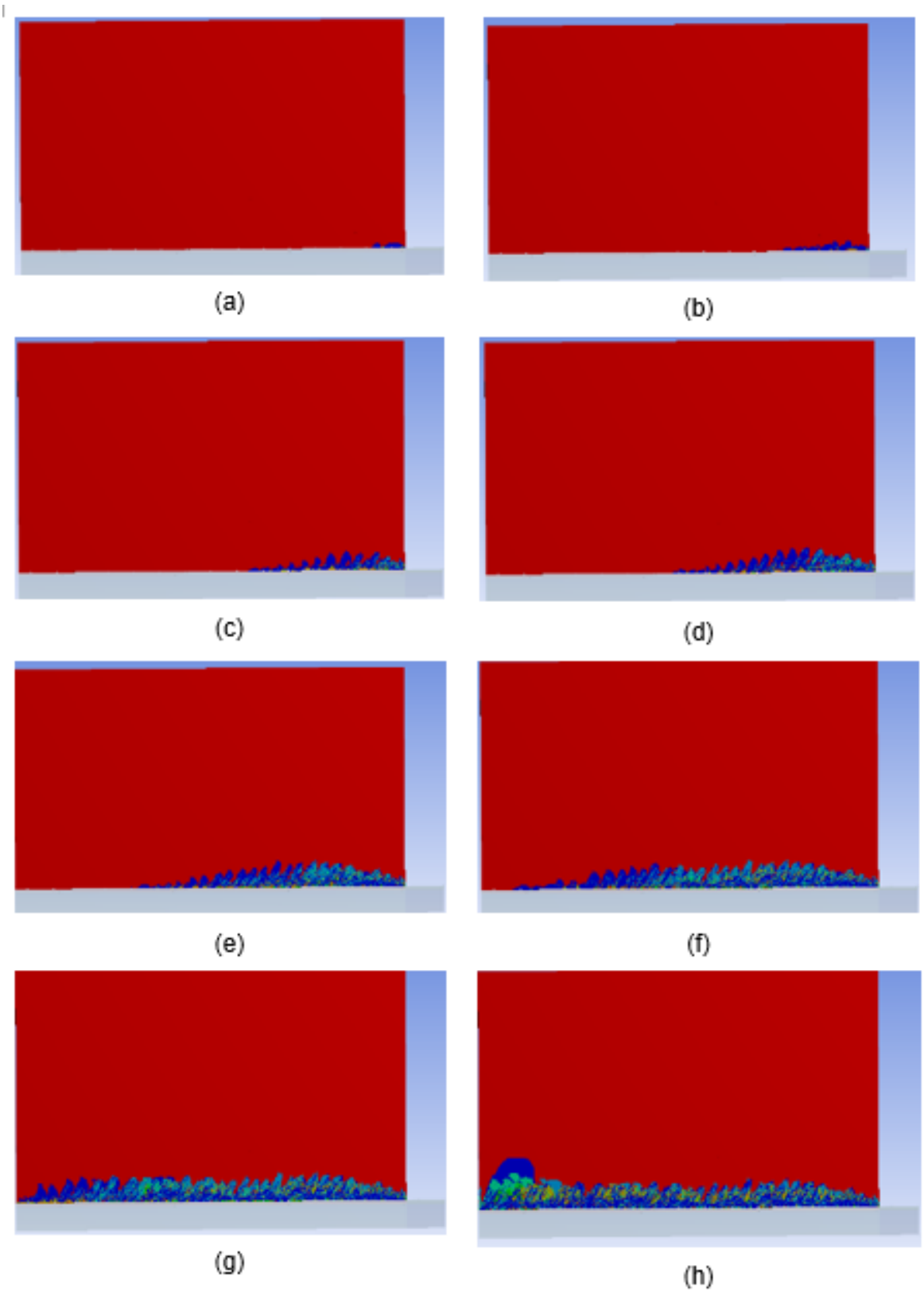

Figure 4.17: Progressive crack growth during the different stages of the pull-out

4.3.3 Transient Thermal Analysis Verification

To this extent different components of numerical models such as nonlinear concrete and bond interface model have been numerically modelled and verified. The third component of a numerical model simulating the pull-out under high temperature during a fire event includes the modelling the transient thermal analysis which provides the thermal load, capture rise in temperature and its profile with respect to fire duration in temperature time history. Eurocode norms provide basic guidelines for the analysis of reinforced concrete structures subjected to fire. An example of a simply supported reinforced concrete beam subjected to standard fire is considered. The numerical model was created for simply supported concrete beam exposed to the fire on external faces of the beam with a rectangular cross section of 300mm x 600mm as shown in Figure 4.18. Taking the advantage of symmetry and to save the computational time, a quarter section of the beam is modelled with symmetric boundary conditions applied on the cut-section of beam cross-section. A temperature time history curve as per ISO 834 – EN 1992-2004 guideline was applied on the faces of beam which are exposed to fire.

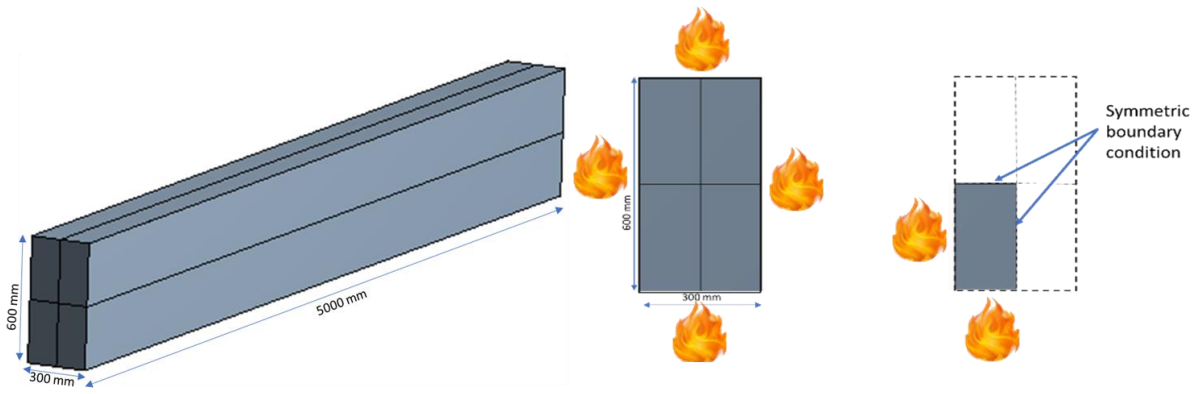

Figure 4.18: RC beam with fire on all exposed surface

The concrete part of the beam is meshed using 3D solid70 8-node brick element with a single temperature degree of freedom. the fire load was applied on the outer faces of the symmetric section as shown in Figure 4.18. Temperature profile of the beam cross-section is plotted at response of the beam is calculated at every 10 seconds. The temperature profiles are constant along the beam length. Results of transient thermal analysis were plotted as (a) contour plot and (b) iso-lines plot at the interval of

30 mins, 60 mins and 90 mins were plotted and shown in Figure 4.19. Verification of these results are made by comparing the temperature profile iso-lines with iso-lines of the temperature profile of same cross-section with similar thermal load results provided in Annex A in BS EN 1992-1-2 :2004 (Figure 4.20).

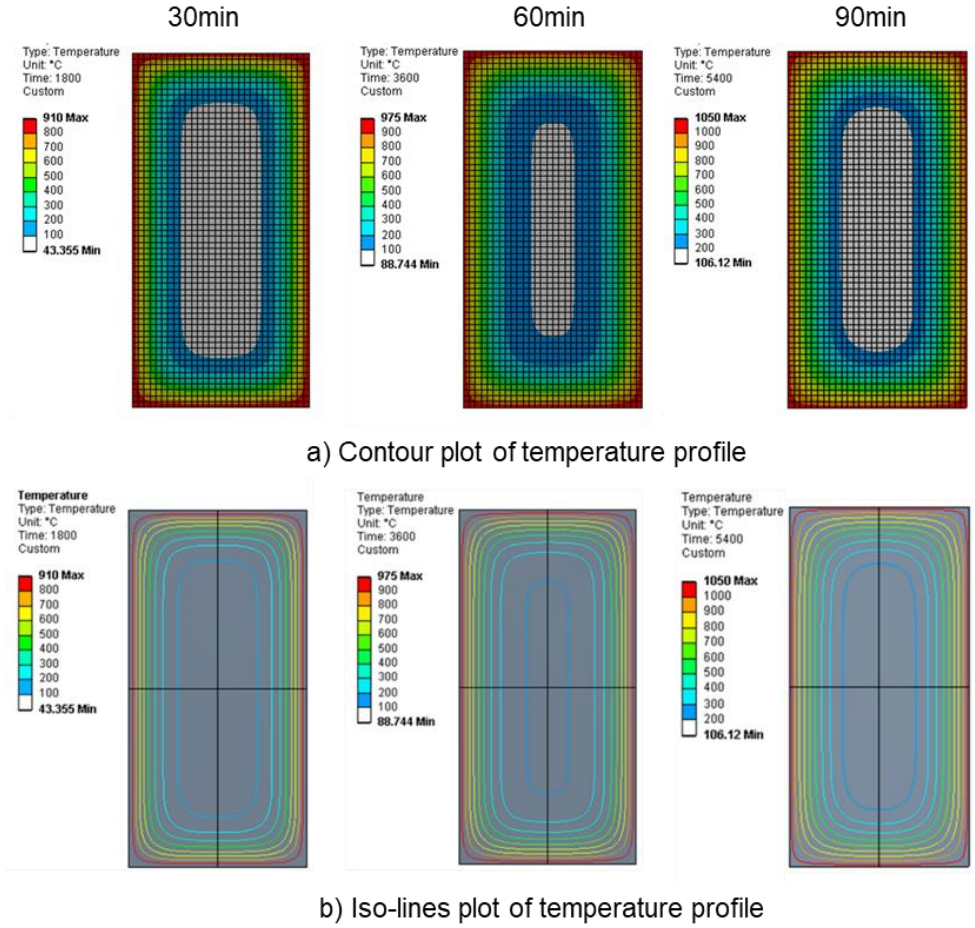

Figure 4.19: Temperature profiles a) contour plot and b) Iso-lines at 30, 60 and 90 minutes

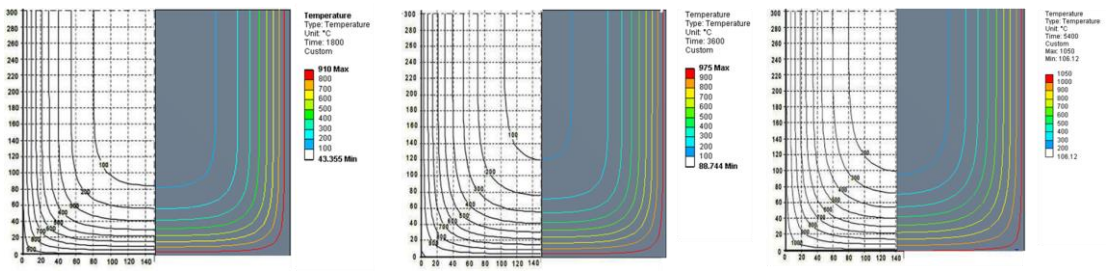

Figure 4.20: Temperature profiles Iso-line at 30, 60 and 90 minutes (quarter-section): EN 1992-1-2 :2004-left: FEA right)

4.4 Numerical Model to study bond stress/bond slip at Rebar-Concrete interface

In this work, the various aspects discussed thus far in this chapter such as methods and mesh elements such as Solid65 and Solid185, numerical models are used to develop a numerical model in ANSYS to examine the bond slip behaviour between concrete and rebars (both SMA and Steel) in order to achieve the second AIM of this work. The manner in which the numerical model was developed, the meshing conditions applied to the CAD models, the boundary conditions applied, the physics governing both thermal and structural analysis are all presented as follows. A flow chart is provided in Figure 4.21 for ease of understanding. Figure 4.22 shows the workflow and also highlights the corresponding software modules that are employed for various steps involved in the numerical simulations.

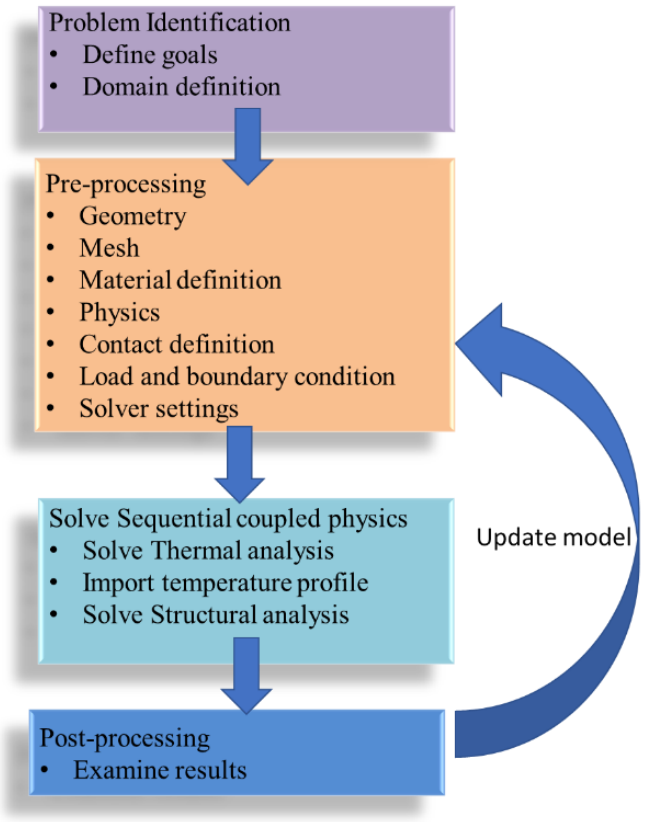

Figure 4.21: Simulation workflow

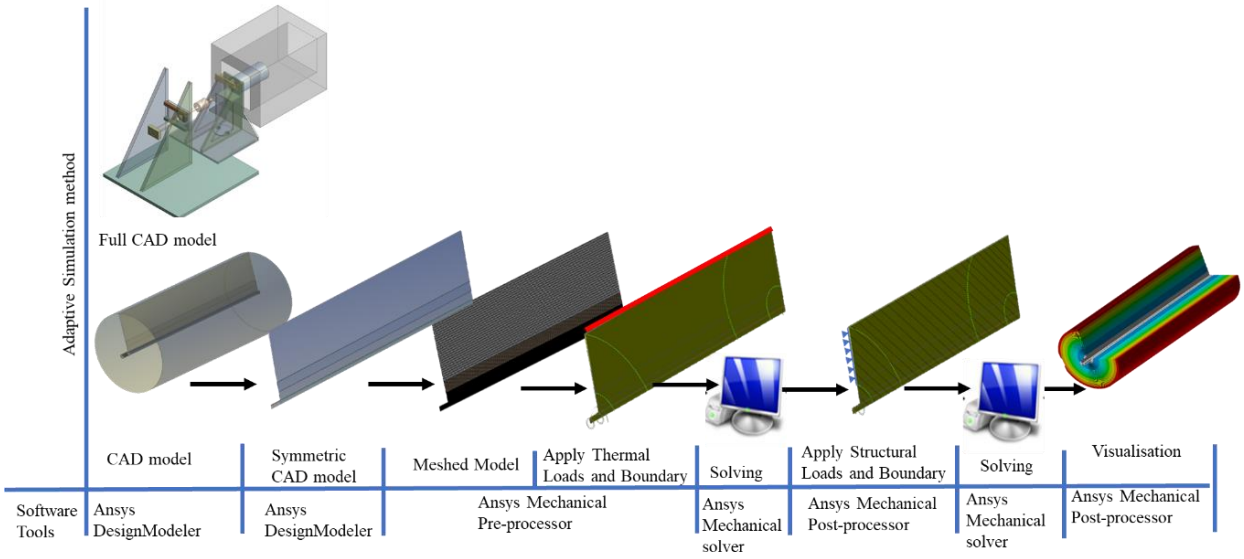

Figure 4.22: Adaptive simulation method and the software tools employed

4.4.1 Establishing the goal and domain identification

The first step is to define the goal of the numerical study. For the purpose of this research the second aim is the goal, which is to investigate the bond stress and behaviour at the SMA-concrete interface under high temperature. The domain in this study is essentially the experimental apparatus developed in Chapter 3 and as shown in Figure 4.23. A CAD model of the above apparatus was developed to assist in the numerical studies. The CAD model is shown in Figure 4.24.

Figure 4.23: Experiment apparatus developed in Chapter 3.

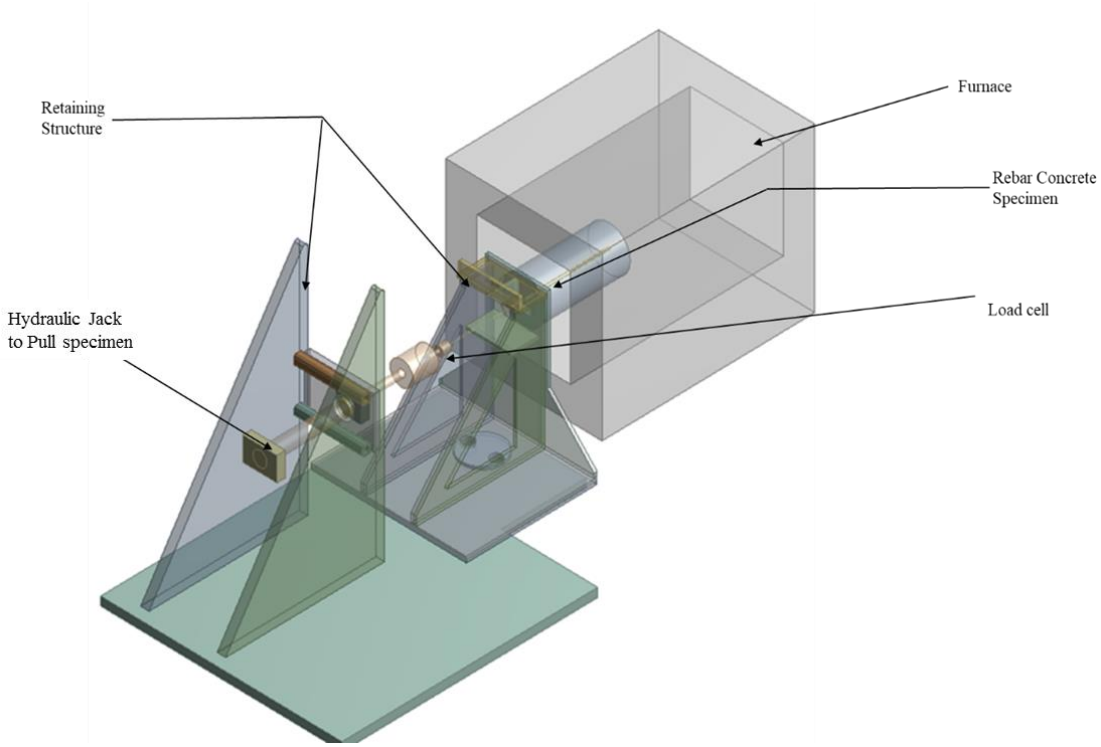

Figure 4.24: CAD model of the experiment apparatus (developed in Chapter 3).

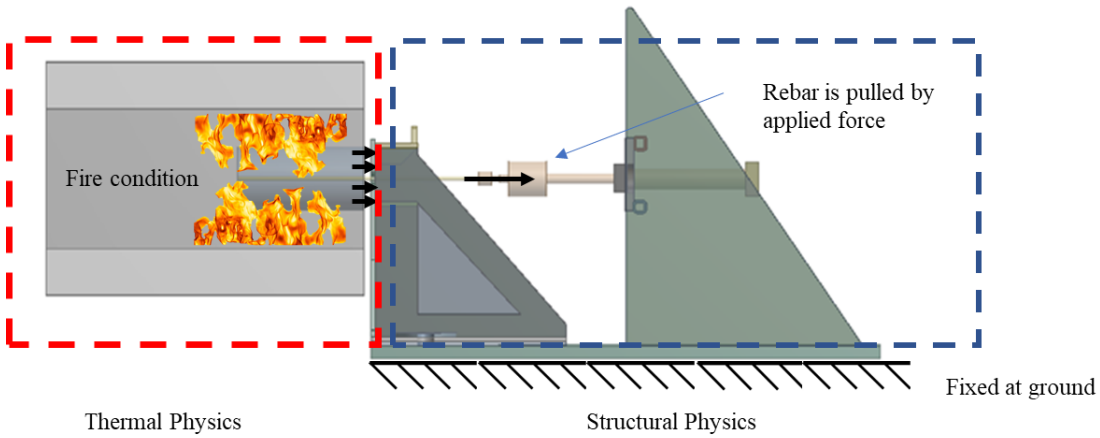

Figure 4.25: CAD model side view (Thermal and Structural Domain)

Unlike physical experiments, numerical models do not require all the components/parts to be present to conduct simulations. In most cases the simulation is carried out on the most critical components of interest. All other components are implied in the boundary conditions. In this study, the domain under consideration is only the SMA-concrete specimen under high temperature condition.

Since the specimen is heated and the effect of heat is altering the structural behaviour, the numerical model needs to address both thermal and structural physics involved in the simulation. In Figure 4.25 the domain considered in this work for Thermal and Structural studies are identified. The red dotted rectangular block encloses the furnace where the specimen is heated to mimic a fire event and hence transient thermal analysis is considered (as it follows the time-temperature fire curve) as input. The second section enclosed by blue dots is a region where the pulling of the specimen happens and therefore the physics that governs the analysis is the structural analysis (where the force applied and slip distance were measured).

4.4.2 Step 1-CAD Model

Taking advantage of the symmetric nature of the SMA-concrete model (Figure 4.26a), further simplification of the CAD model was possible. The CAD model was built using ANSYS DesignModeler. The dimensions of the concrete cylinder were maintained to be the same as the concrete specimen casted for the physical experiments carried out in Chapter 3 (Section 3.3.6). A small 1-degree wedge section is considered for the numerical analysis as shown in Figure 4.26b. Such a section allowed for full consideration of the 3D model albeit with relatively lower mesh size. The low mesh size in turn significantly lowered the computational time for the numerical analysis carried out.

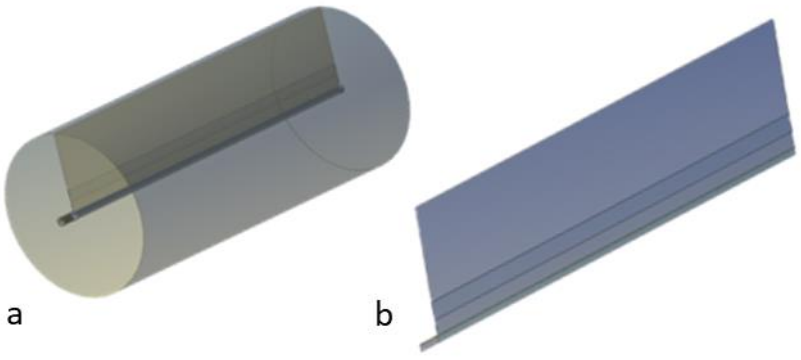

Figure 4.26: a) Symmetric Model b) Wedge

Various representations are made as alternatives that simplify the CAD model to the most essential components for numerical studies as identified in Figure 4.27. For

example, the retaining structure is replaced in numerical model by applying an appropriate boundary condition (support condition shown in Figure 4.28) to the model.

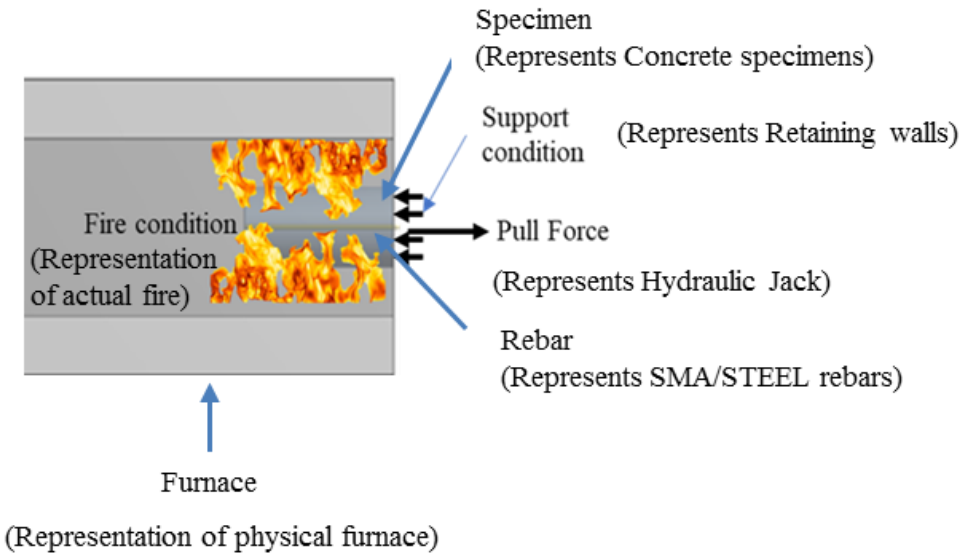

Figure 4.27: Simplified CAD domain modelled for numerical analysis

4.4.3 Step 2-Meshing

The specimen setup model consists of 3 main parts in the model i.e. concrete, rebar and concrete-rebar interface (Figure 4.28). Solid65, an 8-noded brick element is used to model the concrete part of the specimen. Solid185, an 8-noded brick element is used to model the SMA rebar, and the interface between the concrete and SMA rebar is modelled using Inter205, an 8-noded cohesive interface element. The concrete Solid65 element models for the non-linear behaviour of concrete material includes the capability of cracking and crushing based on the specified compressive strength and tensile strength of concrete. This cracking and crushing capability of concrete element allows the removal of stiffness of individual elements which are cracked or crushed to be part of global stiffness matrix, thereby allowing to model the progressive failure. The Inter205 elements is created using the surface nodes of the SMA rebar and concrete at the interface location (Figure 4.28).

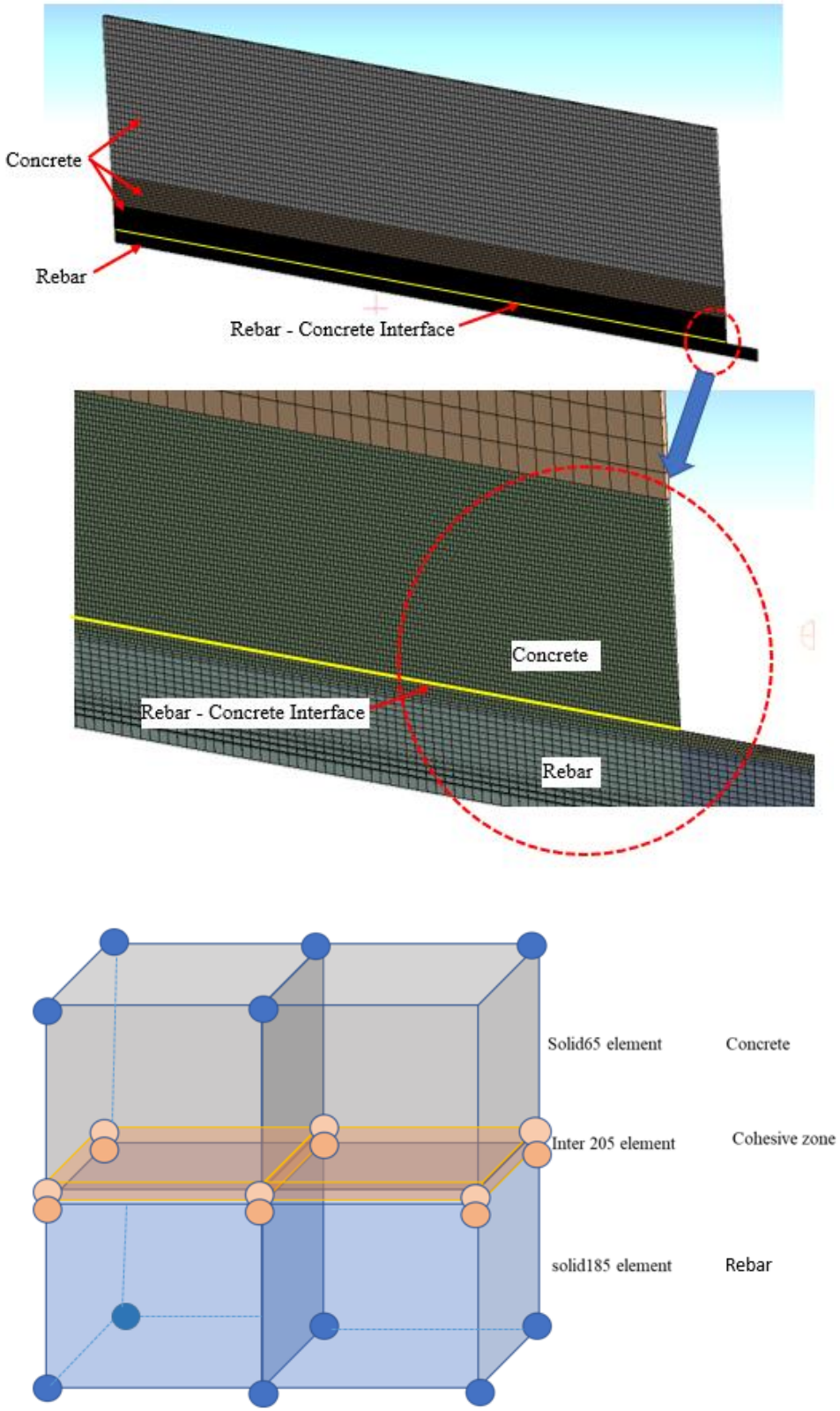

Figure 4.28: Meshing of the symmetric model and mesh at the rebar-concrete interface

4.4.4 Step 3-Materials

4.4.4.1 Concrete:

The structural analysis includes the temperature dependent degradation of the properties of the materials (Table 4.3). Based on the temperature, the program picks up the material properties based on temperature dependent degradation data defined in material definition. Figure 4.29, Figure 4.30, Figure 4.31 show a) relative tensile strength degradation, b) relative compressive strength degradation and c) relative elastic modulus with respect to temperature (Phan et al. 2002; Xuhong et. al. 2013). The data from the above-mentioned curves were utilised in this work.

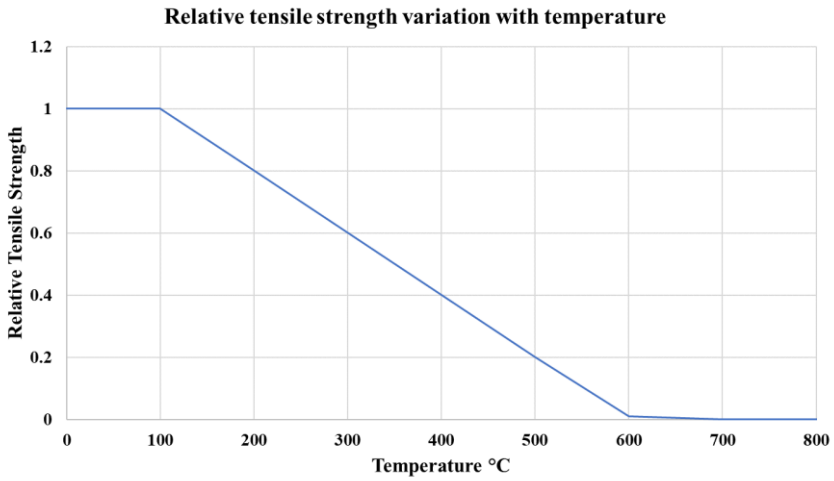

Figure 4.29: Concrete-Relative tensile strength degradation with temperature

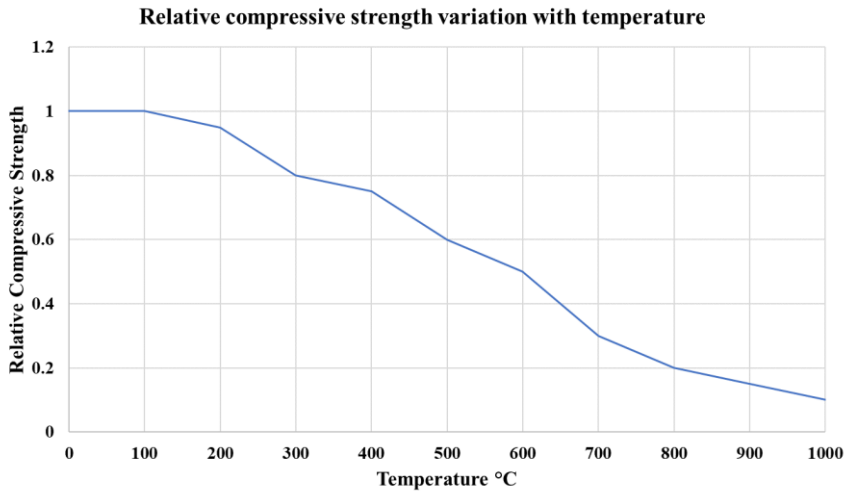

Figure 4.30: Concrete-Relative compressive strength degradation with temperature

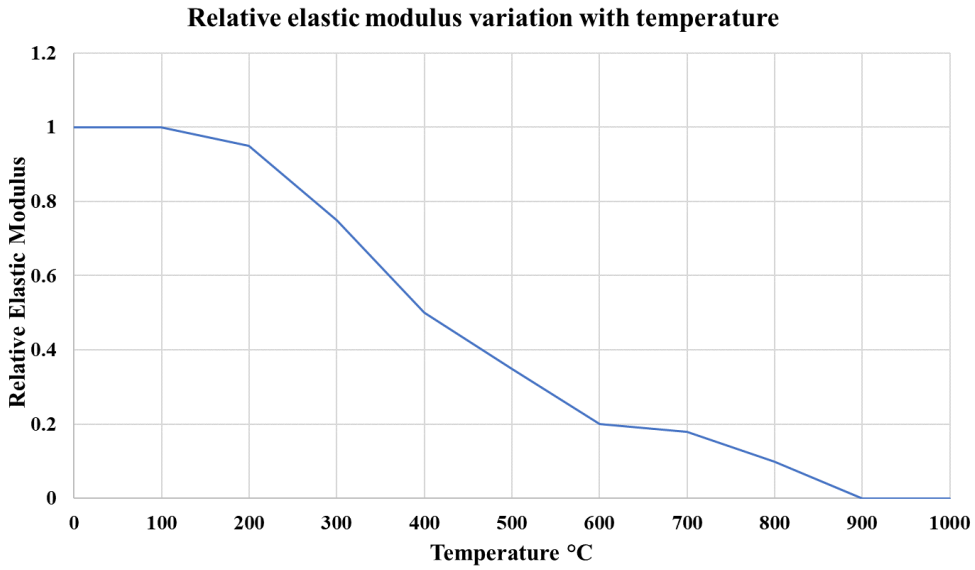

Figure 4.31: Relative elastic modulus degradation with temperature (Concrete)

Table 4.3: Relative strength degradation properties of Concrete under fire condition

Concrete Grade	Fire Duration	Uniaxial Tensile strength (MPa)	Uniaxial Compressive strength (MPa)	Modulus of elasticity (E)
M30	No fire condition	3	30	29128
	30 Min	2.7	27	26215
	60 Min	1.8	18	17476
M40	No fire condition	3.79	40	32800
	30 Min	3.411	36	29520
	60 Min	2.27	24	19680
M50	No fire condition	4.24	50	34800
	30 Min	3.816	45	31320
	60 Min	2.544	30	20880

4.4.4.2 SMA NiTi – Material

Sadiq et al. 2013 used NiTi based SMA material to study the effect of heat treatment on the recovery stresses of SMA. The phase transformation was found to be around 105°C (refer Chapter 3) for samples which were heat treated at 400°C. The Elastic modulus of SMA used was 65 GPa at room temperature. The modulus of elasticity increases with the increase in SMA temperature, till about 300°C and then decreases

as the rebar temperature reaches above 400°C (Sadiq et al. 2013). The data from Sadiq et. al. work was employed in this work for SMA materials.

4.4.4.3 Steel:

Steel rebars were used to benchmark the SMA-concrete bond behaviour. The steel rebars selected were of the same dimensions of the SMA rebars. The dimensions were kept the same so that a reasonable comparison can be made and correlation can be drawn between the two different rebars for their respective bond behaviour with concrete. Figure 4.32 and Figure 4.33 shows the a) relative elastic modulus and b) relative yield strength degradation with respect to temperature (Heidarpour et al. 2014; Wang et al. 2014; Chiew 2014). These values were employed in this work where required (Table 4.4).

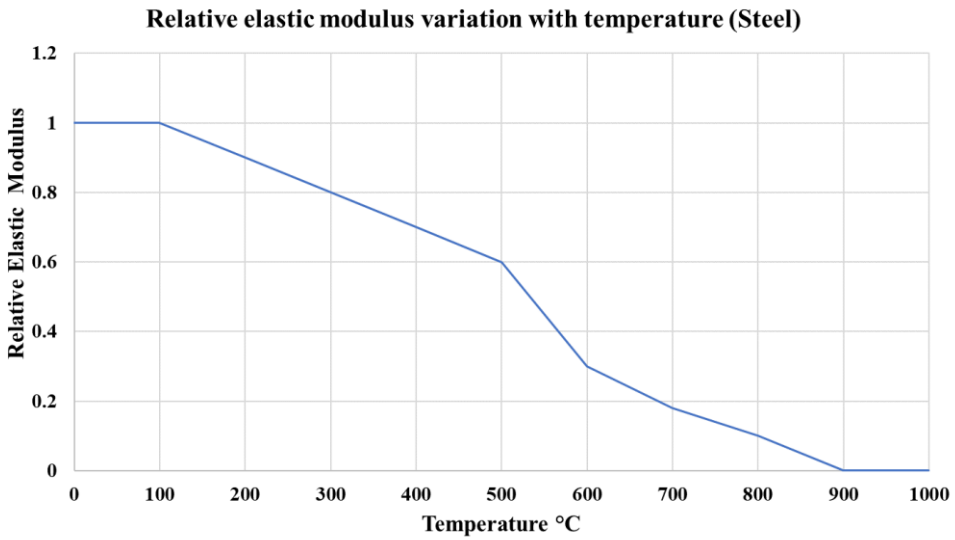

Figure 4.32: Relative elastic modulus variation with temperature (steel)

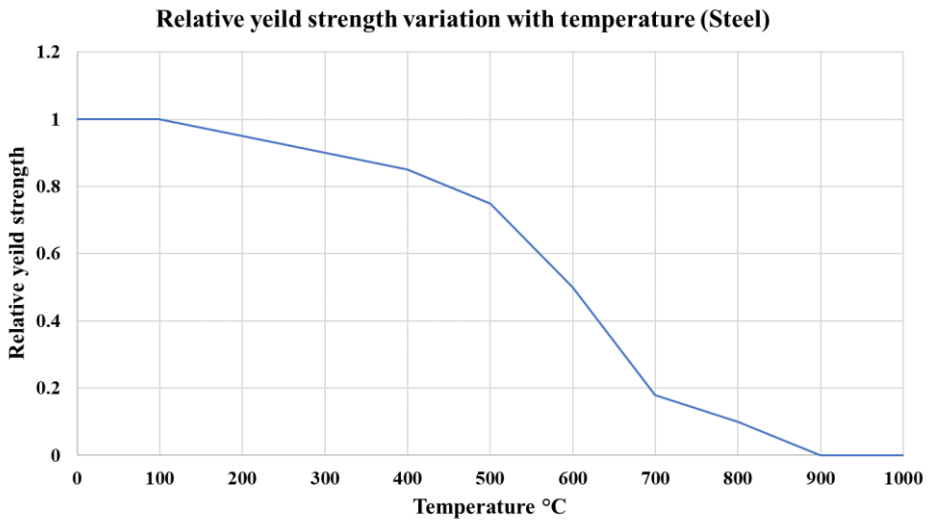

Figure 4.33: Relative yield strength variation with temperature (steel)

Based on Figure 4.33 of the relative strength degradation of Young's modulus the material properties for each fire duration time were evaluated and used as input for performing the numerical analysis. Table 3.2 list the material properties of the mild steel used in the analysis for different fire exposed duration.

Table 4.4: Relative strength degradation properties of Steel under fire condition

Mild Steel Grade	Fire Exposure Duration (Min)	Modulus of Elasticity E (MPa)
	No fire condition	2.00E+05
250	30 Min	1.90E+05
	60 Min	1.40E+05

4.4.5 CZM Bilinear Model-Modelling the interface between SMA and Concrete

In this section, an explanation is provided as to how the data from the experiments are utilised in deriving the various values required for modelling the interface between SMA and concrete. In order to model the SMA-concrete interface, a popular model from the literature called the CZM Bilinear model is employed. The model requires the following inputs:

- Maximum tangential traction;
- Tangential displacement jump at completion of debonding;

- Ratio; and
- Non dimensional weigh parameter.

Maximum tangential traction and tangential displacement jump values for SMA for the various temperature conditions experienced during a fire event could not be found in literature. Hence physical experiments were conducted in this work (Chapter 3) to obtain data concerning the above two parameters. To this extent, the data generated for SMA rebar that was inserted to a depth of 300mm into the concrete and exposed to no fire conditions are presented below as an example.

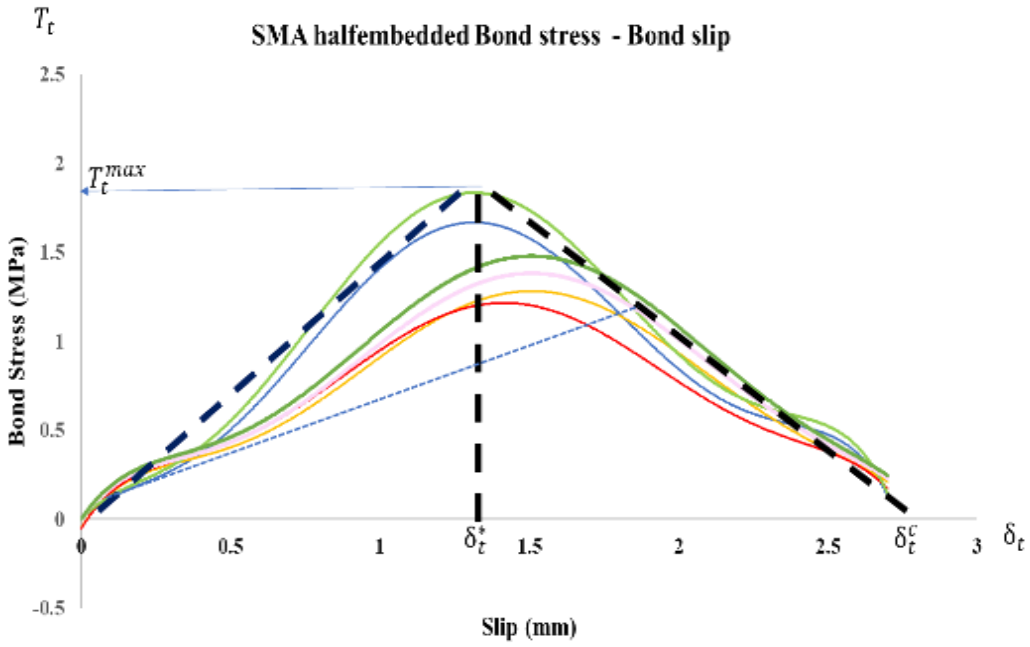

Figure 4.34: Relative compressive strength degradation with temperature

From the above example, the specimen sample (NF-FL-E1-SMA) is considered. The name suggests that the specimen is SMA rebar-based concrete, with the depth of rebar being 300mm and that it is subjected to no heat exposure during the pull-out test conducted as part of physical experiments. From the chart (Figure 4.34), it can be noted that the two values for maximum tangential traction (T_t^{max}) and Tangential Displacement jump (δ_t^*) are 1.8E+06 Pa and 0.0013 m respectively (refer Table 4.5). These values are henceforth used in the numerical analysis as required (structural

analysis) to mimic the bond behaviour between SMA and Concrete for the above-mentioned condition.

Table 4.5: CZM Bilinear Model Parameters

CZM Model Bilinear Inputs	Value	Units
Maximum tangential traction	1.8E+06	Pa
Tangential Displacement jump at completion of debonding	0.0013	m
Ratio (ratio of δ_t^* to δ_t^c)	0.5	
Non dimensional weigh parameter	1	

In similar ways the values of all four parameters (Maximum tangential traction, Tangential displacement jump at completion of debonding, Ratio and Non dimensional weigh parameter) were derived or calculated and are presented below in Table 4.6.

Table 4.6: List of CZ parameters extracted from the experimental test study

S.No.	Specimen Name	Max. Traction (τ) MPa	Traction Displacement (δ*) mm	Ratio (δ*)/(δc)	Weight Parameter
1	NF-FL-E1-SMA	1.51	1.4	0.52	1
2	NF-FL-E2-SMA	1.49	1.45	0.54	1
3	30F-FL-E1-SMA	1.18	1.5	0.56	1
4	30F-FL-E2-SMA	1.08	1.65	0.61	1
5	60F-FL-E1-SMA	0.95	1.5	0.56	1
6	60F-FL-E2-SMA	0.8	1.5	0.56	1
7	NF-HL-E1-SMA	1.82	1.3	0.48	1
8	NF-HL-E2-SMA	1.75	1.3	0.48	1
9	30F-HL-E1-SMA	1.39	1.5	0.56	1
10	30F-HL-E2-SMA	1.49	1.5	0.56	1
11	60F-HL-E1-SMA	1.35	1.4	0.52	1
12	60F-HL-E2-SMA	1.39	1.55	0.57	1
13	NF-FL-E1-Steel	3.34	1.15	0.67	1
14	NF-FL-E2-Steel	3.25	1.15	0.67	1
15	30F-FL-E1-Steel	3.18	1.15	0.67	1
16	30F-FL-E2-Steel	3.21	1.15	0.67	1

17	60F-FL-E1-Steel	1.98	1.15	0.67	1
18	60F-FL-E2-Steel	1.96	1.05	0.61	1
19	NF-HL-E1-Steel	3.61	1.15	0.67	1
20	NF-HL-E2-Steel	3.59	1.15	0.67	1
21	30F-HL-E1-Steel	3.17	1.05	0.61	1
22	30F-HL-E2-Steel	3.18	1.1	0.67	1
23	60F-HL-E1-Steel	1.81	1.1	0.67	1
24	60F-HL-E2-Steel	1.78	1.1	0.67	1

Depending on the fire condition, material involved and the depth to which rebar is inserted, a corresponding data set from the physical experiments was drawn upon as inputs to define the parameters of the CZM bilinear model while defining the material characteristics of the interface in the structural analysis.

4.5 Step 4-Numerical Analysis

This section acts as the connector between Chapter 3 (Physical experiments) and this current Chapter (numerical experiments). It was mentioned earlier that the data from the experiments are used in the development of numerical models (Section 4.4.5). The following flowchart (Figure 4.35) provides this insight and also sheds light on how the outcomes or results from the physical and numerical experiments come together in verifying and validating the numerical model developed in this work.

While the physical experiments were developed in Chapter 3 which achieved Aim1, the following sections of this Chapter explains the development of numerical models and the conduct of numerical experiments concerning both the thermal and structural aspects of rebar and concrete interface modelling. Essentially two numerical Models are developed as mentioned below with the results of thermal analysis feeding into structural analysis:

- Thermal Analysis: deals with the thermal response of the complete specimen (concrete, rebar and their interface); and
- Structural Analysis: also deals with the complete specimen (as above) concerning the structural aspects of the specimen while taking into account.

- the thermal response at any given point in time over the duration of the experiment; and
- the behaviour of the interface material for specific thermal and other load conditions.

The following novel numerical modelling method developed to examine and study the bond stress behaviour between Rebar (both SMA and steel) and concrete at the cohesion zone under the influence of both thermal and structural loading is one of the major contributions of this thesis to the scientific literature. First the thermal analysis methodology adopted is discussed leading into the structural analysis. The manner in which the data flows is shown in Figure 4.36.

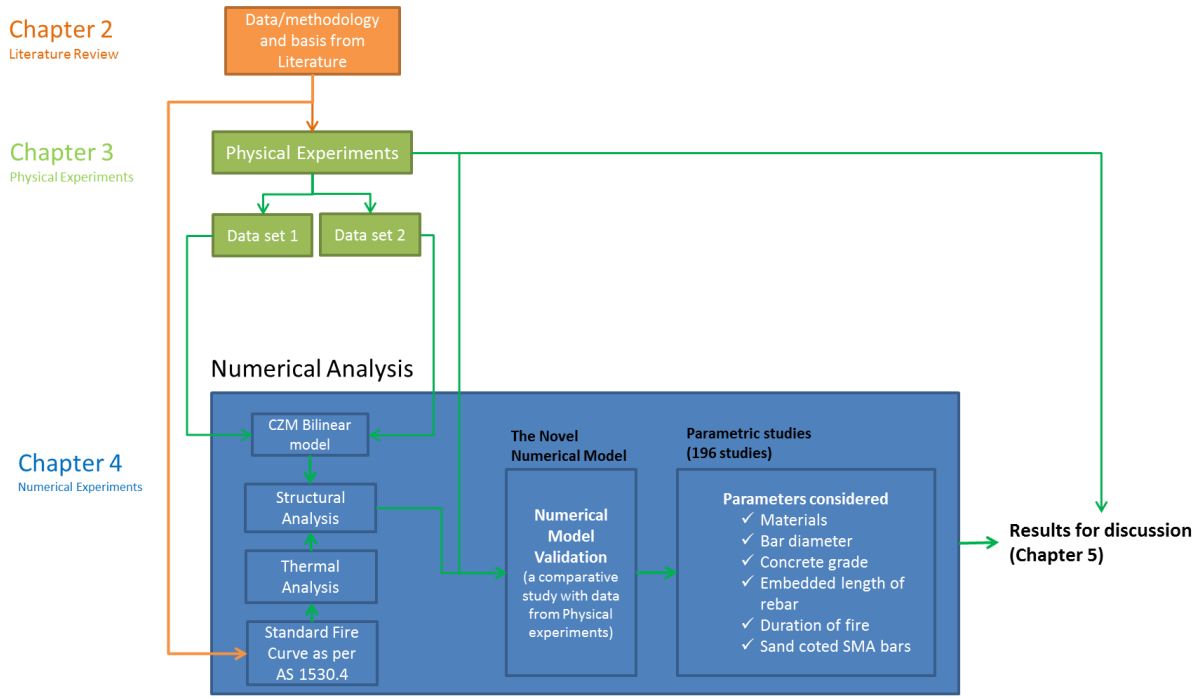

Figure 4.35: The association between chapters and the data flow

4.5.1 Thermal Analysis: Modelling the specimen response to fire

The bonding between the concrete-rebar during a fire event (or at high temperature) depends on the two physics involved i.e. structural and thermal both of which will affect the bonds overall response. In situations like this, when two physics are involved it is called as coupled physics, i.e. the effect of one physics affect the behaviour of the other. In the specific case that is under consideration in this study, the effect of

temperature on the specimen (concrete-SMA) will affect both the materials and hence the bonding between the same. This coupled physics problem can be addressed in two ways (1) one-way coupling and 2) two-way coupling) when it comes to numerical modelling based on the how tightly the said physics are coupled.

In one-way coupling, the change in behaviour in one physics affects the other physics, for example rise in temperature (thermal) can cause the expansion (structural deformation) but the change in deformation doesn't cause the increase in temperature. Whereas, in two-way coupling the change is affected both ways, i.e. thermal condition has an effect on the physical properties of the material and change in physical properties affect the thermal behaviour of the material. In such analysis, where one-way coupling of physics is dominant, a sequential coupling is considered.

In sequential coupling, the thermal and the structural physics are solved one after the other in a two-step manner. Firstly, a numerical model is solved for the thermal conditions, the results of which are exported as thermal loading / thermal profile for consideration in structural analysis. The work-flow of the two-step sequential coupling analysis is in Figure 4.36.

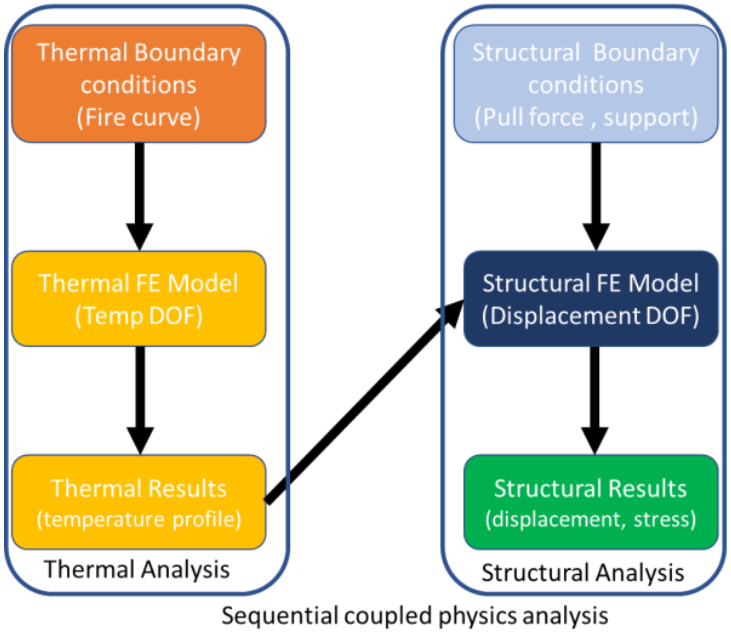

Figure 4.36: Sequential coupling flow

For the reasons mentioned above, it is essential to understand the temperature profile inside the specimen (during a fire event or high temperature condition). Heat transfer through specimen material does alter the physical and mechanical properties of the materials which indirectly affect the bond behaviour and bond strength. In the setting up of the thermal analysis study, the respective thermal properties of materials (such as thermal conductivity (λ), specific heat (cp) and density (ρ)) were applied to concrete, steel and SMA.

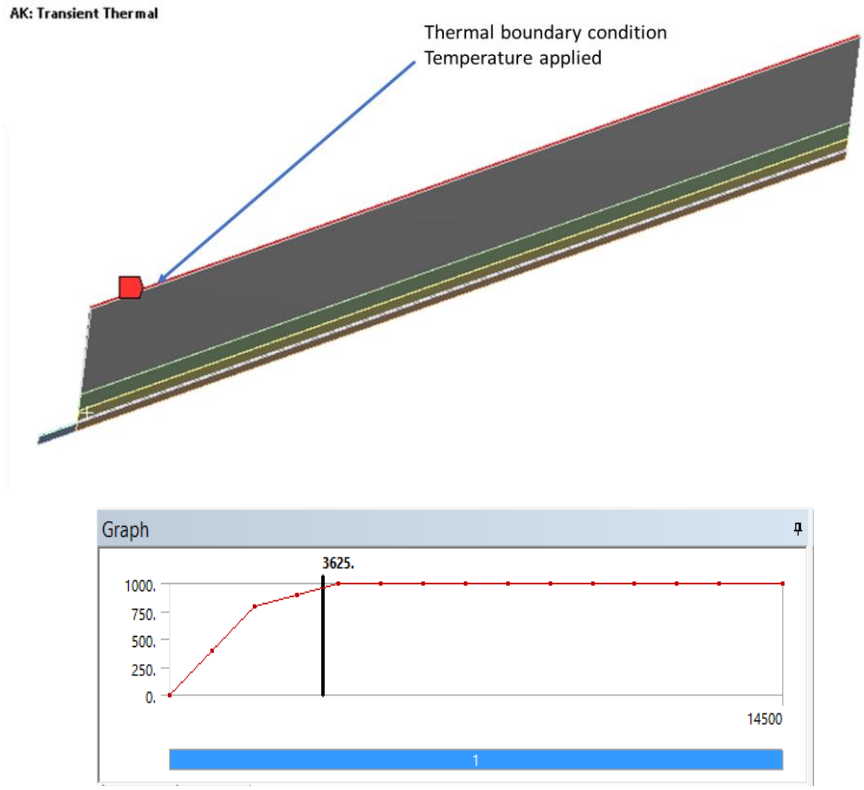

Figure 4.37: Thermal boundary condition as applied

It was assumed that the fire is in direct contact with the concrete specimen and the temperature boundary condition was applied directly on the outer surface of the specimen as shown in Figure 4.37. The transient thermal load applied on to the specimen was governed by the fire curve AS1530.4 as shown in Figure 4.38.

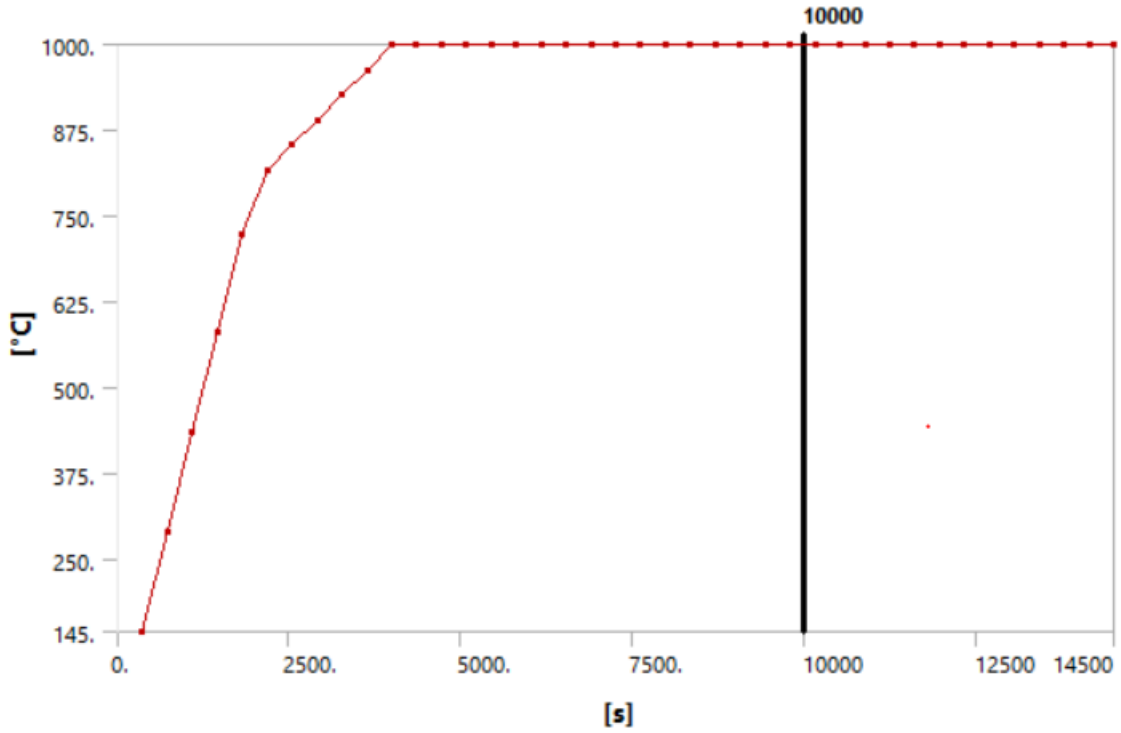

Figure 4.38: Temperature-time fire curve

A full transient thermal analysis was used to obtain the temperature gradient profile for three specific time points over the period of the analysis: 1) at the start under no fire condition 2) at 30mins and 3) at 60mins. The numerical model was solved using a direct solver by adopting the time step as mentioned by Bergheau et al. 2008.

Only one thermal analysis was required to capture the thermal profile of the specimen under investigation. The same profile is used for all the specimens in the various parametric studies undertaken in this work. This is due to the fact that the material's thermal property remains the same. Another reason is also to reduce unwarranted computational power in solving the full transient structural analysis for each case of the parametric study. Since this thermal profile is applied in the structural analysis that is discussed in the following section, it was important to highlight the key aspects of the thermal profile in this section as described below.

It is quite obvious that at the start of the experiment (at time zero) there was no thermal load applied on to the specimen and hence no thermal profile was generated. It is for this reason that an image showing the thermal profile is not presented in this work.

However, at time 30min and 60min there was temperature profiles generated for the concrete block as shown in Figure 4.39a, Figure 4.39b (3d model) and Figure 4.40 (2d wedge). For 30mins of testing the following can be noted (refer Figure 4.40).

- The temperature at the specimen's surface reached around 720°C;
- Nearly half way between the external surface of specimen and the rebar the temperature of the concrete specimen is in the vicinity of 240°C; and
- At the rebar's outer surface, the interface between concrete and rebar the temperature was found to be the lowest at 110°C.

.

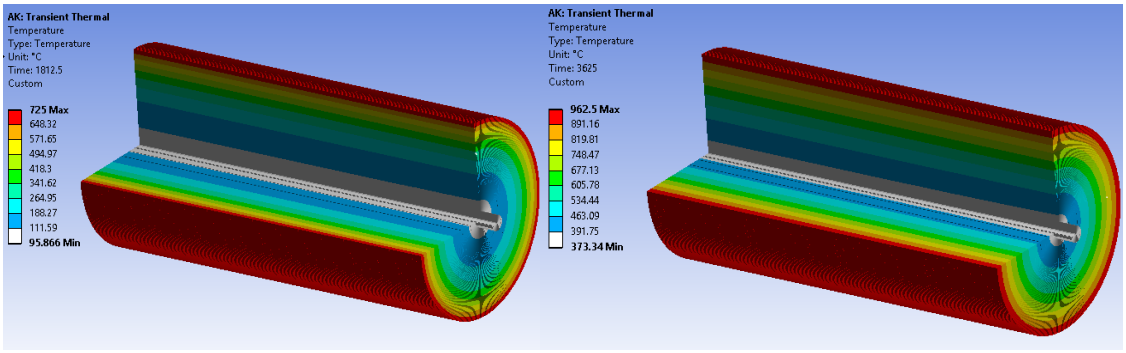

Figure 4.39: 3D expanded view of temperature profile a) at 30 mins duration b) at 60 mins duration

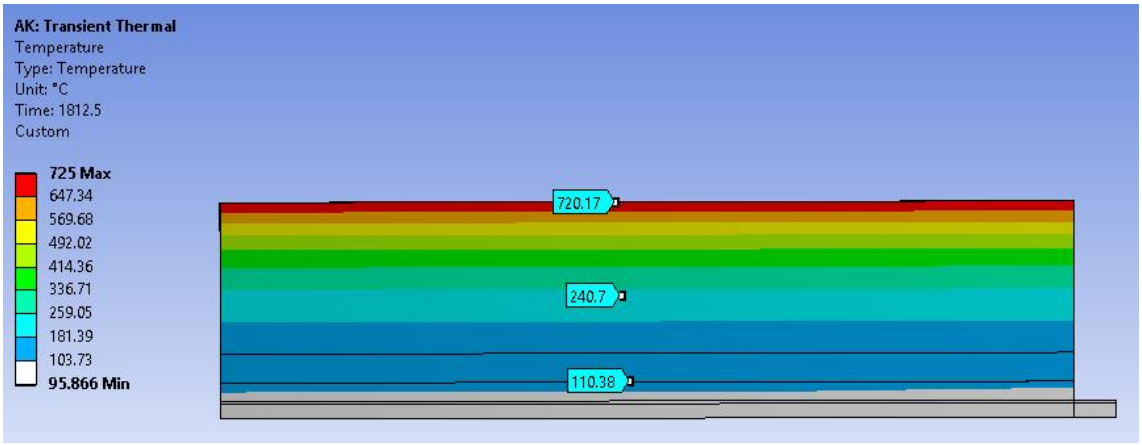

Figure 4.40: Temperature profile at 30 mins fire duration

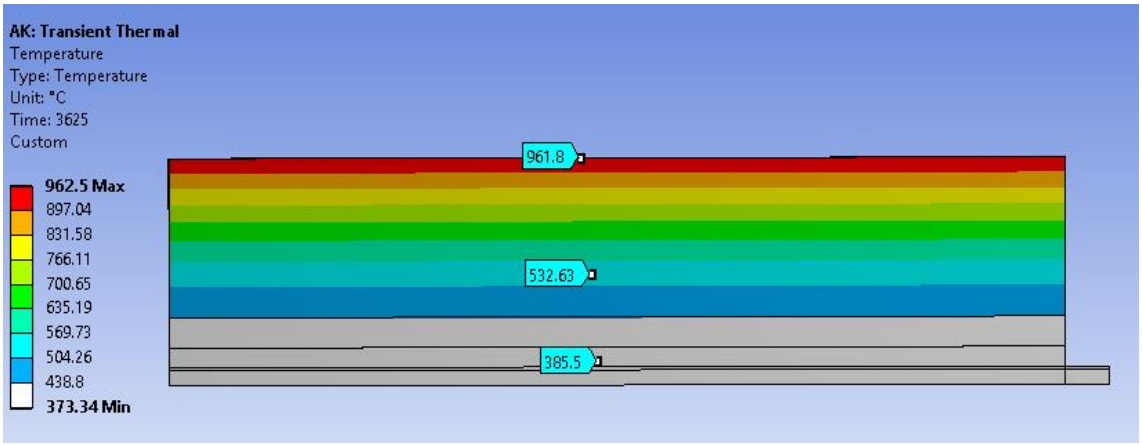

Figure 4.41: Temperature profile at 60 mins fire duration

Likewise, around one hour of fire exposure, the following key observations can be made (Figure 4.41):

- The temperature at the specimen's surface was nearing 960°C;
- At nearly half way between the external surface of specimen and the rebar the temperature of the concrete specimen is in the vicinity of 530°C; and
- At the rebar's outer surface, the interface between concrete and rebar the temperature was found to be the lowest at 385°C.

Figure 4.42 shows two thermal profiles: 1) temperature profile on the specimen surface as applied by the fire curve and 2) the thermal response of the specimen at the interface of the concrete and the rebar. It is evident that the temperature at the location of the interface remains just below 110°C at about 30min of fire exposure. Likewise, it can also be noted that the core temperature does not reach about 400°C until about 60min of exposure. Such a find leads to interesting outcomes when smart materials SMA are used alongside the steel rebars. These materials gain strength which is inversely proportional to that of steel. These aspects are explored and analysed in detail in Chapter 5 - Results and discussion. It is hence important to understand the implications of such behaviour. The application of thermal loading and its effect on the structural strength of the bond interface is discussed next.

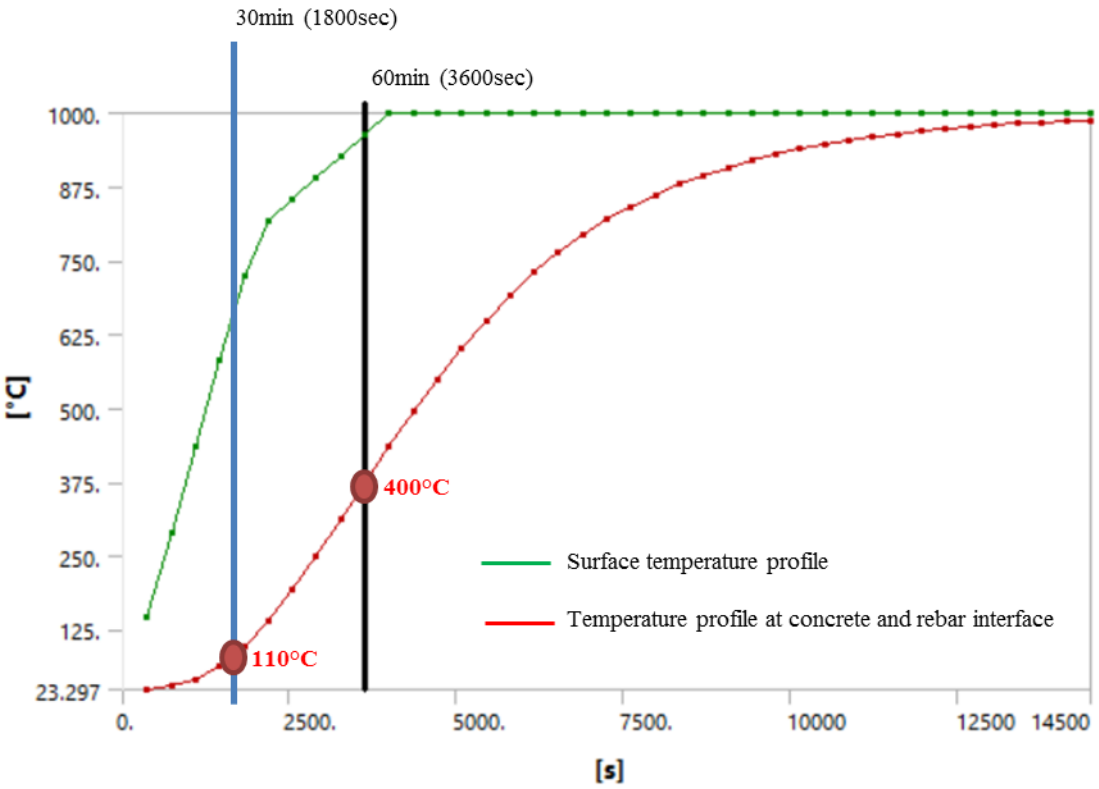

Figure 4.42: Temperature profiles of the specimen

4.5.2 Structural Analysis – Modelling specimen response to pull-out testing

To perform the sequentially coupled thermal-structural analysis, the above discussed temperature profiles were imported from thermal analysis environment to the structural analysis environment so that the pull-out analysis can be performed that can essentially mimic pulling of rebar while the concrete was exposed to fire (as performed on physical model in Chapter 3). The pull-out test using numerical methods is discussed next. As a first step a CAD model of the domain is required.

Step 1-CAD Model of the domain for structural analysis

In order to establish the domain of interest the complete experiment needs to be put into perspective. For convenience, Figure 4.43 is repeated below (Figure 4.43) where in the CAD model which is representative of the apparatus of the physical experiment is shown.

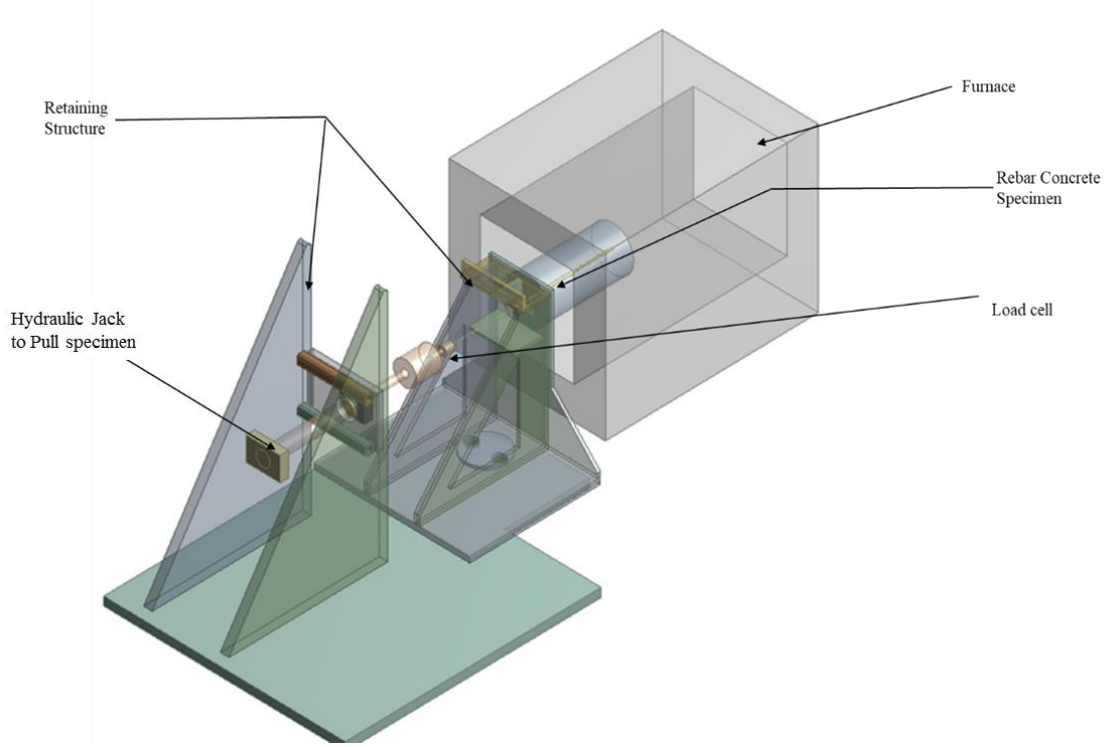

Figure 4.43: CAD model of the experiment apparatus (developed in Chapter 3).

Like the thermal model, structural model of interest too only requires the CAD model of concrete, rebar and their interface in an assembly state that is representative of the castings created in Chapter 3. The isolated CAD model showing the three components of the rebar-concrete specimen is shown in Figure 4.44. The model being symmetric in nature (cylindrical shape), only a section of the model (1Degree angle) is sufficient to study the structural load response. Therefore, the model is further simplified to a wedge (a section of the full model) as shown in Figure 4.45. It is this model that is used for all the structural analysis studies undertaken in this work including the parametric studies (discussed towards the end of this section). On identifying the domain and developing the required CAD model of the domain, the next step involved is to generate appropriate mesh for each of the specimen components. The profile and statistics of the respective domains (concrete, rebar and interface) are shown in Table 4.7.

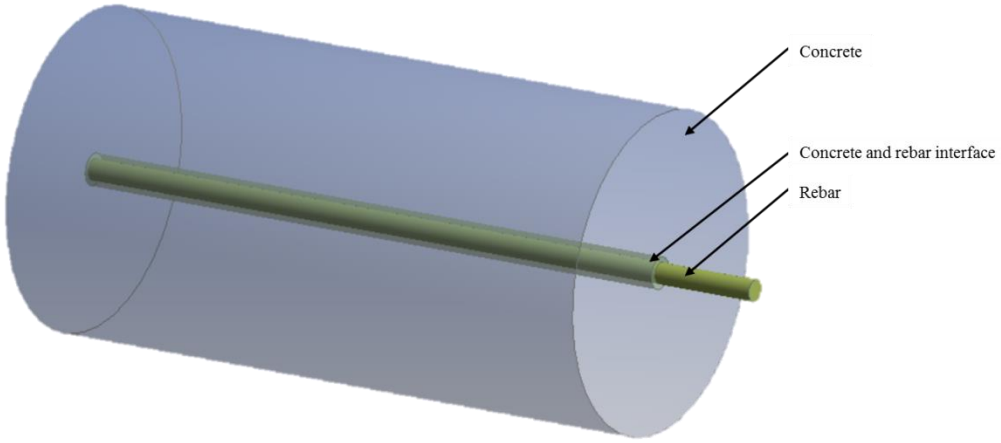

Figure 4.44: 3D CAD model of the Rebar-Concrete Model showing the Three components

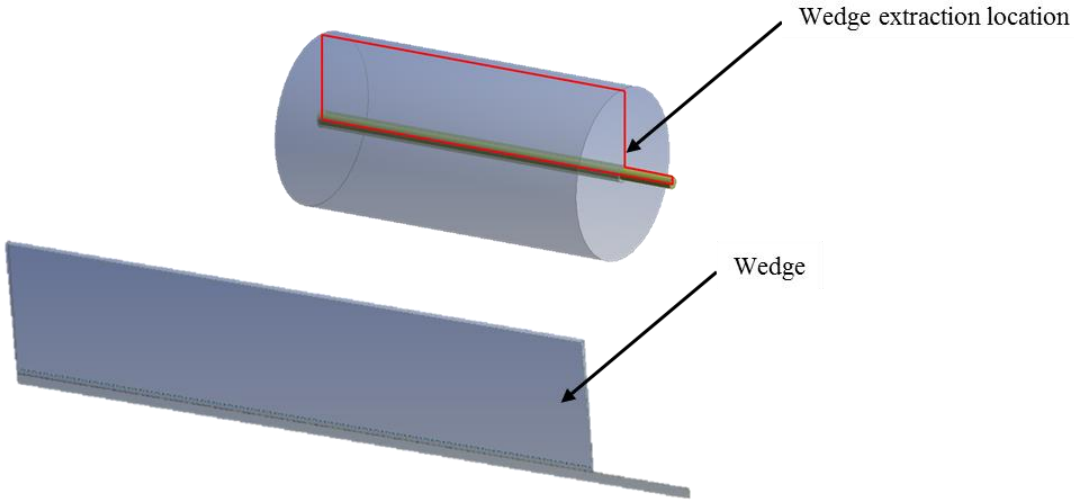

Figure 4.45: 2D wedge of the Rebar-Concrete Model (location of the wedge as showing the inset)

Table 4.7: Profile and statistics of the specimen domain

Object Name	*Solid*	*Solid*	*Solid*	*Solid*
State	Meshed			
Graphics Properties				
Visible	Yes			
Glow	0			
Shininess	1			
Transparency	1			
Specularity	1			
Definition				
Suppressed	No			
ID (Beta)	276	279	288	669
Stiffness Behavior	Flexible			
Coordinate System	Default Coordinate System			
Reference Temperature	By Environment			
Reference Frame	Lagrangian			
Material				
Assignment	sma			
Nonlinear Effects	Yes			
Thermal Strain Effects	Yes			
Bounding Box				
Length X	12.5 mm	4. mm	1.0052 mm	
Length Y	0.19635 mm	3.4906e-002 mm	4.3676e-002 mm	
Length Z	300. mm		15. mm	300. mm
Properties				
Volume	531.78 mm³	20.944 mm³	0.58912 mm³	11.782 mm³
Mass	4.1745e-003 kg	1.6441e-004 kg	4.6246e-006 kg	9.2486e-005 kg
Centroid X	17.051 mm	2.6666 mm	4.5185 mm	
Centroid Y	7.4399e-002 mm	1.1635e-002 mm	1.9716e-002 mm	
Centroid Z	150. mm		-7.5003 mm	150. mm
Moment of Inertia Ip1	31.308 kg·mm²	1.2331 kg·mm²	8.6716e-005 kg·mm²	0.69363 kg·mm²
Moment of Inertia Ip2	31.36 kg·mm²	1.2332 kg·mm²	8.7099e-005 kg·mm²	0.69363 kg·mm²
Moment of Inertia Ip3	5.1681e-002 kg·mm²	1.4615e-004 kg·mm²	3.8446e-007 kg·mm²	7.688e-006 kg·mm²
Statistics				
Nodes	8428	1510	948	18024
Elements	3900	1200	390	7505
Mesh Metric	None			

Step 2-Mesh for structural analysis

The numerical model consists of 3D volumetric solid elements and is selected for their unique characteristics from the element library of ANSYS. More specifically, Solid65 (8-noded) brick element was selected to cater for the non-linear behaviour of concrete material. The Solid65 elements in ANSYS is an 8-noded brick element with structural degrees of freedom (i.e. 3 displacements i.e. ux, uy and uz. Solid65 also has a special ability to model the concrete with its cracking, crushing and stress failure criteria.

To model the rebar, Solid185 element is considered. This element is an 8-noded brick element and it's been selected over the other 20-noded brick element for the reason that the nodes of concrete and rebar element should be coincident in order to create the interface between the two using the cohesive zone approach.

The concrete and SMA rebar interface were modelled using Inter205 8-nodded cohesive element. The Inter205 element was created using the surface nodes of the SMA rebar and concrete at the interface location. In addition, this process allowed to model the interface between the two surfaces. The tangential and normal separation was specified through the cohesive zone material model as discussed in the aforementioned section (refer Section 4.2.2).

The different types of mesh elements used are shown in Figure 4.46 where the concrete elements, rebar Solid185 element and the interface element are shown Red, Green and Yellow. The interface Inter205 element is a zero-thickness element which was created using the coincident nodes of the rebar material and concrete material. A coincident mesh was created at the interface with a mesh sizing of 0.2mm to capture the bond behaviour in detail.

The mesh controls that were applied to simulate the mesh are shown in Table 4.8. A complete view of the meshed wedge is shown in Figure 4.47. The meshed model used for numerical analysis is shown in Figure 4.47. The statistics of the mesh generated are shown in the Table 4.9.

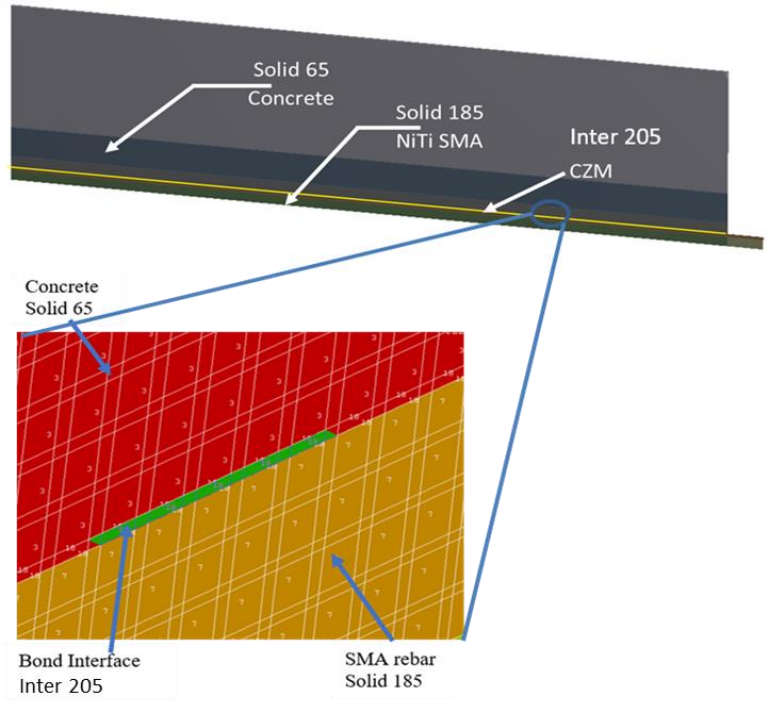

Figure 4.46: Numerical Model – Showing element type and the respective material

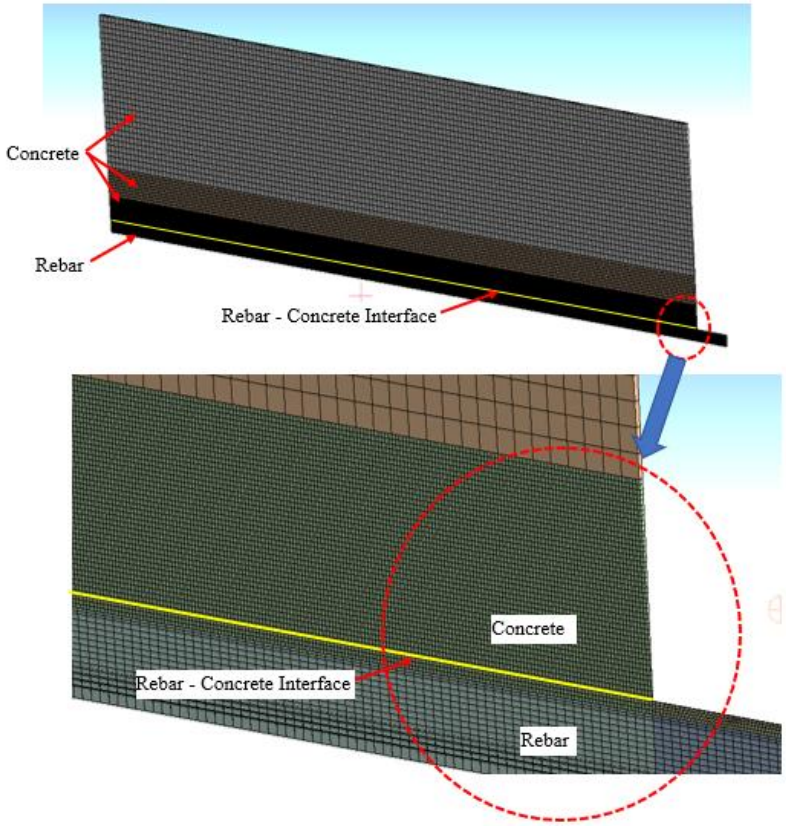

Figure 4.47: Numerical Model – Domain Mesh

Table 4.8: Mesh controls

Object Name	*Sweep Method 3*	*Edge Sizing 2*	*Edge Sizing*	*Edge Sizing 3*
State	Fully Defined	Suppressed		
Scope				
Scoping Method	Geometry Selection			
Geometry	1 Body	3 Edges	2 Edges	
Definition				
Suppressed	No	Yes		
Method	Sweep			
Element Midside Nodes	Use Global Setting			
Src/Trg Selection	Automatic			
Source	Program Controlled			
Target	Program Controlled			
Free Face Mesh Type	Quad/Tri			
Type	Number of Divisions			
Sweep Num Divs	Default			
Sweep Bias Type	No Bias			
Element Option	Solid			
Active		No, Suppressed		
Number of Divisions		2	400	
Behavior		Hard		
Bias Type		No Bias		

Table 4.9: Mesh settings and statistics

Object Name	*Mesh*
State	Solved
Defaults	
Physics Preference	Mechanical
Relevance	0
Sizing	
Use Advanced Size Function	Off
Relevance Center	Coarse
Element Size	1.0 mm
Initial Size Seed	Active Assembly
Smoothing	Medium
Transition	Fast
Span Angle Center	Coarse
Minimum Edge Length	3.4907e-002 mm
Inflation	
Use Automatic Inflation	None
Inflation Option	Smooth Transition
Transition Ratio	0.272
Maximum Layers	5
Growth Rate	1.2
Inflation Algorithm	Pre
View Advanced Options	No
Patch Conforming Options	
Triangle Surface Mesher	Program Controlled
Patch Independent Options	
Topology Checking	Yes
Advanced	
Number of CPUs for Parallel Part Meshing	Program Controlled
Shape Checking	Aggressive Mechanical
Element Midside Nodes	Dropped
Straight Sided Elements	
Number of Retries	Default (4)
Extra Retries For Assembly	Yes
Rigid Body Behavior	Dimensionally Reduced
Mesh Morphing	Disabled
Defeaturing	
Pinch Tolerance	Please Define
Generate Pinch on Refresh	No
Automatic Mesh Based Defeaturing	On
Defeaturing Tolerance	Default
Statistics	
Nodes	115560
Elements	54634
Mesh Metric	None

Step 3-Boundary conditions for structural analysis

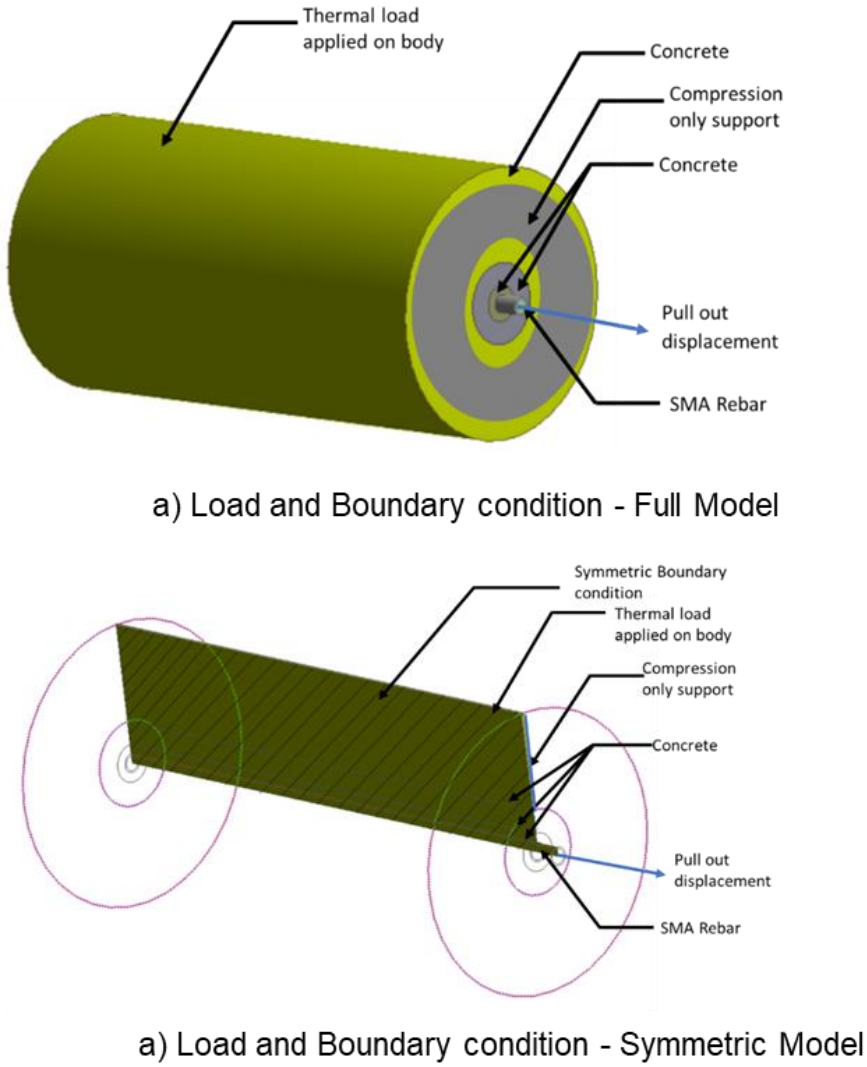

Figure 4.48: Load and Boundary condition – Pull-out simulation

The domain under consideration for the pull-out test and corresponding boundary conditions that are applied to the model are shown in Figure 4.48. The model is constrained on face using compression only support constraint, which represents the specimen, is rested against a rigid wall. One-way sequential thermal-structural model was set up, and thermal profile generated as a result of the thermal analysis discussed in the previous section is applied to the outer wall of the wedge to mimic the fire conditions of the furnace in the physical experiments (in other words, thermal load is applied to the outer wall of the concrete).

A known displacement value of 10mm is applied to the rebar so as to measure the reaction force (force required to pull out the rebar by 10mm). The direction of the arrow in Figure 4.48 shows the direction of pull. The displacement mimics the pull-out action as experienced during the conduct of the physical experiments. Following the creation of a CAD model of the domain and subsequently generating the mesh, the boundary conditions are applied to the wedge. The location and type of boundary conditions as applied to the wedge are shown in Figure 4.48.

Step 4-Material properties for structural analysis

It is typical in the literature that materials used for the pull studies in analysing the bond stress values were based on the assumption that the material is not subject to any transient conditions, such as varying ambient temperature. Such time/temperature dependent variations require the materials to be treated as having non-linear properties. This study involves the concrete being exposed to extreme heat replicating a fire event and as such is time dependent. The required material data to conduct such time and temperature dependent numerical studies is nearly absent in the literature. It is for this reason that physical experiments were conducted in this thesis (Chapter 3) to generate the required data sets. A sample of such a data set for M30 grade concrete and various fire exposure duration is shown in Table 4.10.

Table 4.10: Material model used in analyses

Model Test Condition	Concrete grade (M30)			Rebar Material		Interface Model					
				Structural Steel	SMA	SMA - Concrete			Steel -Concrete		
	Uniaxial Tensile strength (MPa)	Uniaxial compressive strength (MPa)	Modulus of elasticity (MPa)	Modulus of elasticity (MPa)	Modulus of elasticity (MPa)	Maximum Tangential traction, σ_{max} (MPa)	Tangential displacement, $\delta_{c,}$ (mm)	Ratio (alpha) $\alpha = \delta^*/\delta_c$	Maximum Tangential traction, σ_{max} (MPa)	Tangential displacement, δ_c (mm)	Ratio (alpha) $\alpha = \delta^*/\delta_c$
No fire condition	3	30	29128	2.00E+05	6.50E+04	1.8	1.3	0.5	3.5	1.17	0.69
30 Min	2.7	27	26215	1.90E+05	6.50E+04	1.5	1.5	0.58	3	1.16	0.68
60 Min	1.8	18	17476	1.40E+05	7.80E+05	1.25	1.5	0.58	1.75	1.2	0.71

The values for concrete and steel (rebar) are derived from the standard degradation chart used in the literature (Phan et al. 2002; Xuhong et al. 2013) and discussed in (Section 1.4.1). For convenience the charts are shown below in Figure 4.49 and Figure

4.50 respectively. The values of standard degradation used in this study (for the case of NF-FL-SMA-D10-M30) are tabulated in Table 4.10. For SMA rebar, there are two values for modulus of elasticity (austenite and martensite) depending on the state of transformation the material exists. This data on modulus of elasticity for SMA was sourced from literature (Šittner et al. 2014). The SMA rebar in the test specimen is not undergoing any deformation or under any stress condition as it is not under any pre-loading condition, Hence the shape memory effect of SMA is not playing a significant role in test conditions.

Also, when it comes to material definition of the interface (both SMA-concrete and Steel-concrete) in the cohesive zone, there exists no data in the literature. It is for this reason that physical experiments were conducted in this work (Chapter 3). The experiments generated the required data that would assist in completing the material definition for modelling the cohesive zone, CZM. For convenience the chart showing the data set generated for maximum tangential traction (σ_{max}) and tangential displacement (δc) for specimen NF-HL-E2-SMA marked by the dotted line as shown in Figure 4.51 The development of numerical model that would take into account the non-linear behaviour (under conditions of fire) of the cohesive zone is taken up for the first time in this work. The results shall validate a novel method of analysing the interface bond stress between various materials that are subjected to high temperatures. All the above discussed data is shown in Table 4.10 and the same was used in the developing the numerical model to conduct structural analysis on the specimen.

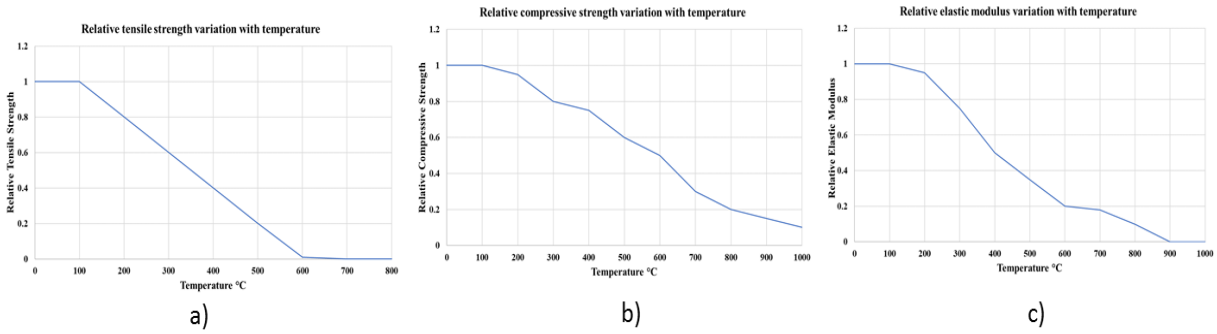

Figure 4.49: Concrete-Relative degradation with temperature a) tensile strength b) compressive strength and c) elastic modulus

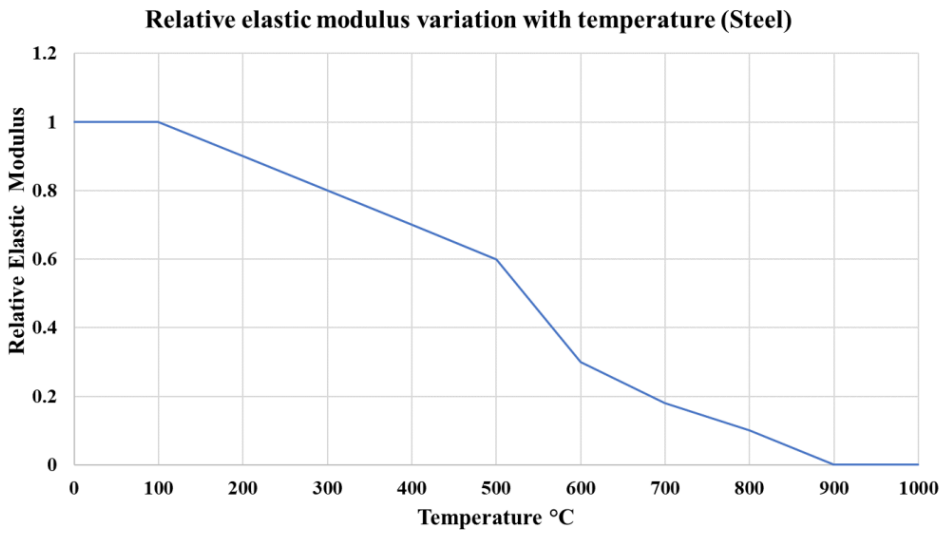

Figure 4.50: Steel-Relative degradation with temperature a) yield strength and b) elastic modulus

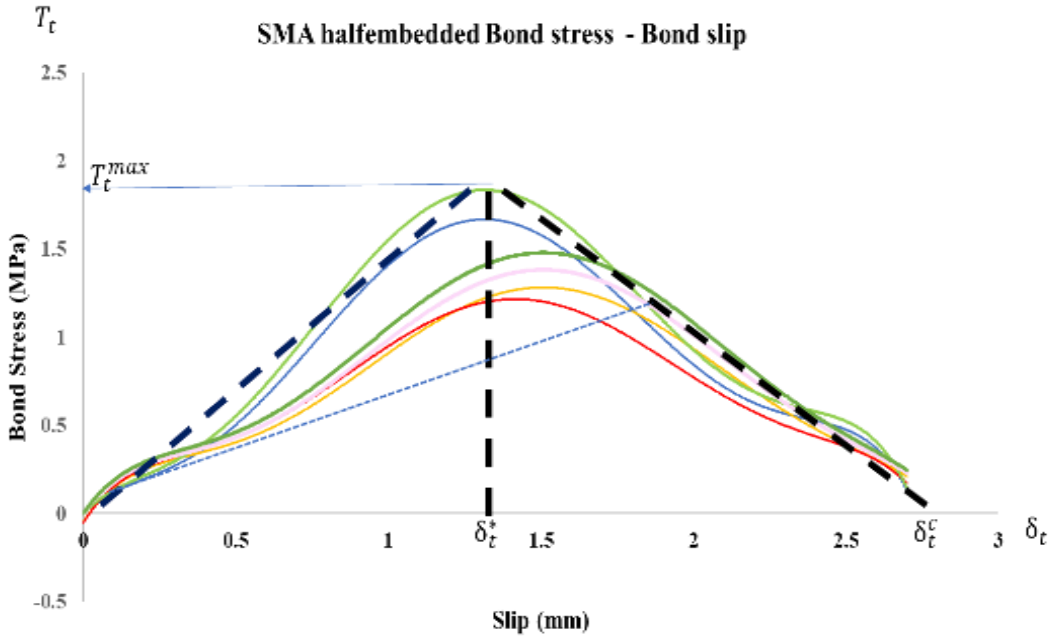

Figure 4.51: Specimen interface-bond stress vs slip

Step 5- Solving the numerical model

Having defined the model for the boundary conditions, developing the mesh, and assigning the required material properties the domain was prepared for solving. The following solver conditions were employed in this work.

With the physics defined and the boundary conditions specified in the previous step (Step 4) the model was ready for solving. The simulations were developed using a machine (a desktop computer) with significantly higher processing capabilities when compared to the usual standard desktop units. The machine used was custom built to exploit the GPU capabilities of the NVIDIA Tesla processors. The Tesla C2075 processor delivers parallel processing ability to a standard desktop, meaning that simulations could be performed faster. By adding two Tesla processor boards, it was possible to accelerate some of the most complex calculations exponentially faster than by simply adding a second CPU. The specifications of the machines are presented below:

- Operating system: Windows 7 Professional (Service Pack 1);
- Processor: Intel® Xenon® CPU x5690 @3.47GHz (8 processors);
- Installed memory (RAM): 8 GB;
- System type: 64-bit operating system; and
- GPU processor: NVIDIA Tesla C2075 (2 Nos.)

4.5.3 Convergence accuracy and results

The order of accuracy of the approximation is determined by the exponent on the mesh spacing or time step factor of the largest term in the truncated part of the series expansion, which is the first term excluded from the approximation. Increasing the order accuracy of an approximation generally implies that errors are reduced more quickly with mesh or time step size refinement. Unfortunately, in addition to increasing the computational load, high-order approximations are also generally less robust (that is, less numerically stable) than their low order counterparts. In order to achieve more accurate solutions, second order accurate approximations are employed although they are computationally intensive.

A measure of how well the solution is converged can be obtained by plotting the residuals for each equation at the end of each time step. The level of convergence required depends on the purpose of the simulation (whether qualitative or quantitative results are required). Although the required convergence level depends on the model

and on individual requirements, the following guidelines concerning the residual levels are used in the simulation studies undertaken in this thesis.

- Values larger than 10^{-4} may be sufficient to obtain a qualitative understanding of the flow field;
- 10^{-4} is relatively loose convergence, but may be sufficient for many engineering applications;
- 10^{-5} is good convergence, and usually sufficient for most engineering applications; and
- 10^{-6} or lower is very tight convergence and is occasionally required for geometrically sensitive problems.

The numerical models developed were solved to achieve a converged solution. The convergence value was set at 10^{-6} for reasons mentioned above. Newton-Raphson approach evaluates the difference between the loads corresponding to the element stresses and applied loads. A minimum of 500 and a maximum of 5000 sub-steps were defined to achieve the convergence criteria mentioned above. Automatic time stepping function in ANSYS program controls the sub-step size. For the above solver conditions, the solution in this work had indeed converged as shown in the Figure 4.52.

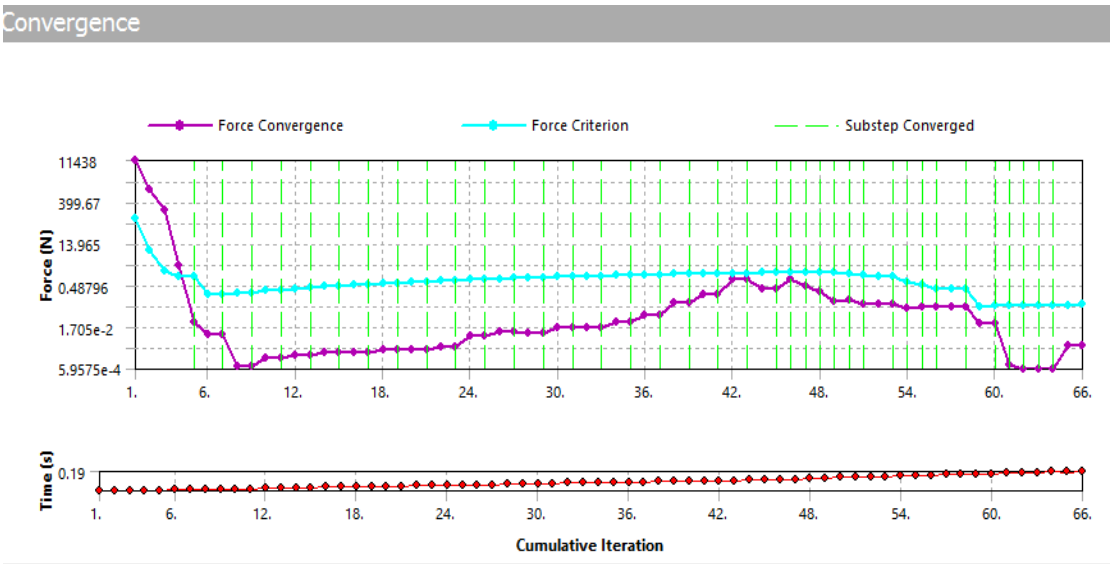

Figure 4.52: Convergence chart

4.6 Numerical Studies – Results and Discussion

A numerical method of examining various concrete specimens was considered in this Chapter. A new method of studying the bond stress at the interface was proposed that uses mesh elements that respond to the nonlinear behaviour of the rebar and concrete under the conditions of fire. Since the data required to define such mesh elements were absent in the literature, experiments were carried out as described in Chapter 3 that resulted in the generation of required data sets (Table 3.12-Chapter 3) on bond stress values of specimens that are subjected to conditions of fire. The above-mentioned data sets were employed in the CZM model to analyse the nonlinear behaviour of the SMA-concrete interface for the first time in this work. To this extent, the numerical framework, methodology and the numerical experiments conducted using the novel numerical approach are discussed in this Chapter thus far. The results of the numerical experiments are presented next wherein the results from the thermal analysis that predicts the thermal profile of the specimen is discussed first followed by the results on the nonlinear structural analysis that employs such above-mentioned thermal profile.

4.6.1 Results- Thermal Analysis

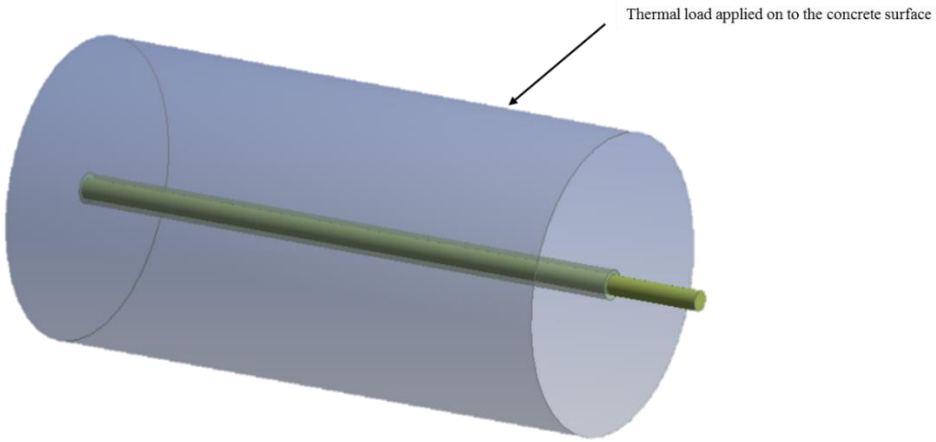

Figure 4.53: Thermal load on specimen

In order to replicate the conditions of fire in a furnace (as elaborated in Chapter 3), in the numerical studies the thermal load was applied to the surface of the concrete as

shown in Figure 4.53. Full transient thermal analyses were performed using fire curve (AS 1530.4) to obtain the temperature profile. The thermal response of the concrete-Interface-SMA rebar and concrete-Interface-steel rebar are studied first as a step leading to the use of such a thermal profile in the structural analysis. A full transient thermal analysis was used to obtain the temperature gradient profile for three specific time points over the period of the analysis 1) at the start under no fire condition, 2) at 30mins, and 3) at 60mins. While the methodology and the numerical setup including the solving of the numerical model was discussed as in Chapter 5, in this section the results of the thermal analysis on both the above-mentioned specimen types are discussed in detail.

4.6.1.1 Concrete-Steel Specimen Thermal Analysis results

All materials respond to thermal loading in a way that is unique and one that is defined by their respective thermal conductive properties. In general, metals are to be expected to conduct heat at a rate that is faster than non-metals such as concrete. In this study, the rebar material is metal (both SMA and steel) which is used in conjunction with concrete (a non-metal). It is important to note the temperature the metal rebars reach in an event of fire so as to understand their failure modes. In the experimental study the temperature profile with respect to time is capture by the thermocouple which recorded the temperature at surface of the specimen (T1), halfway between external surface & concrete rebar (T2) and at rebar interface (T3) (Figure 3.43). Thermal analysis temperature results are probed at the same location as per the experimental thermocouple probe results and are shown in Figure 4.54. In both the experiments and numerical analysis, the temperature can be seen to have ramped up to heat the specimen surface; the response of the specimen is noted at about 3600sec (60min). It can be noted that at about 60min, there is very close agreement of the temperature values between the physical experiment and the numerical study. In this case the temperature of the SMA rebar at the interface is 380°C and 330°C for experiment and numerical studies respectively.

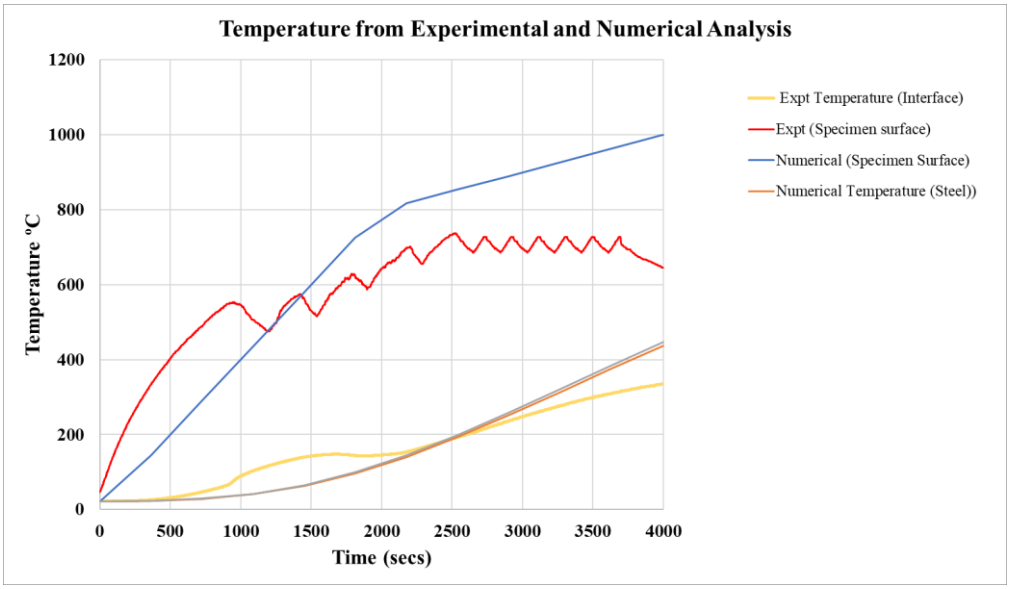

Figure 4.54: Temperature profile SMA rebar full insert: Experimental Vs Numerical

The difference in the surface temperature from the numerical and experimental is mainly attributed to two main reason 1) In numerical analysis the time-temperature fire curve input data was directly applied on the specimen surface, whereas in experimental studies the fire curve was given by FP21 controller to the electric furnace, the controller was not able to ramp up the temp with smaller increment and hence fluctuation on the temperature profile T1 (Expt-surface) can be observed and 2) was the heat loss from the furnace was delaying the temperature rise with respect to time. On the other hand, there was no losses and heat was directly applied on the specimen surface in the numerical analysis. To improve the correlation numerical model for thermal analysis to incorporate the heat loss due to convection on furnace and use the advanced controller to capture the fire curve with smaller increments.

In the CAD model (Figure 4.55) there are three zones identified 1) concrete 2) interface between concrete and steel rebar and 3) steel rebar. The response of the interface to the thermal load applied on the specimen is critical to the bond stress between the above-mentioned and as a consequent the strength specimen (Figure 4.56).

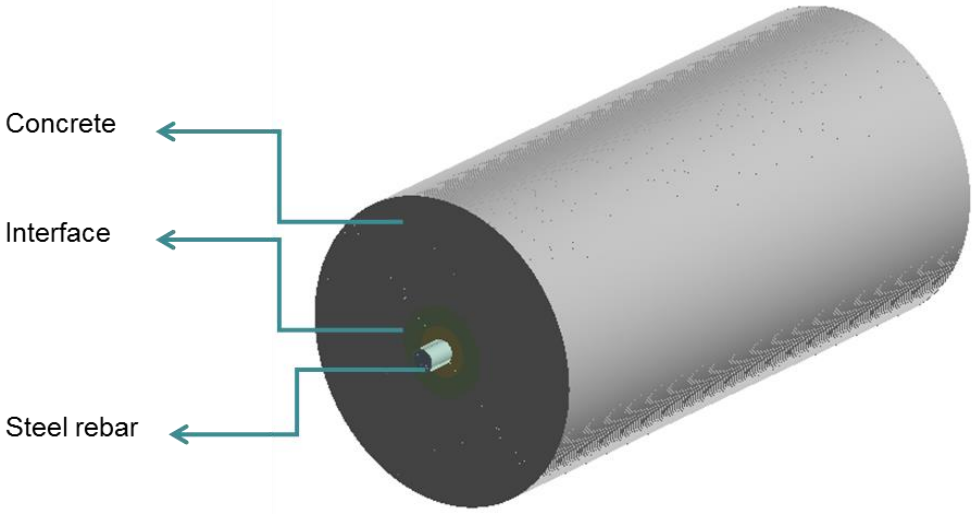

Figure 4.55: 3D CAD of Concrete-Steel rebar and the interface

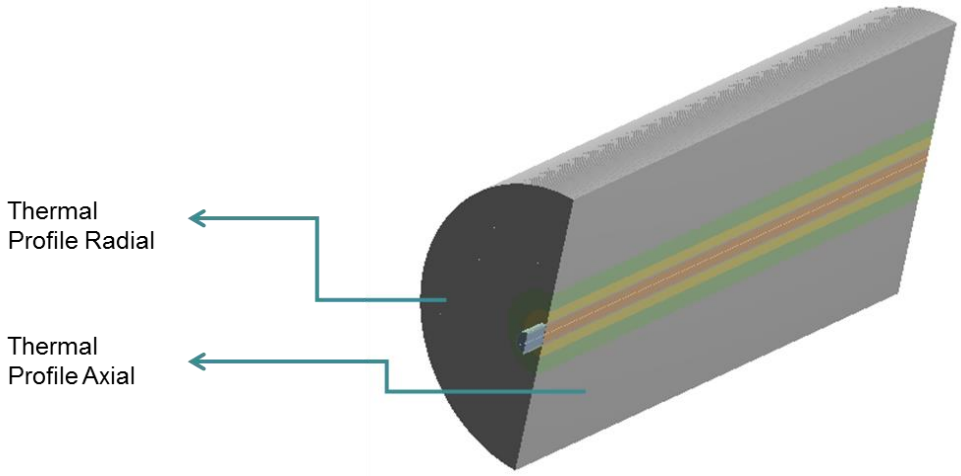

Figure 4.56: 3D Cross-section identifying the locations (to read thermal profiles)

[NOTE: For convenience all Figures mentioned in this section are presented towards the end of this section.]

The location from which the data for the thermal profiles are recorded is shown in Figure 4.56 The response is noted for three-time intervals:

1. At start under no fire condition;
2. At 30mins; and
3. At 60mins.

In general, it can be said that the effect of heating has caused gradual increase in the temperature of the concrete surface from room temperature to about 930°C over a period of 60min. 3D cross-sectional view of the concrete and its corresponding temperature at the above said time points is shown in Figure 4.58.

In Figure 4.59 and Figure 4.60, the 2D cross-section thermal profiles along the axial and radial direction of the specimen are shown respectively. It is evident from the thermal profile that the steel rebar temperature remains below 95°C from the start of the experiment to about 30min from which time there is gradual increase leading to 60min at which point the rebar temperature is about 375°C. A further comparison of the thermal profiles (Figure 4.61, Figure 4.62 and Figure 4.63) at the above-mentioned points in time reveals that the thermal load applied on to the surface of the concrete had indeed penetrated the interface and reached the steel rebar (heating from room temperature to 96˚C at about 30min and further to 375˚C at 60min duration). It is also important to note in the above-mentioned figures that the inner wall temperature of the concrete and the outer wall temperature of the interface had the same temperature readings, meaning that the heating of the interface had occurred as expected and that the heat passed through the interface at levels that ensured uniform temperature of the interface. Likewise, the heat from the interface can also be seen to have transferred to the steel rebar without any hindrance, since the inner wall of the interface and the outer wall of the rebar had matching temperature profiles at every time frame that the results were captured.

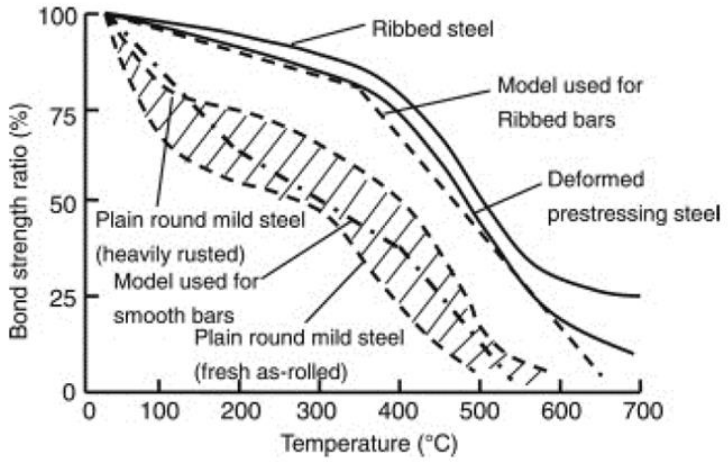

Figure 4.57: Bond strength degradation between concrete and steel rebars (Lublóy et al. 2014)

One of the most important observation is that for the conditions for which the specimen was subjected to, the steel rebar temperature had indeed reached temperatures close to 400°C. Lubloy et al. studied the bond behaviour of steel-concrete under high temperature and based on the material degradation, with the rising temperature steel rebar starts losing its bond strength significantly as shown in Figure 4.57 (Lublóy et al. 2014). In this work, SMA was investigated for use as rebar. The results of which are discussed following the figures mentioned in this section.

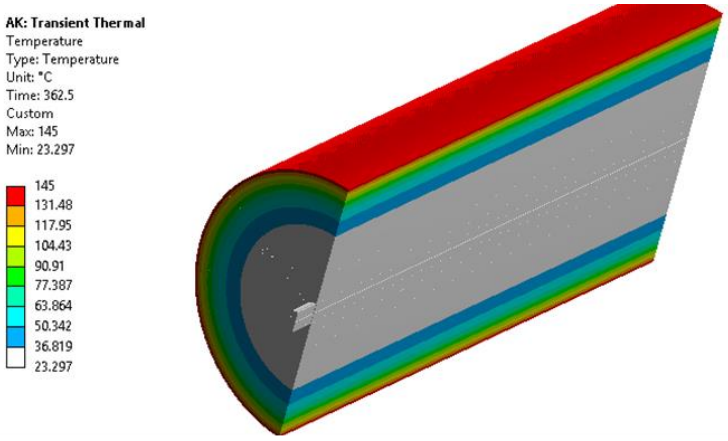

(a)

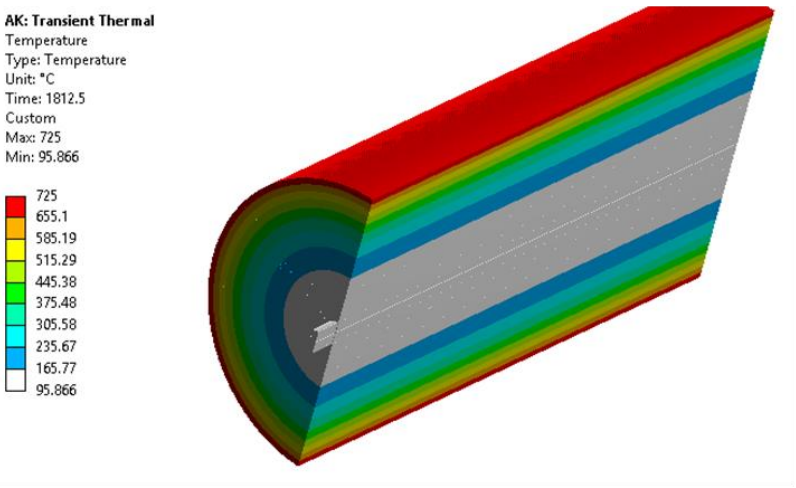

(b)

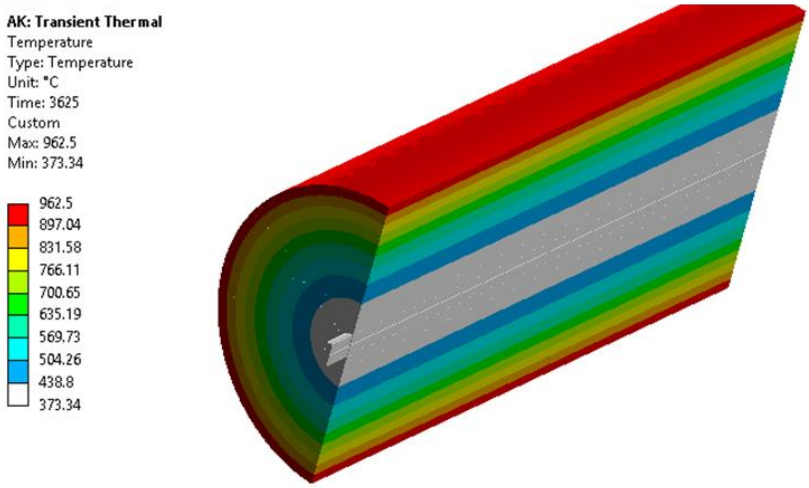

(c)

Figure 4.58: 3D Thermal profile of the Concrete-Steel Rebar and interface at (a) Start (b) 30min and (c) 60min fire exposure

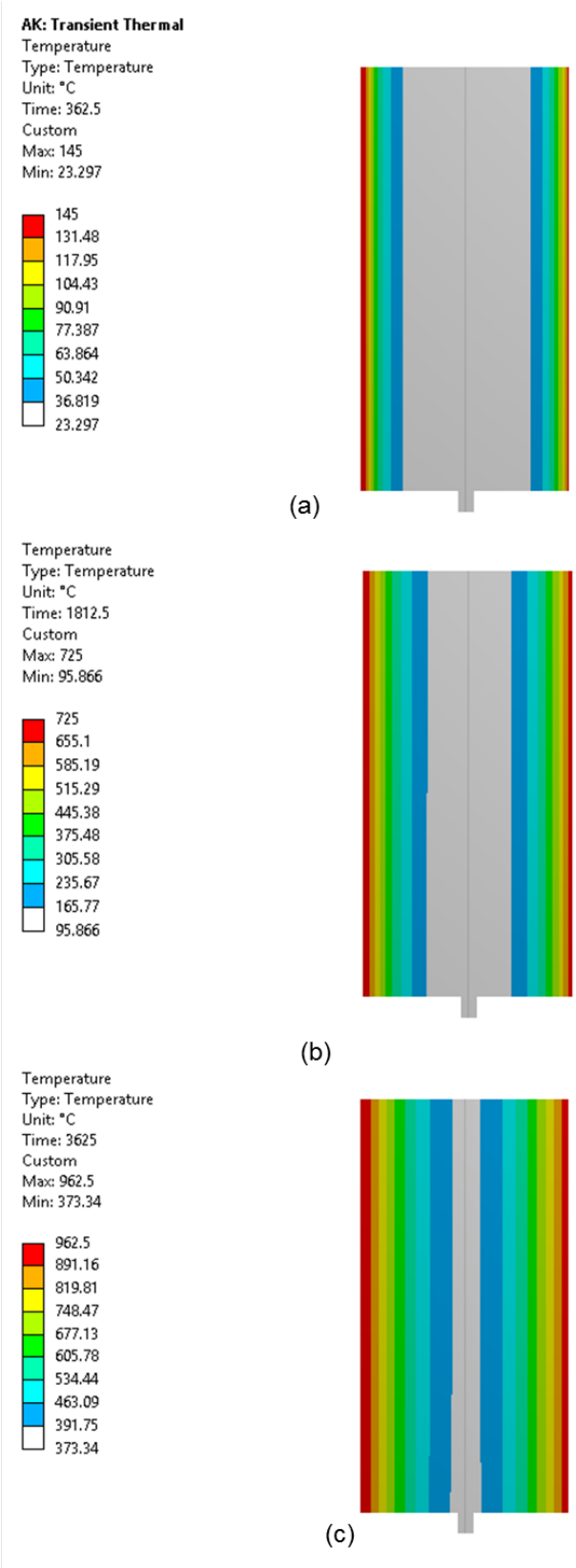

Figure 4.59: 2D Axial Thermal profile of the Concrete-Steel Rebar and interface at (a) Start (b) 30min and (c) 60min fire exposure

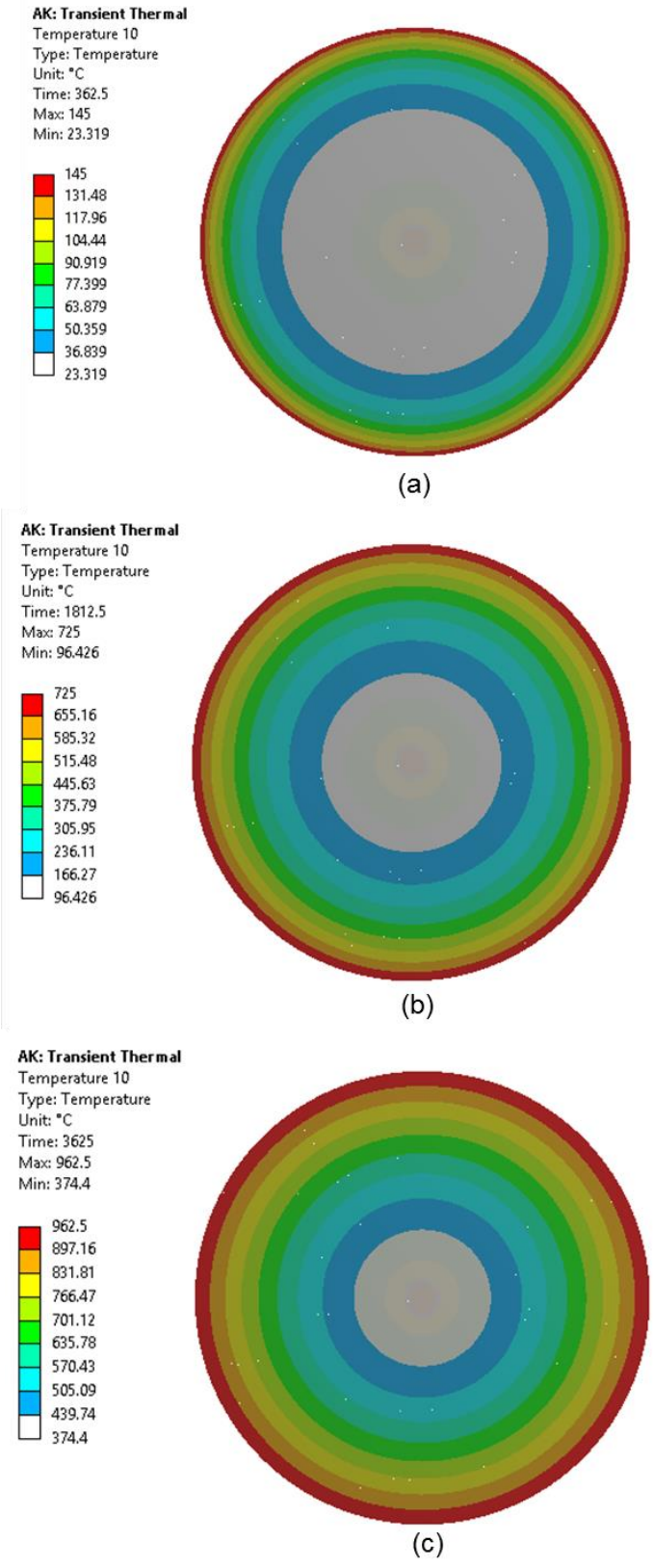

Figure 4.60: 2D Radial Thermal profile of the Concrete-Steel Rebar and interface at (a) Start (b) 30min and (c) 60min fire exposure

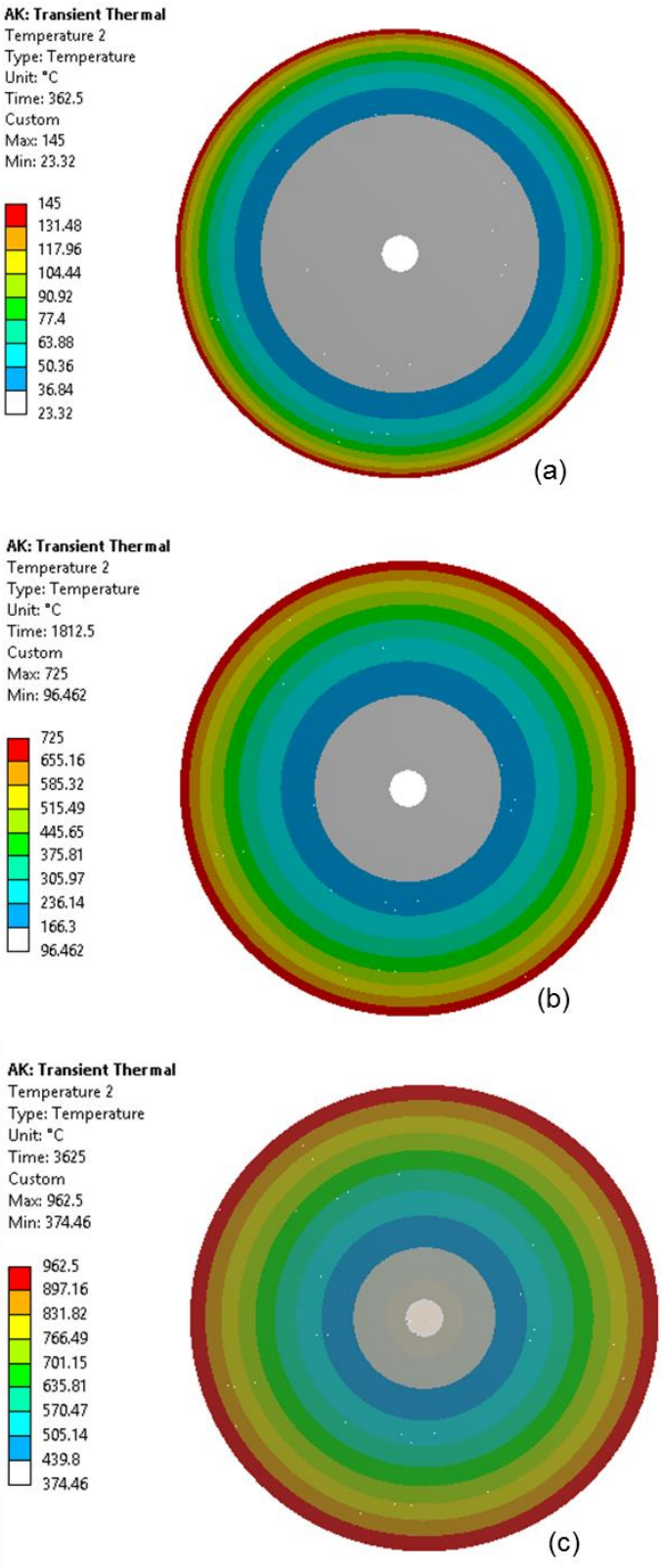

Figure 4.61: 2D Radial Thermal profile of the Concrete at (a) Start (b) 30min and (c) 60min fire exposure

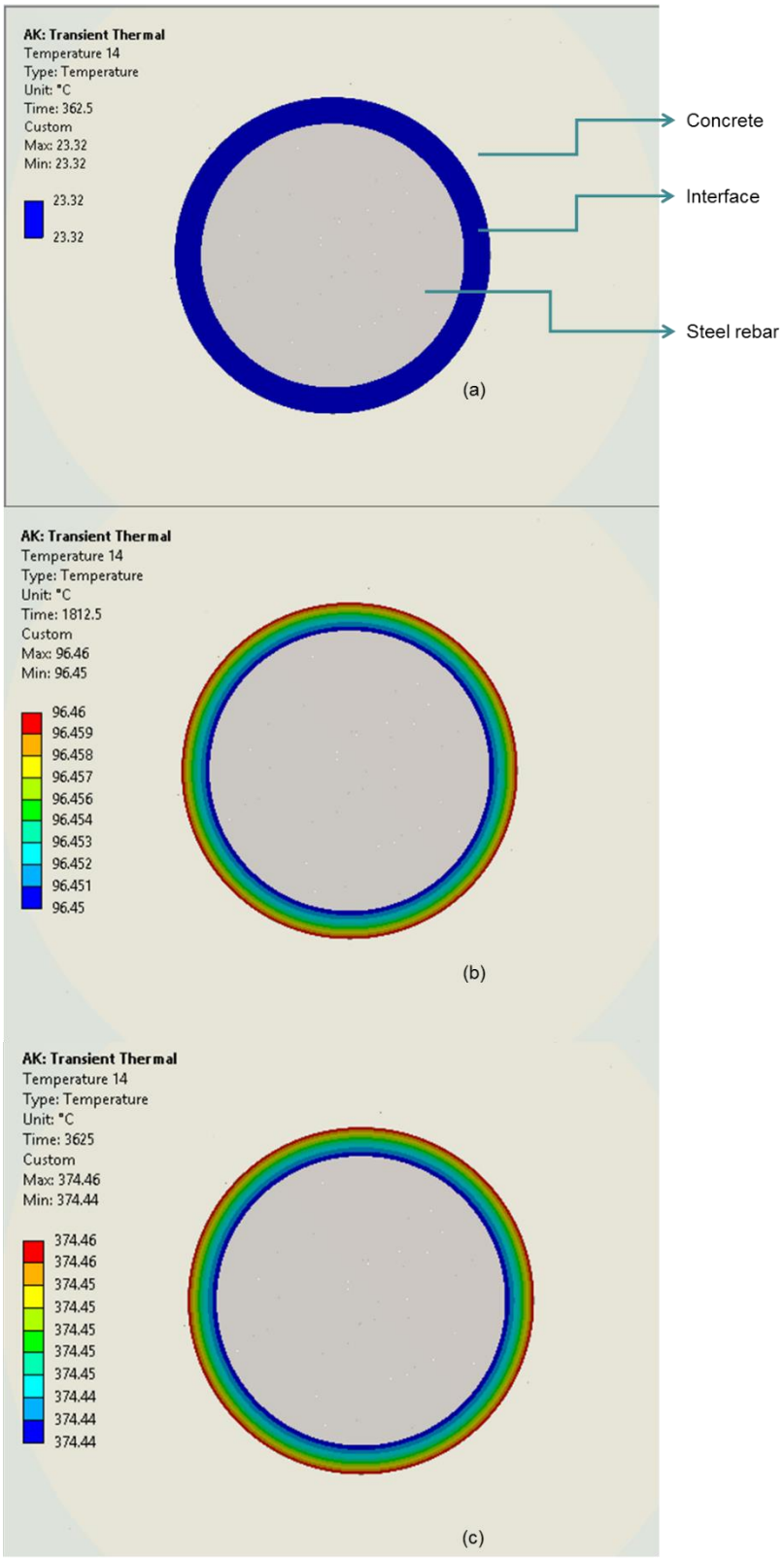

Figure 4.62: 2D Radial Thermal profile of the Concrete-Steel Rebar Interface at (a) Start (b) 30min and (c) 60min fire exposure

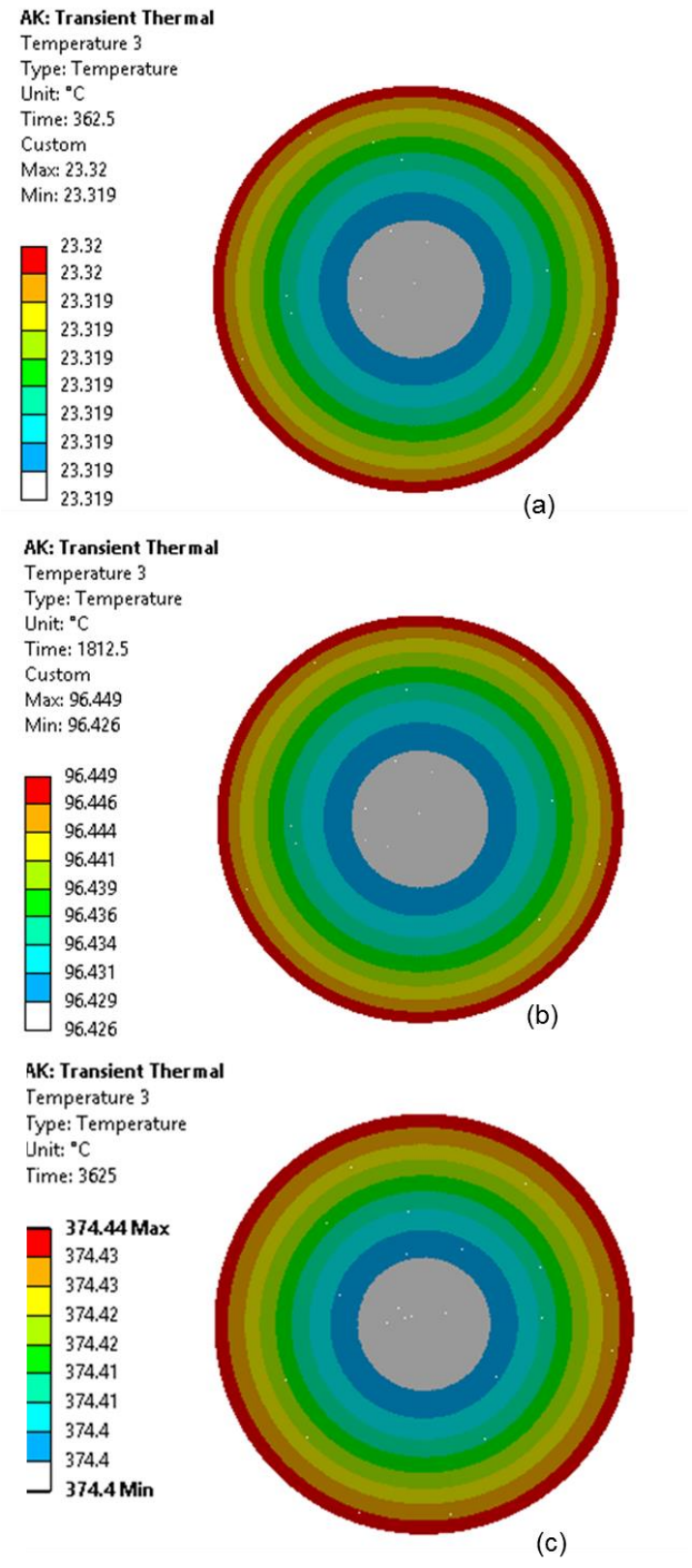

Figure 4.63: 2D Radial Thermal profile of the Steel Rebar at (a) Start (b) 30min and (c) 60min fire exposure

4.6.1.2 Concrete-SMA Specimen Thermal Analysis results

The numerical study involved the study of bond stress between two sets of specimens 1) involving steel rebar and 2) involving SMA rebar. The results on the steel rebar were discussed in the previous section. In this section the results concerning the SMA rebar is discussed. The location on the specimen from where the thermal profiles are record for the discussion in this section remain the same as shown in Figure 4.56. The thermal response is noted for three-time intervals as in the precious case with steel rebar:

1. At start under no fire condition;
2. At 30mins; and
3. At 60mins.

In the case of SMA rebars in concrete, it can be said that the effect of heating has caused gradual increase in the temperature of the concrete from room temperature to about 930°C over a period of 60min. 3D cross sectional view of the concrete and its corresponding temperature at the above said time points is shown in Figure 4.64.

In Figure 4.65 and Figure 4.66, the 2D cross-section thermal profiles along the axial and radial directions of the specimen are shown respectively. It is evident from the thermal profile that the SMA rebar temperature remains below 145˚C from the start and reaching 725˚C at about 30min into the experiment and reaching 962˚C at the 60min. A further comparison of the thermal profiles (Figure 4.67, Figure 4.68 and Figure 4.69) at the above mentioned points in time reveals that the thermal load applied on to the surface of the concrete had indeed penetrated the interface and reached the steel rebar (heating from room temperature to 99˚C at about 30min and further to 383˚C at 60min duration). It is also important to note in the above mentioned figures that the inner wall temperature of the concrete and the outer wall temperature of the interface had the same temperature readings, meaning the heating of the interface had occurred as expected and that the heat passed through the interface at levels that ensured uniform temperature of the interface. Likewise, the heat from the interface can also be seen to have transferred to the SMA rebar without any hindrance,

since the inner wall of the interface and the outer wall of the rebar had matching temperature profiles at every time frame that the results were captured.

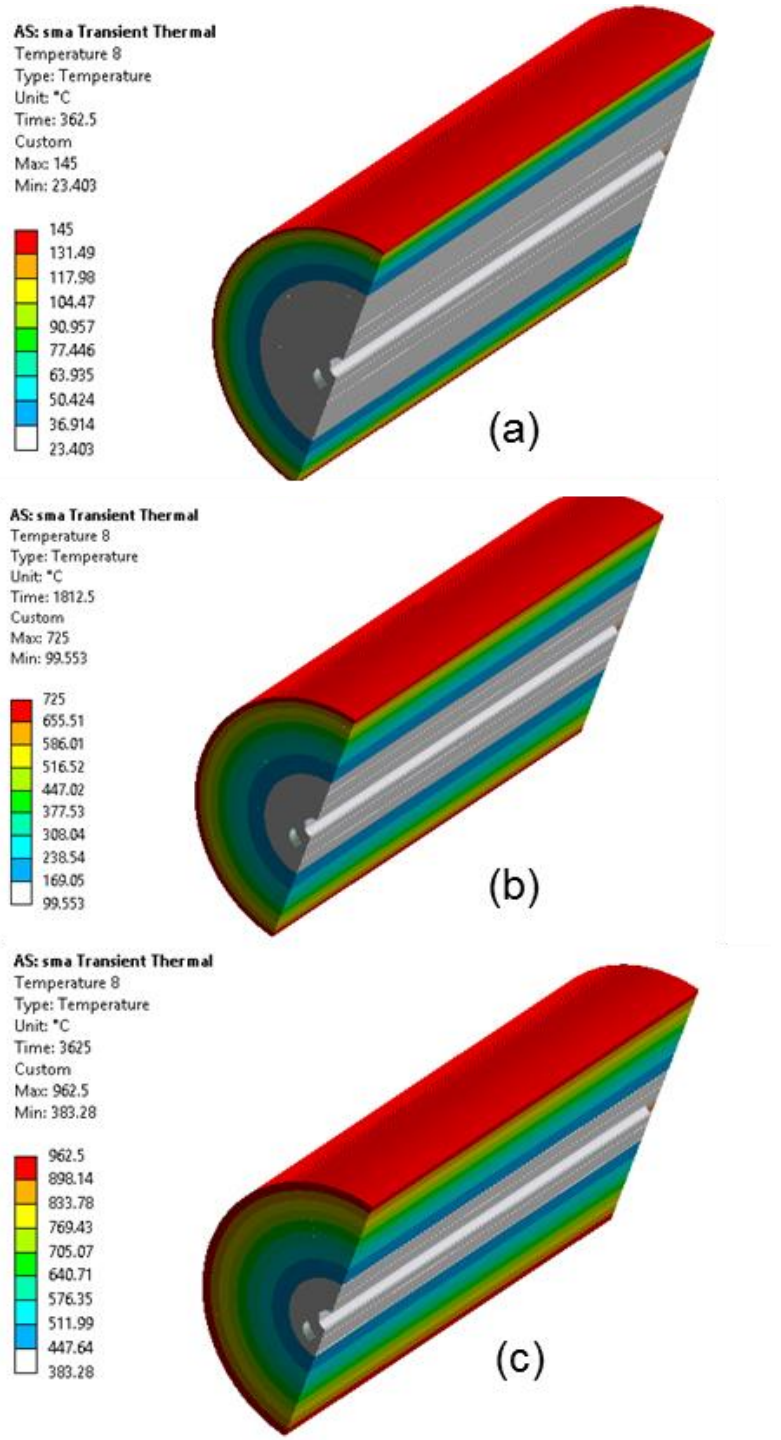

Figure 4.64: 3D Thermal profile of the Concrete-SMA Rebar and interface at (a) Start (b) 30min and (c) 60min fire exposure

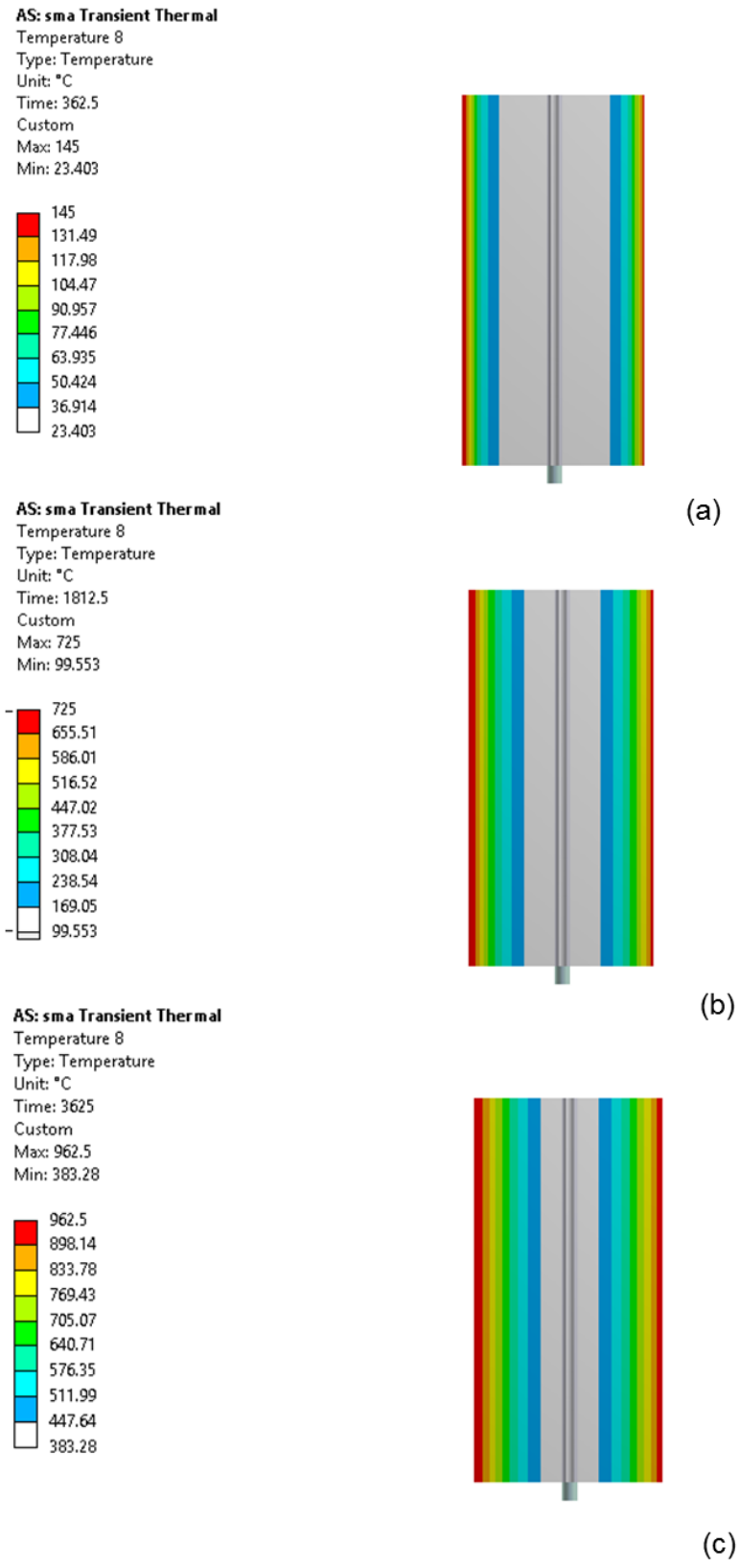

Figure 4.65: 2D Axial Thermal profile of the Concrete-SMA Rebar and interface at (a) Start (b) 30min and (c) 60min fire exposure

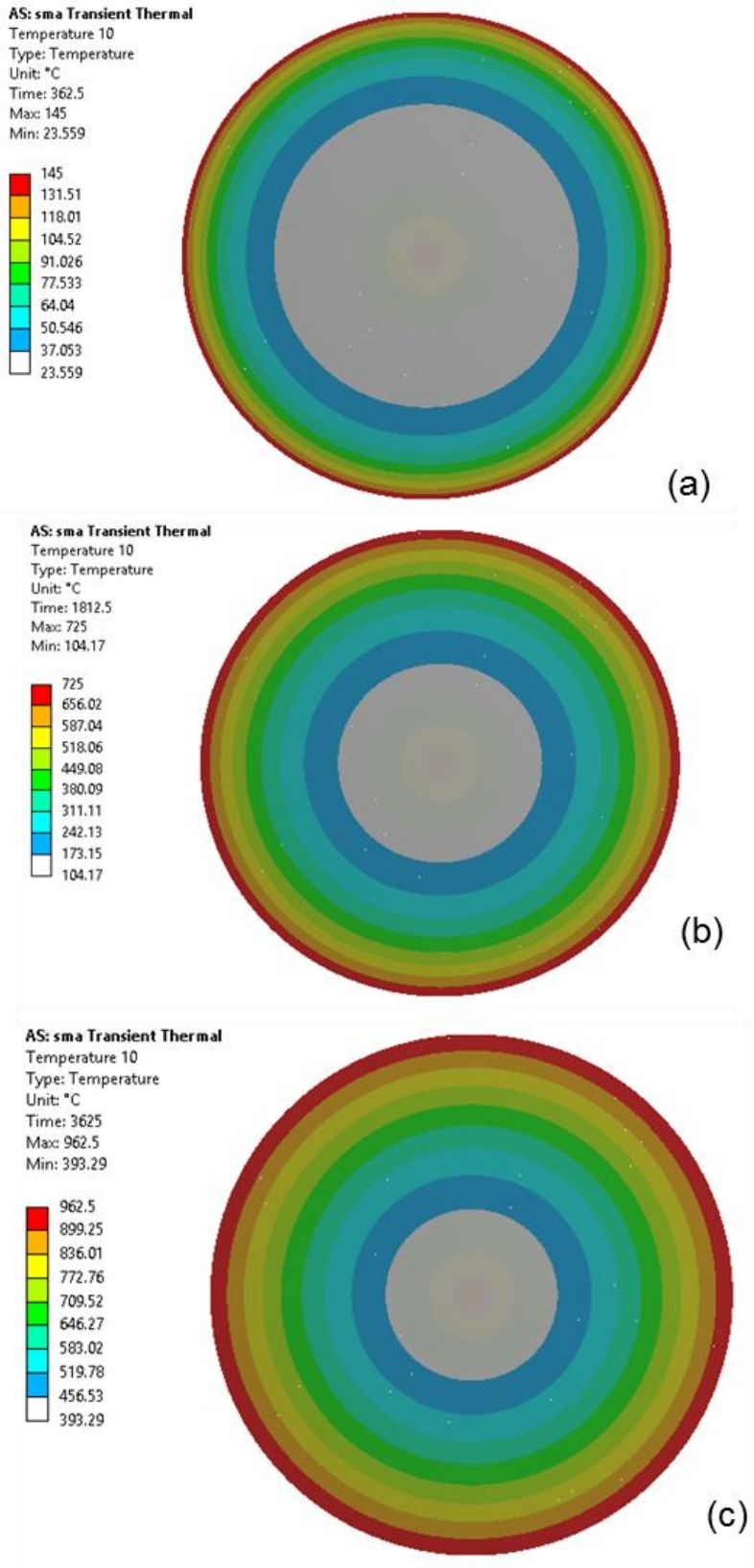

Figure 4.66: 2D Radial Thermal profile of the Concrete-SMA rebar and the interface at (a) Start (b) 30min and (c) 60min fire exposure

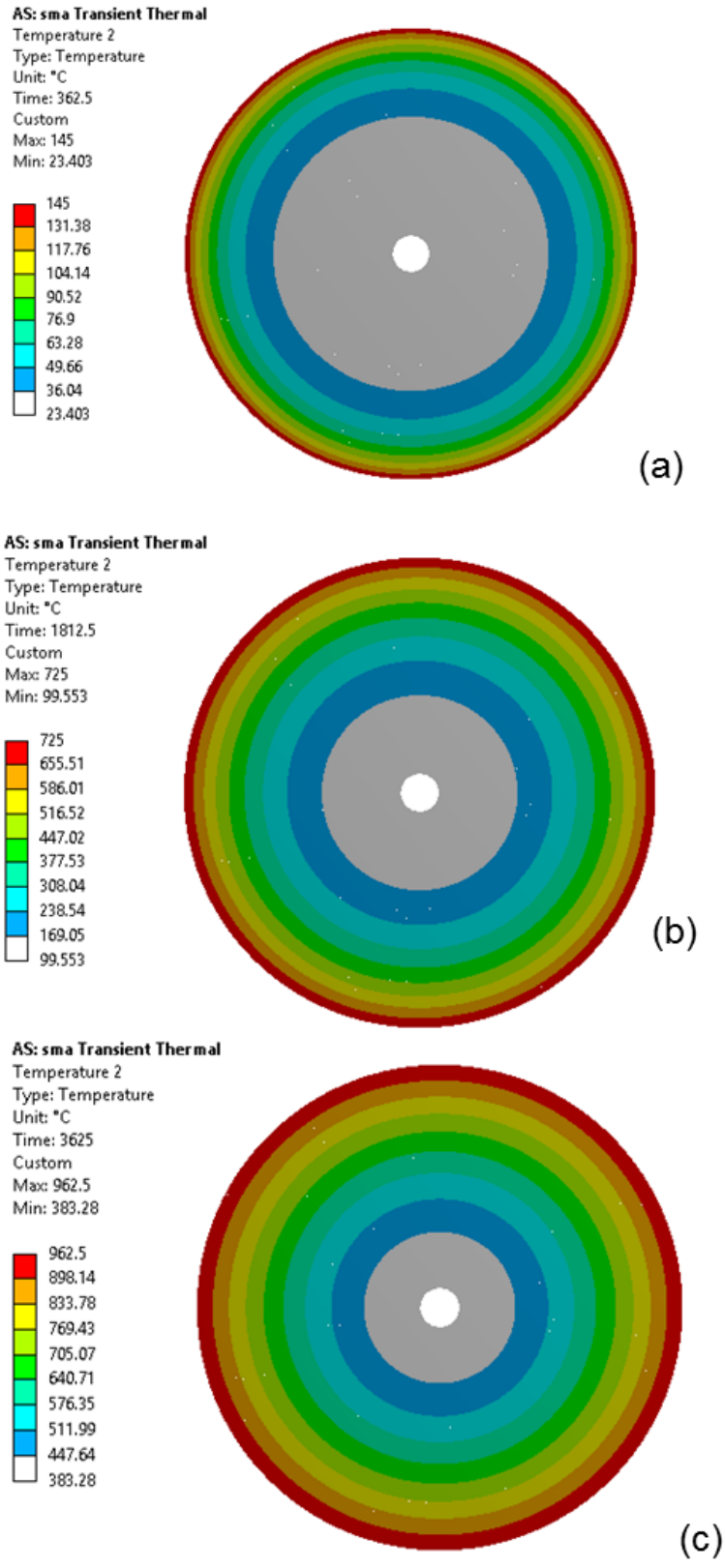

Figure 4.67: 2D Radial Thermal profile of the Concrete (specimen with SMA rebar) at (a) Start (b) 30min and (c) 60min fire exposure

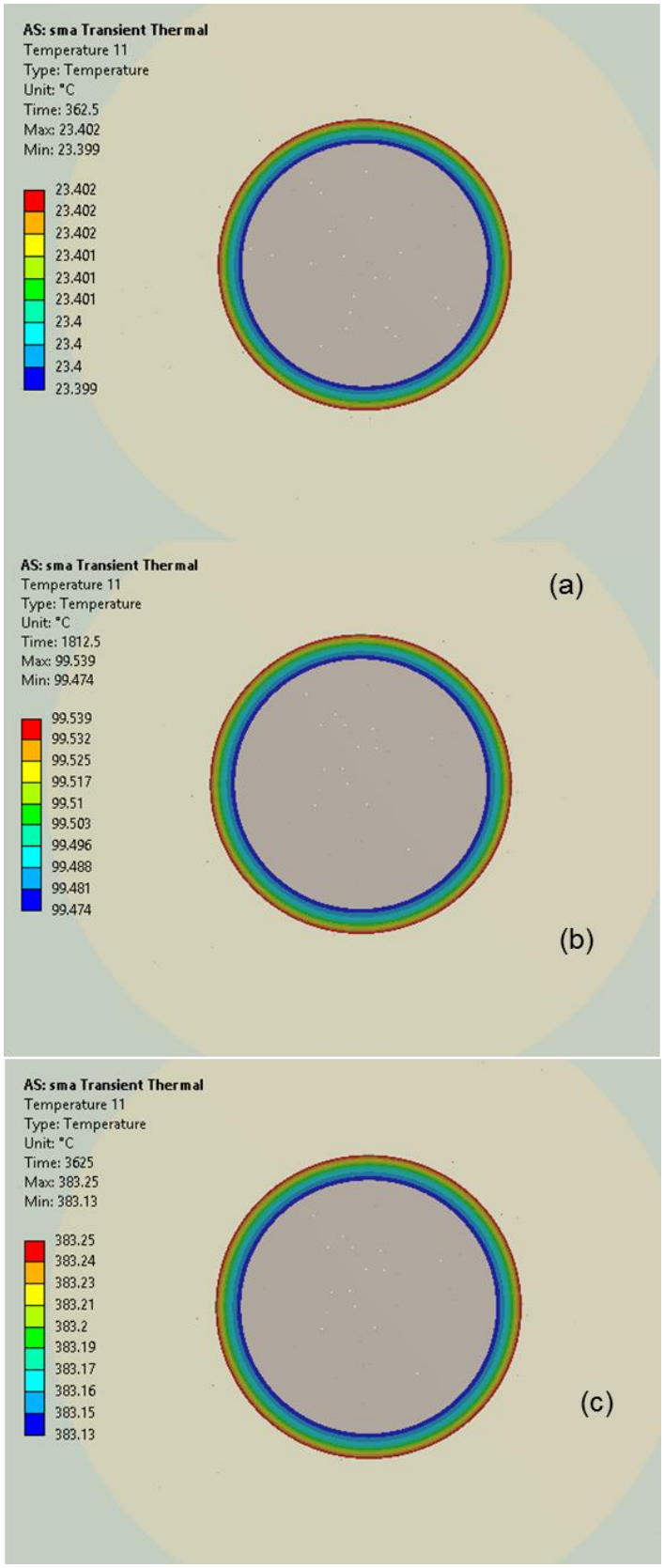

Figure 4.68: 2D Radial Thermal profile of the Concrete-SMA Rebar Interface at (a) Start (b) 30min and (c) 60min fire exposure

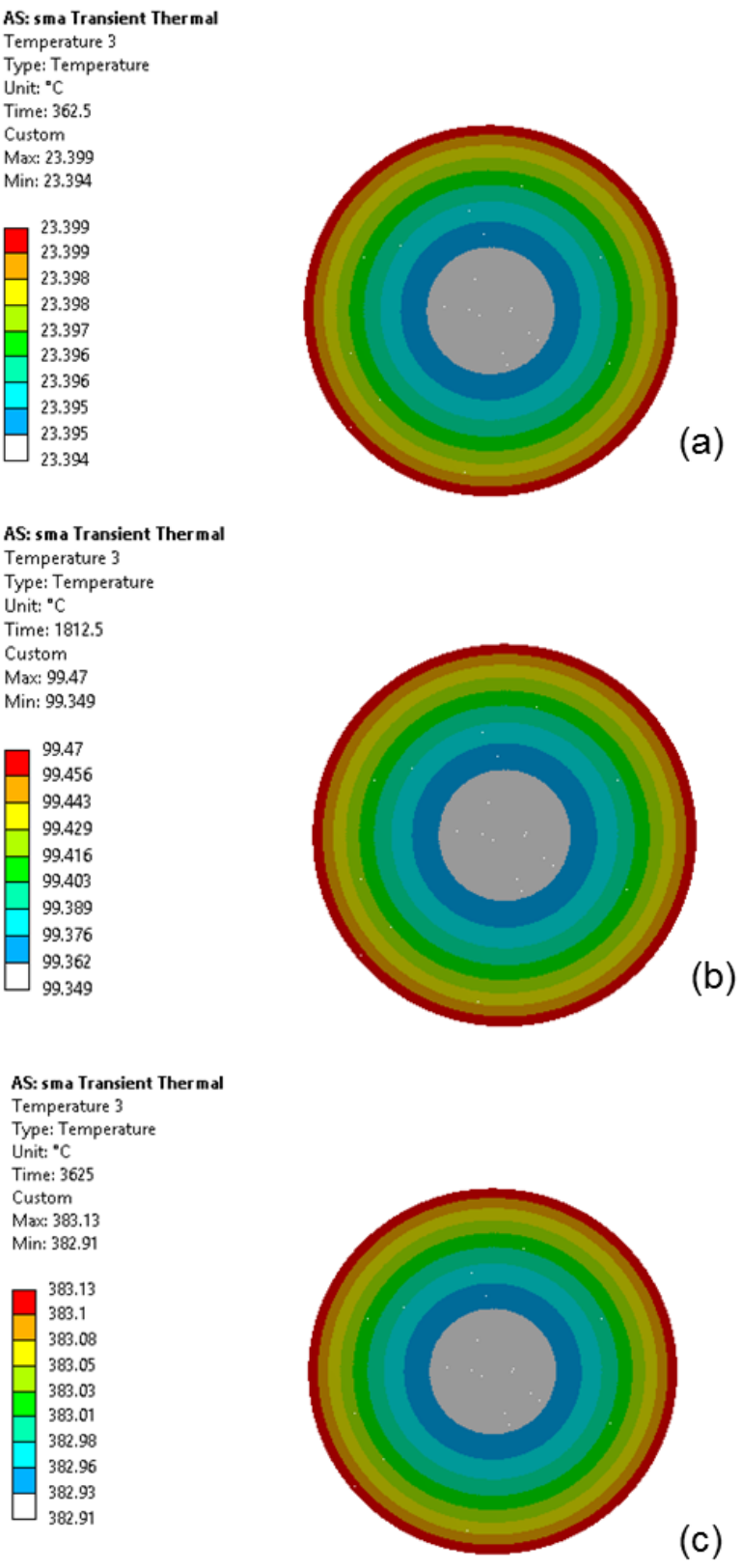

Figure 4.69: 2D Radial Thermal profile of the SMA Rebar at (a) Start (b) 30min and (c) 60min fire Exposure

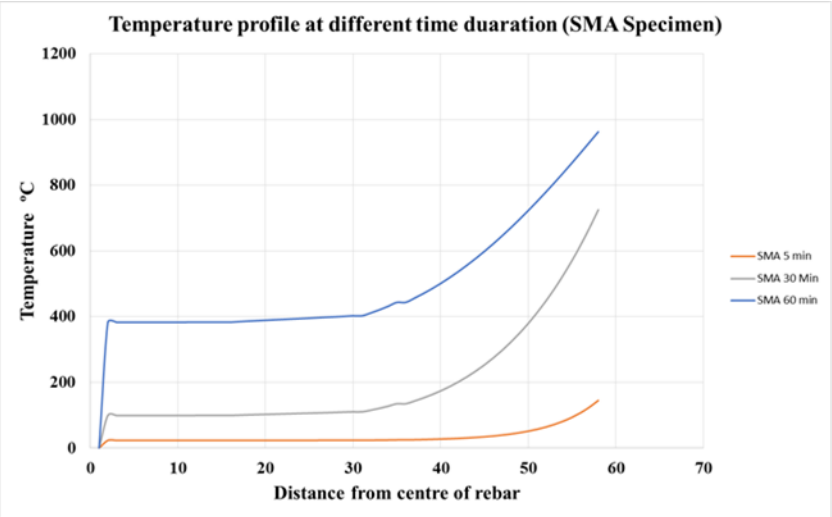

(a)

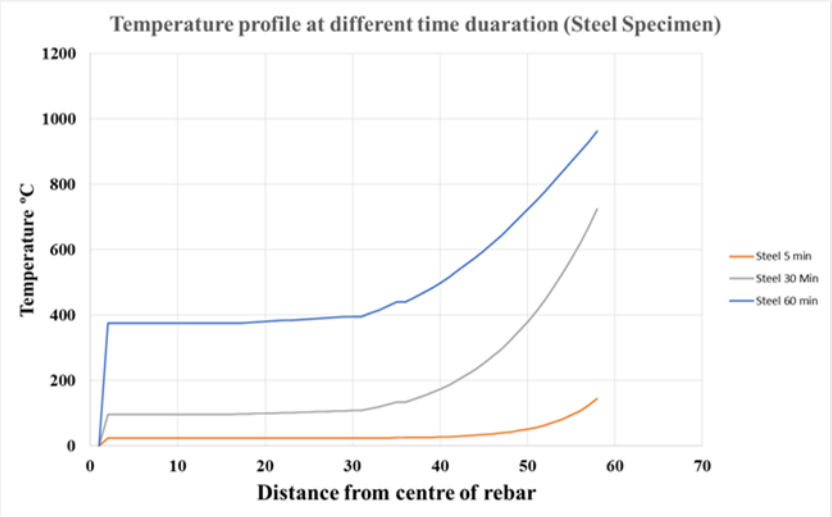

(b)

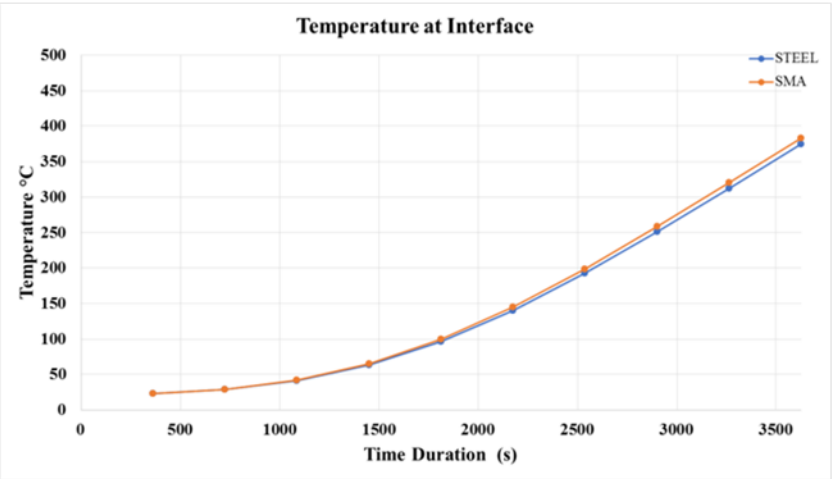

(c)

Figure 4.70: Similarities in thermal profiles between Steel and SMA rebar concrete specimens

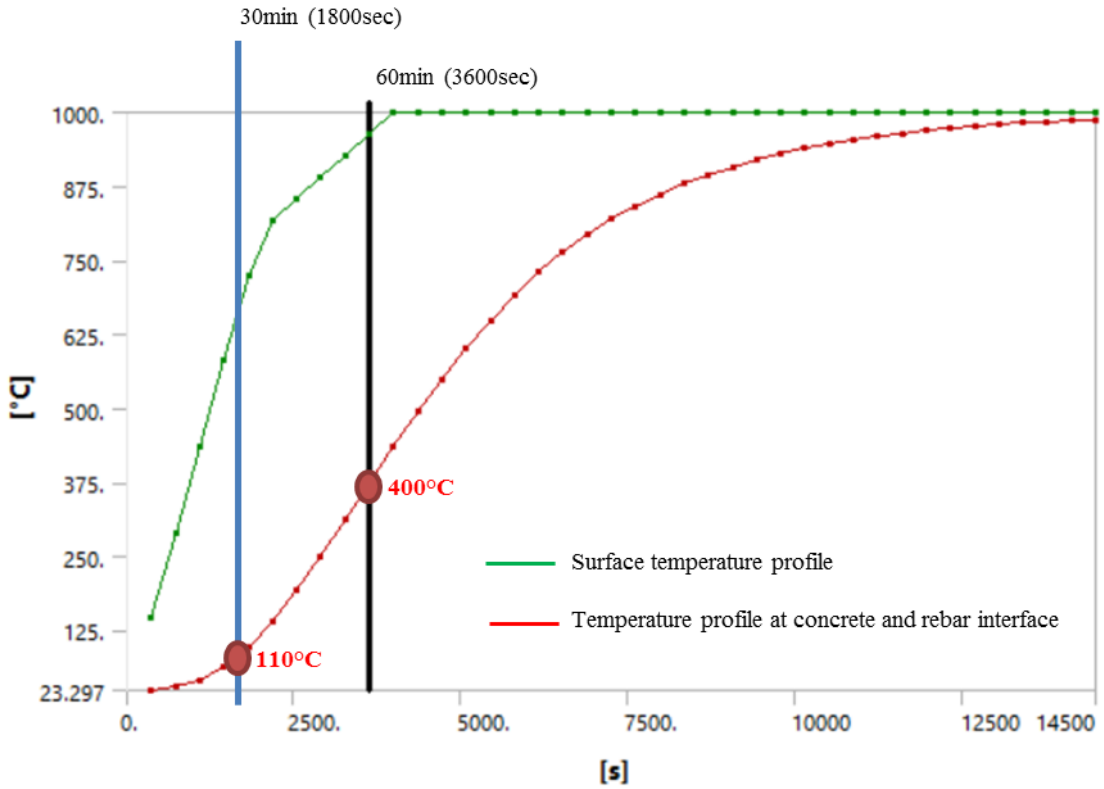

Figure 4.71: Temperature profiles of the specimens (both steel and SMA) as a close approximation

The similarities in the trend in both the concrete-steel rebar and in the case of concrete-SMA rebar are very close as can be noted in Figure 4.70. The similarity between the above two mentioned cases more evident at the interface can be seen in Figure 4.70 (c). While in the case of Concrete-SMA the temperature profile consistently showed marginally higher figures as compared to Concrete-steel rebar specimens. However, in both cases that were tested for the thermal response the bar temperatures were close to 400˚C. In fact, the steel and SMA rebars had reached a temperature of 374˚C and 383˚C respectively.

At the above-mentioned temperature of 400˚C, Steel rebar starts losing strength as explained in the previous section. On the contrary the SMA which is a smart material that is trained to regain its shape at about 400˚C gains strength. The use of the two rebars is a situation that may be ideal and one that is bound to increase the fire resistance rating of the structure. The following charts show the inverse relationship in their respective strengths between SMA and Steel rebar at about 400˚C.

A single chart that approximates and summaries the thermal profile and that reflects very closely the thermal response of both SMA and steel rebars in concrete as shown in Figure 4.70 for quick reference. For the purpose of conducting the structural analysis though, the most accurate data as generated for both SMA and Steel rebar-based studies discussed thus far shall be used.

4.6.2 Results- Nonlinear structural analysis

While in the previous section the thermal response of various specimens considered in this work was discussed in detail, the intent of such an exercise was to generate the required thermal profile for use in the structural analysis of the specimens. The application of thermal profile onto the specimen is dealt with in a novel way in this thesis, where the interface is made to respond to both thermal and structural loading effect. Such a method of examination of the interface is new to the literature and is a significant contribution of this work to the existing knowledge in the literature. The methodology for such a study was elaborately discussed earlier in this chapter. In this section the results of the structural analysis on the specimens considered in this work are presented with a view to examine and establish the interface bond stress. In achieving such a goal and by validating the results against the physical experiments the first objective of AIM 2 of this research is achieved. To this extent, first the structural analysis results on steel-concrete specimens are presented next, followed by the results on SMA-concrete specimens. Like the previous section, the figures discussed in this section are presented towards the end of the respective sections to maintain the flow arguments.

4.6.2.1 Bond stress between Steel-concrete

In order to examine the bond stress behaviour using the novel numerical method developed in this work, first it is important to establish the area of focus. In this case, it is the wedge (Figure 4.72b) rather than the entire specimen model (Figure 4.72a) that is of concern for reasons mentioned earlier. This domain is identified in the figure below for quick reference in Figure 4.72(b).

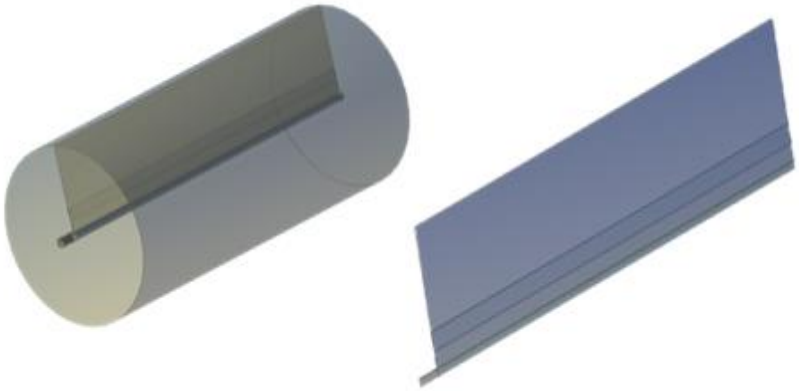

Figure 4.72: a) Symmetric Model b) Wedge

In the pull-out study conducted in the numerical work, it is the pulling force on the rebar that creates the required pull effect and as a consequence, there is displacement that happens on the bar. The quantum of displacement though is based on the surface roughness, material, bonding with concrete to name a few. The above-mentioned parameters were taken into account as part of the numerical model setup.

Since the displacement is a response to the pull force, the maximum amount of force required to pull the rebar out of the concrete is shown in Figure 4.73. In the figure, the force shown is per wedge. In order to obtain the full force value, the force value needs to be multiplied by a value of 360 (for a full 360-degree model with 360 wedges of one-degree angle each). From the figure it can be noted that the force drops quite significantly as the temperature of the concrete builds over the 60min period of testing (while all other parameters being the same). Till about 30 min the influence of temperature did not seem to have an effect on the steel rebar-concrete bond. This can be attributed to the poor thermal conductivity of the concrete as discussed in the previous section (Section 5.3.1.1). The maximum and minimum force being 79.6N and 49.8N for no fire and 60min of fire exposure conditions respectively (For 1° wedge symmetric model). The low force required to pull the rebar out at higher temperatures could indicate the softening of the concrete. More importantly, the above variations indicate the influence of thermal loading on the interface and as an extension on the rebar. The fact that the interface is responding to both the thermal and structural load renders the novel method adopted in this work to study the interface functional. How

effective this method has been can be arrived at by analysing other data that is available from the structural analysis.

For every action there is an equal and opposite reaction. For the force that is applied on the bar, there has to be a displacement (or a movement) of the bar that should be observed as the bar is pulled out of the concrete specimen. The displacement results for steel-concrete specimens are presented in Figure 4.74. While there seems to be no displacement of the concrete in each of the case that was examined, there had been a displacement of the rebar from the model albeit with varying degree of displacement value (minimum and maximum being 0.83 and 0.99mm respectively). In other words, the displacement shown represents the displacement of the interface. Therefore, the effect of such displacement on the bonding between the rebar and concrete needs to be examined.

In Figure 4.75 the interface on the concrete side is shown for the three fire duration conditions. The red areas (value 16 as indicated in the legend) represent the elements of mesh that are un-disturbed during the pull test. However, the blue areas (value 1 as indicated in the legend) are elements that have undergone displacement as a result of the pull test to the greatest degree. Other colours represent displacement of varying degree between the above two mentioned values. Other views and details of the interface showcasing the displaced elements are shown in Figure 4.74 and Figure 4.75.

It is evident in Figure 4.75 and Figure 4.76 that the elements are subjected to displacement on all three test cases. It is also evident that the displacement of elements is more evident as the concrete becomes softer due to longer exposure to the thermal loading. In the 60min exposure case that is considered, it can evidently be noted that the elements across the length of the steel rebar and within the close proximity of the outer surface of the rebar have all indeed undergone displacement (Figure 4.76). Such an effect is bound to result in cracks if this situation was to present itself in real life scenario and in the specimens that are subjected to physical testing (as discussed in Chapter 3). The results from these numerical studies and the physical experiments are compared towards the end of the next section.

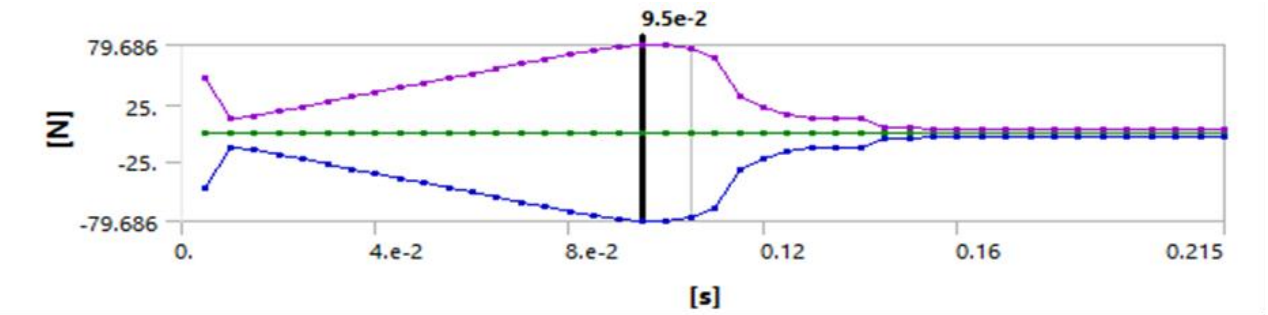

(a)

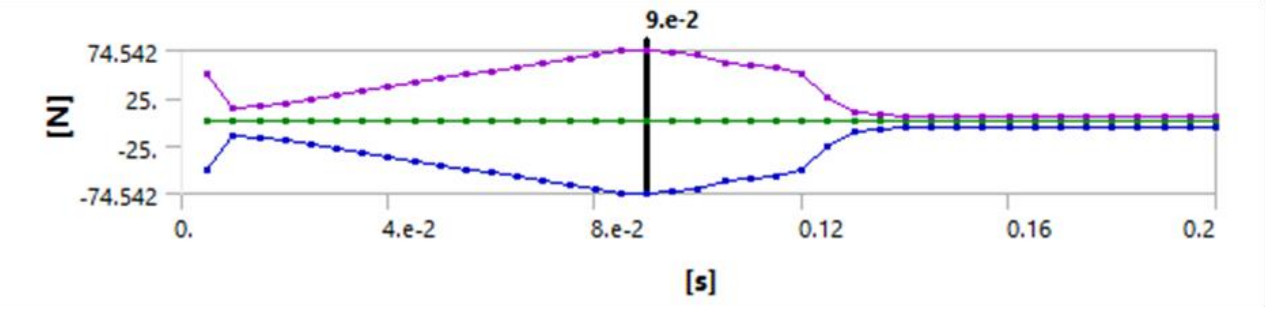

(b)

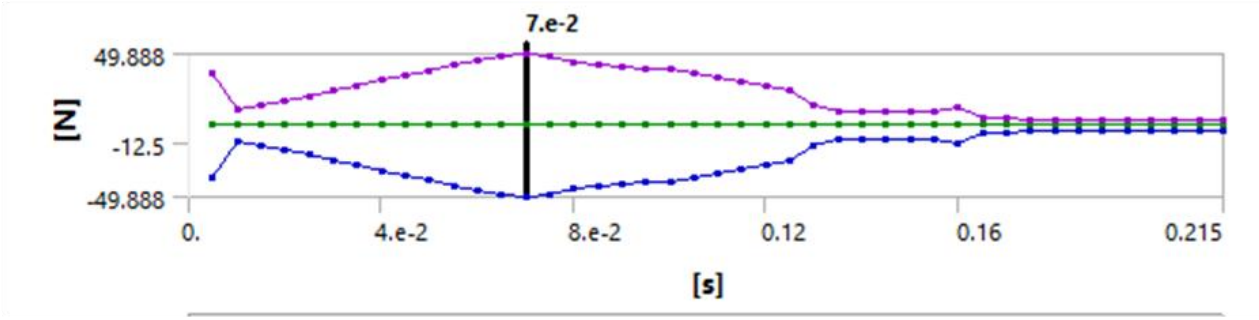

(c)

Figure 4.73: Resultant force for full insert Steel rebar-Concrete Specimen at a) No Fire b) 30min of Fire exposure (c) 60min of Fire exposure

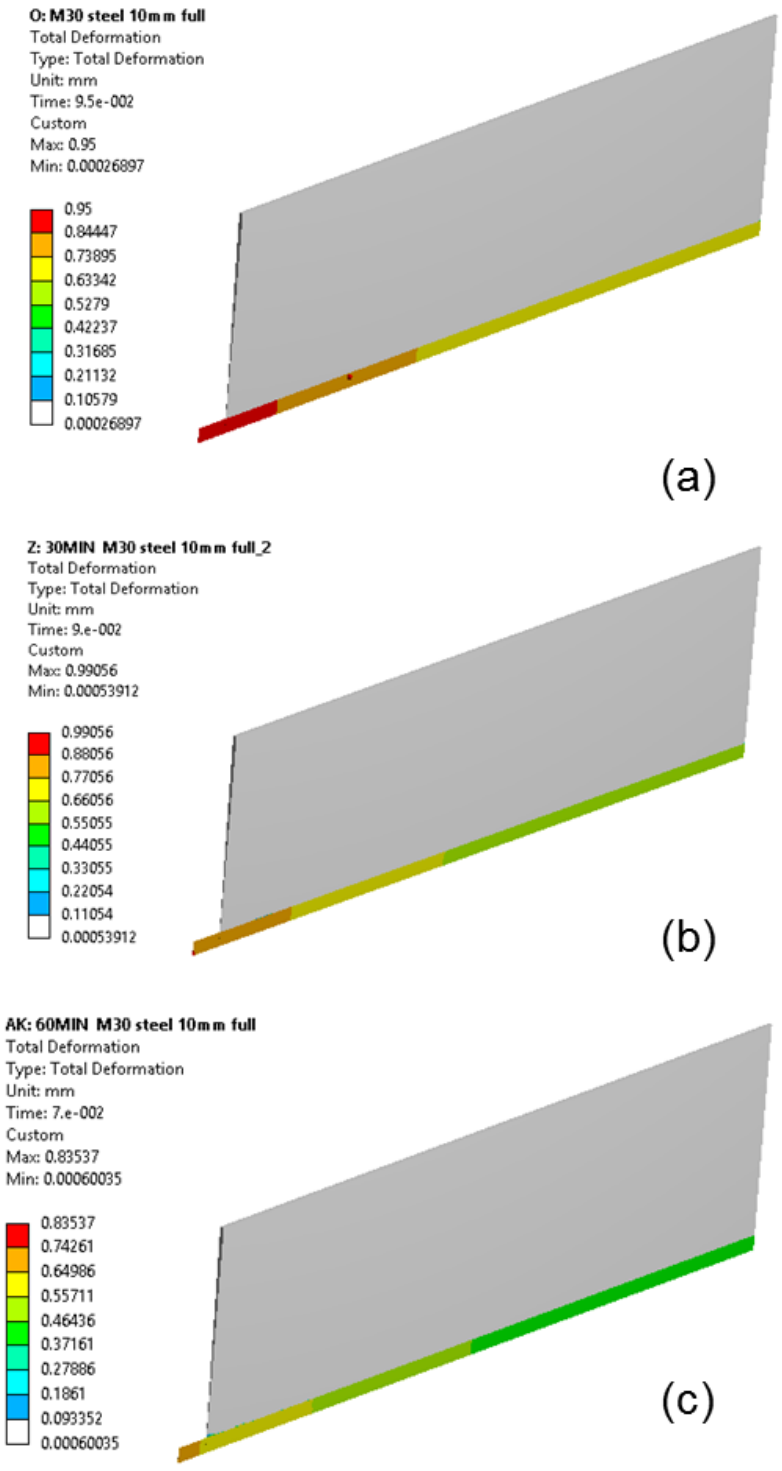

Figure 4.74: Full insert Steel rebar displacement profile for a) No Fire b) 30min of Fire exposure (c) 60min of Fire exposure and for respective loads shown in Figure 4.73

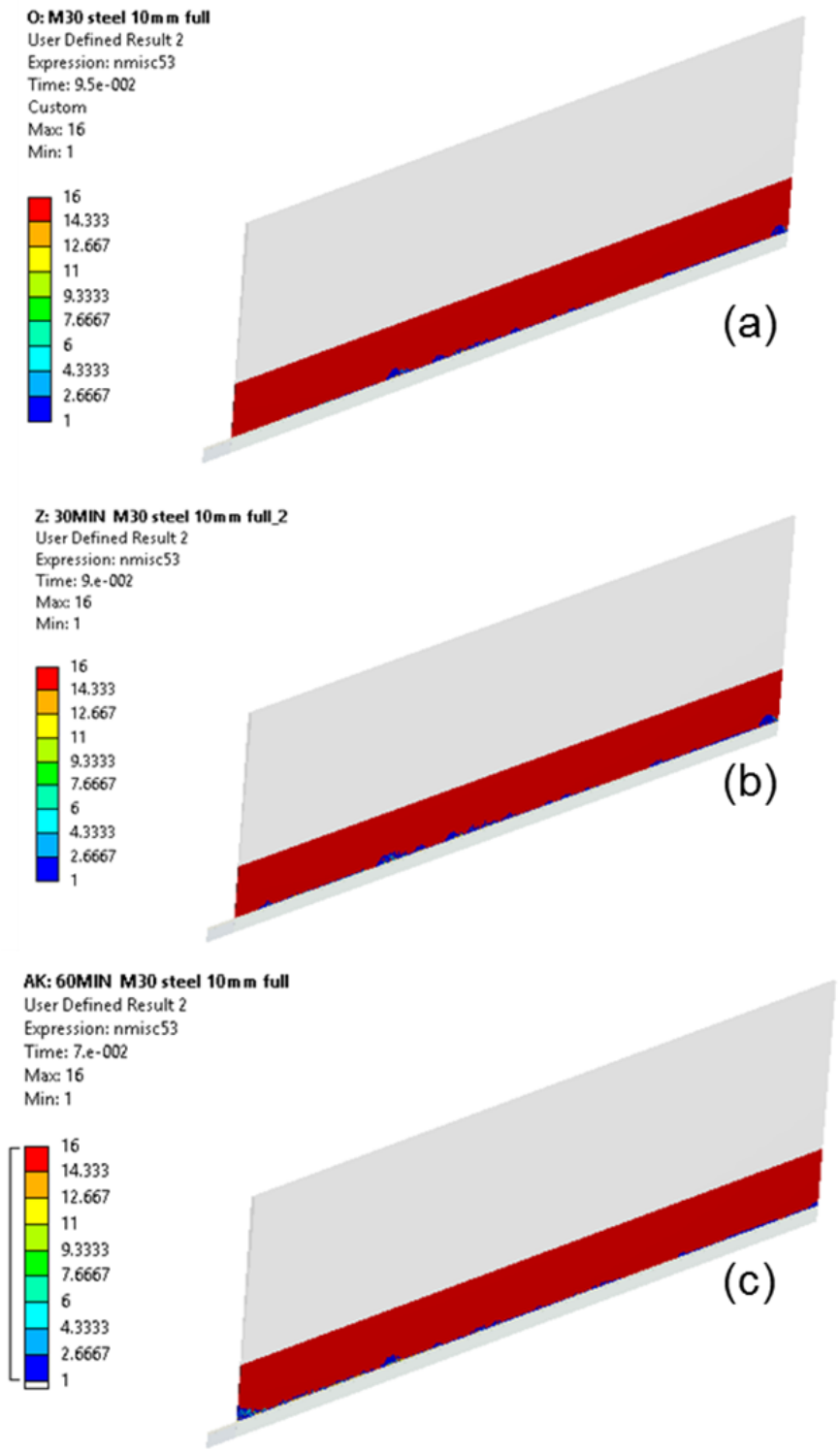

Figure 4.75: Full insert Concrete interface element displacement profile for a) No Fire b) 30min of Fire exposure (c) 60min of Fire exposure and for respective loads shown in Figure 4.73

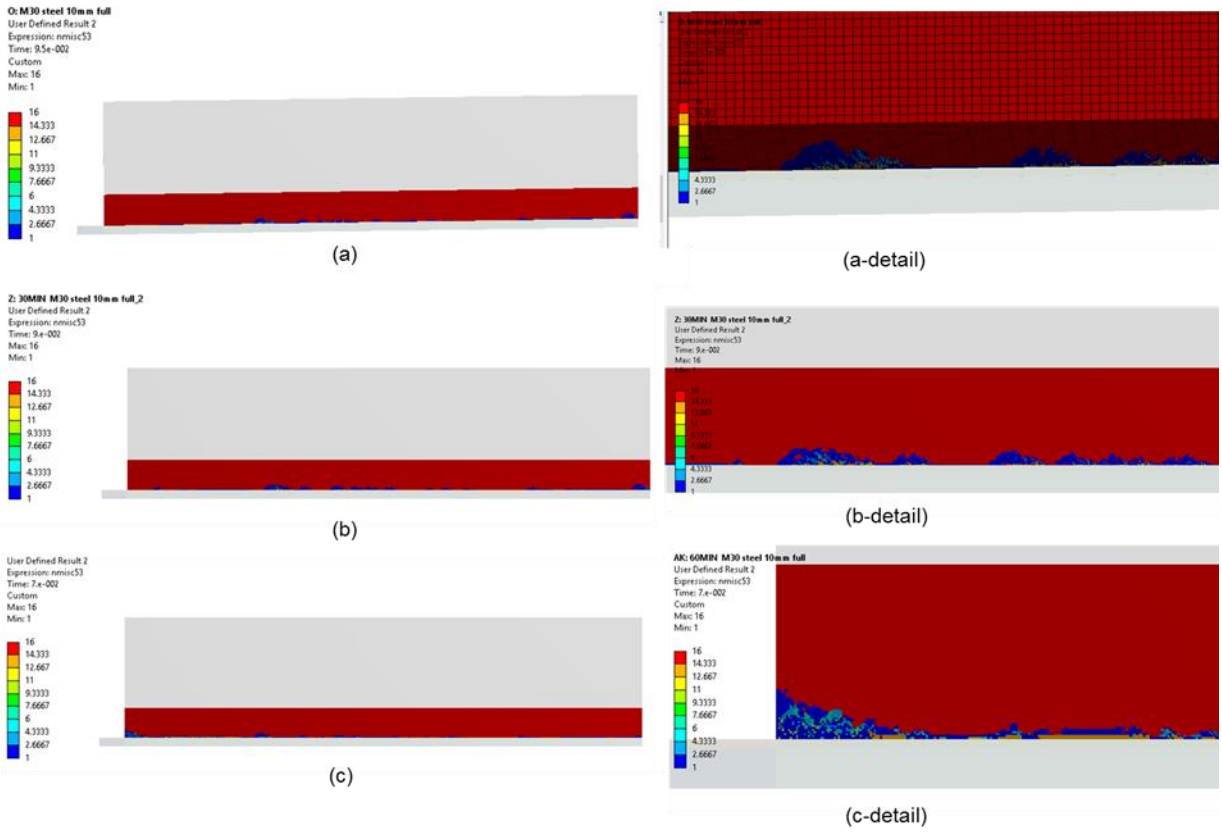

Figure 4.76: Axial section view of Full insert steel rebar Concrete interface element displacement profile for a) No Fire b) 30min of Fire exposure (c) 60min of Fire exposure and for respective loads shown in Figure 4.73

Table 4.11: Bond Stress at interface from numerical Analysis for full steel rebar insert

Interface Bond Stress - Steel rebar full insert into concrete							
	From Numerical experiments FORCE VS DISPLACEMENT CHART				**BOND STRESS** calculated using corresponsing force observed in the force vs displacement chart		
Maximum Displacement [mm]	**NF Steel**	**30min f steel**	**60min f steel**		**NF Steel**	**30min f steel**	**60min f steel**
	Force Reaction 5 (Total) [N]						
5.00E-02	5	5	5		0.191	0.191	0.191
0.1	12.751	13.628	10.913		0.487	0.520	0.417
0.15	15.532	16.091	13.441		0.593	0.615	0.513
0.2	19.641	20.011	16.986		0.750	0.764	0.649
0.25	23.888	24.126	20.654		0.912	0.921	0.789
0.3	28.153	28.275	24.343		1.075	1.080	0.930
0.35	32.421	32.432	28.017		1.238	1.239	1.070
0.4	36.689	36.59	31.532		1.401	1.397	1.204
0.45	40.957	40.748	35.104		1.564	1.556	1.341
0.5	45.226	44.906	38.572		1.727	1.715	1.473
0.55	49.494	49.064	42.162		1.890	1.874	1.610
0.6	53.762	53.222	45.498		2.053	2.033	1.738
0.65	58.03	57.38	48.634		2.216	2.191	1.857
0.7	62.298	61.538	49.888		2.379	2.350	1.905
0.75	66.567	65.693	48.553		2.542	2.509	1.854
0.8	70.833	69.802	43.823		2.705	2.666	1.674
0.85	74.914	73.853	42.845		2.861	2.821	1.636
0.9	78.389	74.542	41.241		2.994	2.847	1.575
0.95	79.686	73.353	39.834		3.043	2.802	1.521
1	78.951	69.874	38.912		3.015	2.669	1.486
1.05	75.674	61.847	36.43		2.890	2.362	1.391
1.1	67.375	59.553	33.736		2.573	2.274	1.288
1.15	32.986	55.634	30.583		1.260	2.125	1.168
1.1768	23.806	49.889	27.449		0.909	1.905	1.048
1.1968	16.137	25.251	24.901		0.616	0.964	0.951
1.2201	13.37	10.502	14.495		0.511	0.401	0.554
1.2495	12.877	6.8784	10.197		0.492	0.263	0.389
1.4	12.573	5.9386	9.4508		0.480	0.227	0.361
1.45	5.377	5.6786	9.3203		0.205	0.217	0.356
1.5	4.2916	5.6013	9.5823		0.164	0.214	0.366
1.55	4.0843	5.5676	10.082		0.156	0.213	0.385
1.6	4.0524	5.5622	12.901		0.155	0.212	0.493
1.65	4.046	5.5606	5.8875		0.155	0.212	0.225
1.7	4.0446	5.56	4.496		0.154	0.212	0.172
1.75	4.0442	5.5585	4.1601		0.154	0.212	0.159
1.8	4.0441	5.5594	4.073		0.154	0.212	0.156
1.85	4.0439	5.5597	4.0543		0.154	0.212	0.155
1.9	4.0439	5.5599	4.0495		0.154	0.212	0.155
1.95	4.044	5.5601	4.0482		0.154	0.212	0.155
2	4.0441	5.5602	4.0478		0.154	0.212	0.155
2.05	4.0442		4.0476		0.154	0.000	0.155
2.1	4.0443		4.0475		0.154	0.000	0.155
2.15	4.0445		4.0475		0.154	0.000	0.155

Table 4.11 shows the force-displacement chart for the full-length steel embedded rebar for no-fire, 30mins and 60 mins fire condition pull-out numerical simulation. The highlighted values in the cell can be traced back to Figure 4.73. The bond stress was calculated as per the explanation provided in Chapter 2 (Section 2.2.2). For

convenience, the equation is given below as per the equations provided by Apparao et al. 2002.

$$\tau = \frac{P}{\pi\, d_b\, l_b}$$ Equation 4.19

where ,

P: load (N),

l_b: embedment length (mm), and

d_b: diameter of the rebar (mm)

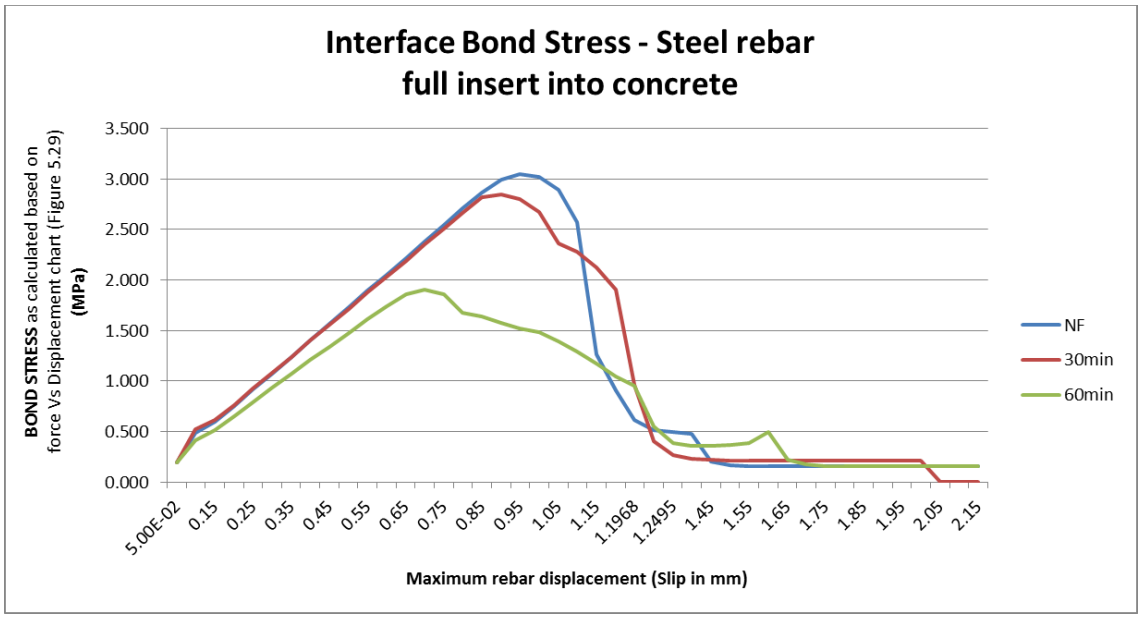

Figure 4.77: Bond Stress at interface from numerical Analysis for full steel rebar insert under No Fire, 30min and 60min of Fire exposure for respective loads shown in Figure 4.73

The AIM 2 of this research is to study the bond stress at the interface of the concrete and rebar through numerical methods, where-in the thermal loading is considered as part of the non-linear structural studies on the specimen that is subjected to fire exposure. The stress figures achieved via the numerical Method developed in this work was compared to the corresponding data set from the experiments carried out on physical experiments (in Chapter 3).

4.6.3 Validation of Numerical Method developed in this work- A comparison with Physical Experiments

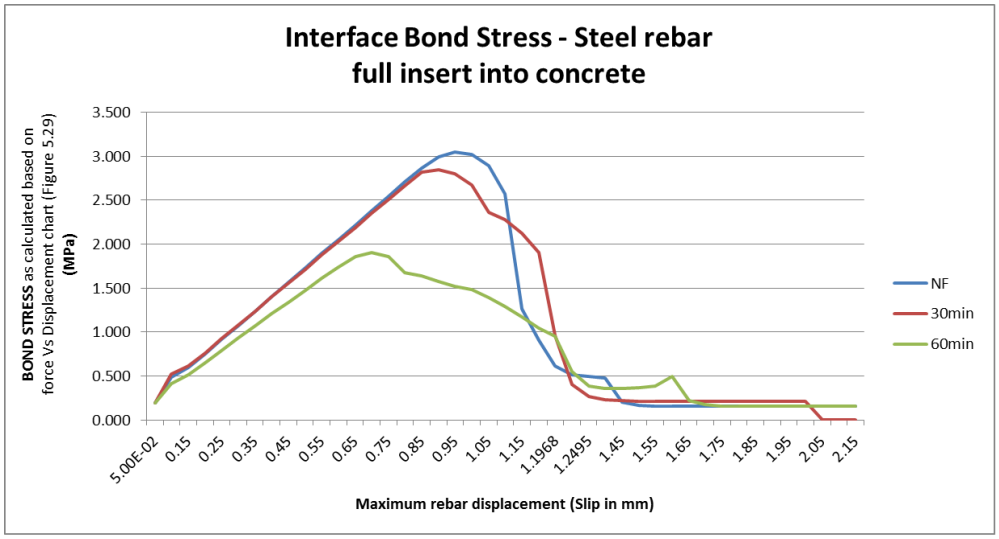

(a)

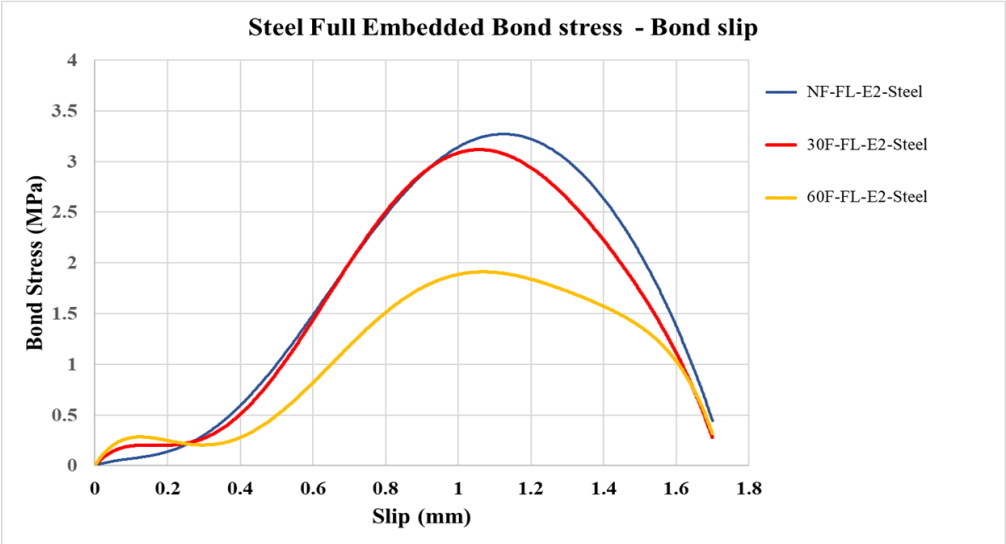

(b)

Figure 4.78: Comparison of Bond Stress values from (a) numerical experiments results and (b) Physical experiment results

The bond stress values achieved via the numerical experiments were found to be in close agreement with the corresponding values from the physical experiments. For example, the bond stress value between a steel rebar inserted fully into the concrete for no fire condition was found to be 3.5 MPa and 3.1 MPa for physical experiment and numerical studies respectively. Likewise, it can also be noted that the peak stress

occurred at about 1.05mm slipped (displacement of the rebar). The results can be found to be in such close agreement for the two fire conditions tested (30min and 60min) too. In the case of 30min fire exposure, the maximum Bond Stress value noted was just under 3 MPa in both physical experiments and numerical experiments. Likewise, the maximum stress peaked at about 1mm slip value (displacement of rebar) in both physical and numerical experiments. Such a close match in values between physical and numerical experiments undoubtedly validated the numerical model/method developed in this work.

The achievement of the data presented in Figure 4.77 and the subsequent comparison done (refer Figure 4.78) that establishes the tight agreement of the bond stress values obtained from physical and numerical experiments establishes the successful achievement of AIM 2. Having successfully validated the novel numerical method and model developed in this work, the novel model was put to use to examine the bond stress behaviour of the remaining eleven specimens considered in this work. The corresponding Figures, Tables and Charts that were developed from the results obtained from the numerical simulations are presented next (Figure 4.79 -Figure 4.82). These results follow the sequence of tables and figures presented in this section thus far and segregated based on the specimen name. For convenience the list of specimens can be found in Table 4.12. is provided below.

Table 4.12: List of specimens examined using numerical method developed in this work

Sno	Specimen	Force Displacement		Displacement contour plot		Contour plot of element cracking/displacing at interface		Contour plot of element cracking/displacing at interface	
1	NF-FL-Steel-M30 –D10	Figure 5.30	a	Figure 5.31	a	Figure 5.32	a	Figure 5.33	a
2	30F-FL-Steel-M30–D10		b		b		b		b
3	60F-FL-Steel-M30-D10		c		c		c		c
4	NF-HL-Steel-M30 –D10	Figure 5.36	a	Figure 5.37	a	Figure 5.38	a	Figure 5.39	a
5	30F-HL-Steel-M30–D10		b		b		b		b
6	60F-HL-Steel-M30-D10		c		c		c		C
7	NF-FL-SMA-M30 –D10	Figure 5.42	a	Figure 5.43	a	Figure 5.44	a	Figure 5.45	a
8	30F-FL-SMA-M30–D10		b		b		b		b
9	60F-FL-SMA-M30-D10		c		c		c		C
10	NF-HL-SMA-M30 –D10	Figure 5.48	a	Figure 5.49	a	Figure 5.50	a	Figure 5.51	a
11	30F-HL-SMA-M30–D10		b		b		b		b
12	60F-HL-SMA-M30-D10		c		c		c		C

Table 4.12 tabulates the list of figures for each specimen showing the result for the force-displacement chart, displacement contour plot, contour plot for the element cracking/displacing at the interface and the zoom view of the same for no fire, 30 mins and 60 mins fire durations. (a, b, and c for No fire, 30 mins and 60mins fire duration).

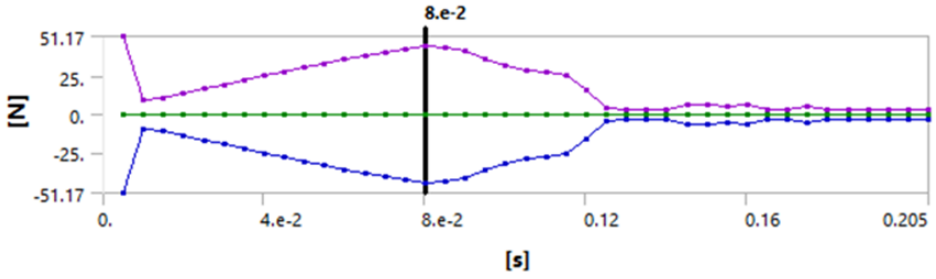

(a)

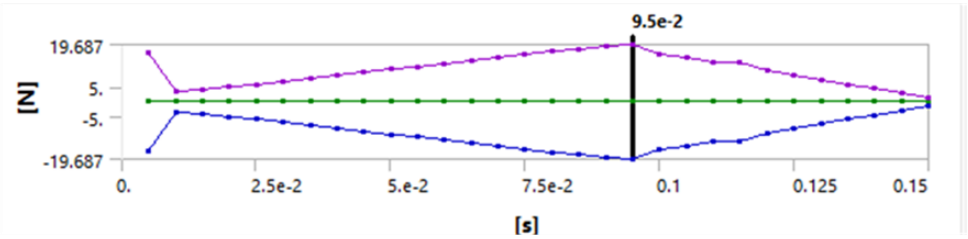

(b)

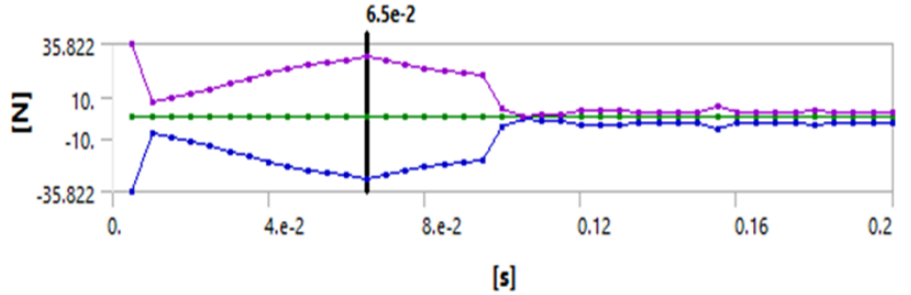

(c)

Figure 4.79: Resultant force for half insert Steel rebar-Concrete Specimen at a) No Fire b) 30min of Fire exposure (c) 60min of Fire exposure

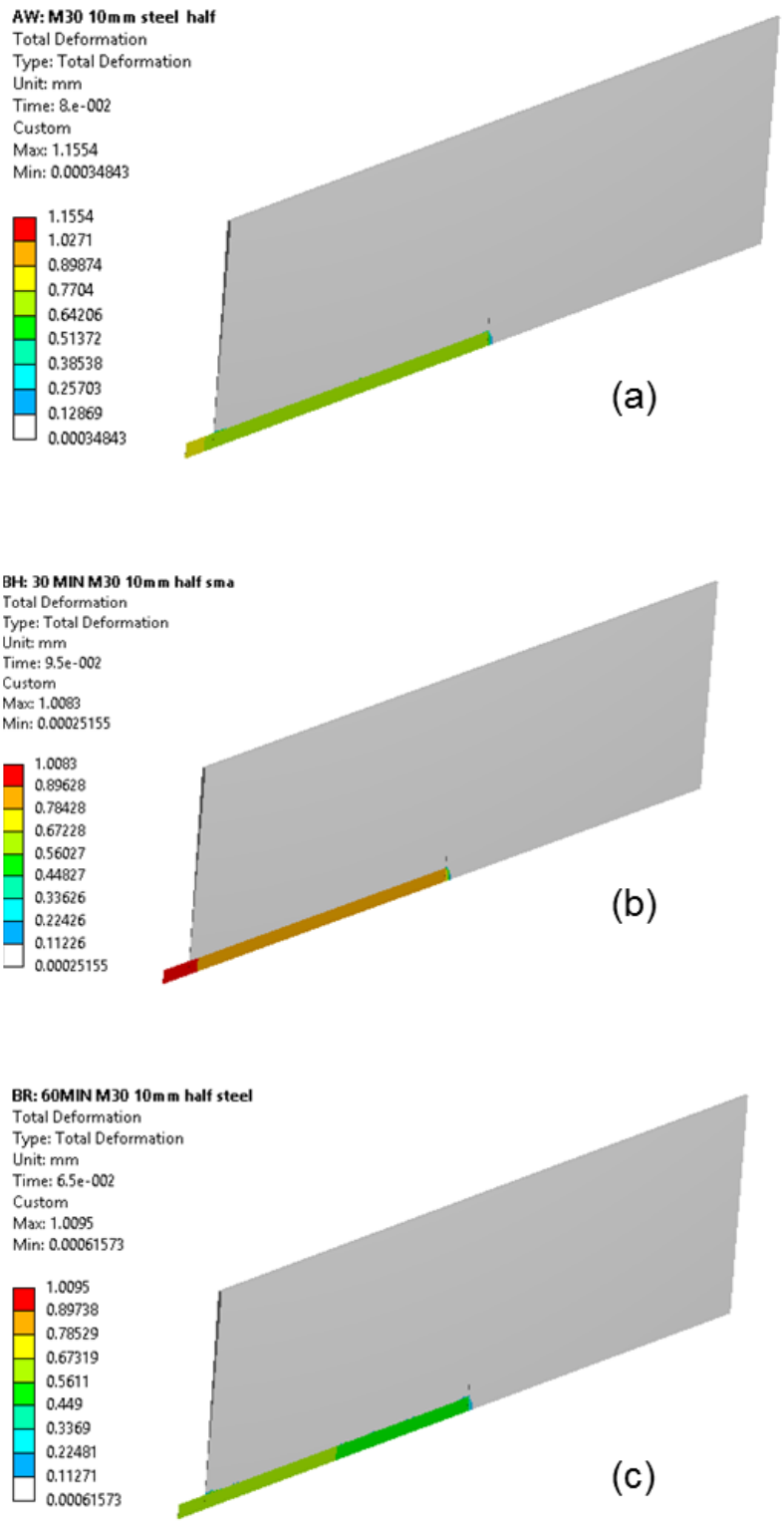

Figure 4.80: Half insert Steel rebar displacement profile for a) No Fire b) 30min of Fire exposure (c) 60min of Fire exposure and for respective loads shown in Figure 4.79.

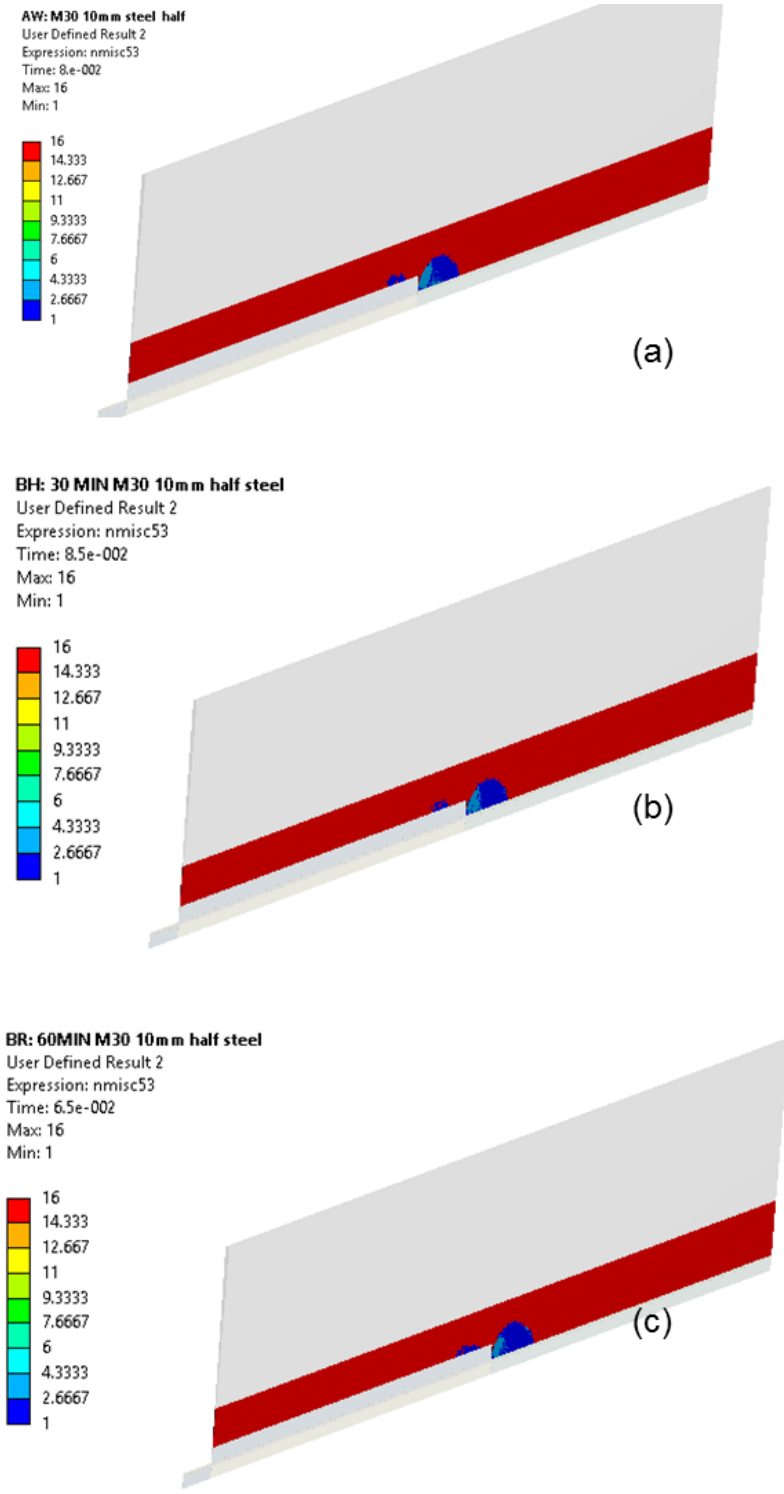

Figure 4.81: Half insert Concrete interface element displacement profile for a) No Fire b) 30min of Fire exposure (c) 60min of Fire exposure and for respective loads shown in Figure 4.79.

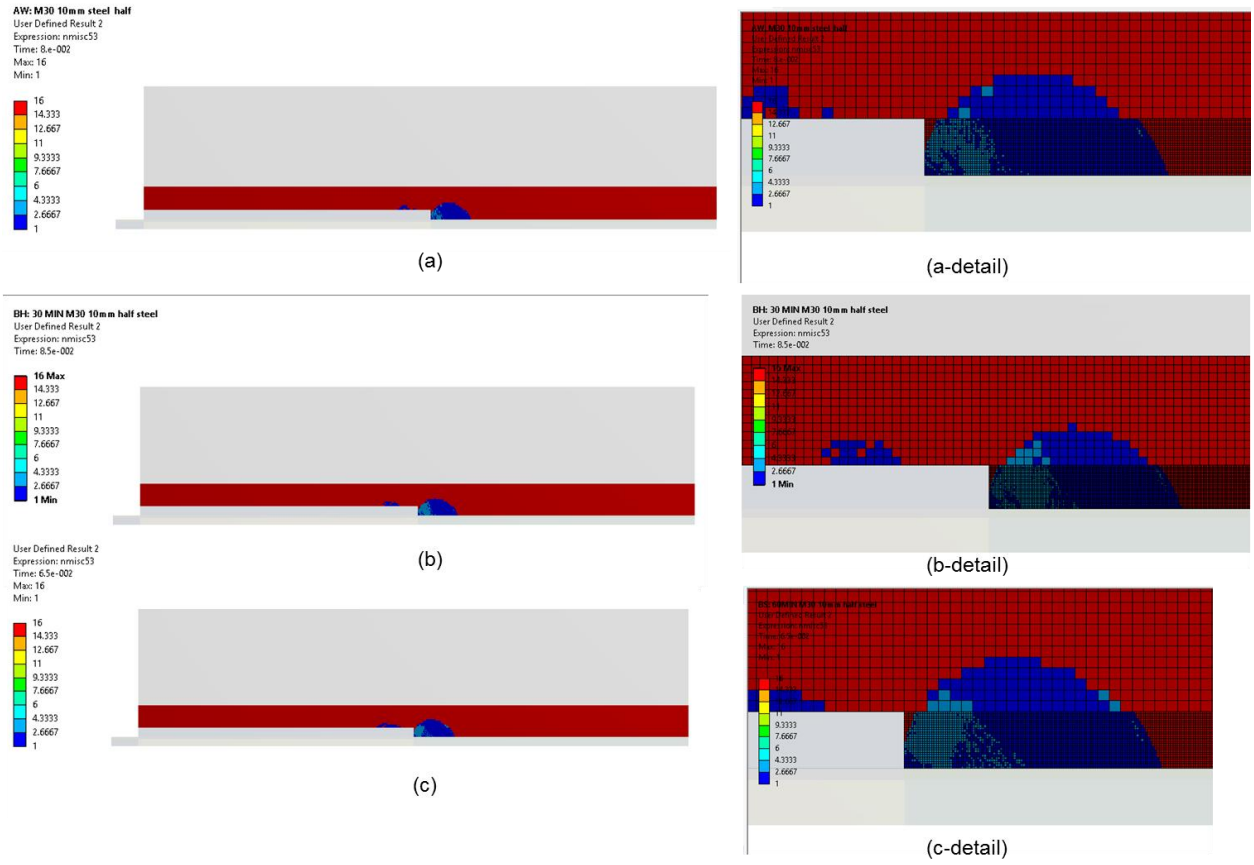

Figure 4.82: Axial section view of half insert steel rebar Concrete interface element displacement profile for a) No Fire b) 30min of Fire exposure (c) 60min of Fire exposure and for respective loads shown in Figure 4.79.

Table 4.13: Bond Stress at interface from numerical Analysis for half insert steel rebar

Interface Bond Stress - Steel rebar half insert into concrete

Force Values From Numerical experiments FORCE VS DISPLACEMENT CHART (Figure 5.35)					**BOND STRESS** calculated using corresponsing force observed in the force vs displacement chart		
Maximum	**NF Steel**	**30min f steel**	**60min f steel**		**NF**	**30min**	**60min**
5.00E-02	1	1	1		0.076	0.076	0.076
0.1	9.8692	9.0499	7.7466		0.754	0.691	0.592
0.15	11.152	10.065	9.2151		0.852	0.769	0.704
0.2	13.915	12.505	11.66		1.063	0.955	0.891
0.25	16.778	15.044	14.122		1.282	1.149	1.079
0.3	19.646	17.59	16.591		1.501	1.344	1.267
0.35	22.518	20.135	19.084		1.720	1.538	1.458
0.4	25.388	22.67	21.494		1.939	1.732	1.642
0.45	28.162	25.057	23.703		2.151	1.914	1.811
0.5	30.875	27.403	26.049		2.358	2.093	1.990
0.55	33.412	29.819	27.107		2.552	2.278	2.071
0.6	36	32.206	27.279		2.750	2.460	2.084
0.65	38.244	34.266	29.895		2.921	2.617	2.284
0.7	40.685	36.13	28.177		3.108	2.760	2.152
0.75	43.157	37.58	25.839		3.297	2.871	1.974
0.8	44.784	38.309	24.05		3.421	2.926	1.837
0.85	43.52	37.101	22.455		3.324	2.834	1.715
0.9	41.774	36.501	21.281		3.191	2.788	1.626
0.95	35.758	33.675	20.253		2.731	2.572	1.547
1	31.554	30.247	4.5999		2.410	2.310	0.351
1.05	29.02	26.877	0.11314		2.217	2.053	0.009
1.1	27.455	23.361	1.8098		2.097	1.784	0.138
1.15	26.064	19.862	1.8475		1.991	1.517	0.141
1.1768	16.23	8.8354	3.3413		1.240	0.675	0.255
1.1968	4.6882	5.5492	3.1128		0.358	0.424	0.238
1.2201	3.0831	5.2181	3.7707		0.236	0.399	0.288
1.2495	3.0448	5.3529	2.1641		0.233	0.409	0.165
1.4	3.4998	5.7613	2.1058		0.267	0.440	0.161
1.45	6.7203	6.3169	2.3702		0.513	0.483	0.181
1.5	5.904	6.9357	2.7736		0.451	0.530	0.212
1.55	5.7614	7.5637	5.1767		0.440	0.578	0.395
1.6	6.903	8.1669	2.2687		0.527	0.624	0.173
1.65	3.2654	8.7259	2.0578		0.249	0.667	0.157
1.7	3.1903	9.2251	2.041		0.244	0.705	0.156
1.75	5.0849	9.6803	2.0318		0.388	0.739	0.155
1.8	3.1237	10.081	3.4919		0.239	0.770	0.267
1.85	2.978	11.659	2.1464		0.227	0.891	0.164
1.9	2.9654	9.7556	2.0484		0.227	0.745	0.156
1.95	2.9645	8.7479	2.0414		0.226	0.668	0.156
2	2.9648	8.2964	2.041		0.226	0.634	0.156
2.05	2.9512	7.928			0.225	0.606	0.000
2.1		6.8215			0.000	0.521	0.000
2.15		6.4271			0.000	0.491	0.000
		6.4606			0.000	0.493	0.000
		6.7543			0.000	0.516	0.000
		7.1933			0.000	0.549	0.000

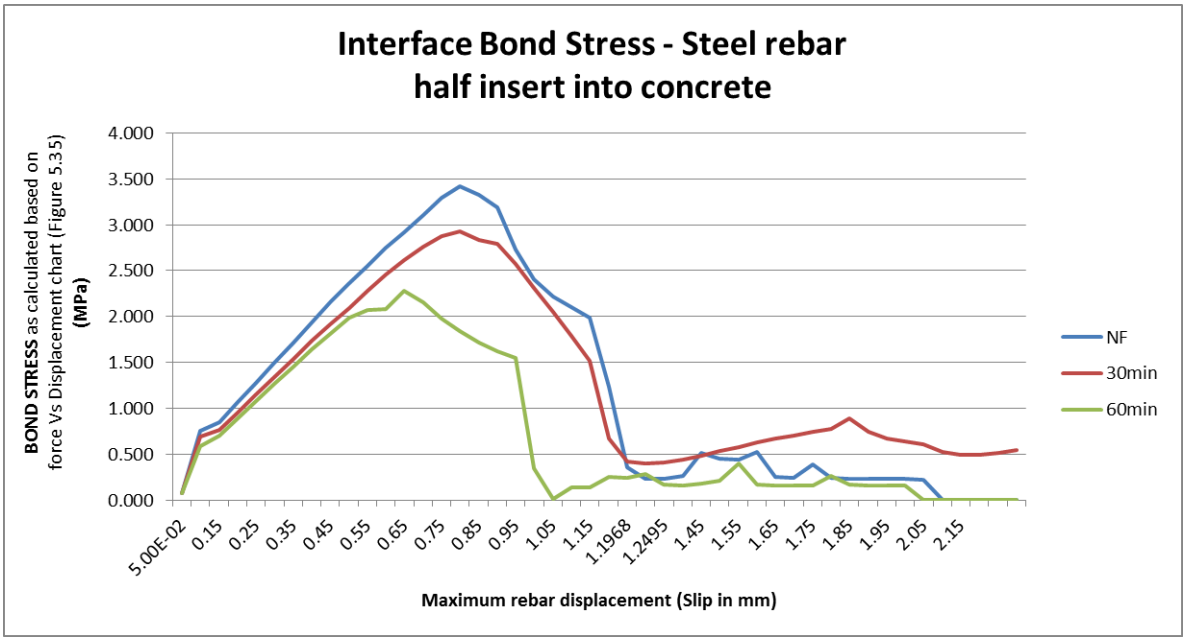

Figure 4.83: Bond Stress at interface from numerical Analysis for full steel rebar insert under No Fire, 30min and 60min of Fire exposure for respective loads shown in Table 4.13

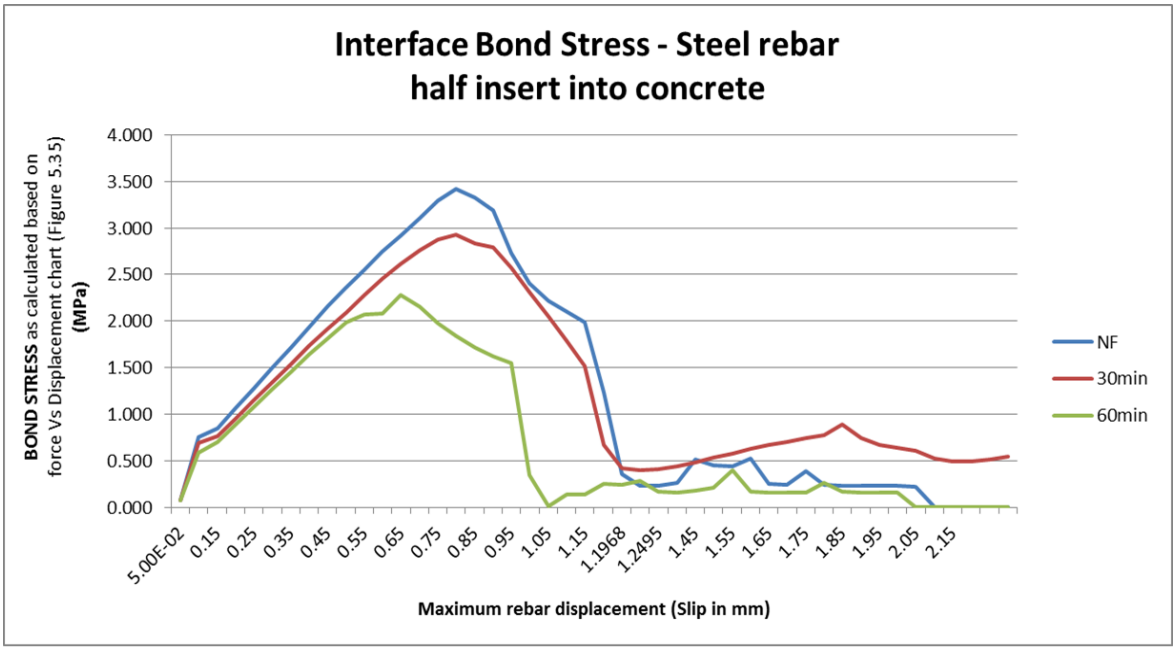

(a)

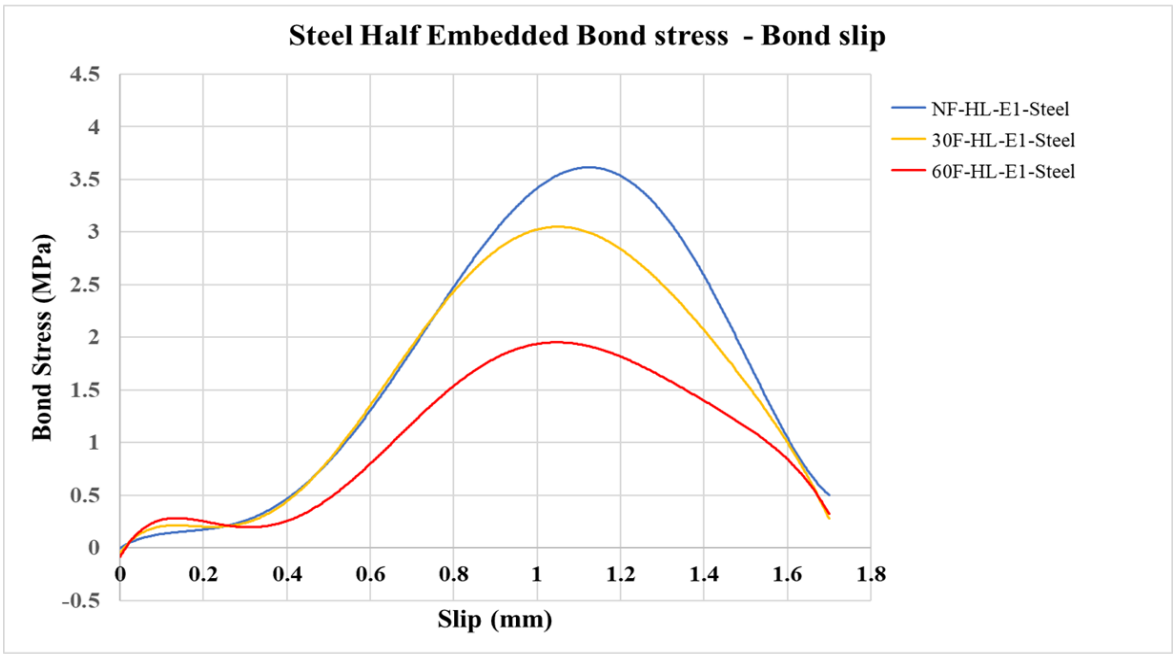

(b)

Figure 4.84: Comparison of Bond Stress values from (a) numerical experiments results and (b) Physical experiment results

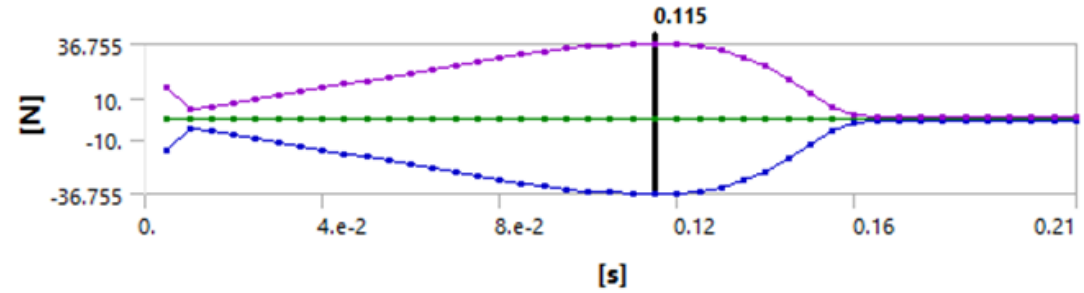

(a)

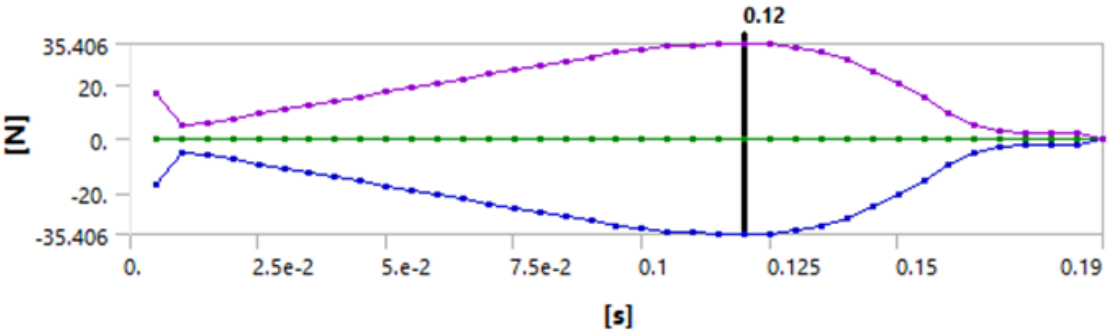

(b)

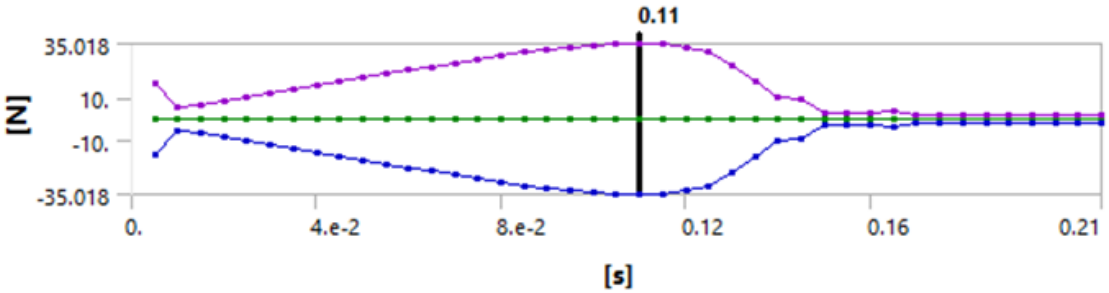

(c)

Figure 4.85: Resultant force for Full insert SMA rebar-Concrete Specimen at a) No Fire b) 30min of Fire exposure (c) 60min of Fire exposure

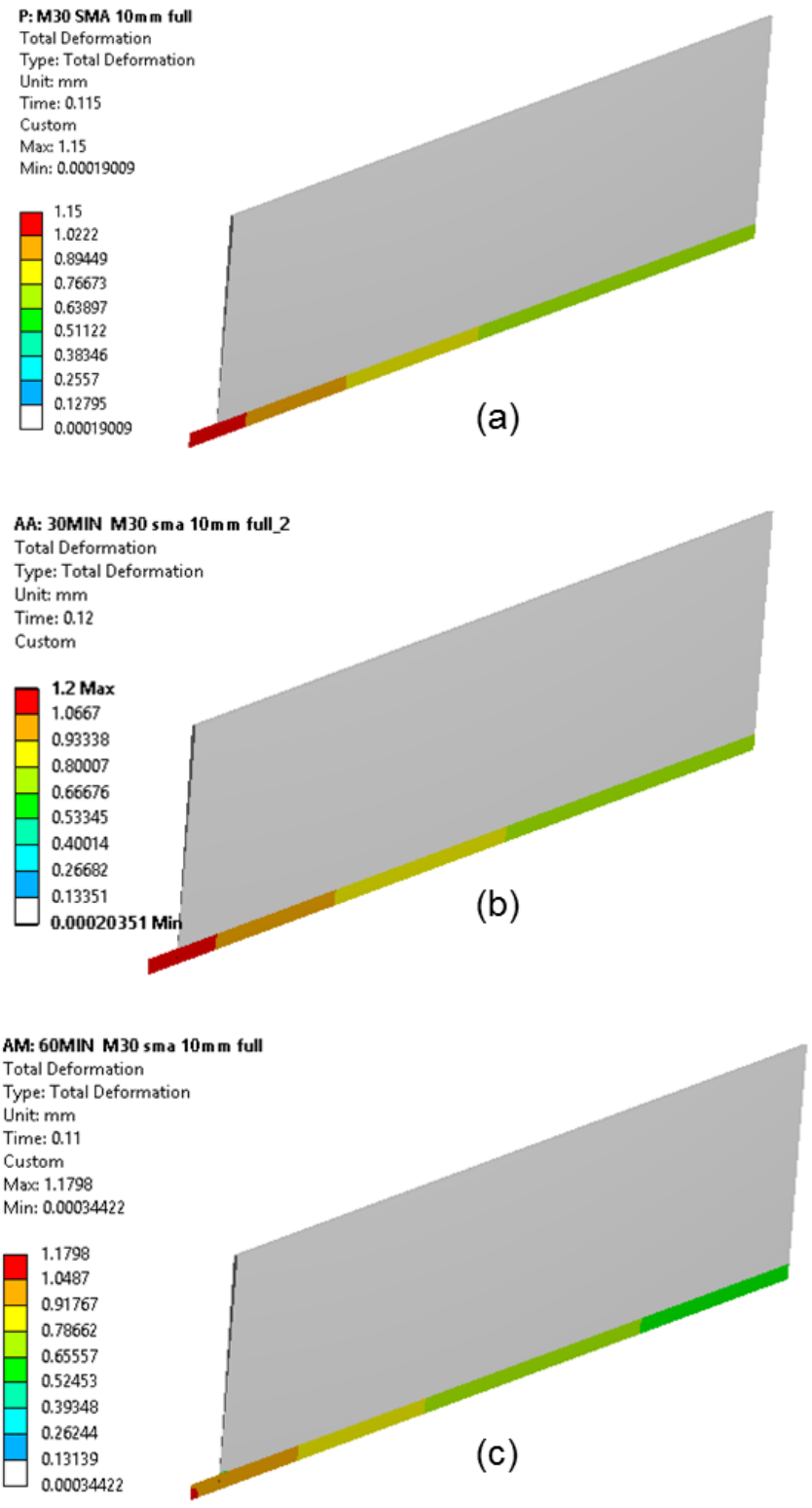

Figure 4.86: Full insert SMA rebar; displacement profile for a) No Fire b) 30min of Fire exposure (c) 60min of Fire exposure and for respective loads shown in Figure 4.85.

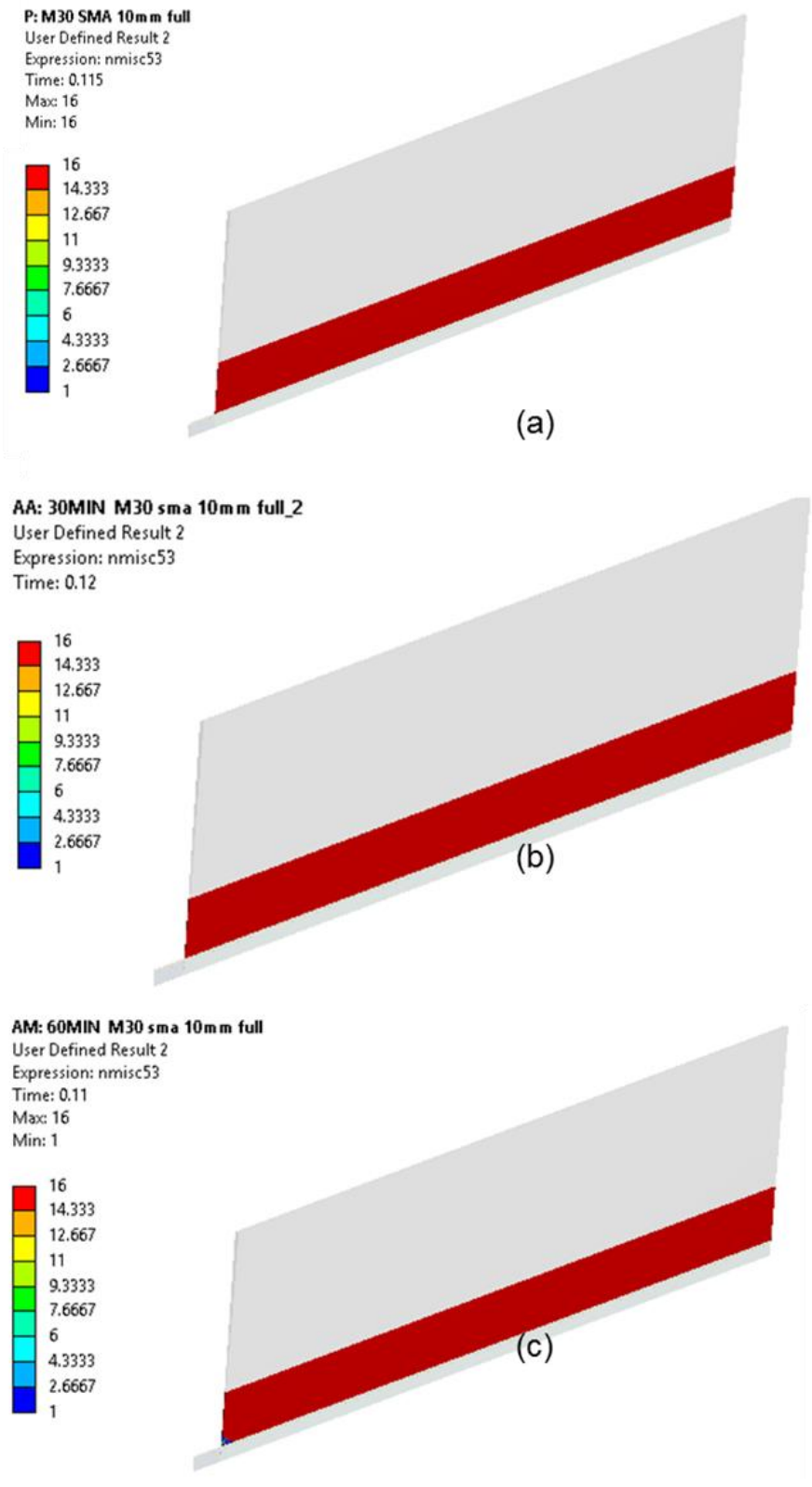

Figure 4.87: Full insert SMA rebar; Concrete interface element displacement profile for a) No Fire b) 30min of Fire exposure (c) 60min of Fire exposure and for respective loads shown in shown in Figure 4.85.

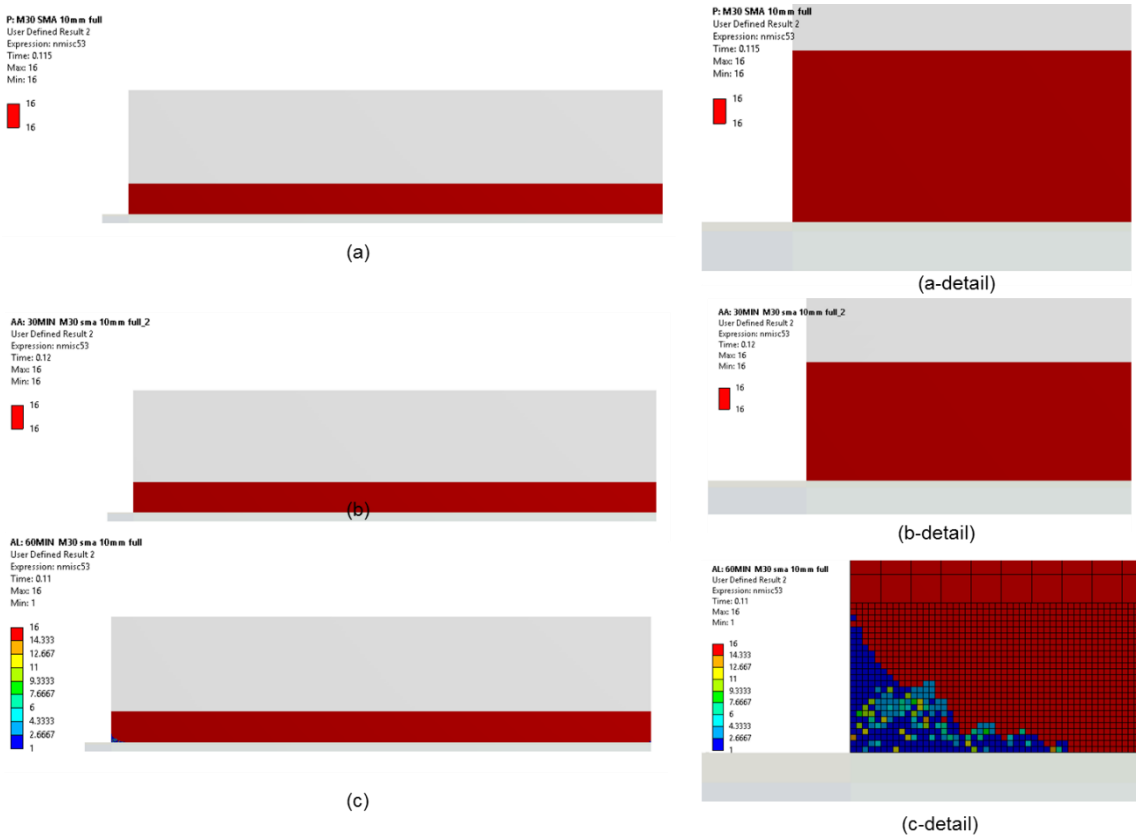

Figure 4.88: Axial section view of Full insert SMA rebar Concrete interface element displacement profile for a) No Fire b) 30min of Fire exposure (c) 60min of Fire exposure and for respective loads shown in Figure 4.85

Table 4.14: Bond Stress at interface from numerical Analysis for full insert SMA rebar

Interface Bond Stress - SMA rebar full insert into concrete

Force Values From Numerical experiments FORCE VS DISPLACEMENT CHART (Figure 5.41)					**BOND STRESS** calculated using corresponsing force observed in the force vs displacement chart		
Maximum	**NF Steel**	**30min f steel**	**60min f steel**		**NF**	**30min**	**60min**
5.00E-02	3	3	3		0.115	0.115	0.115
0.1	4.7297	4.98	5.2091		0.181	0.190	0.199
0.15	6.1478	6.0748	6.4889		0.235	0.232	0.248
0.2	7.9267	7.6468	8.2309		0.303	0.292	0.314
0.25	9.738	9.2789	10.028		0.372	0.354	0.383
0.3	11.553	10.921	11.834		0.441	0.417	0.452
0.35	13.369	12.566	13.642		0.511	0.480	0.521
0.4	15.184	14.211	15.45		0.580	0.543	0.590
0.45	17	15.856	17.259		0.649	0.606	0.659
0.5	18.815	17.5	19.067		0.719	0.668	0.728
0.55	20.631	19.145	20.875		0.788	0.731	0.797
0.6	22.447	20.79	22.679		0.857	0.794	0.866
0.65	24.262	22.435	24.382		0.927	0.857	0.931
0.7	26.078	24.08	26.141		0.996	0.920	0.998
0.75	27.893	25.725	27.774		1.065	0.982	1.061
0.8	29.709	27.37	29.485		1.135	1.045	1.126
0.85	31.524	29.015	31.13		1.204	1.108	1.189
0.9	33.16	30.515	32.493		1.266	1.165	1.241
0.95	34.488	32.145	33.507		1.317	1.228	1.280
1	35.518	33.369	34.337		1.357	1.274	1.311
1.05	36.25	34.312	34.844		1.384	1.310	1.331
1.1	36.673	34.978	35.018		1.401	1.336	1.337
1.15	36.755	35.353	34.769		1.404	1.350	1.328
1.1768	36.433	35.406	33.619		1.391	1.352	1.284
1.1968	35.565	35.069	31.237		1.358	1.339	1.193
1.2201	33.648	34.179	24.721		1.285	1.305	0.944
1.2495	30.335	32.253	17.638		1.159	1.232	0.674
1.4	25.669	29.247	10.508		0.980	1.117	0.401
1.45	19.822	25.318	8.9325		0.757	0.967	0.341
1.5	13.012	20.661	3.0023		0.497	0.789	0.115
1.55	5.9853	15.466	2.3865		0.229	0.591	0.091
1.6	2.1908	9.9152	2.4008		0.084	0.379	0.092
1.65	1.4219	4.8013	3.4293		0.054	0.183	0.131
1.7	1.2816	2.6892	2.2084		0.049	0.103	0.084
1.75	1.2563	2.1033	1.9687		0.048	0.080	0.075
1.8	1.2518	1.9521	1.9094		0.048	0.075	0.073
1.85	1.251	1.9135	1.8937		0.048	0.073	0.072
1.9	1.2508	0	1.8897		0.048	0.000	0.072
1.95	1.2508		1.8887		0.048	0.000	0.072
2	1.2508		1.8884		0.048	0.000	0.072
2.05	1.2508		1.8883		0.048	0.000	0.072
2.1	1.2508		1.8883		0.048	0.000	0.072

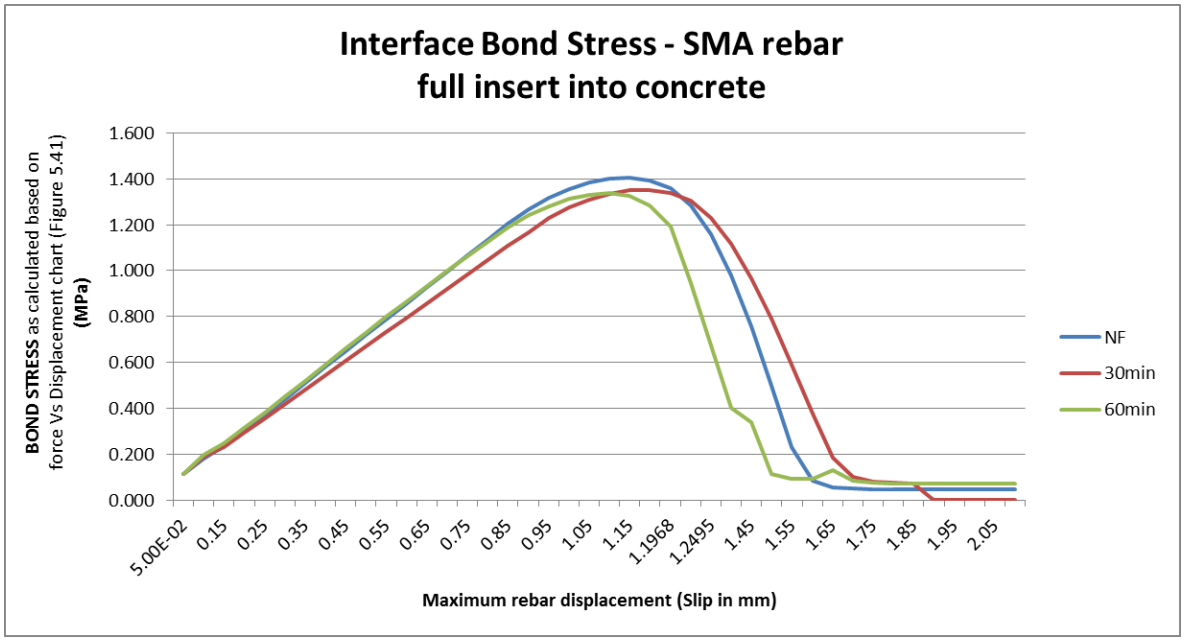

Figure 4.89: Bond Stress at interface from numerical Analysis for full SMA rebar insert under No Fire, 30min and 60min of Fire exposure for respective loads shown in Table 4.14

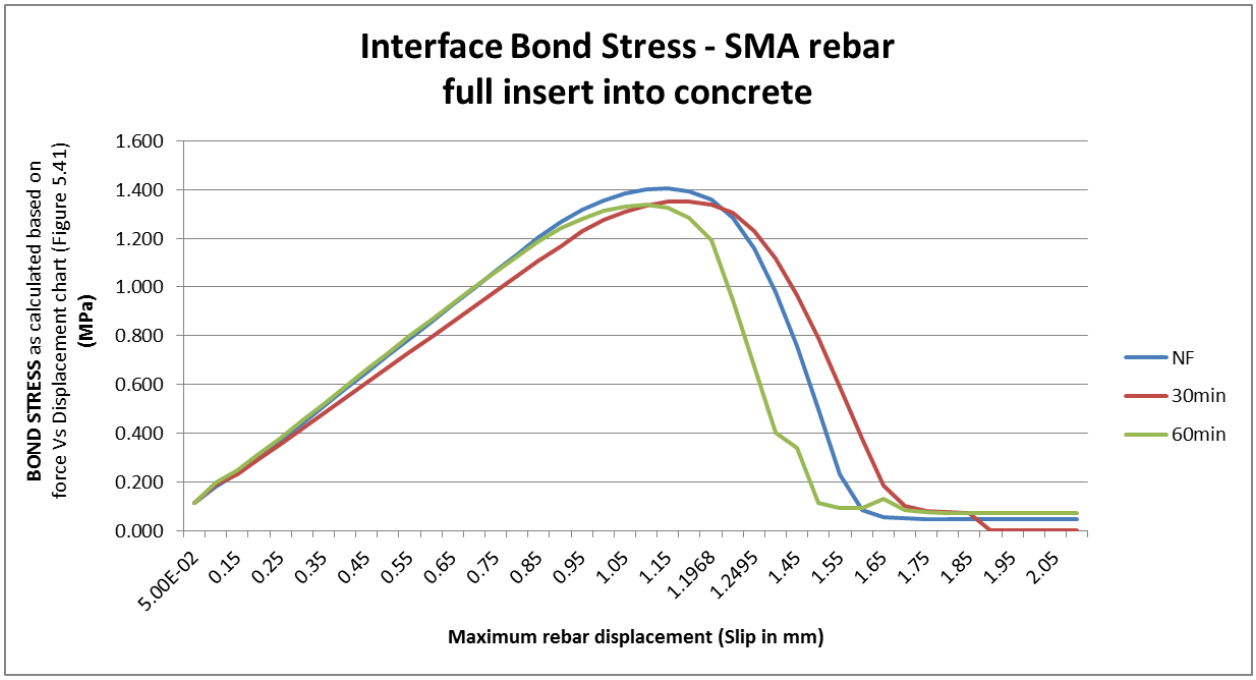

(a)

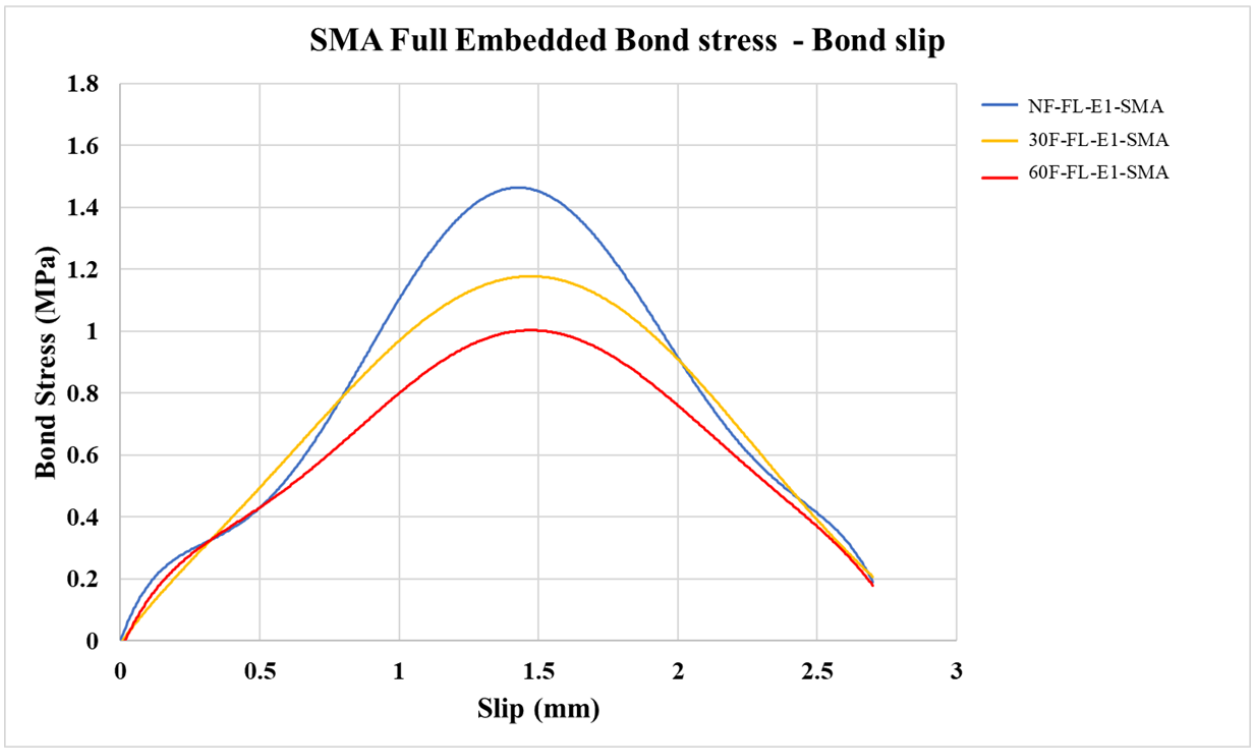

(b)

Figure 4.90: Comparison of Bond Stress values from (a) numerical experiments results and (b) Physical experiment results

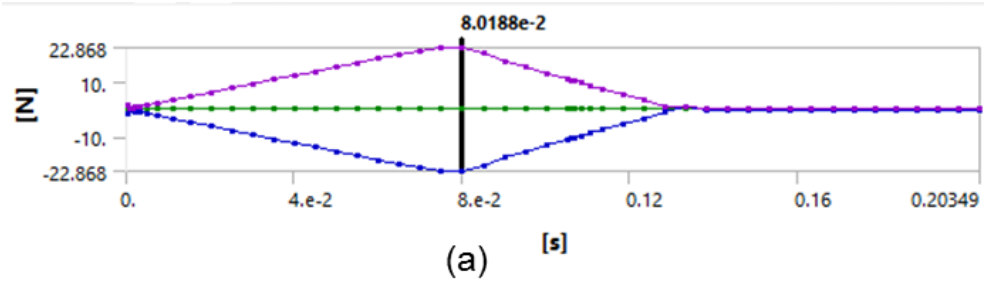

(a)

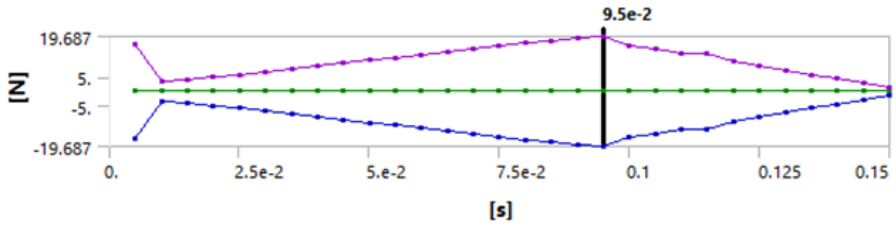

(b)

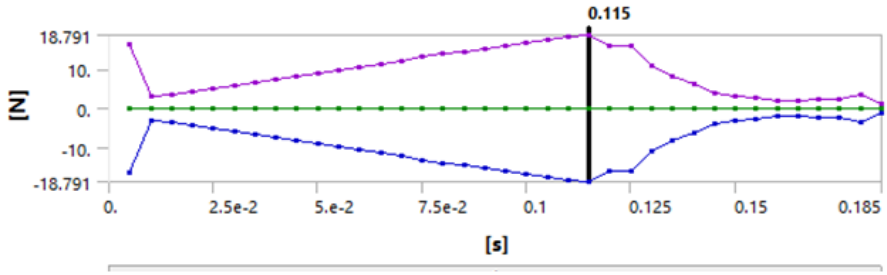

(c)

Figure 4.91: Resultant force for half insert SMA rebar-Concrete Specimen at a) No Fire b) 30min of Fire exposure (c) 60min of Fire exposure

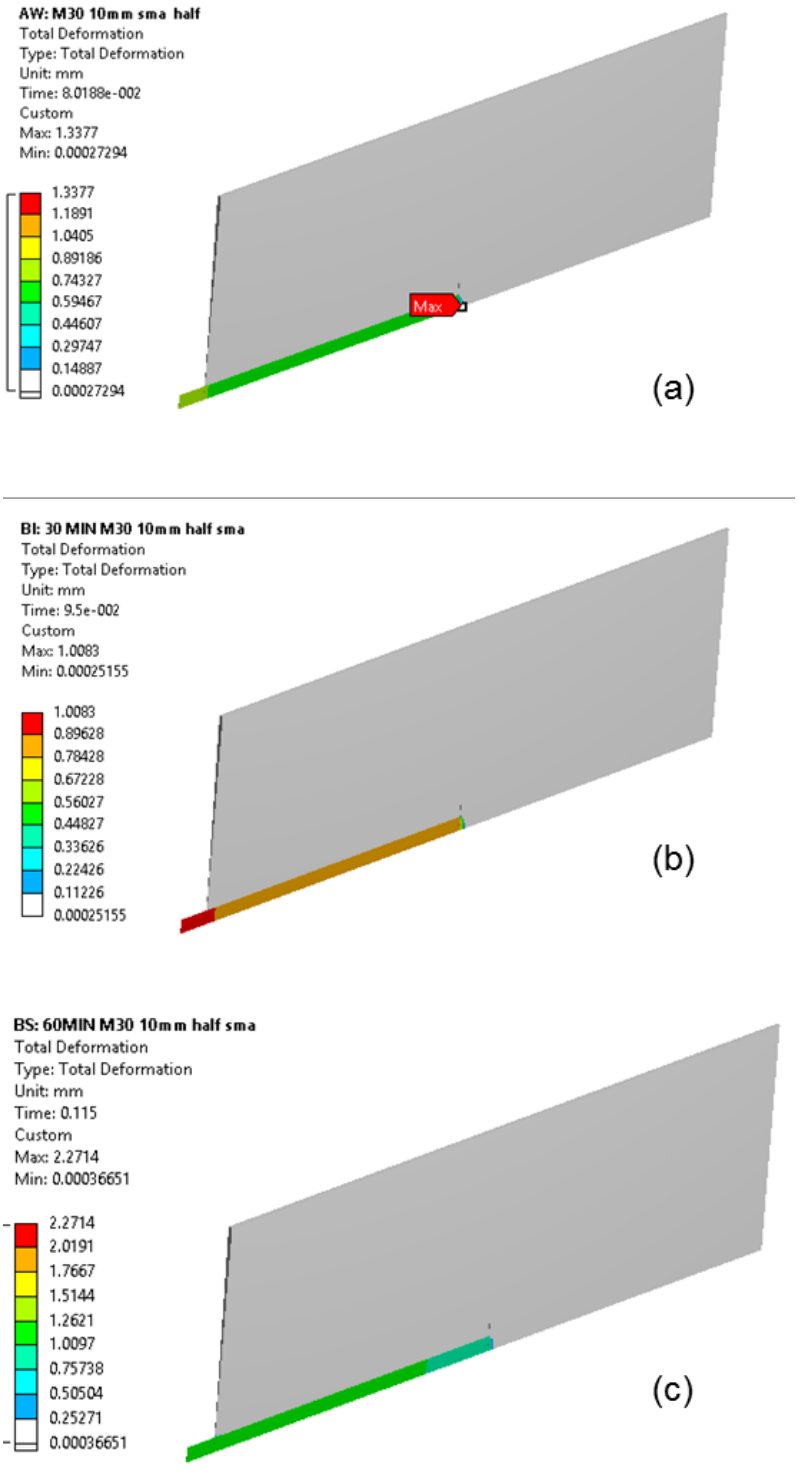

Figure 4.92: Half insert SMA rebar; displacement profile for a) No Fire b) 30min of Fire exposure (c) 60min of Fire exposure and for respective loads shown in Figure 4.91.

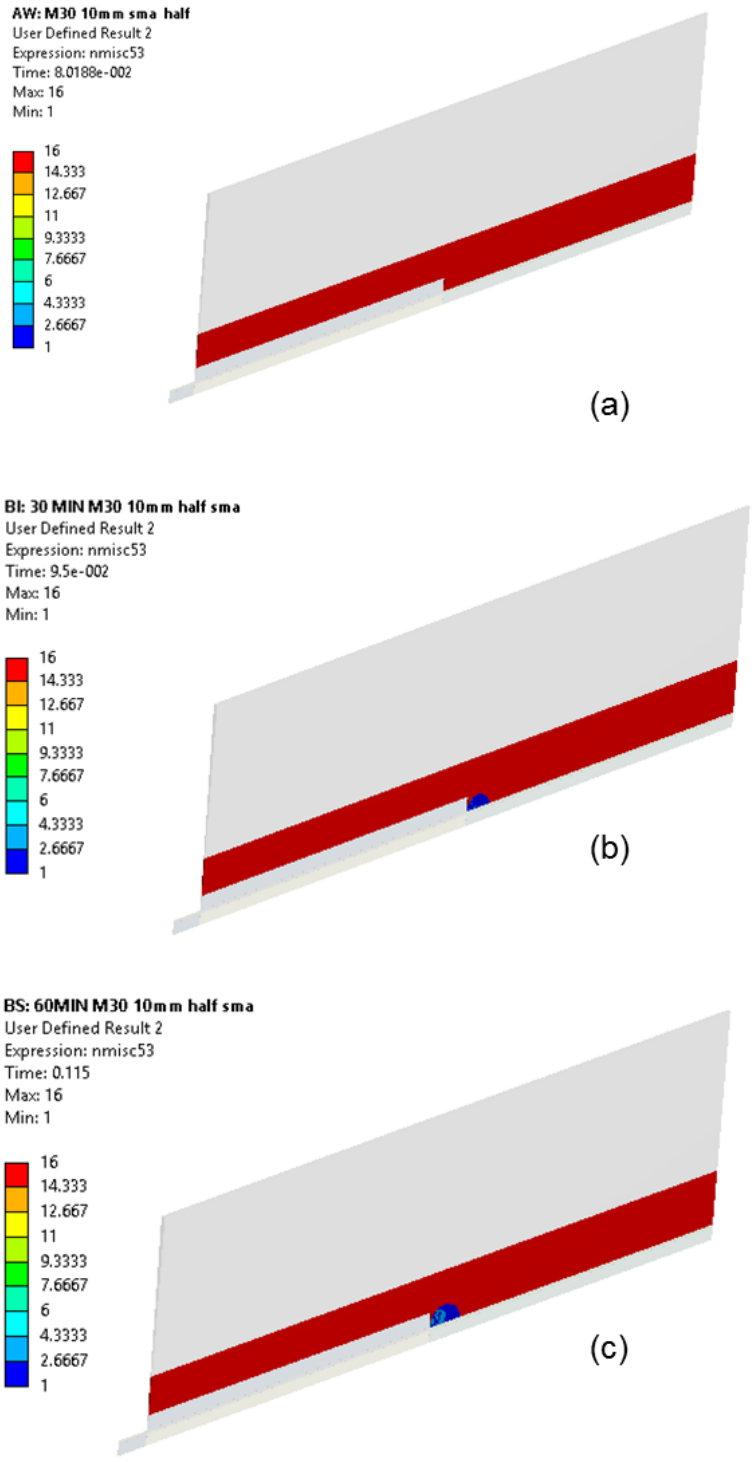

Figure 4.93: Half insert SMA rebar; Concrete interface element displacement profile for a) No Fire b) 30min of Fire exposure (c) 60min of Fire exposure and for respective loads shown in Figure 4.91

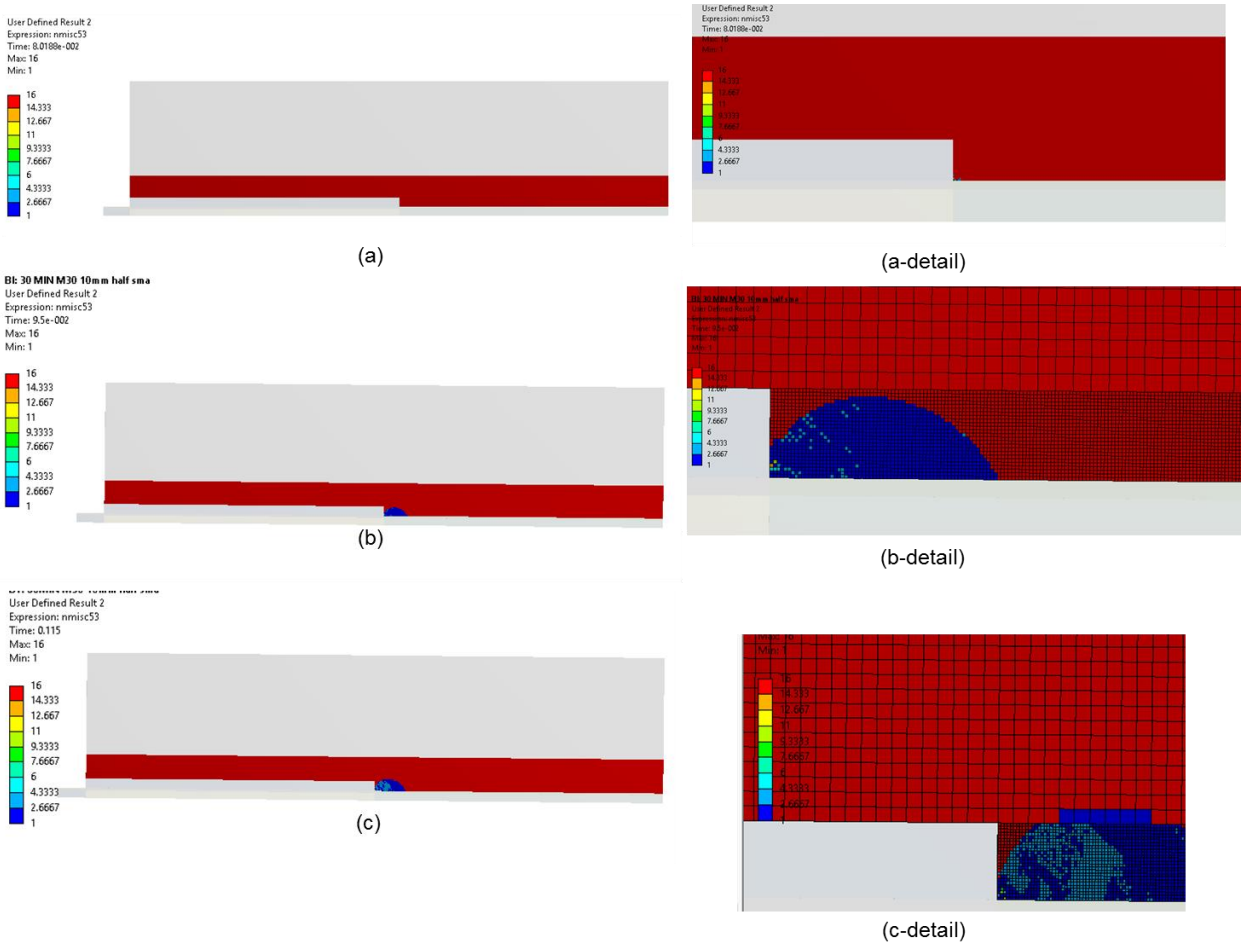

Figure 4.94: Axial section view of Half insert SMA rebar Concrete interface element displacement profile for a) No Fire b) 30min of Fire exposure (c) 60min of Fire exposure and for respective loads shown in Figure 4.91

Table 4.15: Bond Stress at interface from numerical Analysis for half insert SMA rebar

Interface Bond Stress - SMA rebar half insert into concrete

Force Values From Numerical experiments FORCE VS DISPLACEMENT CHART (Figure 5.47)					**BOND STRESS** calculated using corresponsing force observed in the force vs displacement chart		
Maximum	**NF Steel**	**30min f steel**	**60min f steel**		**NF**	**30min**	**60min**
5.00E-02	1	1	1		0.076	0.076	0.076
0.1	0.48107	3.5537	3.1058		0.037	0.271	0.237
0.15	0.57127	4.016	3.3676		0.044	0.307	0.257
0.2	0.80551	4.9922	4.1416		0.062	0.381	0.316
0.25	1.1657	6.0135	4.9567		0.089	0.459	0.379
0.3	1.7074	7.0392	5.7755		0.130	0.538	0.441
0.35	2.5208	8.0654	6.5946		0.193	0.616	0.504
0.4	3.7395	9.0917	7.4138		0.286	0.694	0.566
0.45	4.8726	10.118	8.233		0.372	0.773	0.629
0.5	6.4105	11.144	9.0521		0.490	0.851	0.691
0.55	7.9066	12.171	9.8712		0.604	0.930	0.754
0.6	9.4516	13.197	10.69		0.722	1.008	0.817
0.65	11.004	14.223	11.51		0.841	1.086	0.879
0.7	12.532	15.249	12.329		0.957	1.165	0.942
0.75	14.079	16.276	13.148		1.075	1.243	1.004
0.8	15.627	17.302	13.965		1.194	1.322	1.067
0.85	17.174	18.255	14.671		1.312	1.394	1.121
0.9	18.722	19.27	15.399		1.430	1.472	1.176
0.95	20.271	19.687	16.021		1.548	1.504	1.224
1	21.751	16.57	16.807		1.661	1.266	1.284
1.05	22.784	15.004	17.561		1.740	1.146	1.341
1.1	22.868	13.366	18.276		1.747	1.021	1.396
1.15	20.811	13.692	18.791		1.590	1.046	1.435
1.1768	17.716	10.614	16.003		1.353	0.811	1.222
1.1968	15.548	8.9377	15.922		1.188	0.683	1.216
1.2201	13.4	7.4343	11.006		1.024	0.568	0.841
1.2495	11.216	5.9534	8.4115		0.857	0.455	0.643
1.4	10.765	4.4767	6.1187		0.822	0.342	0.467
1.45	10.358	3.0001	3.8648		0.791	0.229	0.295
1.5	9.7532	1.5234	3.2794		0.745	0.116	0.250
1.55	8.8469		2.6217		0.676	0.000	0.200
1.6	7.4874		1.8101		0.572	0.000	0.138
1.65	5.4481		1.9209		0.416	0.000	0.147
1.7	3.2992		2.1969		0.252	0.000	0.168
1.75	1.1502		2.4759		0.088	0.000	0.189
1.8	0.99871		3.6734		0.076	0.000	0.281
1.85	0.34936		1.2679		0.027	0.000	0.097
1.9	0.37476				0.029	0.000	0.000
1.95	0.38038				0.029	0.000	0.000
2	0.38765				0.030	0.000	0.000
2.05	0.39535				0.030	0.000	0.000
2.1	0.4031				0.031	0.000	0.000

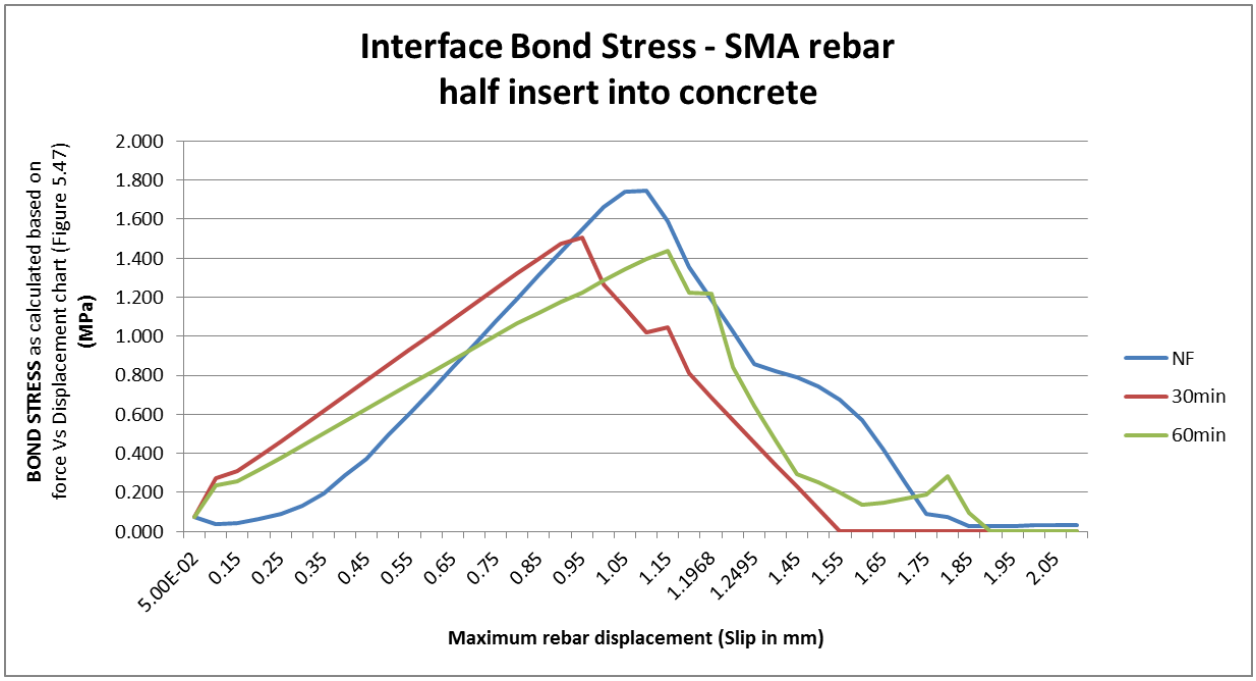

Figure 4.95: Bond Stress at interface from numerical Analysis for full SMA rebar insert under No Fire, 30min and 60min of Fire exposure for respective loads shown in Table 4.15

4.7 Numerical Studies - Results and Discussion

Following the generation of the required data sets on the bond stress of both SMA and Steel rebar based concrete specimens the thesis set to explore the possibility of applying such data to a novel method of analysing concrete-rebar interface (that is subjected to fire conditions) using numerical simulations. It is for the first time that such a study was attempted, and a successful development of the numerical model contributes greatly to the advancement of knowledge in the literature. The numerical studies in this thesis were divided into two major sections a) thermal analysis b) non-linear structural analysis. To this extent, in order to establish the thermal profile of the specimen's thermal analysis of the specimen was carried out. Since materials remained the same and the thermal properties remain the same over a period of 60min, only one thermal analysis was carried out as discussed in section 4.5.1. The results are discussed next following which the results from the non-linear structural analysis is discussed. The results of the thermal analysis on SMA rebar-based specimen heated for 60min is shown in Figure 4.96, while the thermal profile at start (No Fire) and 30min of fire exposure is also discussed in this chapter. Such thermal profiling studies were taken up on specimen with steel rebar too for conformation of

the thermal profile generated. The similarities in the trend in both the Concrete-steel rebar and in the case of Concrete-SMA rebar are very close. In both cases that were tested for the thermal response the rebar temperatures were close to 400°C. In fact, the steel and SMA rebars had reached a temperature of 374°C and 383°C respectively.

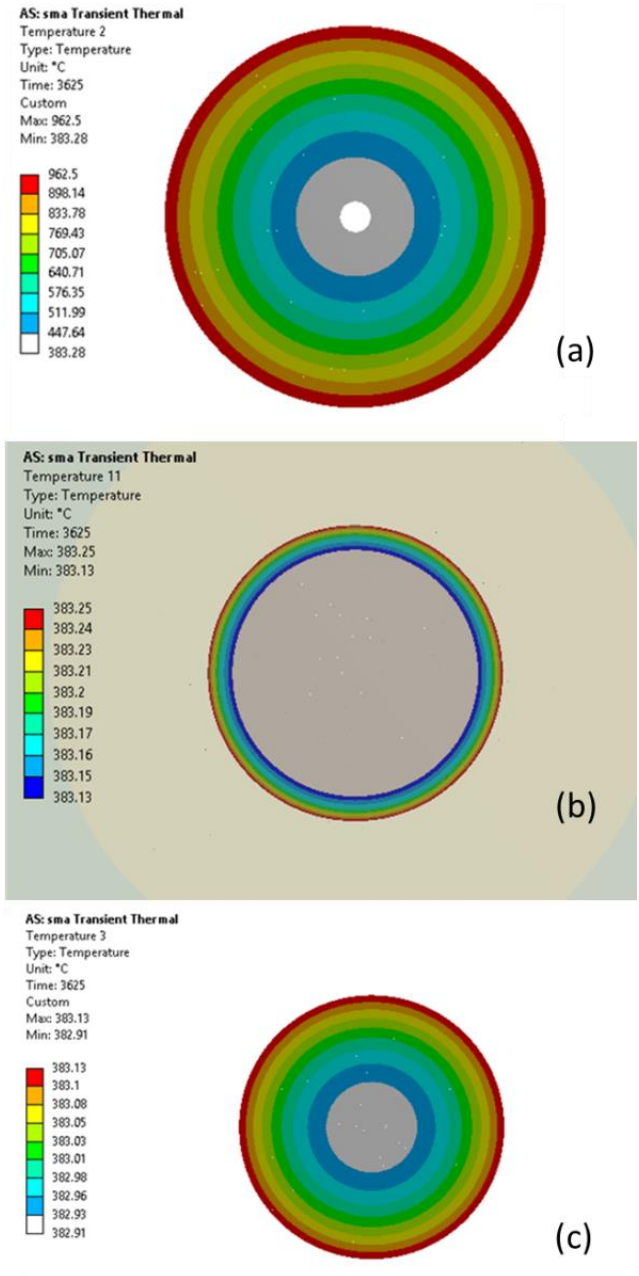

Figure 4.96: 2D Radial Thermal profile at 60min of thermal exposure (a) Concrete (b) Concrete-SMA rebar interface and (c) SMA Rebar

A failure mode of a specimen (SMA rebar that is fully inserted into concrete) that was subjected to pull-out test both experimentally and numerically is shown in Figure 4.97. In the physical testing of the specimen, at about 60 mins of thermal exposure and the specimen was subjected to the pull-out test. The specimen was analysed for cracks and the results are shown in Figure 4.97 (a) and (b). It can be noted from these figures that the rebar had smoothly pulled out of the specimen without cracking the concrete. The interface looks smooth and clean without any rupture. This is evident from any lack of concrete residue on the SMA rebar. In order to establish the consistency of the numerical model/method developed in this work, it is essential to observe similar results on the corresponding model used in numerical study. In Figure 4.97(b) the results from numerical study are presented. The results of the numerical study too predict a smooth pull-out of the rebar as observed in the case of physical experiments. This reiterates the accuracy of the novel method developed to analyse bond stress as a response to both thermal and structural loading.

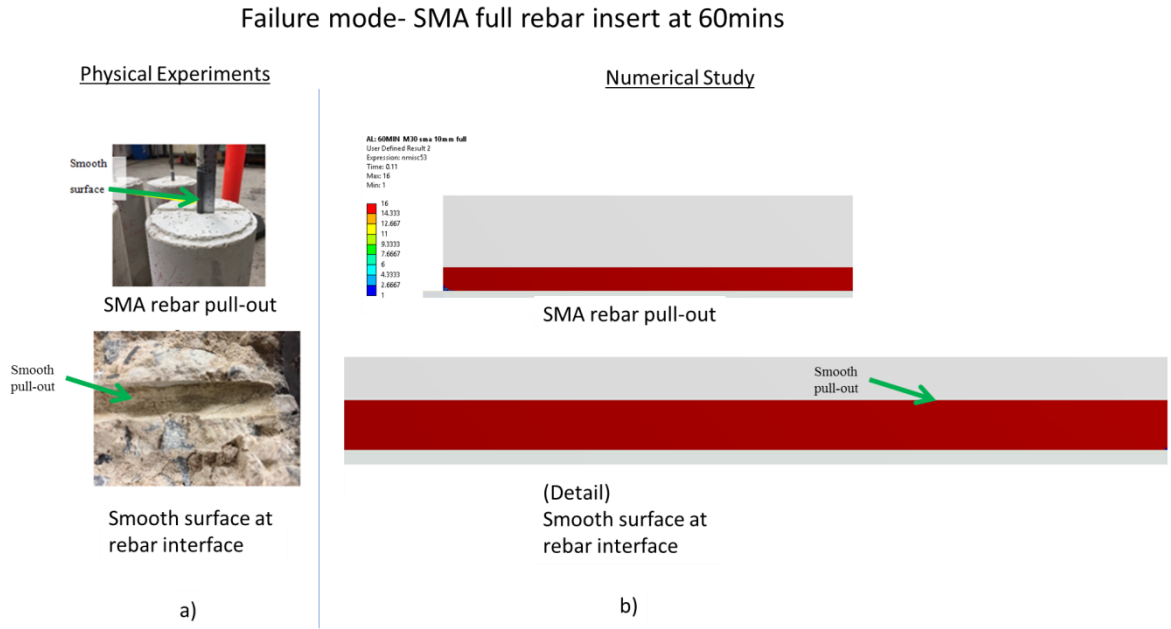

Figure 4.97: Failure Modes: Pull out test under high temperature a) physical experiment and b) numerical study

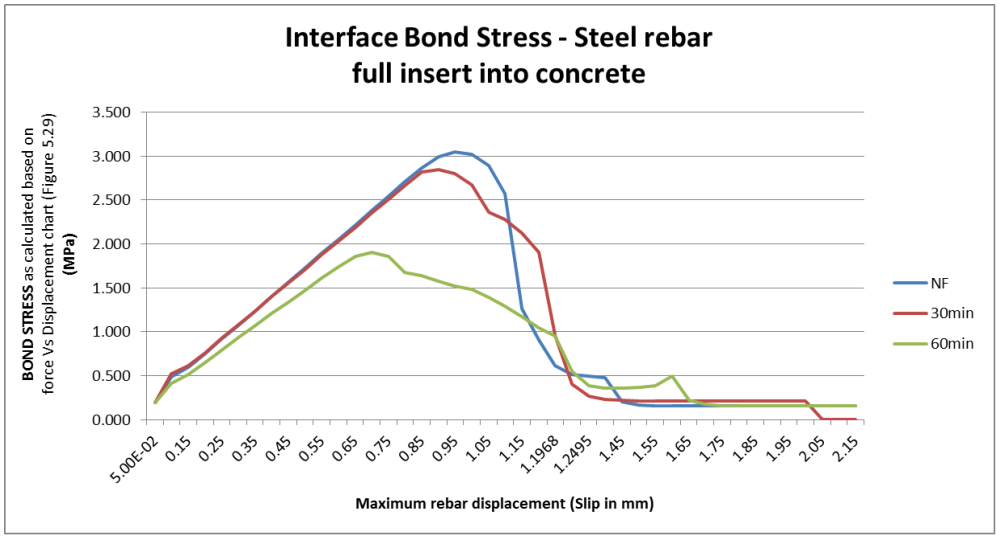

(a)

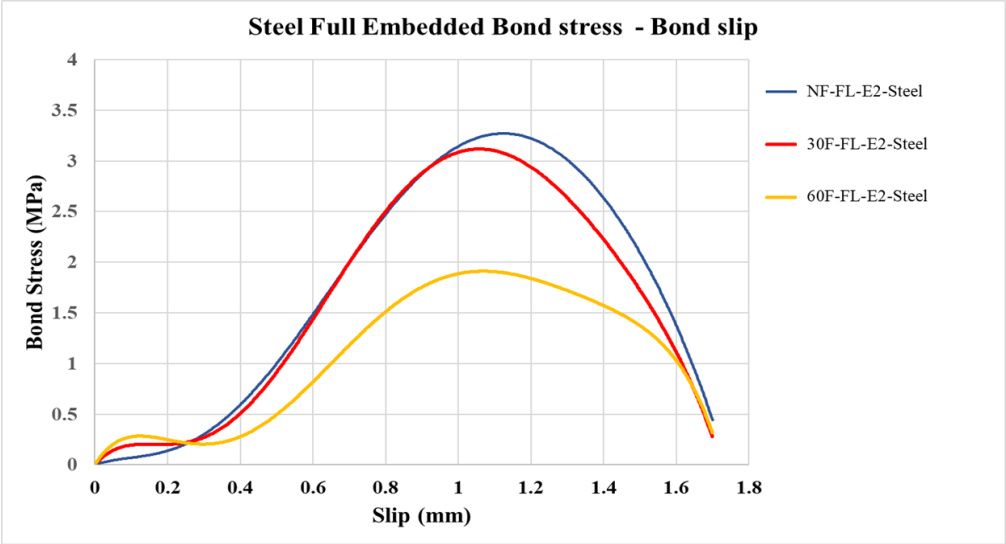

(b)

Figure 4.98: Comparison of Bond Stress values from (a) numerical experiments results and (b) Physical experiment results

The bond stress values achieved via the numerical experiments were found to be in close agreement with the corresponding values from the physical experiments. For example, the bond stress value between a steel rebar inserted fully into the concrete for no fire condition was found to be 3.5 MPa and 3.1 MPa for physical experiment and numerical studies respectively. Likewise, it can also be noted that the peak stress occurred at about 1.05mm slipped (displacement of the rebar). The results can be found to be in such close agreement for the two fire conditions tested (30min and 60min) too. In the case of 30min fire exposure, the maximum Bond Stress value noted

was just under 3MPa in both physical experiments and numerical experiments. Likewise, the maximum stress peaked at about 1mm slip value (displacement of rebar) in both physical and numerical experiments. Such a close match in values between physical and numerical experiments undoubtedly validated the numerical model/method developed in this work. The achievement of the data presented in Figure 4.77 and the subsequent comparison done (refer Figure 4.78) that establishes the tight agreement of the bond stress values obtained from physical and numerical experiments establishes the successful achievement of AIM 2.

Having established that for similar thermal and structural inputs the specimen in both experimental and numerical study responded in similar ways, it was decided to employ the novel numerical method developed in this work to examine the bond stress at the interface of all the specimens that were tested in experimental studies. In all, 12 specimens were subjected to the nonlinear testing using the numerical model developed in this work. In effect, six specimens each were examined with steel and SMA rebars. The six specimens in each group were further divided into two groups a) half insert of rebar and b) full insert of rebar. The examination of the 12 specimens allowed for the comparison of the bond stress for the specimens in the respective grouping. The following two figures (Figure 4.99 and Figure 4.100) summaries these results and key findings.

Figure 4.99 is a chart that shows the bond stress values (as observed from the numerical experiments) on specimens that had rebar inserted to half the length of the concrete (150mm depth). Likewise, Figure 4.100 is a chart that shows the bond stress values (as observed from the numerical experiments) on specimens that had rebar inserted to full length of the concrete (300mm depth). In both the above-mentioned cases, it could be noted that at elevated temperatures (400˚C achieved at around 60mins of fire exposure), in the cohesive zone (the concrete-rebar interface) the steel rebar starts losing its strength (as a reflection of the falling bond stress values). The loss of strength (3MPa to 1.5MPa) can be noted at around 1mm displacement value and continues a rapid decline till about 1.75mm displacement due to sustained fire exposure.

On the contrary, the SMA rebar continues to gain strength as the temperature of the rebar-concrete interface approaches 400˚C. This is evident from the increased bond stress values which raise from about 1MPa to about 1.5MPa. An inverse relationship in the bond stress values is established between SMA and steel rebar for specimens that are exposed to 60min of fire conditions.

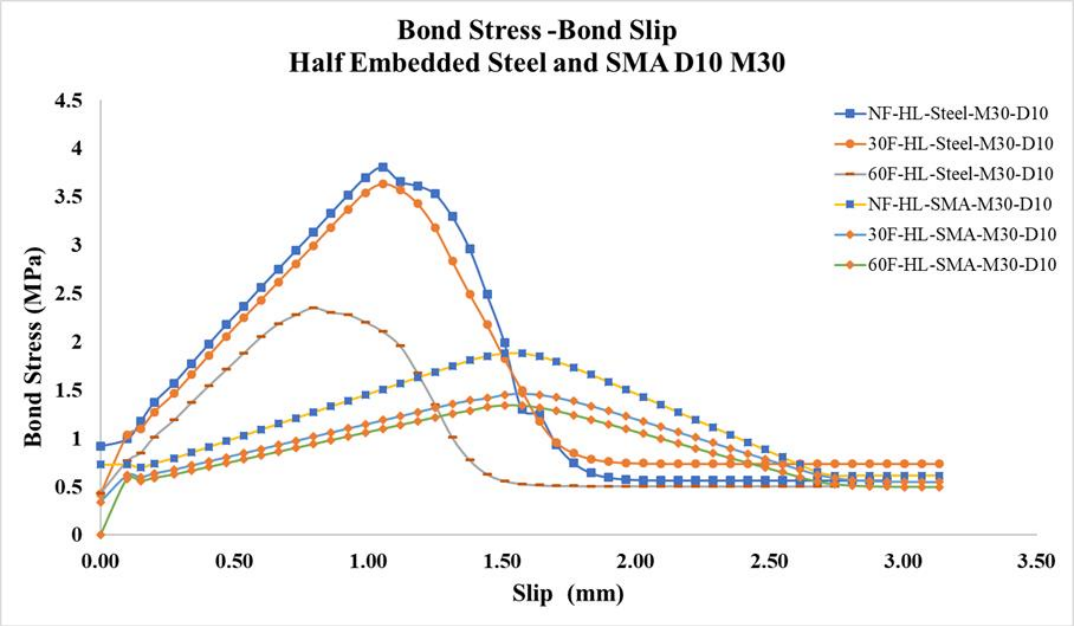

Figure 4.99: Effect of fire duration on bond stress of Half embedded rebar – SMA and Steel M30)

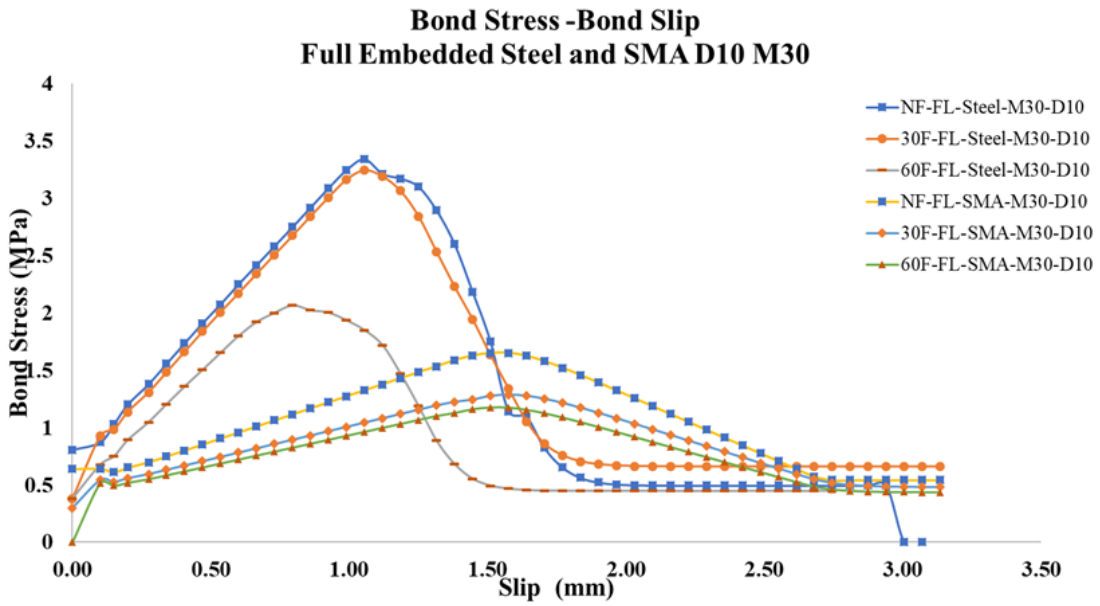

Figure 4.100: Effect of fire duration on bond stress of Full embedded rebar – SMA and Steel M30)

Figure 4.101 shows the plot for concrete M30, SMA and steel rebar 10mm and under three fire exposure conditions and for both physical (denoted by “E” followed by a number in the specimen name) and numerical experiments (denoted by “FEA” in the specimen name). It can be observed that there is good correlation between the experimental test result and numerical simulation results. The bond stress of steel is generally higher because of the surface friction and material modules of elasticity of the steel at normal temperature. It can also be noted that as the temperature the concrete specimens with steel rebars increases as response to thermal loading, the bond stress value begins to drop. For example, at around 30 minutes (the interface temperature is around 110°C as discussed earlier in this Chapter) there is 4 % reduction in steel rebar bond stress and as heating of the specimens continue to about 60min (where the concrete-rebar steel interface reaches a temperature of 400°C), the bond stress drop quite significantly by 42%. This can be attributed to the significant reduction in the elastic modulus of steel at such temperatures.

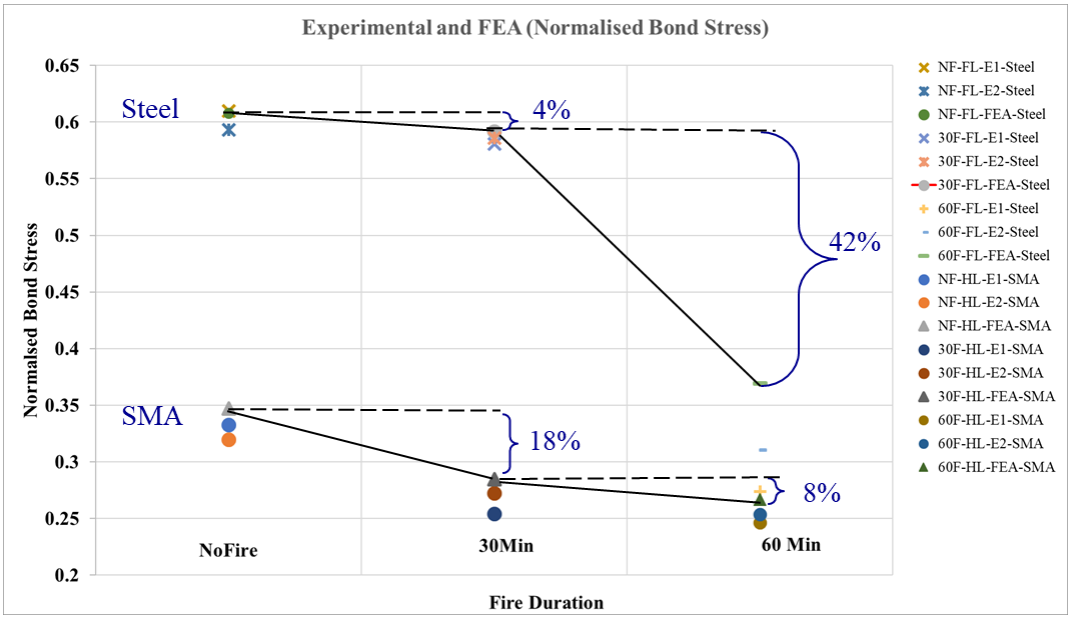

Figure 4.101: Experimental and FEA correlation

On the other hand, in the case of concrete with SMA rebars shown an 18% reduction in SMA rebar concrete bond stress at about 30min and about 8% at about 60min of fire exposure conditions. This can be explained by the fact that at about 400°C, the SMA rebars undergoes austenite phase transformation and gains stiffness because

of increased modulus of elasticity. Interestingly, the overall drop in the bond stress at 60 minutes fire duration in SMA bar is not as significant as steel bar (refer to Figure 4.101).

In all of the above cases it can be noted that the bond stress values noted for a particular case in the physical experiment is in very close and tight agreement with the bond stress prediction made by the numerical experiments; the average margin of error was less than 10% which validates the numerical model. Such a situation further validates and confirms the effectiveness of the novel non-destructive numerical method of testing a specimen's bond stress developed in this work. The development of such a numerical method to study the bond stress at the interface of concrete and rebar that are subjected to thermal loading successfully achieves AIM 2 of this thesis.

AIM 2 Achieved

"Develop a numerical model to study the bond stress and bond slip behaviour in the cohesive zone of SMA-concrete and steel-concrete specimens under various fire conditions"

A comprehensive analysis and comparison of the results from both the physical and numerical experiments validate the novel numerical model developed in this work. Such a situation presents an opportunity to further apply such numerical model to examine various other parameters that were exempted from both numerical and physical experiments considered in this work thus far. Such studies will assist in the development of an empirical equation which achieves the Aim 3 of this work. The manner in which the numerical results presented in this Chapter interacts with the rest of the Chapters in this thesis is shown in Figure 4.102.

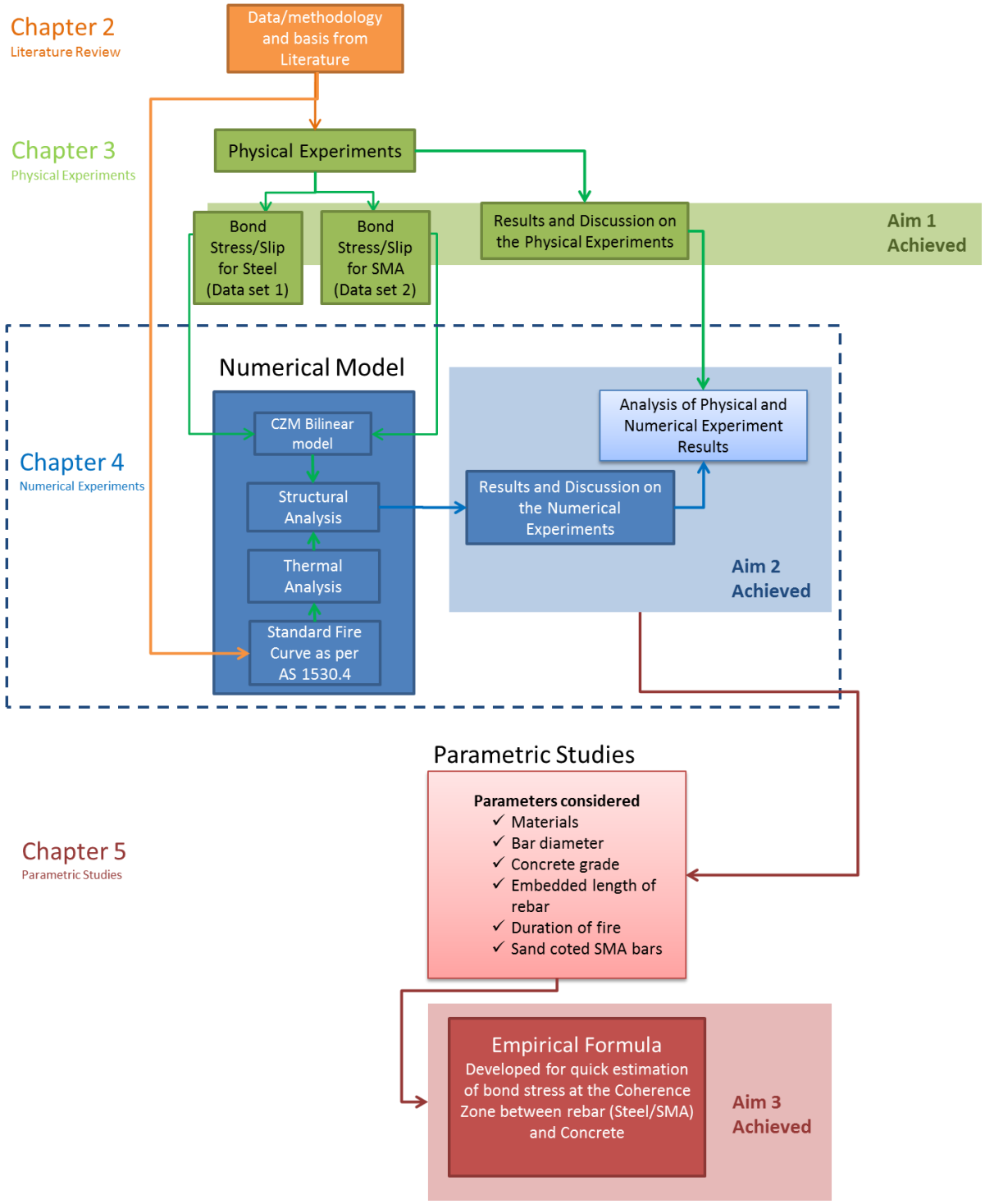

Figure 4.102: Interaction of numerical results with other Chapters

CHAPTER 5: Parametric Studies

In Chapters 3, only a limited number of specimens (M30 Concrete, NiTi SMA, steel rebar, both of 10mm diameter) were examined to understand the bond stress between rebar and concrete while the specimen was subjected to both thermal and structural loading. The constraint was mainly due to the high cost of the materials involved and the long-time frame involved in conducting each physical experiment (mainly related to heating and cooling of the furnace). The results of the physical experiments allowed for the defining of various parameters in a novel numerical model (in Chapter 4) that predicts the interface response to thermal and structural loading. A validation study between the results of the physical and numerical experiments established the accuracy of the numerical model developed in this work in Chapter 4. The novel numerical model developed in this work allows for the study of bond stress between rebar and concrete interface without the need for physical apparatus or experimentation. This situation presented an opportunity to conduct further studies on the influence of various other parameters on the bond stress of SMA-concrete. Such a parametric study will conclusively establish the importance of each of the parameters considered. This Chapter is divided into two main sections 1) Parametric studies and 2) Regression analysis. First the parametric studies conducted in this work are presented and clearly identify the parameters that have the greatest influence on the bond stress values. Such parameters are then be subjected to a regression analysis in the latter half of this Chapter. The regression analysis leads to the development of an empirical formula that allows for quick estimation of bond stress at the interface of the rebar and concrete that is subjected to various conditions of fire. Such a formula achieves the Aim 3 of this thesis. The Aim 3 and the corresponding objectives are:

- To develop an empirical equation for quick assessment of the bond stress that takes into account the influence of fire on the concrete;
    - To employ the numerical model developed in AIM 2 to conduct parametric studies on various specimens developed;

- Regression analysis of parametric study;
- To develop empirical equation taking into consideration the outcome of the parametric study taken up in AIM2 that facilitates quick bond stress calculations; and
- To validate the empirical equation against the results of the experiments conducted in this work and also against work from literature.

5.1 The parametric studies

The numerical model developed in this work in Chapter 4 to predict the bond stress in the cohesive zone is employed in this section to examine and to identify the parameters that have the greatest influence on the bond stress. The following parameters are considered for this exercise:

- Rebar diameter (8, 10 and 12 mm);
- Rebar Material (SMA and Steel);
- Concrete grade (M30, M40 and M50);
- Embedded length of rebar (150 mm and 300 mm);
- Duration of fire (No fire, 30mins and 60mins); and
- Sand coating on the rebar (300µm).

5.1.1 Effect of bar diameter

To study the influence of the bar diameter on bond stress, three different bar diameters (i.e. D8, D10 and D12) and concrete grades (M30, M40 and M50) were considered in this parametric study. Each of the above parameters was observed for three different fire exposure times 1) no fire (NF), 2) 30min of fire exposure (30F) and 3) 60min of fire exposure (60F). The observations made on the bond stress for half and full embedded SMA rebar case are presented in Figure 5.1 and Figure 5.2 respectively.

The bond stress distribution works on the interface area between the rebar and concrete. The increase in the bar diameter increases the interface surface area, which

leads to an increase in the chemical adhesion and frictional area. It is noted in the above-mentioned Figures that the bond stress increases with the increase in the bar diameter. It can also be noted that for the same concrete grade, fire condition and embedded length, an increase in the bar diameter correspondingly increases the pull-out force thereby increasing the bond stress. It was found that the increase in bond stress from diameter 8mm to 10 mm was around 12%, for the same embedded length, whereas it was around 22% for 10mm to 12mm bar diameter. Moreover, the increase in bar diameter does reduces the concrete cover, which contribute in dropping of the bond stress. For example, for rebar diameter more than 22mm the bond stress reduces with increase in the bar diameter (Muntasir et al. 2016).

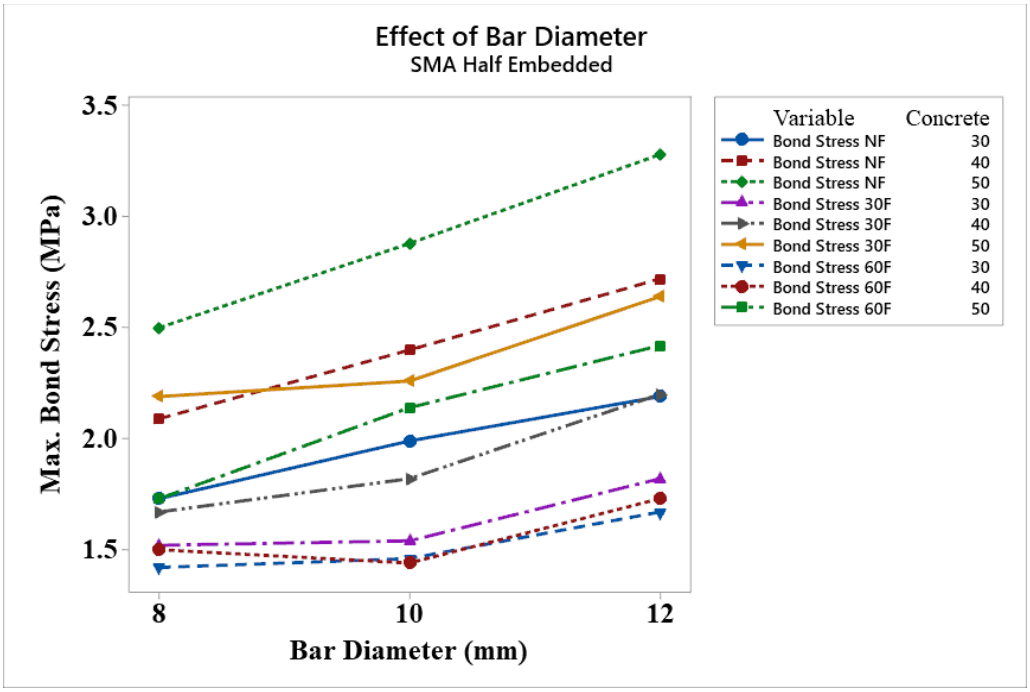

Figure 5.1: Effect of bar diameter on bond stress (Half embedded length)

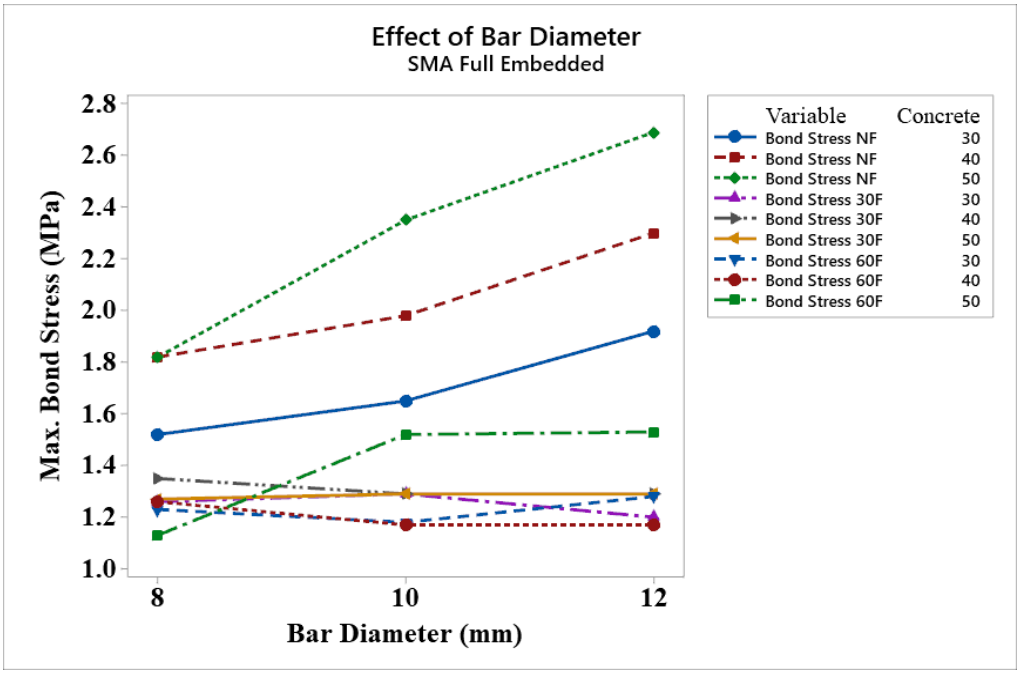

Figure 5.2: Effect of bar diameter on bond stress (Full embedded length)

5.1.2 Effect of concrete grade

The force transfer in a reinforced concrete specimen takes place through the bond between the concrete and rebar and is directly proportional to the strength of the materials involved. In the case of concrete, the grade of concrete denotes concretes strength. Higher the grade, higher is the strength (for example M30, M50). Concrete strength is one of the important factors that influences the bond strength. This is due to the fact that the shear and tangential separation at the interface between the bar and concrete is mostly governed by the concrete strength.

Figure 5.3 shows the plot of normalised bond stress for different bar diameter (8, 10 and 12mm) with different concrete grades (M30, M40 and M50). The response of the bond stress for different bar diameter and the fire expose duration is noted. It can be observed that there is an increase in the bond strength of around 20% to 22% by just changing the grade from M30 to M40 and from M40 to M50. It is evident that the bond stress increases with the increase in the concrete grade. Similar trend is observed in the case of full embedded rebar as well, as presented in Figure 5.14.

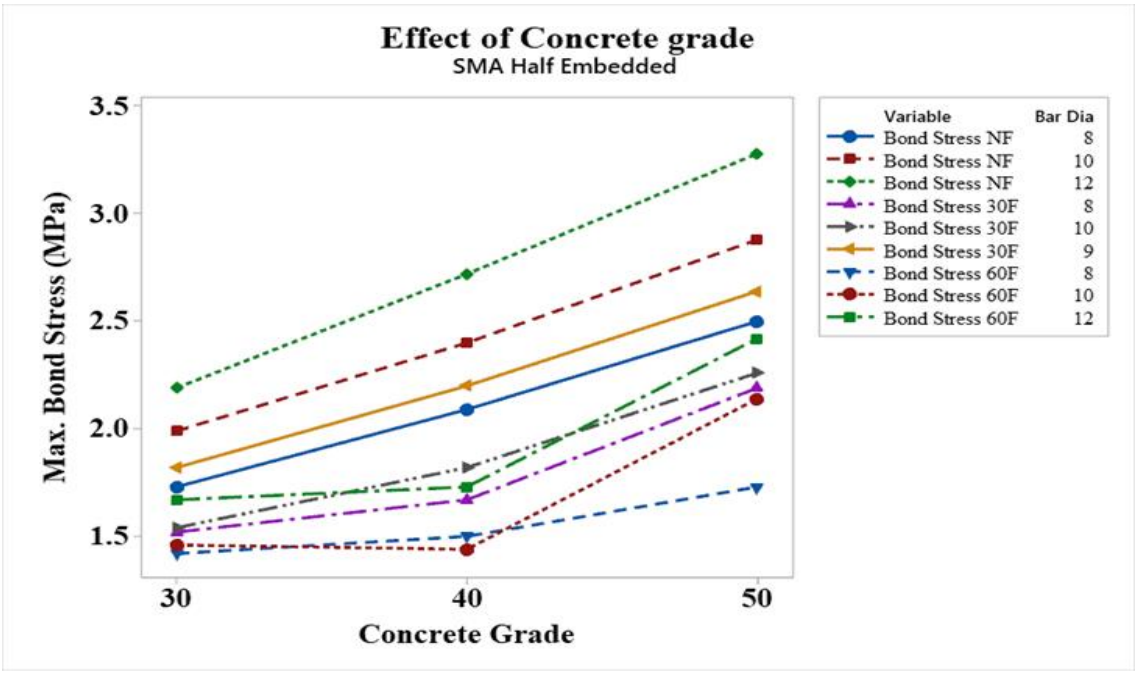

a)

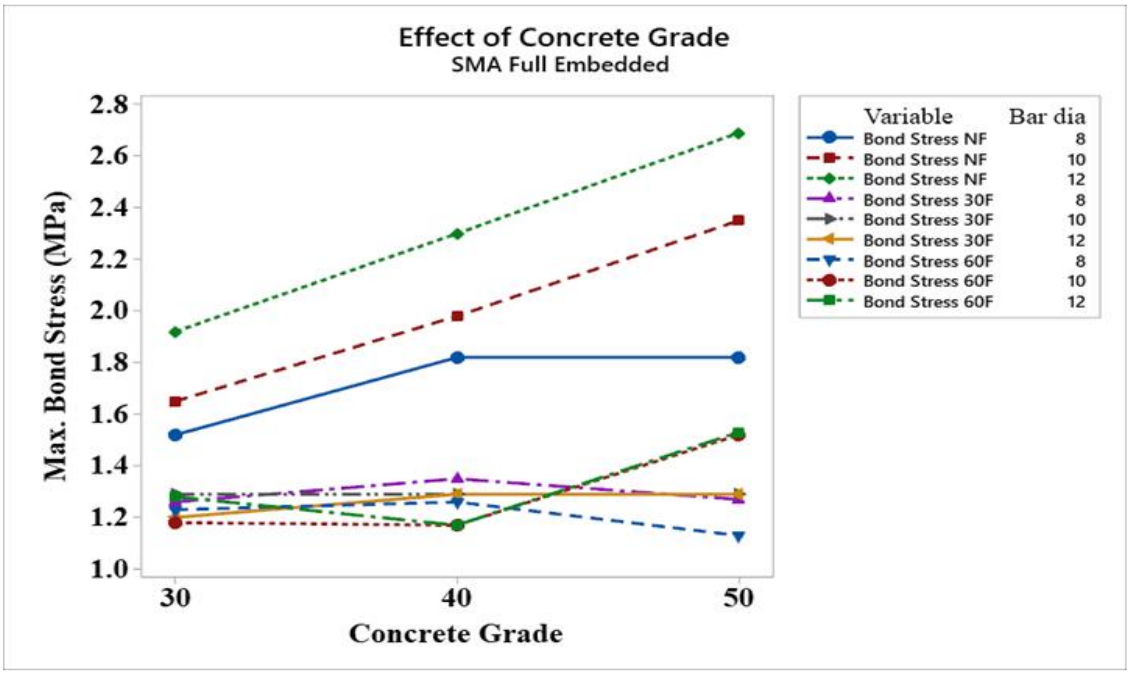

b)

Figure 5.3: Effect of concrete grade on bond stress a) SMA Half embedded and b) SMA Full embedded

5.1.3 Effect of embedded length

Two different embedment lengths were considered for the parametric study so as to study its effect on the bond strength. Essentially, full (300mm) and half embedment length (150mm) of SMA rebars of 8, 10 and 12mm diameter were considered. In Figure 5.4 and Figure 5.5, the normalised bond stress values as determined for the half and full embedded lengths for the above mentioned parameters are presented. The bond stress follows a trend that is comparable between the two insert depths considered. It is observed that the bond stress of the half-embedded length is on the higher side by around 14% as compared to the full embedment length (Figure 5.4). The main reason for the bond stress in the half embedment length being on the higher side is due to the low surface area available at the interface to resist the pull-out force. The following two charts (Figure 5.4 and Figure 5.5) show the bond stress values as predicted for M50 grade concrete for both half and full rebar insert depths, different rebar diameters and fire exposure durations.

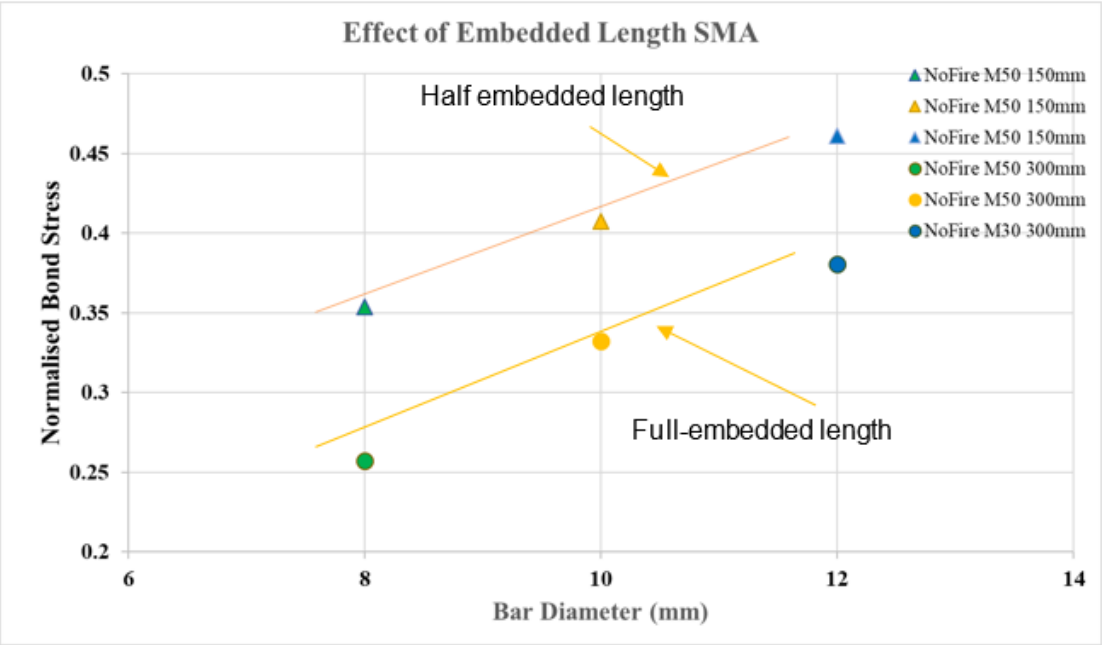

Figure 5.4: Effect of embedded length on bond stress (No Fire condition – M50)

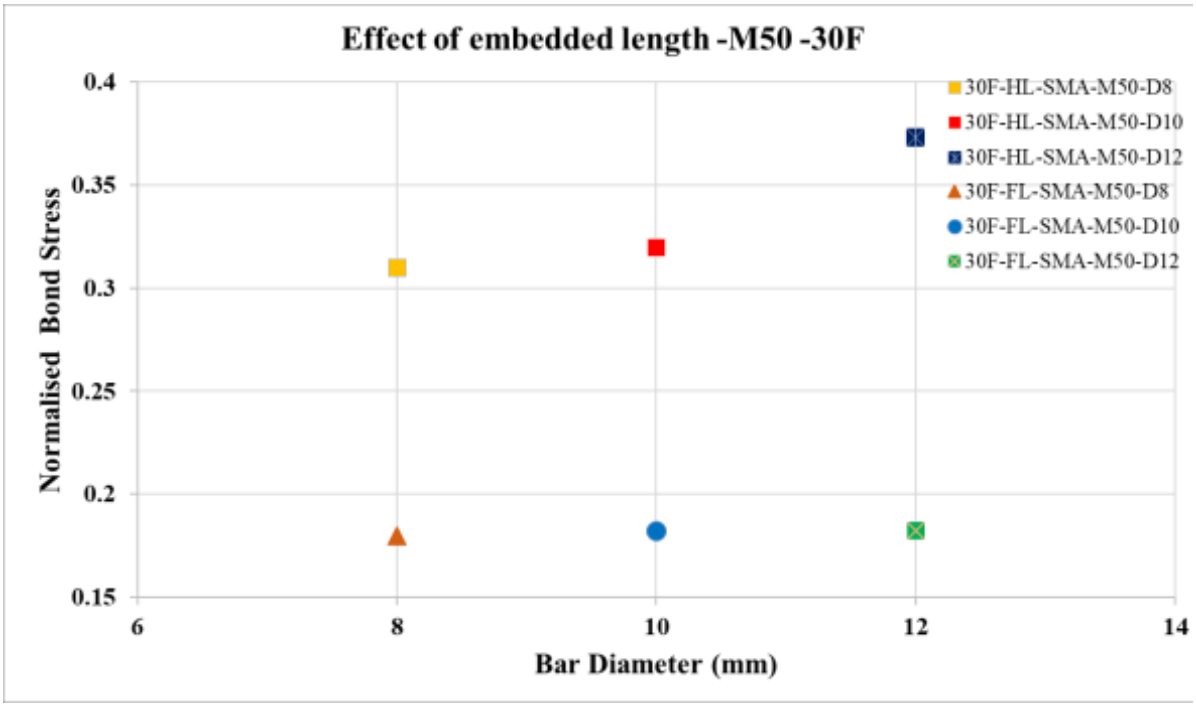

(a)

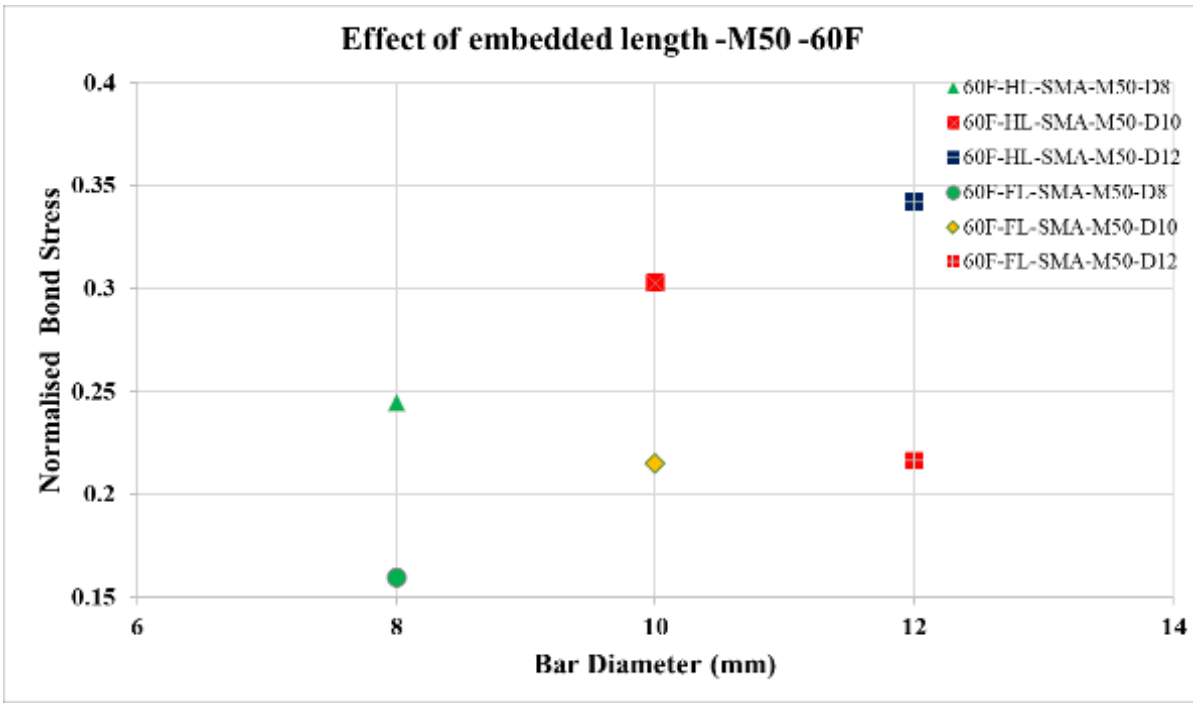

(b)

Figure 5.5: Effect of embedded length of SMA rebar on bond stress in M50 concrete at a) 30min and b) 60min fire exposure

5.1.4 Effect of fire exposure duration

As understood from the discussion thus far, the bond stress is dependent on embedded length, rebar diameter and more importantly the strength of the concrete and rebar interface. SMA are known to exhibit structural properties that are different to that of steel when exposed to fire conditions. Hence the fire exposure time was also considered as one of the parameters in the parametric studies.

SMA offers a unique capability wherein it exhibits increased stiffness as it undergoes a phase transformation between martensite to austenite under the influence of high temperature. Such behaviour is contradictory to that of steel, where in steel rebar shows a loss in stiffness under high temperature. At room temperature (no fire condition), a steel rebar having the same diameter as an SMA rebar, displays significantly higher stiffness than that of the SMA rebar. Typically, at room temperature, the bond stress of steel bar is around 2 times higher as compared to SMA. However, when exposed to conditions of fire and higher temperatures, SMA is expected to gain strength and rightly so the following points are made from the parametric studies conducted in this work.

Figure 5.6 and Figure 5.7 compares the maximum bond stress for different rebar diameter (8, 10 and 12 mm) in combination with different concrete grade (M30, M40 and M50) under three different fire exposure times 1) No fire, 2) 30Min and 3) 60min. In general, it can be seen that there is a drop in maximum bond stress at about 30 min of fire exposure. It is to be noted that at 30 min, the temperature at the SMA rebar-concrete interface did not reach the phase transformation temperature; and hence the SMA was yet to gain the intended stiffness at 30min of fire exposure. On the contrary, at 60min fire exposure, the SMA rebar temperature was noted to be close to 400°C. It is at this temperature that the SMA undergoes phase transformation and hence there is not much reduction in bond stress. On the contrary the bond strength seemed to have increased for rebars of 12mm diameters. Similar observations can be drawn for both full and half embedment rebar specimens (refer Figure 5.6 and Figure 5.7). The above-mentioned figures show the bond stress plot for a 10 mm diameter SMA rebar under different fire conditions and concrete grade (M30, M40 and M50).

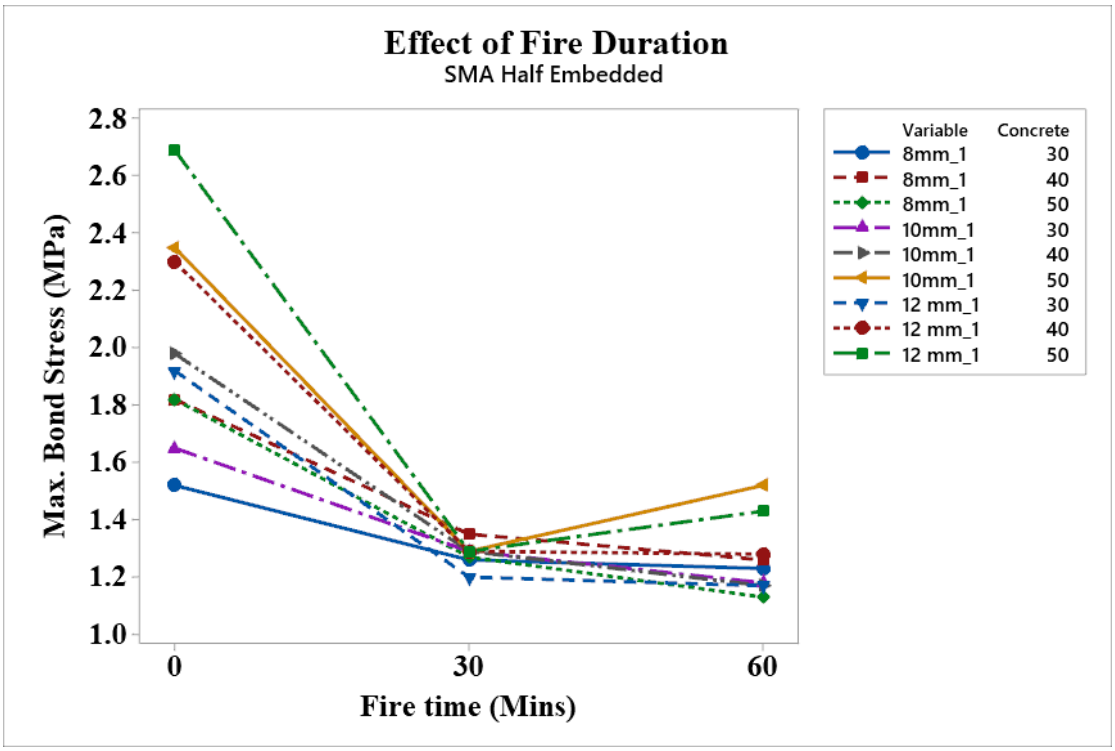

Figure 5.6: Effect of fire duration on bond stress (rebar half insert)

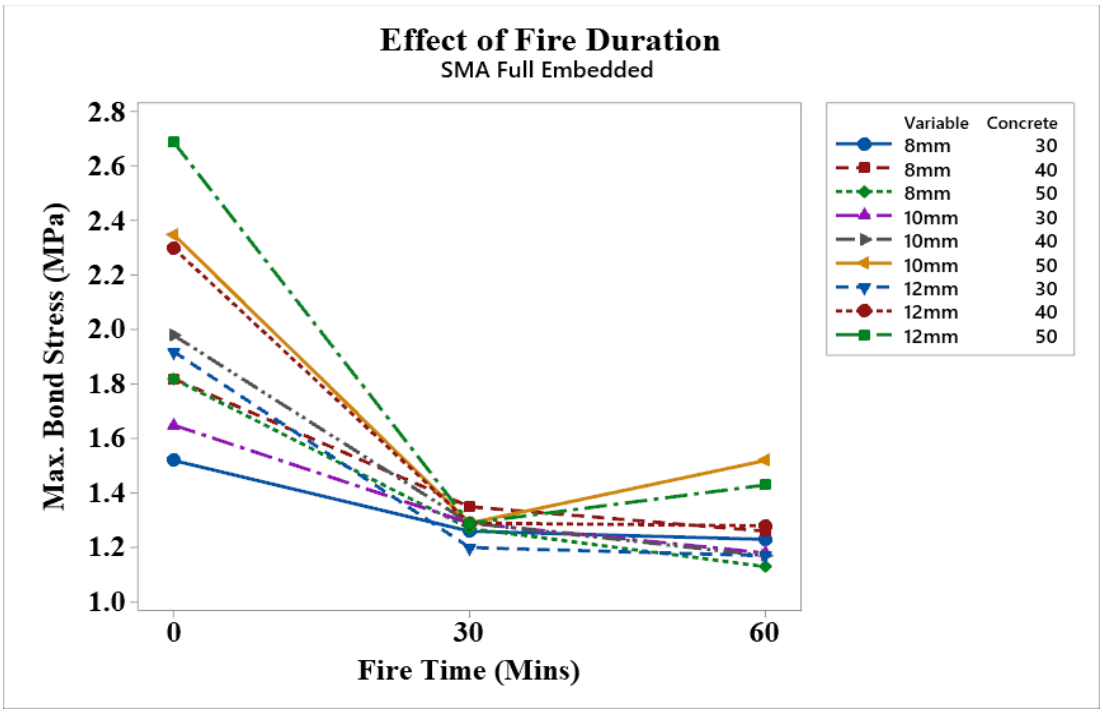

Figure 5.7: Effect of fire duration on bond stress (rebar full insert)

5.1.5 Effect of sand coating

SMA has lower bond strength as compared to steel rebars owing to its smooth surface. To overcome this limitation, sand coating is provided onto the SMA rebar. The purpose of the sand coating is to improve the surface friction. For the purpose of the parametric studies undertaken in this work, 300μm sand coated SMA bar is considered. For this exercise, the concrete grade considered was M50. Figure 5.8 shows a chart that compares the bond stress vs displacement values of SMA and sand Coated SMA rebars, for No fire, 30min and 60min of fire exposure. There is clearly a significant improvement in the bond stress of the sand coated rebar as compared to standards SMA rebar for all three fire conditions (Figure 5.8) that they were exposed to.

From Figure 5.9 it can be observed that the bond strength of sand coated SMA bar has shown more than 41% increase in bond strength. This effectively means the difference between steel and sand coated SMA is about 16% as compared to 56% between steel and standard SMA rebar. There seems to be about 40% improvement in the bond stress values of sand coated SMA even when they are subjected to fire exposure (both 30 and 60min) as noted in Figure 5.9.

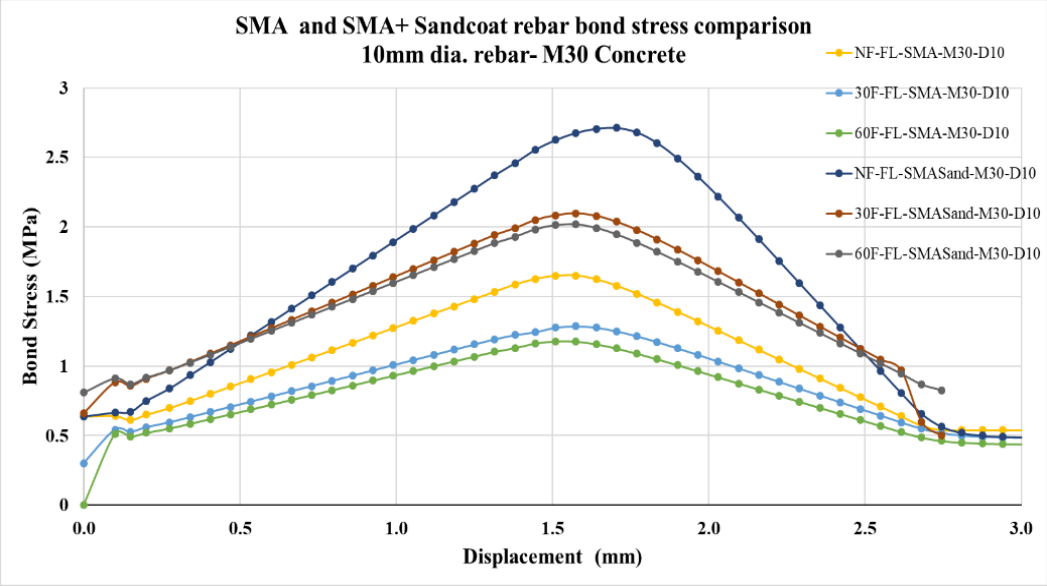

Figure 5.8: Effect of sand coating on bond stress (Full embedded length – M30)

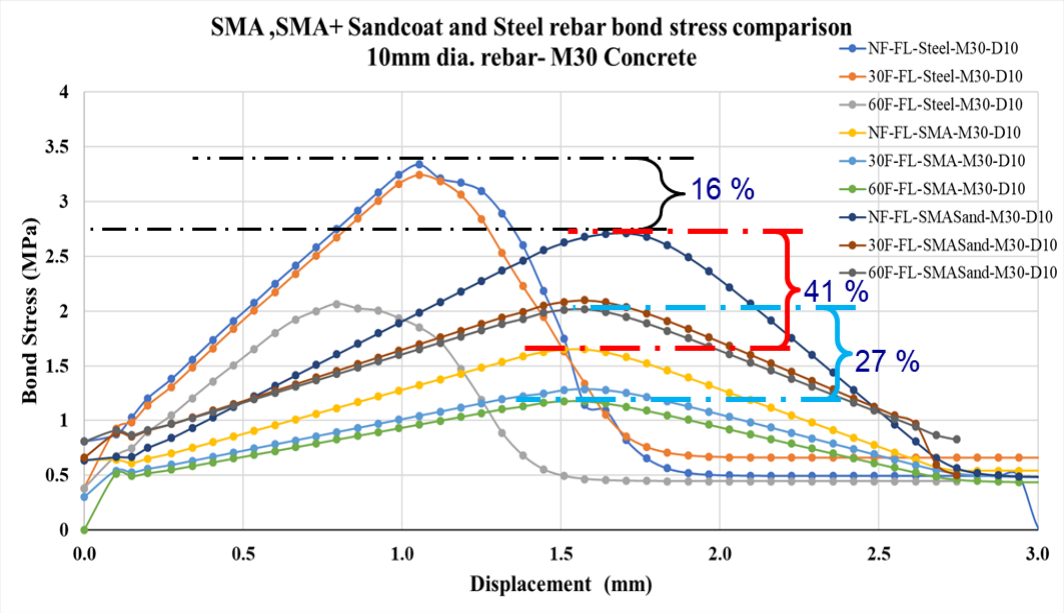

Figure 5.9: Effect of sand coating on bond stress (Full embedded length - SMA-steel – M30)

5.1.6 Key highlights of the parametric studies

Results from parametric studies of the pull-out studies showed a clear trend in how the various parameters affect the bond stress. Importantly, the current study which is carried out on plain rebar is purely to understand the bond stress behaviour between SMA and concrete, and for the same reason plain SMA and plain steel rebar were considered for the comparative analysis.

The influencing parameters from the parametric studies conducted using the numerical model developed in this thesis were combined together and were plotted in the 3D surface plots to understand the influence that each parameter has on bond stress. Figure 5.10 and Figure 5.11 show the different parameters that were considered in the parametric studies and how they had influenced the bond stress as such. The factors which seemed to influence the bond stress the most are concrete grade, rebar material, embedded length of the rebar, rebar diameter and material degradation of concrete and rebar material under high temperature. The above-mentioned parameters were all considered in the development of the empirical formula using regression analysis which is discussed next.

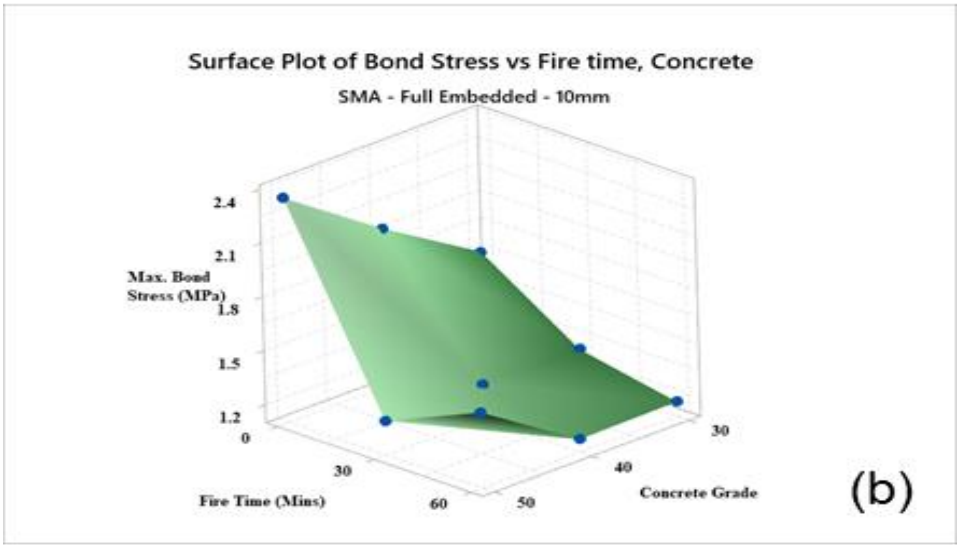

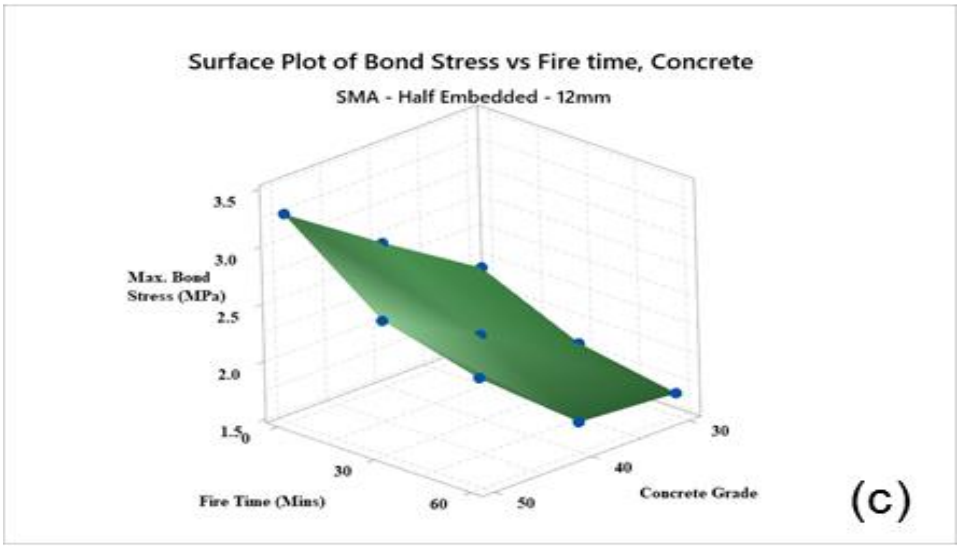

Figure 5.10: Influence of parameters on (a) 8mm (b) 10mm and (c) 12mm diameter SMA fully embedded rebar

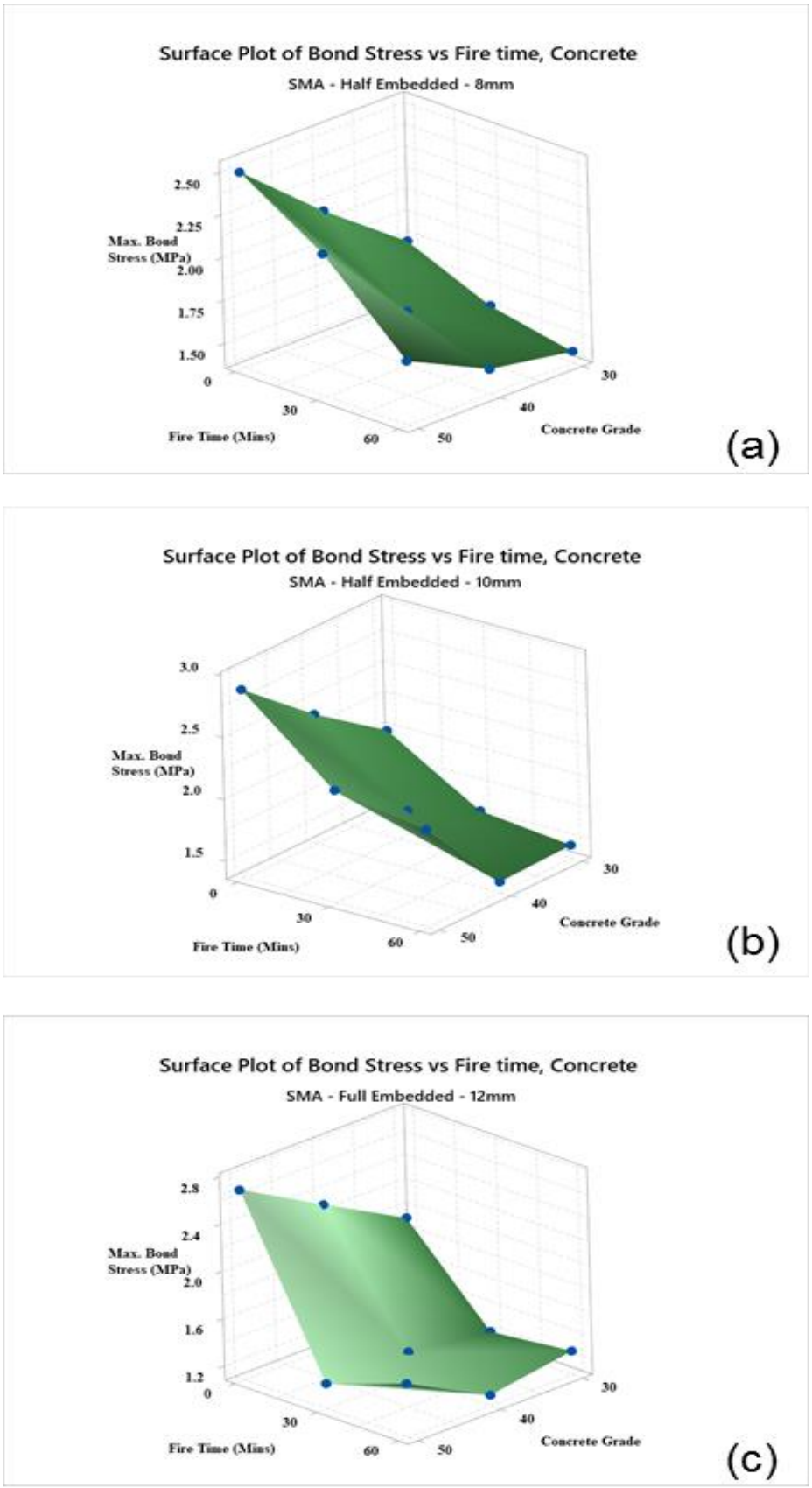

Figure 5.11: Influence of parameters on (a) 8mm (b) 10mm and (c) 12mm diameter SMA half embedded rebar

5.2 Empirical Equation

Regression analysis is a powerful statistical method that allows for the examination of the relationship between two or more variables of interest i.e. dependent and independent variables. In this research, the dependent variable is the bond stress (τ), which is also known as criterion variable. The factors which affect the bond stress and influence this dependent variable are called as independent variable. In this work, the parameters considered in the numerical and parametric studies i.e. bar diameter, embedded length, rebar material, concrete grade and degradation of the concrete and rebar material are the independent variables.

Regression analysis allows to achieve a good understanding on the influence of the independent variables (concrete grade, rebar material, bar diameter, material degradation etc.) (both positive and negative) on the dependent variable (bond stress). It also allows to mathematically determine how strongly a variable affects the dependent variables and quantifies the same. Technically, regression analysis model is based on the sum of squares, which is a mathematical way to find the dispersion of data points. The goal of a model is to get the smallest possible sum of squares and draw a line that comes closest to the data.

Since there were several independent variables identified in this work, a multivariate regression analysis was carried out (using the data analysis tool in Microsoft Excel) to establish the correlation between bond strength (the dependent variable) and the independent variables. When the number of independent variables is high, literature suggests the use of stepwise regression (SR) as a robust approach to determine the best combination of independent variables in predicting the dependent variable (Cevik et al. 2010).

Regression analysis produces an output summary which consists of regression statistics and correlation coefficients. The regression statistics consists of Multiple R, R Square, adjusted R Square, standard error and observations. Multiple R is the Correlation Coefficient that measures the strength of a linear relationship between two variables. R square (R^2) is the coefficient of determination, which is used as an

indicator of the goodness of fit. It shows how many points fall on the regression line. The R^2 value is calculated from the total sum of squares. More precisely, it is the sum of the squared deviations of the original data from the mean. Adjusted R Square is the R square adjusted for the number of independent variables in the model.

Standard error is another goodness-of-fit measure that shows the precision of the regression analysis conducted- the smaller the number, the more certainty about the regression equation that is developed. While R^2 represents the percentage of the dependent variables variance that is explained by the model, Standard Error is an absolute measure that shows the average distance that the data points fall from the regression line. The observations are the number of samples used in the regression analysis. The correlation coefficients (identified as $\beta_1, \beta_2, \beta_3$ etc) also called as parameter coefficients are the respective multiplying factor (constant value) generated for the respective parameter selected. The correlation coefficient can be any value between -1 and 1, and its absolute value indicates the relationship strength. The larger the absolute value, the stronger the relationship. The negative value indicates negative strong relationship, positive value indicates positive strong relationship and if the correlation coefficient is zero, it means it's not related.

5.2.1 Regression Analysis – Discussion on Case studies

Based on the discussion on the parametric studies in the previous section, key parameters that influenced the bond stress the most were identified for the regression analysis. These are:

1) Embedded length;
2) Bar diameter;
3) Degradation of concrete (concrete modulus); and
4) Rebar material (rebar modulus).

In Table 5.1 the bond stress values as observed during the parametric studies for the various combinations of the above four identified parameters are presented. A total of 92 cases (as indicated in Table 5.1) are considered in this work for the regression analysis covering the various permutation and combination of the aforementioned

parameters. These cases were specifically selected in a manner that represents a sample which consists of all the combination of the parameters considered in this work.

Table 5.1: Partial list of dependent and independent variables as derived from parametric studies

S.No.	Bond stress	Bar Dia	Rebar Modulus	embedded	Concrete modulus
1	1.29	8.00	65.00	150.00	29.13
2	1.26	8.00	61.75	150.00	26.22
3	1.23	8.00	60.00	150.00	17.48
4	1.51	10.00	65.00	150.00	29.13
5	1.29	10.00	61.75	150.00	26.22
6	1.18	10.00	60.00	150.00	17.48
7	1.92	12.00	65.00	150.00	29.13
8	1.20	12.00	61.75	150.00	26.22
9	1.28	12.00	60.00	150.00	17.48
10	1.82	8.00	65.00	150.00	32.80
11	1.26	8.00	61.75	150.00	29.52
12	1.35	8.00	60.00	150.00	19.68
13	1.98	10.00	65.00	150.00	32.80
14	1.29	10.00	61.75	150.00	29.52
15	1.17	10.00	60.00	150.00	19.68
16	2.30	12.00	65.00	150.00	32.80
17	1.29	12.00	61.75	150.00	29.52
18	1.17	12.00	60.00	150.00	19.68
19	1.82	8.00	65.00	150.00	34.80
20	1.27	8.00	61.75	150.00	31.32
21	1.13	8.00	60.00	150.00	20.88
22	2.35	10.00	65.00	150.00	34.80
23	1.29	10.00	61.75	150.00	31.32
24	1.52	10.00	60.00	150.00	20.88
25	2.69	12.00	65.00	150.00	34.80
26	1.29	12.00	61.75	150.00	31.32
27	1.53	12.00	60.00	150.00	20.88
28	1.52	8.00	65.00	300.00	29.13
29	1.26	8.00	61.75	300.00	26.22
30	1.23	8.00	60.00	300.00	17.48
31	1.32	10.00	65.00	300.00	29.13
32	1.29	10.00	61.75	300.00	26.22
33	1.18	10.00	60.00	300.00	17.48
34	1.92	12.00	65.00	300.00	29.13
35	1.20	12.00	61.75	300.00	26.22
36	1.28	12.00	60.00	300.00	17.48
37	1.82	8.00	65.00	300.00	32.80

38	1.26	8.00	61.75	300.00	29.52
39	1.35	8.00	60.00	300.00	19.68
40	1.98	10.00	65.00	300.00	32.80
41	1.29	10.00	61.75	300.00	29.52
42	1.17	10.00	60.00	300.00	19.68
43	2.30	12.00	65.00	300.00	32.80
44	1.29	12.00	61.75	300.00	29.52
45	1.17	12.00	60.00	300.00	19.68
46	1.82	8.00	65.00	300.00	34.80
47	1.27	8.00	61.75	300.00	31.32
48	1.13	8.00	60.00	300.00	20.88
49	2.35	10.00	65.00	300.00	34.80
50	1.29	10.00	61.75	300.00	31.32
51	1.52	10.00	60.00	300.00	20.88
52	2.69	12.00	65.00	300.00	34.80
53	1.29	12.00	61.75	300.00	31.32
54	1.53	12.00	60.00	300.00	20.88
55	3.34	10.00	210.00	300.00	29.13
56	3.25	10.00	199.50	300.00	26.22
57	3.18	10.00	105.00	300.00	17.48
58	3.21	10.00	210.00	300.00	29.13
59	1.98	10.00	199.50	300.00	26.22
60	1.96	10.00	105.00	300.00	17.48
61	3.61	10.00	210.00	150.00	29.13
62	3.59	10.00	199.50	150.00	26.22
63	3.17	10.00	105.00	150.00	17.48
64	3.18	10.00	210.00	150.00	29.13
65	1.81	10.00	199.50	150.00	26.22
66	1.78	10.00	105.00	150.00	17.48
67	3.34	8.00	210.00	300.00	29.13
68	3.03	8.00	199.50	300.00	26.22
69	1.97	8.00	105.00	300.00	17.48
70	4.03	8.00	210.00	300.00	32.80
71	3.67	8.00	199.50	300.00	29.52
72	2.37	8.00	105.00	300.00	19.68
73	4.42	8.00	210.00	300.00	34.80
74	4.04	8.00	199.50	300.00	31.32
75	2.72	8.00	105.00	300.00	20.88
76	3.34	10.00	210.00	300.00	29.13
77	3.24	10.00	199.50	300.00	26.22
78	2.06	10.00	105.00	300.00	17.48
79	4.10	10.00	210.00	300.00	32.80
80	3.75	10.00	199.50	300.00	29.52
81	2.52	10.00	105.00	300.00	19.68
82	4.20	10.00	210.00	300.00	34.80
83	4.24	10.00	199.50	300.00	31.32
84	2.81	10.00	105.00	300.00	20.88

85	3.35	12.00	210.00	300.00	29.13
86	3.28	12.00	199.50	300.00	26.22
87	2.17	12.00	105.00	300.00	17.48
88	4.26	12.00	210.00	300.00	32.80
89	3.95	12.00	199.50	300.00	29.52
90	2.58	12.00	105.00	300.00	19.68
91	4.77	12.00	210.00	300.00	34.80
92	4.37	12.00	199.50	300.00	31.32
93	2.85	12.00	105.00	300.00	20.88

Formulation of the empirical equation

A multiple linear regression model with k predictor variables x1, x2, ..., xk and a response y, can be written as

$$y = \beta 0 + \beta 1x1 + \beta 2x2 + \ldots \beta kxk$$

As before, there are the residual terms of the model and the distribution assumption we place on the residuals will allow us later to do inference on the remaining model parameters and interpret the meaning of the regression coefficients β0, β1, β2, ..., βk in this model.

More complex models may include higher powers of one or more predictor variables, e.g.

$$y = \beta 0 + \beta 1x + \beta 2x2$$

or interaction effects of two or more variables

$$y = \beta 0 + \beta 1x1 + \beta 2x2 + \beta 12x1x2$$

Models of this type can be called linear regression models as they can be written as linear combinations of the β-parameters in the model. The x-terms are the weights and they may be non-linear in x. Models with two predictor variables (say x1 and x2) and a response variable y can be understood as a two-dimensional surface in space. The shape of this surface depends on the structure of the model. The observations are

points in space and the surface is plotted to best approximate the observations. For example: The simplest multiple regression model for two predictor variables is

$$y = \beta 0 + \beta 1x1 + \beta 2x2$$

In general, the regression analysis output can be expressed in the linear equation as shown in equation. The equation relates dependent variable (on left hand side) with the independent variable (on right hand side).

$$P0 = \beta_1(\mathrm{P1}) + \beta_2(\mathrm{P2}) + \beta_3(\mathrm{P3}) + \beta_4(\mathrm{P4}) \qquad \text{Equation 5.1}$$

Where, P0 is a dependent parameter and P1, P2, P3 and P4 are the independent parameters which defines the relationship with dependent parameter using the coefficients of parameter $\beta_1, \beta_2, \beta_3$ and β_4 respectively. These coefficients provide the information about the weightage and how it affects (i.e. positively or negatively) the output results. The positive constant value signifies that the parameter affects output positively and negative constant value signifies the parameters affect the output negatively.

For the regression analysis carried out in this study, the dependent parameters P1, P2, P3 and P4 are bond stress (τ_{max}) and independent parameters are bar diameter (d_b), rebar modulus (R_m), embedded length (l_d) and concrete modulus (E_c) respectively. Substituting P0, P1, P2, P3 and P4 with. $\tau_{max}, d_b, \mathrm{R_m}, l_d$ and E_c respectively in Equation 5.1 results in the following equation.

$$\tau_{max} = \beta_1(d_b) + \beta_2(R_m) + \beta_3(l_d) + \beta_4(E_C)$$

where,

τ_{max} = maximum bond strength (MPa)

E_c = modulus of elasticity of concrete

d_b = bar diameter

l_d = embedded length

R_m = modulus of elasticity of bar

In order to establish the respective values for the coefficients of parameter $\beta_1, \beta_2, \beta_3$ and β_4 accepted regression analysis methodology from the literature (Abbas et al. 2017) is adopted. An excel work book was developed to conduct the Multiple Parameter Regression Analysis using the governing equations mentioned above and based on the methodology commonly adopted for such a work book in general. A partial view of the excel sheet is shown in Figure 5.13.

The inputs for the regression analysis are the dependent and independent parameters as identified in Table 5.1. The outcome of the regression analysis resulted in identifying the coefficients of parameter β_1, β_2, β_3 and β_4 as shown in
Table 5.2 and as identified in the summary output of the regression analysis as indicated in the partial view of regression analysis excel work-sheet (Figure 5.13)

Equation 5.2 is derived from the regression analysis conducted on the data from the numerical parametric analysis on the plain rebar and hence does not account for the ribbed rebars or deformed rebars. Moreover, the bond stress in ribbed or deformed rebar also depends on factors such as relative rib area, rib factors and surface preparation of the rebar in addition to the parameters studied in the numerical parametric studies. To incorporate the effect of the ribbed or deformed rebar a rib factor (R_f) is introduced. The rib factor calculations are based on parameters pertaining to ribbed rebar, such as friction, ribs spacing, relative rib area and length of embedded rebar. The total bond stress evaluated by Equation 5.2 multiplied by rib factor R_f.

$$\tau_{max} = (0.0053\, d_b + 0.0136\, R_m - 0.00044 l_d + 0.02137 E_C) \quad \text{Equation 5.2}$$

Table 5.2: Coefficient for parameters in Empirical equation

Parameters	Component	Coefficient	Units	Abbreviation
Bond stress	-	-	MPa	τ_{max}
Bar diameter	P1	$\beta_1 = 0.0053$	mm	d_b
Rebar modulus	P2	$\beta_2 = 0.0136$	GPa	R_m

Embedded Length	P3	β_3 = -0.00044	mm	l_d
Concrete Modulus	P4	β_4 = 0.02137	MPa	E_c

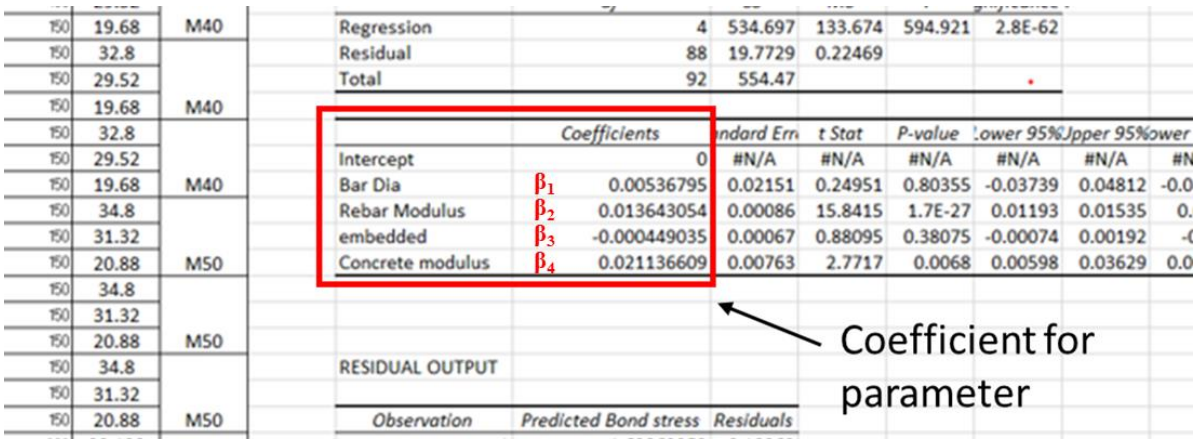

Figure 5.12: Regression Analysis – Coefficient for parameter

The transfer of forces from the rebar to the surrounding concrete by chemical adhesion, frictional forces arising from the roughness & relative slip between the bar and the surrounding concrete and mechanical interlocking or bearing of the rebar ribs against the concrete surface. Based on the coefficient and normalised value of coefficient the weightage and physical interpretation of the parameters included in the regression analysis can be summarised in the Table 5.3 below.

Table 5.3: Coefficient for parameters in Empirical equation: Weightage and Interpretation

Parameter	**Coefficient of empirical equation**		**Physical interpretation**
	Value	**Normalised Value**	
Rebar diameter	0.0053	0.24	In the case of the smooth bars, wherein rupture caused by slipping occurs, the bond is mainly carried out by using the chemical adhesion between the concrete and the rebar. When that connection is broken, the strength that leads to the slipping appears due to

			friction, being that its intensity depends on the type of the surface of the bar. Therefore, the force capable of breaking the bond is proportional to the size of the area of the bar in contact hence it can be seen that as the bar diameter increase the increase in the bond stress.
Rebar Modulus	0.0136	0.63	The force transmitted by rebar to the surrounding concrete depends on the elongation which is based on rebar modulus. This elongation results in transfer of tensile stress to the surrounding concrete results in more damage to the surrounding concrete thus reducing the bond stress.
Concrete modulus	0.0213	1	The increase tensile stresses in the surrounding concrete with pullout force until reaching the limit of tensile strength resulting in splitting and cracking failure. Thus, the bond strength increases from the increasing of tensile strength capacity of the concrete which is proportional to the concrete grade
Embedded length	0.0004	0.02	The smooth rebars have no ribs to have the mechanical interlocking to offer resistance to the force, hence once the when slip occurs the length of the embedded length have very little influence on the bond stress especially in the smooth rebars.

SNo	Bond stress	Bar Dia	Rebar Modulus	embedded	Concrete modulus	
1	1.52	8	65	150	29.128	
2	1.26	8	61.75	150	26.215	
3	1.23	8	60	150	17.476	M30
4	1.65	10	65	150	29.128	
5	1.29	10	61.75	150	26.215	
6	1.18	10	60	150	17.476	M30
7	1.92	12	65	150	29.128	
8	1.2	12	61.75	150	26.215	
9	1.28	12	60	150	17.476	M30
10	1.82	8	65	150	32.8	
11	1.26	8	61.75	150	29.52	
12	1.35	8	60	150	19.68	M40
13	1.98	10	65	150	32.8	
14	1.29	10	61.75	150	29.52	
15	1.17	10	60	150	19.68	M40
16	2.3	12	65	150	32.8	
17	1.29	12	61.75	150	29.52	
18	1.17	12	60	150	19.68	M40
19	1.82	8	65	150	34.8	
20	1.27	8	61.75	150	31.32	
21	1.13	8	60	150	20.88	M50
22	2.35	10	65	150	34.8	
23	1.29	10	61.75	150	31.32	
24	1.52	10	60	150	20.88	M50
25	2.69	12	65	150	34.8	
26	1.29	12	61.75	150	31.32	
27	1.53	12	60	150	20.88	M50
28	1.52	8	65	300	29.128	
29	1.26	8	61.75	300	26.215	
30	1.23	8	60	300	17.476	M30
31	1.65	10	65	300	29.128	
32	1.29	10	61.75	300	26.215	
33	1.18	10	60	300	17.476	M30

SUMMARY OUTPUT

Regression Statistics	
Multiple R	0.982007645
R Square	0.964339014
Adjusted R Square	0.951759662
Standard Error	0.474017402
Observations	92

Regression statistics

ANOVA

	df	*SS*	*MS*	*F*	*gnificance F*
Regression	4	534.697	133.674	594.921	2.8E-62
Residual	88	19.7729	0.22469		
Total	92	554.47			

	Coefficients	*ndard Err*	*t Stat*	*P-value*	*Lower 95%*	*Upper 95%*	*ower 98.0%*
Intercept	0	#N/A	#N/A	#N/A	#N/A	#N/A	#N/A
Bar Dia	0.00536795	0.02151	0.24951	0.80355	-0.03739	0.04812	-0.04561
Rebar Modulus	0.013643054	0.00086	15.8415	1.7E-27	0.01193	0.01535	0.0116
embedded	-0.000449035	0.00067	0.88095	0.38075	-0.00074	0.00192	-0.001
Concrete modulus	0.021136609	0.00763	2.7717	0.0068	0.00598	0.03629	0.00307

Coefficient for parameter

RESIDUAL OUTPUT

Observation	*Predicted Bond stress*	*Residuals*
1	1.62362352	-0.10362
2	1.522990229	-0.26299
3	1.33022346	-0.10022
4	1.642911005	0.00709
5	1.542277714	-0.25228
6	1.349510945	-0.16951

Figure 5.13: Regression analysis – Statistics

In the following Figures (Figure 5.14 - Figure 5.17) some of the key highlights of the regression analysis are shown using scattered plots. The line fit plots show the variation in the bond stress values with respect to the individual parameters and for both predicted data and the data from the parametric studies. It can be noted that in each of the above-mentioned Figures, the trend line of the regression analysis matches closely with the results from the numerical parametric studies. It is further noted that the embedded length affects the bond stress negatively, whereas bar diameter, rebar modulus and concrete modulus affect the bond stress positively.

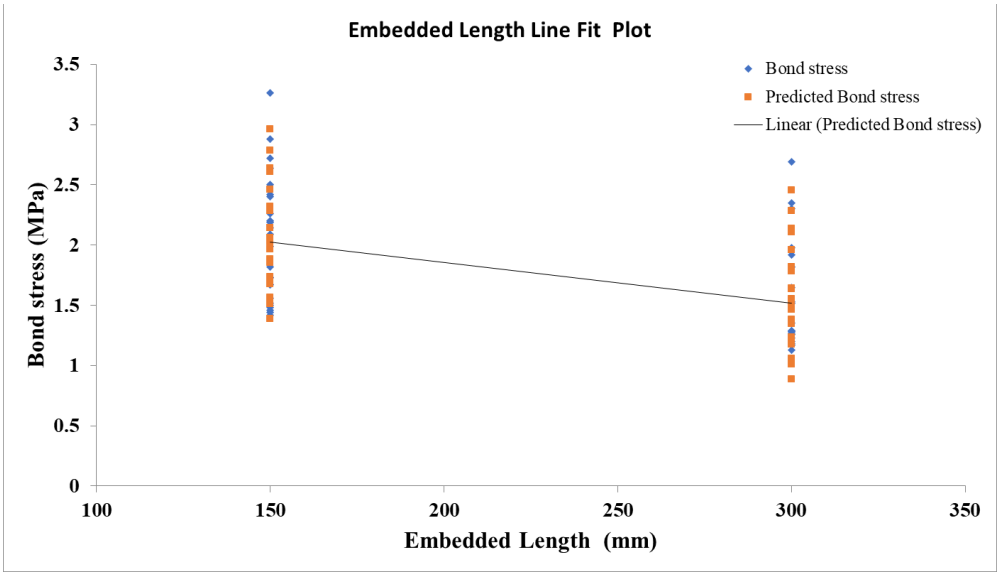

Figure 5.14: Line fit plot for the embedded length variable

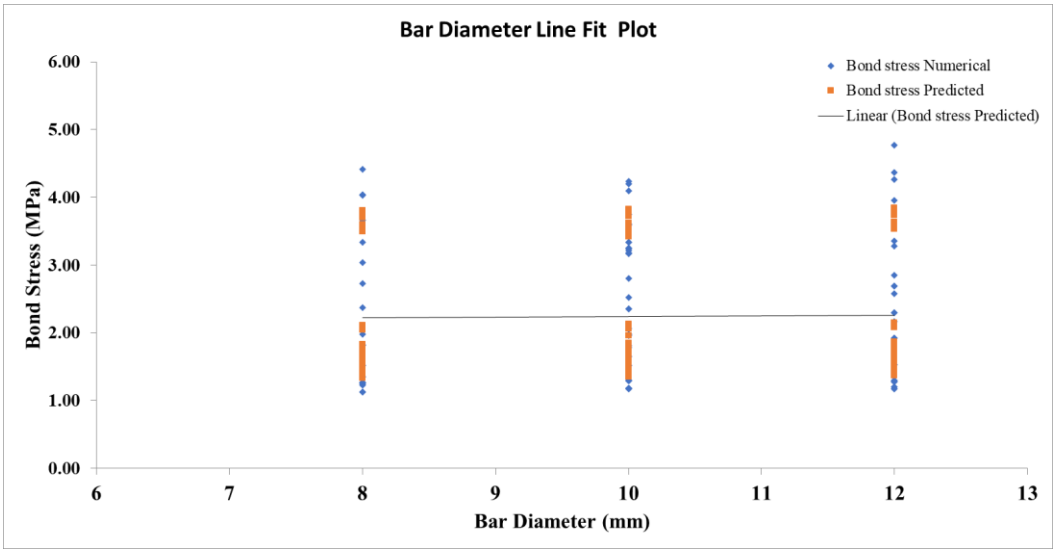

Figure 5.15: Line fit plot for the bar diameter variable

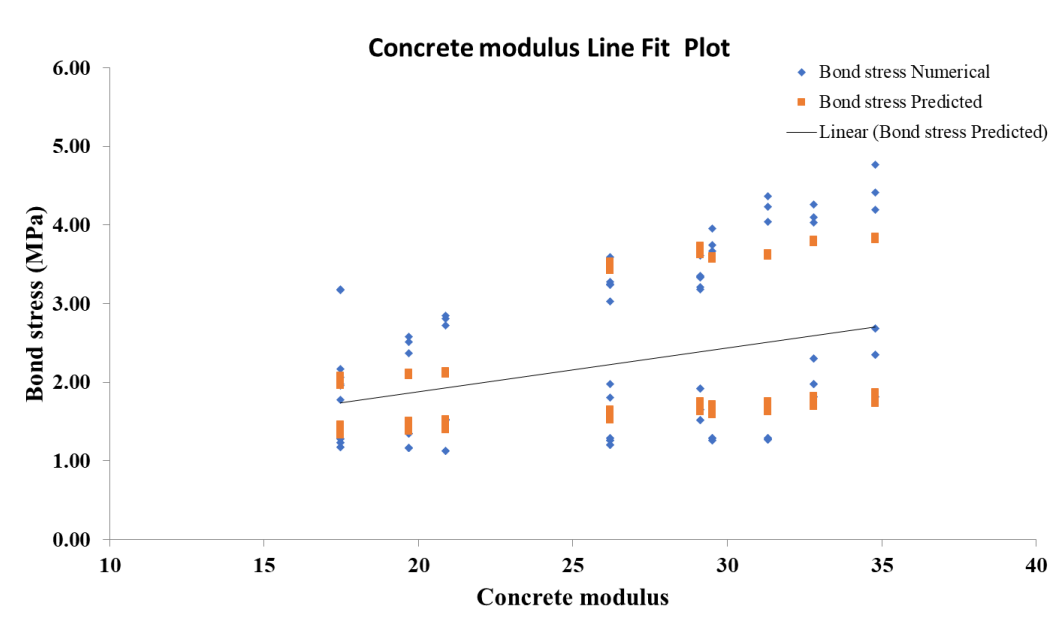

Figure 5.16: Line fit plot for the concrete modulus variable

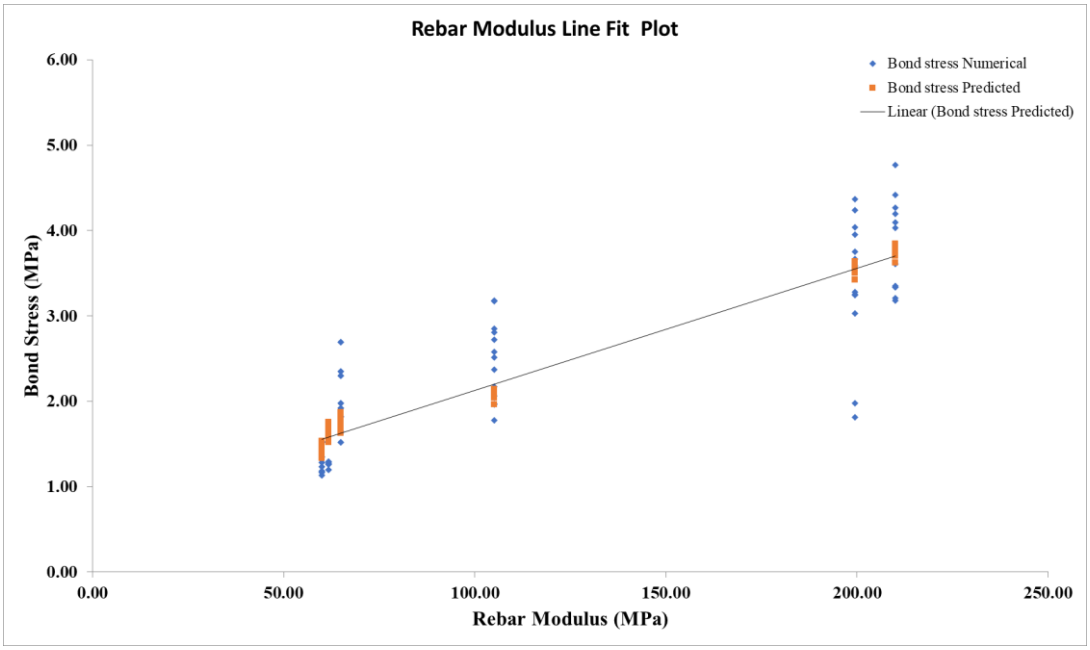

Figure 5.17: Line fit plot for the rebar modulus variable

In all the studies taken up in this work (physical, numerical, parametric and the regression) only plain surfaced rebars were considered. Whereas it is common for rebars to have ribs to provide additional bond strength. Therefore, in order to incorporate such an effect in the equation developed (Equation 5.2) using the regression analysis Rib factor is included and is calculated as shown below.

Rib factor (R_f)

Rib factor is a term which includes the details about the deformed or ribbed rebar. Rib factor is evaluated from the equation below. The rib factor is proportional to the following factors:

- Relative rib area;
- Friction;
- Embedded length; and
- Spacing of ribs.

$$R_f = \frac{\pi l_d \, F_R \, \mu}{0.056 \, (l_d - S_R)} \qquad \text{Equation 5.3}$$

where,

l_d = embedded length of rebar

μ = static coefficient of friction of rebar with concrete

S_R = spacing of transversal ribs

F_R = relative rib area

Furthermore, relative rib area (F_R) is defined as the ratio between the projected rib area and the cylindrical surface area of one rib space. F_R is based on the angle of the ribs, height of ribs and spacing of the ribs on the rebar. The relative rib area (F_R) is calculated by Equation 5.3.

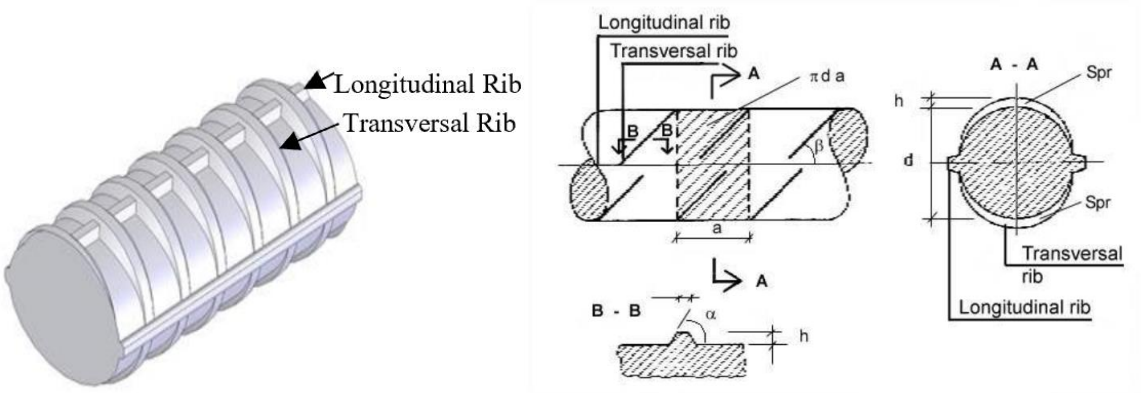

Figure 5.18: Definition of relative rib area, F_R. (Jokela 1979)

d_b = bar diameter

a = length between the transverse ribs and

S_{PR} = projective area of the transversal ribs

F_R = Relative rib area

The bond stress value for the ribbed rebar is then calculated as a product of the Rf calculated in Equation 5.3 and the sum of all the independent variables in the empirical equation (Equation 5.2). Therefore, the new empirical equation in relation to the ribbed rebars is given as follows.

$$\tau_{max} = (0.0053\, d_b + 0.0136\, R_m - 0.00044 l_d + 0.02137 E_C)\, R_f \quad \text{Equation 5.4}$$

Sand Roughness factor (K_R)

It is understood from the parametric studies that sand coating can significantly improve the bond strength. Equation 5.2 the empirical equation can incorporate the rebar surface coating e.g. sand coated rebar. To integrate the effect of the sand coated rebar sand roughness factor (K_R) is introduced (Muntasir et al. 2016) and K_R is calculated as follows

$$K_R = 0.17\, \alpha^2 - 1.92\, \alpha + 6.5 \quad \text{Equation 5.5}$$

where,

K_R = sand roughness factor

α = sand size coefficient (α = 2/sand size in mm)

The sand roughness factor includes the effect of the surface modification in improved concrete adhesion with rebar. The surface modification of sand coated rebar mainly depends on the sand grain size. The sand roughness factor increases with the increase in sand grain size coefficient. The bond stress in such cases can then be evaluated as product of the K_R and the sum of all the independent variables in the empirical Equation 5.2. Therefore, the new empirical equation in relation to the surface roughness is given as:

$$\tau_{max} = (0.0053\, d_b + 0.0136\, R_m - 0.00044 l_d + 0.02137 E_C) K_{\mathrm{R}} \quad \text{Equation 5.6}$$

A combination of sand coating along with the rib effect can then be represented as

$$\tau_{max} = (0.0053\, d_b + 0.0136\, R_m - 0.00044 l_d + 0.02137 E_C) K_{\mathrm{R}}\, R_f \quad \text{Equation 5.7}$$

For the plain rebar and no surface preparation K_R = 1 and R_f = 1; for ribbed rebar and surface coating Rf the values are derived as explained above.

Equation 5.7 is an novel empirical equation developed in this work for the quick assessment of bond stress.

Having developed an empirical equation for quick assessment bond stress it is important to validate and test the accuracy of the equation for robustness in predicting the bond stresses. The validation of the empirical is discussed next.

5.2.2 Validation of case studies for empirical equation

The empirical equation developed in this work is validated through a benchmarking study with the results compared against the results of bond stress values as experienced or predicted by:

1) the experimental studies;
2) numerical studies; and
3) experimental data from the literature.

To this extent, first the bond stress results of both the numerical and physical experiments are compared. In Figure 5.19 and Figure 5.20 a comparison is made between the maximum bond stress values as obtained from experimental tests,

numerical studies and the empirical formula for SMA and steel rebar respectively (10 mm diameter). From Figure 5.19 it can be noted that the SMA rebar at 30 mins and 60 mins fire duration for half embedded length shows the empirical equation predicted bond stresses value matches closely with the experimental results. Whereas the predicted value for the full embedded rebar for 30 min and 60 min fire duration is on the higher side (around 5 %) when compared to the numerical and experimental study results. Similar trend has been observed in Figure 5.20, where the empirical equation bond stress value is in close proximity of the numerical and experimental results for all the cases of fire duration except for 60 min fire duration. From the chart it can be noted that the bond stress values between the three types of studies mentioned above are in good agreement overall.

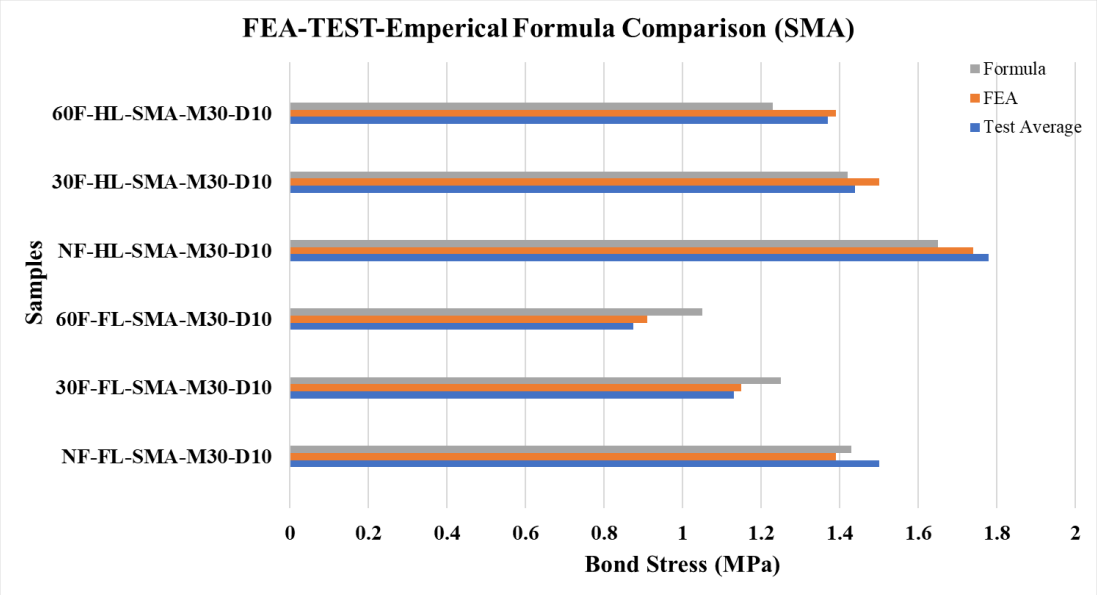

Figure 5.19: FEA-Test-Empirical formula comparison (SMA)

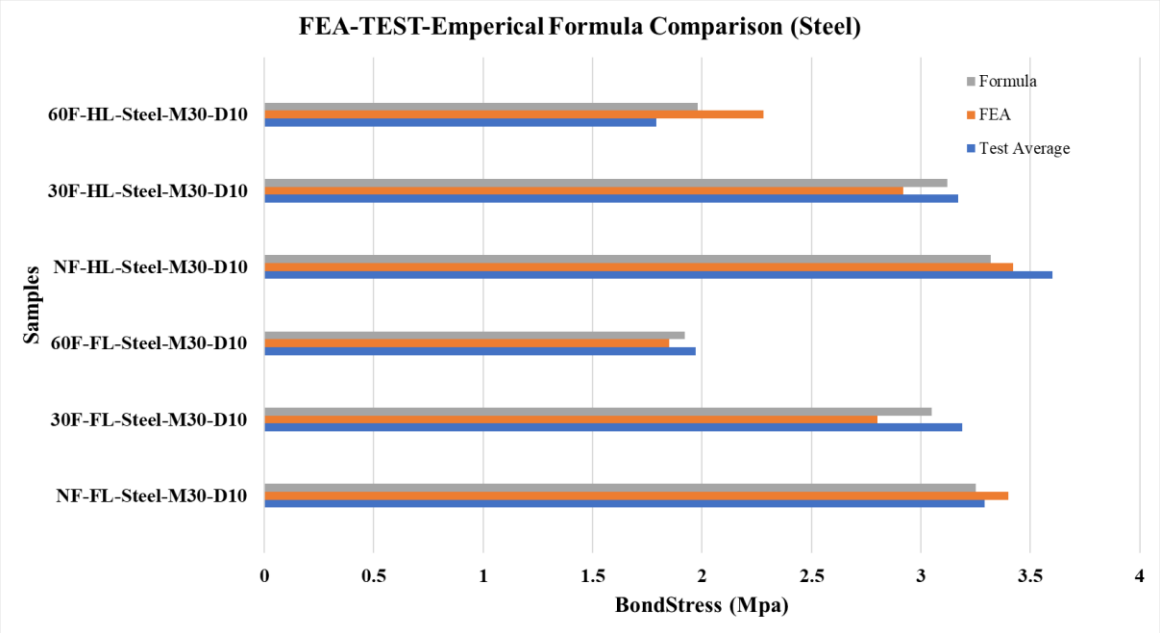

Figure 5.20: FEA-Test-Empirical formula comparison (Steel)

Having established a good agreement between the physical, numerical and the empirical formula, couple of cases from the literature was selected to test the error margins. In Case 1 (Apparao et al. 2002), a 16 mm deformed rebar with an embedment length of 150mm was pulled out from M40 Grade concrete specimen. Figure 5.21 shows the typical bond stress-slip response. The maximum bond stress value observed by the authors was 8 MPa (for unconfined specimen). For similar inputs as Apparao et al. (Table 5.4), the empirical equation developed in this work predicted the bond stress to be 8.56MPa which is in good agreement with the test results.

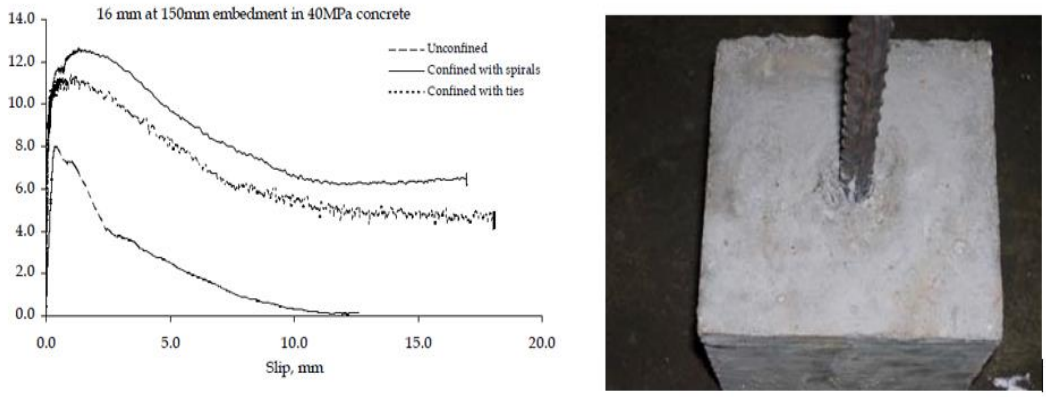

Figure 5.21: Bond-slip response pull-out test (Apparao et al. 2002)

Table 5.4: Statistics used for bond stress evaluation for pullout test (Apparao Rao)

S.No.	Description	Value
1	Bar diameter	16 mm
2	Concrete grade M40	40 MPa
3	Steel grade 415 (E)	200 GPa
4	Bar embedded length	150 mm
5	Relative rib area F_R	0.1
7	Rib spacing	7.5 mm
8	Friction between rebar concrete	0.4
9	Rib factor calculated area R_F (based on eqn)	2.36
10	**Bond stress calculated τ_{max} based on eqn**	**8.56 MPa**
11	Bond stress evaluated by experiment (Apparao et al. 2002)	8.0 MPa

In Case 2 (Katz et al. 1999), experiments on bond stress was conducted at high temperature and for steel rebar based concrete specimen. The degradation in bond stress was observed on the ribbed steel rebar at various temperatures (20°C, 105°C, 210°C and 260°C). For the same temperature conditions and the material modulus considered by Katz et al. 1999 (Table 5.5) and other parameters as identified in Table 5.6 , the empirical formula developed in this work predicted the bond stress values that were in good agreement with that of Katz et al. 1999 as shown in Table 5.7 and Figure 5.22.

Table 5.5: Material degradation used for evaluation

Temperature	Material modulus	
	Steel rebar (GPa)	Concrete (GPa)
20°C	210	35
105°C	146	31.5
210°C	126	29.75
260°C	79	12.92

Table 5.6: Statistics used for bond stress evaluation for pull-out test (Katz et al. 1999)

S.No.	Description	Value
1	Bar diameter	12 mm
2	Concrete grade M40	35 MPa
3	Steel grade	210 GPa
4	Bar embedded length	60 mm
5	Relative rib area F_R	0.12
7	Rib spacing	7.7 mm
8	Friction between rebar concrete	0.4
9	Rib factor calculated area R_f (based on equation)	2.83

Table 5.7: Comparison of bond stress (Katz et al. 1999)

Temperature	Bond Stress	
	Katz et al. 1999 Test	Empirical output
10°C	10.1	10.2
105°C	8.39	8.43
210°C	6.63	7.21
260°C	3.5	3.25

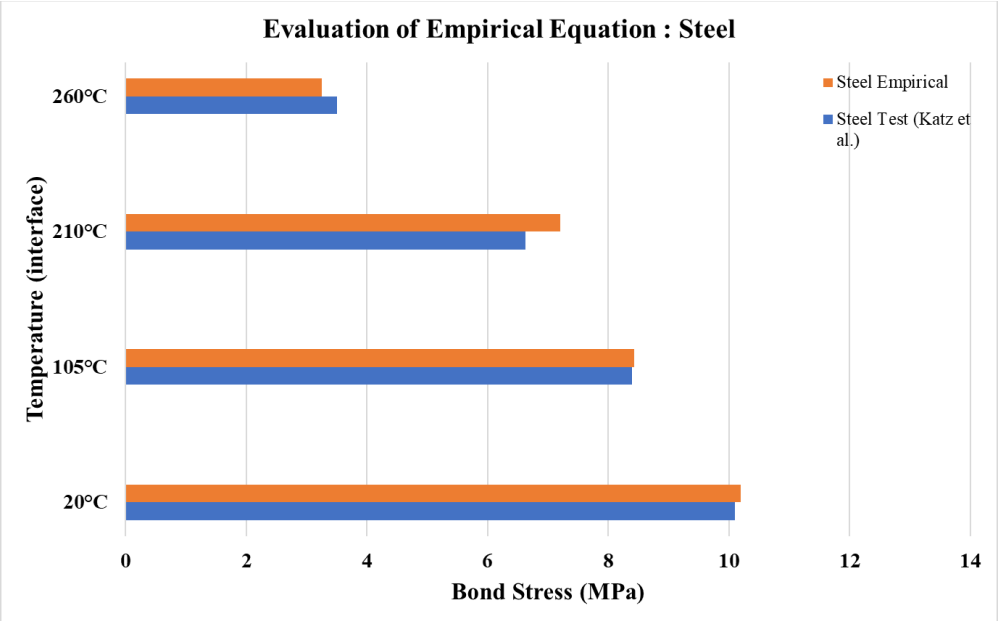

Figure 5.22: Katz Test-Empirical formula comparison (Steel Test)

5.2.3 Estimating the error margin

To understand the accuracy of the empirical formula developed in this work it was important to estimate the error margin in the bond stress values noted between the physical and numerical experiments with respect to bond stress value predicted by the empirical Equation 5.6. Table 5.8 summaries the bond stress values as observed during both physical and numerical experiments for both steel and SMA rebar-based specimens considered in this work. Also, comparison is made between the bond stress values observed in specific studies in the literature and the bond stress values predicted for similar cases by the empirical model developed in this work.

In the case of SMA based specimens, the percent error was between 1.39 % and 20.6%. The highest error was noted for the full embedded no-fire conditions test specimen (the corresponding numerical model being NF-FL-SMA-M30-D10), whereas the lowest percentage difference of 1.39 % was observed for the half embedded specimen 30min fire duration SMA test specimen (the corresponding numerical model being 30F-HL-SMA-M30-D10). Likewise, in the case of steel rebar embedded specimens, the percent error range was noted to be between 1.22% and 13.16%. The highest error was noted for the full embedded 60 min fire duration steel (60F-FL-Steel-M30-D10), whereas the lowest percentage difference of 1.22 % was observed for the full-embedded specimen no fire steel test specimen (the corresponding numerical model being NF-FL-STEEL-M30-D10).

Table 5.8: Estimation of error in empirical equation with respect to physical test and numerical model

Case study	Case	Bond Stress (MPa)			% Error with empirical equation	
		Physical test	Numerical analysis test	Empirical equation	Numerical Model	Test
SMA and Steel rebar physical test and numerical model	NF-FL-SMA-M30-D10	1.5	1.39	1.43	2.88	4.67
	30F-FL-SMA-M30-D10	1.13	1.15	1.25	8.70	10.62
	60F-FL-SMA-M30-D10	0.87	0.91	1.05	15.38	20.69
	NF-HL-SMA-M30-D10	1.78	1.74	1.65	5.17	7.30
	30F-HL-SMA-M30-D10	1.44	1.5	1.42	5.33	1.39
	60F-HL-SMA-M30-D10	1.37	1.39	1.23	11.51	10.22
	NF-FL-Steel-M30-D10	3.29	3.4	3.25	4.41	1.22
	30F-FL- Steel -M30-D10	3.19	2.8	3.05	8.93	4.39

	60F-FL- Steel -M30-D10	1.97	1.85	1.92	3.78	2.54
	NF-HL- Steel -M30-D10	3.6	3.42	3.32	2.92	7.78
	30F-HL- Steel -M30-D10	3.17	2.92	3.12	6.85	1.58
	60F-HL- Steel -M30-D10	1.79	2.28	1.98	13.16	10.61
Apparao et al.	16 mm ribbed rebar M40	8	-	8.56	-	7.00
Katz et al.	Steel rebar at 20°C	10.1	-	10.2	-	0.99
	Steel rebar at 105°C	8.39	-	8.43	-	0.48
	Steel rebar at 210°C	6.63	-	7.21	-	8.75
	Steel rebar at 260°C	3.5	-	3.25	-	7.14

From Table 5.8 it can be said that the overall percentage error is below 10% except in case of 60 min fire duration full embedded SMA test (Corresponding numerical model 60F-FL-SMA-M30-D10). The overall response of the result from the empirical equation was deemed to be acceptable thereby validating the empirical equation developed in this work. The proposed working range for the empirical equation is governed by the parameters and factors that are considered in this work. These are:

1) Temperature range - up to 900ºC;
2) SMA Materials – NiTi Alloy;
3) Bar Diameter – 8mm to 12mm;
4) Concrete grade – M30 to M50; and
5) Fire duration up to 1 hour.

The successful development of an empirical formula that can predict bond stress as established in this section thus far achieves the third and final aim (AIM3) of this research. The empirical formula is presented below.

$$\tau_{max} = (0.0053\, d_b + 0.0136\, R_m - 0.00044 l_d + 0.02137 E_C)\, R_f\, K_R \quad \text{Equation 5.8}$$

where,

τ_{max} = maximum bond strength (MPa)

E_c = Modulus of elasticity of concrete

d_b = bar diameter

l_d = embedded length

R_m = modulus of elasticity of bar

R_f = rib factor

K_R= sand roughness factor

AIM 3 Achieved

"Develop an empirical equation for quick assessment bond stress"

5.2.4 Summary of Parametric Studies and Regression Analysis

The numerical model developed in this work (in Chapter 4) to predict the bond stress in the cohesive zone was further employed in parametric studies. The parameters that are considered for the parametric studies are shown in Figure 5.23.

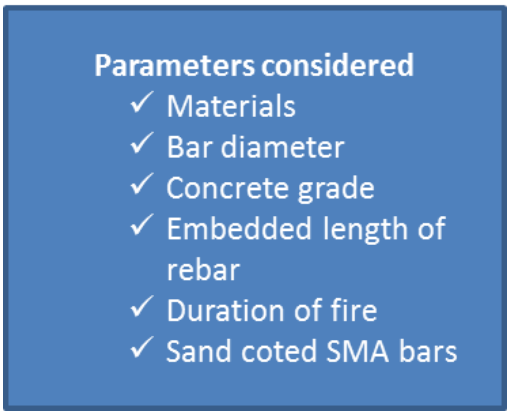

Figure 5.23: Parameters considered for further studies

In addition, the materials of various grades of concrete such as M30, M40 and M50 were considered. Three rebar types namely, the plain steel rebar, the plain SMA rebar and sand coated SMA rebar were considered. Likewise, the rebar diameters 8, 10 and 12 mm were considered. The parameter variance is shown in Table 5.9.

Table 5.9: The parameter variance

Parameters	Parameters variance
Rebar Material	SMA (NiTi) Steel
Rebar Diameter	8 mm 10 mm 12 mm
Embedded length	Half embedded Full embedded
Concrete Grade	M30 M40 M50
Duration of Fire Exposure	No Fire 30 mins 60 mins
Sand Coating (SMA)	300μ sand size

Table 5.10: Number of Parametric Numerical Simulation

	Steel Rebar		SMA Rebar		SMA Rebar with coating	
	Full Embedment		Full Embedment		Full Embedment	
Rebar Diameter (8mm)	M30	0 Fire	M 30	0 Fire	M30	0 Fire
		30 min		30 min		30 min
		60 min		60 min		60 min
	M40	0 Fire	M 40	0 Fire	M40	0 Fire
		30 min		30 min		30 min
		60 min		60 min		60 min
	M50	0 Fire	M 50	0 Fire	M50	0 Fire
		30 min		30 min		30 min
		60 min		60 min		60 min
Rebar Diameter (10mm)	M30	0 Fire	M 30	0 Fire	M30	0 Fire
		30 min		30 min		30 min
		60 min		60 min		60 min
	M40	0 Fire	M 40	0 Fire	M40	0 Fire
		30 min		30 min		30 min
		60 min		60 min		60 min
	M50	0 Fire	M 50	0 Fire	M50	0 Fire
		30 min		30 min		30 min
		60 min		60 min		60 min
Rebar Diameter (12mm)	M30	0 Fire	M 30	0 Fire	M30	0 Fire
		30 min		30 min		30 min
		60 min		60 min		60 min
	M40	0 Fire	M 40	0 Fire	M40	0 Fire
		30 min		30 min		30 min
		60 min		60 min		60 min
	M50	0 Fire	M 50	0 Fire	M50	0 Fire
		30 min		30 min		30 min
		60 min		60 min		60 min

	Steel Rebar		SMA Rebar		SMA Rebar with coating	
	Half Embedment		Half Embedment		Half Embedment	
Rebar Diameter (8mm)	M30	0 Fire	M30	0 Fire	M30	0 Fire
		30 min		30 min		30 min
		60 min		60 min		60 min
	M40	0 Fire	M40	0 Fire	M40	0 Fire
		30 min		30 min		30 min
		60 min		60 min		60 min
	M50	0 Fire	M50	0 Fire	M50	0 Fire
		30 min		30 min		30 min
		60 min		60 min		60 min
Rebar Diameter (10mm)	M30	0 Fire	M30	0 Fire	M30	0 Fire
		30 min		30 min		30 min
		60 min		60 min		60 min
	M40	0 Fire	M40	0 Fire	M40	0 Fire
		30 min		30 min		30 min
		60 min		60 min		60 min
	M50	0 Fire	M50	0 Fire	M50	0 Fire
		30 min		30 min		30 min
		60 min		60 min		60 min
Rebar Diameter (12mm)	M30	0 Fire	M30	0 Fire	M30	0 Fire
		30 min		30 min		30 min
		60 min		60 min		60 min
	M40	0 Fire	M40	0 Fire	M40	0 Fire
		30 min		30 min		30 min
		60 min		60 min		60 min
	M50	0 Fire	M50	0 Fire	M50	0 Fire
		30 min		30 min		30 min
		60 min		60 min		60 min

The bond strength of concrete for the above-mentioned variations was examined on close to 200 virtual specimens. The matrix on the number of analysis conducted in this work using the Numerical Model developed is shown in Table 5.10. Regression analysis performed on the identified parameters resulted in the development of the following empirical formula.

$$\tau_{max} = (0.0053\, d_b + 0.0136\, R_m - 0.00044 l_d + 0.02137 E_C)\, R_f\, K_R$$

This formula was tested against a case each from the physical and numerical experiments conducted in this work and two from the literature. The bond stress values predicted by the above said empirical equation were found to be in close agreement with all other studies conducted in this thesis and that from the literature. The overall error margin was found to be less than 10%.

Hence a new formula that allowed for quick estimation of the bond stress at the interface was deemed to have been developed which achieves the third and final Aim of this thesis.

The manner in which all of the Aims and objectives have been achieved is shown in the Figure 5.24. In the following Chapter the key results and findings from the physical experiments (Chapter 3), numerical experiments (Chapter 4), the parametric studies (Chapter 5) are discussed and summarised.

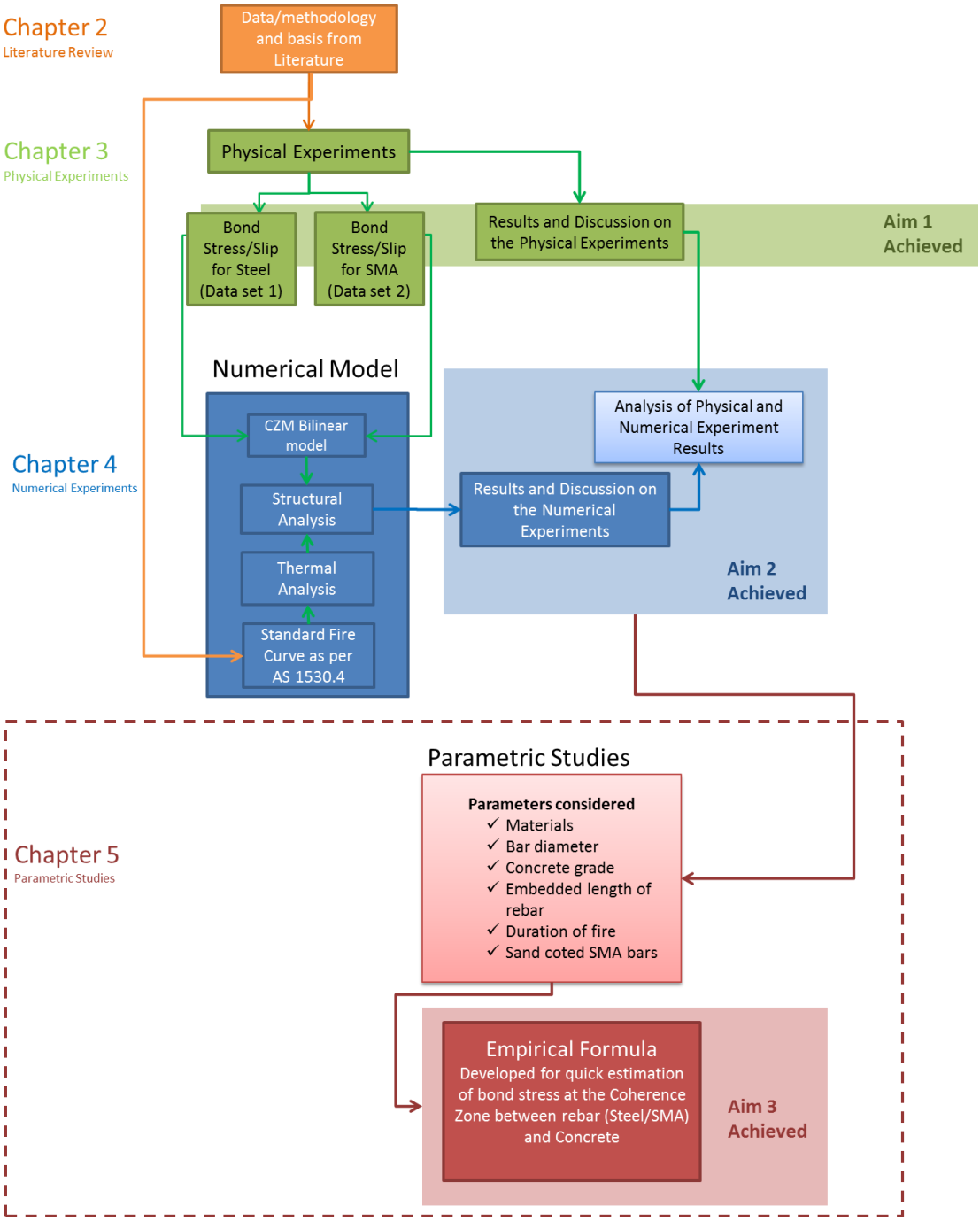

Figure 5.24: Achieving AIM 1, 2 and 3 (Results flow)

CHAPTER 6: Summary of Results and Key Highlights

6.1 Introduction

A comprehensive analysis of the results from the experimental, numerical and parametric studies conducted in this work are presented Chapters 3, 4 and 5 respectively. Key results from each of the above-mentioned Chapters are summarised in this chapter in a manner that clearly establishes and addresses each of the research question framed in Chapter 1 and the specific aims developed in Chapter 2. First the results concerning the physical experiments are discussed. More specifically, the bond stress values that were derived from the force and slip values observed during the physical experiments on 12 specimens are presented. Such a data set achieves the first aim of this thesis. Key aspects of the results from the numerical studies are then presented. The results from the physical and numerical experiments are compared to establish the validity and accuracy of the numerical model developed in this work. The validation of the numerical model achieves the second aim of this work. The validated numerical model was employed to study the influence of various parameters on the bond stress resulting in the identification of the four key parameters. These parameters were then selected to be used in the regression analysis so as to establish their weightage and relationship in estimating the bond stress. Such an effort led to the development of an empirical formula for quick evaluation of bond stress in specimens which are subjected to conditions of fire. The development of such an empirical formula achieves the final aim of this thesis.

6.2 Results – Physical Experiments

In the experimental studies, both steel and SMA were used as rebars in the concrete specimens. While steel as a rebar is well understood in the literature, the knowledge on the SMA rebar that is subjected to fire conditions seems to be very limited in the literature. For this reason, it was essential to first establish the phase transformation temperature of the SMA. It is this temperature that governs the maximum applicable

thermal load beyond which the smart material loses its shape retaining ability. In this thesis, parametric study was conducted on samples extracted from the SMA rebar using a differential scanning calorimeter (DSC 8500). The data obtained suggests that in the case of the SMA samples, the phase transformation limit increases with the increase in the heat treatment temperature. The highest phase transformation temperature for the SMA under investigation was found to be 105°C for a sample that was annealed at 400°C. Based on these observations, all of the SMA rebars used in this thesis were heat treated at 400°C.

From the results of the physical experiments, the data related to force and displacement were retrieved and applied to the equation,

$$\tau = \frac{P}{\pi\, d_b\, l_b} \qquad \text{Equation 6.1}$$

Where, τ is the calculated bond stress value. This value was calculated from the value of force (P) as noted at any given point during the pull-out test for a known embedded length l_b of the rebar and the diameter of the rebar l_b. The τ data set was further plotted against the displacement (slip) noted during the experiment to establish the maximum bond stress value (τ_t^{max}) and other parameters of concern such as tangential displacement (δ_t^*), Ratio (ratio of δ_t^* to δ_t^c) and non-dimensional weigh parameter. The process was repeated for 24 specimens (12 with steel rebars and 12 with SMA rebars) and the corresponding data on τ vs displacement was plotted. In total there were 24 specimens that were tested. The summary of the maximum bond stress values (τ_t^{max}) for each of the 24 specimens tested in this work is presented in Table 6.1 and Table 6.2.

The failure modes were examined and documented for the validation of the numerical model developed in this thesis as part of achieving AIM 2. An important observation was made in the process of analysing the specimens during the failure analysis. The specimens with SMA rebar all pulled out clean from the concrete during the pull-out tests as compared to the specimens with steel rebar. This behaviour is attributed to the smooth surface finish of the SMA rebars. This also indicated that the bond stress

of SMA rebar specimen was lesser as compared to a specimen of similar nature but with a steel rebar.

The bond stress values between SMA-concrete and steel-concrete specimens as calculated from the force and other values as explained earlier for each of the specimens is tabulated in Table 6.1 and Table 6.2 respectively and are presented in Chapter 3 and are shown in this section for the quick reference. It could be noted that there are 2 tests for each specimen type. The tests were duplicated to get the average values.

Table 6.1: Summary of data on SMA-concrete rebar pull-out tests

Specimen Tested	Rebar Material	Fire exposed duration (mins)	Embedded Length (mm)	Concrete Grade	Force (kN)	Max Bond Stress (Mpa)
NF-FL-E1-SMA	SMA	No Fire	300	M30	14.23	1.51
NF-FL-E2-SMA	SMA	No Fire	300	M30	14.04	1.49
30F-FL-E1-SMA	SMA	30	300	M30	11.12	1.18
30F-FL-E2-SMA	SMA	30	300	M30	10.18	1.08
60F-FL-E1-SMA	SMA	60	300	M30	8.95	0.95
60F-FL-E2-SMA	SMA	60	300	M30	7.5	0.8
NF-HL-E1-SMA	SMA	No Fire	150	M30	8.5	1.82
NF-HL-E2-SMA	SMA	No Fire	150	M30	8.24	1.75
30F-HL-E1-SMA	SMA	30	150	M30	6.5	1.39
30F-HL-E2-SMA	SMA	30	150	M30	7.02	1.49
60F-HL-E1-SMA	SMA	60	150	M30	6.36	1.35
60F-HL-E2-SMA	SMA	60	150	M30	6.55	1.39

Table 6.2: Summary of data on steel-concrete rebar pull-out tests

Specimen Tested	Rebar Material	Fire exposed duration (mins)	Embedded Length (mm)	Concrete Grade	Force (kN)	Max Bond Stress (Mpa)
NF-FL-E1-Steel	Steel	No Fire	300	M30	31.53	3.34
NF-FL-E2- Steel	Steel	No Fire	300	M30	30.7	3.25
30F-FL-E1-Steel	Steel	30	300	M30	30.01	3.18
30F-FL-E2-Steel	Steel	30	300	M30	30.3	3.21
60F-FL-E1-Steel	Steel	60	300	M30	18.7	1.98
60F-FL-E2-Steel	Steel	60	300	M30	18.5	1.96
NF-HL-E1-Steel	Steel	No Fire	150	M30	17.01	3.61
NF-HL-E2-Steel	Steel	No Fire	150	M30	16.93	3.59
30F-HL-E1-Steel	Steel	30	150	M30	14.95	3.17
30F-HL-E2-Steel	Steel	30	150	M30	15.01	3.18
60F-HL-E1-Steel	Steel	60	150	M30	8.62	1.81
60F-HL-E2-Steel	Steel	60	150	M30	8.41	1.78

The above two complete data sets record the maximum force and the corresponding maximum bond stress for the specified test case. Following charts of bond stress vs bond slip were plotted one each for half and full embedded steel rebar inside concrete respectively (Figure 6.1 a, b) and another similar set for half and full embedded SMA rebar inside concrete respectively (Figure 6.2 a, b).

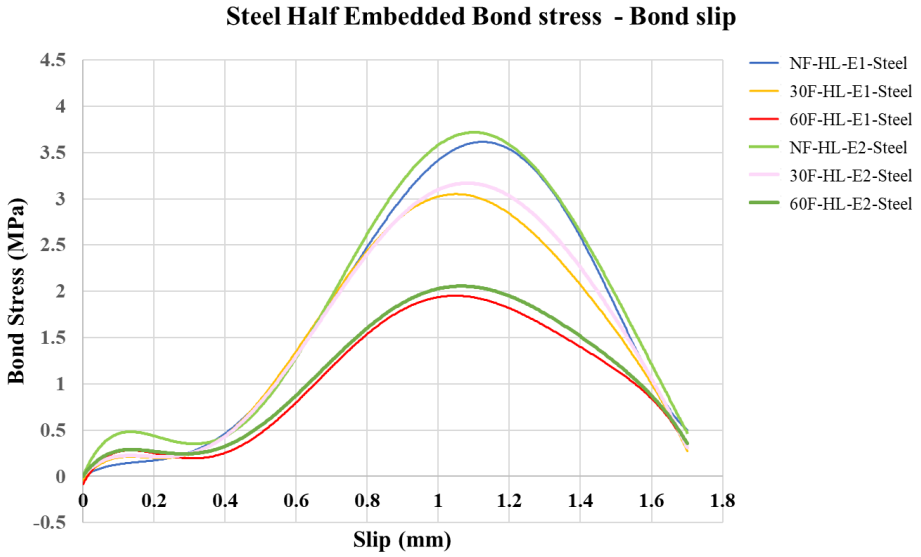

(a) Steel-Concrete (half embedded)

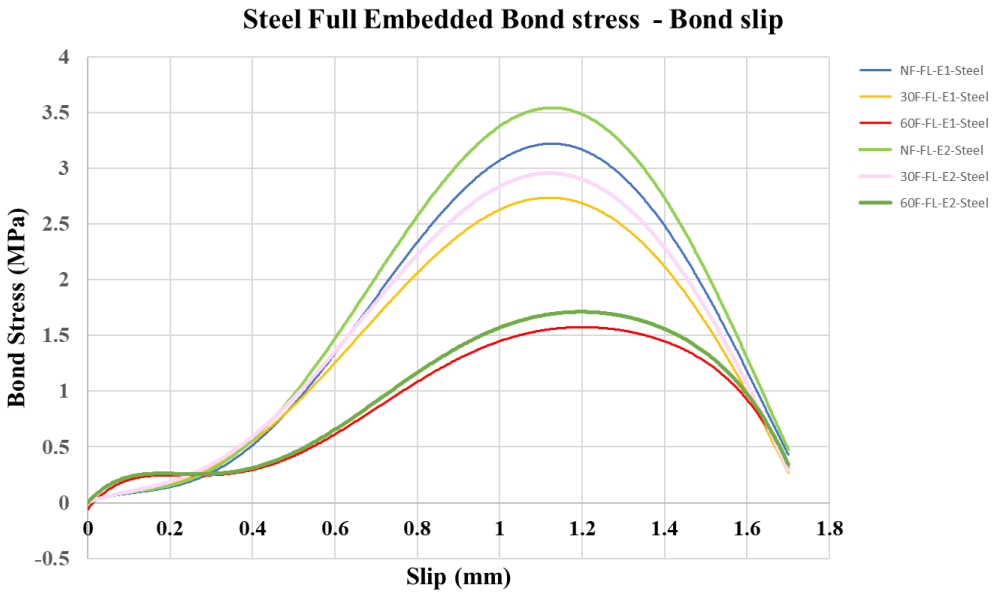

(b) Steel-Concrete (full embedded)

Figure 6.1: Steel-Concrete a) half embedded and b) full embedded, bond stress at various conditions and parameters

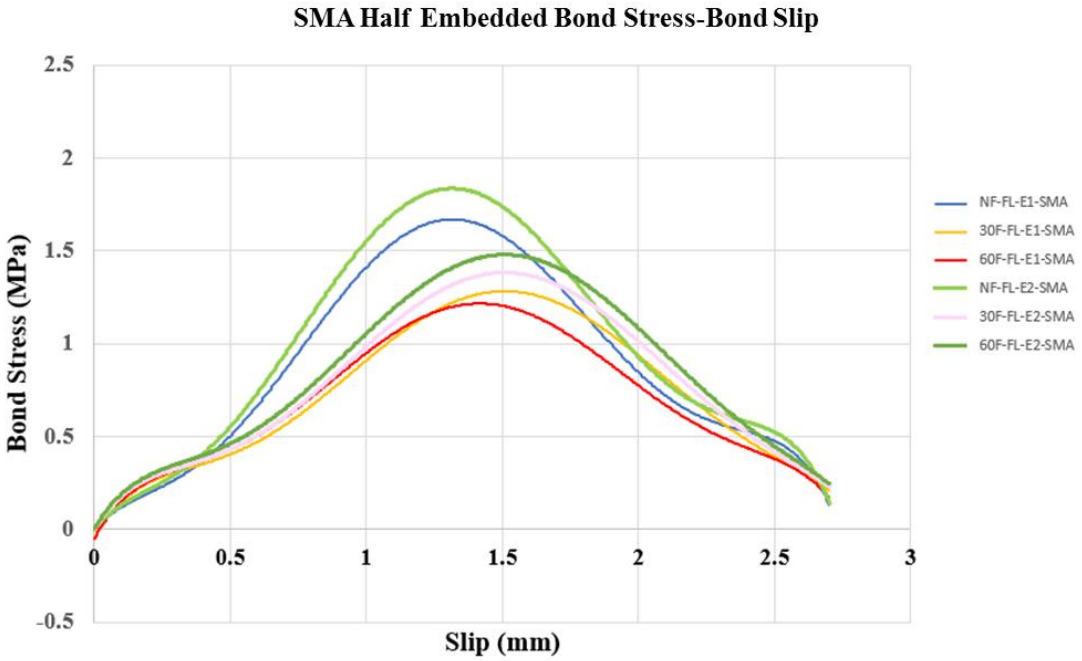

(a) SMA-Concrete (half embedded)

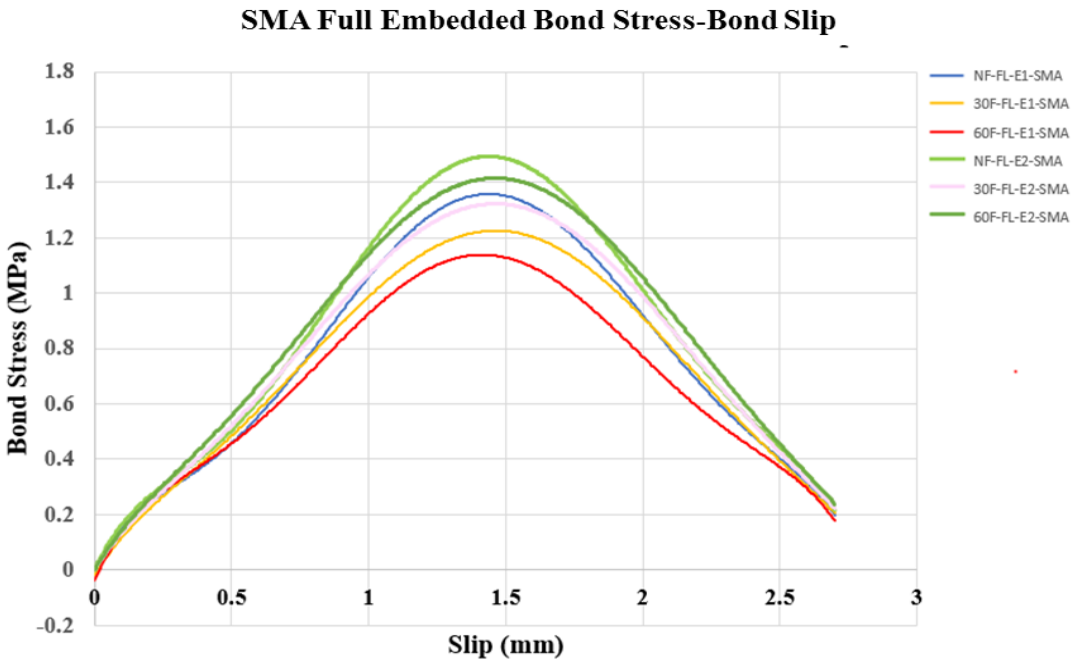

(b) SMA-Concrete (full embedded)

Figure 6.2: SMA-Concrete a) half embedded and b) full embedded, bond stress at various conditions and parameters

A data set created as shown in Table 6.3 for all the specimens considered in this work provides all of the parameters required to define the respective interface material of the cohesive zone (CZM Bilinear model) in the numerical studies. The information generated on the parameters as presented in Table 6.3 contributes greatly in numerical model method of analysing bond stress between SMA-concrete and steel-concrete rebars that are exposed to high temperatures. As numerical model presented now takes into account the non-linear structural effects that are influenced by thermal loading. The absence of such temperature specific data and the model related information in the literature made the requirement of physical experiments absolute necessary in this work. The experimental studies conducted and the resulting data set generated achieved AIM1 of this thesis.

Table 6.3: Displacement, Ratio and Non dimensional weigh parameter

Sno.	Specimen Name	Max. Traction (τ) MPa	Traction Displacement (δ*) mm	Ratio (δ*)/(δc)	Weight Parameter
1	NF-FL-E1-SMA	1.51	1.4	0.52	1
2	NF-FL-E2-SMA	1.49	1.45	0.54	1
3	30F-FL-E1-SMA	1.18	1.5	0.56	1
4	30F-FL-E2-SMA	1.08	1.65	0.61	1
5	60F-FL-E1-SMA	0.95	1.5	0.56	1
6	60F-FL-E2-SMA	0.8	1.5	0.56	1
7	NF-HL-E1-SMA	1.82	1.3	0.48	1
8	NF-HL-E2-SMA	1.75	1.3	0.48	1
9	30F-HL-E1-SMA	1.39	1.5	0.56	1
10	30F-HL-E2-SMA	1.49	1.5	0.56	1
11	60F-HL-E1-SMA	1.35	1.4	0.52	1
12	60F-HL-E2-SMA	1.39	1.55	0.57	1
13	NF-FL-E1-Steel	3.34	1.15	0.67	1
14	NF-FL-E2-Steel	3.25	1.15	0.67	1
15	30F-FL-E1-Steel	3.18	1.15	0.67	1
16	30F-FL-E2-Steel	3.21	1.15	0.67	1
17	60F-FL-E1-Steel	1.98	1.15	0.67	1
18	60F-FL-E2-Steel	1.96	1.05	0.61	1
19	NF-HL-E1-Steel	3.61	1.15	0.67	1
20	NF-HL-E2-Steel	3.59	1.15	0.67	1
21	30F-HL-E1-Steel	3.17	1.05	0.61	1
22	30F-HL-E2-Steel	3.18	1.1	0.67	1
23	60F-HL-E1-Steel	1.81	1.1	0.67	1
24	60F-HL-E2-Steel	1.78	1.1	0.67	1

The generation of the above-mentioned data set achieves Aim1 of this thesis.

AIM 1 Achieved

"Conduct experimental studies to understand the bond stress behaviour of concrete-steel rebar and concrete-SMA rebars that are subjected to high temperature"

6.3 Results – Numerical Studies

Following the generation of the required data sets on the bond stress of both SMA and steel rebar based concrete specimens the thesis set to explore the possibility of applying such data to a novel method of analysing concrete-rebar interface (that is subjected to fire conditions) using numerical simulations. It is for the first time that such a study was attempted and a successful development of the numerical model contributes greatly to the advancement of knowledge in the literature.

The numerical study involved the study of bond stress between two sets of specimens 1) involving steel rebar and 2) involving SMA rebar. The numerical studies (as explained in Chapter 4) in thesis were divided into two major sections a) thermal analysis b) non-linear structural analysis. To this extent, in order to establish the thermal profile of the specimens, thermal analysis of the specimen was carried out. Since materials remained the same and the thermal properties remain the same over a period of 60min, only one thermal analysis was carried out. The results are discussed next following which the results from the non-linear structural analysis is discussed. The thermal response is noted for three-time intervals as in the previous case with steel rebar:

4. At start under no fire condition;
5. At 30mins; and
6. At 60mins.

An example of the results of the thermal analysis on SMA rebar-based specimen heated for 60min is shown in Figure 4.96. Such thermal profiling studies were taken up on specimen with steel rebar too for conformation of the thermal profile generated. The similarities in the trend in both the concrete-steel rebar and in the case of concrete-SMA rebar were found to be very close. In both the cases that were tested for the thermal response the rebar temperatures were close to 400°C. In fact, the steel and SMA rebars had reached a temperature of 374°C and 383°C respectively.

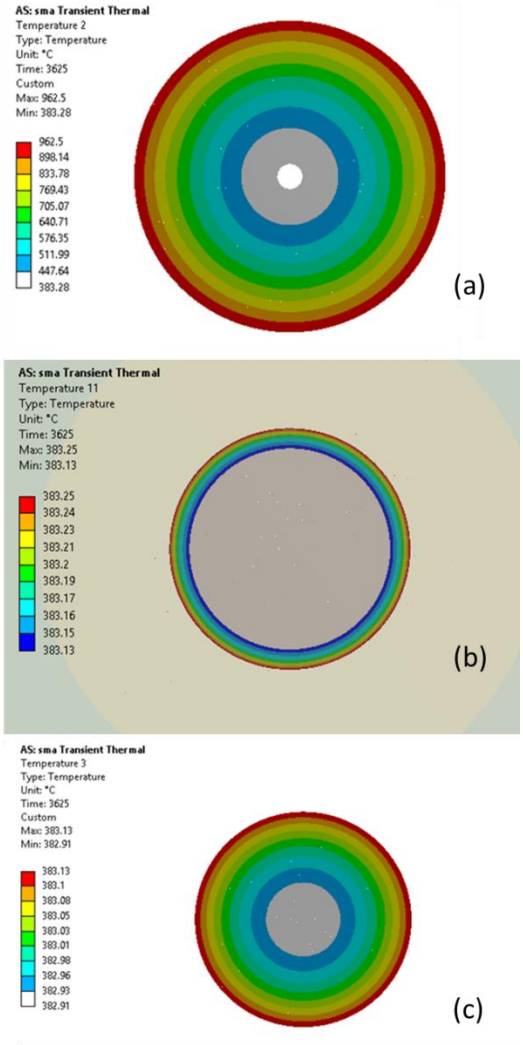

Figure 6.3: 2D Radial Thermal profile at 60min of thermal exposure (a) Concrete (b) Concrete-SMA rebar interface and (c) SMA Rebar

Equipped with the thermal profile and the data sets from Table 6.3 the cohesive zone model (CZM) and thermal parameters were defined for the nonlinear structural analysis. This is the first time such a CZM is being employed that takes into account the SMA related data and combines it with the thermal and structural loading to predict the bond stress at the interface of the concrete and rebar specimen. The observations made on the SMA rebar Concrete specimen is discussed below.

In the pull-out study conducted in the numerical work (non-linear structural analysis), it is the pulling force on the rebar that creates the required pull effect and as a consequence there is displacement that happens on the bar. The quantum of displacement is determined based on the surface roughness, material, bonding with

concrete to name a few. The above-mentioned parameters were taken into account as part of the numerical model setup.

It is evident that the elements in concrete were subjected to displacement on all three fire exposure durations to varying degree and in both SMA and steel rebar specimens. It was also evident that the displacement of elements was more pronounced as the concrete becomes softer due to longer exposure to the thermal loading in both the SMA and Steel rebar-based specimens. The displacement was more noticeable in the case of steel rebar as compared to the SMA rebar-based specimens. Such an effect is bound to result in cracks in the steel rebar specimen if this situation was to present itself in real life scenario. The smooth pull-out of the SMA rebar can be explained by its smooth surface finish as compared to steel rebar. The results from SMA rebar specimen are shown in Figure 6.4. The bond stress observed for this specimen is presented in Figure 6.5. Similar data sets were generated for each of the 12 specimens considered in the numerical studies.

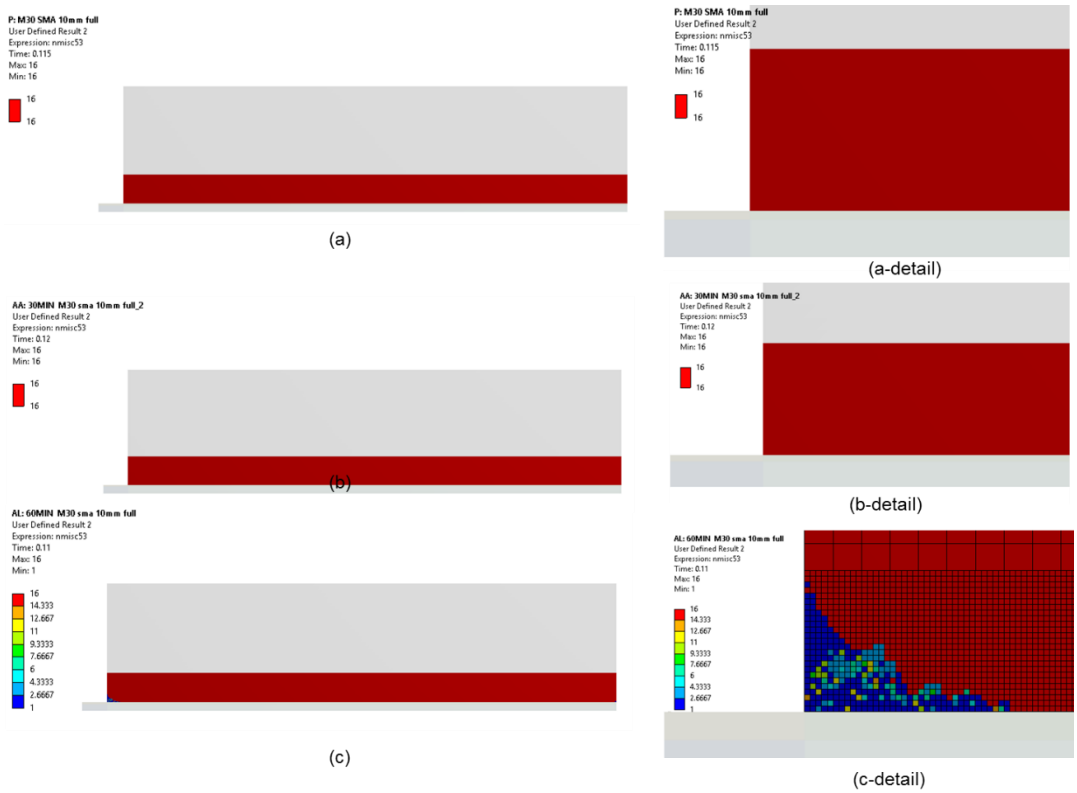

Figure 6.4: Axial section view of Full insert SMA rebar Concrete interface element displacement profile for a) No Fire b) 30min of Fire exposure (c) 60min of Fire exposure and for respective loads shown in Figure 4.81

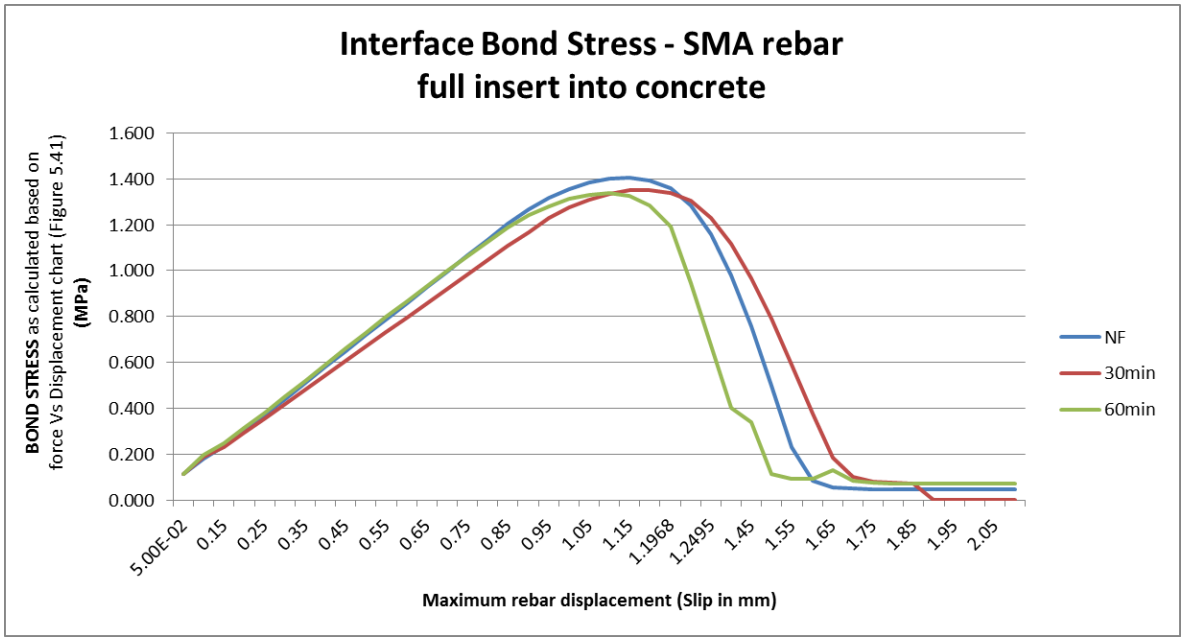

Figure 6.5: Bond Stress at interface from Numerical Analysis for full SMA rebar insert under No Fire, 30min and 60min of Fire exposure for respective loads shown in Table 4.14

To understand the accuracy of the numerical model developed in this work it was important to compare and contrast the results of the physical and numerical experiments. This aspect is dealt with next.

6.4 Compare and contrast experimental Vs numerical results

In this section, a comparison is made between various aspects of the physical experiments (Chapter 3) and Numerical studies (Chapter 4). Essentially, the accuracy of the novel numerical method developed in this work is established by comparing:

a) The thermal loading conditions;
b) Failure mode analysis;
c) Normalised bond stress: response of specimen to thermal and structural loading;
d) Bond Stress values comparison; and
e) Estimating the error margin.

6.4.1 *The thermal input conditions*

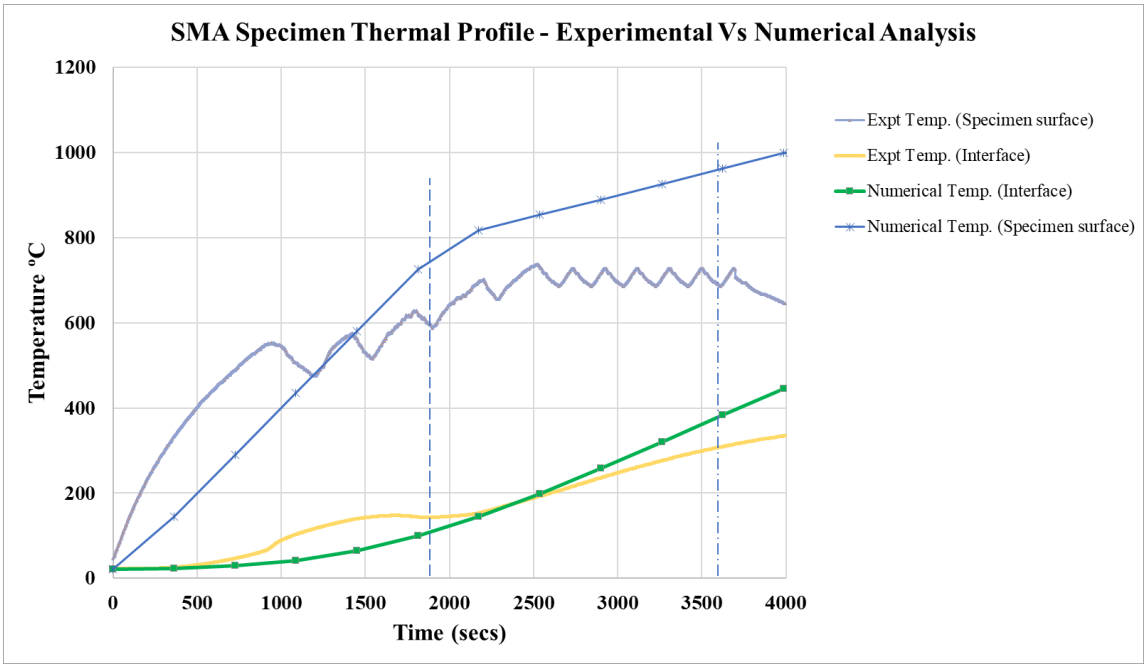

Figure 6.6: Temperature profile SMA rebar full insert: Experimental Vs Numerical

In order to provide a level comparison, it is essential to first establish that the input conditions are the same for both experiments and numerical analysis. Furthermore, it is important to establish that the temperature at the core of the specimens (interface) is in agreement. Figure 6.6 provides information on the above-mentioned topics. In both the experiments and numerical analysis, the temperature can be seen to have ramped up to heat the specimen surface; the response of the specimen is noted at about 3600sec (60min). It can be noted that at about 60min, there is very close agreement of the temperature values between the physical experiment and the numerical study. In this case the temperature of the SMA rebar at the interface is 380°C and 330°C for experiment and numerical studies respectively. Having established that the numerical model responds to thermal loading in similar ways to the specimen from the physical experiments, it was time to examine the numerical model and the physical specimen for failures.

6.4.2 Failure mode analysis

When a specimen is subjected to thermal and structural loading it is bound to respond in ways that are unique to the specimen. In this section, the failure modes of similar specimens from both physical experiments and the corresponding model from the numerical study are compared.

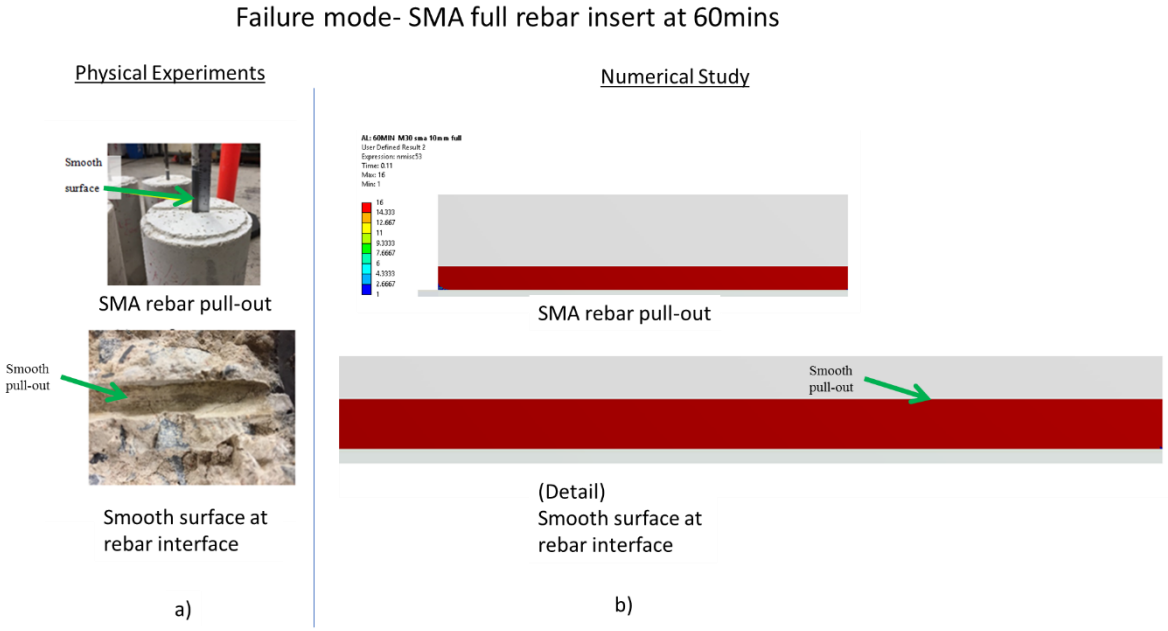

Figure 6.7: Failure Modes: Pull-out test under high temperature a) physical experiment and b) numerical study

A comparison of SMA rebar that is fully embedded to concrete and that was subjected to pull-out test both experimentally and numerically is shown in Figure 6.7. In the physical testing of the specimen, at about 60mins of thermal exposure and the specimen was subjected to the pull-out test. The specimen was analysed for cracks and the results are shown in Figure 6.7 (a) and (b). It can be noted from these figures that the rebar had smoothly pulled out of the specimen without cracking the concrete. The interface looks smooth and clean without any rupture. This evident from any lack of concrete residue on the SMA rebar. In order to establish the consistency of the numerical model/method developed in this work it is essential to observe similar results on the corresponding models used in numerical study. In Figure 6.7 (b) the results from numerical study are presented. The results of the numerical study too predict a smooth pull-out of the rebar as observed in the case of physical experiments.

This reiterates the accuracy of the novel method developed to analyse bond stress as a response to both thermal and structural loading.

Having established that for similar thermal and structural inputs the specimen in both experimental and numerical study responded in similar ways it was decided to study the bond stress at the interface of all the specimens that were tested in both experimental and numerical studies; the purpose of this thesis.

6.4.3 Normalised bond stress: response of specimen to thermal and structural loading

To understand the mechanism of bond stress of SMA rebar in comparison with steel rebar and to plot the results for different grade of the concrete in the same plot, as normalised bond stress is used. The normalised bond stress is calculated using the maximum bond stress as listed in Table 3.8 & Table 3.9 and then dividing it by the flexural strength of the particular grade concrete (maximum bond stress / √Fc). Figure 6.8 shows the normalised bond stress obtained from test result from two sets of experiments (E1 & E2) and numerical simulation for different tested fire conditions.

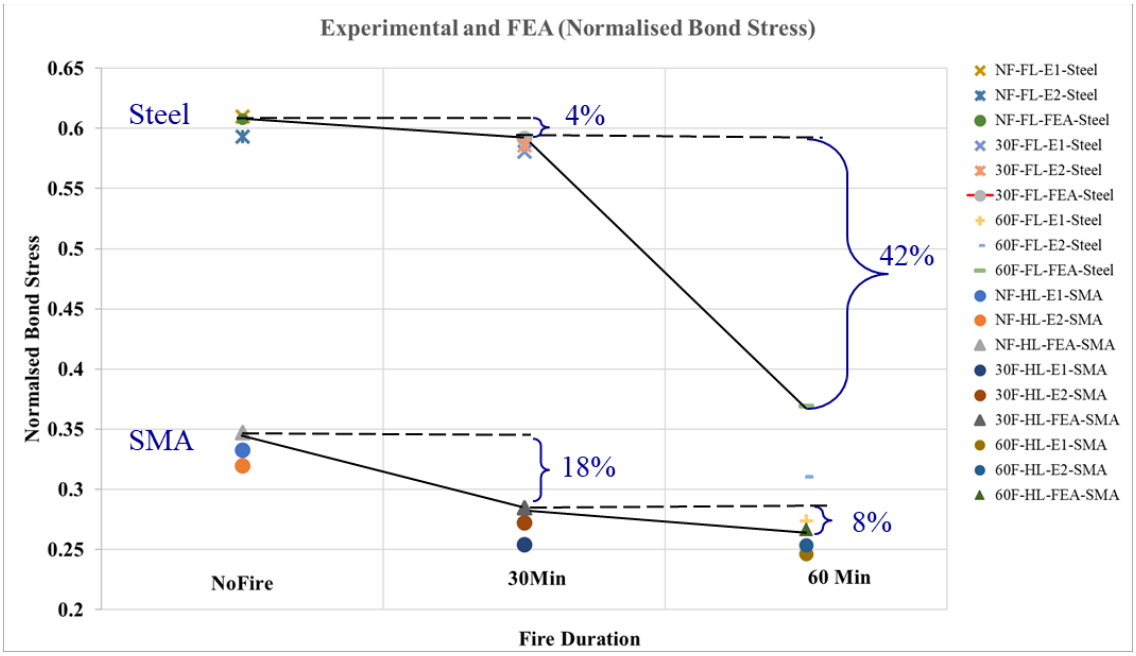

Figure 6.8: Experimental and FEA correlation

Figure 6.8 shows the plot for concrete grade M30, SMA and steel rebar of 10mm and under three different aforementioned fire conditions and for both physical experiments (denoted by “E” followed by a number in the specimen name) and numerical studies (denoted by “FEA” in the specimen name). It can be observed that there is good correlation between the experimental test results and numerical simulation results. The bond stress of steel is generally higher because of the surface friction and material modules of elasticity of the steel at normal temperature. It can also be noted that as the temperature the concrete specimens with steel rebars increases as response to thermal loading, the bond stress value begins to drop. For example, at around 30 minutes (the interface temperature is around 110°C as discussed earlier in this Chapter) there is 4% reduction in steel rebar bond stress and as heating of the specimens continues to about 60min (where the concrete-rebar steel interface reaches a temperature of 400°C), the bond stress drops quite significantly by 42%. This can be attributed to the significant reduction in the elastic modulus of steel at such temperatures.

On the other hand, in the case of concrete with SMA rebars shown, an 18% reduction in SMA rebar concrete bond stress at about 30min and about 8% at about 60min of fire exposure conditions. This can be explained by the fact that at about 400°C, the SMA rebars undergoes austenite phase transformation and gains stiffness because of increased modulus of elasticity. Interestingly, the overall drop in the bond stress at 60 minutes fire duration in SMA bar is not as significant as steel bar (refer to Figure 6.8).

In all of the above cases, it can be noted that the normalised bond stress values noted for a particular case in the physical experiment is in very close and tight agreement with the bond stress prediction made by the numerical experiments. Such a situation further validates and confirms the effectiveness of the novel non-destructive numerical method of testing a specimen’s bond stress developed in this work.

The AIM 2 of this research is to study the bond stress at the interface of the concrete and rebar through numerical methods, where in the thermal loading is considered as part of the non-linear structural studies on the specimen that is subjected to fire

exposure. The stress figures achieved via the numerical model developed in this work was compared to the corresponding data set from the experiments carried out on physical experiments (in Chapter 3).

6.4.4 Bond Stress comparison- Numerical Vs Physical Experiments

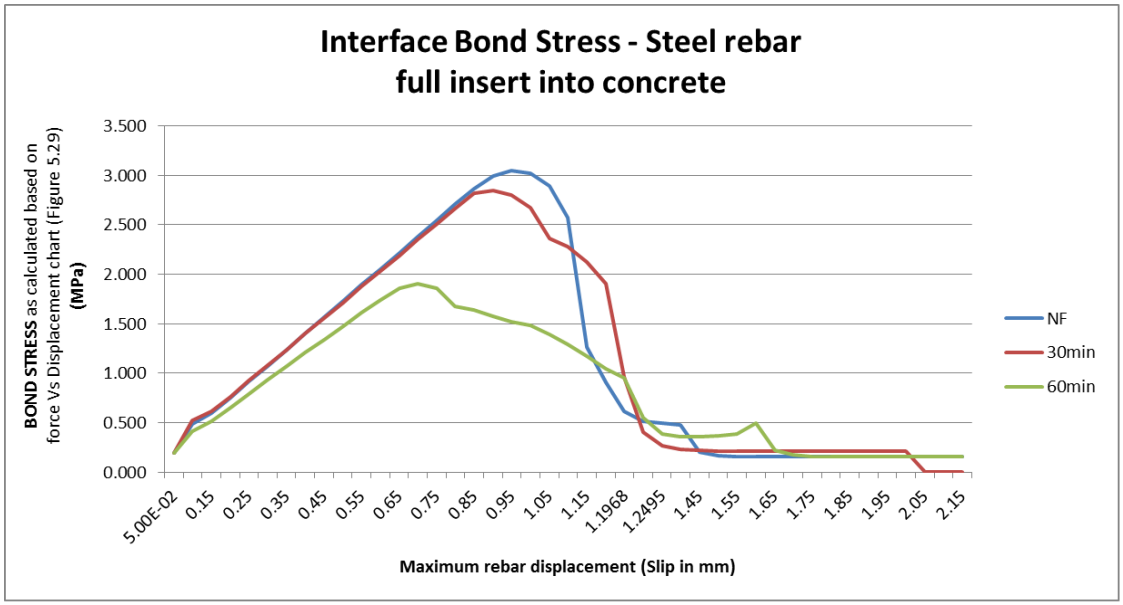

(a)

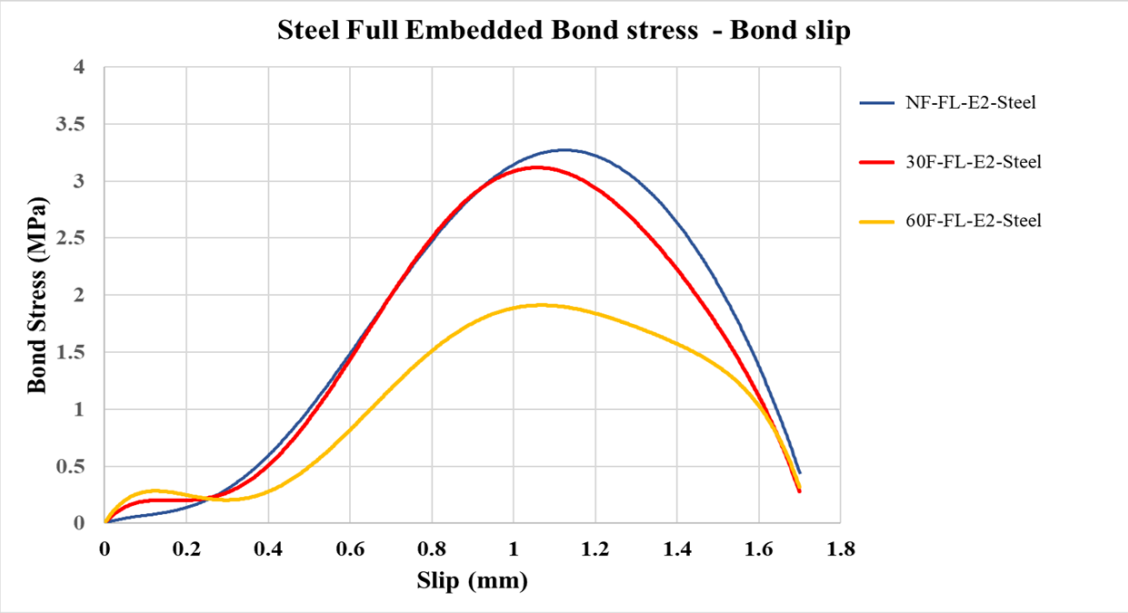

(b)

Figure 6.9: Comparison of Bond Stress values from (a) Numerical experiments results and (b) Physical experiment results

From Figure 4.74 it can be said that the bond stress values achieved via the numerical experiments were found to be in close agreement with the corresponding values from the physical experiments. For example, the bond stress value between a steel rebar inserted fully into the concrete for No fire condition was found to be 3.5 MPa and 3.1 MPa for physical experiment and numerical studies respectively. Likewise, it can also be noted that the peak stress occurred at about 1.05mm slipped (displacement of the rebar). The results can be found to be in such close agreement for the two fire conditions tested (30min and 60min) too. In the case of 30min fire exposure, the maximum Bond Stress value noted was just under 3 MPa in both physical experiments and numerical experiments. Likewise, the maximum stress peaked at about 1mm slip value (displacement of rebar) in both physical and numerical experiments. Such a close match in values between physical and numerical experiments undoubtedly validated the numerical model/method developed in this work. The error margin is estimated.

6.4.5 Estimating the error margin

To understand the accuracy of the numerical model developed in this work it was important to estimate the error margin in the bond stress values noted between the physical and numerical experiments. In Table 6.4, the bond stress values as observed during both physical and numerical experiments for both (a) steel and (b) SMA rebar-based specimens considered in this work is presented. Two tests were carried out for each specimen type and an average bond stress value is adopted to be compared with the experimental results.

In the case of SMA-based specimens (Table 6.4 a) the percent error range was noted to be between 1.4% and 7.3%. The highest error was noted for the full embedded no-fire conditions NF-FL-E2-SMA (the corresponding numerical model being NF-FL-SMA-M30-D10), whereas the lowest percentage difference of 1.4 % was observed for the half embedded specimen 60F-HL-E2-SMA (the corresponding numerical model being 60F-HL-SMA-M30-D10). Likewise, in the case of steel rebar embedded specimens (Table 6.4 b), the percent error range was noted to be between 5% and 27%. The highest error was noted for the full embedded no-fire conditions 60F-HL-E2-

Steel (the corresponding numerical model being 60F-FL-Steel-M30-D10), whereas the lowest percentage difference of 5 % was observed for the half-embedded specimen 60F-HL-STEEL-M30-D10. The higher value of 27% can be discarded as a discrepancy as can be noted in Figure 6.8. Based on the information provided in Table 6.4 (a) and (b) it can be said that the overall percentage error is below 10% and deemed to be acceptable thereby validating the numerical method developed in this work.

Table 6.4: Estimation of error in bond stress between results from physical and numerical experiments for (a) SMA and (b) Steel rebar

Specimen Name	Fire Duration	Embedded Length	Force (kN)			Max. Bond Stress			% Error
			Expt. test	Avg.	Numerical	Expt. test	Average	Numerical	
NF-FL-E1-SMA	No Fire	300 mm	14.23	14.13	13.10	1.51	1.5	1.39	7.3
NF-FL-E2-SMA			14.04			1.49			
30F-FL-E1-SMA	30 Mins	300 mm	11.12	10.65	12.25	1.18	1.13	1.15	1.7
30F-FL-E2-SMA			10.18			1.08			
60F-FL-E1-SMA	60 Mins	300 mm	8.95	8.22	10.36	0.95	0.875	0.91	4.0
60F-FL-E2-SMA			7.5			0.8			
NF-HL-E1-SMA	No Fire	150 mm	8.5	8.37	8.2	1.82	1.785	1.74	2.5
NF-HL-E2-SMA			8.24			1.75			
30F-HL-E1-SMA	30 Mins	150 mm	6.5	6.76	7.06	1.39	1.44	1.5	4.1
30F-HL-E2-SMA			7.02			1.49			
60F-HL-E1-SMA	60 Mins	150 mm	6.36	6.45	6.59	1.35	1.37	1.39	1.4
60F-HL-E2-SMA			6.55			1.39			

(a)

Specimen Name	Fire Duration	Embedded Length	Force (kN)			Max. Bond Stress			% Error
			Expt. test	Avg.	Numerical	Expt. test	Average	Numerical	
NF-FL-E1-Steel	No Fire	300 mm	31.53	31.11	32.04	3.34	3.24	3.4	6.0
NF-FL-E2-Steel			30.7			3.25			
30F-FL-E1-Steel	30 Mins	300 mm	30.01	30.15	26.39	3.18	3.19	2.8	11.95
30F-FL-E2-Steel			30.3			3.21			
60F-FL-E1-Steel	60 Mins	300 mm	18.7	18.6	17.43	1.98	1.97	1.85	6.56
60F-FL-E2-Steel			18.5			1.96			
NF-HL-E1-Steel	No Fire	150 mm	17.01	16.97	16.11	3.61	3.6	3.42	5.0
NF-HL-E2-Steel			16.93			3.59			
30F-HL-E1-Steel	30 Mins	150 mm	14.95	14.98	13.76	3.17	3.175	2.92	8.0
30F-HL-E2-Steel			15.01			3.18			
60F-HL-E1-Steel	60 Mins	150 mm	8.62	8.51	10.76	1.81	1.79	2.285	27
60F-HL-E2-Steel			8.41			1.78			

(b)

In all of the above cases it can be noted that the bond stress values noted for a particular case in the physical experiment are in very close and tight agreement with the bond stress prediction made by the numerical experiments. Such a situation further validates and confirms the effectiveness of the novel non-destructive numerical method of testing a specimen's bond stress developed in this work. The development of such a numerical method to study the bond stress at the interface of concrete and rebar that are subjected to thermal loading successfully achieves AIM 2 of this thesis.

AIM 2 Achieved

"Develop a Numerical model to study the bond stress and bond slip behaviour in the cohesive zone of SMA-concrete and Steel-concrete specimens under various fire conditions"

6.5 Results - Parametric Studies and Development of Empirical Formula

Having successfully validating the numerical model developed in this work against the physical experiments (Chapter 3), the accuracy and stability of the numerical model is established beyond any reasonable doubt. It was therefore conceived to use the novel numerical model to conduct a parametric study on the various parameters that influence the bond stress at concrete and rebar interface and their influence on each other. Such an understanding will provide the required knowledge to develop an empirical formula to quickly predict the bond stress behaviour. The development of the empirical is the third aim of this thesis. The manner in which it is achieved is presented next.

The numerical model developed in this work to predict the bond stress in the cohesive zone was further employed in parametric studies that involved the parameters such as Rebar diameter, Concrete grade, Embedded length of rebar, Duration of fire and Effect of sand coating on the rebar. In all 92 cases were considered for the parametric

studies which resulted in identifying the parameters that had the most influence on the bond stress at the interface. These four parameters are:

- Embedded length of the rebar;
- Bar diameter;
- Modulus of concrete at various temperatures; and
- Modulus of rebar at various temperatures.

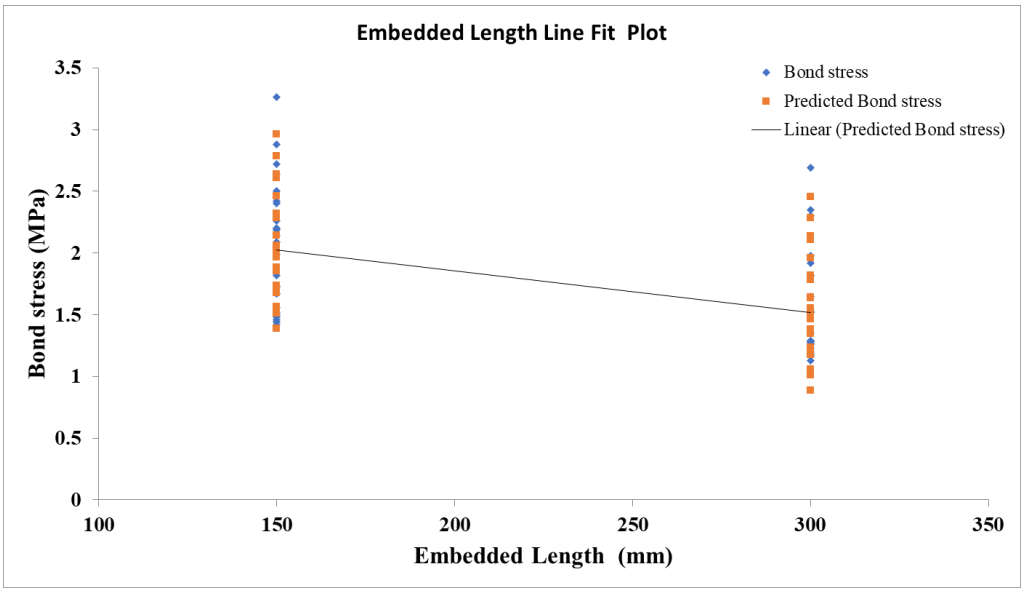

Figure 6.10: Line fit plot for the Embedded length variable

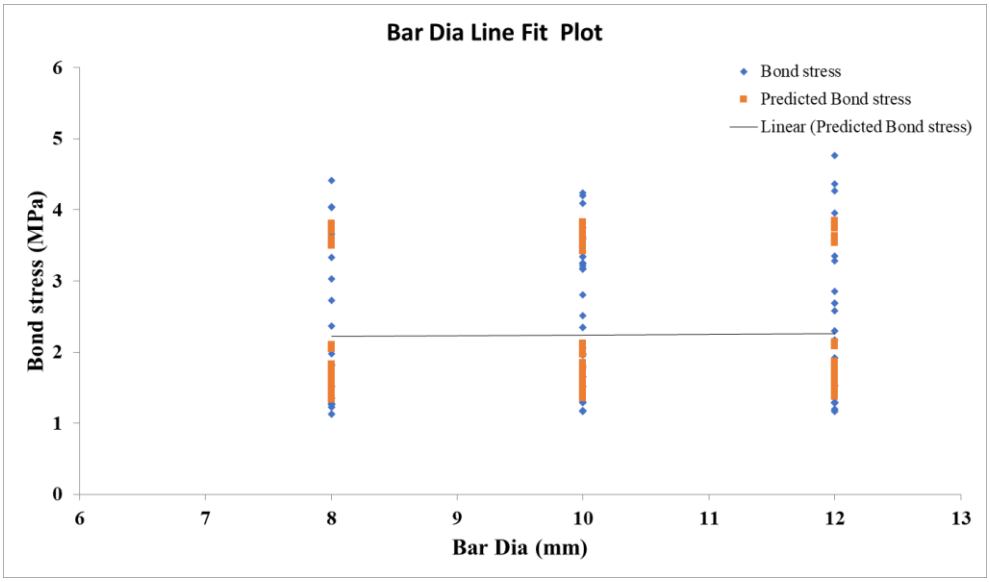

Figure 6.11: Line fit plot for the Bar diameter variable

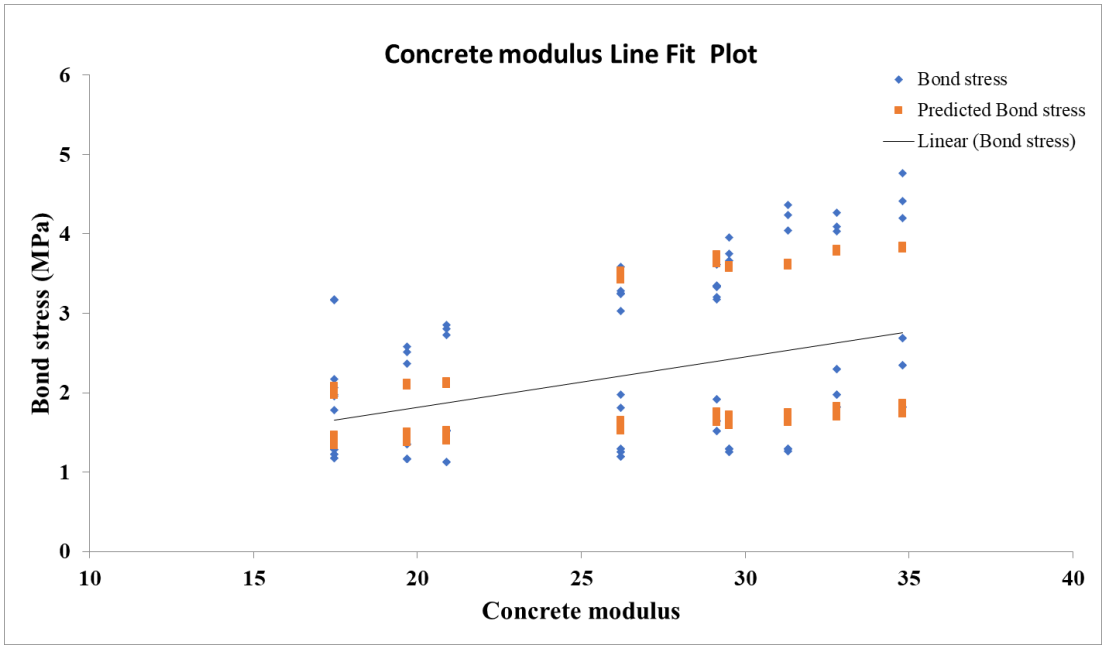

Figure 6.12: Line fit plot for the concrete modulus variable

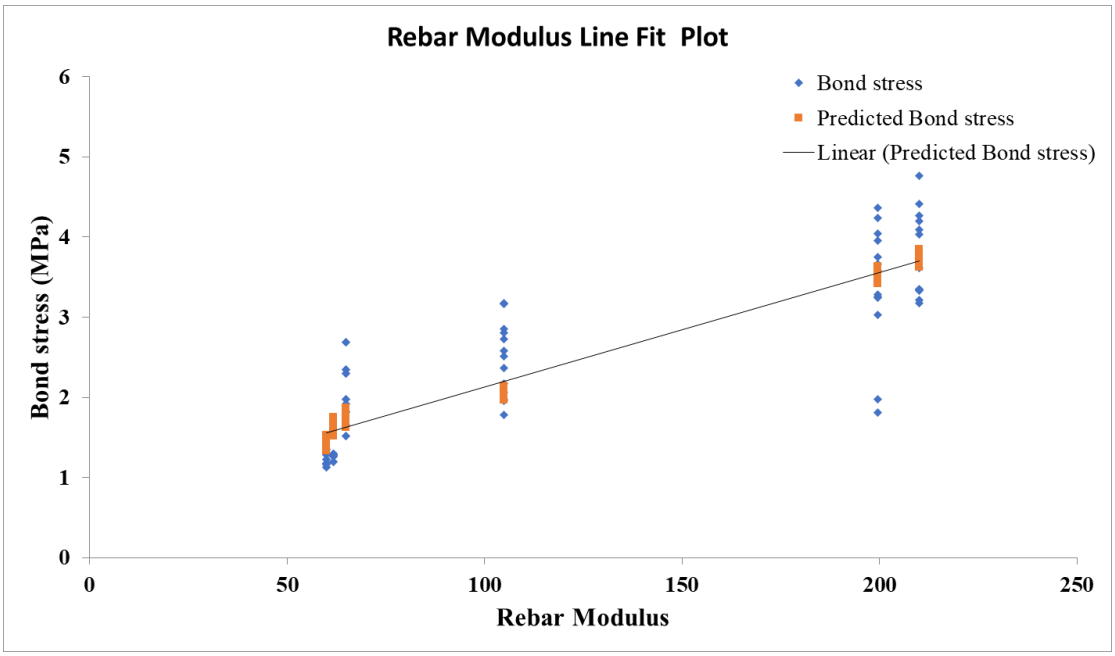

Figure 6.13: Line fit plot for the rebar modulus variable

Regression analysis performed on the identified parameters resulted in the development of an empirical formula.

$$\tau_{max} = (0.0053\, d_b + 0.0136\, R_m + 0.02137 E_C - 0.00044 l_d)\, R_f K_R$$

Equation 6.2

AIM 3 Achieved

"Develop an empirical equation for quick assessment bond stress"

The formula was tested against a case each from the numerical analysis conducted in this work and one from literature. The results were a close match. Hence a new formula that allowed for quick estimation of the bond stress at the interface was developed. Development of such a formula achieved AIM3 of this research.

The correctness of the empirical equation was tested through a benchmarking study where the parameters from the study conducted by Apparao et al. (2002) were considered to derive the bond stress values using the empirical equation developed in this work. Likewise, similar cases were selected from both the physical and numerical experiments conducted in this work and tested against the bond stress values predicted by the equation. First the benchmark studies against the parameters from literature are discussed followed by the discussion on the numerical and physical experiments conducted in this work.

Apparao et al. (2002) conducted experimental studies where in 16 mm deformed rebar is pulled out from M40 Grade concrete at 150mm embedment length. Figure 6.14 shows a typical bond stress-slip response. The maximum bond stress was found to be 8 MPa for unconfined specimen.

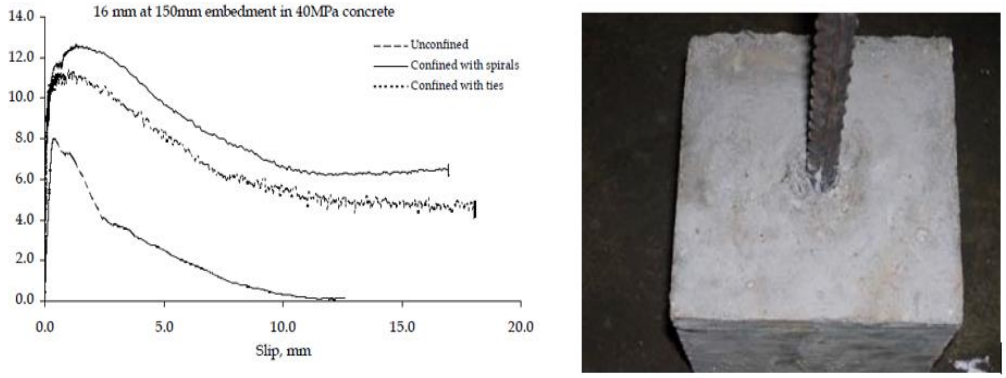

Figure 6.14: Bond-slip response pull-out test (Apparao et al. 2002)

Table 6.5 shows the statistics used for evaluation of the bond stress. While Apparao et al. 2002 predicted the bond stress for the mentioned conditions using experimental means to be 8Mpa, the **empirical equation developed in this work predicted this value to be 8.56MPa**, which is in good agreement with the results from the literature.

Table 6.5: Statistics used for bond stress evaluation for pullout test (Apparao et al. 2002)

S.No.	Description	Value
1	Bar diameter	16 mm
2	Concrete grade M40	40 MPa
3	Steel grade 415 (E)	200 GPa
4	Bar embedded length	150mm
5	Relative rib area F_R	0.1
7	Rib spacing	7.5
8	Friction between rebar concrete	0.4
9	Rib factor calculated area R_F (based on eqn)	2.36
10	**Bond stress calculated τ_{max} based on eqn**	**8.56 MPa**
11	Bond stress evaluated by experiment (Apparao et al. 2002)	8.0 MPa

Another case (Katz et. al 1999) from the literature was tested wherein the authors conducted experimental studies on the bond stress of specimens that were subjected to high temperature pull-out. The parameters from Katz et. al studies were employed

in the empirical formula developed in this work to test the accuracy of the bond stress predictions. The comparison of bond stress values as noted by Katz et. al and the estimations provided by the empirical formula developed in this work is presented in Table 6.6. It can be noted from Table 6.6 that the empirical formula developed has estimated the bond stress values that are a very close match to the respective values noted in the experimental studies conducted by Katz et. al. The parameters considered in the experimental studies are as shown in Table 6.7.

Table 6.6: Comparison of bond stress (Katz et al. 1999)

Temperature	**Bond Stress**	
	Katz et al. 1999 Test	**Empirical output**
10°C	10.1	10.2
105°C	8.39	8.43
210°C	6.63	7.21
260°C	3.5	3.25

Table 6.7: Statistics used for bond stress evaluation for pullout test (Katz et al. 1999)

S.No.	**Description**	**Value**
1	Bar diameter	12 mm
2	Concrete grade M40	35 MPa
3	Steel grade	210 GPa
4	Bar embedded length	60 mm
5	Relative rib area F_R	0.12
7	Rib spacing	7.7
8	Friction between rebar concrete	0.4
9	Rib factor calculated area R_F	2.83

Having established that the empirical formula closely estimated the bond stress values against similar works in the literature, it was deemed essential to test the estimation of the empirical equation to the predictions noted in the numerical studies and the values derived from the physical experiments conducted in this work. Figure 6.15 and Figure 6.16 compares the maximum bond stress obtained by experimental tests, numerical studies and from the proposed empirical formula for 10mm diameter SMA

and steel rebar respectively. The chart compares for different embedded length and fire conditions for M30 concrete grade. From the chart it can be seen that the results are in good agreement overall.

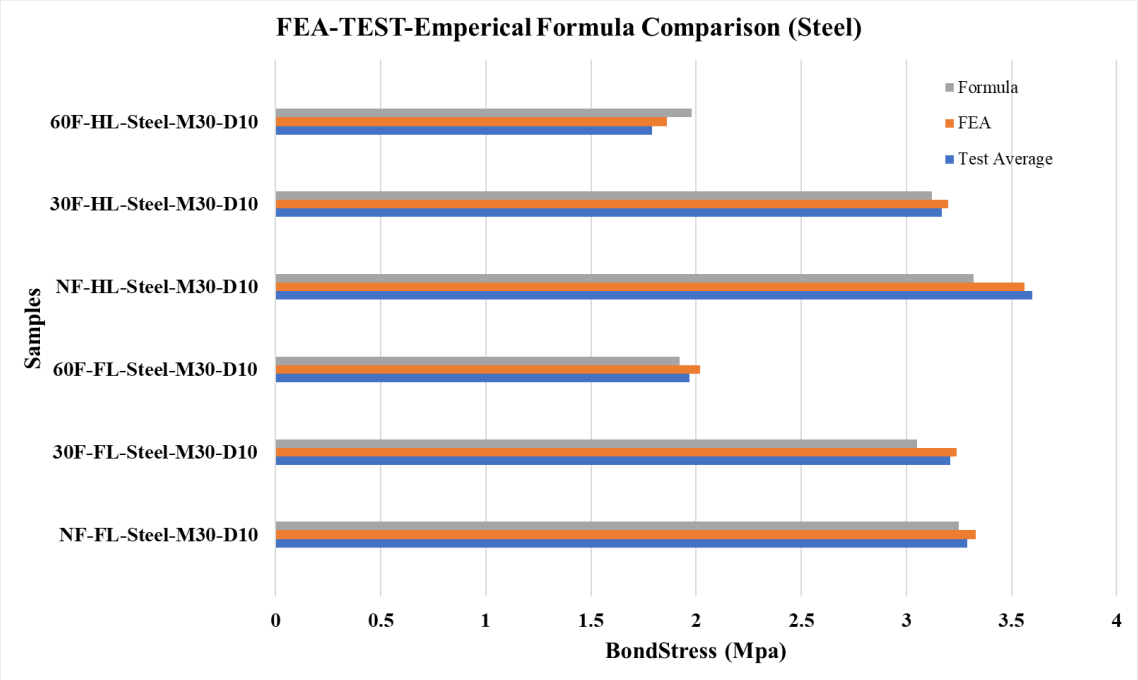

Figure 6.15: Bond stress benchmark numerical (FEA), physical (Test) and empirical formula comparison (steel)

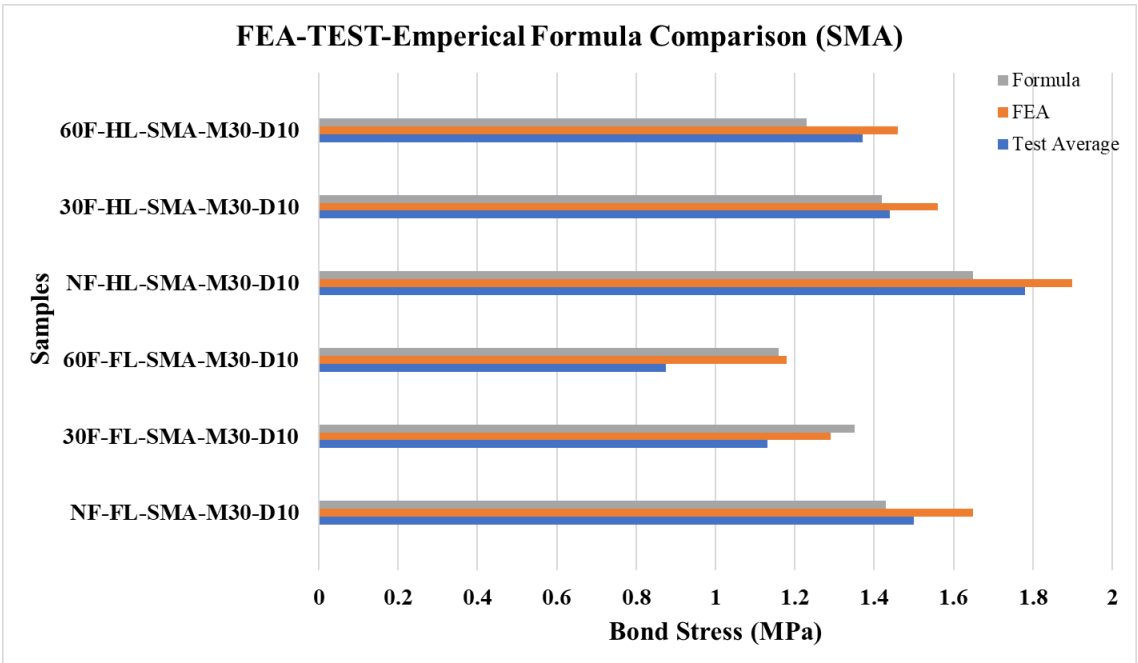

Figure 6.16: Bond stress benchmark Numerical (FEA), Physical (Test) and Empirical formula comparison (SMA)

From Figure 6.15 and Figure 6.16 and from the benchmark studies against the experimental studies found in literature (as discussed above), it can be conclusively said that the empirical formula developed in this work not only provides a means of quickly estimating the bond stress at the interface of metal rebar and concrete, it further validates the physical and numerical experiments conducted in this work. Hence a novel formula is developed in this work that allows for quick prediction of the bond stresses, which achieves the final aim of this thesis.

The manner in which all of the aims and objectives are achieved is summarised in the flow chart (Figure 5.24) and presented below as Figure 6.17. In the following chapter, the conclusions of thesis are drawn. The limitations of this work are described and key recommendations are made for future scope of work.

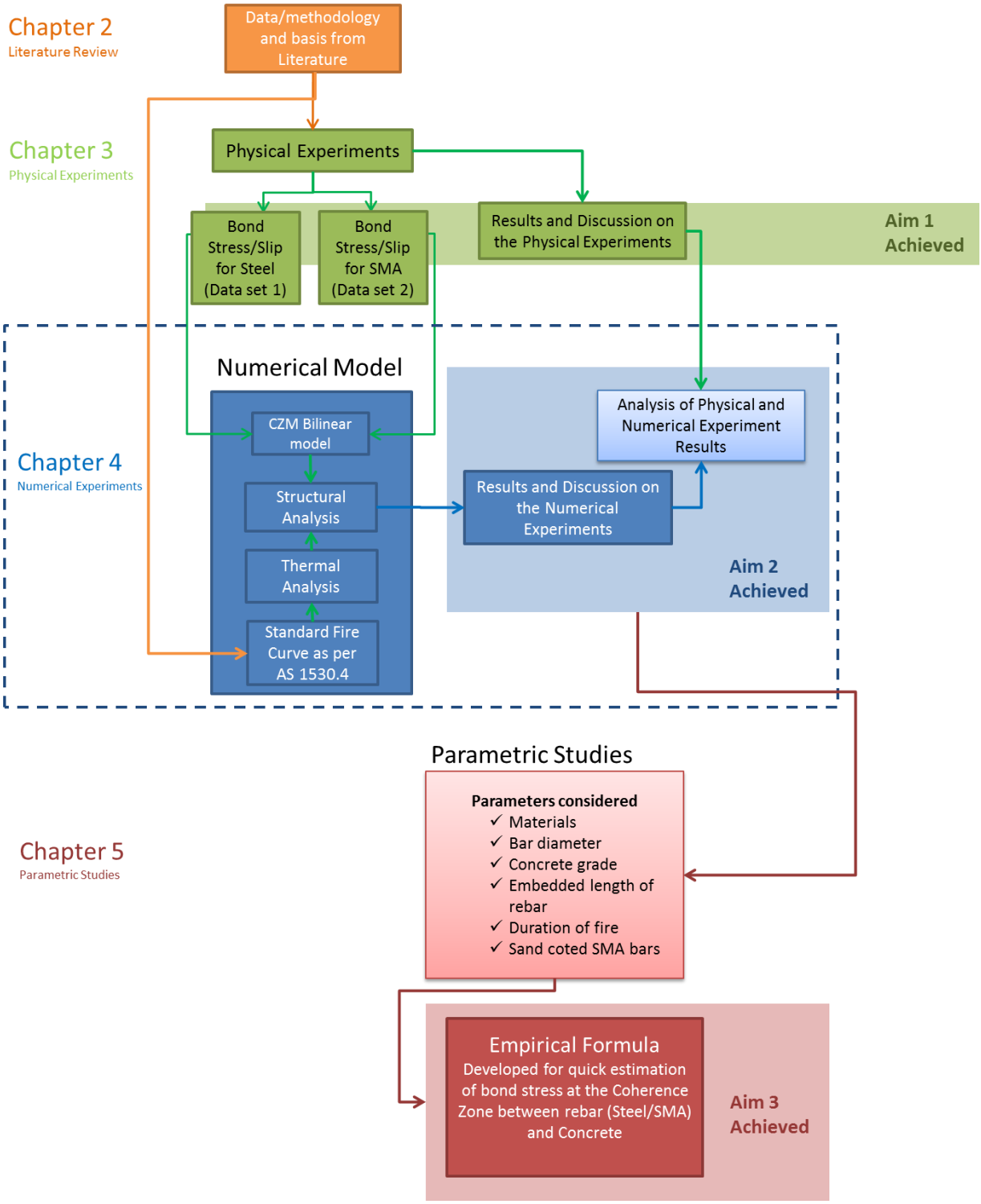

Figure 6.17: Achieving AIM 1, 2 and 3 (Results flow)

CHAPTER 7: Conclusions and Recommendations

7.1 Introduction

In successfully addressing the three fundamental aims set out at the beginning of this work, three significant conclusions are drawn. These conclusions can be viewed as the significant contributions of this thesis to the existing knowledge on the non-destructive methods of analysing bond stress between smart material based rebars and concrete when subjected to conditions of fire. The first conclusion is that a data set on the bond stress between a) SMA rebar-concrete and b) steel rebar-concrete for varying conditions of fire exposure duration and embedded length of the rebar is developed. Another significant conclusion is that the use of cohesive zone modelling using the datasets mentioned above allowed for the development of a non-destructive method of analysing bond stress using numerical models which take into account the effect of fire on the concrete specimens. Essentially, a quicker, cost effective and an alternative to the physical pull-out test experiments is developed that can model both the effect of thermal and structural loading and predict the bond stress values that are in good agreement with the physical experiments. In fact, it is established (via validation studies) that the percentage error in the bond stress predictions between physical and numerical experiments (based on the numerical method developed in this work) are well below 10%. A parametric study was conducted based on the novel numerical method developed in this work to further identify the various parameters (rebar material, rebar embedded length, rebar diameter, fire exposure duration, and concrete grade) that govern and influence the bond stress values. A regression analysis was carried out based on the above parameters identified. Finally, from the regression analysis, it is concluded that an empirical formula is developed for quick assessment of the bond stress between concrete and rebar that take into account the effect of fire.

This chapter is divided into three sections. In the first section, the conclusions of the research are drawn upon based on the results obtained in Chapter 5. The connections are established between the results and the research questions. The contributions of this research to the existing literature on the non-destructive methods of analysing bond stress on specimens that are subjected to conditions of fire are highlighted. The implications of such a novel numerical method developed and the data sets generated is discussed next. The limitations of this study are considered and presented in view of the limited SMA materials, the time and cost of physical experiments that was restrictive to conducting more in-depth studies. The potential to further develop the ideas and contributions of this work are discussed in the concluding section of this chapter.

7.2 Conclusions

Reinforced concrete is used widely across the construction industry for its versatility, strength and durability. One of the main constituents of concrete is steel. At room temperature, the steel rebars improve the strength of concrete significantly. However, under conditions of fire when the temperature can reach as high as 900°C in just under 60 minutes of fire exposure, (during a fire event) both the concrete and reinforcing steel lose their respective strength. It is confirmed in the literature that on an average the steel loses around 50% of its strength when the temperature reaches around 400°C. This situation leads to catastrophic failure of structures and leaving very little time to save lives and the property. Design for fire safety includes numerous active and passive measures such as increased concrete cover or providing insulation on the concrete. However, these measures (especially for structural fire protection of concrete elements) have their own limitations such as continuous weakening of structural materials that are exposed to fire.

To overcome the above-mentioned limitations, smart material such as shape memory alloy (SMA) could potentially be employed. The excellent physical and mechanical properties of SMA have made them successful candidates for use in structural engineering applications. The use of shape memory alloys (SMAs) has increasingly expanded in recent decades finding their way into commercial products in the construction, aerospace, medical and other industries.

This thesis aimed at exploring the possibility of using one such smart material as a potential candidate for rebars in concrete. The hypothesis is that SMA's can be trained to remember shapes at certain temperature and that such ability can counter act where steel rebars are expected to lose strength. Exploring such a possibility required extensive literature survey on the topic of concern. It was noted from the literature that there were numerous studies (both physical and numerical experiments) on steel-concrete interaction. More specifically the bond stress between steel rebars and concrete has been extensively studied with well-established experimental methods and processes. The physical experiments are typically pull-out tests carried out on the specimens. Such experiments require the construction of the physical specimens and require a lot of mechanical gear to conduct the tests. Specimens almost always result in physical damage (in other words these are destructive tests) and hence several specimens are required to confirm outcomes. All these activities are costly and time consuming. To overcome the above-mentioned issue, an alternative approach has evolved in the literature. The use of numerical models and methods has provided a means of examining the bond stress in a non-destructive manner and one that was quick and less expensive, since fewer physical specimen needed to be prepared.

Therefore, in this thesis it was decided to employ the numerical method of testing the hypothesis discussed earlier. To this extent the following three research questions evolved:

1) Are there any existing studies that modelled the interface response to thermal exposure during fire event using numerical methods?
2) Is there sufficient data available to model such an interface? and
3) Is there a means to validate the results from such numerical experiments using other mathematical methods (such as empirical formula) without getting into physical experiments?

Comprehensive review of the literature to provide answers to the above questions was inconclusive. Such numerical models, methods and data sets could not be found in

the literature. It is from these gaps in the literature that the following three AIMs of this thesis evolved.

- Conduct experimental studies to understand the bond stress behaviour of concrete-steel rebar and concrete-SMA rebars that are subjected to high temperature;
- Develop a numerical model to study the bond stress and bond slip behaviour in the cohesive zone of SMA-concrete and steel-concrete specimens under various fire conditions; and
- Develop an empirical equation for quick assessment of bond stress that takes into account the influence of fire on the concrete.

The main findings of this study are reported in the following section: the significance in relation to the research questions will be established.

7.3 Main findings, significance and contributions

A numerical method relies heavily on how well the model is defined. The definition includes defining the materials and the corresponding parameters, boundary conditions and the likes. It is in this respect that data set from achieving AIM 1 proves essential to the successful outcome of AIM 2. The response (maximum bond stress) at interface of SMA-concrete and the steel-concrete specimens to a combination of fire exposure and structural loading was not available in the literature. As a consequence, this work set out to fill this gap in the literature by conducting physical experiments on both the above said specimen categories.

SMA rebars needed to be characterised for their use as rebar in concrete specimens. In this process the phase transformation temperature was established through testing of the samples extracted from the SMA rebars using differential scanning calorimeter. The heat flow through the specimen and the reference were monitored for any differential heating. Any difference in the heat flow indicated that an endothermic or exothermic transformation had occurred in the tested material. In Figure 7.1 the data

obtained during the testing on the phase transformations of the three sample (annealed at 150°C, 250°C and 400°C) is presented.

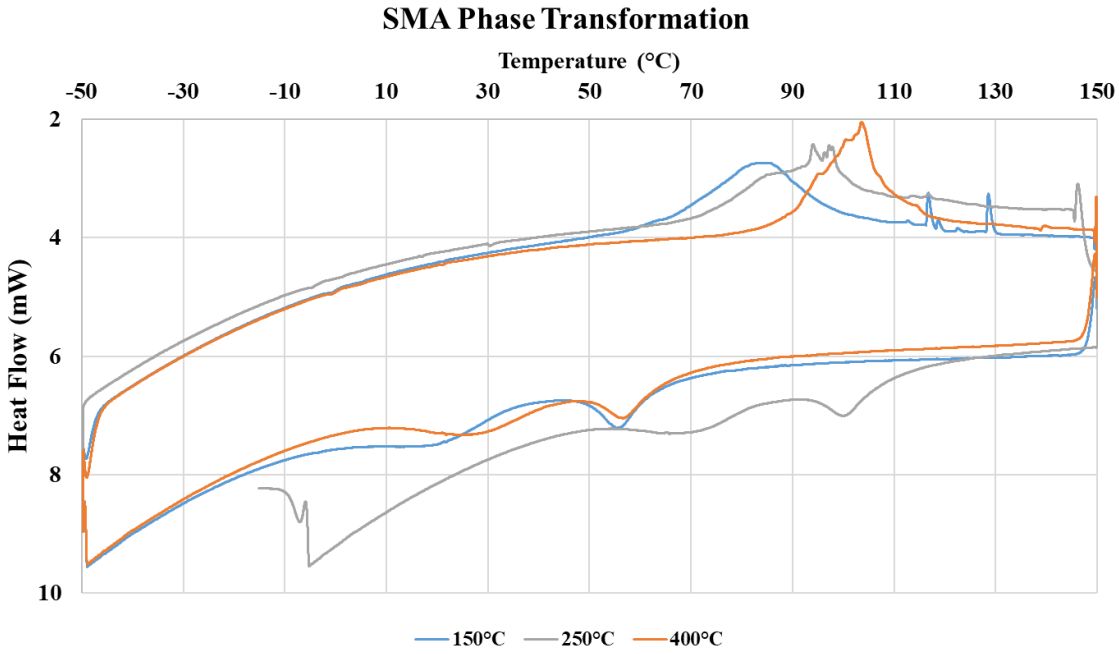

Figure 7.1: Phase transformation of samples at different heat treatment

The data suggests that in the case of the SMA samples, the phase transformation limit increases with the increase in the heat treatment temperature. The highest phase transformation temperature for the SMA under investigation was found to be 105°C for a sample that was annealed at 400°C. Based on these observations, all of the SMA rebars used in this thesis were heat treated at 400°C. This study in itself is a contribution to the literature in that the phase transformation response of the SMA (NiTi alloy) is established.

Both SMA and steel rebars were employed in this work. Over 24 concrete specimens (12 each SMA and steel rebars respectively) were tested in the pull test physical experiments for three fire conditions a) No Fire, b) 30min fire exposure and c) 60min fire exposure. The force vs displacement data for each of the above mention specimen cases was recorded and the corresponding bond stress was calculated using the formula;

$$\tau = \frac{P}{\pi\, l_b\, d_b}$$ Equation 7.1

It is from this equation that respective bond stresses were calculated and bond slip vs displacement charts were created. Essentially, the τ values for the respective test case was further plotted against the displacement (slip) noted during the experiment to establish the Maximum Bond stress value (τ_t^{max}) and other parameters of concern such as Tangential Displacement (δ_t^*), Ratio (ratio of δ_t^* to δ_t^c) and Non dimensional weigh parameter. The summary Maximum Bond stress values ($\tau_t^{\max}$) for each of the 24 specimens tested in this work is presented in Table 7.1.

The comprehensive experimental study conducted in this work that included several parameters such as rebar materials, embedded length of rebars, fire exposure duration, resulted in the generation of the valuable data set that is crucial for the development of the numerical experiments concerning the bond stress at the intersection of rebar and concrete in general and more specifically the modelling of the cohesive zone (interface) as a response to both thermal and structural loading. The data set that evolved of the physical experiments is a significant contribution to the literature and achieves Aim1 of this thesis and paves way to conduct numerical experiments.

Table 7.1: Summary of data on Maximum tangential traction, Tangential Displacement, Ratio and Non dimensional weigh parameter

Sno.	Specimen Name	Max. Traction (τ) MPa	Traction Displacement (δ*) mm	Ratio (δ*)/(δc)	Weight Parameter
1	NF-FL-E1-SMA	1.51	1.4	0.52	1
2	NF-FL-E2-SMA	1.49	1.45	0.54	1
3	30F-FL-E1-SMA	1.18	1.5	0.56	1
4	30F-FL-E2-SMA	1.08	1.65	0.61	1
5	60F-FL-E1-SMA	0.95	1.5	0.56	1
6	60F-FL-E2-SMA	0.8	1.5	0.56	1
7	NF-HL-E1-SMA	1.82	1.3	0.48	1
8	NF-HL-E2-SMA	1.75	1.3	0.48	1
9	30F-HL-E1-SMA	1.39	1.5	0.56	1
10	30F-HL-E2-SMA	1.49	1.5	0.56	1
11	60F-HL-E1-SMA	1.35	1.4	0.52	1
12	60F-HL-E2-SMA	1.39	1.55	0.57	1
13	NF-FL-E1-Steel	3.34	1.15	0.67	1
14	NF-FL-E2-Steel	3.25	1.15	0.67	1
15	30F-FL-E1-Steel	3.18	1.15	0.67	1
16	30F-FL-E2-Steel	3.21	1.15	0.67	1
17	60F-FL-E1-Steel	1.98	1.15	0.67	1
18	60F-FL-E2-Steel	1.96	1.05	0.61	1
19	NF-HL-E1-Steel	3.61	1.15	0.67	1
20	NF-HL-E2-Steel	3.59	1.15	0.67	1
21	30F-HL-E1-Steel	3.17	1.05	0.61	1
22	30F-HL-E2-Steel	3.18	1.1	0.67	1
23	60F-HL-E1-Steel	1.81	1.1	0.67	1
24	60F-HL-E2-Steel	1.78	1.1	0.67	1

It is mentioned earlier that 24 physical specimens were tested in the course of conducting the physical experiments. In the numerical experiments, representations that correspond to each of the 24 specimens were adopted in the form of CAD model and the assignment of suitable material properties. The numerical experiments were carried out in two phases 1) to generate thermal profile and 2) to assess the specimen response to non-linear structural loading which takes into account the thermal

response. While thermal studies could be performed without the need for data derived (Table 7.1), the structural analysis could not proceed without the same. It was decided that only one thermal profile was sufficient for a reason that for given thermal load, material properties, physical dimensions of rebar, the rebar location and rebar diameter, the response of concrete over 60min duration would not change much. Hence only one thermal profile was required that would be applied to the 24 models during the structural analysis. The thermal profile of concrete, interface of concrete-steel rebar and that of the fully embedded rebar itself is shown in figure for fire exposure duration of 60mins. From the figure it can be noted that the core temperature is in the vicinity of 400°C. It was earlier mentioned that 400°C is a critical temperature beyond which the SMA rebar loses its memory retaining ability. Therefore, from the observation made from the thermal profile it could be said that the conditions are suitable for SMA use in lieu of steel rebar.

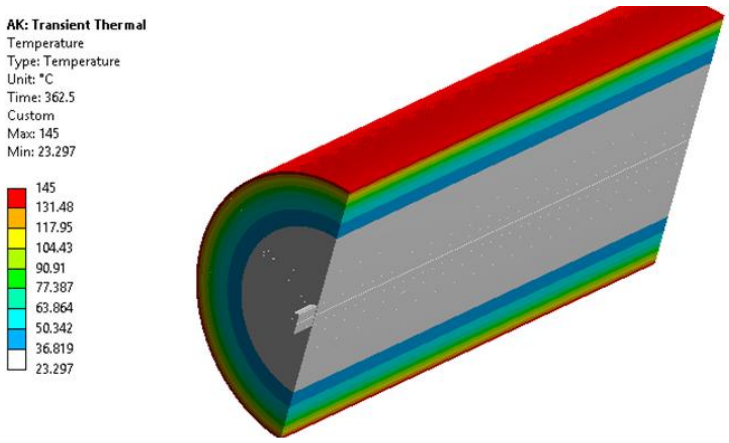

(a)

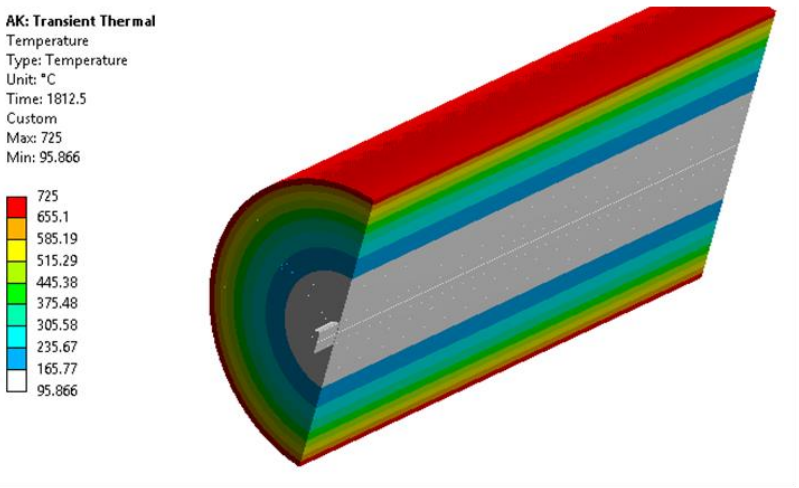

(b)

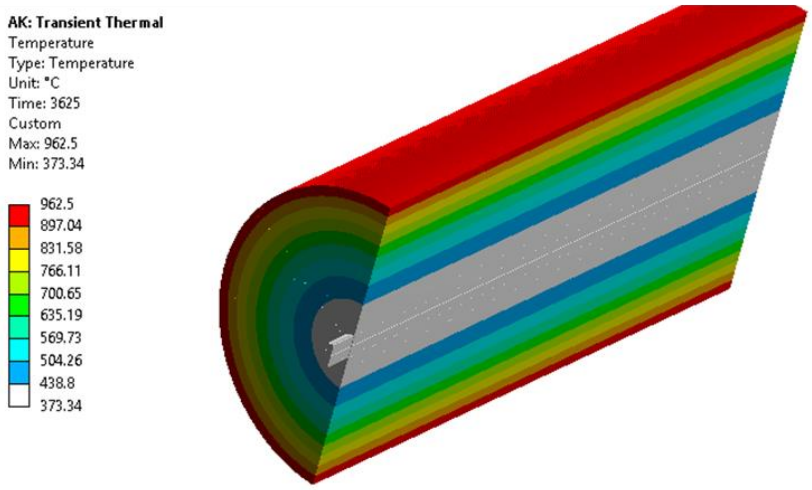

(c)

Figure 7.2: 3D Thermal profile of the Concrete-Steel Rebar and interface at (a) Start (b) 30min and (c) 60min fire exposure

In order to proceed further with the structural analysis, the material properties of concrete and rebar were retained. However, to enable the interface response in a way that is reflective of the physical experiments, it was decided to apply a cohesive zone model (by appropriate selection of mesh elements such as Solid65, Inter205 and Solid185 for concrete, interface and rebar respectively in ANSYS). While concrete material properties were adopted to define concrete and SMA and Steel rebar properties for respective rebars, the properties of the interface were defined by parameters that were taken from the data set generated from physical experiments mentioned earlier (Table 7.1). In addition, the thermal profile generated was also applied on to the specimen model to define the thermal characteristics at any given point over the 60min exposure. It is for the first time that such an attempt is made to examine bond stress at the interface using numerical methods where the interface is made to accept data generated from real world experiments and is further made to respond to both thermal and structural loading.

The results from numerical experiments were compared to the ones from the physical experiments where in the failure modes were analysed to confirm the accuracy of the numerical model developed in this work. The results of the non-linear structural analysis on SMA-concrete specimen where in the rebar is fully embedded into concrete and is subjected to 60min of fire exposure is shown below. These results allow for validation of the numerical model developed in this work. In the physical testing of the specimen, after 60mins of thermal exposure and subjected to the pull-out test, the specimen was analysed for cracks and other failures. It can be noted from the Figure 7.3 (a) that the rebar had smoothly pulled out of the specimen without cracking the concrete. The interface looks smooth and clean without any rupture. This is evident from any lack of concrete residue on the SMA rebar. In order to establish the consistency of the numerical model/method developed in this work it is essential to observe similar results on the corresponding model used in numerical study. In Figure 7.3 (b) the results from numerical study are presented. The results of the numerical study too predict a smooth pull-out of the rebar as observed in the case of physical experiments. This reiterates the accuracy of the novel method developed to analyse bond stress as a response to both thermal and structural loading.

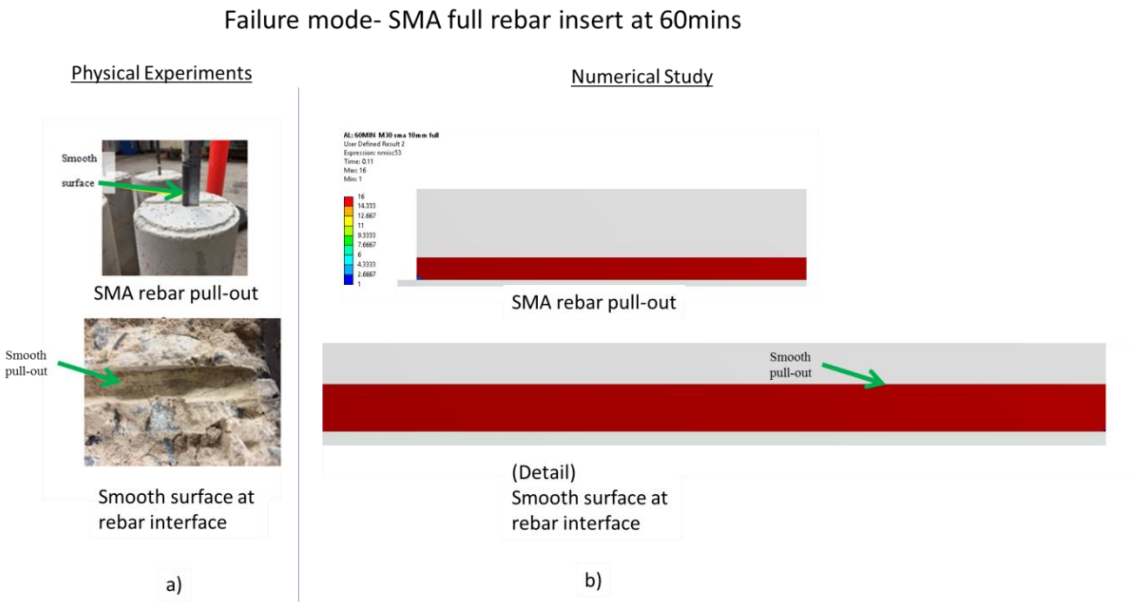

Figure 7.3: Failure Modes: Pull out test under high temperature a) physical experiment and b) numerical study

Specimens with SMA rebars show an 18% reduction in SMA rebar concrete bond stress at about 30min and about 8% at about 60min of fire exposure conditions. This can be explained by the fact that at about 400°C, the SMA rebars undergoes austenite phase transformation and gains stiffness because of increased modulus of elasticity. Interestingly, the overall drop in the bond stress at 60 minutes fire duration in SMA bar is not as significant as that of the steel bar (refer to Figure 7.4).

In all of the 24 specimen cases considered, it can be noted that the bond stress values noted for a particular case in the physical experiment is in very close and tight agreement with the bond stress prediction made by the numerical experiments. The bond stress predictions from numerical analysis on both SMA and Steel rebar are shown in Figure 7.5 and Figure 7.6 for both half and full embedded rebars respectively. Such a situation further validates and confirms the effectiveness of the novel non-destructive numerical method of testing a specimen's bond stress developed in this work.

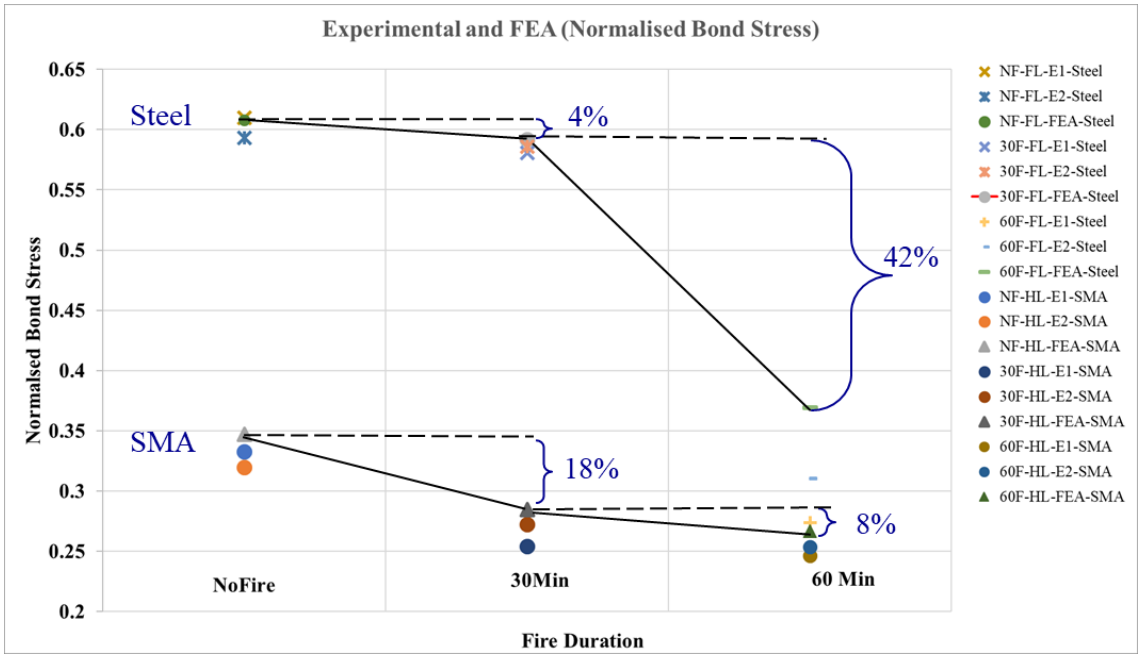

Figure 7.4: Experimental and FEA correlation

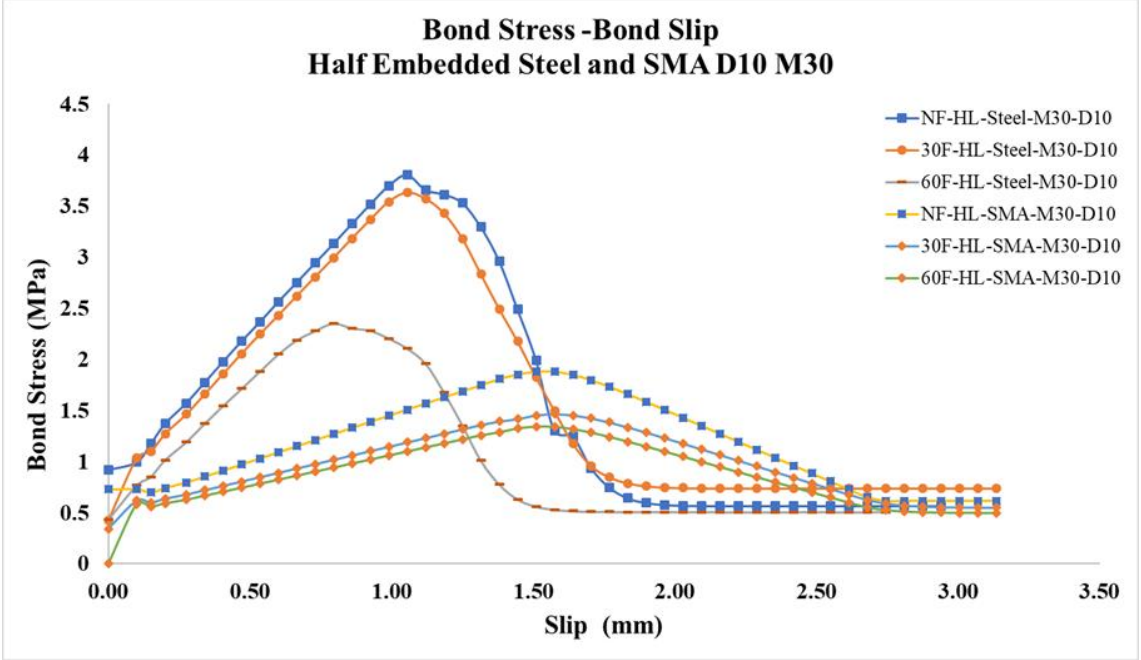

Figure 7.5: Effect of fire duration on bond stress of Half embedded rebar – SMA and Steel M30)

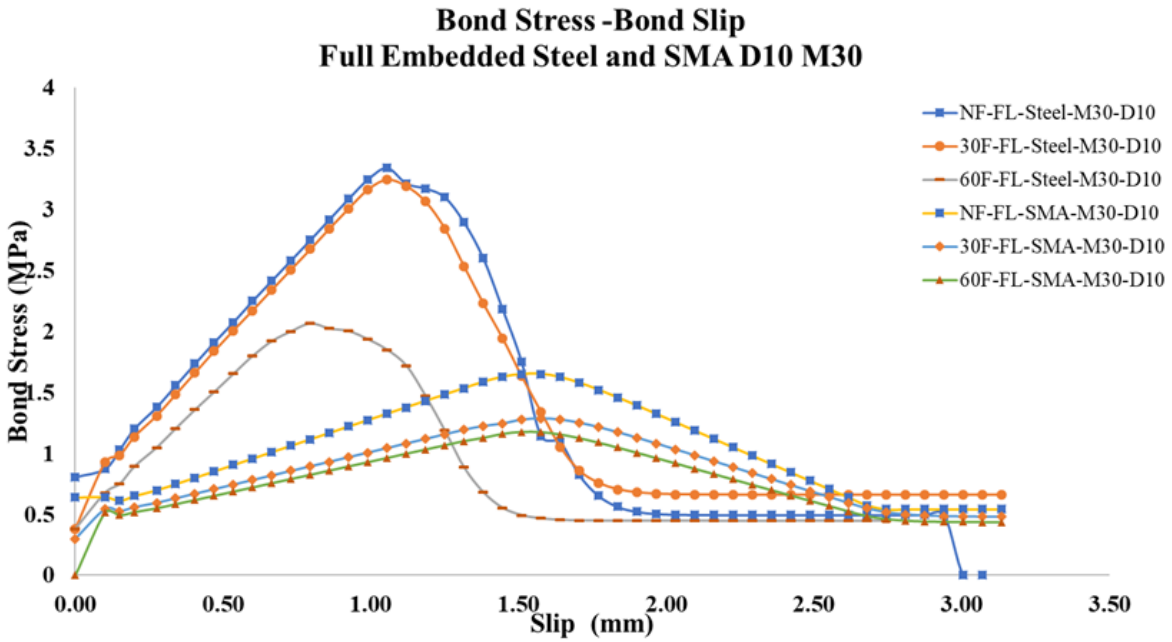

Figure 7.6: Effect of fire duration on bond stress of Full embedded rebar – SMA and Steel M30)

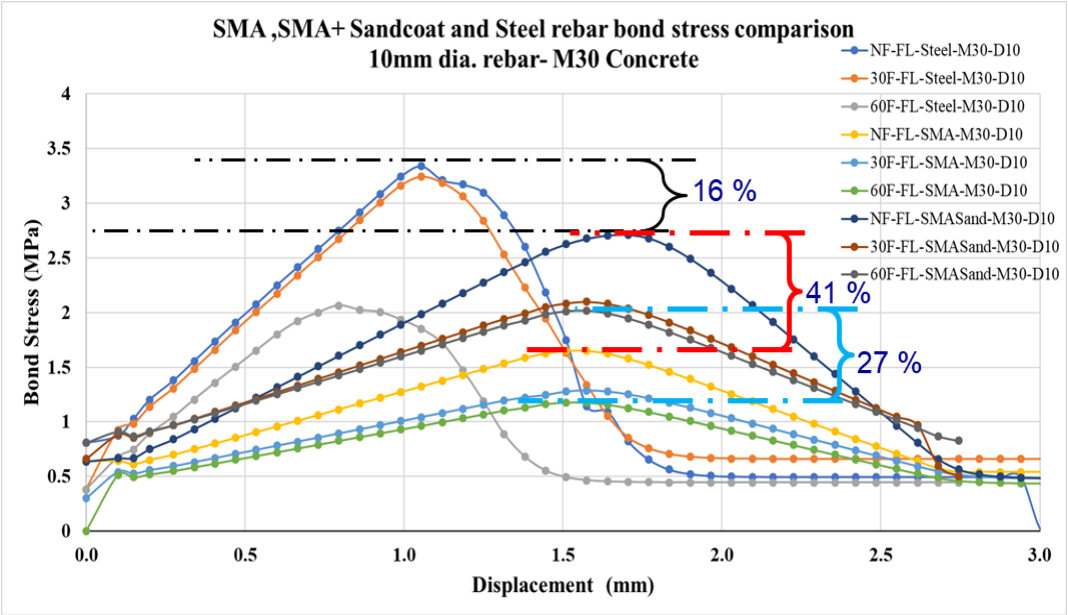

Figure 7.7: Effect of sand coating on bond stress (Full embedded length - SMA-steel – M30)

A comparative study on SMA, sand coated SMA rebar and steel made suggested the effectiveness of the sand coated SMA rebars. It is shown that the sand coated SMA rebars had the advantage of comparable strength with that of steel rebars at about the 60min exposure to fire (1.5mm displacement). It must be noted that from this point onwards, the SMA further gains strength reaching a maximum of about 2 MPa, on the

contrary, specimen with steel rebar had lost significant strength (-25%) and had dropped to about 1.5 MPa during the same period (Figure 7.7).

On successfully developing a numerical method of analysing the bond stress the thesis proceeded to examine the influence of various parameters that influence the bond stress so as to identify the key parameters for the conduct of a regression analysis that will assist in the development of an empirical formula (for quick estimation of bond stresses). The key parameters and their respective variation of parameters such as concrete grade, bar diameter, embedded length, fire exposure duration and its effect on bond stress were studied and plotted in 3d surface plot for understanding the positive and negative influence on the bond stress (Figure 7.8).

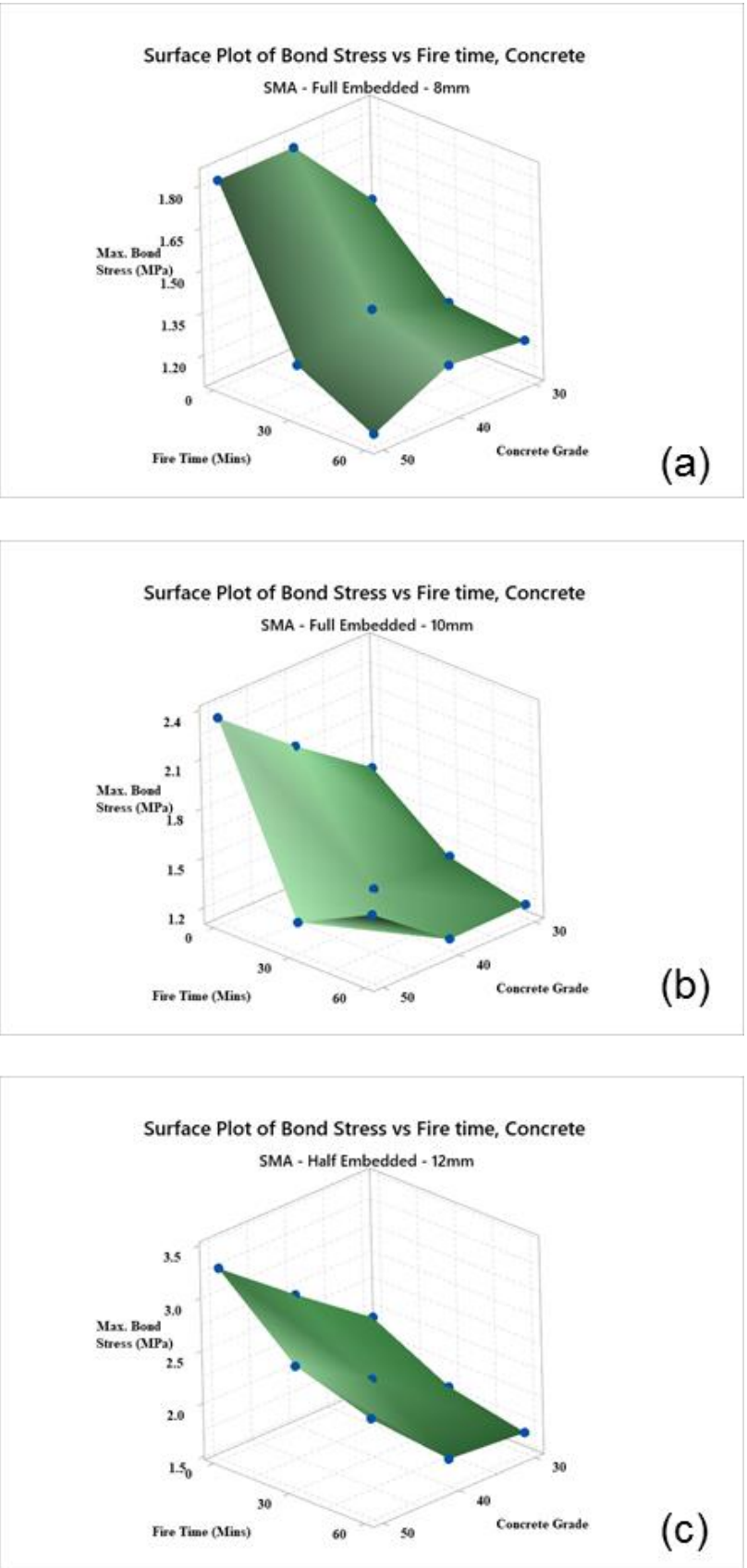

Figure 7.8: Influence of parameters on (a) 8mm (b) 10mm and (c) 12mm diameter SMA fully embedded rebar

7.4 Limitation and constraints of the current studies

The experimental study was limited in scope mainly due to two reasons: 1) expensive resources especially SMA material and 2) the length of time for each physical experiment (as one complete day was required to cool down the oven before the next sample can be tested). The numbers of samples that can be tested were limited; therefore, the experimental program was designed to get more information on bond strength rather than observing variation of other parameters such as bar diameter or concrete grade.

7.5 Recommendation for future works

This thesis highlights the significant advantages of using SMA rebars as reinforcement in concrete more so under conditions of fire accidents. Shape memory alloys can be efficiently used in the hybrid reinforced beam to improve the fire resistance level. The following recommendations are made for future studies on the application of SMA to improve the structural integrity of reinforced concrete that is subjected to conditions of fire:

- The current research can be extended to SMA rebar with ribs;
- Sand coated SMA rebar bond strength under high temperature need to be explored and confirmed through experimental studies;
- Further studies may examine the possibilities of increasing the bond stress by considering parameters such as rebar coated with epoxy materials, sand grain size and length of sand coating; and
- A full scale SMA hybrid simply supported reinforced concrete beam can be studied under a real fire scenario to understand the effect of high temperature on bond stress and fire resistance level with varying SMA to steel reinforcement ratio.

Abbas V, Rijun S, & Keith, C, 2017, 'Modelling of Factors Affecting Bond Strength of Fibre Reinforced Polymer Externally Bonded to Timber and Concrete', *World Academy of Science, Engineering and Technology International Journal of Structural and Construction Engineering,* vol. 11, no. 12.

Achillides, Z, & Pilakoutas, K, 2004, 'Bond behavior of fiber reinforced polymer bars under direct pullout conditions', *Journal of Composites for Construction*, vol. 8, no. 2, pp. 173-181

Achillides, Z, 1998, Bond behaviour of FRP bars in concrete, Doctoral Thesis, The University of Sheffield, UK.

Al-Sulaimani, G, Kaleemullah, M, Basunbul, I, & Rasheeduzzafar, 1990, 'Influence of corrosion and cracking on bond behavior and strength of reinforced concrete members', *ACI Structural Journal*, vol. 87, no. 2, pp. 220–231.

Alam, M, Youssef, M, & Nehdi, M, 2007, 'Utilizing shape memory alloys to enhance the performance and safety of civil infrastructure: a review', *Canadian Journal of Civil Engineering*, vol. 34 no. 9, pp. 1075-1086.

Al-Sulaimani, G, Kaleemullah, M, Basunbul, I, & Rasheeduzzafar, 1990, 'Influence of Corrosion and Cracking on Bond Behavior and Strength of Reinforced Concrete Members', *Structural Journal*, vol. 87, no. 2, pp. 220-231.

Al-Zuhairi, A, & Al-Fatlawi, W, 2013, 'Numerical prediction of bond-slip behaviour in simple pull-out concrete specimens', *University of Baghdad Engineering Journal*, vol. 19, pp. 1-12.

AS 1530 : *Australian Standards for Fire test to Building Material;* Standards Australia.

AS 3600-2009: *Australian Standards for Construction of Concrete Building Structures;* Standards Australia.

AS 1379-2007: *Australian Standards for Specification and Supply of Concrete;* Standards Australia.

AS/NZS 4671:2001: *Australian/New Zealand Standard for Steel Reinforcing Materials;* Standards Australia.

Ammon, K, Neta, B, & Lawrence, C, 1999, 'Effect of high temperature on bond strength of FRP rebars', *Journal of Composite for Construction*, vol. 3, no. 2.

Andrade, C, Arteaga, A, Lopez-Hombrados, C, & Vazquez, A, 2001, 'Tests on bonds of galvanized rebar and concrete cured in seawater', *Journal of Materials in Civil Engineering*, vol.13, no. 5, pp. 319–324.

Andrawes, B, Shin, M, & Wierschem, N, 2010, 'Active confinement of reinforced Concrete bridge columns using shape memory alloys', *Journal of Bridge Engineering,* vol. 15, no. 1.

ANSYS Theory Reference, version 15, Swanson Analysis System.

Apparao, G, Sultana, F, Pandurangan, K, & Eligehausen, R, 2002, 'Studies on the pull-out strength of ribbed bars in high-strength concrete', *International Association of Fracture Mechanics for Concrete and Concrete Structures,* vol. 6, no. 295.

Arioz, O, 2007, 'Effects of elevated temperatures on properties of concrete', *Fire Safety Journal*, vol. 42, no. 8, pp. 516-522.

Bangash, M, 1989, 'Concrete and ConcreteStructures: Numerical Modeling and Applications', Elsevier Science Publishers Ltd, London, UK.

Bastami, M, Chaboki-Khiabani, A, Baghbadrani, M, & Kordi, M, 2011, 'Performance of high strength concretes at elevated temperatures, *Scientia Iranica*, *Civil Engineering*, vol. 18, no. 5, pp. 1028-1036.

Barbosa, A, & Ribeiro, G, 1998, 'Analysis of Reinforced concrete Structures Using ANSYS Nonlinear Concrete Model', *Computational Mechanics,* vol. 1, no. 8.

Belaid, F, Arlique, G, & Francois, R, 2001, 'Effect of bar properties on bond strength of galvanized reinforcement', *Journal of Materials in Civil Engineering*, vol. 13, no. 6, pp. 454-458.

Bergheau, J, & Fortunier, R, 2008, *Finite Element Simulation of Heat Transfer,* ISTE - Wiley, 10.1002/9780470611418.part1.

Belarbi, A, Richardson, N, D, Swenty, M, K, & Taber, L, H, 2010, 'Effect of Combination on Reinforcing Bar-Concrete Bond', *Journal of Performance of Constructed Facilities*, ASCE, vol. 24, no. 3.

Benmokrane, B, Tighiouart, B, & Chaallal, O, 1996, 'Bond strength and load distribution of composite GFRP reinforcing bars in concrete', *ACI Materials Journal*, vol. 3, pp. 246-253.

Bratina, S, Saje, M, & Planinc, I, 2007, 'The effects of different strain contributions on the response of RC beams in fire', Engineering Structures, vol. 29, no. 3, pp. 418-430.

Campbell, M, 2006, 'Statistics at square two: understanding modern statistical applications in medicine', BMJ Books Blackwell.

Capua, D, Mari, A, 2007, 'Non-linear analysis of reinforced concrete cross-sections exposed to fire', *Fire Safety Journal*, vol. 42, pp. 139-149.

Castellano, M, 2000, 'Innovative Technologies for Earthquake Protection of Architectural Heritage', *International ICOMOS Congress*, Bethlehem, Palestine.

Casciati, F, Faravelli, L, Hamdaoui, K,2007,'Performance of a base isolator with shape memory alloy bars', *Earthquake Engineering Vibration*, vol. 6, no. 4.

Cardone, D, Dolce, M, Ponzo, F, & Coelho, E, 2004, 'Experimental behavior of R/C frames retrofitted with dissipating and re-centering braces', *Journal of earthquake Engineering*, vol. 8, no. 3, pp. 361-396.

Cairns, J, & Abdullah, R ,1995, 'An evaluation of bond pull-out tests and their relevance to structural performance', *The Structural Engineer Journal of the Institutation of Structural Engineers*, vol. 73, no. 11, pp. 179-185.

Castillo, C, & Durrani, A, 1990, 'Effect of transient high temperature on high-strength concrete', *ACI Materials Journal*, vol. 87, No. 1, pp. 47-53.

CCAA T61, C 2010, *Guide Fire Safety of Concrete Buildings*. *Cement Concrete & Aggregates Australia*, ISBN 978-1-877023-27-9.

Cevik, A, Gogus, M, Guzelbey, Ibrahim, & Filiz, H, 2010, 'Soft computing-based formulation for strength enhancement of CFRP confined concrete cylinders', *Advances in Engineering Software*, vol. 41, pp. 527-536.

Chiew, S, Zhao, M, & Lee, S, 2014, 'Mechanical properties of heat-treated high strength steel underfire/post-fire conditions', *Journal of Constructional Steel Research*, vol. 98, pp. 12–19.

Chih, C, & Tsai, C, 2003, 'Time-Temperature analysis of bond strength of rebar after fire exposure', *Cement and Concrete Research,* vol. 33 no. 10, pp. 1651-1654.

Chen, W, Knog, N, & Wu, D, 2015, 'Dynamic Furnace Temperature Setting Research on Combustion System of Rolling Mill Reheating Furnace', *The 12th International Conference on Combustion & Energy Utilisation – 12ICCEU,* vol. 66, pp. 217-220.

Choi, E, Cho, S, Hu, J, Park, T, & Chung, Y, 2010, 'Recovery and residual stress of SMA wires and applications for concrete structures', *Smart Materials and Structures*, vol. 19, no. 9.

Cho-Liang, T, Chiang, C, Yang, C, & Chun-Ming, C, 2005, 'Tracking concrete strength under variable high temperature', *ACI Materials Journal*, vol. 102, No. 5, pp. 322-329.

Chowdhury, S, 2013, 'Early Age Bond Strength of Reinforcing Bars in High Strength Concrete', *International Conference on Structural Engineering and Construction Management*.

Cioni, P, Croce, P, & Salvatore, W, 2001, 'Assessing fire damage to R.C. elements', *Fire Safety Journal*, vol. 36, pp. 181-199.

Dahmani, L, Khennane, A, & Kaci, S, 2010, 'Crack identification in reinforced concrete beams using ANSYS software', *Strength of Materials*, vol. 42, no. 2, pp. 232-240.

Deng, Z, C, Li, Q, B, & Sun, H, J, 2006, 'Behavior of concrete beam with embedded shape memory alloy wires', *Engineering Structure*, vol. 28, no. 12, pp. 1691-1697.

Diederichs, U, & Schneider, U, 1981, 'Bond strength at high temperatures, *Magazine of Concrete Research*, vol.33, no. 115, pp. 75-84.

Dolce, M, Cardone, D, Ponzo, F, & Valente, C, 2005, 'Shaking Table Tests on Reinforced Concrete Frames Without and with Passive Control Systems', *Earthquake Engineering and Structural Dynamics*, vol. 34, pp. 1687-1717.F

Dwaikat, M, & Kodur, V, 2010, 'Fire Induced Spalling in High Strength Concrete Beams', *Fire Technology,* vol. 46, pp. 251.

EN 1992-1-1 (2004) (English): Eurocode 2: Design of concrete structures - Part 1-1: General rules structural fire design; European Committee for Standardization

Ehsani, M, Saadatmanesh, H, & Tao, S, 1996, 'Design recommendations for bond of GFRP rebars to concrete', *Journal of Structural Engineering*, pp. 247-254.

Eleonora, Z, 2010, 'One Way and Two Way-Shape Memory Effect: Thermo-Mechanical Characterization of Ni-Ti wires', *Cement Concrete & Aggregates Australia, Fire Safety of Concrete Buildings*.

Elghazouli, A, Y, Izzuddin, B, A, & Cashell, K, A, 2009, 'Experimental Evaluation of the Mechanical Properties of Steel Reinforcement at Elevated Temperature', *Fire Safety Journal*, vol. 44, no. 6, pp. 909-919.

Eligehausen, R, Popov, E, & Bertero, V, 1983, 'Local bond stress-slip relationships of deformed bars under generalized excitations', Report No. UCB/EERC-83/23, *Earthquake Engineering Research Center*, University of California, Berkeley.

Ellingwood, B, & Lin, T, 1991, 'Flexure and shear behaviour of concrete beams during fires', *Journal of Structural Engineering*, ASCE, vol. 117, no. 2, pp. 440-458.

Eric, A, Gordon, S, & Mohammad E, 2010, 'Control of an automotive shape memory alloy mirror actuator' *Mechatronics*, vol. 20, pp. 527–534.

Eswanth, P, & Dhinakaran, G, 2017, 'Experimental and Theoretical Investigations on Bond Strength of GFRP Rebars in Normal and High Strength Concrete', *IOP Conference Series: Earth and Environmental Science*, vol. 80, no. 1 012008.

Esko, S, Pekka, T, & Seppo, H 2005, 'Bonding of hot dip galvanised reinforcement in concrete', *Nordic Concrete Federation*, vol. 34, no. 2.

Eurocode2, Design of concrete structures: Part1.2: general rules— structural fire design, *European Committee for Standardization*, Brussels, BS EN 1992-1-2,2004.

Fanning, P, 2001, 'Nonlinear Models of Reinforced and Post-tensioned Concrete Beams', *Journal of structural engineering*.

Ferguson, P, ACI Committee, 1966, 'bond stress- the state of the art, *Journal of the American Concrete Institute,* vol. 63, no. 11, pp. 1167-1190.

Ferguson, P, Robert, I, & Thompson, J, 1962, 'Development length of high strength reinforcing bars in bond', *American Concrete Institute,* vol. 59, no. 17, pp. 887-922.

Fire Safety of Concrete Buildings, Cement Concrete & Aggregates Australia, 2010.

Folic, R, Radonjanin, V, & Malesev, M, 2002, 'The assessment of the structure of Novi Sad Open University damaged in a fire', *Construction and Building Materials*, vol. 16, pp. 427-440.

Garlock, M, Paya-Zaforteza, I, Kodur, V, & Gu, Li, 2012, 'Fire Hazard in Bridges: Review, Assessment and Repair Strategies', *Engineering Structures*, vol. 35, pp. 89-98.

Gao, W, Dia, J, Teng, J, & Chen, G, 2013, 'Finite element modeling of reinforced concrete beams exposed to fire', *Engineering Structures*, vol. 52, pp. 488-501.

Georgali, B, & Tsakiridis, P, 2005, 'Microstructure of Fire-damaged Concrete', *Cement and Concrete Composites*, vol. 27, pp. 255-259.

Georgin, J, & Reynouard, J, 2003, 'Modeling of structures subjected to impact: Concrete behavior under high strain rate', *Cement and Concrete Composites*, vol. 25, pp. 131-143.

Goto, Y, 1971, 'Cracks formed in concrete around deformed tension bars', Journal *Proceedings*, vol. 68, no. 4, pp. 244-251.

Graesser, E, J, & Cozzarelli, F, A, 1991, 'Shape memory alloys as new materials for aseismic isolation', *Journal of Engineering Mechanics ASCE, November 1991,* vol. 117, Issue 11, pp. 2590-2608.

Ha, T, Ko, J, Lee, S, Kim, S, Jung, J, & Kim, D, 2016, 'A case study on the rehabilitation of a fire-damaged structure', Applied Science, vol. 6, no. 5, pp, 126.

Haddad, R, Alsaleh, R, & Nabil, M, 2008, 'Effect of elevated temperature on bond between steel reinforcement and fiber reinforced concrete', *Fire Safety Journal,* vol. 43, no. 5, pp. 334-343.

Ha, T, Ko, J, Lee, S, Kim, S, Jung, J, & Kim, D, 2016, 'A case study on the rehabilitation of a fire-damaged structure'*, Applied Science*, vol. 6, no. 5, pp. 126.

Hager, I, 2013, 'Behaviour of cement concrete at high temperature', *Bulletin of the Polish Academy of Sciences: Technical Sciences*, vol. 61, no. 145.

Hansen, R, & Liepins, A, 1962, 'Behavior of bond under dynamic loading', *Proceedings ACI Journal*, vol. 59, no. 4, pp. 563-583.

Heidarpour, A, Niall S, Asghar, H, Xiao-Ling, Z, & Christopher, R, 2014, 'Mechanical properties of very high strength steel at elevated temperatures', *Fire Safety Journal*, vol. 64, pp. 27-35.

Heikal, M, 2000, 'Effect of temperature on the physico-mechanical and mineralogical properties of Homra pozzolanic cement pastes', *Cement and concrete research*, vol. 30, no. 11, pp. 1835–1839.

Hertz, K, D, 2005, 'Concrete Strength for Fire Safety Design', *Magazine of Concrete Research*, vol. 57, pp. 445-453.

Huang, Z, 2010, 'Modelling the bond between concrete and reinforcing steel in a fire', *Engineering Structures*, vol. 32, no. 11, pp. 3660-3669.

Huang, Z, & Platten, A, 1997, 'Non-linear finite element analysis of planar reinforced concrete members subjected to fire', *ACI Structural Journal*, vol. 94, no. 3, pp. 272-282.

Hui, Y, Giunta, G, Belouettar, S, Huang, Q, Hu, H, & Carrera, E, 2017, 'A free vibration analysis of three-dimensional sandwich beams using hierarchical one-dimensional finite elements', *Composites Part B Engineering*, vol. 110, pp. 7-19.

Janotka, I, & Nürnbergerovà, T, 2005, 'Effect of Temperature on Structural Quality of the Cement Paste and High-strength Concrete with Silica Fume', *Nuclear Engineering and Design,* vol. 235, pp. 2019-2032.

Jokela, J, 1979, 'Betonin ja raudoituksen yhteistoiminta ja suomalaisten betoniterästankojen tartuntaominaisuudet', *Technical Research Centre of Finland*, Espoo, Finland (In Finnish).

Jendele, L, & Cervenka, J, 2006, 'Finite element modeling of reinforcement with bond', *Computers & Structures*. vol. 84, pp. 1780-1791.

Kabir, M, Islam, M. & Chowdhury, M, 2015, 'Bond stress-slip behavior between concrete and steel rebar via pullout test: experimental and finite element analysis', *First International Conference on Advances in Civil Infrastructure and Construction Materials (CICM)*.

Kachlakev, D, & Miller, T, 2001, 'FE Modeling of Reinforced Concrete Structure Strengthened with FRP Lamiates', *FinalReport SPR 316*, Oregon State University.

Kalifa, P, Menneteau, D, & Quenard, D, 2000, 'Spalling and Pore Pressure in HPC at High Temperatures', *Cement and Concrete Research*, vol. 30, pp.1915-1927.

Knaack, A, Kurama, Y, & Kirkner, D, 2010, 'Compressive strength relationships for concrete under elevated temperatures', *ACI Materials Journal*, vol. 107, No. 2, pp. 164-175.

Kodur, V, 2014, 'Properties of Concrete at Elevated Temperatures', *Hindawi Publishing Corporation ISRN Civil Engineering*, vol. 2014, pp. 15.

Kodur, V, & McGrath, R, 2006, 'Effect of silica fume and lateral confinement on fire endurance of high strength concrete columns', *Canadian Journal of Civil Engineering*, vol. 33, pp. 93-102.

Kodur, V, Dwaikat, M, & Dwaikat, M, 2008, 'High temperature properties of concrete for fire resistance modeling of structures', *ACI Materials Journal*, vol. 105, no. 5, pp. 517–527.

Kato, T, 2011, *The use of shape memory alloys (SMAs) in automobiles and trains Shape Memory and Superelastic Alloys Applications and Technologies,* Woodhead Publishing Series in Metals and Surface Engineering, pp. 120-124.

Kyoungsoo, P, & Glaucio, P, 2011, 'Cohesive Zone Models: A Critical Review of Traction-Separation Relationships Across Fracture Surfaces', *ASME Applied Mechanics Review*, vol. 64, no. 6.

Lagoudas, D, C, & Kumar, P, K, Introduction to Shape Memory Alloys, Springer, Boston, MA.

Li, H, Lui, Z, & Ou, Z, 2008, 'Experimental study of a simple reinforced concrete beam temporarily strengthened by SMA wires followed by permanent strengthening with CFRP plates', *Engineering Structures*, vol. 30, pp. 716-723.

Lie, T, T, Celikkod, B, 1991, 'Method to calculate the fire resistance of circular reinforced concrete columns', *ACI Material Journal*, vol. 88, no. 1, pp. 84-91.

Lutz, L, Gergely, P, 1967, 'Mechanics of bond and slip of deformed bars in concrete', *ACI Journal*, vol. 64, no. 11, pp. 711- 721.

Lublóy, É, & Balázs, G, 2014, 'Temperature effects on bond between concrete and reinforcing steel'. *Zbornik radova Građevinskog fakulteta,* vol. 30, pp. 27-35. 10.14415/zbornikGFS26.03.

Mathey, R & Watstein, D 1961,'Investigation of bond in beam and Pull-Out Specimens with High-Yield Strength Deformed Bars, *Journal proceedings*, vol. 57, pp. 1071-1090.

Md Arman, C, & Md Mashfiqul, I, 2015, 'Shear Strength Prediction of FRP-reinforced Concrete Beams: A State-of- the-Art Review of Available Models', *Journal of Civil and Environmental Engineering*, vol. 5, pp. 1-10.

Mehmet A, Barıs, S, Nabi, Y, & Yusuf, A, 2018, 'Assessment of damages on a RC building after a big fire', *Advances in Concrete Construction*, vol. 6, no. 2, pp. 177-197.

Menna, C, Auricchio, F, & Asprone, D, 2015, 'Applications of Shape Memory Alloys in Structural Engineering', *Shape Memory Alloy Engineering*, Butterworth-Heinemann, pp. 369-403.

Ming, H, W, & Schetky McD, S, 2000, 'Industrial applications for shape memory alloys', *Shape Memory and Superelastic Technolgies*, pp.171-182.

Mindess, S, Young, J, & Darwin, D, 2003, Concrete, 2nd edition, Prentice-Hall, Upper Saddle River, NJ.

Muhammad, N, 2008, 'Bond of High Strength Concrete with High Strength Reinforcing Steel', *The Open Civil Engineering Journal*, vol. 2, pp. 143-147.

Mohamed B, Nasser, F, Hany M, 2014, 'Behavior of reinforced concrete short columns exposed to fire', *Alexandria Engineering Journal*, vol. 53, pp. 643-653.

Muntasir, AHM, & Shahira, M, 2016, 'Bond behaviour of smooth and sand coated shape memory alloy (SMA) rebar in concrete', Structures, vol. 5, pp. 186-195.

Machado, L, & Savi, M, 2003, 'Medical application of shape memory alloys', *Brazilian Journal of Medical and Biological Research,* vol. 36, no. 6, pp. 683-691.

Naus, D, 2010, ‘A compilation of elevated temperature concrete material property data and information for use in assessments of nuclear power plant reinforced concrete structures’, *U.S. Nuclear Regulatory Commission, Office of Nuclear Regulatory Research.* Report no: NUREG/CR-7031.

NCC 2015 Building Code of Australia - Volume One; Australian Building Codes Board, Australia.

Nilson, A, H, 1968, ‘Nonlinear Analysis and Reinforced Concrete by the Finite Element Method’, *American Concrete Institute Journal*, vol. 65, no. 9, pp. 757-766.

Ngo, D, & Scordelis, A, 1967, ‘Finite Element Analysis of Reinforced Concrete Beams’, *ACI Journal*, vol. 64, pp. 152-163.

Ozkal, F, M, Polat, M, Yogan, M, Ozturk, M, 2018, ‘Mechanical properties and bond strength degradation of GFRP and steel rebars at elevated temperature’

Panias, D, Sakkas, K, Sofianos, A & Nomikos, P, 2015, ‘Behaviour of Passive Fire Protection K-Geopolymer under Successive Severe Fire Incidents’, *Materials*, vol. 8, pp. 6096-6104.

Park, K, & Paulino, G, 2011, ‘Cohesive Zone Models: A Critical Review of Traction-Separation Relationships Across Fracture Surfaces’. *Applied Mechanics Reviews*, vol. 64, no. 6, pp. 60-80.

Pecce, M, Manfredi, G, Realfonzo, R, & Cosenza, E, 2001, ‘Experimental and analytical evaluation of bond properties of GFRP bars’, *Journal of Materials in Civil Engineering*, pp. 282-29.

Phan, L, T, & Carino, N, J, 1996, ‘Fire Performance of High-Strength Concrete: A Report of the State-of-the-Art NIST’, *Report NISTIR 5934*. pp. 105.

Phan, L, T, & Carino, N, J, 2002, 'Effects of Test Conditions and Mixture Proportions on Behaviour of High strength Concrete Exposed to High Temperatures', *ACI Materials Journal*, vol. 99, No. 1, pp 54-56.

Poon, C, S, Shui, Z, H, & Lam, L, 2004, 'Compressive Behaviour of Fiber Reinforced High Performance Concrete Subjected to Elevated Temperatures', *Cement and Concrete Research* vol. 34. pp. 2215-2222.

Pothisiri, T, & Panedpojaman, P, 2012, 'Modeling of bonding between steel bar and concrete at elevated temperatures', *Construction and Building Materials*, vol. 27, no.1 pp. 130-140.

Royles, R, & Morley, P, 1985, 'Further response of the bond in reinforced concrete to high temperatures', *Magazine of Concrete Research,* vol. 124, pp. 157-163.

Sadiq, H, Wong, M, B, Al-Mahaidi, R, & Zhao, X, L, 2013, 'A novel active fire protection approach for structural steel members using NiTi shape memory alloy', *Smart Material and Structures,* vol. 22, no. 2.

Schneider, U, & Diederichs, U, 1981, 'Physical properties of Steel and Concrete up to Melting and Ablation', *Structural Mechanics in Reactor Technology (SmiRT)*, vol. 6, no.1.

Schneider, U, 1981, 'Behaviour of Concrete under Thermal Steady State and Non-Steady State Conditions', *Fire and Materials,* pp. 103-115.

Sezen H, Moehle J, 2003, 'Bond slip behaviour of reinforced concrete members', digitalunion.osu.edu/r2rsummer05/fisher.533/research_docs/Greece_fib_2003.pdf.

Shan-Shan, H, Buick, D, & Ian, W, 2013, 'Experiments on reverse-channel connections at elevated temperatures', *Engineering Structures*, vol. 49, pp. 973-982.

Shafaei, J, Hosseini, A, & Marefat, M, 2009, '3d finite element modelling of bond-slip between rebar and concrete in pull-out', *The Third International Conference On Concrete And Development*, At Tehran, Iran.

Salah, K & Ouchenane, M, 2007, 'A numerical simulation of bond for pull-out tests: The direct problem', *Asian Journal of Civil Engineering*, vol. 8, no. 5, pp 491-505.

Song, G, 2007, 'Design and control of a Nitinol wire actuated rotary servo', Smart Material and Structures, vol. 16, no. 5.

Shin M, & Andrawes, B, 2010, 'Experimental investigation of actively confined concrete using shape memory alloys ', *Engineering Structures,* vol. 32, no. 3, pp 656-664.

Shook, D, Roschke, N, & Ozbulut, E, 2008, 'Superelastic semi-active damping of a base-isolated structure', *Structural Control and Health Monitoring*, vol. 15, no. 5, pp. 746-768.

Sistonen, E, Tukiainen, P, Peltola, S, Skriko, S, & Huovinen, S, 2002 'Bonding of hot dip galvanised reinforcement in concrete', *Nordic Concrete Federation*, vol. 34, no. 2.

Sittner, P, Heller, L, Pilch, J, Curfs, C, Alonso, T, & Favier, D, 2014, 'Young's Modulus of Austenite and Martensite Phases in Superelastic NiTi Wires', *Journal of Material Engineering and Performance*, vol. 23, pp. 2303-2314.

Subramani, T, Manivannan, R, & Kavitha, M, 2014, 'Crack Identification in Reinforced Concrete Beams Using Ansys Software', *Journal of Engineering Research and Applications*, vol. 4, no. 6, pp.133-141.

Tepfers, R, 1979, 'Cracking of reinforced concrete cover along anchored deformed reinforcing bars', *Magazine of Concrete Research,* vol. 31, no.106, pp. 3-12.

Tepfers, R, & DeLorenzis, L, 2003, ‘Bond of FRP Reinforcement in Concrete - a Challenge’, *Mechanics of Composite Materials*, vol. 39, pp. 315-328.

Tighiouart, B, Benmokrane, B, & Gao, D, 1998, ‘Investigation of bond in concrete member with fiber reinforced polymer (FRP) bars’, *Construction and Building Materials*, vol. 12, pp. 453–462.

Ulrich, S, 1988, ‘Concrete at High Temperatures - A General Review’, *Fire Safety Journal*, vol. 13, no. 1, pp. 55-68.

Wahyuni, A, Vimonsatit, S, & Nikraz, H, 2011, 'Shear Behavior of Lightweight Sandwich Reinforced Concrete Slabs', *Advances in Structural Engineering*, vol. 15, pp. 917-921.

Wang, H, & Belarbi, A, 2010, ‘Static and Fatigue Bond Characteristics of FRP Rebars Embedded in Fiber-reinforced concrete’, *Journal of Composite Materials*, pp. 1605-1622.

Wang, X, Q, Tao, Z, Song, T, Y, & Han, L, H, 2014, ‘Stress–strain model of austenitic stainless steel after exposure to elevated temperatures’, *Journal of Constructional Steel Research*, vol. 99, pp. 129-139.

Wittig, P, & Cozzarelli, F, 1992, ‘Shape Memory Structural Dampers: Material Properties, Design and Seismic Testing’, *Technical Report NCEER-92-0013* (State Univ. of New York at Buffalo).

Wong, M, B, & Liu, J, 2014, 'Optimal design of hybrid steel-SMA reinforced concrete beam in fire', ‘*23rd Australasian Conference on the Mechanics of Structures and Materials (ACMSM23)’,* vol. 2, pp. 695-700.

Xu, Y, Wong, Y, Poon, C & Anson, M, 2001, ‘Impact of high temperature on PFA concrete’, *Cement and Concrete Research,* vol. 31, pp. 1065-1073

Xuhong, Q, Frans, B & Henk, K, 2012, 'Dependence of mechanical properties of high strength steel S690 on elevated temperatures', *Construction and Building Materials*, vol. 30, pp. 73–79.

Yaqub, M, Bailey, C, & Nedwell, P, 2011, 'Axial capacity of post heated square columns wrapped with FRP composites', *Cement and Concrete Composite*, vol. 33, pp. 694-701.

Youssef, M, & Moftah, M, 2007, 'General Stress-strain relationship for concrete at elevated temperatures', *Engineering Structures*, vol. 29, no. 10, pp. 2618-2634.

Yi, L, Xinzheng, L, Mingjian, Y, Weiming, Y, & Hong, G, 2015, 'A Case Study on a Fire-Induced Collapse Accident of a Reinforced Concrete Frame-Supported Masonry Structure', *Fire Technology*, vol. 52, pp. 707-729.

Zhang, J, & Qin, F, 2013, 'Three-dimensional modelling of steel fiber reinforced concrete material under intense dynamic loading', *Construction and Building Materials*. vol. 44, pp. 118-132.

Zhong, T & Qing, Y, 2012, 'Residual bond strength in steel reinforced concrete columns after fire exposure', *Fire Safety Journal*, vol. 53, pp. 19-27.

Zhu, B, L, Lu, Z, D, & Hu, K, X, 1990, 'The constitutive relation of concrete and steel under fires'. *Sichuan Building Science*, vol. 1, pp. 37-43.